



UNIVERSIDAD NACIONAL AUTÓNOMA DE MÉXICO
PROGRAMA DE POSGRADO EN CIENCIAS DE LA TIERRA

CENTRO DE GEOCIENCIAS

EVOLUCIÓN ESTRATIGRÁFICA Y PROCEDENCIA DE LA CUENCA DE ANTEPAÍS MEXICANA (CRETÁCICO SUPERIOR-PALEÓGENO) EN EL CENTRO DE MÉXICO

T E S I S

QUE PARA OPTAR POR EL GRADO DE

DOCTOR EN CIENCIAS DE LA TIERRA

PRESENTA

EDGAR JUÁREZ ARRIAGA

TUTOR

Dr. Timothy F. Lawton

Bureau of Economic Geology, The University of Texas at Austin

MIEMBROS DEL COMITÉ TUTOR:

Dra. Elisa Fitz Díaz, Instituto de Geología, UNAM

Dr. Roberto Stanley Molina Garza, Centro de Geociencias, UNAM

Querétaro, Noviembre 2019



Universidad Nacional
Autónoma de México



UNAM – Dirección General de Bibliotecas
Tesis Digitales
Restricciones de uso

DERECHOS RESERVADOS ©
PROHIBIDA SU REPRODUCCIÓN TOTAL O PARCIAL

Todo el material contenido en esta tesis esta protegido por la Ley Federal del Derecho de Autor (LFDA) de los Estados Unidos Mexicanos (México).

El uso de imágenes, fragmentos de videos, y demás material que sea objeto de protección de los derechos de autor, será exclusivamente para fines educativos e informativos y deberá citar la fuente donde la obtuvo mencionando el autor o autores. Cualquier uso distinto como el lucro, reproducción, edición o modificación, será perseguido y sancionado por el respectivo titular de los Derechos de Autor.

Declaración de ética

Declaro conocer el Código de Ética de la Universidad Nacional Autónoma de México, plasmado en la Legislación Universitaria. Con base en las definiciones de integridad y honestidad ahí especificadas, aseguro mediante mi firma al calce que el presente trabajo es original y enteramente de mi autoría. Todas las citas de, o referencias a la obra de otros autores aparecen debida y adecuadamente señaladas, así como acreditadas mediante los recursos editoriales convencionales.

Edgar Juárez Arriaga

*A Eiza, Balam y Miriam,
A mis padres María Ninfa y Silvestre
por ser el origen de todo*

*..como no estás experimentado en las cosas del mundo
todas las cosas que tienen algo de dificultad, te parecen imposibles.
Confía en el tiempo, que suele dar dulces salidas a muchas amargas dificultades.*

Miguel de Cervantes Saavedra
El Quijote

Evolución estratigráfica y procedencia de la cuenca de antepaís Mexicana (Cretácico Superior-Paleógeno) en el centro de México

Contenido

Agradecimientos	<i>i</i>
Resumen	<i>iii</i>
Abstract	<i>vi</i>
Parte I	Introducción
	1
	I.I Marco geológico
	3
	El orógeno mexicano
	3
	La cuenca de antepaís mexicana
	6
	I.II Hipótesis
	9
	I.III Justificación
	12
	I.IV Objetivo principal y objetivos particulares
	12
Parte II	Metodología
	14
	II.I Trabajo de campo y colecta de muestras
	14
	II.II Petrografía de rocas sedimentarias clásticas
	14
	II.III Geocronología U-Pb en granos de circón detrítico
	15
	II.IV Termocronología (U-Th)/He en circón
	17
	II.V Fechas dobles (U-Th)/(He-Pb) en granos individuales de circón detrítico
	18
	II. VI Estructura de la tesis
	19
Parte III	Evolución estratigráfica y procedencia de la cuenca de antepaís mexicana (CAM) en el centro de México
	21
	III.I El orógeno mexicano y la cuenca antepaís mexicana. <i>The Cretaceous-Paleogene Mexican orogen: Structure, basin development, magmatism and tectonics.</i>
	21

III.II	El relleno de la cuenca de antepaís mexicana durante el Cretácico Tardío-Paleógeno. <i>Sediment provenance, sediment-dispersal systems, and major arc-magmatic events recorded in the Mexican foreland basin, North-Central and Northeastern Mexico.</i>	51
III.III	Evolución de la cuenca de antepaís mexicana en el centro de México: exhumación y erosión a lo largo del transecto Tolimán-Tamazunchale. <i>Late Cretaceous-Paleocene stratigraphic and structural evolution of the central Mexican fold and thrust belt, from detrital zircon (U-Th)/(He-Pb) ages</i>	77
Parte IV.	Conclusiones	95
Parte V.	Referencias	99
Parte VI.	Apéndice 1	111
	Apéndice 2	112
	Apéndice 3	128
	Apéndice 4	139
	Apéndice 5	142

Agradecimientos

Agradezco al Dr. Gerardo Carrasco Nuñez, Director del Centro de Geociencias de la UNAM durante el periodo 2014-2018, así como a la Dra. Lucia Capra Pedol actual directora del Centro por facilitarme el uso de las instalaciones y el apoyo brindado durante el desarrollo de este proyecto. Al Consejo Nacional de Ciencia y Tecnología (CONACyT) por la beca de manutención otorgada, así como a la Coordinación de Estudios de Posgrado por el apoyo económico brindado para la realización de trabajos de campo.

Al Dr. Timothy F. Lawton por favorecerme con su asesoría en el desarrollo de esta investigación. Agradezco su invaluable ayuda y consejos brindados, las innumerables charlas y el trabajo de campo donde compartió conmigo su experiencia y entusiasmo. Por su guía y la meticulosidad de sus comentarios que fueron fundamentales para el desarrollo y conclusión de esta investigación. A Tim agradezco también su gran calidad humana y ética que me han hecho crecer en distintos aspectos de mi vida personal y profesional. Tim es sin duda, una de las personas que más ha influenciado en mi y para quien mis agradecimientos resultan insuficientes. Mil y un gracias por alentarme a mirar de una forma distinta la Tierra y el cielo.

Agradezco a los doctores Elisa Fitz Díaz y Roberto S. Molina Garza por el apoyo y seguimiento brindado durante todo el proceso de este proyecto. Las observaciones y sugerencias hechas en distintas etapas de esta investigación la enriquecieron enormemente. Hago un reconocimiento especial a la Dra. Elisa Fitz por compartir su conocimiento sobre el cinturón de pliegues y cabalgaduras Mexicano. Manifiesto mi gratitud por su saber y ayuda durante varias temporadas de campo que resultaron altamente enriquecedoras.

Expreso mi especial agradecimiento al Dr. Luigi A. Solari del Centro de Geociencias, por las discusiones sobre aspectos clave en geocronología, estadística aplicada al análisis de datos geológicos y sobre la geología del sur de México. Sus sugerencias y la estrecha colaboración que mantuvimos fue determinante para la exitosa conclusión de este trabajo.

Agradezco también al Dr. Yam Zul E. Ocampo Díaz de la Universidad Autónoma de San Luis Potosí por sus enseñanzas en campo y en el estudio petrográfico. Al Dr. Carlos Ortega Obregón del Centro de Geociencias por su apoyo y enseñanza en la adquisición y procesamiento de datos geocronológicos en granos de circón. Al Dr. Uwe Martens por su enseñanza en aspectos finos en el análisis e interpretación de edades U-Pb, su capacidad y dedicación me permitieron comprender el significado geológico de las edades obtenidas. Gracias al Dr. Daniel F. Stockli y la M. en C. Lisa Stockli de la Universidad de Texas en Austin, por su apoyo en la adquisición e interpretación de edades geo- y termoconológicas. Agradezco el tiempo dedicado para compartir conmigo su conocimiento, experiencia y guía tanto en el laboratorio como fuera de él. Asimismo estoy agradecido por su hospitalidad y atenciones durante mi estancia de investigación en el *UTChron Geo- and Thermochronology Laboratory* en Jackson School of Geosciences de la Universidad de

Texas en Austin. Expreso mi gratitud al Dr. Danny Stockli por compartir sus conocimientos durante varias temporadas de campo en el centro y sureste de México.

Al Dr. Gerardo Aguirre Díaz por su disponibilidad para discutir distintos aspectos sobre el vulcanismo en el centro de México y las lecturas recomendadas para abordar este tema.

El contenido y estilo de este trabajo ha sido mejorado en gran medida por las sugerencias de los miembros del Jurado de examen de grado, el cual estuvo integrado por los doctores Luigi A. Solari, Michelangelo Martini, Timothy F. Lawton, Elisa Fitz Díaz y Felipe de Jesús Escalona Alcázar, a quienes agradezco sus atinados comentarios y por el tiempo dedicado.

Agradezco igualmente al Dr. Alexander Iriondo y a María Concepción Arredondo de la Rosa por la asistencia y facilidades otorgadas para la obtención de imágenes de cátodoluminiscencia de granos de circón. También agradezco al Dr. James Pindell de *Tectonic Analysis Ltd.*, por permitirme el uso de datos geo- y termocronológicos del centro de México.

De igual manera, le doy las gracias al personal de la Biblioteca del campus UNAM-Juriquilla en especial a Teresita de Jesús Pérez Cruz, así como a José Luís Casiano Casiano, de la Biblioteca Conjunta de Ciencias de la Tierra de la UNAM, por atender generosamente a mis solicitudes de información bibliográfica.

En el trabajo de campo fui apoyado por los M. en C. Rodrigo Gutiérrez Navarro, Mildred Zepeda Martínez y Erick Juárez Arriaga, así como por Artemiza González Cervantes, David G. Garrido Amaya y María Guadalupe González Díaz.

Para la realización de este trabajo tuve el apoyo técnico y la asesoría de Manuel Albarrán Murillo y Juan Tomás Vázquez Ramírez, quienes me brindaron todas las facilidades para la separación mineral y la preparación de láminas delgadas, respectivamente.

Aprecio el apoyo y la gestión administrativa de los doctores Luis Mariano Cerca Martínez y Carlos Mendoza como responsables del Posgrado en Ciencias de la Tierra en el Centro de Geociencias durante mis estudios, así como el apoyo administrativo brindado por Marta Pereda Miranda, Armando Ramírez Morán y Blanca L. Rendón Juárez.

Esta investigación fue financiada por el CONACyT, proyecto CB-240932 otorgado a T.F. Lawton/L.A. Solari; recursos adicionales fueron proporcionados por UNAM-PAPIIT, proyecto IN105714 otorgado a T.F. Lawton y la Coordinación de Estudios de Posgrado de la Universidad Nacional Autónoma de México.

Resumen

Nuevas secciones estratigráficas medidas en el centro y noreste de México junto con datos petrográficos y un vasto conjunto de edades geocronológicas (1394 nuevos análisis U-Pb individuales en granos de circón detritico), procedentes de rocas del Cretácico Superior-Paleógeno indican que estos depósitos se acumularon en una cuenca flexural dentro del margen continental y estrechamente relacionados a un arco magmático activo. Estas características son consistentes con las de una cuenca de antepaís de retro-arco (*retro-foreland basin*); la cuenca cretácica en México es definida aquí como la *cuenca de antepaís mexicana*. Al igual que su contraparte en el norte, la cuenca de antepaís cordillerana en los Estados Unidos, la cuenca mexicana migró por delante de la cuña orogénica hacia el este con el tiempo. La cuenca de antepaís mexicana está asociada al evento de acortamiento del orógeno mexicano e incluye las cuencas de Parras, La Popa, Sabinas y Tampico-Misantla, así como depocentros no nombrados en la Mesa Central y el cinturón de pliegues y cabalgaduras mexicano. Datos geocronológicos y petrográficos provenientes de sucesiones sedimentarias en la transversal de Parras, la Mesa Central y la parte central del cinturón de pliegues y cabalgaduras mexicano, así como de datos previamente publicados del Grupo Difunta (Campaniano-Eoceno) en el noreste de México indican que las potenciales áreas fuente que aportaron sedimentos a la cuenca de antepaís tienen variaciones temporales y geográficas. Los componentes de edad incluyen granos arqueanos que constituyen un componente de edad subordinado. Los grupos de edad principales son: Proterozoico (~1750-920 Ma), Pan-africano (~652-544 Ma), Cámbrico-Silúrico (~490-420 Ma), Jurásico (~164-156 Ma), Cretácico-Paleógeno (~145-60 Ma). Se interpreta que este conjunto de granos deriva de tres principales fuentes: 1) el *arco magmático mexicano* que se desarrolló simultáneamente en el oeste de México; 2) rocas del basamento y de la cubierta del terreno Guerrero, acrecionado a la margen occidental de México desde el final del Cretácico Temprano; y 3) rocas sedimentarias del Triásico-Cretácico Superior que fueron exhumadas en la parte frontal de la cuña durante su avance hacia el este. Los datos de paleocorrientes medidos en las distintas áreas de estudio apoyan el aporte de sedimentos desde el oeste de México.

Los depósitos iniciales de la cuenca de antepaís afloran en la Mesa Central y corresponden a depósitos de gravedad y olistolitos pertenecientes a la arenisca Mineral de Pozos y calciturbiditas intercaladas con turbiditas siliciclásticas no diferenciadas del Cenomaniano tardío-Turoniano. Durante el Turoniano-Coniaciano, sucesiones de turbiditas de la Formación Soyatal se depositaron en la parte proximal de la cuenca, mientras se depositaban pelagitas carbonatadas de las formaciones Indidura y Agua Nueva en la parte más distal. La subsidencia continuó a lo largo del Cretácico Tardío a medida que la cuenca y su relleno compuesto por sucesiones clásticas migraban hacia el este. Durante el Santoniano-Campaniano temprano pelagitas carbonatadas se intercalaron con capas de toba y arenisca ricas en ceniza de las formaciones Caracol y San Felipe. En el Campaniano tardío-Eoceno una potente sucesión de depósitos fluviales y deltaicos pertenecientes al Grupo Difunta se depositó adyacente al frente del cinturón de pliegues y cabagaduras en el noreste de México. Esta sucesión incluye parte de los depósitos más jóvenes de la cuenca de antepaís. Datos petrográficos y geocronológicos de areniscas del Grupo Difunta indican la presencia de granos proterozoicos (~1.7, 1.4 y 1.1. Ga), que se interpreta derivan del basamento de Laurencia. En contraste, en las sucesiones equivalentes depositadas en el centro de México (e.g., formaciones Méndez y Chicontepec), los granos proterozoicos constituyen un componente subordinado derivado posiblemente del reciclado de rocas sedimentarias del oeste de México. De acuerdo a las edades U-Pb en circón detrítico, los depósitos de la parte superior del Grupo Difunta se correlacionan con las sucesiones marino profundas de la Formación Chicontepec del Paleoceno-Eoceno temprano de la cuenca Tampico-Misantla.

En este trabajo se propone que la cuenca del antepaís mexicana registra dos eventos magmáticos de gran volumen y corta duración en el arco magmático mexicano. El evento más antiguo se registra en los depósitos de la parte proximal de la cuenca, éste se caracteriza por abundantes granos líticos volcánicos y edades U-Pb entre ~98-92 Ma que indican el aporte de un gran volumen de detritos volcánicos derivado de un evento magmático sindepositacional. Un segundo evento magmático prominente es registrado en estratos del Santoniano-Campaniano en la parte distal de la cuenca, constituidos por pelagitas carbonatadas intercaladas con capas de toba y arenisca tobácea, los cuales contienen edades U-Pb entre ~85-74 Ma.

Finalmente, las edades de enfriamiento (U-Th)/He en granos de circón detrítico derivadas de un conjunto de areniscas cretácicas de la cuenca de antepaís ubicadas en la parte central del cinturón de pliegues y cabalgaduras en el centro-este de México definen tres conjuntos de edad que se interpreta corresponden a eventos de exhumación individuales: 1) ~136-120 Ma, 2) ~99-80 Ma, y 3) ~66-56 Ma. A excepción del evento más antiguo, estas edades revelan una correspondencia entre episodios de exhumación y eventos de deformación previamente reconocidos en el cinturón de pliegues y cablagaduras mexicano.

Abstract

New stratigraphic sections measured in central and northeastern Mexico, petrographic data and a robust data set of geochronological ages (1394 new individual U-Pb analyses in detrital zircon grains) from Upper Cretaceous-Paleogene rocks indicate that these sedimentary successions accumulated in a flexural basin inboard of the continental margin and closely related to an active magmatic arc. These characteristics are consistent with that of a retro-foreland basin; the Cretaceous basin is defined here as the *Mexican foreland basin*. Like the Cordilleran foreland basin in the United States, the Mexican foreland basin migrated eastward with time, ahead of an advancing orogenic wedge. The Mexican foreland basin was associated with shortening of the Mexican orogen and includes the Parras, La Popa, Sabinas and Tampico-Misantla basins, as well as unnamed depocenters in the Mesa Central and the Mexican fold-thrust belt. Geochronological and petrographic data from sedimentary successions in the Parras transverse sector of the fold-thrust belt, the Mesa Central and the central part of the Mexican fold-thrust belt, as well as previously published data of the Difunta Group (Campanian-Eocene) in northeastern Mexico indicate that potential sediment sources that supplied detritus to the foreland basin have temporal and geographical variations. Age components include Archean grains that constitute a minor age component. The main age groups of the sandstones include Proterozoic (~1750-920 Ma), Pan-African (~652-544 Ma), Cambrian-Silurian (~490-420 Ma), Jurassic (~164-156 Ma), and Cretaceous-Paleogene (~145-60 Ma) grains. This age set is interpreted to be derived from three main sources: 1) the Mexican magmatic arc that developed simultaneously in western Mexico; 2) rocks of the basement and cover of the Guerrero terrain, accreted to the western margin of Mexico in latest Early Cretaceous time; and 3) sedimentary rocks of the Upper Triassic-Cretaceous succession, which was exhumed in the frontal part of the wedge during its eastward advance. Paleocurrent data in the different study areas are consistent with the contribution of sediments from western Mexico.

The initial deposits of the Mexican foreland basin crop out at the Mesa Central and consist of deposits of sediment-gravity flows and olistoliths belonging to the informal Mineral de Pozos sandstone and calciturbidites that interfinger with unnamed siliciclastic turbidites of late

Cenomanian-Turonian age. During Turonian-Coniacian time, turbidite successions of the Soyatal Formation were deposited in the proximal part of the basin, while carbonate pelagites of the Indidura and Nueva Agua formations were deposited in the most distal part of the basin. Subsidence continued during the Late Cretaceous as the depocenter and its fill composed of clastic successions migrated eastward with time. During the Santonian-early Campanian, carbonate pelagites were interbedded with tuff beds and sandstone rich in volcanic ash of the Caracol and San Felipe formations. In the late Campanian-Eocene, a thick succession of sandstone-rich fluvial and deltaic deposits of the Difunta Group was deposited adjacent to the front of the fold-thrust belt in northeastern Mexico. This succession includes part of the youngest deposits of the Mexican foreland basin. Petrographic and geochronological data of sandstones of the Difunta Group indicate the presence of Proterozoic grains (~1.7, 1.4 and 1.1. Ga), which can be interpreted as derived from basement provinces in southern Laurentia. In contrast, the equivalent Late Cretaceous-Paleogene successions deposited in central Mexico (e.g., Méndez and Chicontepec formations) contain Proterozoic grains that constitute a subordinate age component and possibly derived from reworking of sedimentary rocks from western Mexico. On the basis of U-Pb detrital zircon ages, uppermost strata of the Difunta Group are correlated with the deep marine successions of the Paleocene-lower Eocene Chicontepec Formation of the Tampico-Misantla basin.

This research indicates that the Mexican foreland basin records two magmatic events of great volume and short duration in the Mexican magmatic arc. The oldest event is recorded in the proximal strata of the basin, which are characterized by abundant volcanic lithic grains and U-Pb ages between ~98-92 Ma that indicate the contribution of a large volume of volcanic detritus derived from a syndepositional magmatic event. A second prominent magmatic event is recorded in Santonian-Campanian beds in the distal part of the basin, consisting of carbonate pelagites interbedded with tuff and tobaceous sandstone beds, which contain U-Pb ages between ~85 and ~74 Ma.

Analyses of (U-Th)/He ages in detrital zircon grains derived from a small set of Cretaceous sandstones of the foreland basin located in the central part of the Mexican fold-thrust belt of central-eastern Mexico define three cooling age groups, which are interpreted to correspond to a three

individual exhumation events: 1) ~136-120 Ma, 2) ~99-80 Ma, and 3) ~66-56 Ma. Except for the oldest event, these cooling age clusters correspond to exhumation episodes and deformation events previously reported in the central Mexican fold-thrust belt.

Parte I

Introducción

Las sucesiones sedimentarias del Cretácico Tardío en el centro de México han sido comúnmente consideradas parte de la cuenca mesozoica del centro de México (Carrillo-Bravo, 1971). No obstante, la historia geológica de dichas rocas fue luego vinculada al desarrollo y evolución del orógeno que constituyó la Sierra Madre Oriental durante el Cretácico Tardío-Paleógeno (e.g., Suter, 1980, 1987; Carrillo y Suter, 1982; Suter et al., 1997) y ha sido recientemente reevaluada como parte del orógeno mexicano (*Mexican orogen*, Fitz-Díaz, et al., 2018), lo que permite distinguirlas de las sucesiones del Jurásico Superior y Cretácico Inferior del centro y noreste de México. Estudios recientes han permitido reevaluar la relación entre la deformación del Cretácico Tardío-Paleógeno y los depósitos sinorogénicos en la cuenca de antepaís adyacente, sentando las bases para comprender la relevancia de este evento de deformación sobre la evolución de la cuenca asociada. En esta investigación se documenta y define la *cuenca de antepaís mexicana* (CAM) como una entidad paleogeográfica desarrollada al sur de la cuenca de antepaís cordillerana del Mesozoico tardío (Fig. 1). Como se discute en las siguientes secciones, el relleno de esta cuenca contiene el registro de dos eventos geológicos contemporáneos: la evolución del orógeno mexicano y el desarrollo de un arco volcánico activo a lo largo de la margen occidental de México. A diferencia de lo que es posible observar en el centro-oeste y suroeste de E.U.A., donde el sistema de cuenca de antepaís se desarrolla en un amplio cratón y su registro está ampliamente preservado, la CAM resulta relevante porque su evolución ocurre sobre el lado continental que se estrecha hacia el sur y buena parte de su registro sedimentario en el centro y este de México está extensivamente deformado. Los mejores afloramientos de la CAM se encuentran en cortes carreteros y arroyos donde la sucesiones alcanzan algunas decenas de metros debido a que comúnmente están truncadas por fallas. Las interpretaciones de esta investigación se basan en los resultados derivados de la aplicación de métodos de estratigrafía y sedimentología clásicas (e.g., medición y descripción de columnas estratigráficas, medición de paleocorrientes e identificación de litofacies) petrografía de areniscas y técnicas analíticas modernas como el fechamiento doble (U-Th)/(He-Pb) en granos de circón individual. La información disponible junto con los nuevos datos

generados en esta investigación permiten comprender de mejor manera la relación espacial y temporal de la deformación del Cretácico Tardío-Paleógeno sobre la evolución de la CAM,

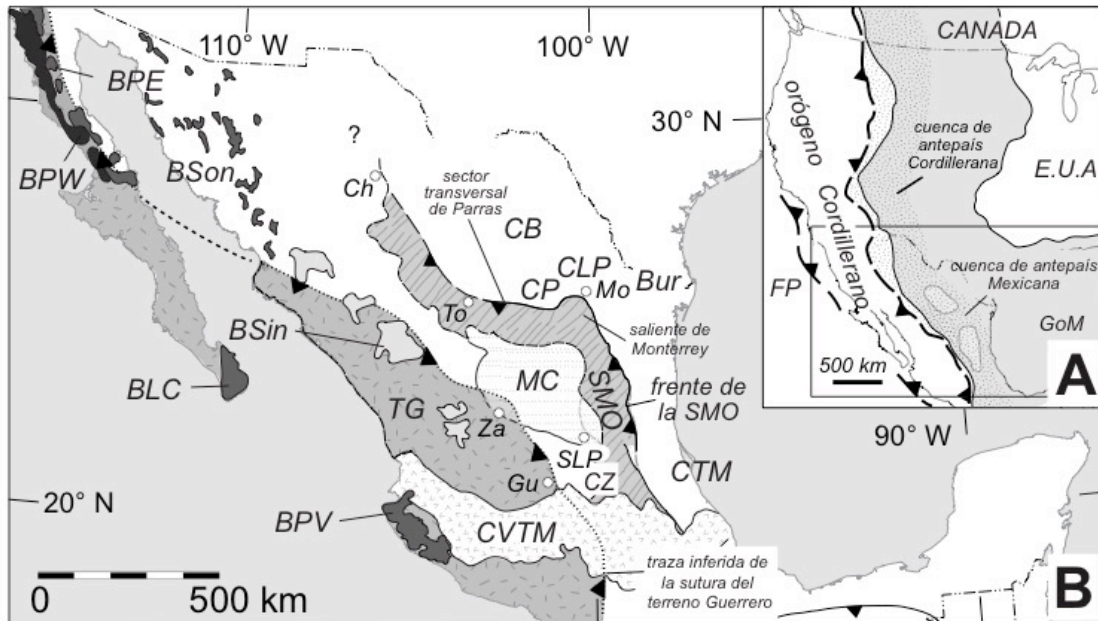


Figura 1. **(A)** Paleogeografía del orógeno cordillerano y la cuenca de antepaís cordillerana durante el Cenomaniano tardío. La CAM representa la extensión sur de la cuenca de antepaís cordillerana (área punteada), que ocupa la parte occidental del mar interior de América del Norte (*Western Interior Seaway*). Explicación: FP, placa Farallón; GoM, Golfo de México. **(B)** Ubicación de las principales características geográficas y geológicas del norte y centro de México. Terreno Guerrero (TG); provincias fisiográficas de México mencionadas en el texto: CVTM, cinturón volcánico transmexicano; MC, Mesa Central; SMO, cinturón de pliegues y cabalgaduras de la Sierra Madre Oriental o cinturón de pliegues y cabalgaduras mexicano. Componentes de la cuenca de antepaís mexicana: Bur, cuenca de Burgos; CB, cuenca de Sabinas; CLP, cuenca de La Popa; CP, cuenca de Parras; CTM, cuenca Tampico-Misantla; CZ, cuenca de Zimapán. Rocas plutónicas y volcánicas del arco cordillerano mexicano, mencionadas en texto: BLC, batolito de Los Cabos; BPE, batolito peninsular oriental; BPV, batolito de Puerto Vallarta; BPW, batolito peninsular occidental; BSin; batolito de Sinaloa; BSon, batolito de Sonora. Ciudades (puntos blancos): Ch, Chihuahua; Gu, Guanajuato; Mo, Monterrey; SLP, San Luis Potosí; To, Torreón; Za, Zacatecas.

particularmente sobre los efectos de estructuras de deformación regionales con la generación y dispersión de sedimentos en el cinturón de pliegues y cabalgaduras mexicano (CPCM). Este trabajo aporta aspectos cruciales para la mejor comprensión de la evolución del CPCM y la CAM así como para la distribución de los recursos presentes en la región.

I.1 Marco geológico

El orógeno mexicano

La formación de cinturones montañosos u orogénos es resultado de la convergencia de placas tectónicas (Dewey y Horsfield, 1970; Dahlen y Suppe, 1988; Dahlen, 1990; Selzer *et al.*, 2007, entre otros). Esto ocurre durante la colisión de dos masas continentales o como resultado de la subducción de la litosfera oceánica bajo la litosfera continental; su evolución está influenciada por la geometría de la subducción, así como por la naturaleza e historia geológica de las placas convergentes (Garzanti *et al.*, 2007). El orógeno cordillerano del oeste de América del Norte forma parte del cinturón orogénico circum-Pacífico donde se ha llevado a cabo la subducción de la litosfera oceánica formando un gran cinturón montañoso circular a nivel global, el cual comenzó desde la ruptura del supercontinente Pangea en el Triásico (Dickinson, 2004). La evolución posterior del orógeno cordillerano incluyó la acreción tectónica de arcos de islas que acrecentaron el margen continental de América del Norte durante el Jurásico-Cenozoico temprano (Coney *et al.*, 1980), en el que se formó durante el Cretácico un extenso cinturón batolítico (Coney *et al.*, 1980; Dickinson, 2004). El orógeno cordillerano se extiende ~5000 km desde el Golfo de Alaska hasta la desembocadura del Golfo de California (Fig. 1A). Los segmentos más importantes que se han propuesto para entender el orógeno cordillerano en América del Norte durante el Cretácico son Sevier, Laramide y Mexicano; este último fue recientemente documentado por Fitz-Díaz *et al.* (2018). Estos elementos tectónicos son resultado de la subducción de la placa de Farallón a lo largo de la margen occidental de la placa norteamericana (Coney *et al.*, 1980; Dickinson y Lawton, 2001; DeCelles, 2004; Dickinson, 2004; DeCelles *et al.*, 2009; Fitz-Díaz *et al.*, 2018, entre otros). La orogenia Sevier se encuentra en el centro-oeste de los E.U.A. y se extiende hacia Canadá en el norte. La orogenia Laramide formó cadenas montañosas en el centro-oeste y suroeste de los E.U.A. e incluye las serranías de Montana, Wyoming, Utah, Colorado, Nuevo México y Arizona, y se prolonga hacia el sur hasta el norte de Sonora, en el noroeste de México (Lawton, 2008, 2019). El desarrollo de las cuencas y levantamientos en la provincia Laramide concluyó en el Eoceno medio (~50 Ma) (Dickinson, 2004, Lawton, 2008). Más al sur, la cadena montañosa de la Sierra Madre Oriental representa el segmento meridional del orógeno cordillerano en América del Norte

(de Cserna, 1956; Suter, 1984; Dickinson y Lawton, 2001; Fitz-Díaz *et al.*, 2012; 2018), que típicamente ha sido incluida en la provincia Laramide, pero cuya deformación continuó hasta el fin del Eoceno (Dickinson, 2004; Lawton, 2019) (Fig. 1). Este segmento del orógeno cordillerano se ha interpretado con base en la extrapolación de observaciones hechas en el suroeste de los E.U.A., asumiendo la continuidad de estructuras y de la temporalidad de la deformación, mismas que en México consideramos son claramente distintas (ver Parte III, Capítulo I).

El orógeno cordillerano en México se caracteriza por la sobreposición del terreno Guerrero sobre la parte occidental del CPCM (*e.g.*, Mendoza y Suastegui, 2000; Martini *et al.*, 2016). Esta relación hizo suponer que la acreción del terreno Guerrero causó el acortamiento regional en el interior de México (*e.g.*, Freydier *et al.*, 1996; Talavera-Mendoza *et al.*, 2007; Centeno-García *et al.*, 2008). No obstante, datos geológicos disponibles sugieren que el terreno Guerrero se acrecionó al margen mexicano durante la parte tardía del Cretácico Temprano (*e.g.*, Johnson *et al.*, 1999; Dickinson y Lawton, 2001; Martini *et al.* 2014, 2016; Palacios-García y Martini, 2014; Ortega-Flores *et al.*, 2016; Fitz-Díaz *et al.*, 2018), poco antes de la formación del CPCM y por tanto las estructuras de acortamiento en este último no tienen relación en secuencia con el cinturón de sutura del terreno Guerrero adyacente (Martini *et al.*, 2016). Esta evidencia previa indica que el CPCM es un orógeno que marca una etapa distintiva de la evolución tectónica de la margen pacífica de América del Norte (Martini *et al.*, 2012; 2016; Fitz-Díaz *et al.*, 2018).

La propuesta de un segmento orogénico, definido aquí como *orógeno mexicano* se sustenta en la documentación estratigráfica de varios sectores de la cuenca de antepaís asociada, nuevas edades U-Pb de sucesiones sedimentarias sin-orogénicas, fechamientos dobles (U-Th)/(He-Pb) en granos individuales de circon detrítico que aunadas a edades de deformación previas (*e.g.*, Fitz-Díaz *et al.*, 2014; Garduño *et al.*, 2015; Martini *et al.*, 2016) permiten acotar y comprender mejor la evolución geológica de este segmento del orógeno en América del Norte. Por lo tanto, la edad de la deformación, el estilo tectónico dominante y su estrecha relación con un arco magmático activo reflejan variaciones temporales y litosféricas que permiten reconocerlo como la expresión en México del orógeno cordillerano (Fitz-Díaz *et al.*, 2018). La historia de acortamiento de este orógeno se infiere abarcó del Cretácico Tardío-Eoceno tardío e involucró rocas del Triásico-Eoceno

(Campa, 1985; Suter, 1987; Eguiluz *et al.*, 2000; Fitz-Díaz *et al.*, 2012; 2018). El orógeno mexicano presenta características cinemáticas tanto de piel delgada (*thin-skinned style deformation*) como de piel gruesa (*thick-skinned style deformation*) determinadas por la estructura de la corteza heredada (basamento) y las sucesiones sedimentarias mesozoicas depositadas antes del evento de acortamiento (Fitz-Díaz *et al.*, 2018). Este orógeno comparte características cinemáticas con el orógeno Sevier y Laramide en los E.U.A. El orógeno mexicano consiste de tres elementos principales: (1) en su parte occidental, el *hinterland* constituido por rocas de cuenca e ígneas del terreno Guerrero; (2) la cuña orogénica (*foreland orogenic wedge*), referida como cinturón de pliegues y cabalgaduras mexicano, compuesta por rocas carbonatadas del Jurásico Superior-Cretácico Inferior y depósitos clásticos del Cretácico Superior de la CAM que se encuentran imbricadas y plegadas; y (3) estratos deformados del Cretácico Tardío-Eoceno que se extienden desde el noreste hasta el centro de México y pertenecen a la CAM (Fitz-Díaz *et al.*, 2018; Juárez-Arriga *et al.*, 2019a).

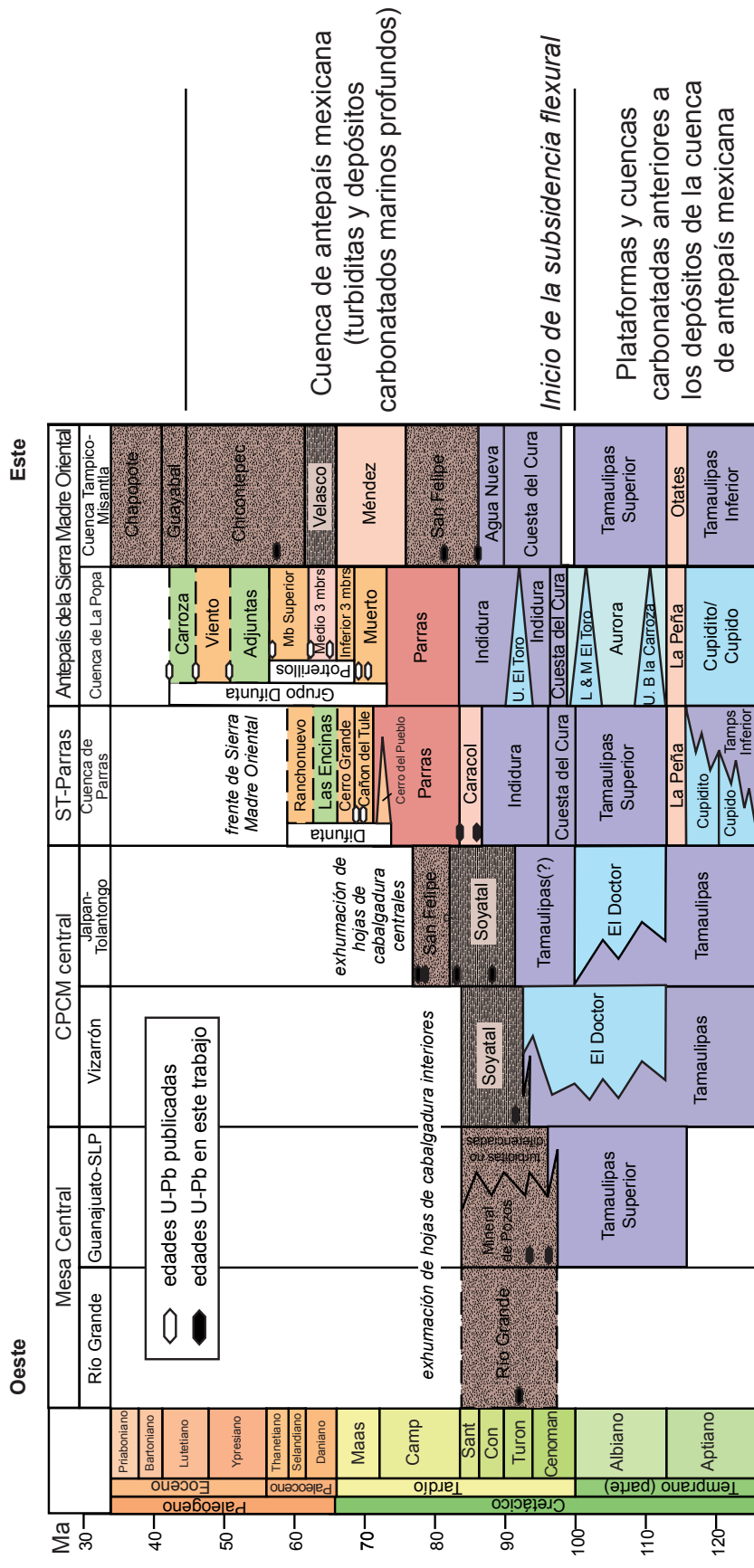
Numerosos estudios indican que el principal mecanismo tectónico que dio origen al acortamiento en el orógeno cordillerano fue posiblemente un incremento en la velocidad de convergencia entre las placas de Farallón y Norteamericana durante el Cretácico Tardío-Eoceno como se ha documentado previamente (*e.g.*, Coney *et al.*, 1980; Engebretson *et al.*, 1984; Saleeby, 2003; DeCelles, 2004; Dickinson, 2004; Solari *et al.*, 2007; Martini y Ferrari, 2011; Fitz-Díaz *et al.*, 2018). Por otro lado, el análisis de las edades de deformación, de plutones sintectónicos en la margen occidental de México, así como de las sucesiones sedimentarias sinorogénicas indica que la CAM se formó en un ambiente de retroarco (*sensu* Ingersoll, 2012). Una descripción más detallada de la formación y evolución del orógeno mexicano se encuentra en el primer artículo de esta tesis (Parte III, Capítulo 1). En dicho trabajo se exponen las características que distinguen este segmento del orógeno cordillerano y se propone un escenario geológico que intenta explicar las variaciones temporales y cinemáticas observadas en México (*e.g.*, Fitz-Díaz *et al.*, 2018).

La cuenca de antepaís mexicana

Asociada a la evolución del orógeno mexicano durante del Cretácico Tardío-Paleógeno temprano se desarrolló la cuenca de antepaís mexicana. La CAM, definida en el Capítulo 2 de esta tesis, representa la continuación geográfica hacia el sur de la cuenca de antepaís cordillerana de América del Norte, sin embargo ha recibido menor atención que su contraparte en los E.U.A. (Juárez-Arriaga *et al.*, 2019a). A diferencia de la provincia Laramide que tuvo en general un carácter amagmático (Dickinson y Snyder, 1978; Lawton, 2019), la evolución del orógeno mexicano estuvo acompañada por magmatismo de arco continental que migró tierra adentro desde el cinturón batolítico en la margen occidental mexicana a lo largo de su evolución (Dickinson y Lawton, 2001; Dickinson, 2004; Fitz-Díaz *et al.*, 2018). Los eventos magmáticos modificaron la extensión y geometría de la CAM a lo largo de su desarrollo al formar topografía positiva y contribuir con el engrosamiento de la corteza, además de que suministraron un volumen importante de detritos a la cuenca. La historia de subsidencia y sedimentación de la CAM inicia posiblemente en la parte temprana el Cenomaniano, poco tiempo después de que el terreno Guerrero fuera acrecionado a la margen occidental de México (*e.g.*, arco Alisitos, Busby *et al.*, 2006; cuenca de Arperos, Martini *et al.*, 2014; 2016) (Fig. 2). Ya almagamado el terreno Guerrero, la subducción de la placa de Farallón causó la formación de un arco magmático que se desarrolló en la margen continental y se mantuvo activo a lo largo de la historia de acortamiento del retro-arco (Cretácico Tardío-Paleógeno temprano). Por analogía con otros segmentos del orógeno cordillerano (*e.g.*, provincia Laramide, Dickinson y Snyder, 1978), la subducción subhorizontal de la placa de Farallón bajo Norte América parece ser el modelo que mejor explica el acortamiento de la conterza en el interior de México. El acortamiento en el transpaís (*hinterland*) generó la formación de una cuña orogénica que causó la subsidencia en la CAM. Por su posición con respecto al arco magmático y su desarrollo del lado continental del orógeno, la CAM corresponde a una cuenca de antepaís de retoarco (*retro-foreland basin*, *sensu* Dickinson, 1976; Ingersoll, 2012). A lo largo de su evolución, la cuenca fue flanqueada al oeste por el arco magmático activo y el CPCM, este último constituyó la topografía más elevada. La presencia de este arco definido como *arco magmático mexicano* (Juárez-Arriaga *et al.*, 2019a) se basa en una extensa área de batolitos del Cretácico Tardío-

Paleógeno en el oeste de México (Zimmermann *et al.*, 1988; Kimbrough *et al.*, 2001; Henry *et al.*, 2003; Ortega-Rivera, 2003; Valencia *et al.*, 2013; Ortega-Gutiérrez *et al.*, 2014). Adicionalmente un robusto conjunto de edades U-Pb en granos de circón volcánico de primer ciclo y datos petrográficos en areniscas de la CAM sugieren al menos dos episodios magmáticos particularmente voluminosos que son discutidos en el segundo artículo de esta tesis (*i.e.*, Juárez-Arriaga *et al.*, 2019a). El arco magmático mexicano abarcó la margen occidental de México, la cual ya estaba constituida por el terreno Guerrero recientemente acrecionado, desde el sur de la actual Sonora hasta Jalisco donde tuvieron su nacimiento redes de drenaje que erosionaron el armazón volcánico y cuyos sedimentos fueron transportados a la cuenca. Este sistema de transporte predominantemente transversal estuvo activo durante el Cenomaniano-Turoniano y acarrió sedimentos derivados del arco, el basamento y de rocas sedimentarias que estuvieron expuestas en el oeste de México. Un segundo mecanismo de transporte de sedimentos volcanoclásticos fueron nubes de ceniza producto de eventos explosivos a lo largo del arco que fueron transportados por viento hacia la CAM durante el Santoniano-Campaniano alcanzando sus partes más distales en el este (Juárez-Arriaga *et al.*, 2019a). Como se discute más adelante (Parte III, Capítulo II), la historia de la CAM estuvo estrechamente asociada a la historia del arco magmático mexicano lo cual permitió que su relleno contenga un abundante registro de granos de circón provenientes de este arco contemporáneo (Fitz-Díaz *et al.*, 2018; Juárez-Arriaga *et al.*, 2019a).

La CAM incluye las cuencas de Parras, La Popa, Sabinas y Tampico-Misantla, así como turbiditas deformadas expuestas en la Mesa Central (que anteriormente fueron consideradas parte de la cuenca mesozoica del centro de México; *e.g.*, Carrillo-Bravo, 1971) y las cuencas presentes en el cinturón de pliegues y cabalgaduras mexicano como la cuenca de Zimapán (Fig. 1). Las sucesiones sedimentarias de la CAM pueden dividirse en: (1) *depósitos proximales*, estratos depositados en la margen occidental de la CAM, particularmente, aquellos que estuvieron adyacentes a la cuña tectónica en su etapa inicial y que fueron subsecuente imbricados e incorporados a la cuña orogénica. Los afloramientos tienen una extensión vertical limitada a algunos metros y se encuentran localmente bien expuestos a lo largo de arroyos y cortes carreteros (Fig. 3). (2) *Depósitos distales*, estratos depositados en la parte oriental de la CAM,



Cuenca de antepais mexicana
(turbiditas y depósitos
carbonatados marinos profundos)

Inicio de la subsidencia flexural

Plataformas y cuencas
carbonatadas anteriores a
los depósitos de la cuenca
de antepais mexicana

- Depósitos carbonatados**
- Rampa carbonatada
 - Plataforma carbonatada
 - Carbonatos de cuenca;
 - Calciturbiditas
- Depósitos Siliciclasticos**
- Capas rojas;
 - Estratos fluviales
 - Areniscas marinas;
 - Depósitos de frente deltaico
 - Lutita de plataforma
 - Lutita de prodelta;
 - Foredeep
 - Turbiditas ricas en arena
 - Turbiditas ricas en lodo

Figura 2. Correlación estratigráfica en la región central de México. Los colores púrpura y azul de esta tabla de correlación indican las plataformas y cuencas carbonatadas y lutitas del Cretácico Temprano. Las calciturbiditas de las sucesiones de carbonatos más antiguas se interdigitan con turbiditas siliciclásticas en la parte occidental de la CAM. Los ambientes siliciclásticos (marrón) migraron hacia el este con el tiempo, hacia la parte exterior del CPCM. La edad del límite superior de las sucesiones de la CAM en el oeste se desconocen porque los estratos son truncados por erosión al ser exhumados durante el avance progresivo hacia el este de la cuña orogénica.

los cuales constituyen las sucesiones menos deformadas y actualmente presentes en las cuencas de Sabinas, Parras, La Popa y Tampico-Misantla (Fig. 4).

I.II Hipótesis

De acuerdo al modelo de evolución tectónica del CPCM central, la cuña orogénica migró hacia el este generando distintos episodios de deformación y exhumación (Fitz-Díaz *et al.*, 2014; 2018). Lo anterior permite inferir que las fuentes de sedimento cambiaron a través del tiempo y pueden reconocerse a partir de las variaciones en las edades de enfriamiento de los granos de circón detrítico, así como en la composición de las areniscas procedentes de la parte proximal, intermedia y distal de la cuenca. Por ejemplo, las rocas del basamento del terreno de Guerrero exhumadas en el oeste deben haber aportado detritos de diferente composición y granos de circón con edades de enfriamiento distintas a los detritos y granos de circón derivados posteriormente de estratos del Cretácico Inferior y Cretácico Superior exhumados en la parte central del CPCM.

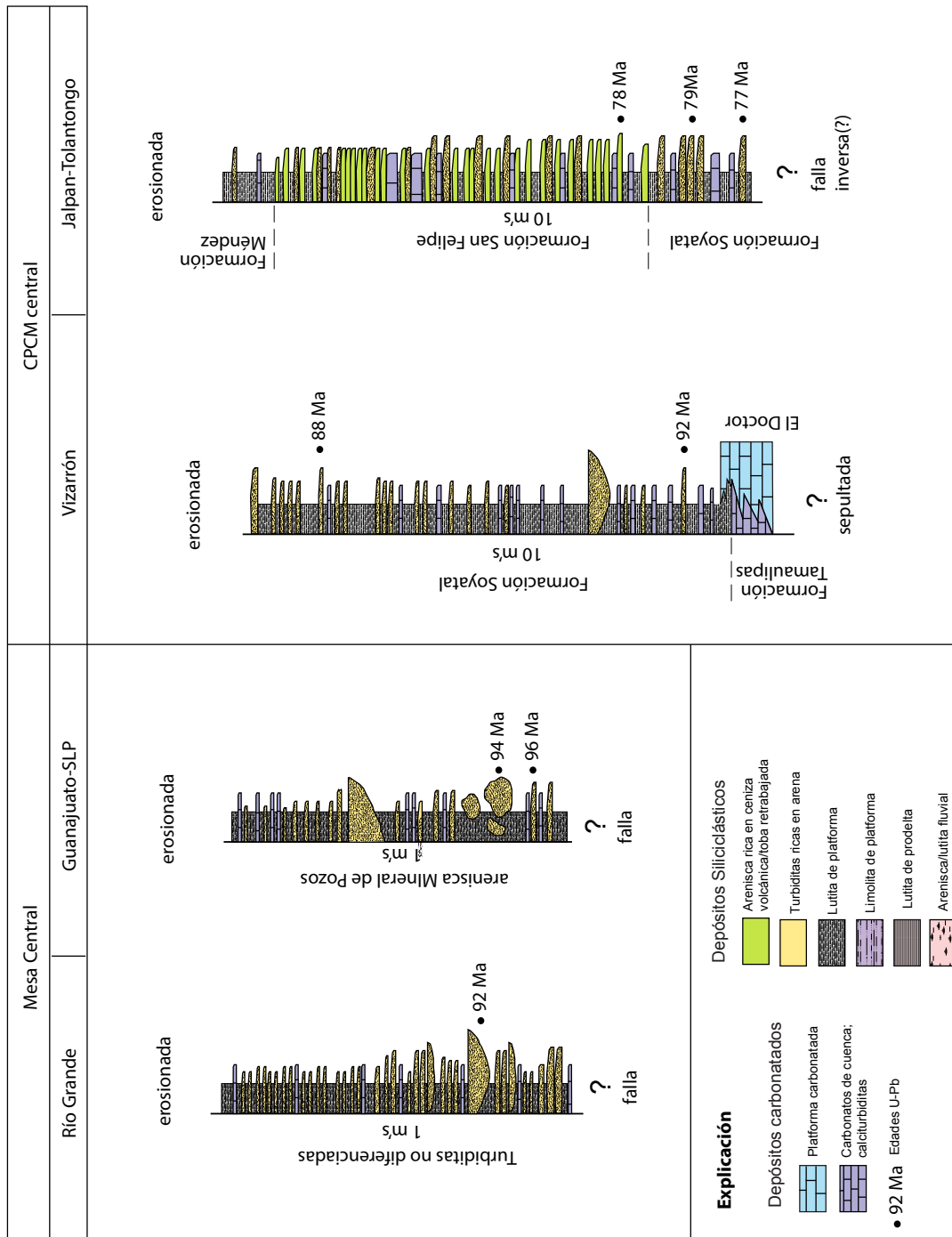


Figura 3. Columnas estratigráficas sintéticas que representan los *depósitos proximales* de la cuenca de antepaís mexicana (la ubicación dentro de la cuenca se indica en la Fig. 2). Las columnas muestran las variaciones estratigráficas y enfatizan las diferencias en espesor de las sucesiones sedimentarias dependiendo de su posición dentro de la CAM.

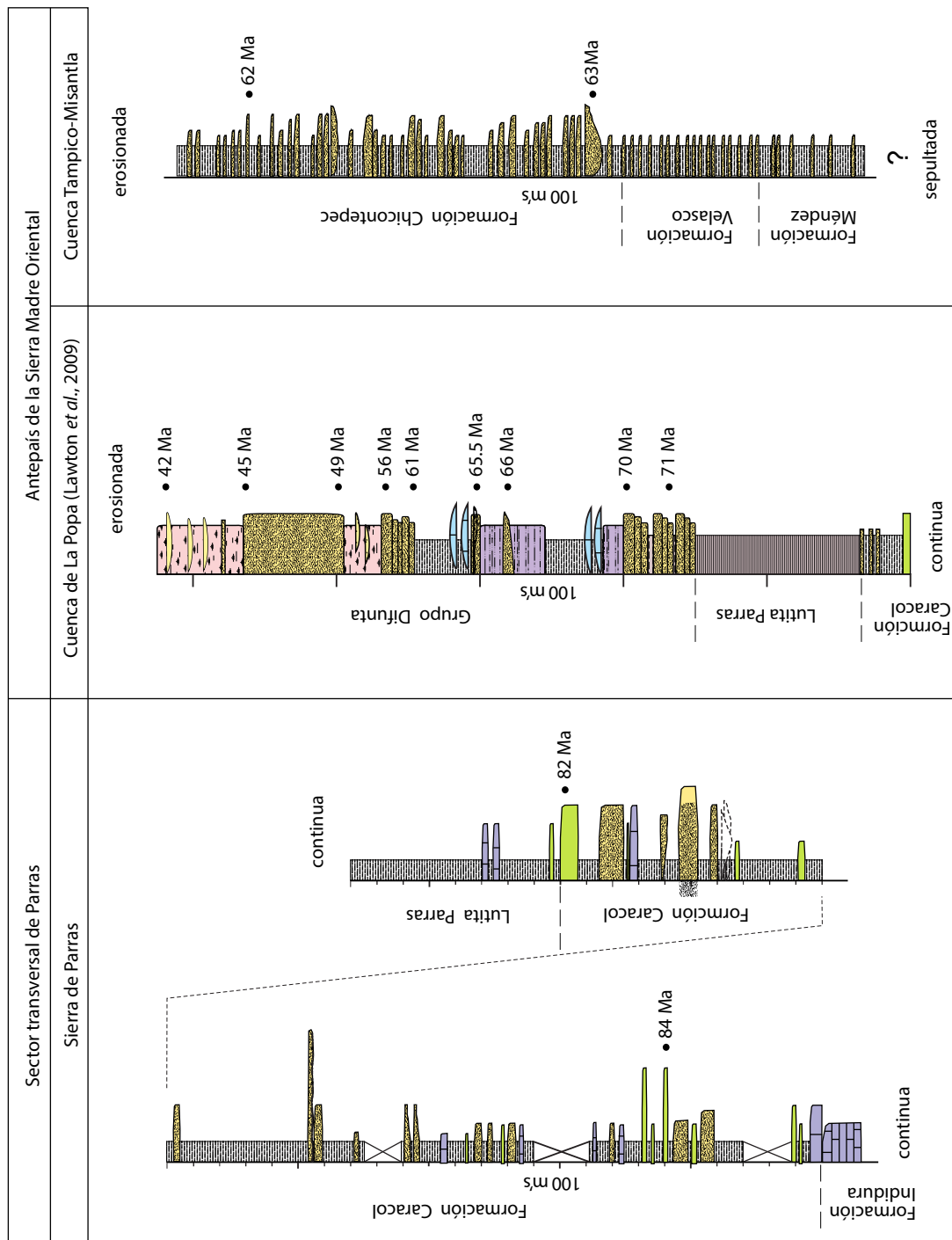


Figura 4. Columnas estratigráficas sintéticas que representan los *depósitos distales* de la cuenca de antepaís mexicana, las cuales muestran las variaciones estratigráficas y enfatizan las diferencias en espesor de las sucesiones sedimentarias dependiendo de su posición dentro de la CAM. La ubicación dentro de la cuenca se indica en la figura 2. Estas columnas sintetizan datos documentados en Lawton *et al.* (2009), Juárez-Arriaga *et al.* (2019a y 2019b).

I.III Justificación

Aunque se ha avanzado en el conocimiento de la geología del centro del país en años recientes (e.g., Carrillo-Bravo, 1971; Tardy y Maury, 1973; López-Ramos, 1979; Suter, 1980, 1987; Eguiluz *et al.*, 2000; Eguiluz, 2011; Alzaga-Ruiz *et al.*, 2009), los resultados obtenidos resultan insuficientes para comprender la relevancia que tuvo la deformación del Cretácico Tardío-Paleógeno sobre la generación y dispersión de sedimentos en la CAM. El presente trabajo tiene como meta integrar los datos disponibles en la literatura geológica y la generación de nueva información proveniente de localidades escasamente documentadas o no estudiadas, para mejorar la comprensión de la evolución de la CAM asociada al CPCM. Este estudio contribuye al conocimiento de las potenciales fuentes de sedimento y a constreñir la edad de los depósitos de la CAM en el centro de México. Para alcanzar esta meta se aplicaron metodologías de estratigrafía clásica, así como el uso de conceptos y técnicas analíticas modernas. Las edades de cristalización (U-Pb) en granos de circón fueron usadas para calcular la edad máxima de depósito (*maximum depositional age*, MDA) de las sucesiones siliciclásticas de acuerdo a los criterios discutidos por Dickinson y Gehrels (2009). Este trabajo incluye también los primeros fechamientos dobles (U/Th)/(He-Pb) en granos individuales de circón detrítico procedentes de tres unidades cretácicas expuestas en el centro de México que en combinación con datos petrográficos permiten evaluar la influencia de eventos de exhumación en la generación y dispersión de sedimentos. La integración de ambos conjuntos de datos, como se describe más adelante, permitieron una mejor comprensión del relleno sedimentario de la cuenca de antepaís mexicana y su evolución temporal proporciona un marco geológico preciso que contribuye a la comprensión de la distribución de recursos energéticos asociados a este sistema.

I.IV Objetivo principal y objetivos particulares

El objetivo principal de este trabajo es documentar la evolución estratigráfica de la CAM, la cual está asociada al desarrollo del CPCM durante el Cretácico Tardío-Eoceno. La investigación se enfocó en los afloramientos presentes en el noreste y centro de México e incluyen rocas de la Mesa Central, el sector transversal de Parras y la parte central del CPCM.

Adicionalmente se plantearon los siguientes objetivos particulares.

i. Identificar las posibles fuentes de sedimento que rellenaron la cuenca de antepaís mexicana. Para cumplir con este objetivo se aplicaron metodologías de estratigrafía clásica, así como el uso de conceptos y técnicas analíticas modernas como el fechamiento de granos de circón por U-Pb y (U-Th)/He en circón.

ii. Identificar los posibles patrones de dispersión que acarrearón sedimentos a la CAM. Para lograr este objetivo se integró un vasto conjunto de nuevas edades U-Pb en circón que aunado a datos petrográficos y direcciones de paleocorrientes permitieron construir sólidas hipótesis de procedencia y de patrones de dispersión de sedimentos durante el Cretácico Tardío-Paleógeno. Adicionalmente, la distribución de detritos volcánicos documentada fue evaluada en el contexto de modelos de circulación atmosférica para Norte América durante el Cretácico Tardío.

iii. Evaluar la influencia de los eventos de deformación de la parte central del CPCM en la producción y dispersión de sedimentos en la CAM asociada durante el Cretácico Tardío-Paleógeno. Para lograr este objetivo se construyó un sólido conjunto de datos petrográficos, geo- y termocronológicos procedentes de unidades cretácicas presentes a lo largo del transecto geológico Tolimán-Tamazunchale (estados de Querétaro-San Luis Potosí) ubicado en la parte central del CPCM.

Parte II

Metodología

II.I Trabajo de campo y colecta de muestras

En el trabajo de campo se aplicaron metodologías de estratigrafía clásica que incluye la medición y descripción de columnas estratigráficas, reconocimiento e interpretación de litofacies, medición de estructuras de paleocorrientes, identificación de discordancias y de estructuras de deformación. Veinticinco columnas estratigráficas cortas (~6-25 m de espesor) de la CAM fueron documentadas la Mesa Central, el sector transversal de Parras, la curvatura de Monterrey y en centro del CPCM. Las columnas más completas (~125 y ~430 m de espesor) medidas en la curvatura de Monterrey y el sector transversal de Parras, respectivamente, son discutidas en el Capítulo II. Las interpretaciones presentadas en esta tesis se basan en el análisis de 14 muestras petrográficas, 18 muestras geocronológicas y 3 muestras utilizadas para realizar fechamientos dobles (U-Th)/(He-Pb). Las muestras fueron colectadas con respecto a rasgos geológicos importantes (e.g., discordancias, cambios litológicos y posición con respecto a estructuras de deformación). Cada muestra está posicionada dentro de columnas estratigráficas en las que se destaca su litología, contenido fósil, estructuras sedimentarias primarias e indicadores de dirección de paleocorrientes cuando estuvieron presentes (e.g., estructuras de flauta y de arrastre). Estas consideraciones complementan las interpretaciones presentadas y están encaminadas a mejorar la comprensión de variaciones obtenidas en los espectros de edad U-Pb en los granos de circón detrítico analizados.

II.II Petrografía de rocas sedimentarias clásticas

Para cada muestra geocronológica se elaboró una sección delgada. Las rocas clásticas fueron clasificadas de acuerdo al esquema de clasificación de areniscas de Folk (1974). La mitad de cada sección delgada fue teñida con cobaltonitrito de sodio para el reconocimiento modal de feldespato potásico. Para cada muestra se contaron un total de 400 granos del armazón siguiendo la técnica de conteo de Gazzi-Dickinson y así minimizar la dependencia de la composición al tamaño de grano (Ingersoll *et al.*, 1984). Los conteos fueron graficados en los diagramas ternarios de

procedencia QtFL y QmFLt (Dickinson, 1985) y LmLvL (Ingersoll y Suczek, 1979). Los minerales accesorios y los granos bioclásticos no fueron incluidos en los diagramas ternarios. Los parámetros de conteo de puntos se muestran en el Apéndice 1.

II.III Geocronología U-Pb en granos de circón detrítico

Una de las metas más comunes al realizar estudios geocronológicos en granos de circón detrítico es constreñir la edad de sucesiones sedimentarias siliciclásticas, particularmente cuando los depósitos carecen de fósiles diagnósticos de edad (Fedo *et al.*, 2003; Dickinson y Gehrels, 2009). La geocronología U-Pb en granos de circón detrítico provee de edades de cristalización (~900°C) que comúnmente se usan para establecer edades estratigráficas absolutas (*e.g.*, Reiners *et al.*, 2005; DeCelles *et al.*, 2007). La premisa principal es que la edad de depósito debe ser menor que (o igual a) la edad del circón detrítico más joven o grupo de circones más jóvenes (Dickinson y Gehrels, 2009). Sin embargo es común que los resultados obtenidos correspondan únicamente a la edad máxima de depósito (DeCelles *et al.*, 2007). Las edades de cristalización pueden aproximarse a la edad de depósito cuando se presentan granos de circón volcánico procedentes de una fuente contemporánea, ya que su depósito es instantáneo por lo que constituyen granos sindepositacionales. En algunos casos la estimación de la edad de las sucesiones sedimentarias en el noreste y centro de México mejoraron cuando dentro de éstas existieron capas de toba que fueron analizadas y sus edades, interpretadas como edades de emplazamiento, fueron usadas para constreñir las MDA obtenidas a partir de granos de circón detrítico.

La geocronología U-Pb en circones detríticos es una técnica probada y ampliamente utilizada para evaluar hipótesis de procedencia por medio de la comparación de edades U-Pb de circones detríticos de una muestra desconocida con las edades de un conjunto de circones detríticos de referencia bien establecido (*e.g.*, Gehrels y Dickinson, 1995; Gehrels, 2000; Lawton *et al.*, 2009; Leier y Gehrels, 2011). Numerosas investigaciones recientes muestran que la combinación de metodologías de estratigrafía clásica complementadas con datos derivados de técnicas analíticas modernas proporcionan información trascendente para entender la influencia de la deformación en el relleno de cuencas de antepaís (*e.g.*, Fildani *et al.*, 2003; Soegaard *et al.*, 2003; Dickinson y

Gehrels, 2008; Lawton *et al.*, 2009; Romans *et al.*, 2010; Fosdick *et al.*, 2011; Raines *et al.*, 2013; Roigé *et al.*, 2016; Malkowski *et al.*, 2017; Calle *et al.*, 2018; Pujols *et al.*, 2018).

Cada muestra geocronológica consiste de 3-5 kg de roca para obtener 150 granos de circón detrítico por muestra que luego fueron analizados por ablación láser asociada con un espectrómetro de masas de plasma inductivamente acoplado (LA-ICPMS, por sus siglas en inglés). Esta técnica analítica requiere que los granos tengan al menos ~60 μm de diámetro, pues los cráteres de ablación varían de 25-50 μm de diámetro y de 7-8 μm en profundidad. Debido a lo anterior las muestras geocronológicas analizadas están constituidas predominantemente por areniscas de grano mediano a grueso (250 μm a <2 mm) con tonos oscuros –tonalidad comúnmente dada por la abundancia de minerales pesados– ya que éstas tienen las mejores posibilidades de contener circones detríticos con tamaños adecuados para esta técnica. Las muestras fueron analizadas en el Laboratorio de Estudios Isotópicos (LEI) del Centro de Geociencias, UNAM-Juriquilla de acuerdo a los procedimientos descritos por Solari *et al.* (2018), el Geo- and ThermoChronometry Laboratory de la Universidad de Texas en Austin según la metodología descrita por Hart (2015), Hart *et al.* (2016) y Pujols *et al.* (2018). Adicionalmente, una muestra fue analizada en Arizona LaserChron Center de la Universidad de Arizona de acuerdo a los procedimientos descritos por Gehrels *et al.* (2008).

Para cada muestra se analizaron entre 120-150 granos de circón detrítico para obtener un conjunto de datos estadísticamente representativo que permitiera identificar los principales componentes de edad en cada muestra (*e.g.*, Vermeesch, 2004). En el caso de las muestras de toba se realizó el análisis de 40-50 granos para calcular la edad de cada muestra, la cual se interpretó como edad de emplazamiento. Para ampliar nuestro conocimiento y elaborar interpretaciones más robustas sobre el registro de edades de circón en el relleno de la cuenca de antepaís mexicana, las nuevas edades U-Pb fueron analizadas conjuntamente con edades U-Pb de la CAM previamente publicadas (*e.g.*, Lawton *et al.*, 2009; Ortega-Flores *et al.*, 2014; Velasco-Tapia *et al.*, 2016).

El análisis de datos y las interpretaciones hechas en esta investigación se basan en edades U-Pb concordantes; los filtros de concordancia utilizados se detallan en la metodología de cada

publicación. El análisis de las edades U-Pb incluye histogramas, curvas de probabilidad relativa y media ponderada (*weighted mean age*) calculadas por medio del software Isoplot 4.15 (Ludwig, 2012). Las edades isotópicas y edades corregidas son proporcionadas en los Apéndices 2 y 3. El marco temporal seguido en este trabajo se basa en la escala del tiempo geológico (*Geologic Time Scale*) propuesta por Cohen *et al.* (2013).

II.IV Termocronología (U-Th)/He en circón

La termocronometría (U-Th)/He en granos de circón se basa en el incremento de helio dentro del cristal a partir de la decadencia radioactiva del U y Th, la cual se mantiene por debajo de la temperatura de cierre $\sim 180^{\circ}\text{C}$ (Reiners, 2005; Reiners *et al.*, 2005). Por encima de esta temperatura el He escapa del cristal por difusión y la edad calculada por esta técnica será cero (Payton y Carrapa, 2013). La baja temperatura de cierre del sistema (U-Th)/He en granos de circón permite la reconstrucción de la historia térmica de la corteza superior, particularmente es posible fechar eventos de exhumación tectónica y determinar la historia de sepultamiento de una cuenca sedimentaria (*e.g.*, Saylor *et al.*, 2012; Domènech *et al.*, 2016; Hart *et al.*, 2016; Pujols *et al.*, 2018; Juárez-Arriaga *et al.*, 2019b).

Los granos de circón volcánico de primer ciclo tienen una edad de cristalización (U-Pb) y enfriamiento (ZHe) prácticamente idéntica (Reiners *et al.*, 2005; Saylor *et al.*, 2012; Pujols *et al.*, 2018). La inclusión de granos volcánicos en el análisis de las edades ZHe puede distorcionar las interpretaciones de la historia térmica de una región, por ejemplo, pueden llevar a la interpretación errónea de tasas de exhumación muy altas (Ruiz *et al.*, 2004; Saylor *et al.*, 2012). El fechamiento doble en granos individuales de circón se emplea para identificar la presencia de granos de circón volcánico de primer ciclo en sucesiones sedimentarias donde hay posibilidad de aporte de detritos volcánicos sinsedimentarios. Para reconocer estos granos se considera la diferencia entre la edad de cristalización y la edad de enfriamiento (Δt) según los criterios discutidos por Saylor *et al.* (2012). Si Δt es menor que la incertidumbre 2σ de la edad ZHe, el grano se interpreta como un circón volcánico de primer ciclo y se excluye de los cálculos e interpretaciones posteriores.

Basados únicamente en la distribución modal de las edades de enfriamiento detríticas (DZHe) se identificaron los principales eventos de enfriamiento que en este caso, pueden ser atribuidos a diferentes episodios tectónicos en la evolución del CPCM central.

II.V Fechas dobles (U-Th)/(He-Pb) en granos individuales de circón detrítico

Dada su presencia en una variedad de litologías, su resistencia a la descomposición mecánica o química y la posibilidad de aplicar a un solo grano de circón dos técnicas isotópicas independientes: U-Pb y (U-Th)/He, estos granos son una poderosa herramienta para realizar tanto estudios evolución térmica en la corteza superior y de procedencia. El fechamiento doble en un grano único evita interpretaciones ambiguas basadas en un solo sistema isotópico y pueden ayudar a discriminar entre fuentes potenciales con edades de cristalización similares (*i.e.*, U-Pb). El uso de edades de cristalización y enfriamiento procedentes de un único grano debe proporcionar una única combinación, característica del área fuente de la cual se derivó el sedimento. Esta metodología permite además investigar la evolución temporal y espacial de procesos de exhumación y deformación en cinturones de pliegues y cabalgaduras (*e.g.*, Saylor *et al.*, 2012; Juárez-Arriga *et al.*, 2019b).

Además de realizar fechamientos U-Pb en granos de circón detrítico, este estudio incluye fechamientos por (U-Th)/He (ZHe) para refinar las interpretaciones de procedencia e identificar eventos de exhumación tectónica en el CPCM central. Un subconjunto de granos de circón se seleccionó para ser fechado por U-Th/He y obtener edades de enfriamiento (ZHe) siguiendo los criterios siguientes: (1) un tamaño mayor a 60 μm , (2) ausencia de inclusiones y fracturas y, (3) abundancia relativa de los componentes de edad U-Pb para cada muestra seleccionada (más detalles y fundamento teórico sobre esta técnica analítica en Wolfe y Stockli, 2010; Pujols *et al.*, 2018; Ruiz-Arriaga, 2018). Para cada muestra se obtuvieron entre 11-17 edades ZHe, las cuales registran el tiempo de enfriamiento a una temperatura de $\sim 180^\circ\text{C}$ (*e.g.*, Reiners *et al.*, 2005).

En el Capítulo 3 se presentan los resultados de edades dobles U-Pb y ZHe en granos de circón individual. Estos datos fueron analizados para refinar las interpretaciones de procedencia y para evaluar el modelo de evolución tectónica del CPCM central, es decir la migración de la deformación

hacia el este durante distintos episodios de deformación (e.g., Fitz-Díaz *et al.*, 2014). Todas las fechas dobles (U-Th)/(He-Pb) se obtuvieron a partir de un grano circón individual en el Geo- and Thermochronometry Laboratory de la Universidad de Texas en Austin y se incluyen en el Apéndice 4.

II.V Estructura de la tesis

La Parte III comprende tres capítulos, cada uno de ellos corresponde a un artículo publicado. Las interpretaciones de estas investigaciones se basan en edades U-Pb y U-Th /He en granos de circón volcánico y detrítico, y están sustentadas en conceptos de estratigrafía moderna.

El Capítulo 1 corresponde a un artículo de revisión en el que se describe y define el *orógeno mexicano* como parte del sistema orogénico cordillerano. El análisis de un robusto conjunto de datos que incluye edades de deformación, edades máximas de depósito de las sucesiones sedimentarias sinorogénicas y edades de plutones sintectónicos en la margen occidental de México permite hacer las siguientes inferencias: (1) los datos indican que este evento orogénico fue el resultado de la subducción de la placa de Farallón a lo largo de la margen occidental mexicana. (2) Simultáneamente, al inicio del evento de acortamiento ocurrió el ahogamiento de las plataformas carbonatadas en el oeste y el inicio de la sedimentación siliciclástica en la CAM. (3) Durante la evolución del orógeno mexicano ocurrió un continuo y voluminoso magmatismo continental en la margen pacífica de México. Este arco constituyó una fuente abundante de sedimentos volcánicos para la CAM, así como de circones que permitieron establecer la edad de sus depósitos. La CAM constituye así una cuenca de retroarco (*sensu* Dickinson, 1976; Ingersoll, 2012) que al igual que su contraparte en el norte, migró con el tiempo hacia el este por delante de la cuña orogénica.

En el Capítulo 2 se propone el término *cuenca de antepaís mexicana*, la cual representa la continuación hacia el sur de la cuenca de antepaís cordillerana. La CAM agrupa a las sucesiones sedimentarias del Cretácico Tardío-Paleógeno que actualmente se extienden desde el norte de la faja volcánica transmexicana, en el centro del país, hasta los estados del noreste de México. Con base en un robusto conjunto de edades U-Pb en granos de circón volcánicos de primer ciclo y

detríticos, datos petrográficos y análisis de paleocorrientes se determina que buena parte del relleno sedimentario de la CAM provino de un arco magmático activo durante el Cretácico Tardío-Paleógeno en la margen continental del occidente de México (*arco magmático mexicano*). Los principales mecanismos de dispersión de sedimentos son discutidos considerando que las fuentes en el arco fueron múltiples y simultáneamente activas durante el Cretácico Tardío.

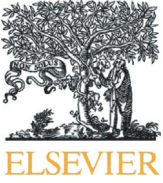
El Capítulo 3 se enfoca en el análisis de fechas dobles (U-Th)/(He-Pb) en granos individuales de circón detrítico para entender la correspondencia entre episodios de exhumación, como consecuencia del avance de la cuña orogénica hacia el este, con la sedimentación sinorogénica en la cuenca de antepaís mexicana en el centro de México. Las fechas dobles proceden de tres areniscas del Cretácico Superior localizadas en la parte central del cinturón de pliegues y cabalgaduras mexicano. Estas edades fueron complementadas con datos geocronológicos (U-Pb en circón detrítico), petrográficos y bioestratigráficos para constreñir mejor el tiempo de los eventos de deformación en el CPCM y la producción de sedimentos. Tres principales eventos de enfriamiento fueron identificados en el centro de México, los cuales se corresponden con pulsos de deformación previamente interpretados en la región (*e.g.*, Fitz-Díaz *et al.*, 2014; Garduño-Martínez, *et al.*, 2015; Guerrero-Paz *et al.*, *aceptado*). El evento de enfriamiento más joven reconocido es coincidente con la edad máxima de depósito de la Formación Chicontepec, sin embargo las edades de U-Pb no definen la claramente la fuente de sus sedimentos. En contraste, el análisis petrográfico y bioestratigráfico indica que la mayor parte de los componentes de la muestra de la Formación Chicontepec deriva de la erosión de calizas localizadas directamente en el flanco occidental de esta unidad dentro del CPCM.

Parte III

Evolución estratigráfica y procedencia de la cuenca de antepaís mexicana (CAM) en el centro de México

III.I El orógeno mexicano y la cuenca antepaís mexicana

Fitz-Díaz, E., Lawton, T.F., **Juárez-Arriaga, E.**, Chávez-Cabello, G., 2018. *The Cretaceous-Paleogene Mexican orogen: Structure, basin development, magmatism and tectonics*: Earth-Science Reviews, v. 183, 56-84. <http://dx.doi.org/10.1016/j.earscirev.2017.03.002>



Contents lists available at ScienceDirect

Earth-Science Reviews

journal homepage: www.elsevier.com/locate/earscirev

Invited review

The Cretaceous-Paleogene Mexican orogen: Structure, basin development, magmatism and tectonics

Elisa Fitz-Díaz^{a,*}, Timothy F. Lawton^b, Edgar Juárez-Arriaga^c, Gabriel Chávez-Cabello^d^a Instituto de Geología, Universidad Nacional Autónoma de México, Ciudad Universitaria, Ciudad de México, Mexico^b Centro de Geociencias, Universidad Nacional Autónoma de México, Juriquilla, Qro. 76230, Mexico^c Posgrado en Ciencias de la Tierra, Universidad Nacional Autónoma de México, Juriquilla, Qro. 76230, Mexico^d Facultad de Ciencias de la Tierra, Universidad Autónoma de Nuevo León, Linares, N.L. 67700, Mexico

ARTICLE INFO

Article history:

Received 31 May 2016

Received in revised form 17 February 2017

Accepted 2 March 2017

Available online 6 March 2017

Keywords:

Cordilleran orogen
 Mexican fold-thrust belt
 Guerrero terrane
 Laramide orogen
 Sevier orogen
 Arperos basin

ABSTRACT

The Mexican orogen is the expression in Mexico of the Cordilleran orogenic system. The orogen extends the length of Mexico, a distance of 2000 km from the state of Sonora in the northwest to the state of Oaxaca in the south. The Mexican orogen consists of (1) a western *hinterland* of accreted oceanic basinal rocks and magmatic arc rocks generally known as the Guerrero volcanic superterrane, (2) a *foreland orogenic wedge*, commonly termed the Mexican fold and thrust belt (MFTB), composed of imbricated and folded Upper Jurassic-Lower Cretaceous carbonate rocks and Upper Cretaceous foreland-basin strata, and (3) an assemblage of variably folded and inverted Late Cretaceous to Eocene *foreland basins* that lie northeast and east of the MFTB. The Mexican orogen encompasses the entire country, spanning several physiographic provinces and deformational domains that display both thin-skinned and thick-skinned structural styles determined by inherited crustal structure and contrasting pre-kinematic sedimentary sections. The orogen contains kinematic characteristics of both the Sevier and Laramide orogens in the United States (U.S.), and deformation in the Mexican orogen spanned the deformational history of those U.S. orogens. The overall trend of the Mexican orogen is NW-SE, although it displays local trend variations. At presently exposed levels, the orogen consists of folded and reverse-faulted Mesozoic-Eocene strata. Lower Cretaceous strata of the deformed foreland are dominated by carbonate rocks, whereas time-equivalent strata in the hinterland consist of deformed plutons belonging to one or more magmatic arcs, as well as turbidites, pillow lavas and altered mafic rocks deposited in an offshore basin prior to consolidation of fringing arc systems to mainland Mexico. Upper Cretaceous syntectonic strata of the foreland orogenic wedge constitute siliciclastic turbidite successions that grade eastward to carbonate pelagites of the distal foreland basin, which was starved of siliciclastic sediment input. Uppermost Cretaceous and Paleogene strata of the foreland basin constitute a shelfal, deltaic and coastal plain fluvial succession in northeastern Mexico and a succession of turbidites in the Tampico-Misantla basin east of the MFTB.

Structural geometry of the orogen was controlled by the spatial distribution of pre-Cretaceous crustal elements, such as Jurassic extensional basins and basement blocks, and detachment horizons at varying stratigraphic levels, as well as the direction of structural vergence, which is dominated by NE-directed tectonic transport throughout the belt. Jurassic evaporite horizons and Upper Jurassic carbonaceous shale units provide detachment surfaces in some parts of the orogen. The structural style of the MFTB is generally thin-skinned, although high-angle faults are present at several localities, where the steep faults cut thin-skinned, shallowly-dipping faults, detachment horizons and associated folds. Strain magnitude decreases toward the foreland and generally satisfies critical wedge predictions. Values of shortening >70% are present in the hinterland of central Mexico; these decrease systematically to values <15% to the front of the fold belt where upper Eocene onlap successions in the Gulf of Mexico coastal plain unconformably overlie deformed strata of the orogenic wedge. Exceptions to this pattern of regional shortening values are well documented and are related to lateral variations in mechanical properties caused by facies variations, notably massive platform carbonates as contrasted with thinly-bedded basinal carbonates.

Shortening history in the Mexican orogen approximately spanned Late Cretaceous-Eocene time. Deformation timing has been constrained using Ar-Ar systematics on illite generated by layer-parallel slip in the limbs of *chevron* folds. Estimates of deformation timing are in good agreement with the age of synorogenic sedimentary successions, and with ages of syn-tectonic plutons. Published data from central Mexico suggest episodic pulses of deformation between 93–80 Ma, 75–64 Ma and 55–43 Ma, which postdate the closure of the Arperos basin. Each

* Corresponding author at: Universidad Nacional Autónoma de México, Instituto de Geología, Av. Universidad 3000, 04510 México, D. F., Mexico
 E-mail address: elisaf@geologia.unam.mx (E. Fitz-Díaz).

of these shortening events affects rock units lying progressively farther to the east to yield a temporal eastward advance of deformation and sedimentation. Effects of successively younger shortening were superimposed on the westernmost exposures of the thrust belt and are evidenced on a map scale by abrupt trend variations in orogen-interior folds, compared to generally linear or broadly arcuate axial traces of frontal folds. Although potential tectonic mechanisms for shortening in the Mexican orogen remain debated, our analysis indicates that orogenic wedge development took place in a retroarc setting that postdated consolidation of the hinterland oceanic assemblages, which lay offshore western Mexico during Albian time. Orogen development followed a protracted period of early Mesozoic extension that affected most of the Mexico due to the combined effects of Laurentia-Gondwana separation and long-term Triassic-Jurassic rollback of a paleo-Farallon plate. Slab rollback ultimately resulted in the development of a marginal basin, the Arperos basin, between a rifted Late Jurassic magmatic arc and mainland Mexico. Initial shortening in the Mexican orogen, which followed Arperos basin closure and Guerrero superterrane accretion by ~5–10 Ma, was coeval with voluminous magmatism on the Pacific margin of Mexico, drowning of the western carbonate platforms and onset of foreland-basin sedimentation in Cenomanian time. Subduction of the Farallon slab from early Late Cretaceous to Eocene time was thus the primary driving mechanism of shortening in the Mexican orogen.

© 2017 Elsevier B.V. All rights reserved.

Contents

1.	Introduction	57
1.1.	Historical perspective: from the Sierra Madre Oriental to the Mexican fold and thrust belt.	58
1.2.	Structures vs. tectonic events	60
2.	Paleogeographic and stratigraphic synthesis of Mexico prior to development of the Mexican orogen	62
3.	Basin development in the Mexican orogen	63
3.1.	Pre-consolidation marginal-basin deposits	63
3.2.	Deformed foreland basin deposits of the MFTB	65
3.2.1.	Imbricated foreland basin deposits, MFTB	65
3.2.2.	Extant foreland basin.	66
3.3.	Chihuahua and Sabinas basins.	66
4.	Shortening deformation in the MFTB	67
4.1.	Sonora	68
4.2.	Section A-A': Chihuahua basin.	69
4.3.	Section B-B': Mesa Central-Coahuila block-Sabinas basin.	70
4.4.	Section C-C': Central Mexico basin from Zacatecas to Nuevo León.	72
4.5.	Section D-D': Central Mexico	72
4.6.	Section E-E': Morelos Guerrero platform	73
4.7.	Section F-F': Cuicateco assemblage-Veracruz basin	73
4.8.	MFTB deformation summary	73
5.	Syn-orogenic magmatism	74
6.	Timing of deformation in the Mexican orogen	76
7.	Tectonic evolution of Mexico during the Mesozoic and the development of the Mexican orogen	77
8.	Conclusions	78
	Acknowledgments	79
	References	79

1. Introduction

The Mexican orogen is the areally most extensive tectonic feature in Mexico and has a spectacular topographic expression in the Sierra Madre Oriental and the Sierra Madre del Sur (Fig. 1). Because it includes the entire Sierra Madre Oriental physiographic province, the belt has been termed the Sierra Madre Oriental orogenic belt or Sierra Madre Oriental orogen in the literature, but temporally equivalent shortening deformation in fact encompassed the entire modern crustal domain lying between the Pacific Ocean and the Gulf of Mexico. The Mexican orogen has a length of >2000 km and is hundreds of km wide along an elongate zone that extends northward from the Tehuantepec Isthmus in Oaxaca to northwestern Sonora. The structures in the foreland of the Mexican orogen have a generally NW-SE trend in central Mexico that changes to almost E-W in northeastern Mexico at the Monterrey salient and back again to NW-SE in northwestern Mexico at the Torreón reentrant (Fig. 1). To the south, the MFTB bifurcates to form two separate belts of deformation that flank the southern Mexico metamorphic terranes block, including an eastern belt that continues into the

Morelos-Guerrero platform (Fries, 1956) and a western belt that follows the Zongolica range (Fig. 1).

The Mexican orogen consists of thrust faults and folds involving Mesozoic and Paleogene sedimentary strata of eastern Mexico (de Cserna, 1956; Suter, 1984, 1987; Eguiluz de Antuñano et al., 2000; Gray and Lawton, 2011; Fitz-Díaz et al., 2014a,b; Fig. 2), and locally involves basement rocks (e.g., Chávez-Cabello, 2005; Zhou et al., 2006; Mauel et al., 2011). As in the thrust belt of the Canadian Rocky Mountains (Bally et al., 1966; Price, 1981) and the Sevier and Laramide orogens in the United States (Armstrong, 1974; Weil and Yonkee, 2012), the Mexican thrust belt (Coney, 1981; Campa, 1985) was formed on the external, foreland side of the Cordilleran orogenic system (Fig. 2), which resulted from protracted Jurassic-Paleogene subduction along the western edge of the North America plate (Coney, 1989; Oldow et al., 1989; Dickinson and Lawton, 2001; Dickinson, 2004; DeCelles, 2004; Evenchick et al., 2007). We regard the Mexican thrust belt, or Mexican fold and thrust belt (MFTB) as only the foreland part of the overall orogenic wedge that developed in Late Cretaceous-Paleogene time. A western hinterland part of the wedge occupies much of western Mexico (Fig. 1). The

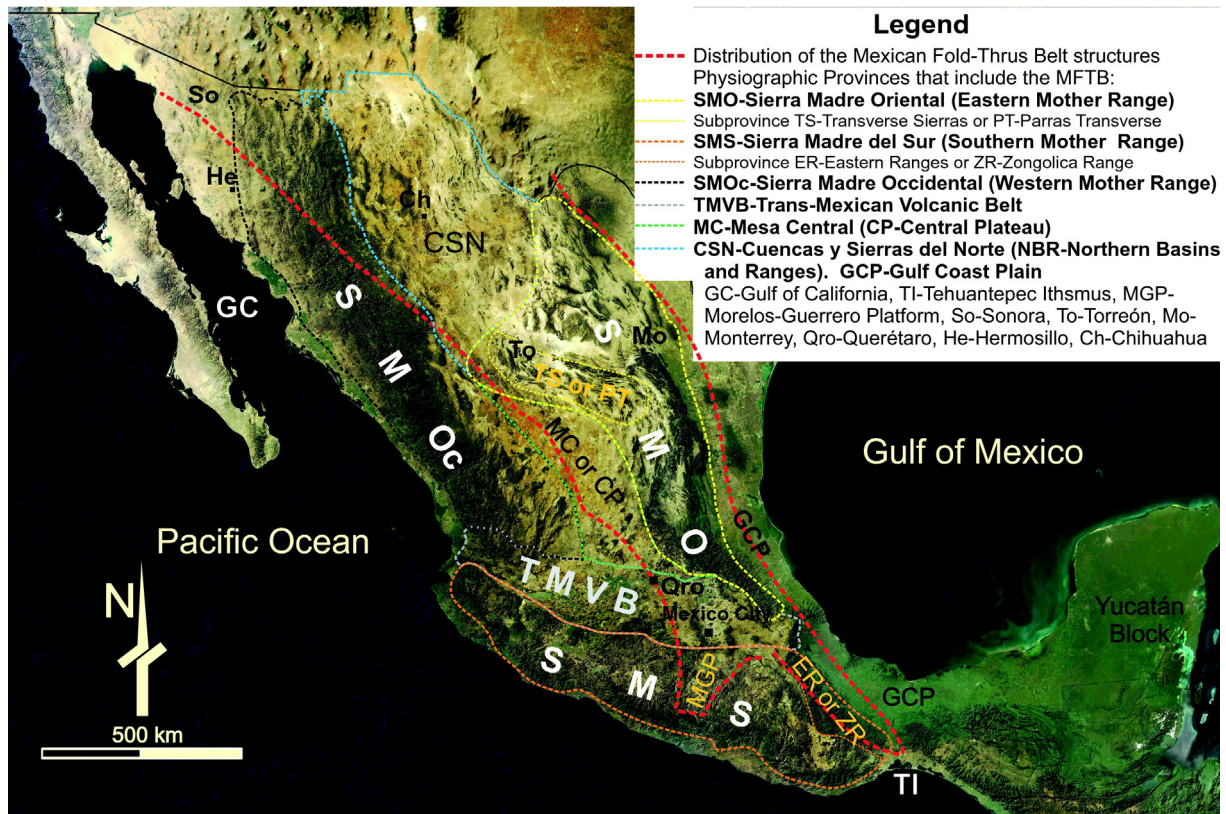


Fig. 1. Landsat image showing the distribution of the main physiographic elements of Mexico and the distribution of the Mexican fold and thrust belt (MFTB) delineated with a dashed red line. The MFTB includes the Sierra Madre Oriental, the Mesa Central and Cuencas y Sierras del Norte and Sierra Madre del Sur, and is partly intruded and covered by rocks of the Sierra Madre Occidental and of the Trans-Mexican Volcanic Belt.

hinterland is composed of young crustal elements assembled by terrane accretion (Centeno-García, 2005), arc-related magmatism (Tardy et al., 1994; Jones et al., 1995), low-grade metamorphism (Eliás-Herrera et al., 2000) and localized penetrative deformation (Salinas-Prieto, 1994; Johnson et al., 1999). Pre-orogenic rocks formed coeval with Jurassic rifting (Salvador, 1987) and Early Cretaceous drifting (Goldhammer and Johnson, 2001) in the Gulf of Mexico. The hinterland and foreland domains of the Cordilleran orogenic system in Mexico are separated by a suture of complexly deformed rocks of the Arperos basin, which opened between the Late Jurassic and the Early Cretaceous (Freydier et al., 1998; White and Busby, 1987; Almazán-Vázquez, 1988; Martini et al., 2014) and was deformed in the Albian (Johnson et al., 1999; Martini et al., 2013, 2014; Martini and Ortega-Gutiérrez, in press; Martini et al., 2016; Ortega-Flores et al., 2015).

Although we focus in this review on advances in understanding the Late Cretaceous-Paleogene deformation, syn-orogenic sedimentation and magmatism of the MFTB in the foreland of the Mexican orogen, we also consider new findings on the evolution of the Guerrero terrane in order to establish temporal and spatial connections of deformation episodes, syn-orogenic sedimentary patterns, and magmatism that permit an integrated view of tectonic processes, test existing tectonic models and support those models that consistently explain the origin and evolution of the MFTB. We define the rocks of the Guerrero volcanic superterrane (e.g., Dickinson and Lawton, 2001), or simply Guerrero terrane, which have debated affinity to continental basement of Mexico by virtue of their oceanic character, to constitute the hinterland of the Mexican orogen.

This review also offers a perspective on how knowledge regarding the MFTB has built up through time, as well as on knowledge of different aspects of the tectonic evolution of Mexico that might have influenced the development of the MFTB, including the post-Pangea crustal architecture of Mexico and Mesozoic paleogeography and stratigraphy, Late

Cretaceous-Paleogene deformation patterns, timing of deformation in the MFTB, syn-orogenic sedimentation, opening and evolution of the Arperos-Alisitos basin and subsequent accretion of the Guerrero terrane, as well as arc-related magmatism and subduction dynamics on the Pacific flank of Mexico. We also compare the parallelism of deformation processes in the hinterland and foreland Cordilleran domains (Guerrero terrane and MFTB, respectively) and review tectonic models to explain the formation of the MFTB. In particular we address four key points:

1. The architecture of Mexican fold and thrust belt, and the influence of inherited paleogeographic elements on Late Jurassic-Paleogene stratigraphy and deformation patterns;
2. Spatial and temporal relations of deformation and sedimentation;
3. Evolution of subduction-related magmatism within the MFTB;
4. A review of tectonic models that integrally explain deformation propagation, magmatism and foreland basin migration within a broad paleotectonic framework that integrates the Guerrero terrane, the Arperos-Alisitos basin and the MFTB.

1.1. Historical perspective: from the Sierra Madre Oriental to the Mexican fold and thrust belt

Prior to the 1950s and into the 1960s, most geological studies in Mexico were focused on mining exploration and definition of regional stratigraphy (e.g., Baker, 1922; Kellum, 1930; Imlay, 1936; King, 1944; Rogers et al., 1961). Only a few pioneer studies were dedicated to describing structures of the Sierra Madre Oriental in NE Mexico (e.g., Böse, 1923; Kellum et al., 1936; Heim, 1940; Álvarez, 1949). Because many of these studies were carried out by geologists from the U.S., a connection or continuity of structures of the Sierra Madre Oriental to structures farther north was suggested (e.g., Humphrey, 1956).

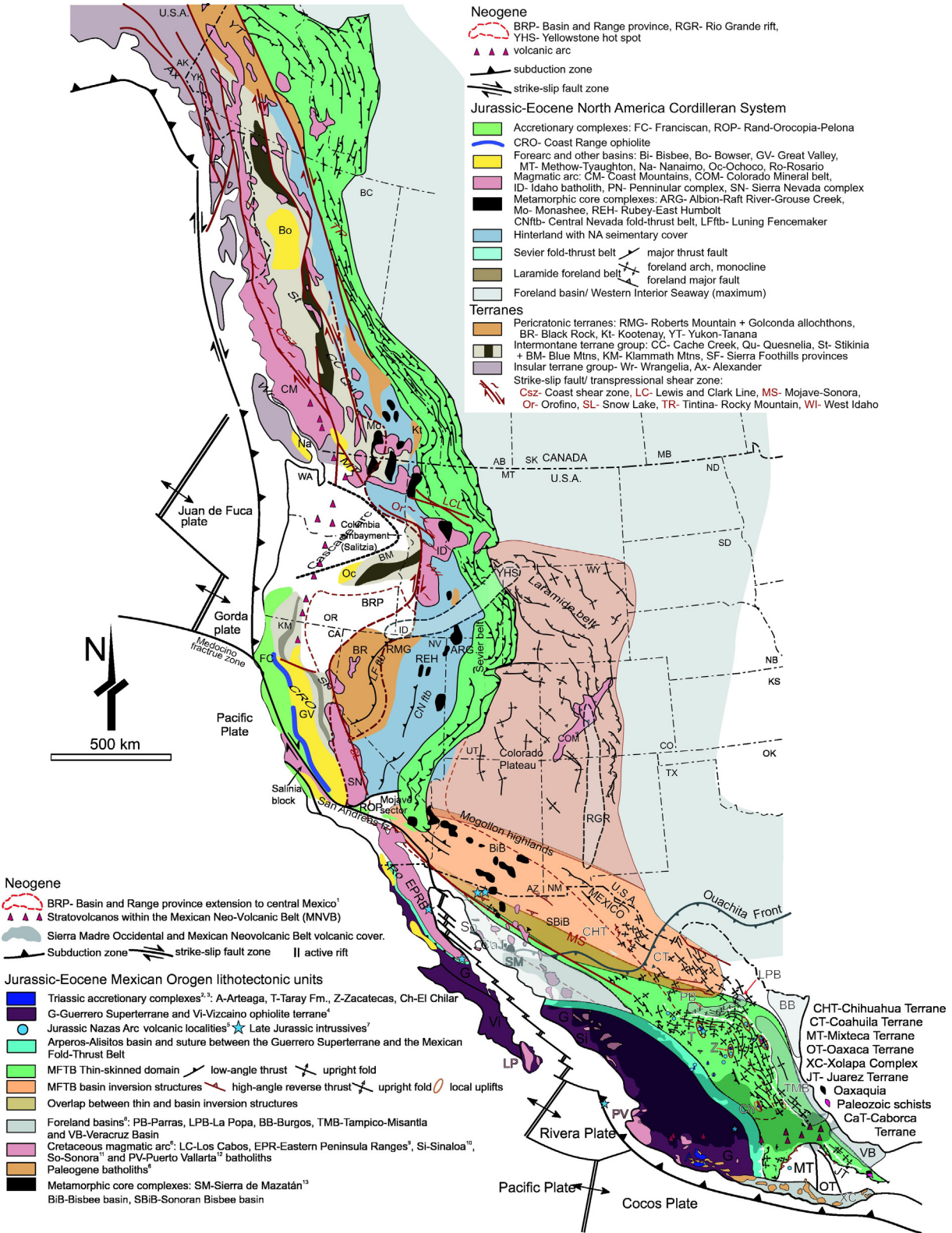


Fig. 2. The North American Cordilleran system, including the Mexican orogen, adapted from Yonkee and Weil (2015). The map includes current distribution of major tectonic elements of the cordilleran orogenic system in Mexico, including Triassic-Jurassic? accretionary complexes, forearc basins, backarc suture basin in Mexico (Arperos basin), hinterland magmatic arc (Guerrero terrane), hinterland metamorphic core complexes, Sevier fold-thrust belt, Laramide foreland belt, and overlap of thin-skinned and thick-skinned domains on the Mexican fold-thrust belt and foreland basins in Mexico. Details of the U.S.-Canada area available in Yonkee and Weil (2015). Major frontal thrusts of the MFTB are indicated with white lines with triangular barbs. References: ¹Aranda-Gómez and Mcdowell, 1998, ²Centeno-García, 2005; ³Barboza-Gudiño et al., 2010, ⁴Campa and Coney, 1983, ⁵Jones et al., 1995; Ortega-Gutiérrez et al., 2014, ⁷Martini and Gutiérrez, 2016a, Martini et al., 2016b, ⁸Goldhammer, 1999; ⁹Walawender et al., 1990, ¹⁰Henry et al., 2003, ¹¹Ramos-Velázquez et al., 2008, ¹²Schaaf et al., 2003, ¹³Wong and Gans, 2008. The distribution of thin-skinned and thick-skinned structures near the Mexico-USA border considers works by Pubellier et al. (1995) and Lawton (2000, 2008).

The first classic work on the Sierra Madre Oriental by Zoltan de Cserna (1956) presented a map, detailed structural cross-sections, and a kinematic interpretation of folds and thrusts of a broad area that included the Monterrey salient and the Parras transverse sector between Monterrey and Torreón (Fig. 1). De Cserna later included these features in the first tectonic map of Mexico (de Cserna, 1961) and framed the patterns of deformation in a broader tectonic context (Guzman, 1963). Guzman and de Cserna (1963) also applied the term, “Mexican structural belt,” to a group of structures in eastern Mexico formed between the Late Jurassic and Pliocene, and proposed the term, *Hidalgoan orogeny*, for an early Eocene shortening event, which they correlated with the Laramide orogeny.

The 1960s and 1970s saw more modern structural studies and kinematic interpretation of the MFTB. Carrillo-Bravo (1961, 1965, 1971) contributed iconic works on stratigraphy and structure of the MFTB in central Mexico. Mark Tardy (Tardy et al., 1975; Tardy, 1980) revised the geology of the Sierra Madre Oriental in the Mesa Central and Monterrey salient, and applying concepts of Alpine geology, analyzed the effect of pre-orogenic basin architecture on deformation styles of the region.

In the 1980s, with significant advances in understanding of Cordilleran tectonics, Campa and Coney (1983) divided the Mexican territory into tectono-stratigraphic terranes and defined the Sierra Madre terrane as: “...a sequence of folded and imbricated thrust-faulted upper Mesozoic limestones, shale, and sandstone layers of the superjacent Gulf of Mexico transgressive sequence deformed during the Late Cretaceous-early Tertiary Laramide orogeny.” Mesozoic strata were inferred to overlie a succession of Paleozoic sedimentary and metamorphic units with a Precambrian basement in this terrane. Campa (1985) pointed out that the Mexican thrust belt also includes parts of adjacent tectono-stratigraphic terranes, including the Juárez, Mixteco, Coahuila and Chihuahua terranes. Campa (1985) considered the Mexican thrust belt as a transposed tectonic element emplaced at the border between the Guerrero terrane to the west and the eastern autochthonous foreland terranes of Mexico, in the Cordilleran orogenic system.

The 1990s saw continued growth in general understanding of MFTB structural geology and kinematics. As the result of regional mapping projects, Suter (1990) and Carrillo-Martínez (1997) generated remarkable advances in understanding the MFTB in central Mexico (Suter, 1984, 1987, 1990; Carrillo-Martínez, 1989, 1990); through their work, this is probably the best known part of the MFTB. Padilla y Sánchez mapped and analyzed the geometry of structures of the Monterrey salient (Padilla y Sánchez, 1982, 1985). Based in part on this mapping, Marrett and Aranda-García (1999) interpreted the structures of the Monterrey salient and central Mexico in light of advances on kinematic models of structures in fold-thrust belts, and of the orogenic wedge theory. Eguiluz de Antuñano et al. (2000) likewise presented an integrated review of the tectonics of the Sierra Madre Oriental that synthesized published and unpublished data by PEMEX on stratigraphy and large-scale structure of the belt.

Since 2000, studies have focused on understanding kinematics and tectonics (Salinas-Prieto et al., 2000; Ortuño-Arzate et al., 2003; Zhou et al., 2006; Nieto-Samaniego et al., 2006; Alzaga-Ruiz et al., 2009; Roure et al., 2009; Fischer et al., 2009; Fitz-Díaz et al., 2008; Fitz-Díaz et al., 2011a, González-León et al., 2012; Martini et al., 2013), sedimentation (Hernández-Romano et al., 1998; Giles and Lawton, 1999; Lawton, 2008; Lawton et al., 2009; Gray and Lawton, 2011; Ocampo-Díaz et al., 2016), magmatism (González-León et al., 2000, 2011; Valencia-Moreno et al., 2001; Chávez-Cabello, 2005; Cerca et al., 2007; Ramos-Velázquez et al., 2008; Martini et al., 2009), fluid-rock interaction and thermal structure (Gray et al., 2001; Fischer et al., 2009; Ferket et al., 2003; Fitz-Díaz et al., 2011b; Nemkin et al., 2015) and timing and propagation of deformation (Gray et al., 2001; Gray and Lawton, 2011; Cuéllar-Cárdenas et al., 2012; Fitz-Díaz and van der Pluijm, 2013; Fitz-Díaz et al., 2014a,b; Heller and Liu, 2016) along specific transects or areas of the thrust belt. This manuscript is based on a

review of classic and recent publications to produce an updated overview of the MFTB.

1.2. Structures vs. tectonic events

The term, “fold-thrust belt” is a concept in structural geology that describes a province, generally of significant topography, dominated by shortening structures (folds and thrusts) affecting stratified rocks at very low metamorphic facies to surface conditions. Such belts lie on the continental, or foreland, edges of wider orogenic belts. Because of the belt’s proximity to the surface, deformation, erosion and sedimentation are interacting processes in fold-thrust belts (Dahlstrom, 1970; Chapple, 1978; Price, 1981; Beaumont, 1981; Beaumont et al., 1992; McClay, 1992; DeCelles, 1994; Lawton, 2008) and advances in orogenic wedge numerical models have illustrated the intimate feedback relationships among these processes (Willet, 1999; Stockmal et al., 2007; Cruz et al., 2010); nevertheless, deformation, magmatism and metamorphism are dominant processes in the internal, hinterland part of orogenic belts in the vicinity of plate boundary (Monger et al., 1982; Barton and Hanson, 1989; Brown, 1993).

For the foreland orogenic wedge, we use a slight modification of the term, Mexican thrust belt, proposed by Campa (1985) because it perfectly suits the topical content of this review. The Mexican fold thrust belt, as defined here (Fig. 1), constitutes a widespread geographic province distributed along a mountainous fringe from southern Oaxaca to Sonora (Fig. 1). The belt includes all shortening structures involving Mesozoic sedimentary units, and locally basement rocks that were formed in the Late Cretaceous-Paleogene in the Mexican foreland of the Cordilleran orogenic system. We add the word “fold”, to the term “Mexican Thrust Belt” of Campa (1985) because a significant portion of this belt is dominated by folds that are unrelated to thrusts (Fitz-Díaz, 2010; Fitz-Díaz et al., 2011a, 2012), which is a characteristic style in Mexico and is different from the thrust belt style of the Rocky Mountains, which is dominated by thrusts (Bally et al., 1966; Armstrong, 1968; Price and Farmor, 1985). The MFTB includes thin-skinned and thick-skinned structures, which are represented in two domains, green and light orange in map of Fig. 2, with an overlap among them in pale brown. The Sevier and Laramide belts of the U.S. are also mapped with similar colors, respectively.

The Sevier belt or Sevier orogen is distributed along a sinuous band on the western side of the Colorado Plateau in the southwestern U.S. (Fig. 2; Armstrong, 1968) and western Canada (Price and Farmor, 1985). The Sevier orogen consists of folds and thrusts that in cross-section are confined within an orogenic wedge tapering to the east (Fig. 2 in Weil and Yonkee, 2012). The age of deformation in this belt took place between the Hauterivian and early Eocene (see Fig. 12 and references in Yonkee and Weil, 2015) and crustal shortening has been attributed to an increase in convergence rates between the North American plate and subducting Farallon oceanic plate from the Jurassic to the Early Cretaceous. It has been speculated that the rate of trench rollback was likely lower than the rate of the overriding North American plate motion, thus causing convergence of the subduction hinge, with intraplate shortening and development of the Sevier belt as a consequence (DeCelles, 2004; Fig. 6B–D, in Yonkee and Weil, 2015).

Coney (1976) defined the Laramide orogen on the basis of deformation style and time of formation between Maastrichtian and middle Eocene (Dickinson et al., 1988; DeCelles, 2004). The faults in the Laramide province are typically high-angle reverse faults with 10s of km of along-strike extent that accommodate significant vertical displacements, involve basement rocks, and are commonly associated with km-scale drape folds (Friedman et al., 1976; Figs. 5D and 6D of Yonkee and Weil, 2015). Despite contrasting styles of deformation, there is substantial temporal overlap of shortening in the Sevier and Laramide belts. In central Utah, displacement along low-angle thrusts at the front of the thrust belt continued until middle to late Eocene time and thus temporally overlapped the main phase of basement deformation that occurred

farther to the east (Lawton and Trexler, 1991; Lawton et al., 1993). Moreover, as Lawton (2008) pointed out “basement-involved disruption of the orogenic foreland never did take place in the Canadian Cordillera; therefore, the temporal definition of the Laramide orogeny is an artificial construct in Canada.” In addition to basement-cored uplifts of the Colorado Plateau (Davis, 2009), thick-skinned structures are also present in California, Arizona, New Mexico, and extend into the states of Sonora, Chihuahua and Coahuila in northern Mexico (Fig. 2; Drewes, 1988; Hennings, 1994; Pubellier et al., 1995; Jacques-Ayala, 1999; Jacques Ayala et al., 2009; Lawton, 2008; Haenggi, 2002; Chávez-Cabello, 2005). The development of crustal-scale basement-involved structures has been associated with an increase in basal traction as a consequence of flat-slab subduction (Dickinson and Snyder, 1978; Jordan and Allmendinger, 1986), or subduction of thick, buoyant oceanic plateaus (Liu et al., 2010).

Due to the trend of structures of the MFTB and their continuity to the north, they have historically been related to the Laramide orogeny (Humphrey, 1956; De Cserna, 1956; Campa and Coney, 1983; Eguiluz de Antuñano et al., 2000; Nieto-Samaniego et al., 2006; Cerca et al., 2007; Cuéllar-Cárdenas et al., 2012), regardless of their deformation style or timing (Coney, 1976). In Fig. 2 we use the same color for thin-skinned structures in the MFTB as for those in the Sevier belt on the basis of kinematic affinity, and the thick-skinned structures have a

similar color to the Laramide province. This does not necessarily imply that the thin-skinned structures of the MFTB were formed during the Sevier orogeny or that the thick-skinned features were formed during the Laramide orogeny. In fact, we now know that the thin-skinned structures of the MFTB are younger than most of the Sevier structures. Thick-skinned structures in northern Mexico, on the other hand, in general correspond better in space, time and style with Laramide structures. Most thick-skinned structures of the MFTB in northern Mexico are flanked by reactivated normal faults, previously active during the formation and subsidence of Middle Jurassic–Early Cretaceous sedimentary basins (e.g., Bisbee, Chihuahua and Sabinas basins, Fig. 3), which presumably formed as a consequence of the opening of the Gulf of Mexico and were later inverted (Mckee et al., 1990; Lawton, 2000; Haenggi, 2001, 2002; Mael et al., 2011; Chávez-Cabello, 2005).

In the absence of detailed kinematic studies, age or specific data about their origin, most shortening structures within the MFTB of general Late Cretaceous–Paleogene age, irrespective of geographic location, or their thin- or thick-skinned style, have been interpreted as part of the Laramide orogen. We believe that this indiscriminate correlation is inappropriate for most structures in the MFTB, which, although dominantly thin-skinned, include a variety of structural styles. Moreover, although the Sevier, Laramide and MFTB orogens all lie in the foreland of the Cordilleran orogenic system, the geodynamics along the western

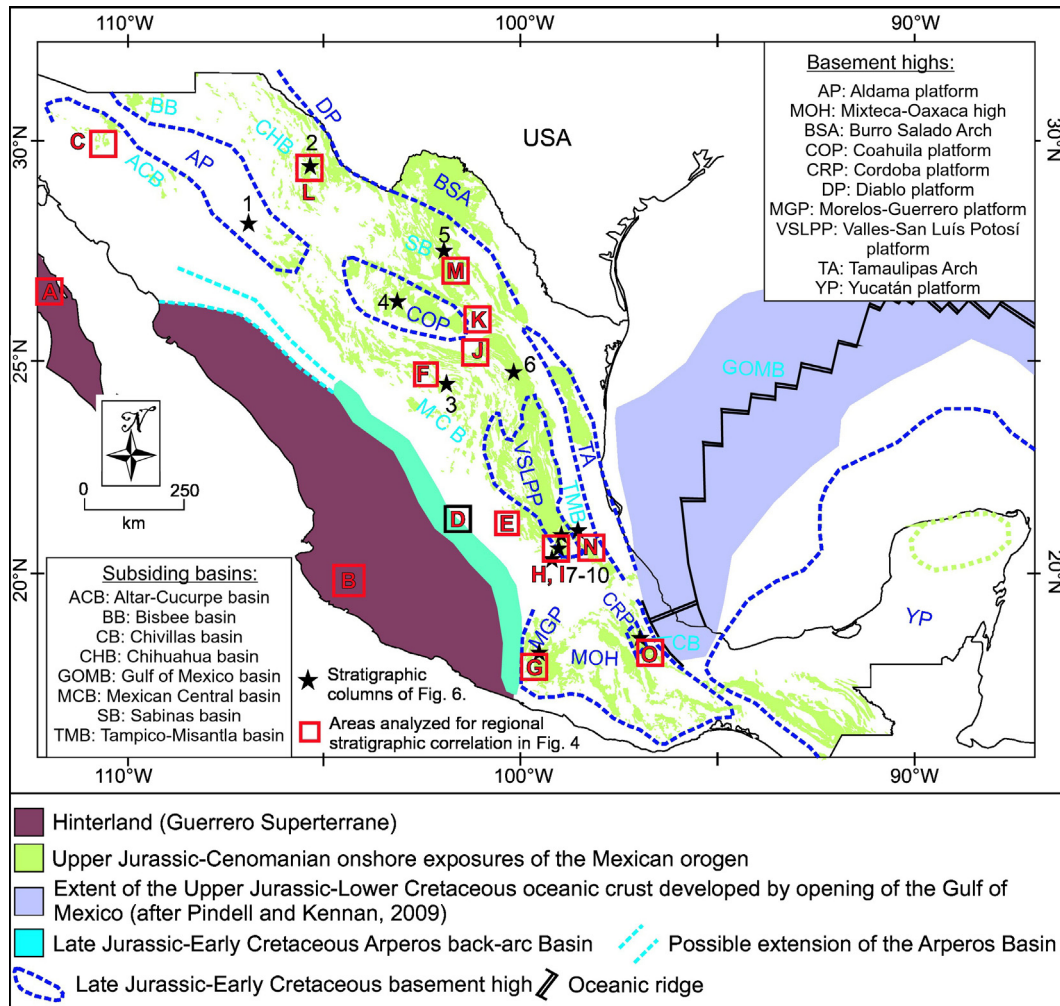


Fig. 3. Modified geologic map of Fig. 10 in Martini and Ortega-Gutiérrez (in press) showing the location and extension of the Late Jurassic–Cenomanian stratigraphic successions developed during the drift and cooling stage. The distribution of shallow and deep marine successions developed on basement highs and subsiding basin, respectively, are differentiated in the map. We use this figure as a reference for Cretaceous platforms and basins, for which the stratigraphic columns in Figs. 4 and 5, were synthesized. The authors of this figure recomplied exposures of the Late Jurassic–Cenomanian successions from the available 1:250'000 maps of the Servicio Geológico Mexicano, as well as from Suter (1987), Carrillo-Martínez (1989), McKee et al. (1990), Lehmann et al. (1999), Silva-Romo et al. (2000), Haenggi (2002), Humphrey and Díaz (2003), López-Doncel (2003), Cerca et al. (2007), Barboza-Gudiño et al. (2010), Mendoza-Rosales et al. (2010), García Barragán and Jacques-Ayala (1999).

margin of North America were so variable, in both time and space (Hildebrand, 2009), that it would be impossible that all thrust belts were formed in the same tectonic scenario, especially considering the great length of the belt. In addition, continental-arc magmatism accompanied the entire time span of deformation in Mexico, as reviewed below, whereas the Laramide orogeny of the U.S. was largely amagmatic (e.g. Dickinson and Snyder, 1978). For the above reasons, we propose redefinition of the Late Cretaceous–Eocene deformed belt in all its structural variability as the Mexican orogen. For instance, the accretion to Mexico of the Guerrero superterrane is restricted to western Mexico, yet Guerrero rocks were the source of much of the sediment in the foreland basins.

Finally, the Laramide orogeny may have a tectonic cause related to distribution of crustal heterogeneities in the Farallon slab. Recent inverse convection models (Liu et al., 2010) have suggested that the timing and distribution of thick-thinned Laramide deformation resulted from the passage of a conjugate of the Shatsky oceanic plateau under the southwestern U.S. between 90 and 68 Ma, while its companion, the conjugate Hess oceanic plateau, passed under northern Mexico later, from 65 to 50 Ma ago. In summary, preserved evidence in the crust and poorly preserved evidence from the subducting plates deciphered from inverse convection models (Liu et al., 2010; Liu and Stegman, 2011) support the idea that the Mexican orogen has sufficient structural variation and potentially different tectonic drivers to warrant its consideration as a separate entity, distinct from its northern counterparts in the Cordilleran orogenic system.

2. Paleogeographic and stratigraphic synthesis of Mexico prior to development of the Mexican orogen

Most post-Proterozoic basement rocks in Mexico were added to older Precambrian basement rocks on the southern edge of the North American continent in northwestern Mexico (Ruiz et al., 1988) or to Oaxaquia (Ortega-Gutiérrez et al., 1995), a suite of Grenville age granulites also known as the Middle American terrane (Keppie and Ortega-

Gutiérrez, 2010), during the progressive assembly of Pangea in the Paleozoic (Poole et al., 2005; Ortega-Gutiérrez et al., 2003). Precambrian and Paleozoic metamorphic and magmatic rocks are classified as basement rocks and are indicated with the same pattern for simplification in stratigraphic columns as indicated in Table 1.

The subsequent history of the breakup of Pangea, the persistent subduction on the western margin of Mexico and the opening of the Gulf of Mexico deeply influenced the Mesozoic paleogeography and stratigraphy of Mexico, as described by Martini and Ortega-Gutiérrez (in press). Following the Gondwana-Laurentia collision along the Ouachita belt (Viele and Thomas, 1989; Poole et al., 2005), and the emplacement of plutons of the Permo-Triassic arc (Torres et al., 1999, drawn in pale purple in the cross-sections, as indicated in Table 1), Pangea experienced a stage of thermal doming in northeastern Mexico and southeastern U.S. in the Late Triassic (Dickinson et al., 2010). During the uplift, a gigantic volume of siliclastic detritus was transported from the dome toward the continental margin of western Mexico, where it is recorded by deposits of quartz-rich sandstone interbedded with phyllite in the fluvial El Alamar Formation and the Zacatecas Formation, which represents deposits of the Potosi submarine fan (Centeno-García and Silva-Romo, 1997; Barboza-Gudiño et al., 2014). Finer-grained deposits with similar populations of detrital zircons are exposed in central Mexico in El Chilar complex (Ortega-Flores et al., 2014), and as far south as the state of Michoacán, on the western margin of Mexico, in the Arteaga complex (Centeno-García, 2005), providing a perspective of the extent of this enormous depositional system that covered both the future foreland and hinterland of the Cordilleran orogenic system. These units are drawn in purple in the cross-sections and stratigraphic columns.

In Early to Middle Jurassic time, felsic volcanic rocks were locally emplaced in central Mexico in the vicinity of the Mesa Central, presumably during the development of the Nazas volcanic arc, related to subduction of the Farallon plate on the Pacific margin of Mexico (Jones et al., 1995; Torres et al., 1999; Bartolini et al., 2003); nevertheless, detailed stratigraphic analyses of these deposits suggest they are

Table 1

Color code of the lithotectonic groups represented in stratigraphic columns of Figs. 4 and 6 and cross-sections of Fig. 8. Lithology and tectonic environment during deposition constitute criteria for defining lithostratigraphic groups.

Color code	Lithostratigraphic groups
	Quaternary alluvial and colluvial deposits.
	Neogene clastic deposits of the Gulf of Mexico coastal plain.
	Paleogene intrusions (syn-or post-tectonic if they cross-cut structures).
	Paleogene marine synorogenic deposits along the Gulf of Mexico plain.
	Paleogene redbeds overlying Upper Cretaceous turbidites or shallow marine deltaic deposits.
+ + +	Upper Cretaceous intrusive rocks (syn or post tectonic if cross-cut structures).
.....	Upper Cretaceous shallow marine deltaic deposits.
-----	Upper Cretaceous synorogenic turbidites.
	Deepwater carbonate units deposited from Late Jurassic through Early Cretaceous time, during the drift period of the Gulf of Mexico.
	Shallow water carbonates deposited from the Late Jurassic through the Early Cretaceous, during the drift period of the Gulf of Mexico.
	Volcanic and volcanoclastic rocks deposited in and adjacent to the Arperos basin and the Alisitos arc during Late Jurassic and Early Cretaceous time.
^ ^ / - -	Middle to Upper Jurassic evaporites and carbonaceous shale.
	Clastic marine deposits formed during the opening of the Gulf of Mexico.

dominated by felsic volcanoclastic rocks, rather than volcanic deposits and only in Sonora and the southwestern U.S. are caldera-like structures and Lower to Middle Jurassic granitoids preserved (Lipman and Hagstrum, 1992; Riggs et al., 1993; Anderson et al., 2005a,b). These rocks are indicated in sky blue (Table 1) and seem to be present in both the hinterland and foreland of the Mexican orogen (Ortega-Flores et al., 2015).

Adjacent to eastern Mexico, rifting in the Gulf of Mexico began somewhat later in the Middle Jurassic (Ross and Scotese, 1988; Pindell and Kennan, 2009). The *horsts* and *grabens* formed during the rifting stage controlled the distribution of onshore Mexico evaporites and redbeds (inverted-v pattern and pale blue, respectively in cross-sections and columns, see Table 1) that filled the nascent basins. Carbonate platformal (bright green) and basinal facies (dark green) were deposited atop basement highs and within structural lows, respectively, during subsequent drifting stage of the Gulf of Mexico from the Late Jurassic to the Cenomanian (Fig. 3; Wilson, 1990; Goldhammer, 1999).

In the Guerrero terrane, volcanism and plutonism were the dominant Late Jurassic–Early Cretaceous geologic processes, as intra-arc basins and the backarc Arperos basin filled with deepwater volcanoclastic sediments, in part including the Mezcalera Formation (Eguiluz de Antuñano and Campa, 1982) for most of the Early Cretaceous. In the correlation table (Fig. 4) we include composite stratigraphic columns of the Guerrero terrane because its position in the hinterland of the Cordilleran orogenic system influenced formation of the MFTB, and the basement rocks of the Guerrero terrane were an important source of sediments in the synorogenic foreland basin. Thus, deformational episodes in the Guerrero terrane, evident as depositional hiatuses in the stratigraphic column, can be related to episodes of sedimentation to the east. We therefore use no color code for units in the Guerrero terrane, but rather emphasize intervals marked by hiatuses.

Near the end of the Early Cretaceous, emplacement of magmatic rocks into the Guerrero terrane dominated the tectonics of the western margin of Mexico; however, carbonate and clastic deposits, which include a thick interval of redbeds, also accumulated in the hinterland (Altamira-Areyan, 2002). In the foreland to the east, synorogenic turbidites were deposited and preserved to form a record of foreland-basin development from late Cenomanian through Maastrichtian time (pale green in stratigraphic columns of Fig. 4). These turbidites are overlain by fluvial deposits (orange) on the western side of the MFTB and by clastic marine deposits (salmon colored) on the eastern edge of the belt. Around the Gulf of Mexico margin, Neogene clastic deposits that overlie the Paleogene strata are indicated in yellow in the cross sections. Finally, we also include thick Quaternary alluvial and colluvial deposits in pale yellow.

The color code of Table 1 allows us to establish stratigraphic correlations across Mexico, and is used in the cross-sections in order to calibrate tectonostratigraphic relations and illustrate the mechanical stratigraphy of the MFTB.

3. Basin development in the Mexican orogen

The stratigraphic record of the Mexican orogen can be divided into two major tectonostratigraphic assemblages, which include (1) an assemblage of deep water strata and mafic volcanic rocks deposited in an offshore basin or basins prior to accretion of the Guerrero terrane, and (2) syntectonic strata deposited in a foreland basin that developed adjacent to the orogenic wedge. We term the former assemblage, which constitutes the fill and basement of the Arperos basin, *pre-consolidation marginal-basin deposits*. These rocks were formed prior to shortening in the orogen and were subsequently thrust over the continental margin to form a pervasively deformed suture zone between the Guerrero terrane and deformed Paleozoic to Mesozoic rocks on the flank of the Proterozoic core of eastern Mexico. The latter deposits, which formed adjacent to an orogenic wedge, which began to develop after the accretion of Guerrero, are termed simply the *foreland basin fill*.

3.1. Pre-consolidation marginal-basin deposits

The combined effects of Laurentia–Gondwana separation and long-term Triassic–Jurassic retreat or rollback of a paleo-Farallon plate ultimately resulted in the development of the Arperos basin, a marginal basin between a rifted Late Jurassic magmatic arc and mainland Mexico. The Arperos basin spanned an imprecisely defined time interval, but published data suggest that the basin developed between Late Jurassic and Early Cretaceous time (Lapierre et al., 1992; Freydiep et al., 1996; Ortíz-Hernández et al., 2003; Martini et al., 2011). The Arperos Formation (Late Jurassic–Early Cretaceous) consists of highly deformed flysch-like detrital strata and volcanic rocks (Ortíz-Hernández et al., 2003; Martini et al., 2011). Less deformed parts of the Arperos Formation are composed of rhythmic interbeds of fine- to coarse-grained sandstone, gray to black siltstone, claystone, and uncommon cherty and calcareous shale that rest conformably on pillow lavas, diabasic dikes, and volcanic-lithic turbidites (Ortíz-Hernández et al., 2003; Martini et al., 2011). Volcanic-lithic turbidites of the informal Cuestecita formation were originally included in the Arperos Formation by Martini et al. (2011), but reassigned to the Cuestecita formation on the basis of field relations (Martini et al., 2012; Figs. 4, 5).

Following closure of Arperos basin and collision of the Guerrero terrane with mainland Mexico, the volcanic arc rocks and siliciclastic strata of the basin were buried by Upper Cretaceous sedimentary successions, such as the Mexcala and La Escondida formations (Fig. 4) deposited along the western margin of the MFTB (e.g., de Cserna, 1976; Ortíz-Hernández et al., 2003; Palacios-García and Martini, 2014; Ortega-Flores et al., 2015). La Escondida phyllite is a foliated siliciclastic unit exposed in the western part of Sierra de Zacatecas. The unit consists of thin to medium beds of alternating fine- to medium-grained metasandstone interbedded with gray phyllite (Ortega-Flores et al., 2015).

Detrital zircon ages of strata deposited in the Arperos basin are distinctive and permit their discrimination from subsequent foreland basin deposits derived from the orogenic wedge. The dominant detrital-zircon age component in the Cuestecita formation consists of Late Jurassic–Early Cretaceous grains (64%; 160 of 250 analyses; Martini et al., 2012). Older Proterozoic grains, characteristic of basement rocks in southwestern Laurentia, are absent (Fig. 5). A main age peak at ~132 Ma and continuously distributed grain ages between ~156 and 117 Ma, in combination with a volcanic-lithic composition, are compatible with derivation from the Alisitos arc developed on the Guerrero terrane. No sources of this age range are known to be present on the eastern side of the suture zone. The young grains yield a calculated maximum depositional age of 120 ± 1 Ma (middle Aptian; Fig. 5). Like the Cuestecita formation, La Escondida phyllite contains a prominent component of Early Cretaceous ages with a prominent age peak at ~136 Ma, and a component of Late Jurassic grains, both of which can be attributed to magmatic rocks of the Guerrero terrane. Nevertheless, Ortega-Flores et al. (2015) inferred, from the presence of Grenvillian (~1.3–1.1 Ga) and pan-African (~700–550 Ma) zircon age components and a quartzose composition, that La Escondida phyllite also contains recycled detritus from the Mexican mainland, and thus represents an eastern petrofacies of the Arperos basin. The young grains yield a calculated maximum depositional age of 110 ± 2 Ma (Albian; Fig. 5). In summary, detrital zircon ages from deposits on both flanks of the Arperos basin suggest that deposition in the basin, which was closely linked to an active arc, appears to have been finished by late Early Cretaceous time. We regard La Escondida phyllite and Cuestecita formation as an important record of deposition within the Arperos basin, which was deformed during formation of the suture boundary between the Guerrero terrane and mainland Mexico. Subsequent to deformation during the closure of the marginal basin, the basinal rocks constituted part of the hinterland of the eastward-migrating orogenic wedge.

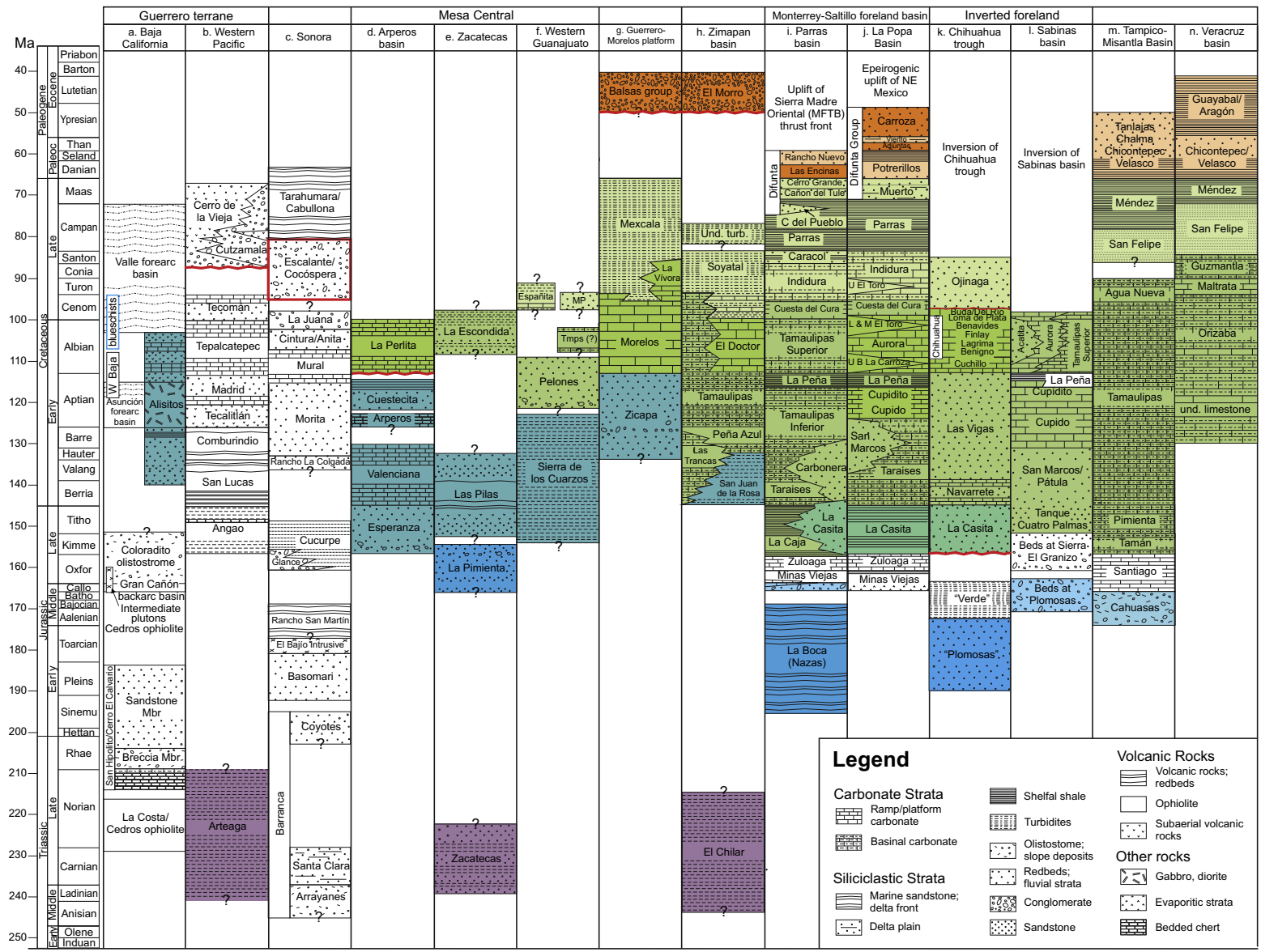


Fig. 4. Correlation chart of the Mesozoic and Cenozoic stratigraphy from selected areas of the hinterland and foreland of the MFTB. This table shows the simplified correlation of the main lithotectonic units as indicated in Table 1. Columns located in western and northwestern Mexico complete the geologic framework (Fig. 3), but the uncolored units are not included on cross sections of Fig. 8. Columns of the **Guerrero Terrane** or MPSM include: Vizcaíno Peninsula (Busby-Spera, 1988; Boles and Landis, 1984; Johnson et al., 1999; Kimbrough and Moore, 2003; Busby, 2004; Payne et al., 2004; Carreño and Smith, 2007); Western Pacific (Pantoja-Alor and Estrada-Barraza, 1986; Guerrero-Suástegui, 1997; Omaña-Pulido, 2012; Martini et al., 2009; Centeno-García et al., 2011). **Sonora:** (González-León and Lawton, 1995) and **Mesa Central:** Arperos (Lapierre et al., 1992; Freyrier et al., 1996; Ortiz-Hernández et al., 2003; Martini et al., 2011; Martini et al., 2012; Martini et al., 2014); Zacatecas (Escalona-Alcázar et al., 2009, 2014; Ortega-Flores et al., 2015) and Western Guanajuato (Palacios-García and Martini, 2014; Martini and Gutiérrez, 2016a; Martini et al., 2016b; Juárez-Arriaga et al., 2016a). **Guerrero-Morelos platform** (Fitz-Díaz, 2001; Sierra-Rojas and Molina-Garza, 2014). **Zimapán basin** (Ortega-Flores et al., 2014; Juárez-Arriaga et al., 2016a; Juárez-Arriaga et al., 2016b). **Monterrey-Salttillo foreland basin:** Parras basin (McBride et al., 1974; Lawton et al., 2009). La Popa basin (McBride et al., 1974; Lawton et al., 2009). **Inverted foreland:** Chihuahua Trough (Haenggi, 2002; Eguiluz-de Antuñaño, 2011); Sabinas basin (Haenggi, 2002; Eguiluz de Antuñaño, 2001; Eguiluz-de Antuñaño, 2011). **Tampico-Misantla basin** (Suter, 1987; Fitz-Díaz et al., 2012). Finally, the **Veracruz basin** (Ortuño-Arzate et al., 2003).

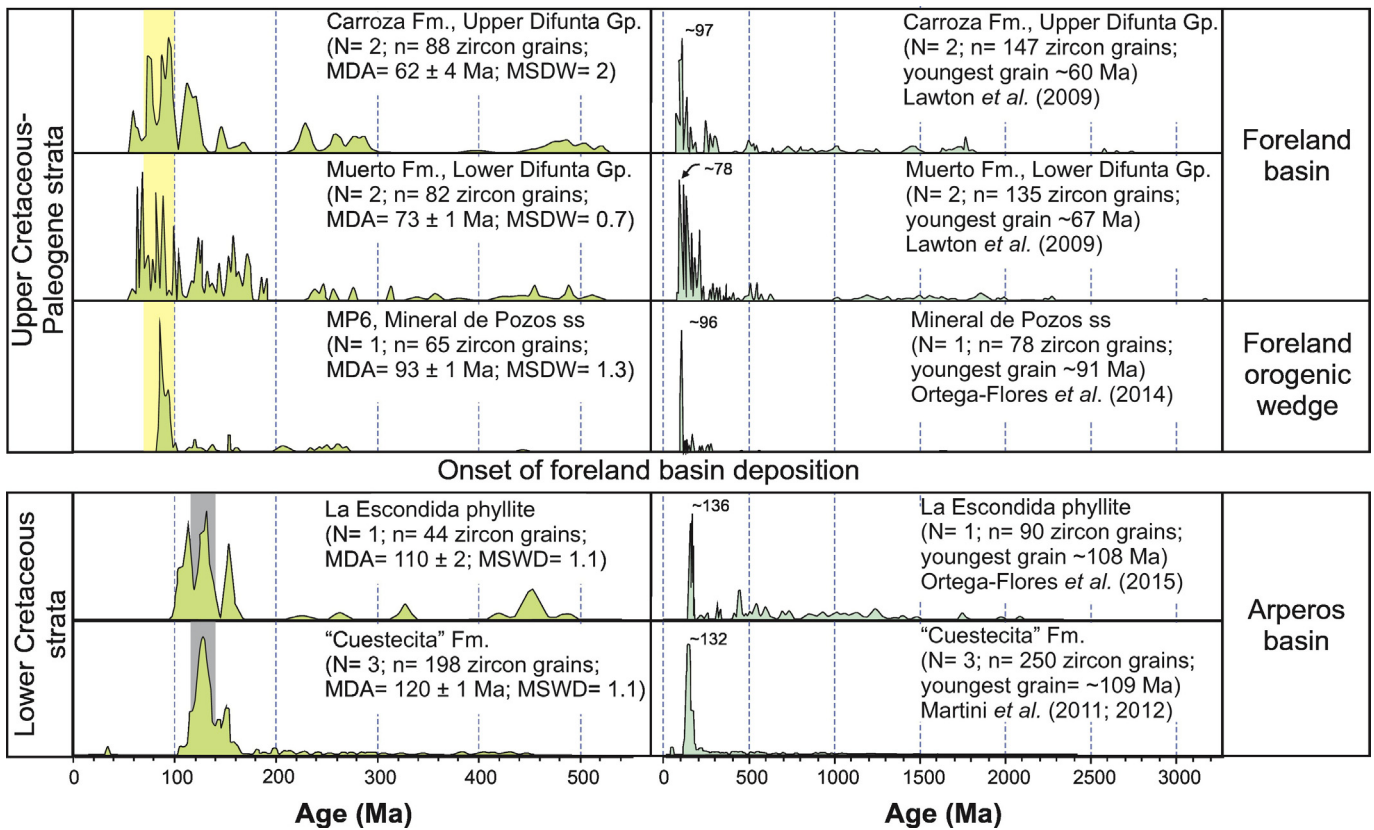


Fig. 5. Comparison of detrital zircon relative age-probability curves from selected localities (see Fig. 7 for location of samples). Geographic variation is evident in MDAs and the component ages of the selected strata. Detrital zircon ages of Cuestecita formation and La Escondida phyllite can be attributed to sources in the Guerrero terrane and plutonic rocks intruded into it (see text for details). These units lack Late Cretaceous detrital zircons, but Early Cretaceous ages are dominant, with age peaks at ~132 and ~136 Ma, respectively. The onset of foreland basin deposition is near early-middle Cenomanian time according to detrital zircon ages in the Mineral de Pozos sandstone, which is located in the Cenomanian foredeep near the western flank of the foreland basin. Deposits of the foreland basin contain a distinctive three-fold Laurentian age distribution (peaks near 1.7 Ga, 1.4 Ga and 1.1 Ga); Mineral de Pozos sandstone, sample MP6; lower Difunta Group, Muerto Formation, samples 05DEL01, 05DEL02; and upper Difunta Group, Carroza Formation, samples 03LP1, 03LP2, in Lawton et al., 2009, right column. The three age peaks characteristic of Laurentian basement (e.g., Karlstrom et al., 2004) are absent from samples of the oldest deposits (right column). The dominant young age component of foreland basin strata includes grains with ages equivalent to La Posta intrusive event of southern California and the “type” La Posta of the Baja California Peninsula (~100–90 Ma) in the detrital samples (left column). MDA = maximum depositional age calculated from individual U–Pb grain analyses. Vertical gray bar is interpreted age range of Arperos basin fill and is inferred to represent the time span of magmatic activity of the Early Cretaceous Alisitos arc. Yellow bar is the age range of the Late Cretaceous magmatic arc of western Mexico.

3.2. Deformed foreland basin deposits of the MFTB

Strata deposited in the foreland basin adjacent to the evolving MFTB can be divided into (1) strata deposited adjacent to the early thrust wedge and subsequently imbricated and incorporated into the orogenic wedge and (2) strata that reside in an assemblage of less-deformed foreland basins, including the Sabinas, Parras, La Popa, Tampico-Misantla and Veracruz basins (Fig. 2).

3.2.1. Imbricated foreland basin deposits, MFTB

A tract of pervasively thrust and folded turbidites underlies the Mesa Central of northern Mexico, continues northward along an apparently narrower belt northward into Chihuahua, and extends southward beneath the Trans-Mexican volcanic belt into southern Mexico. These siliciclastic rocks include unnamed turbidites (formerly termed Caracol Formation; de Cserna, 1976), the informal Mineral de Pozos sandstone (Ortega-Flores et al., 2014), and the Soyatal (Wilson et al., 1955; Hernández-Jaúregui, 1997) and Concepción del Oro (Ocampo-Díaz et al., 2016) formations of early Late Cretaceous age (late Cenomanian-Santonian; Fig. 4). The sandstones constitute a wide range of facies characteristic of submarine fan deposits, including upward-coarsening and upward-fining stratal successions, rhythmic thin sandstone beds in thick siltstone and shale successions, and boulder conglomerate supported in a mudstone matrix. We interpret these facies as depositional lobes, channel complexes, basin-plain deposits

and slope-related slump deposits, respectively (e.g., Posamentier and Walker, 2006). The sources and dispersal directions of these deep-water sandstones are not yet well known, although local southeast-directed flute casts indicate axial transport parallel to the inferred foredeep of the foreland basin. As with the Arperos basin fill, sandstone compositions are rich in volcanic-lithic detritus (Ocampo-Díaz et al., 2016). The siliciclastic turbidites are depositionally intercalated with turbidites composed exclusively of extrabasinal and intrabasinal carbonate grains, or calciturbidites, with west-directed paleocurrents.

Detrital zircon content of the foreland basin strata is different from that of the Arperos basin fill and serves to discriminate the foreland basin strata on the basis of grain age and provenance. The Mineral de Pozos sandstone contains detrital zircons that yield Proterozoic ages with peaks at ~1.7, 1.4, and 1.1 Ga (Fig. 5), a continuum of Middle Jurassic and Early Cretaceous grains, and Late Cretaceous grains in the range ~100–92 Ma. The young grains yield a calculated maximum depositional age of 93 Ma (early Turonian) and thus indicate foreland deposition by early Late Cretaceous time. The old grains are characteristic of basement in southwestern Laurentia (e.g., Karlstrom et al., 2004), whereas Late Jurassic and Early Cretaceous grains are compatible with derivation from the Guerrero terrane. The dominant source for Late Cretaceous detrital zircons was contemporary magmatism along the western margin of the recently accreted Guerrero terrane, indicating concurrent subduction of the Farallon slab (e.g., Kimbrough et al., 2001; Ortega-Rivera, 2003). The extrabasinal carbonate grains of the calciturbidites were derived from strata of exposed Lower Cretaceous platforms of eastern

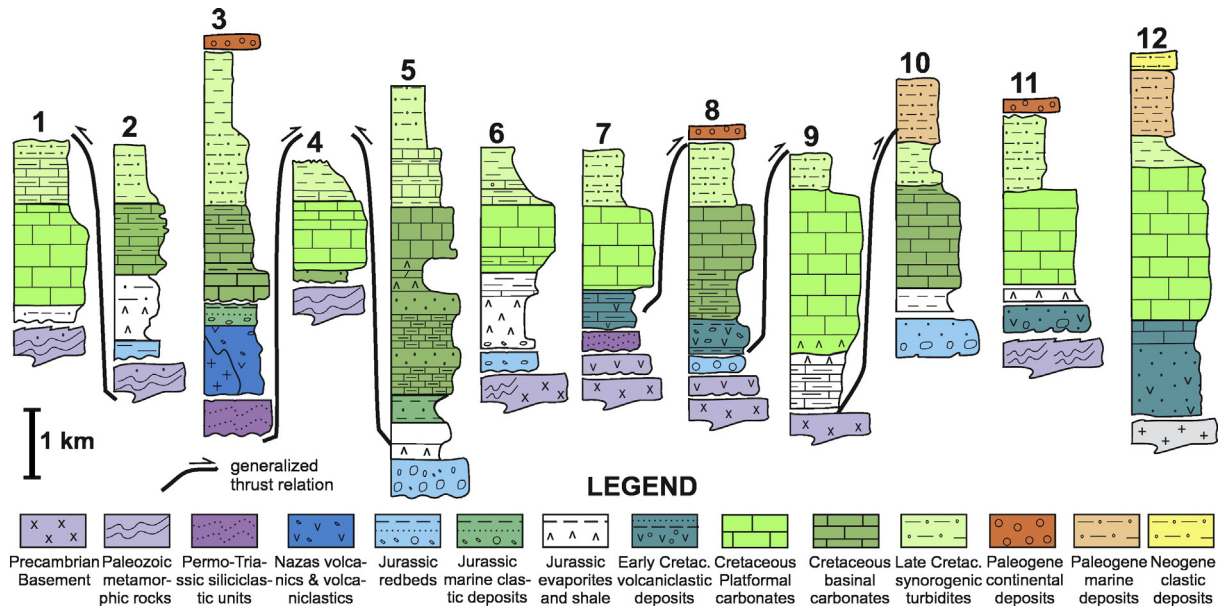


Fig. 6. Stratigraphic columns of different Cretaceous paleogeographic elements of eastern Mexico (location is indicated in Fig. 3), which show stratigraphic variations and emphasize thickness variations among Late Jurassic–Early Cretaceous basins and platforms (Fig. 4). As the exposure of most pre-Cretaceous units is limited, we used the Cretaceous carbonates as a reference horizon to look at deformation variations along the cross-sections shown in Figs. 7 and 8. Notice the distribution of evaporites and carbonaceous shale under the platformal and basal carbonate successions, which in most of the MFTB served as the basal or local detachment horizon. These columns synthesize data reported in López-Ramos (1982), Suter (1987), Carrillo-Martínez (1989), McKee et al. (1990), Hennings (1994), Jones et al. (1995), Goldhammer (1999), Haenggi (2001), Eguiluz de Antuñano (2001), Fitz-Díaz (2001), Ortuño-Arzate et al. (2003), López-Doncel (2003).

Mexico (e.g., Wilson and Ward, 1993), which persisted into the Late Cretaceous on the Valles-San Luis Potosí platform (Fig. 3; Carrillo-Bravo, 1971). Deep-water deposition, axial paleocurrent directions and intercalation of sediment derived from opposite flanks of the basin indicate deposition in the rapidly subsiding foredeep depozone of a foreland basin (e.g., DeCelles and Giles, 1996). The width of the basin, from the initial thrust front near the Arperos basin suture zone, to likely sediment sources for the calciturbidites in the Valles-San Luis Potosí platform, was approximately 200 km. Former carbonate platforms on the distal flank of the foredeep probably formed important residual topography, similar to that of the Miocene Apennine foreland basin system (Critelli et al., 2007).

3.2.2. Extant foreland basin

North and west of the MFTB lie individual, but formerly connected depocenters, including the Parras, La Popa and Tampico-Misantla basins, of a nearly continuous foredeep that probably extended around the front of the MFTB prior to advance of the Monterrey salient into the foredeep (e.g., Ye, 1997a). Although shortened and inverted by Paleogene deformation as discussed earlier, this part of the foreland basin experienced less deformation and uplift than the adjacent MFTB and therefore preserves the most complete foreland-basin stratigraphic succession. It includes a three-fold succession of older deep-water carbonates, intermediate deep-water siliciclastics and younger shallow-water and continental deposits analogous to the stratigraphic succession in an evolving underfilled to overfilled foreland basin (Sinclair, 1997a,b; Gupta and Allen, 2000; Allen et al., 2001). The deep-water carbonates include the Cuesta del Cura, Indidura and Agua Nueva formations (Fig. 4; Barboza-Gudiño et al., 2004; Ángeles-Villeda et al., 2005). These formations consist of deep-water pelagic carbonate and subordinate shale, which in combination with overlying foraminifer carbonate mudstones, shales and tuffs of the Caracol and San Felipe formations, represent a deepening-upward succession at the beginning of Late Cretaceous time that signals widespread drowning of the Lower Cretaceous carbonate depositional system. Overlying shale and subordinate sandstone of the intermediate siliciclastic succession, which includes the Parras and Méndez formations, record influx of siliciclastic

sediments in the distal MFTB in Santonian time. North of the Parras transverse belt, in the Parras and La Popa basins, the upper shallow-water succession, which includes shallow marine, deltaic and continental deposits of the Difunta Group, was deposited between late Campanian and early Eocene time by sediment-dispersal systems oriented parallel to the basin axis (Weidie and Murray, 1967; McBride et al., 1974; Lawton et al., 2009). Contemporary latest Cretaceous–Paleogene strata in the Tampico-Misantla basin consist of distal mud-rich turbidites of the Méndez and Velasco formations and the sandier Paleocene–Eocene Chicontepec Formation (Fig. 4). Ye (1997a,b) suggested that dispersal systems of the Difunta Group connected down-dip into the Chicontepec Formation of the Tampico-Misantla basin, a hypothesis that has not yet been rigorously tested with provenance data. Why the Tampico-Misantla basin never experienced a phase of shallow-water deposition similar to that of the Parras and La Popa basins is an important unanswered question concerning Mexican foreland evolution, but may be related to accentuated flexure of the narrow width of continental crust that lay between the orogenic wedge and the Gulf of Mexico.

Because the synorogenic sedimentary basin linked to development of the orogenic wedge developed for its entire subsidence history on the continental side of an active continental margin magmatic arc (see below), it represents a retroarc foreland basin (sensu Ingersoll, 2012).

3.3. Chihuahua and Sabinas basins

Upper Cretaceous strata are not widely preserved in either the Chihuahua basin or the Sabinas basin, because both of these basins were uplifted during shortening of the foreland region (Haenggi, 2002) and as a result of late Paleogene epeirogenic uplift of eastern and northeastern Mexico (Gray et al., 2001). Thin stratigraphic sections of Cenomanian–Turonian strata are present on the northeastern flank of the Chihuahua basin, in the Sabinas basin (Eguiluz de Antuñano, 2001) and locally on the Coahuila block, where the strata are preserved beneath the hanging wall of the San Marcos reverse fault. These strata consist of pelagic limestone intercalated with carbonate-rich litharenite and shale layers of Turonian age (Alonso-Manuel, 2016). They may

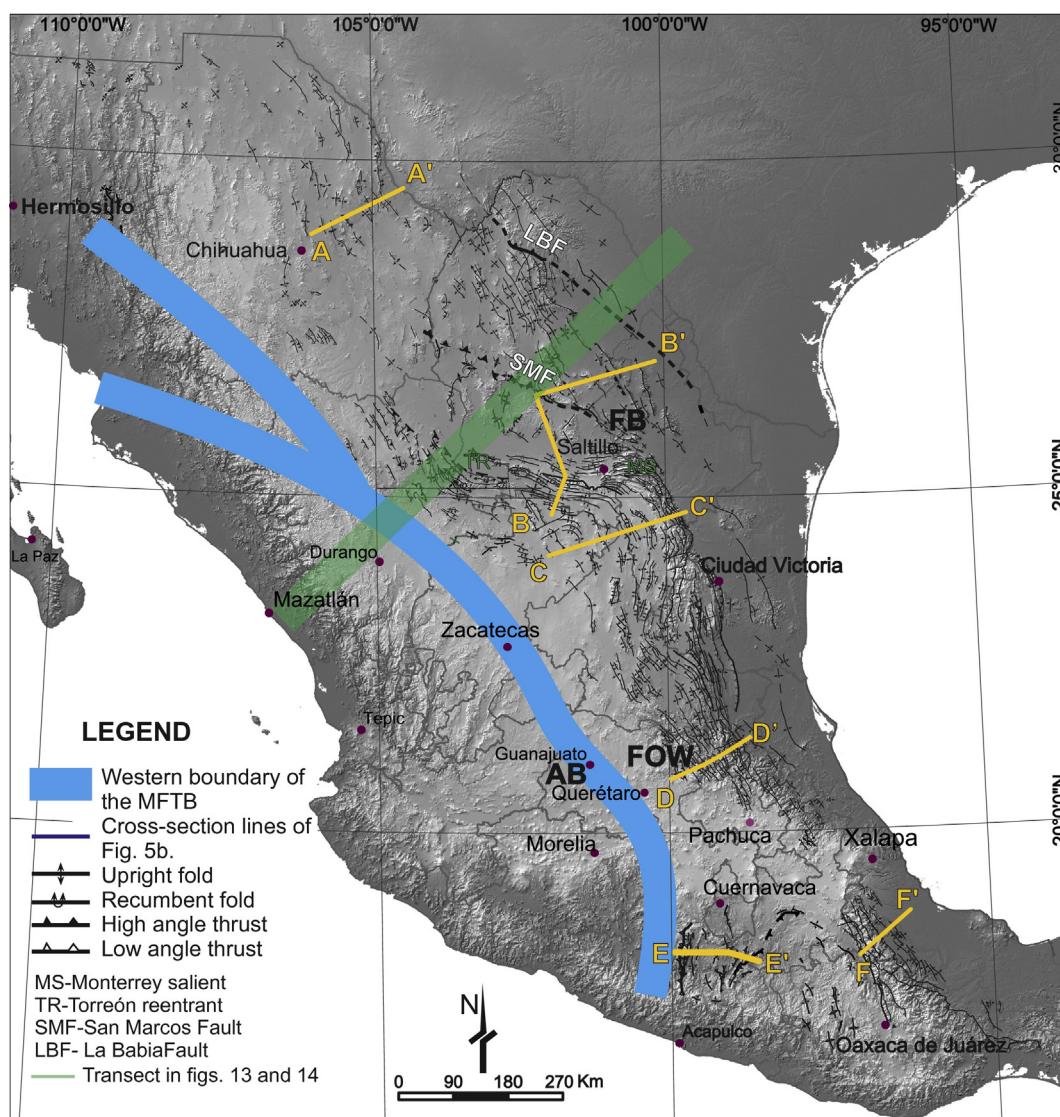


Fig. 7. Digital elevation model of Mexico, in which the distribution of structures of the MFTB and of its western boundary, the Arperos suture, as well as the location of the regional cross-sections of Fig. 8 across the MFTB are shown. Notice the change of fold axis trend, which is dominantly NW-SE in Northern Mexico, and shows variable orientations and spacing in the Coahuila platform (CP), and then again fold are concentrated in a belt that goes around the CP with a NW-SE on its western margin, to E-W trend on its southern margin, along the Parras transverse range. The structures around the Monterrey salient continue with a NNW-SSE trend. In southern Mexico the belt bifurcates, with a western branching into the Morelos-Guerrero platform, where folds have an average N-S trend and on an eastern leg along the Zongolica range, where folds are NW-SE oriented. The location of selected localities for detrital zircon provenance analysis of Fig. 6 are also indicated with tags letters: AB-Arperos basin, FOW-Foreland orogenic wedge, FB-Foreland basin.

record long-wavelength dynamic subsidence coincident with initial emplacement of the Farallon slab beneath Mexico and attendant onset of downwelling of asthenosphere in the mantle wedge above the slab (e.g., Heller and Liu, 2016).

4. Shortening deformation in the MFTB

In order to analyze the diverse structures in the Mexican fold and thrust belt, we use the Lower Cretaceous carbonate platforms and basins (Figs. 3, 4, 6) as a reference for the cross-sections of Figs. 7 and 8. The Lower Cretaceous is widely exposed across the MFTB and accounts for the dominant volume of rocks involved in the deformation. Facies within the Lower Cretaceous carbonates, whether thin-bedded basinal deposits or thick platformal strata, strongly controlled local deformation style within the belt. To illustrate structural variability and the varied architecture of the foreland wedge, we selected six cross-sections in the basis of availability of information and variable structural characteristics in the MFTB. The structural transects include: A-A', the deformed belt of the Chihuahua basin; B-B', beginning on the southern edge of Sierra de

Parras and crossing the Coahuila platform and the southern Sabinas basin; C-C' across the central Mexico basin, primarily of Jurassic and Early Cretaceous age; D-D', of significant structural variability, across basins and platforms in central Mexico; E-E' traversing the Morelos-Guerrero platform; F-F' across the Cordoba platform and Veracruz basin (Figs. 3 and 7).

In order to compare deformation variations along the MFTB, we use approximately the same scale and color code for stratigraphic reference horizons. For simplification, we avoided formational names and used the lithostratigraphic groups described in Table 1 and illustrated in Figs. 4 and 6. We also considered litho-stratigraphic unit thickness variations in the construction of the cross sections, as shown in Fig. 6. However, the columns of Fig. 6 are based on data reported in the literature for specific areas, so they are rough estimates of thickness of the Cretaceous carbonate interval; complex deformation and limited exposures of Triassic and Middle Jurassic units renders their thickness in Fig. 6 approximate. The geometry of the structures along the cross-sections considers the length and thickness of the Cretaceous carbonate units, whereas the structures beneath the Cretaceous were inferred

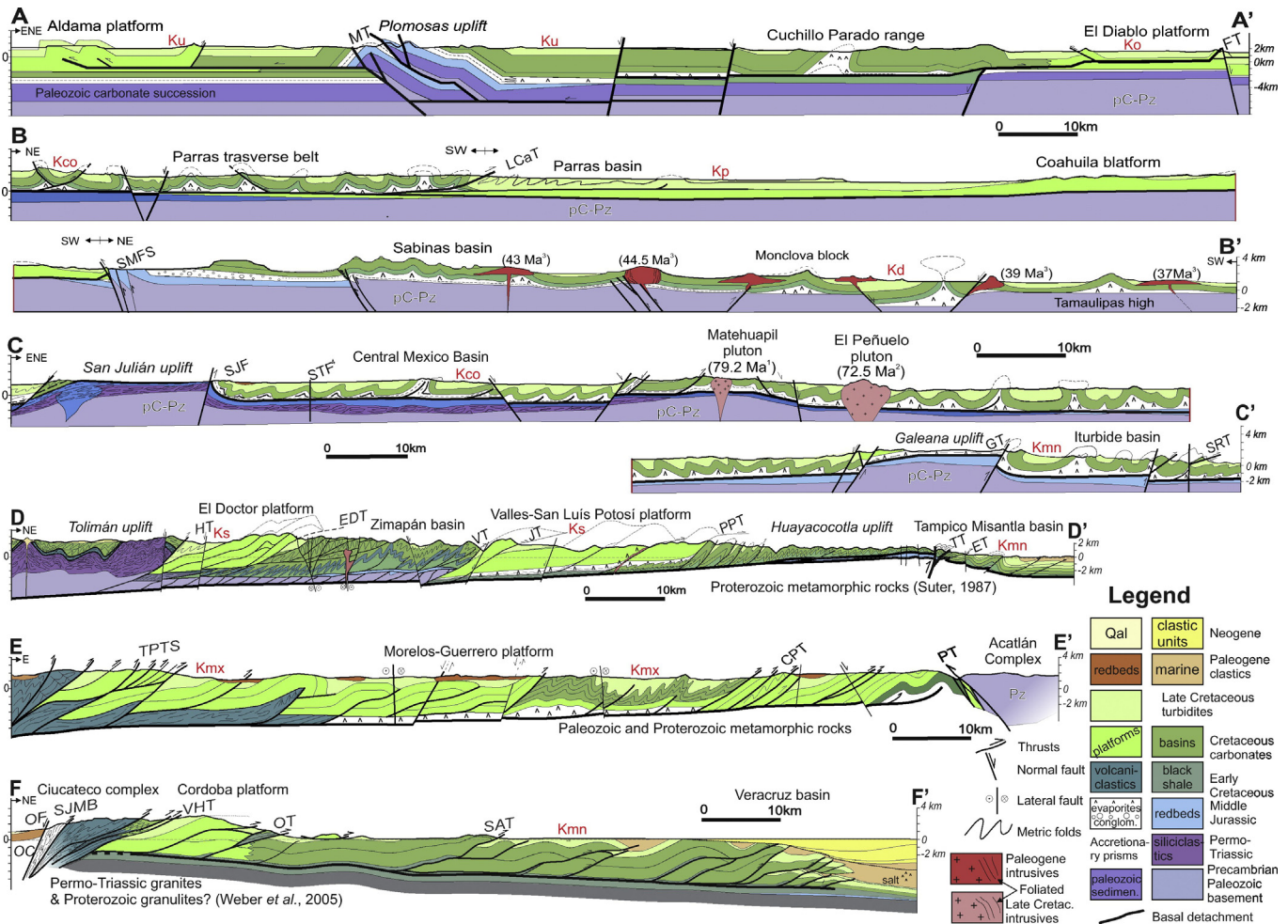


Fig. 8. Selected structural cross-sections of the MFTB, each at about the same scale and with a standard lithostratigraphic color code for comparison (see Table 1 and Figs. 4 and 5). Section A-A' is modified from Hennings (1994). Section B-B' is adapted from work by Quintero-Legorreta and Aranda-García (1985), Eguiluz de Antuñano (2001); Chávez-Cabello (2005) and Bolaños-Rodríguez, 2006. Section C-C' is based on Chávez-Cabello (unpublished) and observations by Jones et al. (1995) in the San Julián block. Section D-D' is adapted from Fitz-Díaz (2010). The western half of section E-E' is adapted from the Cuernavaca geological map (1:250'000) published by the Mexican Geological Service, and the western margin includes work by Salinas-Prieto et al. (2000); the eastern half is based on detailed mapping by Fitz-Díaz (2001). Section F-F' is based on the detailed and careful work by Ortuño-Arzate et al. (2003) and Ángeles-Moreno (2012). MT-Monillas thrust, FT-Frontal thrust, LCaT-La Catana thrust, SMFS-San Marcos fault system, SJF-San Jerónimo fault, STL-San Tiburcio lineament, GT-Galeana thrust, SRT-Santa Rosa thrust, HT-Higuerillas thrust, EDT-El Doctor thrust, JT-Jiliapan thrust, TT-Tetitla thrust, ET-Enramaditas thrust, TPTS-Teloloapan-Pachivia thrust system, CPT-Cruz de Palma thrust, PF-Papalutla fault, SJMB-Sierra de Juárez mylonite belt, VHT-Vista Hermosa thrust, OT-Orizaba thrust, SAT-Sierra Azul thrust, AC-Acatlán Complex, OC-Oaxaca complex, Ko-Ojinaga Fm., Kd-Difunta Group, Kp-Parras Fm., Kco-Concepción del Oro Fm., Ks-Soyatal Fm., Kmn-Mendez Fm., Kmx-Mexcala Fm. 1-Sosa-Valdés, 2-Ramírez-Peña and Chávez-Cabello, 2017, 3-Chávez-Cabello, 2005, 4-Mitre-Salazar, 1989.

from limited exposures, and structural geometry is less well controlled than in the Cretaceous reference horizon. Both columns and cross-section are organized from left to right and top to bottom to correspond with their description from north to south in the following text.

4.1. Sonora

Although we do not include a cross-section from Sonora due to limited exposures of shortening structures involving Cretaceous units, some discussion of deformation style and timing is warranted. Both low-angle and high-angle faults have been reported in northern Sonora. Near Arizpe and to the northeast of Hermosillo, low-angle thrusts affecting Lower Cretaceous strata and pervasive folds with vergence to the east have been observed in different localities (Pubellier et al., 1995). Thick-skinned structures and related foreland basins have also been reported in NE Sonora (e.g., Cabullona basin, González-León and Lawton, 1995; Lawton, 2008). The San Antonio reverse fault on the northeastern flank of the Middle-Late Jurassic Altar-Curcupe basin in north-central Sonora emplaces redbeds of the Lower Cretaceous Bisbee Group over

the synorogenic Cocóspera Formation, which contains interbedded andesite flows and boulders derived from the Bisbee Group (Mauel et al., 2011). Correlative conglomerate in the Escalante Formation of El Chanate Group in Sierra El Chanate, northeast of Caborca, contains clasts of felsic intrusive and pyroclastic rocks, quartzarenite and litharenite. The Cocóspera Formation is unconformably overlain by volcanic and pyroclastic rocks of the Tarahumara Formation (González-León et al., 2011); the Escalante Formation is concordantly overlain by El Charro volcanic complex, which consists of volcanic flows, flow breccias and intermediate to felsic tuffs, and is folded with the underlying El Chanate Group in El Chanate syncline (Jacques-Ayala, 1999).

High-angle faults are slightly younger than the low-angle faults (González-León et al., 2012), and were apparently in part coeval with displacement on the northwesternmost thrusts exposed in Sonora, which preserve a dominant direction of transport to the north, and have ages between 75 and 60 Ma (Iriando et al., 2004). The high-angle reverse faults, such as the San Antonio fault, reactivate normal fault systems that formed during Jurassic basin formation (Mauel et al., 2011); we thus consider them to have originated as basin-

inversion structures (e.g., Coward, 1994; Lowell, 1995). Cross-cutting relations in central Sonora suggest that these structures locally affect previous thin-skinned structures according to Pubellier et al. (1995).

Ages of continental syntectonic clastic strata, combined with the ages of overlying volcanic and volcanoclastic strata, indicate that shortening in Sonora took place between late Cenomanian and late Campanian time (e.g., González-León et al., 2012). A hornblende andesite flow in the Cocóspera Formation yielded a $^{40}\text{Ar}/^{39}\text{Ar}$ hornblende age of 93 ± 1 Ma, and the overlying Tarahumara Group has yielded U-Pb ages ranging ~79–59 Ma in northeastern Sonora (González-León et al., 2011). The lower member of the Escalante Formation has detrital zircon young grain ages of ~97–94 Ma and a sandstone in the upper part of the El Chanate Group contains two young zircon grains of ~76 and 74 Ma (Jacques Ayala et al., 2009). El Charro volcanic complex has yielded a single $^{40}\text{Ar}/^{39}\text{Ar}$ hornblende age of 72 ± 1 Ma (Jacques-Ayala, 1993). El Charro volcanic complex thus probably records shortening during the late Campanian (Jacques-Ayala, 1999; Jacques Ayala et al., 2009) and which may have continued into the Paleogene (e.g., Iriando et al., 2005).

4.2. Section A-A': Chihuahua basin

Cross section A-A' depicts shortening across the Jurassic-Lower Cretaceous Chihuahua basin, or Chihuahua trough. The cross section was based on several years of fieldwork by Hennings (1994), who inferred that shortening in the Chihuahua basin is recorded by km-scale NW-SE oriented folds bounded by high-angle reverse faults in the borders of the basin. The structures record NE-SW shortening of the basin, with thrusting to the northeast onto the Diablo platform on the northeast flank of the basin, and SW-directed onto the intra-basinal Aldama platform, to the southwest (Figs. 3 and 7). Within the basin, Paleozoic and Middle Jurassic strata are exposed in the Plomosas uplift, which consists of imbricated thrust sheets with SW vergence. A single exposure of Proterozoic basement consisting of amphibolite intruded by 1.1 Ga pegmatic granite is present in the uplift at Cerro del Carrizalillo, south of the Conchos River (Dyer and Reyez-Cortes, 1987). Thick sections of Jurassic strata, formerly considered Permian, have recently proven to be Middle Jurassic (Villarreal-Fuentes et al., 2014; Barboza-Gudiño et al., 2016), suggesting that the Plomosas uplift

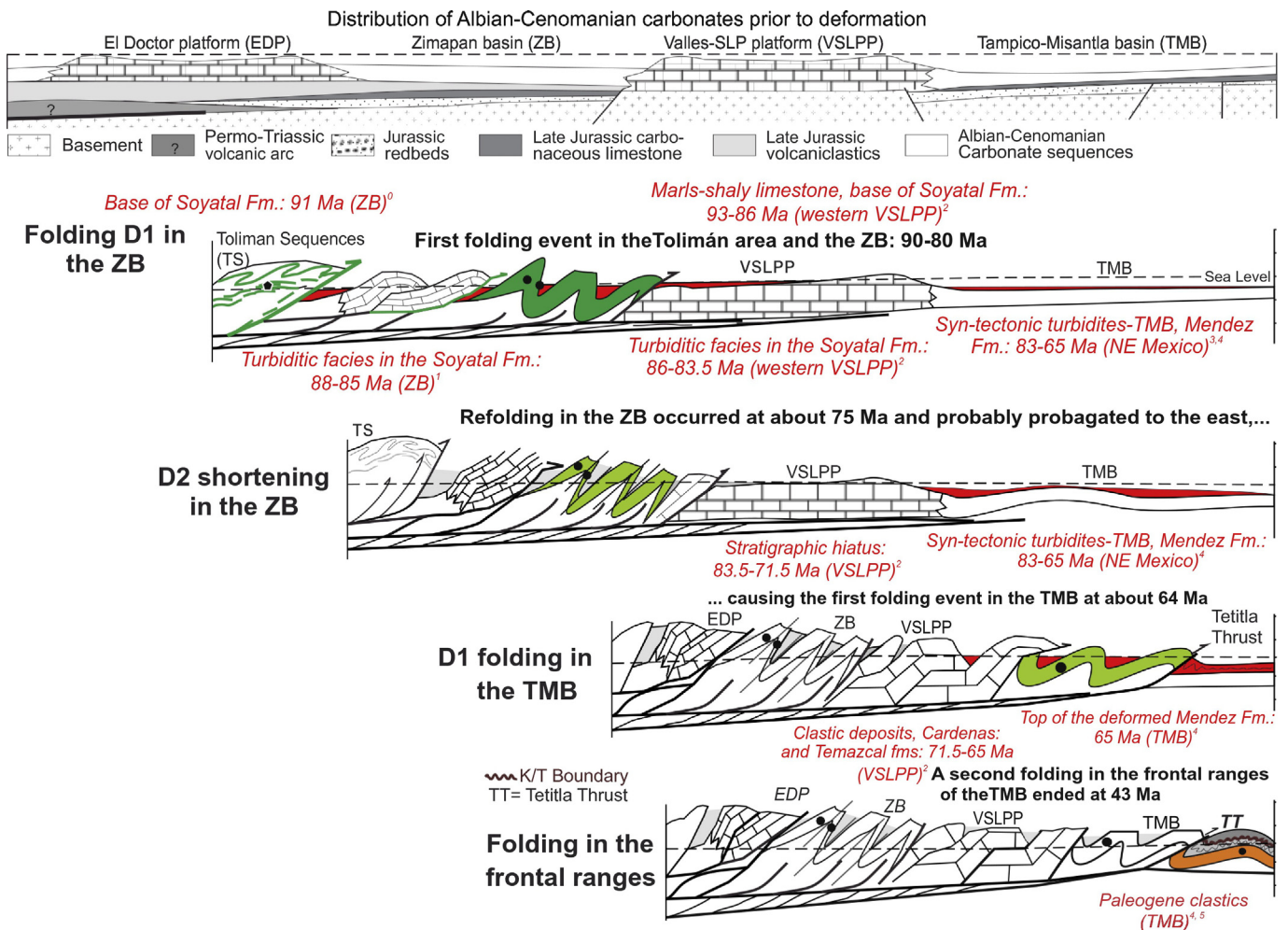


Fig. 9. Schematic model of propagation of deformation of the Mexican fold-thrust belt in central Mexico (modified from Fig. 8 in Fitz-Díaz et al., 2014b). According to Ar/Ar ages and local biostratigraphy, deformation affected rocks of the Tolimán sequences on the western most part of the section in the Coniacian. Then, deformation propagated to the ZB causing folding (F1) until Early Campanian. In the same rocks, a second horizontal shortening pulse sub-parallel to the previous one caused attenuation of high angle inverted forelimbs of asymmetrical folds and re-folding in the middle Campanian. On top of the VSLPP, syn-tectonic turbidites were deposited in the Coniacian-Santonian and then in the Late Campanian-Maastrichtian clastic sediments were deposited directly on top of the platformal carbonates. Ar-illite ages suggest that folding affected the westernmost TMB rocks in the Late Maastrichtian/Paleocene, which makes good sense with the fact that these folds involve local syntectonic turbidites (Mendez Fm., Fig. 4), which is as young as Late Maastrichtian. A folded unconformity separates intensely folded/foliated Campanian-Maastrichtian turbidites from less deformed paleogene deposits in the foothills. Folding was propagated to the foothills (coastal plain of the Gulf of Mexico) until the middle Eocene. 0-Hernández-Jauregui, 1997, 1-Kiyokawa, 1981, 2-Omaña-Pulido, 2012, 3-Suter, 1990, 4-López-Oliva et al., 1998, 5-Alzaga-Ruiz et al., 2009.

represents an inverted Jurassic basin (Fig. 8, A-A'). Evaporite injection enhanced fold hinges in the center of the basins, and also occurred along thick-skinned thrusts on the margins of the basins. Hennings (1994) interpreted the shortening in the Chihuahua basin as dominated by a thin-skinned deformation style with two different detachment horizons, one at the basement level with structures verging to the south on the southern margin, and another detachment localized in evaporites at the Jurassic-Cretaceous boundary, with structures verging to the north on the northern margin.

Haenggi (2001, 2002) interpreted the deformation in the Chihuahua basin as the result of left-lateral oblique compression, involving reactivation of pre-existing faults formed during the formation of the Jurassic-Aptian extensional basin, and as in Sonora presumably related to the opening of the Gulf of Mexico (González-León and Lawton, 1995; Mauel et al., 2011). Haenggi (2002) suggested that evaporites in the basin center favored the formation of open folds, followed by fold amplification accompanied by evaporite injection in anticlinal hinges. Emplacement of reverse faults, principally toward the Diablo platform, and diapiric injection of evaporites along the margins of the basin postdated folding. Despite the evaporite-related local detachments, Haenggi (2002) inferred that thrusts are dominantly basement-involved rather than related to a regional-scale *décollement*, which is consistent with the estimated overall fold-related shortening of 16% in the basin (Hennings, 1994). Synorogenic strata are absent in the Chihuahua basin, but cross-cutting relationships and the ages of tilted volcanic units and syntectonic magmatism in the area indicate the age of deformation to be between 68 and 46 Ma (McDowell and Mauger, 1994).

4.3. Section B-B': Mesa Central-Coahuila block-Sabinas basin

This cross-section illustrates variation of deformation styles in three important Jurassic-Cretaceous paleogeographic elements, the Central Mexico basin to the south, the Coahuila platform and the Sabinas basin to the north, whose deformed equivalents are termed the Parras transverse belt (or sector transversal), the Coahuila block and the Coahuila fold belt, respectively. The orientation of the cross-section line changes to cross structures perpendicularly in each segment (Fig. 7). In the Parras transverse belt, named the "Parras nappe" by Tardy et al. (1974), the deformation of the Central Mexico basin rocks is dominated by tight asymmetrical folds associated with reverse faults, which were displaced along a detachment level in Middle Jurassic evaporites (Fig. 5). Northward, the folds demonstrate north vergence (Quintero-Legorreta and Aranda-García, 1985), and the frontal La Catana thrust emplaces strata of the Central Mexico basin over the strata of the Parras foreland basin, the strata of which formerly overlapped the Coahuila platform but are now largely eroded from the platform (Fig. 8, section B-B'). South of the Parras transverse belt, thrust-related folds have an opposite south vergence. The divergent character of thin-skinned deformation in the Parras transverse belt is peculiar to this segment of the MFTB, and is apparently continuous, following a sinuous belt along the southern margin of the Coahuila platform. Similar double verging structures with significant internal deformation are only known in Sierra del Gallo, Durango (Eguiluz de Antuñano and Campa, 1982), 280 km to the NW, and in the eastern Mesa Central, to the south.

The strata of the Parras foreland basin have tight folds and development of an axial-plane cleavage in the vicinity of the Parras transverse

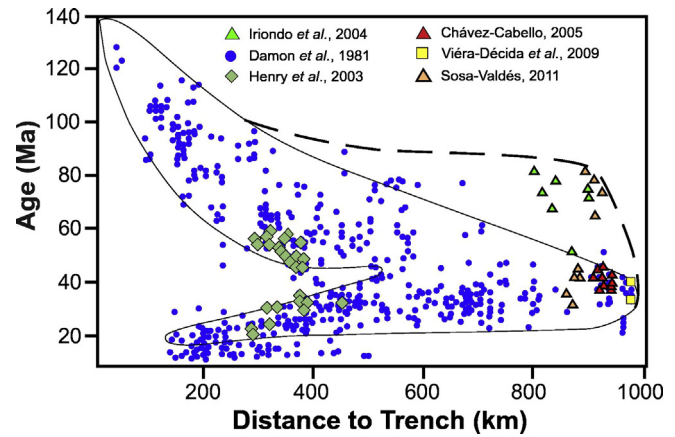
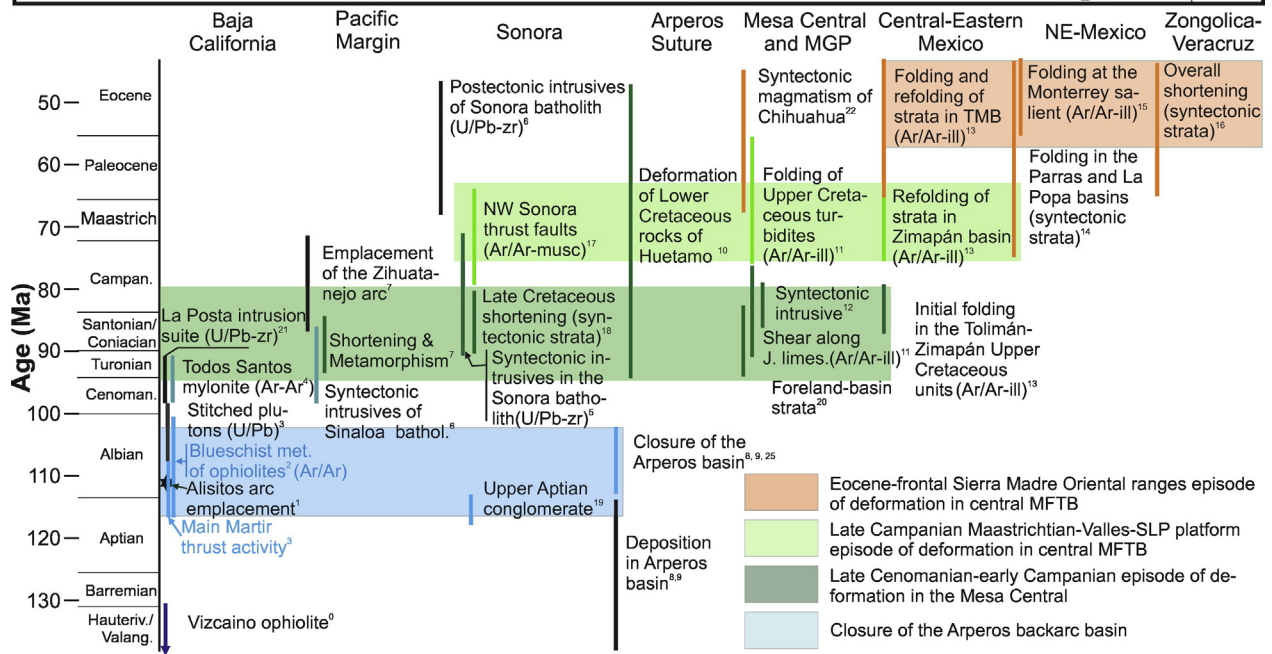
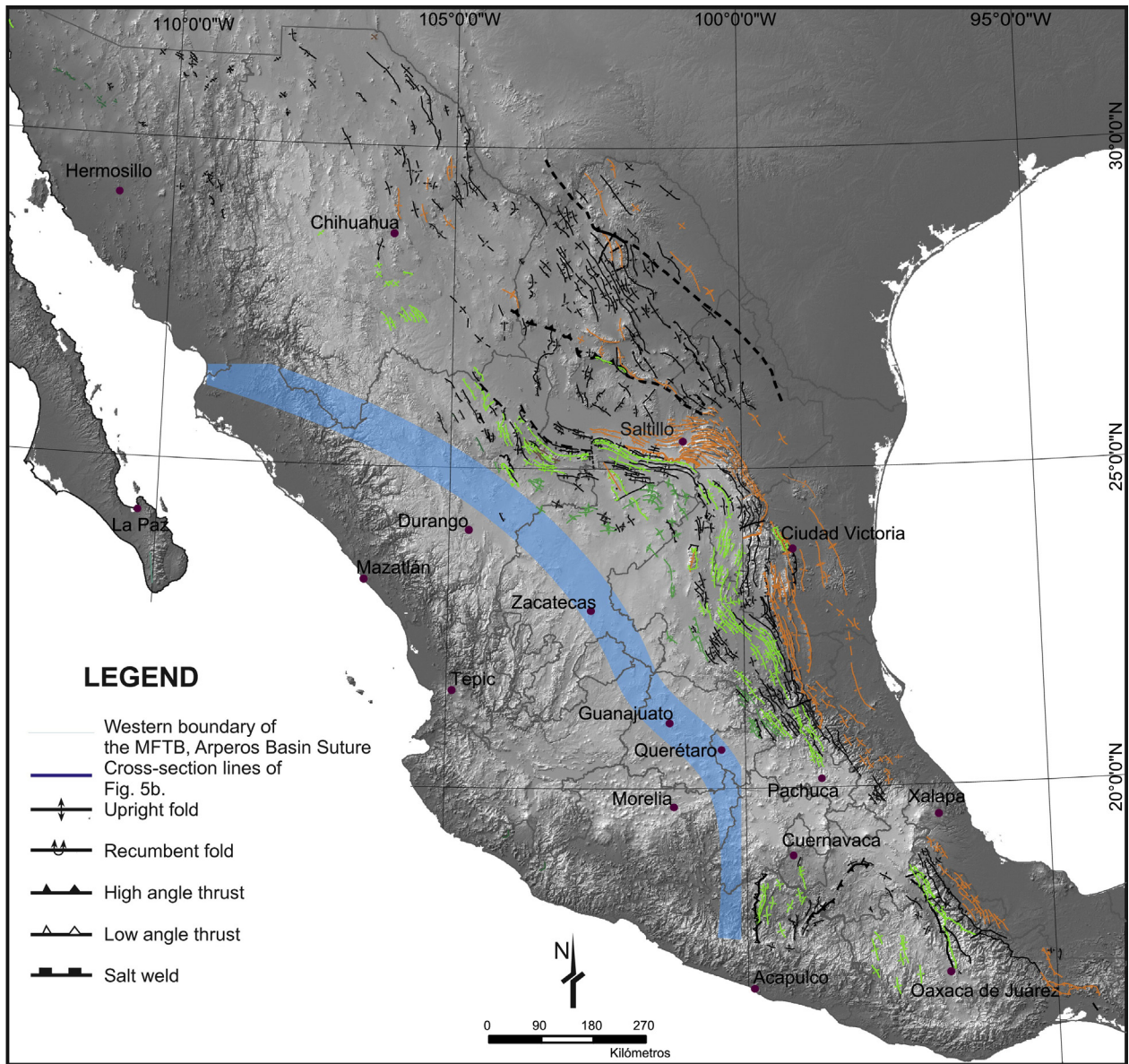


Fig. 10. Migration of magmatism in northern Mexico from Early Cretaceous through Neogene time. Data were plotted in a distance to paleotrench vs. age graph (modified from Damon et al., 1981a,b). We include data reported by Henry et al. (2003), Iriondo et al. (2004), Chávez-Cabello (2005), Solé et al. (2007), Sosa-Valdés (2011). The migration of magmatism to the east has been used as an argument to explain progressive reduction in the subduction angle of the Farallon plate between 80 and 40 Ma, by comparison with the Laramide orogeny (Damon et al., 1981a,b; Ferrari et al., 2005). However, recent data from northern Mexico (dashed line), show that such a migration of magmatism is not very clear in Mexico for such a period of time.

range front and near La Catana thrust. Folds are more open and lose amplitude near the exposures of the Coahuila platform rocks, to the north (section B-B'). Except for dome-like structures and small-displacement north-verging detachment levels observed on its northern edge (Chávez-Cabello, 2005; Bolaños-Rodríguez, 2006), the Coahuila platform has negligible internal deformation and for this reason it is also known as the Coahuila block, a mechanically resistant element constituted by a relatively strong basement, which remained as a high-standing structural element for most of the Mesozoic, as suggested by its stratigraphic record (Fig. 6). The Coahuila block and the low-angle detachment structures on its northern margin, are cut by high-angle reverse faults with southern transport directions. The faults served to uplift and emplace strata of the Sabinas basin onto the adjacent Coahuila platform. Although field observations suggest that there are few high-angle reverse faults along the edge of the platform, as shown in section B-B', the best exposed of these high-angle faults is the San Marcos Fault. Based on detailed mapping and stratigraphic analysis, McKee et al. (1990) concluded that the WNW-ESE oriented San Marcos fault originated as a left lateral fault in the Middle Jurassic during the opening of the Gulf of Mexico, was active as a normal fault in the Early Cretaceous and finally, was converted to a reverse fault in the Paleogene (Chávez-Cabello, 2005).

Folds in the Sabinas basin have a general NW-SW orientation and diverse geometries. On the southern flank of the basin, folds are typically asymmetric fault-propagation folds with steep forelimbs facing south in the Cuatro Ciénegas area (e.g., Sierra La Madera, La Virgen, La Fragua and San Marcos-Pinos anticlines; Chávez-Cabello et al., 2007), whereas nearer the basin center, fold form is gentle to open and slightly asymmetrical with fault-propagation fold geometries (Eguiluz de Antuñano, 2001). Close to the depocenter of the basin, where they are detached on Middle to Late Jurassic salt, folds have irregular shapes in part influenced by large volumes of evaporite injection (i.e. Obayos anticline;

Fig. 11. Timing of deformation in the Mexican orogen. In the upper part we show a digital elevation model of Mexico with major shortening structures in the MFTB. Folds and thrusts are colored according to different episodes of deformation, as shown in the table below. In black are mapped structures of unknown age, in blue those formed during the closure of the Arperos basin in the Albian, deep green are Turonian-Early Campanian in age, pale green are Late Campanian-Massstrichtian and in orange grouped Paleogene structures. Notice that structures are progressively younger to the east. The deformation age table for the MFTB was based on the following references: 0-Moore, 1985, 1-Busby et al., 2006; 2-Baldwin and Harrison, 1992, 3-Johnson et al., 1999, 4-Cuéllar-Cárdenas et al., 2012, 5-Ramos-Velázquez et al., 2008, 6-Henry et al., 2003, 7-Centeno-García et al., 2011, 8-Martini et al., 2014 and Martini et al., 2009, 9-Ortega-Flores et al., 2015, 10-Martini et al., 2011; 11-this work, 2016; 12-Solé et al., 2007, 13-Fitz-Díaz et al., 2014a,b; 14-Gray and Lawton, 2011, 15-Fitz-Díaz et al., 2016, 16-Ortuño-Arzate et al., 2003, 17-Iriondo et al., 2005, 18-González-León et al., 2011, 19-Mauel et al., 2011, 20-this work, 21-Kimbrough et al., 2001, 22-McDowell and Mauger, 1994, 23-Cerca et al., 2007, 24-Delgado-Argote et al., 1992; 25-Eliás-Herrera et al., 2000.



Peterson-Rodríguez et al., 2008). Folds are open and slightly asymmetrical on the northern edge of the basin in the vicinity of La Babia fault trace (Fig. 8). Shortening estimates across the Sabinas basin are on the order of 14% (Eguiluz de Antuñano et al., 2000), which are very similar to those in the Chihuahua basin to the northwest. Both basins have a thick-skinned deformation style characteristic of basin inversion (Lowell, 1995), in which internal open to isoclinal box folds are detached above a thick evaporite horizon within the basin, and basement-involved faults develop fault-propagation folds near the basin edges. As in the Chihuahua basin (Haenggi, 2002), the obliquity between the fold axes and basin-marginal San Marcos and La Babia faults has been explained by reference to left-lateral, basin-scale oblique contraction (Charleston, 1981). Nevertheless, except for syntectonic intrusive bodies with sigmoidal map shapes in the Monclova area (Chávez-Cabello, 2005), no direct supporting kinematic evidence for strike-slip displacement on the faults has been reported.

With respect to the age of deformation along this section, the age of syntectonic intrusives (Chávez-Cabello, 2005), foreland deposits (Gray and Lawton, 2011), and the age of folds in the Monterrey salient (Fitz-Díaz et al., 2016) suggest that the deformation from the Parras foreland basin to the northern edge of the Sabinas basin occurred between 74 and 44 Ma, and was probably younger to the north.

4.4. Section C-C': Central Mexico basin from Zacatecas to Nuevo León

Cross section C-C' illustrates the deformation style of Central Mexico basin strata from the block of San Julián to the Mexican coastal plain near Linares, Nuevo León, along an ENE-WSW transect. A basal detachment zone separating folded strata above from less shortened rocks underneath creates the dominant thin-skinned deformation style. Exposure of rocks and structures on the western half of this transect is limited by Neogene alluvial and colluvial deposits that cover older strata in wide *grabens* (Aranda-Gómez and Mcdowell, 1998); nevertheless, on a regional scale the basal detachment zone can be traced because it is well exposed in the San Julián (Jones et al., 1995) and Galeana uplifts. Fold geometry is not clearly evident on the section because the section line is oblique to fold axes between these two uplifted blocks, but fold vergence and spacing are well illustrated on the basis of field observations.

At the western end of the section, the basal detachment constitutes a low grade mylonite zone localized along the contact between volcanic, volcanoclastic and intrusive Middle Jurassic rocks and highly deformed Triassic siliciclastic deposits of the Taray Formation, interpreted as a subduction complex (Anderson et al., 2005a,b). The mylonite has an SL fabric with the foliation dipping to the west on the western margin, dipping to the east on the eastern margin, and flat in the middle of the San Julián block. Above the detachment, tight asymmetrical folds verging to the east are pervasive in Upper Jurassic and Lower Cretaceous carbonates on the northern edge of the block. On the eastern margin of the block a NW-SE oriented subvertical reverse fault zone affecting the detachment zone is exposed. This reverse fault system might have caused the uplift of rocks of the San Julián block and of the detachment zone. To the east, Upper Cretaceous turbidities, presumably of the Concepción del Oro Formation (Ocampo-Díaz et al., 2016), are exposed. These rocks are folded but the folds are less tight than in the carbonates below and are unconformably covered by thick-bedded limestone-clast conglomerate, the Ahuichila Formation, which is gently folded. To the east, at the Concepción del Oro bend (Rogers et al., 1957), north-verging fault-propagation folds have curved axes that form a salient in map view (Fig. 7). Fold-axis bending might be the result of refolding, which could have happened during displacement of the San Tiburcio fault in the Cenozoic (Mitre-Salazar, 1989). The folds along the segment between San Tiburcio and Galeana, are cut by post-tectonic shallow plutons, such as the Matehuapil (Sosa-Valdés, 2011) and El Peñuelo plutons (González-Guzmán et al., 2009), with U-Pb ages of 79.2 and 72.2 Ma, respectively, which indicates that the thin-

skinned deformation in the area is early Campanian or older; the age of the high-angle faults remains unknown.

To the east of El Peñuelo pluton, the crests of some anticlines are exposed above the surficial deposits (section C-C' in Fig. 8). The anticlines were presumably formed above a basal detachment zone in Middle Jurassic evaporites and limestone that is exposed on the Galeana uplift. The exhumation of this block exposed Triassic and Lower Jurassic clastic sedimentary rocks (Alamar, La Boca and La Joya formations; Figs. 4 and 6) and the basal detachment zone (evaporites of the Minas Viejas Formation; Kroeger and Stinnesbeck, 2003; Cross, 2012), which is cut by high angle reverse fault (GT) on the eastern edge of the Galeana block. This structure seems to be complicated by salt tectonics. At the easternmost end of the section, a train of kilometer-scale asymmetrical folds verging to the east and locally affected by high angle reverse faults, is almost continuously exposed along the Santa Rosa Canyon. At the eastern end of section C-C', the Santa Rosa thrust emplaces Upper Jurassic strata of the Zuloaga Limestone and La Casita Formation over Upper Cretaceous turbidities of the Agua Nueva Formation.

4.5. Section D-D': Central Mexico

The cross-section from Vizarrón to Tamazunchale in central Mexico is probably the most studied section of the MFTB, in part because rocks are very well exposed, and also because regional mapping established consistent stratigraphy (Suter, 1990; Carrillo-Martínez, 1997) and well-documented structural geology (Suter, 1984, 1987; Suter et al., 1997; Carrillo-Martínez, 1989, 1990). Almost 20 years later the fold-belt wedge exposed along the cross-section was revised (Fitz-Díaz, 2010; Fitz-Díaz et al., 2011a) and used as a natural laboratory to analyze the effect of lateral carbonate facies variations on deformation (Fitz-Díaz et al., 2012; Contreras and Suter, 2015), fluid flow and water-rock interaction during folding and faulting within an evolving orogenic wedge (Fitz-Díaz et al., 2011b), illitization and remagnetization during folding of basinal carbonate successions (Fitz-Díaz et al., 2014a; Nemkin et al., 2015), and fold dating with $^{40}\text{Ar}/^{39}\text{Ar}$ in illite (Fitz-Díaz and van der Pluijm, 2013; Fitz-Díaz et al., 2014b).

The knowledge accumulated in studies along the transect containing section D-D', which is oriented ENE-WSW and includes almost the full width of the MFTB along its 130 km length, can be summarized in six major points. 1) This part of the orogen has an overall wedge shape tapering toward the east and a dominantly thin-skinned deformation style (Fitz-Díaz et al., 2011a). 2) Most of the volume of deformed rocks are Upper Jurassic-Lower Cretaceous carbonates distributed in four major paleogeographic elements across the region, which are from east to west the Tampico-Misantla basin (TMB), the Valles-San Luis Potosí platform (VSLPP), the Zimapán basin (ZB), and El Doctor platform (EDP, Fig. 8); to the west, these carbonates are overthrust along the Higuierillas thrust by a suite of rocks included in the Tolimán sequences (Dávila-Alcocer et al., 2009; Fitz-Díaz et al., 2011a). 3) The vertical displacement of the Higuierillas thrust is significantly greater than any other thrust along the section. High-angle faults superimposed on cataclases in the Higuierillas fault zone indicate that later reactivation of this structure probably produced the Tolimán uplift. 4) The Tolimán uplift, like the San Julián, Galeana and Real de Catorce uplifts (Franco-Rubio, 1999), has a folded and faulted detachment zone that separates Triassic siliciclastic units and Lower Cretaceous volcanoclastic rocks. 5) Lithological variations among the Early Cretaceous platforms and basins resulted in contrasting deformation styles dominated by intense folding in the basins and thrust faulting in the platforms. Little displacement took place along intra-formational thrusts and pervasive folding small-scale folding is important in the basins, as compared to greater fault displacement and imbrication with almost no internal deformation in the platformal carbonate successions. 6) The intensity of shortening (from 20 to 70%, Fitz-Díaz et al., 2011a), and temperature (from ~80° to 250 °C, Fitz-Díaz et al., 2011b) and complexity of

deformation decrease eastward, consistent with progressive development of an orogenic wedge.

Geometrical-kinematical comparative analysis of folds in Aptian-Albian carbonates in the Zimapán and Tampico-Misantla basins (Fitz-Díaz et al., 2012), and $^{40}\text{Ar}/^{39}\text{Ar}$ dating of illite produced during fold-associated bed parallel shear (Fitz-Díaz et al., 2014b) indicate that: a) shortening in the basins is accommodated by mesoscopic buckle *chevron* folds, which become progressively tighter and flattened to the west; b) west of the Tetitla thrust near the tip of the orogenic wedge, two generations of folds (F1 and F2) are present in Cretaceous carbonates (Fig. 3); F1 folds are close to tight and pervasive throughout the section whereas F2 folds are open and commonly localized in thinly-bedded and/or fine-grained rocks; c) a single generation of open, m- to km-scale folds, which involve the regional K-Pg boundary angular unconformity, is present east of the Tetitla thrust; nevertheless, d) $^{40}\text{Ar}/^{39}\text{Ar}$ illite ages from four folds and one shear zone along the transect representative of these two phases in each of the two basins, show that fold age is consistently older, beginning at ~85 Ma to the western part of the section and younger, ending at about 43 Ma, in the east; e) the combined illite ages and fold analysis show that the deformation was progressive but episodic from west to the east along this transect as shown in Fig. 9.

4.6. Section E-E': Morelos Guerrero platform

The Morelos-Guerrero platform (MGP) represents the foreland of the Mexican orogen in southern Mexico and unlike section D-D', its deformation has been poorly documented. Except for detailed structural studies by Salinas-Prieto (1994) and Salinas-Prieto et al. (2000) on its western margin and by Fitz-Díaz (2001) and Cerca et al. (2007) on its eastern margin, as well as regional mapping of structures by the Mexican Geological Service (Rivera-Carranza et al., 1998), little of the structural geology has been published. The western boundary between the MGP and hinterland rocks is a highly deformed thrust fan known as the Teloloapan-Pachivia thrust system (TPTS; Salinas-Prieto et al., 2000), in which thrust sheets of platform carbonates are imbricated with Upper Cretaceous turbidites of the Mexcala Formation, with a direction of transport to the east. To the east of the TPTS, a box-fold geometry observed in platform carbonates on a kilometer scale at the surface, along with stratigraphic duplication in the central part of the platform reported in the Tecuman 2 borehole by PEMEX (López-Ramos, 1982), permits us to interpret fault-bend fold imbricates in the lesser known central sector of the section. Farther east, mesoscopic *chevron* folds, and km-scale folds and thrusts have a dominant direction of transport to the east (Fitz-Díaz, 2001). On the eastern edge of the section, east-verging structures are cut by a regional scale, high-angle west-vergent reverse fault, the Papalutla thrust (De Cserna et al., 1980), which emplaced rocks of the Acatlán complex upon the MGP to the west.

Considering the relatively high internal deformation of the rocks in the MGP, the dominant east-vergent structures and the absence of major vertical uplifts, evidenced by the lack of significant stratigraphic discontinuities (such as the exposure of older rocks), makes the structures of this section very similar to those of section D-D' in central Mexico. By analogy we infer an analogous dominant thin-skinned deformation style, with a shallow basal detachment dipping to the west; nevertheless, we have no data that control the depth of the detachment. A progression of deformation from west to east is supported by the fact that the sedimentation of syntectonic turbidites was older, Cenomanian-Turonian, on the western margin of the platform (Hernández-Romano et al., 1997) and younger, Maastrichtian, (Perrillat et al., 2000) to the east.

Cerca et al. (2007) interpreted an initial shortening event in the Morelos-Guerrero platform, affecting the rocks on the eastern margin of the platform, between 68 and 57 Ma and a second strike-slip faulting event, with associated magmatism, affected regional folds and thrusts

between 37 and 29 Ma. At present no ages of deformation have been reported for the western margin of the Morelos-Guerrero platform.

4.7. Section F-F': Cuicateco assemblage-Veracruz basin

This NE-SW cross-section illustrates exposed structures of the northern portion of the Zongolica Range (Ángeles-Moreno, 2006) and buried structures in the Veracruz basin (Ortuño-Arzate et al., 2003). At the southwesternmost end of the section, granulites and granites of the Oaxaca terrane, buried under Cenozoic redbeds, constitute the hanging wall of the Oaxaca normal fault, and northeastward, rocks of the Cuicateco assemblage are exposed. At its western extent, the Cuicateco assemblage includes the Sierra de Juárez mylonite belt (SJMB, Alaniz-Álvarez et al., 1994), which consists of mylonitic diorite migmatites and tonalite gneiss, volcano-sedimentary rocks of the Chivillas Formation (Mendoza-Rosales et al., 2010), and uncommon serpentinites (Delgado-Argote, 1988; Ángeles-Moreno, 2006). According to Alaniz-Álvarez et al. (1996) the SJMB was created by dextral strike-slip movement related to the opening of the Gulf of Mexico and Early Cretaceous reactivation as a reverse fault (Delgado-Argote et al., 1992; Ángeles-Moreno, 2006). Subsequent shortening in the Late Cretaceous and Paleogene probably effected inversion of the former Chivillas pull-apart basin in the southwestern part of section F-F', transferring deformation to the Cordoba platform (Ángeles-Moreno, 2006) and ultimately to the Veracruz basin in the Paleogene (Ortuño-Arzate et al., 2003).

Eastward from the Vista Hermosa thrust, which constitutes the tectonic contact between the Cuicateco assemblage and the Cordoba platform, the cross section is based on the superb cross-section by Ortuño-Arzate et al. (2003), who integrated field observations, seismic interpretations and borehole records to create one of the most complete and detailed cross-sections of the MFTB (Fig. 8). Along this part of the section, imbricated thrust sheets demonstrate east vergence above a basal detachment inclined to the east; however, this is likely not the original dip of the detachment zone, as no evidence for gravitational sliding, such as conjugate updip extension, has been reported or suggested in this area. Paleocene-Eocene growth strata are present in the subsurface and are unconformably buried by Oligocene post-tectonic strata, constraining youngest deformation in the Veracruz basin to the Eocene. This deformation age is consistent with the Paleogene age of deformation of similar structures in the Isthmus of Tehuantepec to the south (Pérez-Gutiérrez et al., 2009).

4.8. MFTB deformation summary

Except for the basin inversion kinematic style in the Chihuahua and Sabinas basins on the northeastern margin of the MFTB, structures are dominantly thin-skinned in the rest of the belt. In the three northernmost sections (A-A', B-B' and C-C'), basement rocks are generally shallower, basement block uplifts are more common than in the southernmost sections, and strata of the Mesozoic section exhibit less internal deformation.

In westernmost outcrops, a conspicuous regional shear zone at the contact between highly deformed siliciclastic Triassic turbidite strata and volcanoclastic units above it (cf., Nazas, La Joya and San Juan de la Rosa formations) could represent the basal detachment of the MFTB wedge, which was locally uplifted by later thick-skinned deformation. To the east, the basal detachment lies in Jurassic-Lower Cretaceous evaporites or carbonaceous shale, and in the Gulf of Mexico coastal plain, the detachment continues in the same stratigraphic level according to seismic interpretations (Alzaga-Ruiz et al., 2009; Roure et al., 2009). In general, rocks above a detachment located in evaporites (e.g., Minas Viejas and Olvido formations, Fig. 4) have less internal deformation than strata above a detachment occupies carbonaceous shale (cf., Santiago Formation in central Mexico), where folds are tighter and or there are more thrust faults (Fitz-Díaz et al., 2011a). Deformation

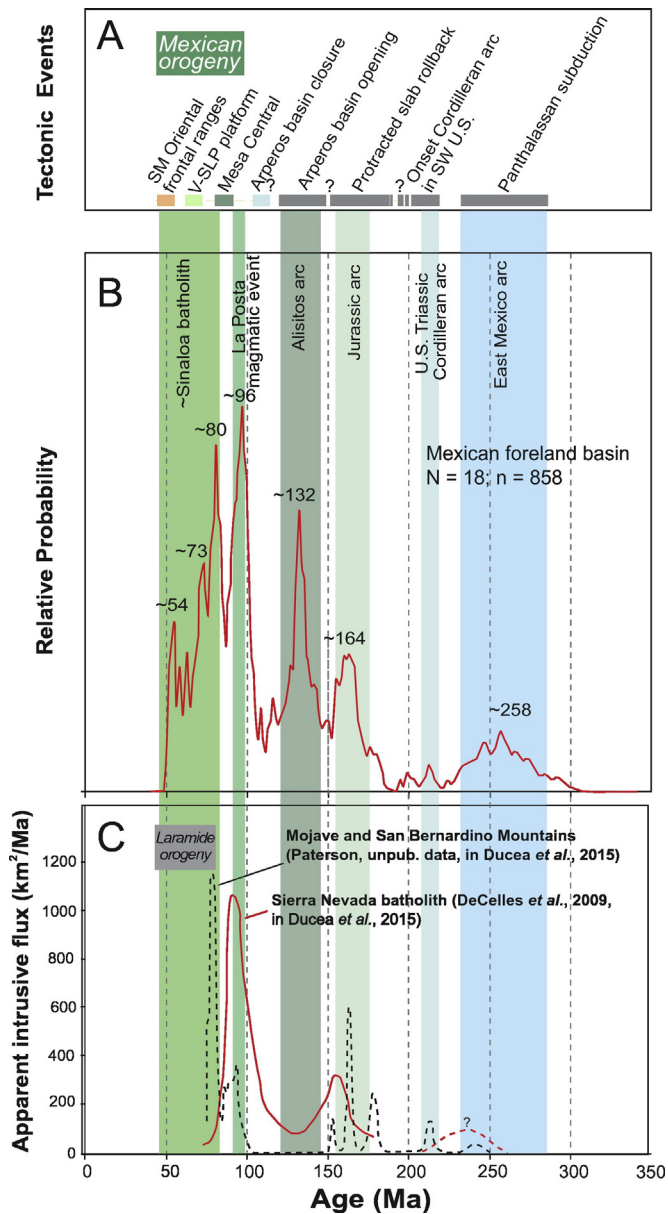


Fig. 12. Mexican orogen and syn-orogenic magmatism. A) Main deformation events of MFTB and southern Laurentia (late Paleozoic–Paleogene, details in the text). Note that Mexican orogen (~98–45 Ma) had a greater temporal history than the Laramide orogen of the U.S. B) Probability distribution of detrital zircons in the foreland basin system of the MFTB. The arc derived grains form three main Late Cretaceous peaks: Early Cenomanian (~96 Ma), early Campanian (~80 Ma) and late Campanian (~73 Ma). A minor peak defined during Ypresian (~52 Ma) results from a single unpublished sample of the Chicontepec Formation. These data support the idea of magmatism migration through time from western to eastern Mexico. C) Relative flux curves of Sierra Nevada batholith and batholithic rocks of southern California interpreted from exposures of igneous rocks of U.S. Cordillera. Note that main Late Cretaceous magmatic peaks match with the interpreted age ranges of La Posta and Sinaloa batholiths of northwestern Mexico.

in platform carbonates is dominated by thrusts and thrust-sheet imbricates, whereas in basinal carbonate successions there is more strain in the rocks that is accommodated by buckle folds, which are unrelated to thrusts (e.g., central Mexico, Fitz-Díaz et al., 2012). On the margins of platforms at changes in mechanical properties of the Cretaceous carbonate interval (Contreras and Suter, 2015), it is common to observe regional scale thrusts, which accommodated considerable displacement for long periods of time (e.g., El Doctor thrust, Garduño-Martínez et al., 2015).

The wavelength of the folds is controlled by the layer thickness of the carbonate horizons, as well as relative competence and thickness

of the rocks of the detachment zone (Hudleston and Treagus, 2010). For instance, in the Zimapán and the Tampico-Misantla basins in east-central Mexico (sensu Suter, 1987), which are mostly composed of thinly-bedded limestone interbedded with chert and shale, relatively tight mesoscopic chevron folds detached above carbonaceous shale are pervasive. In contrast, the Monterrey salient contains a section of thick-bedded carbonate strata >1 km thick (Fig. 4), which overlies hundreds of meters of evaporites, and is overlain by Upper Cretaceous shale. There, the style of shortening consists of a train of detached, kilometer-scale buckle folds developed in the massive limestone strata, which control the fold wavelength (Padilla y Sánchez, 1982).

5. Syn-orogenic magmatism

Subduction-related magmatism accompanied shortening deformation in most of the Mexican orogen during its entire Cenomanian through Eocene history. In this regard, the Mexican orogen differs significantly from the largely amagmatic Laramide orogen of the United States. The Mexican territory has an extensive history of magmatism, mainly in the Sonora region and along a big portion of the Mexican Pacific margin from the Mesoproterozoic to the Miocene (Clark et al., 1982; Damon et al., 1981a,b; Silver and Chappell, 1988; Schaaf et al., 2002; Valencia-Moreno et al., 2001, 2003; Solari et al., 2007; Ortega-Gutiérrez et al., 2014). During the Mesozoic, magmatism was a prevalent process in what is now the hinterland of the Mexican orogen (Guerrero terrane) and included at least two phases of extensional arc-related magmatism (Busby, 2004; Centeno-García et al., 2011). The first phase occurred during the Late Triassic–Late Jurassic and was characterized by intermediate to silicic explosive and effusive volcanism, and was followed by a second phase of arc rifting, during the Late Jurassic–Early Cretaceous, characterized by widespread dike swarms and extensive mafic lavas and hyaloclastites, which are particularly common in the Arperos basin. In the Late Cretaceous, intense calc-alkaline plutonism and silicic volcanism along the Pacific margin (Henry et al., 2003; Valencia et al., 2013; Centeno-García, 2017) took place within an environment of tectonic shortening (Centeno-García et al., 2011).

Syn- and post-orogenic magmatism occurred from the Late Cretaceous to the Miocene, and is concentrated in northwestern and central western Mexico, in the states of Sonora, Sinaloa, Chihuahua, Durango, Jalisco, Colima and Michoacán, although scattered plutons and volcanic rocks are also found to the east, in the states of Coahuila, Nuevo León, Tamaulipas, San Luis Potosí, Zacatecas and Guanajuato (Stein et al., 1994; Ferrari et al., 2005; Molina-Garza et al., 2008; Velasco-Tapia et al., 2011). The Sierra Madre Occidental contains most of the pre-, syn- and post-tectonic magmatic record of the MFTB according to Ferrari et al. (2005), who grouped the subduction related magmatism of this province in four main igneous complexes: (1) Upper Cretaceous to Paleocene plutonic and volcanic rocks; (2) Eocene andesites and lesser dacitic-rhyolites, both of which are included in a “Lower Volcanic Complex” (LVC); (3) silicic ignimbrites emplaced during two pulses of Oligocene (~32–28 Ma) and early Miocene (~24–20 Ma) ages and grouped into the “Upper Volcanic Supergroup” (UVS); and (4) transitional basaltic-andesitic lavas erupted after each ignimbritic pulse and correlated with the Southern Cordillera Basaltic-Andesite (SCORBA) of the southwestern U.S.

Upper Cretaceous–Paleogene plutonic rocks are exposed discontinuously in a belt of large batholiths that extends from northwesternmost Mexico to the vicinity of Michoacán. This belt includes the Puerto Vallarta, Los Cabos, Sinaloa, Sonora and Peninsular Ranges batholiths and marks the location of the continental-margin magmatic arc during shortening of the MFTB. The large-volume eastern part of the Peninsular Ranges batholith of the northern half of the Baja Peninsula was emplaced primarily between 105 and 80 Ma (Ortega-Rivera, 2003), with a major magmatic pulse known as the “La Posta event” between 98 and 92 Ma (Kimbrough et al., 2001). Emplacement of the Los Cabos batholith at the southern tip of the peninsula also began near 100 Ma,

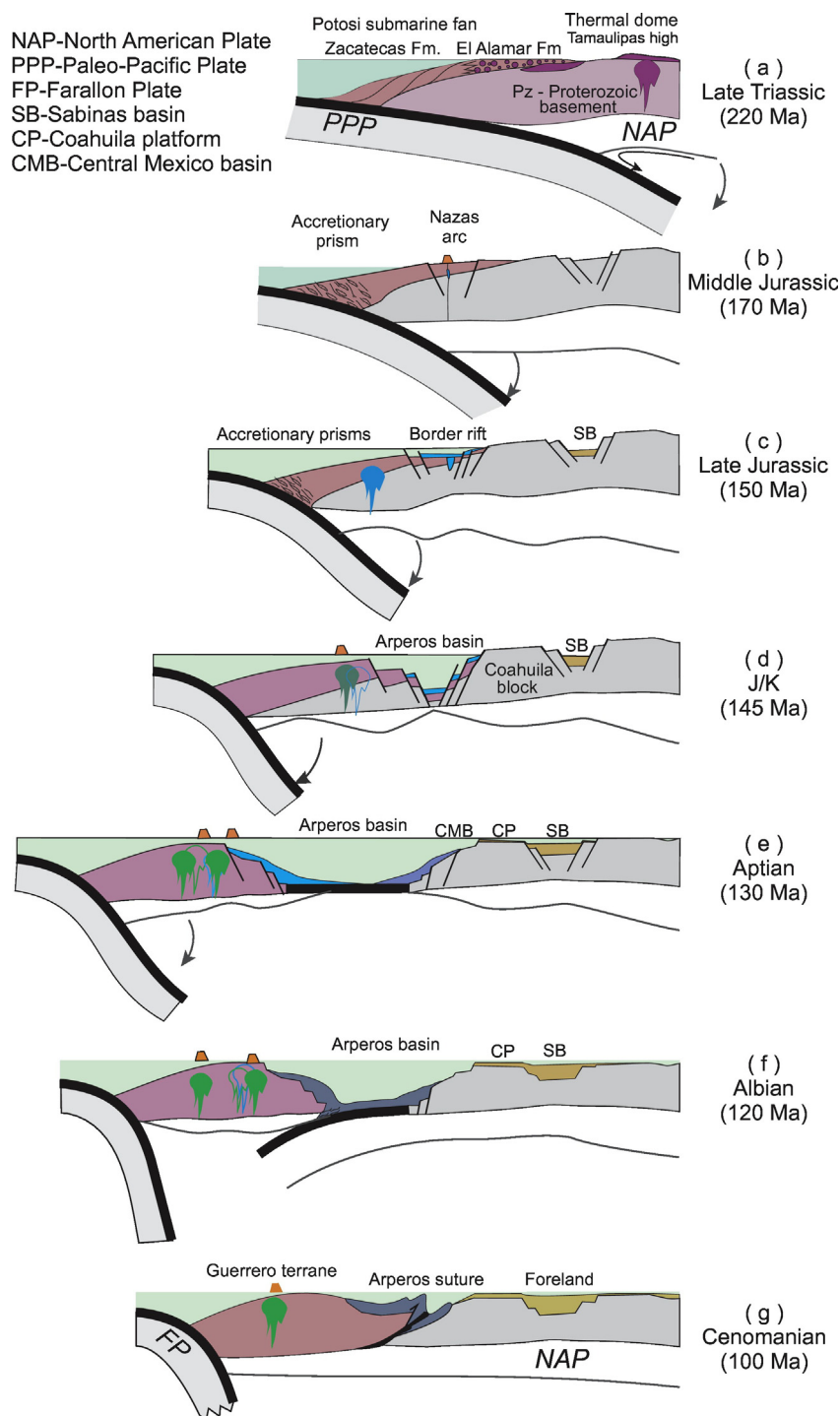


Fig. 13. Mesozoic tectonic evolution of Mexico prior the development of the MFTB viewed along a NE-SW transect from Mazatlán to southern Texas (green line in Fig. 6). a) Late Triassic, erosion of the Permo-Triassic (Torres et al., 1999) and deposition of siliciclastic sediments of the Potosi and El Alamar fans on western Pangaea. b) Beginning rolling back subduction of a paleo-Pacific plate on the western margin of North America, initiation of rifting in the Gulf of Mexico (May 1970; Pindell and Dewey, 1982) and installation of the border rift Nazas Arc. c) Instauration of drifting in the GOM and consolidation of the Nazas arc in western Mexico during the middle Jurassic. d) Back-arc extension in western Mexico that trigger development of Arperos basin during Late Jurassic and end of drifting in GOM basin. e) Drifting in Arperos basin and deposition of Cuestecita and Arperos Formation in the west of the basin and Valenciana and Los Cuarcos in the continental margin in the area of Guanajuato (Martini et al., 2014), end of drifting in the GOM during Late Jurassic. f) Major subsidence in the GOM basin and deposition of argillaceous and carbonate rocks during Early Cretaceous time (Wilson, 1990). g) Closure of Arperos basin during Late Aptian (Martini et al., 2016).

but continued to about 80 Ma (Duque-Trujillo et al., 2014), and the Puerto Vallarta batholith, which was contiguous with the Los Cabos batholith prior to opening of the Gulf of California, likewise has yielded U-Pb crystallization ages of ~100–80 Ma (Schaaf et al., 1995; Valencia et al., 2013). The Sinaloa batholith represents the southern continuation of the Sonora batholithic complex and was apparently a long-lived

magmatic complex, with intrusive ages ranging 101–45 Ma (Henry et al., 2003).

In northeastern Mexico, most Upper Cretaceous-Paleogene igneous rocks constitute small outcrops of volcanic deposits or shallow plutonic bodies emplaced in the sedimentary section. Most of the older rocks are buried beneath younger volcanic or continental deposits. Syntectonic

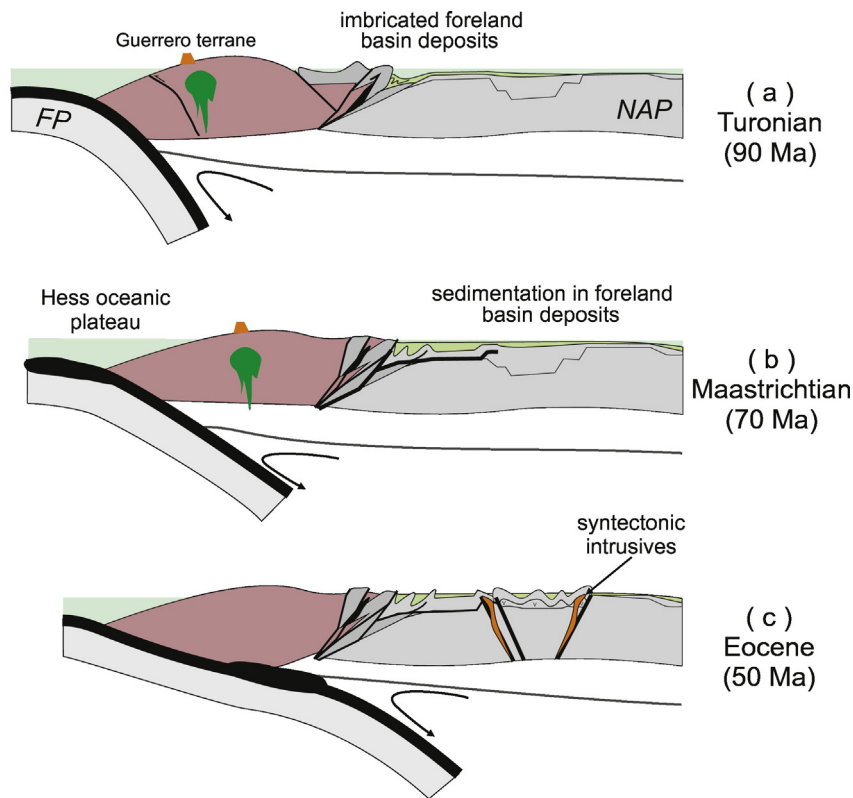


Fig. 14. Tectonic scenarios in which the three episodes of deformation described from the MFTB might have occurred in the Late Cretaceous–Paleogene. Explanation is provided in the text.

plutonic bodies are elongate perpendicular to the direction of shortening and have a strong internal magmatic foliation that is concordant with the structural orientation of hosting folds and thrusts (e.g., Chávez-Cabello, 2005; Solé et al., 2007; Ramírez-Peña and Chávez-Cabello, 2017; Ramírez-Peña and Chávez-Cabello, 2017). Other plutons that cross-cut folds and thrusts and lack an internal fabric coaxial with shortening structures are interpreted as post-tectonic (Molina-Garza et al., 2008). The post-tectonic plutons are commonly Eocene granitic bodies (Fig. 8, section B–B'), whereas syntectonic intrusives range from Late Cretaceous to Paleogene in age and tend to be more mafic in composition than the post-tectonic plutons.

Numerous workers have documented a general eastward migration of magmatism across northern Mexico from the Pacific paleotrench toward the Mexican foreland during MFTB deformation (Fig. 10). Temporal eastward migration of magmatism was first proposed on the basis of data from Sonora (Damon et al., 1981a,b; Clark et al., 1982), where there is evidence that migration accelerated between 70 and 60 Ma (Ramos-Velázquez et al., 2008). Clark et al. (1982) also noted a Late Cretaceous to late Eocene shift from calc-alkalic to high-K calc-alkalic pluton chemistry. Late Eocene magmatism in Coahuila extended nearly 1000 km east of the paleotrench (Chávez-Cabello, 2005). Henry et al. (2003) suggested that further south, at the latitude of the states of Sinaloa and Durango, magmatism migrated only ~100 km eastward between 100 and 45 Ma, reaching a distance ~400 km east of the paleotrench (Fig. 10).

The migration of magmatism through time from western to eastern Mexico, in concert with chemical variation, has been explained by two different tectonic models: (1) A progressive increase in subduction rate and attendant decrease in subduction angle of the Farallon plate under North America, followed by a later plate roll-back as in the southwestern U.S. (Coney and Reynolds, 1977; Damon et al., 1981a,b), or (2) subduction of a thickened segment of the Farallon plate (e.g., an oceanic plateau) to create flat subduction during the latest Cretaceous–early Eocene, and later reestablishment of a steeper subduction angle after the plateau passage (Ferrari et al., 2005). The second model is supported

by recent independent evidence that predicts passage of the Hess conjugate oceanic plateau under northern Mexico from 70 to 50 Ma (Liu et al., 2010). Nevertheless, flat subduction of the Hess conjugate does not explain continued magmatism in the Mexican orogen during latest Cretaceous–Eocene time.

6. Timing of deformation in the Mexican orogen

Deformation timing in the Mexican orogen has been inferred from various sources of geologic data, including (1) ages of syntectonic and cross-cutting plutons (e.g., Johnson et al., 1999; Henry et al., 2003; Chávez-Cabello, 2005; Ramos-Velázquez et al., 2008), (2) the age of syntectonic sedimentary deposits or the ages of angular unconformities in the stratigraphic succession (e.g., Gray and Lawton, 2011; González-León et al., 2011; Centeno-García et al., 2011); and (3) absolute ages of folds, faults and shear zones on the basis of ages of syntectonic mica or illite (Iriondo et al., 2005; Cuéllar-Cárdenas et al., 2012; Fitz-Díaz and van der Pluijm, 2013; Fitz-Díaz et al., 2014a,b; Fitz-Díaz et al., 2016). Data from different sources are summarized in Fig. 11 to provide an overview the timing of deformation in the Mexican orogen.

The time range of deformation interpreted in different structures of the Mexican orogen is organized spatially from west to east and temporally from oldest to youngest in Fig. 10. The table indicates that shortening deformation in the Mexican orogen started in the hinterland in the Early Cretaceous, presumably localized on its western edge along accretionary prisms (Moore, 1985). Stratigraphic relations (Martini et al., 2013, 2014; Ortega-Flores et al., 2015) and $^{39}\text{Ar}/^{40}\text{Ar}$ whole-rock ages of metavolcanic rocks (Eliás-Herrera et al., 2000) and hornblende ages separated from metabasites (Delgado-Argote et al., 1992) indicate the closure of the Arperos basin took place in southern and central Mexico during the Albian (blue band in map and correlation table of Fig. 10). Kinematic studies of structures in southern Mexico indicate that during basin closure, rocks of the Guerrero terrane arc were thrust eastward over the Arperos basin (Salinas-Prieto et al., 2000), producing intense

pervasive deformation characterized by isoclinal folding in metasedimentary rocks (Fitz-Díaz et al., 2008) and localized deformation recorded by anastomosing mylonite zones, such as those exposed in metavolcanic rocks of Valle de Bravo, Estado de México (Fitz-Díaz et al., 2008) or the Sierra de Guanajuato (Martini et al., 2011, 2012). Albian deformation was also determined on the basis U-Pb zircon ages from syntectonic plutons of the Main Martir thrust, on which eastern Peninsular Ranges plutons are thrust over volcanic and sedimentary rocks of the Alisitos arc in Baja California (Johnson et al., 1999). The Main Martir thrust has a direction of transport to the west, which is opposite to that observed in southern Mexico (Fig. 2). Metamorphism of ophiolite assemblages in the footwall of this shear zone, to the west of the Alisitos arc, in the Vizcaino peninsula also occurred during the Albian (Baldwin and Harrison, 1992).

Following closure of the Arperos basin, another shortening event affected the rocks in both the Guerrero terrane and the westernmost side of the MFTB (deep green band, Fig. 10). This episode is as old as Cenomanian (~98–90 Ma) and as young as early Coniacian in the hinterland, according to the age of syntectonic intrusives (Henry et al., 2003) and the age of the Todos Santos mylonite (Cuéllar-Cárdenas et al., 2012). In the westernmost exposures of the Guerrero and Zihuatanejo terranes in Colima and Michoacán, shortening and metamorphism of Upper Jurassic and Lower Cretaceous units occurred between Turonian and Coniacian time (Centeno-García et al., 2011). Despite the above investigations, a scarcity of structural studies in the Guerrero terrane prevents a complete perspective on the kinematics, style and history of deformation between the Turonian and Campanian in the Guerrero terrane. The first folding event in the westernmost exposures of the MFTB occurred during the Turonian-Early Campanian (Fitz-Díaz et al., 2014b). Although a little younger, these structures are in part contemporaneous with shortening structures in the Guerrero terrane described above and for this reason we group them in the same deformation episode, colored with deep green in the structural map and correlation table of Fig. 11. This generation of folds of the MFTB is tight to isoclinal in medium to thinly bedded limestone of the Mesa Central, and their axes show abrupt orientation variations on the map (Fig. 11).

From late Campanian to Maastrichtian time, a second shortening event, which is evidenced by refolding, affected the MFTB. Structures of this event are shown in green in the map and the correlation table of Fig. 11. This generation of folds is relatively more open and widely spaced and is superimposed on older folds in the Zimapán basin (Figs. 8 and 9). During this time, it is possible that the folds of the Parras transverse belt and the Monterrey salient advanced the front of the MFTB further east. The trend of the fold axes of the second episode of deformation is shown in pale green in the map of Fig. 11. These fold axes also show a sinuous trend along a belt in the middle of the MFTB, which is the same as the trend of the older folds, and could also be a result of refolding.

The youngest folds and thrusts in the MFTB are indicated in orange on its eastern front, and are as old as 64 Ma and as young as 42 Ma (middle Eocene) in central Mexico (Fitz-Díaz and van der Pluijm, 2013). In northern Mexico, the folds of the Monterrey salient (Fitz-Díaz et al., 2016), of La Popa (Gray and Lawton, 2011), Sabinas (Chávez-Cabello, 2005) and Chihuahua basins (McDowell and Mauger, 1994) were also formed in this time range. In southern Mexico, the age of growth strata indicate a Paleogene episode of shortening in folds buried beneath the coastal plain of the Gulf of Mexico in the Tampico-Misantla and Veracruz basins (Ortuño-Arzate et al., 2003; Alzaga-Ruiz et al., 2009; Roure et al., 2009). The southernmost structures of the MFTB, in the Isthmus of Tehuantepec, involve 65 Ma old rocks (Pérez-Gutiérrez et al., 2009), and thus likely also formed during the Paleogene shortening episode, which seems to be a pervasive event of deformation in the eastern foothills of the MFTB. Nevertheless, Paleogene structures of the MFTB show very contrasting styles. In northern Mexico the shortening is recorded by a basin-inversion deformation style, whereas in southern Mexico,

particularly in the Veracruz basin, the deformation is thin-skinned (Ortuño-Arzate et al., 2003).

Distribution of structural ages indicates that shortening in the Mexican orogen was older to the west and that thrust deformation advanced eastward progressively and episodically (Fig. 11). Regional patterns of shortening are thus consistent with documented shortening ages along a transect in central Mexico (Fitz-Díaz et al., 2014a, Fig. 9), and therefore the age of shortening episodes can be extrapolated north and south along the MFTB. The oldest folds (Fig. 11, deep green domain) seem to be tightly refolded on the western side of the belt, whereas Campanian-Maastrichtian structures are distributed along a sinuous belt along the eastern front of the Sierra Madre Oriental that continues along the Parras transverse belt. Paleogene structures are located in the inverted foreland of northeastern Mexico and in the Tampico-Misantla and Veracruz basins.

Possible correspondence of magmatic events and shortening in the MFTB can be estimated from the content of detrital zircon age groups in sandstones of the foreland basin (Fig. 12). The shortening events described above from $^{40}\text{Ar}/^{39}\text{Ar}$ ages on neomorphic illite (Fig. 12A) overlap with Late Cretaceous and Paleogene magmatic events recorded as detrital zircon age peaks present in eighteen combined foreland-basin sandstones (Fig. 12B). The detrital-zircon age peaks record the ~100–92 Ma La Posta magmatic event of the Peninsular Ranges batholith and contemporary batholiths on the continental margin, as well as Santonian and late Campanian peaks at ~80 and ~73 Ma, and a prominent peak at ~54 Ma, which is contributed by a single sandstone sample from the Eocene part of the Chicotepec Formation in the Tampico-Misantla basin (Fig. 4). Cenomanian turbidites of the foreland basin, which contain abundant approximately syndepositional zircons derived from the La Posta magmatic event, were quickly deformed by shortening that began in the Turonian. The second influx of zircons into the foreland basin appears to have taken place during continued shortening during the initial Turonian-early Campanian shortening event. The age peak at ~73 Ma corresponds with onset of late Campanian shortening recorded in the Zimapán basin (Fig. 12A, B). Two minor peaks and a major peak at ~54 Ma indicate marked influx of Paleocene zircons to the foreland and corresponds to an interval of rapid subsidence in the Tampico-Misantla basin. This Paleocene influx correlates with shortening ages from the eastern front of the Sierra Madre Oriental.

Estimates of intrusive-flux rates during the life of the continental margin arc in the U.S. (Fig. 12C) demonstrate both similarities and differences with magmatic history, as inferred from our preliminary detrital-zircon data set. The Sierra Nevada batholith experienced a large magmatic episode coeval with the La Posta event, but lacks the Santonian-Campanian event that is prominent in Mexico. Nevertheless, the Santonian-Campanian event is prominent in the San Bernardino Mountains and Mojave Desert of southern California. Paleogene magmatism west of the Eocene province of the U.S. is markedly absent, in contrast to Paleogene syndeformational magmatism indicated by zircon grains from an Eocene sample in the detrital analyses of Fig. 12B. The absence of U.S. Paleogene magmatism illustrates the amagmatic character of the U.S. Laramide event and its difference from the Mexican orogen.

7. Tectonic evolution of Mexico during the Mesozoic and the development of the Mexican orogen

The tectonic evolution of Mexico from Triassic through the end of Early Cretaceous time was dominated by extensional deformation, but we include a summary of that deformation because of its profound influence on style and distribution of Late Cretaceous-Paleogene Mexican deformation. In this section, a sequential model (Fig. 13) of important Triassic-Albian tectonic events is illustrated along a transect from Sinaloa to southern Texas (green line of Fig. 7), followed by a model for deformation of the Mexican orogen itself (Fig. 14). Each step of this tectonic evolution remains controversial and debated.

Extensive exhumation of Upper Permian-Lower Triassic granitoids took place in eastern Mexico, accompanied by deposition of voluminous submarine fans along the western flank of Proterozoic basement in Mexico. The granitoids were emplaced as part of a continental margin arc that persisted along the western margin of Gondwana after its suturing with Laurentia (Torres et al., 1999; Dickinson and Lawton, 2001). The detrital zircon record of the Upper Triassic submarine-fan deposits suggests rapid exhumation of the Permo-Triassic batholith of eastern Mexico and the presence of a Late Triassic magmatic gap (Barboza-Gudiño et al., 2010; Ortega-Flores et al., 2014). Nevertheless, Upper Triassic granite porphyries and Jurassic sandstones with abundant Late Triassic grains have recently been described from the Chihuahua basin in northern Mexico (Villarreal-Fuentes et al., 2014). Although the voluminous Upper Triassic deposits have been attributed to cessation of subduction and development of a passive margin along Mexico's west coast (Centeno-García and Silva-Romo, 1997; Barboza-Gudiño et al., 2010), we suggest that rapid exhumation of the Permo-Triassic granitoid trend of eastern Mexico resulted from flat-slab subduction even as normal subduction continued farther northwest beneath northwestern Mexico and the southwestern U.S., where abundant evidence of Late Triassic magmatism is present in the Chinle Formation and correlative stratigraphic units (Riggs et al., 1993) and in Jurassic strata of northeastern Chihuahua (Fig. 13a; Villarreal-Fuentes et al., 2014).

Early to Middle Jurassic magmatism has been attributed to the Nazas arc, which extended from northwest to southeast across northern Mexico, and is also present in Chiapas (Dickinson and Lawton, 2001; Bartolini et al., 2003; Godínez-Urban et al., 2011; Lawton and Molina-Garza, 2014). The volcanic succession of the arc contains thick siliciclastic successions interbedded with volcanic and pyroclastic rocks and thus has been attributed to arc development in a succession of extensional basins termed an arc-graben depression (Busby-Spera, 1988). Middle and Late Jurassic extension in Mexico and the southwestern USA has been variably attributed to opening of the Gulf of Mexico and attendant processes related to the breakup of Pangea (Stern and Dickinson, 2010; Martini and Ortega-Gutiérrez, in press) and to rollback of a subducting oceanic slab that lay west of Mexico (Lawton and McMillan, 1999; Dickinson and Lawton, 2001). We suggest that extension in Mexico was due to a combination of North America-South America separation (e.g., Pindell and Kennan, 2009) and slab rollback, the latter of which began in Late Triassic-Early Jurassic time (Fig. 13b) and continued through the Jurassic as described below.

The locus of Late Jurassic volcanism lies west of the inferred trace of the Middle Jurassic volcanic arc as recorded by plutons in the Baja California Peninsula and Jalisco (Valencia et al., 2013) and Sinaloa (Vega-Granillo et al., 2008). The Middle and Late Jurassic magmatic trends appear to merge in northern Sonora (e.g., Anderson et al., 2005a,b), but in most of Mexico, continued slab roll back appears to explain Jurassic igneous rock distribution (Fig. 13c).

The Arteaga complex forms the basement of the Guerrero terrane on the Pacific margin of Mexico and contains similar detrital zircon age patterns to those of the Triassic submarine-fan systems of central Mexico. The detrital zircon link suggests that the Arteaga complex was deposited in the same Triassic sedimentary system on the edge of Mexico (Centeno-García, 2005), and implies that the Guerrero terrane was not as allochthonous as formerly thought, but rather that it was separated from the Mexican mainland in the Late Jurassic-Early Cretaceous (Martini et al., 2011, 2013, 2014; Ortega-Flores et al., 2014, 2015, Fig. 13d). At present, we are unsure how far the Guerrero terrane was separated from the Mexican mainland, but the extension of the resulting Arperos basin was likely adequate to produce oceanic crust (Lapierre et al., 1992; Freyrier et al., 1996; Martini et al., 2011, Fig. 13e). Shortening and low grade metamorphism during the closure of the Arperos basin most likely occurred during the Albian (Fig. 13f), as a consequence of west-facing subduction of the newly formed oceanic crust. We base our speculation on the fact that Guerrero rocks were

thrust over the Arperos basin rocks and the fact that the foreland basin developed to the east of the suture. Although considerable internal deformation was accumulated in the Arperos suture (Salinas-Prieto et al., 2000; Fitz-Díaz et al., 2008), no shortening deformation was propagated to the east, as carbonate sedimentation prevailed during that time in the foreland. It is also likely that deformed rocks of the Arperos basin remained beneath sea level as no detrital material derived from the oceanic rocks has been observed in carbonate successions to the east. Finally, we infer a breakup of the paleo-Farallon plate at this point of time as a result of the opposing subduction directions beneath the Guerrero terrane, which might have caused interaction between the two subducting slabs. The paleo-Farallon slab is likely one of the many vertical slab walls observed in seismic tomography data under the Caribbean region interpreted as detached pieces of paleo-Pacific plates (Sigloch and Mihalynuk, 2013).

Paleogene deformation in the MFTB, dominated by thick-skinned structures in northern Mexico (Fig. 14c) and thin-skinned structures in central and eastern Mexico, may have occurred due to geographically distinct mechanisms. For instance, Laramide structures of the Colorado Plateau required of a particular subduction setting that involved flat subduction (Dickinson and Snyder, 1978) presumably of the conjugate Shatsky oceanic plateau (Tarduno et al., 1985; Liu et al., 2010), which caused coupling between the North American and Farallon plates and produced crustal-scale shortening in the southwestern U.S. (see Fig. 6 in Yonkee and Weil, 2015). The conjugate Hess plateau was subducted under northern Mexico in the Paleogene, later than the Shatsky conjugate (Liu et al., 2010), but it did not affect most of Mexico. Nonetheless, there was also an increase in rate of westward North American plate motion during the Paleogene (van der Meer et al., 2010). Thus it is possible that these two combined factors, or one dominating over the other in different places, might have caused the diversity of structure that was characteristic of the MFTB during the Paleogene.

Because the detachment zone in some parts of the MFTB is flat (Fig. 8, sections B-B', C-C') or dips to the east (Fig. 8, section F-F'; e.g., the Veracruz basin), it has been suggested that gravitational sliding drove the deformation (de Cserna, 1956). Nevertheless, there is no evidence in the form of up-dip contemporary conjugate extension reported anywhere within the MFTB similar to that observed in gravitational structures in the Gulf of Mexico (e.g., Peel et al., 1995). Moreover, evidence such as a gradient of shortening, temperature of deformation and topography increasing to the west (Fitz-Díaz et al., 2011a,b, 2012) corroborate the development of an orogenic wedge across the MFTB.

New geological data from the last 15 years pertaining the Mesozoic stratigraphy and structural geology of central Mexico (Martini et al., 2014, and references therein) combine to support progressive closure of the Arperos back-arc basin, along with convergence of the Farallon plate hinge and the North American plate as the principal mechanisms that drove shortening in the Mexican orogen. Plate interactions and shortening were enhanced by acceleration of westward North American plate motion between 90 and 70 Ma, and again during the Paleogene, corresponding to the times of primary deformation recorded in the MFTB.

8. Conclusions

Structural, stratigraphic and geochronological data, including recent studies, cited herein, from the hinterland and foreland of the Mexican fold-thrust belt, support the following general conclusions:

1. The Mexican fold-thrust belt possesses many key aspects, including (a) a variable **deformation style** dominated by basin inversion in the north and thin-skinned and fold-dominated shortening in central and southern Mexico, (b) a characteristic **deformation history** consisting of at least three superimposed belts that propagated

deformation to the east, (c) Late Cretaceous to Eocene **syn-orogenic sedimentation patterns**, and (d) a distinctive **tectonic scenario** which included a collapsed back-arc basin and volcanic superterrane to the west. Although it shares some of these characteristics with the Sevier and Laramide orogens of the U.S., in the aggregate, they clearly distinguish the Mexican orogen from those orogens lying to the north.

- In contrast to the Laramide orogen of the U.S., continental magmatism was a continuous process throughout the evolution of the Mexican orogen. The foreland basin system of the orogen thus constituted a retroarc foreland basin. Volcanic rocks provided voluminous detritus to the evolving basin, and young detrital zircons provide key evidence to stratigraphic age of the foreland-basin strata.
- The arrival of the para-autochthonous Guerrero terrane and attendant closure of the Arperos basin to form the Arperos suture either completely preceded, or were at most the first manifestation of deformation of the Mexican fold-thrust belt. All three tectono-structural elements – volcanic superterrane and oceanic suture of the hinterland, and deformed foreland – together constitute the Mexican orogen.
- The magmatic-flux model, which explains large-scale cycles of subduction-related magmatism, hinterland uplift, linked erosion and sedimentation, and deformation in the foreland (DeCelles et al., 2009), provides a first-order mechanism for the origin of the Mexican fold-thrust belt. We conclude that Late Cretaceous–Paleogene deformation was a result of a single, evolving subduction zone that lay west of the Guerrero terrane, rather than multiple events of terrane accretion or gravity-driven shortening. Active magmatism during the entire history of MFTB shortening likewise implicates the subducted Farallon slab as a principal driver of crustal orogenesis. Moreover, deformation-magmatic cycles coincide with periods of westward acceleration of the North American plate (van der Meer et al., 2010) and further corroborate subduction as the principal tectonic driver of Mexican orogenesis. Nevertheless, the magmatic flux model imperfectly explains patterns of magmatism in northern Mexico, suggesting at least local flat-slab subduction, perhaps related to the passage of the Hess ridge beneath Mexico.

Acknowledgments

This work was supported by CONACYT grants 240662 (to Fitz-Díaz) and 240932 (to Lawton), and group CONACYT project 164454, led by Fernando Ortega Gutiérrez. We thank Gary G. Gray for discussions of Mexican geology in the field, and Carlos Gonzalez-León for sharing his vast knowledge of the geology of Sonora. We express our gratitude to César Francisco Ramírez Peña and to Victoria Urueta Pineda and Laura Luna for their assistance in figure preparation. We also appreciate the support of Arlo Weil to create Fig. 2 in this manuscript. At last, but not least, we thank Matthew E. Brueseke for his useful reviews, as well as to the anonymous reviewer and the Editor.

References

- Alaniz-Álvarez, S.A., Ortega-Gutiérrez, F., Nieto-Samaniego, A.F., 1994. Structural evolution of the Sierra de Juárez mylonitic complex, State of Oaxaca, México. *Rev. Mex. Cienc. Geol.* 11, 147–156.
- Alaniz-Álvarez, S.A., van der Heyden, P., Nieto-Samaniego, A.F., Ortega-Gutiérrez, F., 1996. Radiometric and kinematic evidence for Middle Jurassic strike-slip faulting in southern Mexico related to the opening of the Gulf of Mexico. *Geology* 24, 443–446.
- Allen, P.A., Burgess, P.M., Galewsky, J., Sinclair, H.D., 2001. Flexural-eustatic model for drowning of the Eocene perialpine carbonate ramp and implications for Alpine geodynamics. *Bull. Geol. Soc. Am.* 113, 1052–1066.
- Almazán-Vázquez, E., 1988. Marco paleosedimentario y geodinámico de la formación Alisitos en la península de Baja California. Universidad Nacional Autónoma de México. *Inst. Geol. Rev.* 7, 41–51.
- Alonso-Manuel, F., 2016. Capas Cerro La Bruja, cerca de la Falla de San Marcos, Las Palomas, Coahuila. Bachelor's thesis. Universidad Nacional Autónoma de México (120 pp).
- Altamira-Areyan, A., 2002. Las litofacies y sus implicaciones de la cuenca sedimentaria Cutzamala-Tiquicheo estados de Guerrero y Michoacán, México. Universidad Nacional Autónoma de México, MSc thesis (79 pp).
- Álvarez, M., 1949. Unidades tectónicas de la República Mexicana (incompleta).
- Alzaga-Ruiz, H., Lopez, M., Roure, F., Séranne, M., 2009. Interactions between the Laramide foreland and the passive margin of the Gulf of Mexico: tectonics and sedimentation in the Golden Lane area, Veracruz State, Mexico. *Mar. Pet. Geol.* 26, 951–973.
- Anderson, T.H., Jones, N.W., McKee, J.W., 2005a. The Taray Formation: Jurassic(?) mélange in northern Mexico–tectonic implications. In: Anderson, T.H., Nourse, J.A., McKee, J.W., Steiner, M.B. (Eds.), *The Mojave-Sonora Megashar Hypothesis: Development, Assessment, and Alternatives*. *Geol. Soc. Am. Special Paper Vol.* 393, pp. 427–455.
- Anderson, T.H., Rodríguez-Castañeda, J.L., Silver, L.T., 2005b. Necesitamos distinguir 2005a y 2005b en el texto. Jurassic rocks in Sonora, Mexico: relations to the Mojave-Sonora megashar and its inferred northwestward extension. In: Anderson, T.H., Nourse, J.A., McKee, J.W., Steiner, M.B. (Eds.), *The Mojave-Sonora Megashar Hypothesis: Development, Assessment, and Alternatives*. *Geological Society of America Special Paper Vol.* 393, pp. 51–95.
- Ángeles-Moreno, E., 2006. Petrografía, geología estructural y geocronología del borde noroccidental del terreno Cuicateco, Sierra Mazateca, Estado de Oaxaca, México. Universidad Nacional Autónoma de México, MSc thesis (216 pp).
- Ángeles-Moreno, E., 2012. Geological Map of the Western Border of the Cuicateco Terrane, Southern Mexico. *Geological Society of America MCH102* (1 sheet).
- Ángeles-Villeda, M.E., Hinojosa-Espinosa, J.J., López-Oliva, J.G., Valdés-González, A., Livas-Vera, M., 2005. Estratigrafía y microfácies de la parte sur del Cañón La Boca, Santiago, Nuevo León, México. *Rev. Mex. Cienc. Geol.* 22, 272–281.
- Aranda-Gómez, J.J., McDowell, F.W., 1998. Paleogene extension in the southern Basin and Range province of Mexico: syndepositional tilting of Eocene red beds and Oligocene volcanic rocks in the Guanajuato Mining District. *Int. Geol. Rev.* 40, 116–134.
- Armstrong, R.L., 1968. Sevier orogenic belt in Nevada and Utah. *Bull. Geol. Soc. Am.* 79, 429–458.
- Armstrong, R.L., 1974. Magmatism, orogenic timing, and orogenic diachronism in the Cordillera from Mexico to Canada. *Nature* 247, 348–351.
- Baker, C.L., 1922. General geology of Catorce mining district. *Am. Inst. Min. Met. Eng. Trans.* 66, 42–48.
- Baldwin, S.L., Harrison, T.M., 1992. The PTt history of blocks in serpentinite-matrix mélange, west-central Baja California. *Bull. Geol. Soc. Am.* 104, 18–31.
- Bally, A.W., Gordy, P.L., Stewart, G.A., 1966. Structure, seismic data, and orogenic evolution of southern Canadian Rocky Mountains. *Bulletin of Canadian Petroleum Geology* 14, 337–381.
- Barboza-Gudiño, J.R., Hoppe, M., Gómez-Anguiano, M., Martínez-Macías, P.R., 2004. Aportaciones para la interpretación estratigráfica y estructural de la porción noroccidental de la Sierra de Catorce, San Luis Potosí, México. *Rev. Mex. Cienc. Geol.* 21, 299–319.
- Barboza-Gudiño, J.R., Zavala-Monsiváis, A., Venegas-Rodríguez, G., Barajas-Nigoche, L.D., 2010. Late Triassic stratigraphy and facies from northeastern Mexico: tectonic setting and provenance. *Geosphere* 6, 621–640.
- Barboza-Gudiño, J.R., Ocampo-Díaz, Y.Z.E., Zavala-Monsiváis, A., López-Doncel, R.A., 2014. Procedencia como herramienta para la subdivisión estratigráfica del Mesozoico temprano en el noreste de México. *Rev. Mex. Cienc. Geol.* 31, 303–324.
- Barboza-Gudiño, J.R., Torres-Hernández, J.R., Villasuso-Martínez, R., 2016. Revisión estratigráfica y estructura de la Sierra Plomosa, Chihuahua. *Rev. Mex. Cienc. Geol.* 33, 221–238.
- Bartolini, C., Lang, H., Spell, T., 2003. Geochronology, geochemistry, and tectonic setting of the Mesozoic Nazas arc in north-central Mexico, and its continuation to northern South America. In: Bartolini, C., Buffler, R.T., Blickwede, J. (Eds.), *The Circum-Gulf of Mexico and the Caribbean: Hydrocarbon Habitats, Basin Formation, and Plate Tectonics: America Association of Petroleum Geologists Memoir*. 79, pp. 427–461.
- Barton, M.D., Hanson, R.B., 1989. Magmatism and the development of low-pressure metamorphic belts: implications from the western United States and thermal modeling. *Bull. Geol. Soc. Am.* 101, 1051–1065.
- Beaumont, C., 1981. Foreland basins. *Geophys. J. Int.* 65, 291–329.
- Beaumont, C., Fulsack, P., Hamilton, J., 1992. Erosional control of active compressional orogens. In: McClay, K.R. (Ed.), *Thrust Tectonics*. Chapman and Hall, pp. 1–18.
- Bolaños-Rodríguez, D., 2006. Análisis estructural en el Puerto de las sierras La Fragua, El Granizo, San Marcos-Pinos y áreas aledañas en la parte central de Coahuila. Universidad Nacional Autónoma de México, Bachelor's thesis (74 pp).
- Boles, I.R., Landis, C.A., 1984. Jurassic sedimentary melange and associated facies, Baja California, Mexico. *Geol. Soc. Am.* 93, 513–521.
- Böse, E., 1923. Vestiges of an ancient continent in northeast Mexico. *Am. J. Sci.* 34, 310–337.
- Brown, M., 1993. P–T–t evolution of orogenic belts and the causes of regional metamorphism. *J. Geol. Soc.* 150, 227–241.
- Busby, C., 2004. Continental growth at convergent margins facing large ocean basins: a case study from Mesozoic convergent-margin basins of Baja California, Mexico. *Tectonophysics* 392, 241–277.
- Busby, C., Adams, B.F., Mattinson, J., Deoreo, S., 2006. View of an intact oceanic arc, from surficial to mesozonal levels: Cretaceous Alisitos arc, Baja California. *J. Volcanol. Geotherm. Res.* 149, 1–46.
- Busby-Spera, C.J., 1988. Evolution of a Middle Jurassic back-arc basin, Cedros Island, Baja California: evidence from a marine volcanoclastic apron. *Bull. Geol. Soc. Am.* 100, 218–233.
- Campana, U.M.F., 1985. The Mexican thrust belt. In: Howell, D.G. (Ed.), *Tectonostratigraphic Terranes of the Circum-Pacific Region*. Circum-Pacific Council for Energy and Mineral Resources, Earth Science Series Vol. 1, pp. 299–313.
- Campana, M.F., Coney, P.J., 1983. Tectono-stratigraphic terranes and mineral resource distributions in Mexico. *Can. J. Earth Sci.* 20, 1040–1051.
- Carreño, A.L., Smith, J.T., 2007. Stratigraphy and correlation for the ancient Gulf of California and Baja California Peninsula, Mexico. *Bull. Am. Paleontol.* 317 (146 pp).

- Carrillo-Bravo, J., 1961. Geología del Anticlinorio Huizachal-Peregrina al NW de Ciudad Victoria, Tamaulipas. *Bol. Asoc. Mex. Geol. Petrol.* 13, 1–98.
- Carrillo-Bravo, J., 1965. Estudio geológico de una parte del Anticlinorio de Huayacocotla. *Bol. Asoc. Mex. Geol. Petrol.* 17, 73–96.
- Carrillo-Bravo, J., 1971. La Plataforma Valles-San Luis Potosí. *Bol. Asoc. Mex. Geol. Petrol.* 23, 1–113.
- Carrillo-Martínez, M., 1989. Structural analysis of two juxtaposed Jurassic lithostratigraphic assemblages in the Sierra Madre Oriental fold and thrust belt of central Mexico. *Geofis. Int.* 28, 1007–1028.
- Carrillo-Martínez, M., 1990. Geometría estructural de la Sierra Madre Oriental, entre Peñamiller y Jalpan, Estado de Querétaro. *Rev. Mex. Cienc. Geol.* 9, 62–70.
- Carrillo-Martínez, M., 1997. Hoja Zimapán 14Q-e (7): con resumen de la geología de la hoja Zimapán, estados de Hidalgo y Querétaro. Instituto de Geología, Universidad Nacional Autónoma de México (1 sheet).
- Centeno-García, E., 2005. Review of Upper Paleozoic and Lower Mesozoic stratigraphy and depositional environments of central and west Mexico: constraints on terrane analysis and paleogeography. In: Anderson, T.H., Nourse, J.A., McKee, J.W., Steiner, M.B. (Eds.), *The Mojave-Sonora Megashield Hypothesis: Development, Assessment, and Alternatives*. Geological Society of America Special Paper Vol. 393, pp. 233–258.
- Centeno-García, E., 2017. Mesozoic tectono-magmatic evolution of Mexico: an overview. *Ore Geol. Rev.* 81, 1035–1052.
- Centeno-García, E., Silva-Romo, G., 1997. Petrogenesis and tectonic evolution of central Mexico during Triassic-Jurassic time. *Rev. Mex. Cienc. Geol.* 14, 244–260.
- Centeno-García, E., Busby, C., Busby, M., Gehrels, G., 2011. Evolution of the Guerrero composite terrane along the Mexican margin, from extensional fringing arc to contractional continental arc. *Bull. Geol. Soc. Am.* 123, 1776–1797.
- Cerca, M., Ferrari, L., López-Martínez, M., Martiny, B., Iriondo, A., 2007. Late Cretaceous shortening and early Tertiary shearing in the central Sierra Madre del Sur, southern Mexico: insights into the evolution of the Caribbean–North American plate interaction. *Tectonics* 26, TC3007.
- Chapple, W.M., 1978. Mechanics of thin-skinned fold-and-thrust belts. *Bull. Geol. Soc. Am.* 89, 1189–1198.
- Charleston, S., 1981. A summary of the structural geology and tectonics of the state of Coahuila, Mexico. In: Smith, C.I., Brown, L.F. (Eds.), *Lower Cretaceous Stratigraphy and Structure, Northern Mexico*. Field Trip Guidebook, West Texas Geological Society, Publication Vol. 81-74, pp. 28–36.
- Chávez-Cabello, G., 2005. Deformación y magmatismo Cenozoico en el sur de la Cuenca de Sabinas, Coahuila, México. Ph.D thesis. Universidad Nacional Autónoma de México (226 pp).
- Chávez-Cabello, G., Aranda-Gómez, J.J., Molina-Garza, R.S., Cossío-Torres, T., Arvizu-Gutiérrez, I.R., González-Naranjo, G.A., 2007. The San Marcos fault: a Jurassic multireactivated basement structure in northeastern México. In: Alaniz-Álvarez, S.A., Nieto-Samaniego, Á.F. (Eds.), *Geology of Mexico: Celebrating the Centenary of the Geological Society of Mexico*. Geological Society of America Special Paper Vol. 422, pp. 261–286.
- Clark, K.F., Foster, C.T., Damon, P.E., 1982. Cenozoic mineral deposits and subduction-related magmatic arcs in Mexico. *Bull. Geol. Soc. Am.* 93, 533–544.
- Coney, P.J., 1976. Plate tectonics and the Laramide orogeny. *New Mexico Geological Society Special Publication* 6, 5–10.
- Coney, P.J., 1981. Accretionary tectonics in western North America. In: Dickinson, W.R., Payne, W.D. (Eds.), *Relations of Tectonics to Ore Deposits in the Southern Cordillera*. *Ariz. Geol. Soc. Digest* Vol. 14, pp. 23–37.
- Coney, P.J., 1989. Structural aspects of suspect terranes and accretionary tectonics in western North America. *J. Struct. Geol.* 11, 107–125.
- Coney, P.J., Reynolds, S.J., 1977. Cordilleran benioff zones. *Nature* 270, 403–406.
- Contreras, J., Suter, M., 2015. Mechanical stability model of progradational carbonate platform margins under tectonic loads: deformation of Cretaceous carbonate platforms in the Sierra Madre Oriental fold thrust belt (east central Mexico). *J. Geophys. Res. Solid Earth* 120, 1288–1308.
- Coward, M.P., 1994. Inversion tectonics. In: Hancock, P.R. (Ed.), *Continental Deformation*. Pergamon, Oxford, pp. 289–304.
- Crittelli, S., Le Pera, E., Galluzzo, F., Milli, S., Moscatelli, M., Perrotta, S., Santantonio, M., 2007. Interpreting siliciclastic-carbonate detrital modes in foreland basin systems: an example from Upper Miocene arenites of the central Apennines. In: Arribas, J., Crittelli, S., Johnsson, M.J. (Eds.), *Sedimentary Provenance and Petrogenesis: Perspectives From Petrography and Geochemistry*. Geological Society of America Special Paper Vol. 420, pp. 107–133.
- Cross, G.E., 2012. Evaporite Deformation in the Sierra Madre Oriental, Northeastern Mexico: Décollement Kinematics in an Evaporite-Detached Thin-Skinned Fold Belt. Unpublished Ph.D thesis. University of Texas (547 pp).
- Cruz, L., Malinski, J., Wilson, A., Take, W.A., Hillel, G., 2010. Erosional control of the kinematics and geometry of fold-and-thrust belts imaged in a physical and numerical sandbox. *J. Geophys. Res. Solid Earth* 115, B09404.
- Cuéllar-Cárdenas, M.A., Nieto-Samaniego, Á.F., Levresse, G., Alaniz-Álvarez, S.A., Solari, L., Ortega-Obregón, C., López-Martínez, M., 2012. Límites temporales de la deformación por acortamiento Laramide en el centro de México. *Rev. Mex. Cienc. Geol.* 29, 179–203.
- Dahlstrom, C.D., 1970. Structural geology in the eastern margin of the Canadian Rocky Mountains. *Bull. Can. Petrol. Geol.* 18, 332–406.
- Damon, P.E., Shaffiqullah, M., Clark, K.F., 1981a. Age trends of igneous activity in relation to metallogenesis in the southern Cordillera. In: Dickinson, W.R., Payne, W.D. (Eds.), *Relations of Tectonics to Ore Deposits in the Southern Cordillera*. Tucson, Arizona, Arizona Geological Society Digest Vol. 14, pp. 137–153.
- Damon, P.E., Shaffiqullah, M., Clark, K.F., 1981b. Evolución de los arcosmagmáticos en México y su relación con la metalogénesis. Universidad Nacional Autónoma de México. *Rev. Inst. Geol.* 5, 223–238.
- Dávila-Alcocer, V.M., Centeno-García, E., Valencia, V., Fitz-Díaz, E., 2009. Una nueva interpretación de la estratigrafía de la Región de Tolimán, Estado de Querétaro. *Bol. Soc. Geol. Mex.* 61, 491–497.
- Davis, G.H., 2009. Structural geologic evolution of the Colorado Plateau. In: Kay, S.M., Ramos, V.A., Dickinson, W.R. (Eds.), *Backbone of the Americas; Shallow Subduction, Plateau Uplift, and Ridge and Terrane Collision*. Geological Society of America Memoir Vol. 204, pp. 99–124.
- de Cserna, Z., 1956. Tectónica de la Sierra Madre Oriental de México: entre Terreón y Monterrey. *XX Congreso Geológico Internacional* (87 p).
- de Cserna, Z., 1961. Tectonic map of Mexico. *Geol. Soc. Am. Scale* 1, 2,500,000.
- de Cserna, Z., 1976. Geology of the Fresnillo are, Zacatecas, Mexico. *Geol. Soc. Am. Bull.* 87, 1191–1199.
- de Cserna, Z., Ortega Gutiérrez, F., Palacios, N.M., 1980. Reconocimiento geológico de la parte central de la cuenca del alto Río Balsas, Estados de Guerrero y Puebla. Libro Guía de la Excursión Geológica a la parte central de la cuenca del Alto Balsas, Estados de Guerrero y Puebla. *Sociedad Geológica Mexicana*. pp. 1–33.
- DeCelles, P.G., 1994. Late Cretaceous-Paleocene synorogenic sedimentation and kinematic history of the Sevier thrust belt, Northeast Utah and Southwest Wyoming. *Bull. Geol. Soc. Am.* 106, 32–56.
- DeCelles, P.G., 2004. Late Jurassic to Eocene evolution of the Cordilleran thrust belt and foreland basin system, western U.S.A. *Am. J. Sci.* 304, 105–168.
- DeCelles, P.G., Giles, K.A., 1996. Foreland basin systems. *Basin Res.* 8, 105–123.
- DeCelles, P.G., Ducea, M.N., Kapp, P., Zandt, G., 2009. Cyclicity in Cordilleran orogenic systems. *Nat. Geosci.* 2, 251–257.
- Delgado-Argote, L.A., 1988. Geología preliminar de la secuencia volcanosedimentaria y serpentinitas asociadas del Jurásico (?) del área de Cuicatlán-Concepción Pápalo, Oaxaca. *Rev. Mex. Cienc. Geol.* 7, 127–135.
- Delgado-Argote, L.A., López-Martínez, M., York, D., Hall, C.M., 1992. Geologic framework and geochronology of ultramafic complexes of southern Mexico. *Can. J. Earth Sci.* 29, 1590–1604.
- Dickinson, W.R., 2004. Evolution of the North American Cordillera. *Annu. Rev. Earth Planet. Sci.* 32, 13–45.
- Dickinson, W.R., Lawton, T.F., 2001. Carboniferous to Cretaceous assembly and fragmentation of Mexico. *Bull. Geol. Soc. Am.* 113, 1142–1160.
- Dickinson, W.R., Snyder, W.S., 1978. Plate tectonics of the Laramide orogeny. In: Matthews, V. (Ed.), *Laramide Folding Associated With Basement Block Faulting in the Western United States*. Geological Society of America Memoir Vol. 151, pp. 355–366.
- Dickinson, W.R., Klute, M.A., Hayes, M.J., Janecke, S.U., Lundin, E.R., McKittrick, M.A., Olivares, M.D., 1988. Paleogeographic and paleotectonic setting of Laramide sedimentary basins in the central Rocky Mountain region. *Bull. Geol. Soc. Am.* 100, 1023–1039.
- Dickinson, W.R., Gehrels, G.E., Stern, R.J., 2010. Late Triassic Texas uplift preceding Jurassic opening of the Gulf of Mexico: evidence from U-Pb ages of detrital zircons. *Geosphere* 6, 641–662.
- Drewes, H., 1988. Development of the foreland zone and adjacent terranes of the Cordilleran orogenic belt near the US-Mexican border. In: Schimidt, C.J., Perry Jr., W.J. (Eds.), *Interaction of the Rocky Mountain Foreland and the Cordilleran Thrust Belt*. Geological Society of America Memoir Vol. 171, pp. 447–463.
- Duque-Trujillo, J., Ferrari, L., Orozco-Esquivel, T., López-Martínez, M., Lonsdale, P., Bryan, S.E., Kluesner, J., Piñero-Lajas, D., Solari, L., 2014. Timing of rifting in the southern Gulf of California and its conjugate margins: insights from the plutonic record. *Bull. Geol. Soc. Am.* 127, 702–736.
- Dyer, J.R., Reyex-Cortes, I.A., 1987. The geology of Cerro El Carrizalillo Chihuahua, Mexico, preliminary findings. *Gac. Geol.* 1, 108–128.
- Eguiluz de Antuñano, S.E., 2001. Geologic evolution and gas resources of the Sabinas Basin in northeastern México. In: Bartolini, C., Buffler, R.T., Cantú-Chapa, A. (Eds.), *The Western Gulf of México Basin: Tectonics, Sedimentary Basins, and Petroleum Systems*. American Association of Petroleum Geologists Memoir Vol. 75, pp. 241–270.
- Eguiluz de Antuñano, S.E., Campa, M.F., 1982. Problemas tectónicos del sector de San Pedro del Gallo, en los Estados de Chihuahua y Durango. *Bol. Asoc. Mex. Geol. Petrol.* 34, 5–42.
- Eguiluz de Antuñano, S., Aranda-García, M., Marrett, R., 2000. Tectónica de la Sierra Madre Oriental, México. *Bol. Soc. Geol. Mex.* 53, 1–26.
- Eguiluz-de Antuñano, S., 2011. Cuenca de Sabinas: su significado en el entendimiento de la evolución geológica del noreste mexicano. *Bol. Soc. Geol. Mex.* 63, 285–311.
- Elías-Herrera, M., Sánchez-Zavala, J.L., Macías-Romo, C., 2000. Geologic and geochronologic data from the Guerrero terrane in the Tejuipulco area, southern Mexico: new constraints on its tectonic interpretation. *J. S. Am. Earth Sci.* 13, 355–376.
- Escalona-Alcázar, F.J., Delgado-Argote, L.A., Weber, B., Núñez-Peña, E.P., Valencia, V.A., Ortiz-Acevedo, O., 2009. Kinematics and U-Pb dating of detrital zircons from the Sierra de Zacatecas, Mexico. *Rev. Mex. Cienc. Geol.* 26, 48–64.
- Escalona-Alcázar, F.J., Delgado-Argote, L.A., Nebel, O., Velasco-Tapia, F., Weber, B., Núñez-Peña, E.P., 2014. Maturing arc signatures monitored by trace element and Hf isotope systematics in the Early Cretaceous Zacatecas Volcanic Field, Mexico. *J. Geol.* 122, 549–566.
- Evenchick, C.A., McMechan, M.E., McNicoll, V.J., Carr, S.D., 2007. A synthesis of the Jurassic-Cretaceous tectonic evolution of the central and southeastern Canadian Cordillera; exploring links across the orogen. In: Sears, J.W., Harms, T.A., Evenchick, C.A. (Eds.), *Whence the Mountains? Inquiries Into the Evolution of Orogenic Systems: A Volume in Honor of Raymond A. Price*. Geological Society of America Special Paper Vol. 433, pp. 117–145.
- Ferket, H., Swennen, R.A.J., Ortuño, S., Roure, F., 2003. Reconstruction of the fluid flow history during Laramide foreland fold and thrust belt development in eastern Mexico; cathodoluminescence and $\delta^{18}\text{O}$ - $\delta^{13}\text{C}$ isotope trends of calcite-cemented fractures. *J. Geochem. Explor.* 78, 163–167.

- Ferrari, L., Valencia-Moreno, M., Bryan, S., 2005. Magmatismo y tectónica en la Sierra Madre Occidental y su relación con la evolución de la margen occidental de Norteamérica. *Bol. Soc. Geol. Mex.* 57, 343–378.
- Fischer, M.P., Higuera-Díaz, I.C., Evans, M.A., Perry, E.C., Leticariu, L., 2009. Fracture-controlled paleohydrology in a map-scale detachment fold: insights from the analysis of fluid inclusions in calcite and quartz veins. *J. Struct. Geol.* 31, 1490–1510.
- Fitz-Díaz, E., 2001. Evolución estructural del sinclinal de Zacango en el límite oriental de la Plataforma Guerrero-Morelos, Guerrero, Mexico. Unpublished Bachelor's thesis, Instituto Politécnico Nacional (103 pp).
- Fitz-Díaz, E., 2010. Progressive Deformation, Fluid Flow and Water-Rock Interaction in the Mexican Fold-Thrust Belt, Central Mexico. Unpublished PhD. thesis. University of Minnesota (143 pp).
- Fitz-Díaz, E., van der Pluijm, B., 2013. Fold dating: a new Ar/Ar illite dating application to constrain the age of deformation in shallow crustal rocks. *J. Struct. Geol.* 54, 174–179.
- Fitz-Díaz, E., Tolson, G., Camprubí, A., Rubio-Ramos, M.A., Prol-Ledesma, R.M., 2008. Deformación vetas, inclusiones fluidas y la evolución tectónica de las rocas cretácicas de Valle de Bravo, Estado de México, México. *Rev. Mex. Cienc. Geol.* 25, 59–81.
- Fitz-Díaz, E., Hudleston, P., Tolson, G., 2011a. Comparison of tectonic styles in the Mexican and Canadian Rocky Mountain fold-thrust belt. In: Poblet, J., Lisle, R.J. (Eds.), *Kinematic Evolution and Structural Styles of Fold-and-Thrust Belts*. Geological Society of London, Special Publication Vol. 349, pp. 149–167.
- Fitz-Díaz, E., Hudleston, P., Siebenaller, L., Kirschner, D., Camprubí, A., Tolson, G., Puig, T.P., 2011b. Insights into fluid flow and water-rock interaction during deformation of carbonate sequences in the Mexican fold-thrust belt. *J. Struct. Geol.* 33, 1237–1253.
- Fitz-Díaz, E., Tolson, G., Hudleston, P., Bolaños-Rodríguez, D., Ortega-Flores, B., Serrano, A.V., 2012. The role of folding in the development of the Mexican fold-and-thrust belt. *Geosphere* 8, 931–949.
- Fitz-Díaz, E., Camprubí-Cano, A., Cienfuegos-Alvarado, E., Morales-Puente, P., Schleicher, A., van der Pluijm, B., 2014a. Newly-formed illite preserves fluid sources during folding of shale and limestone rocks; an example from the Mexican Fold-Thrust Belt. *Earth Planet. Sci. Lett.* 391, 263–273.
- Fitz-Díaz, E., van der Pluijm, B., Hudleston, P., Tolson, G., 2014b. Progressive, episodic deformation in the Mexican Fold-Thrust Belt (Central Mexico): evidence from isotopic dating of folds and faults. *Int. Geol. Rev.* 56, 734–755.
- Fitz-Díaz, E., Hall, C.M., van der Pluijm, B.A., 2016. XRD-based $^{40}\text{Ar}/^{39}\text{Ar}$ age correction for fine-grained illite, with application to folded carbonates in the Monterrey salient (northern Mexico). *Geochim. Cosmochim. Acta* 181, 201–216.
- Franco-Rubio, M., 1999. Geology of the basement below the decollement surface, Sierra de Catorce, San Luis Potosí, México. In: Bartolini, C., Wilson, J.L., Lawton, T.F. (Eds.), *Mesozoic Sedimentary and Tectonic History of North-Central Mexico*. Geological Society of America Special Paper Vol. 340, pp. 211–221.
- Freydier, C., Martinez, R.J., Lapiere, H., Tardy, M., Coulon, C., 1996. The Early Cretaceous Arperos oceanic basin (western Mexico) geochemical evidence for an aseismic ridge formed near a spreading center. *Tectonophysics* 259, 343–367.
- Freydier, C., Lapiere, H., Tardy, M., 1998. The Early Cretaceous Arperos oceanic basin (western Mexico). Geochemical evidence for an aseismic ridge formed near a spreading center—reply. *Tectonophysics* 292, 327–331.
- Friedman, M., Handin, J., Logan, J.M., Min, K.D., Stearns, D.W., 1976. Experimental folding of rocks under confining pressure: part III. Faulted drape folds in multithologic layered specimens. *Bull. Geol. Soc. Am.* 87, 1049–1066.
- Fries, C., 1956. Bosquejo geológico de las partes central y occidental del Estado de Morelos y áreas contiguas de Guerrero y México. In 20th International Geological Congress, pp. 17–53.
- Garduño-Martínez, D.E., Puig, T.P., Solé, J., Martini, M., Alcalá-Martínez, J.R., 2015. K-Ar illite-mica age constraints on the formation and reactivation history of the El Doctor fault zone, central Mexico. *Rev. Mex. Cienc. Geol.* 32, 306–322.
- Giles, K.A., Lawton, T.F., 1999. Attributes and evolution of an exhumed salt weld, La Popa basin, northeastern Mexico. *Geology* 27, 323–326.
- Godínez-Urban, A., Lawton, T.F., Garza, R.S.M., Iriondo, A., Weber, B., López-Martínez, M., 2011. Jurassic volcanic and sedimentary rocks of the La Silla and Todos Santos Formations, Chiapas: Record of Nazas arc magmatism and rift-basin formation prior to opening of the Gulf of Mexico.
- Goldhammer, R.K., 1999. Mesozoic sequence stratigraphy and paleogeographic evolution of northeast Mexico. In: Bartolini, C., Wilson, J.L., Lawton, T.F. (Eds.), *Mesozoic Sedimentary and Tectonic History of North-Central Mexico*. Geological Society of America Special Paper Vol. 340, pp. 1–58.
- Goldhammer, R.K., Johnson, C.A., 2001. Middle Jurassic–Upper Cretaceous paleogeographic evolution and sequence-stratigraphic framework of the northwest Gulf of Mexico rim. In: Bartolini, C., Buffler, R.T., Cantú-Chapa, A. (Eds.), *The Western Gulf of Mexico Basin: Tectonics, Sedimentary Basins, and Petroleum Systems*. American Association of Petroleum Geologists Memoir Vol. 75, pp. 45–81.
- González-Guzmán, R., Velasco-Tapia, F., Chávez-Cabello, G., Valencia-Moreno, M., 2009. Estudio petrográfico y geoquímico del intrusivo El Peñuelo, Noreste de México. *GEOS* 29, 181.
- González-León, C.M., Lawton, T.F., 1995. Stratigraphy, depositional environments, and origin of the Cabullona basin, northeastern Sonora. In: Jacques-Ayala, C., González-León, C.M., Roldán-Quintana, J. (Eds.), *Studies on the Mesozoic of Sonora and Adjacent Areas: Geological Society of America, Special Paper*. 301, pp. 121–142.
- González-León, C.M., McIntosh, W.C., Lozano-Santacruz, R., Valencia-Moreno, M., Amaya-Martínez, R., Rodríguez-Castañeda, J.L., 2000. Cretaceous and Tertiary sedimentary, magmatic, and tectonic evolution of north-central Sonora (Arizpe and Bacanuchi Quadrangles), northwest Mexico. *Bull. Geol. Soc. Am.* 112, 600–610.
- González-León, C.M., Solari, L., Solé, J., Ducea, M.N., Lawton, T.F., Bernal, J.P., Santacruz, R.L., 2011. Stratigraphy, geochronology, and geochemistry of the Laramide magmatic arc in north-central Sonora, Mexico. *Geosphere* 1392–1418.
- González-León, C.M., Lawton, T.F., Solari, L., 2012. Cretaceous Tectonics in Sonora: constraining time of the shortening events (abstract). 108th Annual Meeting, Geological Society of America Abstracts With Programs. 44, p. 76.
- Gray, G.G., Lawton, T.F., 2011. New constraints on timing of Hidalgo (Laramide) deformation in the Parras and La Popa basins, NE Mexico. *Bol. Soc. Geol. Mex.* 63, 333–343.
- Gray, G.G., Pottorf, R.J., Yurewicz, D.A., Mahon, K.I., Pevear, D.R., Chuchla, R.J., 2001. Thermal and chronological record of syn- to post-Laramide burial and exhumation, Sierra Madre Oriental, Mexico. In: Bartolini, C., Buffler, R.T., Cantú-Chapa, A. (Eds.), *The Western Gulf of México Basin, Tectonics, Sedimentary Basins, and Petroleum Systems*. 75. American Association of Petroleum Geologists, Memoir, pp. 159–181.
- Guerrero-Suástegui, M., 1997. Depositional History and Sedimentary Petrology of the Huetamo Sequence, Southwestern Mexico. Unpublished MSc thesis, University of Texas (120 pp).
- Gupta, S., Allen, P.A., 2000. Implications of foreland paleotopography for stratigraphic development in the Eocene distal Alpine foreland basin. *Bull. Geol. Soc. Am.* 112, 515–530.
- Guzman, E.J., de Cserna, Z., 1963. Tectonic history of Mexico. In: Kay, S.M., Ramos, V.A., Dickinson, W.R. (Eds.), *Backbone of the Americas: Shallow Subduction, Plateau Uplift, and Ridge and Terrane Collision*. American Association of Petroleum Geologists Memoir Vol. 2, pp. 113–129.
- Haenggi, W.T., 2001. Tectonic history of the Chihuahua trough, Mexico and adjacent USA, part I: the pre-Mesozoic setting. *Bol. Soc. Geol. Mex.* 54, 28–66.
- Haenggi, W.T., 2002. Tectonic history of the Chihuahua trough, Mexico and adjacent USA, part II: Mesozoic and Cenozoic. *Bol. Soc. Geol. Mex.* 55, 38–94.
- Heim, A., 1940. The front ranges of Sierra Madre Oriental, Mexico, from Ciudad Victoria to Tamazunchale. *Ecológ. Geol. Helv.* 33, 313–362.
- Heller, P.L., Liu, L., 2016. Dynamic topography and vertical motion of the U.S. Rocky Mountain region prior to and during the Laramide orogeny. *Bull. Geol. Soc. Am.* (In press).
- Hennings, P.H., 1994. Structural transect of the southern Chihuahua Fold Belt between Ojinaga and Aldama, Chihuahua, Mexico. *Tectonics* 13, 1445–1460.
- Henry, C.D., McDowell, F.W., Silver, L.T., 2003. Geology and geochronology of the granitic batholithic complex, Sinaloa, México: implications for Cordilleran magmatism and tectonics. In: Johnson, S.E., Paterson, S.R., Fletcher, J.M., Girty, G.H., Kimbrough, D.L., Martín-Barajas, A. (Eds.), *Tectonic Evolution of Northwestern México and the Southwestern USA*. Geological Society of America Special Paper Vol. 374, pp. 237–273.
- Hernández-Jaúregui, R., 1997. Sedimentación Sintectónica de la Formación Soyatal (Turoniano Medio-Campaniano) y Modelado Cinemático de la Cuenca de Flexura de Maconí, Querétaro. Unpublished MSc thesis, Instituto Politécnico Nacional.
- Hernández-Romano, U., Aguilera-Franco, N., Martínez-Medrano, M., Barceló-Duarte, J., 1997. Guerrero-Morelos platform drowning at the Cenomanian-Turonian boundary, Huitziltepec area, Guerrero State, southern Mexico. *Cretac. Res.* 18, 661–686.
- Hernández-Romano, U., Aguilera-Franco, N., Buitrón, B.E., 1998. Late Cenomanian fossil association from Morelos, Mexico—stratigraphic implications. *Rev. Mex. Cienc. Geol.* 15, 46–56.
- Hildebrand, R.S., 2009. Did westward subduction cause Cretaceous–Tertiary orogeny in the North American Cordillera? *Geol. Soc. Am. Spec. Pap.* 457, 1–71.
- Hudleston, P.J., Treagus, S.H., 2010. Information from folds: a review. *J. Struct. Geol.* 32, 2042–2071.
- Humphrey, W.E., 1956. Tectonic framework of northeast Mexico. *Trans. Gulf Coast Assoc. Geol. Soc.* 6, 25–35.
- Humphrey, W.E., Díaz, T., 2003. Jurassic and Lower Cretaceous stratigraphy and tectonics of northeast Mexico. In: Wilson, J.L., Jordan, C. (Eds.), *RIO 267*. University of Texas at Austin, Bureau of Economic Geology (152 pp).
- Imlay, R.W., 1936. Geology of the western part of the Sierra de Parras. *Bull. Geol. Soc. Am.* 47, 1091–1152.
- Ingersoll, R.V., 2012. Tectonics of sedimentary basins, with revised nomenclature. In: Busby, C., Azor Pérez, A. (Eds.), *Tectonics of Sedimentary Basins: Recent Advances*. Blackwell Publishing Ltd., pp. 3–43.
- Iriondo, A., Kunk, M.J., Winick, J.A., CRM, 2004. $^{40}\text{Ar}/^{39}\text{Ar}$ dating studies of minerals and rocks in various areas in Mexico. United States Geological Survey/Consejo de Recursos Minerales, Scientific Collaboration (Part II). Open File Report 04-1444 (46 pp).
- Iriondo, A., Martínez-Torres, L.M., Kunk, M.J., Atkinson, W.W., Premo, W.R., McIntosh, W.C., 2005. Northward Laramide thrusting in the Quitovac region, northwestern Sonora, Mexico: implications for the juxtaposition of Paleoproterozoic basement blocks and the Mojave-Sonora megashear hypothesis. In: Anderson, T.H., Nourse, J.A., McKee, J.W., Steiner, M.B. (Eds.), *The Mojave-Sonora Megashear Hypothesis: Development, Assessment, and Alternatives*. Geological Society of America Special Paper Vol. 393, pp. 631–669.
- Jacques-Ayala, C., 1993. The Cretaceous in the Caborca-Santa Ana region, northern Sonora. Ph. D. Thesis: University of Cincinnati, Cincinnati.
- Jacques Ayala, C., Barth, A.P., Wooden, J.L., Jacobson, C.E., 2009. Provenance and U-Pb geochronology of the Upper Cretaceous El Chanate Group, northwest Sonora, Mexico, and its tectonic significance. *Int. Geol. Rev.* 51, 1051–1077.
- Jacques-Ayala, C., 1999. Stratigraphy of El Chanate Group (Late Cretaceous) and its implications for the tectonic evolution of northwestern Sonora, Mexico. *Rev. Mex. Cien. Geol.* 16, 97–120.
- Johnson, S.E., Tate, M.C., Fanning, C.M., 1999. New geologic mapping and SHRIMP U-Pb zircon data in the Peninsular Ranges batholith, Baja California, Mexico: evidence for a suture? *Geology* 27, 743–746.
- Jones, N.W., McKee, J.W., Anderson, T.H., Silver, L.T., 1995. Jurassic volcanic rocks in north-eastern Mexico: a possible remnant of a cordilleran magmatic arc. In: Jacques-Ayala, C., González-León, C.M., Roldán-Quintana, J. (Eds.), *Studies on the Mesozoic of Sonora and Adjacent Areas*. Geological Society of America Special Paper Vol. 301, pp. 179–190.

- Jordan, T.E., Allmendinger, R.W., 1986. The Sierras Pampeanas of Argentina: a modern analogue of Laramide deformation. *Am. J. Sci.* 286, 737–764.
- Juárez-Arriaga, E., Lawton, T.F., Stockli, D., 2016a. Soyatal formation and related strata: onset of sedimentation in the Cretaceous foreland-basin system, central Mexico. American Association of Petroleum Geologists, Annual Convention and Exhibition.
- Juárez-Arriaga, E., Lawton, T.F., Martens, U., Stockli, D., 2016b. Double dating ages of detrital zircon from synorogenic deposits: history of thrust-belt exhumation, central Mexico. Cordilleran Section - 112th Annual Meeting.
- Karlstrom, K.E., Amato, J.M., Williams, M.L., Heizler, M., Shaw, C., Read, A., Bauer, P., 2004. Proterozoic evolution of the New Mexico region: a synthesis. In: Mack, G.H., Giles, K.A. (Eds.), *The Geology of New Mexico: A Geologic History*. New Mexico Geological Society Special Publication Vol. 11, pp. 1–34.
- Kellum, L.B., 1930. Similarity of surface geology in front range of Sierra Madre Oriental to subsurface in Mexican south fields. *Bull. Am. Assoc. Pet. Geol.* 14, 73–91.
- Kellum, L.B., Imlay, R.W., Kane, W.C., 1936. Evolution of the Coahuila Peninsula, Mexico. Relation of structure, stratigraphy and igneous activity to an early continental margin. *Bull. Geol. Soc. Am.* 47, 969–1008.
- Keppie, J.D., Ortega-Gutiérrez, F., 2010. 1.3–0.9 Ga Oaxaquia (Mexico): remnant of an arc/backarc on the northern margin of Amazonia. *J. S. Am. Earth Sci.* 29, 21–27.
- Kimbrough, D.L., Moore, T.E., 2003. Ophiolite and volcanic arc assemblages on the Vizcaino Peninsula and Cedros Island, Baja California Sur, México: Mesozoic forearc lithosphere of the Cordilleran magmatic. In: Johnson, S.E., Paterson, S.R., Fletcher, J.M., Girty, G.H., Kimbrough, D.L., Martín-Barajas, A. (Eds.), *Tectonic Evolution of Northwestern México and Southwestern USA*. Geological Society of America Special Paper Vol. 374, pp. 43–71.
- Kimbrough, D.L., Smith, D.P., Mahoney, J.B., Moore, T.E., Grove, M., Gastil, R.G., Fanning, C.M., 2001. Forearc-basin sedimentary response to rapid Late Cretaceous batholith emplacement in the Peninsular Ranges of southern and Baja California. *Geology* 29, 491–494.
- King, R.E., 1944. *Geology and Paleontology of the Permian Area Northwest of Las Delicias, Southwestern Coahuila, Mexico*. In: King, R.E., Dunbar, C.O., Cloud, P.E. Jr., Miller, A.K. (Eds.), *Geology and Paleontology of the Permian Area Northwest of Las Delicias, Southwestern Coahuila, Mexico*. Geological Society of America Memoir. Vol. 52 pp. 1–33.
- Kiyokawa, M., 1981. Geological Survey of the Pachuca-Zimapán Area, Central Mexico, Professional Report. Metal Agency of Japan and Consejo de Recursos Minerales, Estados Unidos Mexicanos (194 pp).
- Kroeger, K.F., Stinnesbeck, W., 2003. The Minas Viejas Formation (Oxfordian) in the area of Galeana, northeastern Mexico: significance of syndepositional volcanism and related barite genesis in the Sierra Madre Oriental. In: Bartolini, C., Buffler, R.T., Blickwede, J. (Eds.), *The Circum-Gulf of Mexico and the Caribbean: Hydrocarbon Habitats, Basin Formation, and Plate Tectonics*. American Association of Petroleum Geologists Memoir Vol. 79, pp. 515–528.
- Lapiere, H., Ortiz, L.E., Abouchami, W., Monod, O., Coulon, C., Zimmermann, J.L., 1992. A crustal section of an intra-oceanic island arc: the Late Jurassic–Early Cretaceous Guanajuato magmatic sequence, central Mexico. *Earth Planet. Sci. Lett.* 108, 61–77.
- Lawton, T.F., 2000. Inversion of Late Jurassic–Early Cretaceous extensional faults of the Bisbee basin, southeastern Arizona and southwestern New Mexico. In: Lawton, T.F., McMillan, N.J., McLemore, V.T. (Eds.), *Southwest Passage—A Trip Through the Phanerozoic*. New Mexico Geological Society, Guidebook Vol. 51, pp. 95–102.
- Lawton, T.F., 2008. Laramide sedimentary basins. In: Miall, A.D. (Ed.), *Sedimentary Basins of the World*. 5, pp. 429–450.
- Lawton, T.F., McMillan, N.J., 1999. Arc abandonment as a cause for passive continental rifting: Comparison of the Jurassic Mexican Borderland rift and the Cenozoic Rio Grande rift. *Geology* 27, 779–782.
- Lawton, T.F., Molina-Garza, R.S., 2014. U–Pb geochronology of the type Nazas Formation and superjacent strata, northeastern Durango, Mexico: implications of a Jurassic age for continental-arc magmatism in north-central Mexico. *Bull. Geol. Soc. Am.* 126, 1181–1199.
- Lawton, T.F., Trexler, J.H., 1991. Piggyback basin in the Sevier orogenic belt, Utah: implications for development of the thrust wedge. *Geology* 19, 827–830.
- Lawton, T.F., Talling, P.J., Hobbs, R.S., Trexler Jr., J.H., Weiss, M.P., Burbank, D.W., 1993. Structure and stratigraphy of Upper Cretaceous and Paleogene strata (North Horn Formation), eastern San Pitch Mountains, Utah—sedimentation at the front of the Sevier orogenic belt. U.S. Geological Survey, Professional Paper 1787-II (33 pp).
- Lawton, T.F., Bradford, I.A., Vega, F.J., Gehrels, G.E., Amato, J.M., 2009. Provenance of Upper Cretaceous–Paleogene sandstones in the foreland basin system of the Sierra Madre Oriental, northeastern Mexico, and its bearing on fluvial dispersal systems of the Mexican Laramide Province. *Bull. Geol. Soc. Am.* 121, 820–836.
- Lehmann, C., Osleger, D.A., Montañez, I.P., Sliter, W., Vanneau, A.A., Banner, J., 1999. Evolution of Cupido and Coahuila carbonate platforms, early Cretaceous, northeastern Mexico. *Bull. Geol. Soc. Am.* 111, 1010–1029.
- Lipman, P.W., Hagstrum, J.T., 1992. Jurassic ash-flow sheets calderas, and related intrusions of the Cordilleran volcanic arc in southeastern Arizona: Implications for regional tectonics and ore deposits. *Geol. Soc. Am. Bull.* 104, 32–39.
- Liu, L., Stegman, D.R., 2011. Segmentation of the Farallon slab. *Earth and Planetary Science Letters* 311, 1–10.
- Liu, L., Gurnis, M., Seton, M., Saleeby, J., Müller, R.D., Jackson, J.M., 2010. The role of oceanic plateau subduction in the Laramide orogeny. *Nat. Geosci.* 3, 353–357.
- López-Doncel, R., 2003. La Formación Tamabra del Cretácico medio en la porción central del margen occidental de la Plataforma Valles-San Luis Potosí, centro-noreste de México. *Rev. Mex. Cienc. Geol.* 20, 1–19.
- López-Oliva, J.G., Keller, G., Stinnesbeck, W., 1998. El límite Cretácico/Terciario (K/T) en el noreste de México—extinción de foraminíferos planctónicos. *Rev. Mex. Cienc. Geol.* 15, 109–113.
- López-Ramos, E.L., 1982. *Geología de México* (No. 557.2 L6) (454 p).
- Lowell, J.D., 1995. Mechanics of basin inversion from worldwide examples. *Geol. Soc. London, Special Publications* 88, 39–57.
- Marrett, R., Aranda-García, M., 1999. Structure and kinematic development of the Sierra Madre Oriental fold-thrust belt, Mexico. In: Wilson, J.L. (Ed.), *Stratigraphic and Structure of the Jurassic and Cretaceous Platform and Basin Systems of the Sierra Madre Oriental: A Field Book and Related Papers*. South Texas Geological Society, American Association of Petroleum Geologists and SEPM, Annual Meeting, pp. 69–98.
- Martini, M., Ortega-Gutiérrez, 2016. Tectonostratigraphic Evolution of Eastern Mexico During the Break-Up of Pangea: A Review (*Earth Sci. Rev.* this volume).
- Martini, M., Ferrari, L., López-Martínez, M., Cerca-Martínez, M., Valencia, V.A., Serrano-Durán, L., 2009. Cretaceous–Eocene magmatism and Laramide deformation in southwestern Mexico: no role for terrane accretion. In: Kay, S.M., Ramos, V.A., Dickinson, W.R. (Eds.), *Backbone of the Americas: Shallow Subduction, Plateau Uplift, and Ridge and Terrane Collision*. Geological Society of America Memoir Vol. 204, pp. 151–182.
- Martini, M., Mori, L., Solari, L., Centeno-García, E., 2011. Sandstone provenance of the Arperos Basin (Sierra de Guanajuato, Central Mexico): Late Jurassic–Early Cretaceous back-arc spreading as the foundation of the Guerrero terrane. *J. Geol.* 119, 597–617.
- Martini, M., Fitz-Díaz, E., Solari, L., Camprubi, A., Huddlestone, P.J., Lawton, T.F., Tolson, G., Centeno-García, E., 2012. The Late Cretaceous fold-thrust belt in the Peña de Bernal–Tamazunchale area and its possible relationship to the accretion of the Guerrero Terrane. In: Aranda-Gómez, J.J., Tolson, G., Molina-Garza, R.S. (Eds.), *The Southern Cordillera and Beyond: Geological Society of America Field Guide*. 25, pp. 19–38.
- Martini, M., Solari, L., Camprubi, A., 2013. Kinematics of the Guerrero terrane accretion in the Sierra de Guanajuato, central Mexico: new insights for the structural evolution of arc-continent collisional zones. *Int. Geol. Rev.* 55, 574–589.
- Martini, M., Solari, L., López-Martínez, M., 2014. Correlating the Arperos Basin from Guanajuato, central Mexico, to Santo Tomás, southern Mexico: implications for the paleogeography and origin of the Guerrero terrane. *Geosphere* 10, 1–17.
- Martini, M., Solé, J., Garduño-Martínez, D.E., Pi Puig, T., Omaña, L., 2016. Evidence for two Cretaceous superposed orogenic belts in central Mexico based on paleontologic and K–Ar geochronologic data from the Sierra de los Cuarcos. *Geosphere* 12, 1–14.
- Mauel, D.J., Lawton, T.F., González-León, C., Iriondo, A., Amato, J.M., 2011. Stratigraphy and age of Upper Jurassic strata in north-central Sonora, Mexico: southwestern Laurentian record of crustal extension and tectonic transition. *Geosphere* 7, 390–414.
- McBride, E.F., Weidie, A.E., Wolleben, J.A., Laudon, R.C., 1974. Stratigraphy and structure of the Parras and La Popa Basins, Northeast Mexico. *Bull. Geol. Soc. Am.* 84, 1603–1622.
- McClay, K.R. (Ed.), 1992. *Thrust Tectonics*. Chapman and Hall (447 p).
- McDowell, F.W., Mauger, R.L., 1994. K–Ar and U–Pb zircon chronology of Late Cretaceous and Tertiary magmatism in central Chihuahua State, Mexico. *Bull. Geol. Soc. Am.* 106, 118–132.
- McKee, J.W., Jones, N.W., Long, L.E., 1990. Stratigraphy and provenance of strata along the Sandoz fault, central Coahuila, Mexico. *Bull. Geol. Soc. Am.* 102, 593–614.
- Mendoza-Rosales, C.C., Centeno-García, E., Silva-Romo, G., Campos-Madriral, E., Bernal, J.P., 2010. Barremian rift-related turbidites and alkaline volcanism in southern Mexico and their role in the opening of the Gulf of Mexico. *Earth Planet. Sci. Lett.* 295, 419–434.
- Mitre-Salazar, M.L., 1989. La Megafalla Laramídica de San Tiburcio, Estado de Zacatecas. *Rev. Mex. Cienc. Geol.* 47–51.
- Molina-Garza, R.S., Chávez-Cabello, G., Iriondo, A., Porras-Vázquez, M.A., Terrazas-Calderón, G.D., 2008. Paleomagnetism, structure and ⁴⁰Ar/³⁹Ar geochronology of the Cerro Mercado pluton, Coahuila: implications for the timing of the Laramide orogeny in northern Mexico. *Rev. Mex. Cienc. Geol.* 25, 284–301.
- Monger, J.W.H., Price, R.A., Tempelman-Kluit, D.J., 1982. Tectonic accretion and the origin of the two major metamorphic and plutonic welts in the Canadian Cordillera. *Geology* 10, 70–75.
- Moore, T., 1985. Stratigraphy and tectonic significance of the Mesozoic tectonostratigraphic terranes of the Vizcaino Peninsula, Baja California Sur, Mexico. In: Howell, D.G. (Ed.), *Tectonostratigraphic Terranes of the Circum-Pacific Region*. Circum-Pacific Council for Energy and Mineral Resources, Earth Science Series Vol. 1, pp. 315–329.
- Nemkin, S.R., Fitz-Díaz, E., van der Pluijm, B., Van der Voo, R., 2015. Dating synfolding remagnetization: Approach and field application (central Sierra Madre Oriental Mexico). *Geosphere* 11, 1617–1628.
- Nieto-Samaniego, A.F., Alaniz-Álvarez, S.A., Silva-Romo, G., Eguiza-Castro, M.H., Mendoza-Rosales, C.C., 2006. Latest Cretaceous to Miocene deformation events in the eastern Sierra Madre del Sur, Mexico, inferred from the geometry and age of major structures. *Bull. Geol. Soc. Am.* 118, 238–252.
- Ocampo-Díaz, Y.Z.E., Pinzon-Sotelo, M.P., Chávez-Cabello, G., Ramírez-Díaz, A., Martínez-Paco, M., Velasco-Tapia, F., Guerrero-Suastegui, M., Barboza-Gudiño, J.R., 2016. Propuesta nomenclatural y análisis de procedencia de la Formación Concepción del Oro (antes Formación Caracol): implicaciones sobre la evolución tectónica del sur de Norte América durante el Cretácico Tardío. *Rev. Mex. Cienc. Geol.* 33, 3–33.
- Oldow, J.S., Bally, A.W., Ave Lallemand, H.G., Leeman, W., 1989. Phanerozoic evolution of the North American Cordillera, United States and Canada. In: Bally, A.W., Palmer, A.R. (Eds.), *The Geology of North America—An Overview*. Geological Society of America, The Geology of North America A, pp. 139–232.
- Omaña-Pulido, M.L., 2012. Bioestratigrafía, Paleoecología y Paleobiogeografía del Cretácico superior con base en foraminíferos de la parte occidental de la Plataforma Valles-San Luis Potosí. Ph.D. thesis. Universidad Nacional Autónoma de México (198 p).
- Ortega-Flores, B., Solari, L., Lawton, T.F., Ortega-Obrégón, C., 2014. Detrital-zircon record of major Middle Triassic–Early Cretaceous provenance shift, central Mexico: demise of Gondwanan continental fluvial systems and onset of back-arc volcanism and sedimentation. *Int. Geol. Rev.* 56, 237–261.

- Ortega-Flores, B., Solari, L., Escalona-Alcázar, F.D.J., 2015. The Mesozoic successions of western Sierra de Zacatecas, Central Mexico: provenance and tectonic implications. *Geol. Mag.* 1–22.
- Ortega-Gutiérrez, F., Ruiz, J., Centeno-García, E., 1995. Oaxaquia, a Proterozoic microcontinent accreted to North America during the late Paleozoic. *Geology* 23, 1127–1130.
- Ortega-Gutiérrez, F., Elías-Herrera, M., Solari, L.A., Morán-Zenteno, D.J., Weber, B., Luna-González, L., 2003. Deep orogenic systems of Mexico: a 2 Ga history of continental growth, destruction and dispersal. *Earth Sci. Rev.*
- Ortega-Gutiérrez, F., Elías-Herrera, M., Morán-Zenteno, D.J., Solari, L., Luna-González, L., Schaaf, P., 2014. A review of batholiths and other plutonic intrusions of Mexico. *Gondwana Res.* 26, 834–868.
- Ortega-Rivera, A., 2003. Geochronological constraints on the tectonic history of the Peninsular Ranges batholith of Alta and Baja California: tectonic implications for western México. In: Johnson, S.E., Paterson, S.R., Fletcher, J.M., Girty, G.H., Kimbrough, D.L., Martín-Barajas, A. (Eds.), *Tectonic Evolution of Northwestern Mexico and the Southwestern USA*. Geological Society of America Special Paper Vol. 374, pp. 297–335.
- Ortiz-Hernández, L.E., Acevedo-Sandoval, O.A., Flores-Castro, K., 2003. Early Cretaceous intraplate seamounts from Guanajuato, central Mexico: geochemical and mineralogical data. *Rev. Mex. Cienc. Geol.* 20, 27–40.
- Ortuño-Arzate, S., Ferket, H., Cacas, M.C., Swennen, R., Roure, F., 2003. Late cretaceous carbonate reservoirs in the Cordoba platform and Veracruz Basin, Eastern Mexico. In: Bartolini, C., Buffler, R.T., Blickwede, J. (Eds.), *The Circum-Gulf of Mexico and the Caribbean: Hydrocarbon Habitats, Basin Formation, and Plate Tectonics*. American Association of Petroleum Geologists Memoir Vol. 79, pp. 476–514.
- Padilla y Sánchez, R.J., 1982. Geologic Evolution of the Sierra Madre Oriental Between Linares, Concepcion del Oro, Saltillo, and Monterrey, Mexico. Unpublished Ph.D thesis. University of Texas at Austin (217 pp).
- Padilla y Sánchez, R.J., 1985. Las estructuras de la Curvatura de Monterrey, estados de Coahuila, Nuevo León, Zacatecas y San Luis Potosí. *Rev. Mex. Cienc. Geol.* 6, 1–20.
- Palacios-García, N.B., Martini, M., 2014. From back-arc rifting to arc accretion: The Late Jurassic–Early Cretaceous evolution of the Guerrero terrane recorded by a major provenance change in sandstones from the Sierra de los Cuarzos area, central Mexico. *Int. Geol. Rev.* 56, 1377–1394.
- Pantoja-Alor, J., Estrada-Barraza, S., 1986. Estratigrafía de los alrededores de la mina de fierro El Encino, Jalisco. *Bol. Soc. Geol. Mex.* 47, 1–15.
- Payne, J.L., Johnson, M.E., Ledesma-Vázquez, J., 2004. Lower Cretaceous Alisitos Formation at San Isidro: coastal sedimentation and volcanism/Formación Alisitos del Cretácico temprano en Punta San Isidro: Sedimentación costera y vulcanismo. *Cienc. Mar.* 30, 365–380.
- Peel, F.J., Travis, C.J., Hossack, J.R., 1995. Genetic structural provinces and salt tectonics of the Cenozoic offshore US Gulf of Mexico: a preliminary analysis. In: Jackson, M.P.A., Roberts, D.G., Snelson, S. (Eds.), *Salt Tectonics: A Global Perspective*. American Association of Petroleum Geologists Memoir. 65, pp. 153–175.
- Pérez-Gutiérrez, R., Solari, L.A., Gómez-Tuena, A., Valencia, V.A., 2009. El terreno Cuicatenco: ¿cuencia oceánica con influencia de subducción del Cretácico Superior en el sur de México? Nuevos datos estructurales, geoquímicos y geocronológicos. *Rev. Mex. Cienc. Geol.* 26, 222–242.
- Perrillat, M.C., Vega, F.J., Corona, R., 2000. Early Maastrichtian mollusca from the Mexcala Formation of the State of Guerrero southern Mexico. *Jour. Paleon.* 74, 7–24.
- Peterson-Rodríguez, R.H., Aranda-García, M., Yadalberto, J., Alvarado-Céspedes, A.J., 2008. Etapas y estilos de deformación que desarrollaron trampas estructurales en el sector centrooriental de la Cuenca de Sabinas. In: Aranda-García, M., Peterson-Rodríguez, R.H. (Eds.), *Estructuras del Arco de Monterrey y Cuenca de La Popa en la Sierra Madre Oriental y sus analogías para la exploración de hidrocarburos en el Golfo de México, Monterrey, Nuevo León, México*. Guía de Campo y artículos relacionados, 92–99.
- Pindell, J., Dewey, J.F., 1982. Permo-Triassic reconstruction of western Pangea and the evolution of the Gulf of Mexico and Caribbean region. *Tectonics* 1, 179–211.
- Pindell, J.L., Kennan, L., 2009. Tectonic evolution of the Gulf of Mexico, Caribbean and northern South America in the mantle reference frame: an update. In: James, K.H., Lorente, M.A., Pindell, J.L. (Eds.), *The Origin and Evolution of the Caribbean Plate*. Geological Society of London, Special Publication 328, pp. 1–55.
- Poole, F.G., Perry, W.J., Madrid, R.J., Amaya-Martínez, R., 2005. Tectonic synthesis of the Ouachita-Marathon-Sonora orogenic margin of southern Laurentia: stratigraphic and structural implications for timing of deformational events and plate-tectonic model. In: Anderson, T.H., Nourse, J.A., McKee, J.W., Steiner, M.B. (Eds.), *The Mojave-Sonora Megashield Hypothesis: Development, Assessment, and Alternatives*. *Geol. Soc. Am. Special Paper Vol.* 393, pp. 543–596.
- Posamentier, H.W., Walker, R.G., 2006. Deep-water turbidites and submarine fans. In: Walker, R.G. (Ed.), *Facies Models Revisited*. SEPM Special Publication Vol. 84, pp. 397–520.
- Price, R.A., 1981. The Cordilleran foreland thrust and fold belt in the southern Canadian Rocky Mountains. In: McClay, K.R., Price, N.J. (Eds.), *Thrust and Nappe Tectonics*. *Geol. Soc. London, Special Publication* 9, pp. 427–448.
- Price, R.A., Fermor, P.R., 1985. Structure Section of the Cordilleran Foreland Thrust and Fold Belt West of Calgary, Alberta. *Geological Survey of Canada*, 84-14, 1 Sheet.
- Pubellier, M., Rangin, C., Rascon, B., Chorowicz, J., Bellon, H., 1995. Cenomanian thrust tectonics in the Sahuaripa region, Sonora: implications about northwestern Mexico megashields. In: Anderson, T.H., Nourse, J.A., McKee, J.W., Steiner, M.B. (Eds.), *The Mojave-Sonora Megashield Hypothesis: Development, Assessment, and Alternatives*. Geological Society of America Special Paper Vol. 393, pp. 111–120.
- Quintero-Legorreta, O., Aranda-García, M., 1985. Relaciones estructurales entre el Anticlinorio de Parras y el Anticlinorio de Arteaga (Sierra Madre Oriental), en la región de Agua Nueva, Coahuila. *Rev. Mex. Cienc. Geol.* 6, 21–36.
- Ramírez-Peña, C.F., Chávez-Cabello, G., 2017. Age and structural evolution of thin skinned deformation in Zacatecas México: evidence of Sevier orogeny in the Mexican Fold Thrust Belt. *J. S. Am. Earth Sci.* <http://dx.doi.org/10.1016/j.james.2017.01.007>
- Ramos-Velázquez, E., Calmus, T., Valencia, V., Iriondo, A., Valencia-Moreno, M., Bellon, H., 2008. U/Pb and ⁴⁰Ar/³⁹Ar geochronology of the Coastal Sonora Batholith: new insights on Laramide continental arc magmatism. *Rev. Mex. Cienc. Geol.* 25, 314–333.
- Riggs, N.R., Mattinson, J.M., Busby, C.J., 1993. Correlation of Jurassic eolian strata between the magmatic arc and the Colorado Plateau: New U-Pb geochronologic data from southern Arizona. *Geol. Soc. Am. Bull.* 105, 1231–1246.
- Rivera-Carranza, E., De la Teja, M.A., Motolinía-García, O., Miranda-Huerta, A., León-Ayala, V.M., Lemus-Bustos, O., Moctezuma, M.D., 1998. Carta Geológico-Minera Cuernavaca (Cuernavaca Geologic Map). Servicio Geológico Mexicano (Mexican Geological Service), 1 Sheet.
- Rogers, C.L., De Cserna, Z., Tavera, A.E., Ulloa, S., 1957. Geología general y depósitos de fosfatos del distrito de Concepción del Oro, estado de Zacatecas. *Bole. Inst. Nac. Investig. Recur. Miner.* 38, 1–129.
- Rogers, C.L., de Cserna, Z., Tavera-Amezcuza, E., Van Vloten, R., Ojeda-Rivera, J., 1961. Reconocimiento geológico y depósitos de fosfatos del norte de Zacatecas y areas adyacentes en Coahuila, Nuevo León y San Luis Potosí. Consejo de Recursos Naturales no Renovables. *Boletín* 56 (322 p).
- Ross, M.I., Scotese, C.R., 1988. A hierarchical tectonic model of the Gulf of Mexico and Caribbean region. *Tectonophysics* 139–168.
- Roure, F., Alzaga-Ruiz, H., Callot, J.P., Ferket, H., Granjeon, D., Gonzalez-Mercado, G.E., Guilhaumou, N., Lopez, M., Mougín, P., Ortuño-Arzate, S., Séranne, M., 2009. Long lasting interactions between tectonic loading, unroofing, post-rift thermal subsidence and sedimentary transfers along the western margin of the Gulf of Mexico: some insights from integrated quantitative studies. *Tectonophysics* 475, 169–189.
- Ruiz, J., Patchett, P.J., Ortega-Gutiérrez, F., 1988. Proterozoic and Phanerozoic basement terranes of Mexico from Nd isotopic studies. *Bull. Geol. Soc. Am.* 100, 274–281.
- Salinas-Prieto, J.C., 1994. Etude structurale du sud-ouest Mexicain (Guerrero). Analyse microtectonique des deformations ductiles du Tertiaire inférieur. Unpublished Ph.D thesis. Universidad de Orleans (228 pp).
- Salinas-Prieto, J.C., Monod, O., Faure, M., 2000. Ductile deformations of opposite vergence in the eastern part of the Guerrero Terrane (SW Mexico). *J. S. Am. Earth Sci.* 13, 389–402.
- Salvador, A., 1987. Late Triassic-Jurassic paleogeography and origin of Gulf of Mexico basin. *Bull. Am. Assoc. Pet. Geol.* 71, 419–451.
- Schaaf, P., Morán-Zenteno, D., Hernández-Bernal, M., Solís-Pichardo, G., Tolson, G., Köhler, H., 1995. Paleogene continental margin truncation in southwestern Mexico: geochronological evidence. *Tectonics* 14, 1339–1350.
- Schaaf, P., Weber, B., Weis, P., Gross, A., Ortega-Gutiérrez, F., Köhler, H., 2002. The Chiapas Massif Complex (Mexico) revised: new geologic and isotopic data and basement characteristics. In: Miller, H.E. (Ed.), *Contributions to Latin-American Geology*. N. Jb. Geol. Paläont. Abh. Vol. 225, pp. 1–23.
- Schaaf, P., Hall, B.V., Bissig, T., 2003. March. The Puerto Vallarta Batholith and Cuale Mining District, Jalisco, Mexico—high diversity parenthood of continental arc magmas and Kuroko-type volcanogenic massive sulphide deposits. In: Morán-Zenteno, D. (Ed.), *Geologic Transects Across Cordilleran Mexico*. Guidebook for the Field Trips of the 99th Geological Society of America Cordilleran Section Annual Meeting. Instituto de Geología, Universidad Nacional Autónoma de México, Special Publication 1, pp. 183–199.
- Sierra-Rojas, M.I., Molina-Garza, R.S., 2014. La Formación Zicapa del sur de México: revisión estratigráfica, sedimentología y ambientes sedimentarios. *Rev. Mex. Cienc. Geol.* 31, 174–189.
- Sigloch, K., Mihalynuk, M.G., 2013. Intra-oceanic subduction shaped the assembly of Cordilleran North America. *Nature* 496, 50–56.
- Silva-Romo, G., Arellano-Gil, J., Mendoza-Rosales, C., Nieto-Obregón, J., 2000. A submarine fan in the Mesa Central, Mexico. *J. S. Am. Earth Sci.* 13, 429–442.
- Silver, L.T., Chappell, B.W., 1988. The Peninsular Ranges Batholith: an insight into the evolution of the Cordilleran batholiths of southwestern North America. *Transactions of the Royal Society of Edinburgh: Earth Sciences* 79, 105–121.
- Sinclair, H.D., 1997a. Flysch to molasse transition in peripheral foreland basins: the role of the passive margin versus slab breakoff. *Geology* 25, 1123–1126.
- Sinclair, H.D., 1997b. Tectonostratigraphic model for underfilled peripheral foreland basins: an Alpine perspective. *Bull. Geol. Soc. Am. Geol. Soc.* 109, 324–346.
- Solari, L.A., Torres de León, R., Hernández-Pineda, G., Solé, J., Hernández-Treviño, T., Solís-Pichardo, G., 2007. Tectonic significance of Cretaceous–Tertiary magmatic and structural evolution of the northern margin of the Xolapa Complex, Tierra Colorada area, southern Mexico. *Bull. Geol. Soc. Am.* 119, 1265–1279.
- Solé, J., Salinas, J.C., González-Torres, E., Cendejas Cruz, J.E., 2007. Edades K/Ar de 54 rocas ígneas y metamórficas del occidente, centro y sur de México. *Rev. Mex. Cienc. Geol.* 24, 104–119.
- Sosa-Valdés, R., 2011. Geocronología U-Pb del Cinturón de Intrusivos de Concepción del Oro. Unpublished Bachelor's thesis, Universidad Autónoma de Nuevo León (117 pp).
- Stein, G., Lappierre, H., Monod, O., Zimmermann, J.L., Vidal, R., 1994. Petrology of some Mexican Mesozoic-Cenozoic plutons: sources and tectonic environments. *J. S. Am. Earth Sci.* 7, 1–7.
- Stern, R.J., Dickinson, W.R., 2010. The Gulf of Mexico is a Jurassic backarc basin. *Geosphere* 6, 739–754.
- Stockmal, G.S., Beaumont, C., Nguyen, M., Lee, B., 2007. Mechanics of thin-skinned fold and thrust belts: insights from numerical models. In: Sears, J.W., Harms, T.A., Evenchick, C.A. (Eds.), *Whence the Mountains? Inquiries Into the Evolution of Orogenic Systems: A Volume in Honor of Raymond A Volume in Honor of Raymond A. Price*. Geological Society of America Special Paper Vol. 433, pp. 63–98.

- Suter, M., 1984. Cordilleran deformation along the eastern edge of the Valles–San Luis Potosí carbonate platform, Sierra Madre Oriental fold-thrust belt, east-central Mexico. *Bull. Geol. Soc. Am.* 95, 1387–1397.
- Suter, M., 1987. Structural traverse across the Sierra Madre Oriental fold-thrust belt in east-central Mexico. *Bull. Geol. Soc. Am.* 98, 249–264.
- Suter, M., 1990. Hoja Tamazunchale 14Q-e (5): con geología de la Hoja Tamazunchale, estados de Hidalgo, Querétaro y San Luis Potosí. Instituto de Geología, Universidad Nacional Autónoma de México (1 sheet).
- Suter, M., Contreras-Pérez, J., Ochoa Camarillo, H., 1997. Structure of the Sierra Madre Oriental fold-thrust belt in east-central Mexico. In: II Convención sobre la Evolución Geológica de México, Libro-guía de las excursiones geológicas. Excursión 2, 45–63.
- Tarduno, J.A., McWilliams, M., Debiche, M.G., Sliter, W.V., Blake Jr., M.C., 1985. Franciscan Complex Calera limestones: accreted remnants of Farallon Plate oceanic plateaus. *Nature* 317, 345–347.
- Tardy, M., 1980. Contribution à l'étude géologique de la Sierra Madre orientale du Mexique. Unpublished Ph.D thesis. Université de Paris (445 pp).
- Tardy, M., Sigal, J., Glacon, G., 1974. Bosquejo sobre la estratigrafía y la paleogeografía de los flysch cretácicos del sector transversal de Parras, Sierra Madre Oriental, México. Serie Divulgación 2. Universidad Autónoma Nacional de México, Instituto de Geología, pp. 12–28.
- Tardy, M., Longoria, J.F., Martínez-Reyes, J., Mitre-Salazar, L.M., Patiño, M., Padilla y Sánchez, R., Ramírez, C., 1975. Observaciones generales sobre la estructura de la Sierra Madre Oriental: la aloctonía del conjunto cadena alta-altiplano central, entre Torreón, Coah. y San Luis. *Rev. Mex. Cien. Geol.* 75, 1–11.
- Tardy, M., Lapierre, H., Freydier, C., Coulon, C., Gill, J.B., De Lépinau, B.M., Martínez, J.R., Talavera, O.M., Ortíz, E.H., Stein, G., Bourdier, J.L., Yta, M., 1994. The Guerrero suspect terrane (western Mexico) and coeval arc terranes (the Greater Antilles and the Western Cordillera of Colombia): a late Mesozoic intra-oceanic arc accreted to cratonic America during the Cretaceous. *Tectonophysics* 230, 49–73.
- Torres, R., Ruiz, J., Patchett, P.J., Grajales, J.M., 1999. A Permo-Triassic continental arc in eastern Mexico: tectonic implications for reconstructions of southern North America. In: Bartolini, C., Wilson, J.L., Lawton, T.F. (Eds.), *Mesozoic Sedimentary and Tectonic History of North-Central Mexico*. Geological Society of America Special Paper Vol. 340, pp. 191–196.
- Valencia, V.A., Richter, K., Rosas-Elguera, J., López-Martínez, M., Grove, M., 2013. The age and composition of the pre-Cenozoic basement of the Jalisco block: implications for and relation to the Guerrero composite terrane. *Contrib. Mineral. Petrol.* 166, 801–824 (doi: 10.1007/s00410-00013-00908-z).
- Valencia-Moreno, M., Ruiz, J., Barton, M.D., Patchett, P.J., Zürcher, L., Hodkinson, D.G., Roldán-Quintana, J., 2001. A chemical and isotopic study of the Laramide granitic belt of northwestern Mexico: identification of the southern edge of the North American Precambrian basement. *Bull. Geol. Soc. Am.* 113, 1409–1422.
- Valencia-Moreno, M., Ruiz, J., Ochoa-Landín, L., Martínez-Serrano, R., Vargas-Navarro, P., 2003. Geochemistry of the coastal Sonora batholith, Northwestern Mexico. *Can. J. Earth Sci.* 40, 819–831.
- Van Der Meer, D.G., Spakman, W., Van Hinsbergen, D.J., Amaru, M.L., Torsvik, T.H., 2010. Towards absolute plate motions constrained by lower-mantle slab remnants. *Nat. Geosci.* 3, 36–40.
- Vega-Granillo, R., Salgado-Souto, S., Herrera-Urbina, S., Valencia, V., Ruiz, J., Meza-Figueroa, D., Talavera-Mendoza, O., 2008. U–Pb detrital zircon data of the Rio Fuerte Formation (NW Mexico): Its peri-Gondwanan provenance and exotic nature in relation to southwestern North America. *Jour. South Am. Earth Sci.* 26, 343–354.
- Velasco-Tapia, F., González-Guzmán, R., Chávez-Cabello, G., Lozano-Serna, J., Valencia-Moreno, M., 2011. Estudio petrográfico y geoquímico del Complejo Plutónico El Peñuelo (Cinturón de Intrusivos de Concepción del Oro), noreste de México. *Bol. Soc. Geol. Mex.* 63, 183–199.
- Viele, G.W., Thomas, W.A., 1989. Tectonic synthesis of the Ouachita orogenic belt. In: Hatcher Jr., R.D., Thomas, W.A., Viele, G.W. (Eds.), *The Appalachian-Ouachita orogen in the United States. The Geology of North America 2*. Geological Society of America, pp. 695–728.
- Villarreal-Fuentes, J., Levresse, G., Nieto-Samaniego, A.F., Corona-Esquivel, R., 2014. New geological and geochronological data of the Placer de Guadalupe uplift, Mexico: a new piece of the Late Triassic–Jurassic Nazas Arc? *Int. Geol. Rev.* 56, 2000–2014.
- Walawender, M.J., Gastil, R.G., Clinkenbeard, J.P., McCormick, W.V., Eastman, B.G., Wernicke, R.S., Wardlaw, M.S., Gunn, S.H., Smith, B.M., 1990. Origin and evolution of the zoned La Posta-type plutons, eastern Peninsular Ranges batholith, southern and Baja California. In: Anderson, J.L. (Ed.), *The Nature and Origin of Cordilleran Magmatism*. Geological Society of America Memoir Vol. 174, pp. 1–18.
- Weidie, A.E., Murray, G.E., 1967. Geology of Parras Basin and adjacent areas of northeastern Mexico. *AAPG Bull.* 51, 678–695.
- Weil, A.B., Yonkee, W.A., 2012. Layer-parallel shortening across the Sevier fold-thrust belt and Laramide foreland of Wyoming: spatial and temporal evolution of a complex geodynamic system. *Earth Planet. Sci. Lett.* 357, 405–420.
- White, J.D., Busby, C.J., 1987. Deep marine arc apron deposits and syndepositional magmatism in the Alisitos Group at Punta Cono, Baja California, Mexico. *Sedimentology* 34, 911–927.
- Willett, S.D., 1999. Orogeny and orography: The effects of erosion on the structure of mountain belts. *Jour. Geoph. Res.: Solid Earth.* 104 (B12), 28957–28981.
- Wilson, J.L., 1990. Basement structural controls on Mesozoic carbonate facies in northeastern Mexico: A review. In: Tucker, M., et al. (Eds.), *Carbonate platforms, facies, sequences and evolution: International Association of Sedimentologists Special Publication no. 9*, pp. 235–255.
- Wilson, J.L., Ward, W.C., 1993. Early Cretaceous carbonate platforms of northeastern and east-central Mexico. *Memoirs-Am. Asso. Pet. Geol.* V. 84, 35.
- Wilson, B.W., Hernández, J.P., Meave, E.T., 1955. Un banco calizo del Cretácico en la parte oriental del estado de Querétaro México. *Bol. Soc. Geol. Mex.* 18, 1–10.
- Wong, M.S., Gans, P.B., 2008. Geologic, structural, and thermochronologic constraints on the tectonic evolution of the Sierra Mazatán core complex, Sonora, Mexico: new insights into metamorphic core complex formation. *Tectonics* 27, TC4013.
- Ye, H., 1997a. The arcuate Sierra Madre Oriental orogenic belt, NE Mexico: tectonic infilling of a recess along the southwestern North American continental margin, structure, stratigraphy and paleontology of Late Cretaceous-Early Tertiary Parras-La Popa Foreland Basin near Monterrey, Northeast Mexico. *American Association of Petroleum Geologists –Field trip 10*, 82–115.
- Ye, H., 1997b. Sequence Stratigraphy of the Difunta Group in the Parras-La Popa Foreland Basin, and Tectonic Evolution of the Sierra Madre Oriental, NE Mexico. Unpublished Ph.D thesis. The University of Texas at Dallas (197 pp).
- Yonkee, W.A., Weil, A.B., 2015. Tectonic evolution of the Sevier and Laramide belts within the North American Cordillera orogenic system. *Earth Sci. Rev.* 150, 531–593.
- Zhou, Y., Murphy, M.A., Hamade, A., 2006. Structural development of the Peregrina–Huizachal anticlinorium, Mexico. *J. Struct. Geol.* 28, 494–507.

III.II El relleno de la cuenca de antepaís mexicana durante el Cretácico Tardío-Paleógeno

Juárez-Arriga, E., Lawton, T.F., Ocampo-Díaz, Y.Z.E., Stockli, D.F., Solari, L., 2019a. *Sediment provenance, sediment-dispersal systems, and major arc-magmatic events recorded in the Mexican foreland basin, North-Central and Northeastern Mexico*: International Geology Review, <https://doi.org/10.1080/00206814.2019.1581848>

ARTICLE



Sediment provenance, sediment-dispersal systems, and major arc-magmatic events recorded in the Mexican foreland basin, North-Central and Northeastern Mexico

Edgar Juárez-Arriaga^a, Timothy F. Lawton^b, Yam Zul E. Ocampo-Díaz^c, Daniel F. Stockli^d and Luigi Solari^b

^aPosgrado en Ciencias de la Tierra, Centro de Geociencias, Universidad Nacional Autónoma de México, Santiago de Querétaro, México; ^bCentro de Geociencias, Universidad Nacional Autónoma de México, Santiago de Querétaro, México; ^cÁrea de Ciencias de la Tierra, Facultad de Ingeniería, Universidad Autónoma de San Luis de Potosí, San Luis Potosí, México; ^dDepartment of Geological Sciences, Jackson School of the Geosciences, University of Texas at Austin, Austin, TX, USA

ABSTRACT

The Late Cretaceous-Paleogene Mexican foreland basin (MFB), defined herein, represents the southern continuation of the late Mesozoic Cordilleran foreland basin. Sandstone petrography, new detrital-zircon (DZ) U-Pb geochronology, and paleocurrent data indicate that much of the sedimentary fill of the basin was derived from an active Late Cretaceous-Paleogene magmatic arc, termed here the Mexican Cordilleran arc, on the western continental margin of Mexico. The oldest known strata of the proximal foreland basin in the Mesa Central consist of Cenomanian-Turonian turbidites. Sampled sandstones are compositional volcanic litharenites with abundant neovolcanic grains and a dominant, approximately syndepositional DZ age group ranging ~98–92 Ma that records a major magmatic event in the Mexican Cordilleran arc. Santonian-Campanian strata in the distal MFB consist of carbonate pelagites with abundant interbedded tuffs and tuffaceous sandstones. Represented by the Caracol and San Felipe formations deposited in the forebulge and back-bulge depozones, respectively, these strata form an arcuate outcrop belt ~700 km in length. DZ ages ranging ~85–74 Ma in the arc-derived tuffaceous strata record a second prominent magmatic event.

Two principal transport mechanisms delivered volcanogenic sediment to the MFB from multiple, simultaneously active arc sources during Late Cretaceous time: (1) Cenomanian-Turonian east-directed transverse fluvial systems transported volcanic-lithic sand rich in young zircon grains; and (2) airborne ash clouds transported Santonian-Campanian zircon grains to the distal foreland basin in prevailing Late Cretaceous northwesterly winds. Axial transport of sediment derived from active arc sources, Proterozoic basement and derivative sedimentary rocks in northwestern Mexico, in addition to transverse transport from the thrust orogen itself, represents a younger sediment-routing system, modified by advance of the foreland fold-thrust belt, to the Maastrichtian-Paleogene foreland of northeastern Mexico.

ARTICLE HISTORY

Received 21 September 2018
Accepted 9 February 2019

KEYWORDS

Foreland basin-fill; magmatic flare-up; sandstone provenance; northeastern Mexico; southern North American Cordillera


Introduction

The Mesozoic record of magmatism in the North American Cordillera of the western United States includes plutonic and volcanic rocks produced during Late Cretaceous events (Smith 1960; McDowell and Clabaugh 1979; Christiansen *et al.* 1994; DeCelles *et al.* 2009; de Silva *et al.* 2015). Termed magmatic flare-ups, the events took place during time intervals on the order of 5–20 m.y. (Ducea 2001; Ducea and Barton 2007; DeCelles *et al.* 2009; Ducea *et al.* 2015). In the California segment of the Cordilleran arc, these magmatic events are interpreted to have resulted from eastward subduction of the Farallon oceanic plate (Ducea 2001). Belts of Cretaceous-Paleogene plutons along the western margin of Mexico also originated by

subduction of the Farallon plate (Ortega-Gutiérrez *et al.* 2014; Fitz-Díaz *et al.* 2018).

Assessments of the Late Cretaceous-Paleogene magmatic history of western North America based on compilations of plutonic rock ages can be limited by incomplete exposure of or inadequate access to, volcanic and plutonic igneous rocks of the arc. This problem is especially acute in western Mexico where Mesozoic igneous rocks are extensively covered by younger volcanic rocks (e.g. Langenheim and Jachens 2003; Fletcher *et al.* 2007). In such cases, the volcanoclastic content and detrital-zircon record of adjacent sedimentary basins can provide critical evidence for the magmatic history of the arc. For example, the distribution and ages of bentonites and ash-rich strata in deposits of the Cretaceous Western Interior Seaway (Figure 1(a))

CONTACT Edgar Juárez-Arriaga ✉ ejarriaga@geociencias.unam.mx Posgrado en Ciencias de la Tierra, Centro de Geociencias, Universidad Nacional Autónoma de México, Santiago de Querétaro 76001, México

 Supplemental data for this article can be accessed [here](#)

© 2019 Informa UK Limited, trading as Taylor & Francis Group

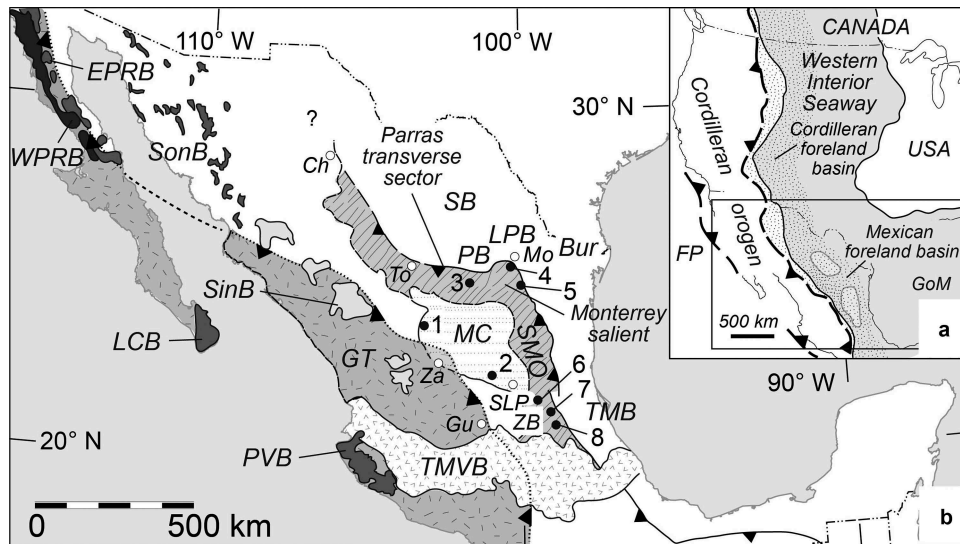


Figure 1. (a) Palaeogeography of Cordilleran orogen, foreland basin and Western Interior Seaway during late Cenomanian-Campanian time. Mexican foreland basin is the southern extension of the Cordilleran foreland basin (stippled), which occupies the western part of Western interior seaway. Explanation: FP, Farallon plate. (b) Locations of geographic and geologic features of northern and central Mexico. Guerrero terrane (GT) is a fringing or exotic magmatic arc, which was accreted near the end of Early Cretaceous time (e.g. Alisitos arc, Busby *et al.* 2006; Martini *et al.* 2014). Physiographic provinces of Mexico described in text: MC, Mesa Central; SMO, Sierra Madre Oriental fold and thrust belt; TMVB, Trans-Mexican volcanic belt. Numbered sample localities: (1) Río Grande, (2) Mexquitic, (3) La Casita Canyon, (4) Huasteca Canyon, (5) Alamar Canyon, (6) Jalpan-Concá, (7) Tezapotla, (8) Agua Zarca. Components of Mexican foreland basin system: SB, Sabinas basin; Bur, Burgos basin; LPB, La Popa basin; PB, Parras basin, ZB, Zimapán basin; TMB, Tampico-Misantla basin. GoM, Gulf of Mexico. Plutonic and volcanic rocks of Mexican Cordilleran arc, defined in text: WPRB, Western Peninsular Ranges batholith; EPRB, Eastern Peninsular Ranges batholith; SonB, Sonora batholith; SinB; Sinaloa batholith; LCB, Los Cabos batholith; PVB, Puerto Vallarta batholith. Cities (white dots): Ch-Chihuahua; To-Torreón; Mo-Monterrey; Za-Zacatecas; SLP-San Luis Potosí; Gu-Guanajuato.

correlate closely with emplacement ages of plutons in the North American Cordillera (Christiansen *et al.* 1994).

Although the detrital zircon record of the Cordilleran foreland basin of the United States has been described extensively, the detrital zircon record and composition of sandstones in a correlative counterpart basin in Mexico remain largely unknown. In this paper, we introduce the name *Mexican foreland basin (MFB)* for a foreland-basin system (e.g. DeCelles and Giles 1996) that developed adjacent to an eastward-advancing, Late Cretaceous-Paleogene fold-thrust belt termed the Mexican orogen (Fitz-Díaz *et al.* 2018). MFB subsidence began immediately following accretion of the Guerrero terrane, a composite oceanic or fringing arc system (Centeno-García *et al.* 2008, 2011; Martini *et al.* 2012, 2013), near the end of Late Cretaceous time. Although initial deep-water fill of the basin resembles that of the collisional Alpine foreland basin (e.g. Sinclair 1997), a pro-foreland basin, the history of subsidence in the MFB corresponded with arc magmatism in western Mexico related to subduction of the Farallon slab, as we describe below; therefore, the tectonic setting of the MFB is consistent with that of a retroarc or retro-foreland basin (e.g. Dickinson 1976).

In cases where retro-foreland basin systems (*sensu* Ingersoll 2012) are linked to adjacent drainage networks within the volcanic carapace of the arc, the basin fill can record arc history because easily eroded volcanogenic material transported to the basin provides a widely distributed record of approximately contemporary magmatism (DeCelles *et al.* 2009; de Silva *et al.* 2015). Detrital zircon (DZ) analysis, integrated with systematic mapping has been applied to the fill of the Cordilleran foreland basin in the United States to identify short-lived magmatic pulses in the North American Cordillera (Laskowski *et al.* 2013; de Silva *et al.* 2015; Ducea *et al.* 2015). Airborne ash erupted during major magmatic events can also provide a direct record of arc magmatism if prevailing atmospheric circulation is from the arc to the basin (e.g. Christiansen *et al.* 1994).

In this study, we present sandstone petrographic data and U-Pb geochronological data from zircon grains in sandstone and tuff of the MFB to augment the record of Cretaceous arc history in western Mexico and evaluate the influence of the magmatic arc on the basin fill. On the basis of new DZ data and U-Pb ages of tuffs interbedded in foreland basin strata, we recognize two major Late

Cretaceous magmatic events in western Mexico with a duration of ~7 and ~11 m.y., suggesting that magmatic activity in the southern part of the Cordilleran arc was similarly episodic. The Late Cretaceous magmatic events correlate with similar ones in the magmatic arc of the United States, but we also recognize an Early Cretaceous magmatic event that corresponds with a coeval episode of low apparent magmatic flux in the California arc to the north (e.g. Ducea 2001); the Early Cretaceous event serves to distinguish the arc history of Mexico from that of the United States and provided an important source for detrital zircons in Mexico. Our study also suggests mechanisms of sediment transport between the arc and the basin and provides a possible explanation for the distribution of tuffs and ash-rich strata in the southern part of the North American Cordillera during Late Cretaceous time.

Geological framework

Foreland-basin sedimentation in Mexico was linked to the development of the Mexican orogen, a deformed belt of variable kinematic style that extends the length of Mexico (Fitz-Díaz *et al.* 2018). In late Early Cretaceous time, volcanic arc rocks and siliciclastic strata of the Guerrero terrane were accreted to western Mexico (Dickinson and Lawton 2001; Busby *et al.* 2006; Martini *et al.* 2014); sedimentation in the adjacent foreland of central Mexico began shortly after the collision. Alternative models for the origin of the Guerrero terrane, whether as an exotic, far-travelled arc (Tardy *et al.* 1994; Dickinson and Lawton 2001; Sigloch and Mihalynuk 2013) or a parautochthonous fragment of North America separated during Late Jurassic–Early Cretaceous marginal-basin formation (Centeno-García *et al.* 2008, 2011; Martini *et al.* 2011; Fitz-Díaz *et al.* 2018) remain a matter of debate. In either case, east-dipping subduction of the Farallon slab beneath Mexico was established by Cenomanian time, roughly synchronous with the age of the oldest deposits of the foreland basin (Kimbrough *et al.* 2001; Centeno-García *et al.* 2011; Ortega-Gutiérrez *et al.* 2014; Fitz-Díaz *et al.* 2018). Late Cretaceous–Paleogene subduction created a continental-margin arc along the western flank of Mexico, which consisted of the newly accreted Guerrero terrane. Because much of the volcanic caparace has been removed by erosion, extensive batholiths in western Mexico (Zimmermann *et al.* 1988; Henry *et al.* 2003; Valencia *et al.* 2013; Ortega-Gutiérrez *et al.* 2014) and the Baja Peninsula (Walawender *et al.* 1990; Kimbrough *et al.* 2001; Langenheim and Jachens 2003; Ortega-Rivera 2003) provide the principal record of the arc (Kimbrough *et al.* 2001). Episodic magmatism during Late Cretaceous–Eocene time was particularly voluminous (Kimbrough *et al.* 2001; Ortega-Gutiérrez *et al.* 2014). In this paper, we refer to the post-accretion, Late Cretaceous–Paleogene

magmatic arc of the Baja Peninsula and western mainland Mexico as the *Mexican Cordilleran arc*. Consistent with previous usage, an Early Cretaceous magmatic arc that developed on the Guerrero terrane prior to its accretion is termed the Alisitos arc (Wetmore *et al.* 2002, 2003; Alsleben *et al.* 2012).

The Mexican foreland basin (MFB) lay on the continental side of the magmatic arc and Mexican orogen (Fitz-Díaz *et al.* 2018). The foreland basin ranges in age from late Cenomanian(?)–Eocene (Figure 2) (Lawton *et al.* 2016) and extends from the suture with the Guerrero terrane to the Gulf of Mexico; much of the early-formed basin was extensively deformed by advance of the Mexican orogen (Figure 1) (Fitz-Díaz *et al.* 2018). The basin includes a broad region of deformed turbidite strata in the Mesa Central, formerly termed the Central Mexican Mesozoic basin (cuenca Mesozoica del Centro de México; Carrillo-Bravo 1971), as well as local stratigraphic inliers in the Sierra Madre Oriental fold-thrust belt, such as the Zimapán basin, and the Burgos, Parras, La Popa, Sabinas and Tampico-Misantla basins (Figure 1(b)), which lie north and east of the Mexican orogen (e.g. Fitz-Díaz *et al.* 2018, and references therein).

Cenomanian(?)–Turonian calciturbidites and siliciclastic turbidites of the Mesa Central constitute the oldest strata of the basin (Figure 2). Younger strata are absent from the Mesa Central, evidently due to erosion during eastward-advancing uplift of the fold-thrust belt (Fitz-Díaz *et al.* 2018). Santonian–Campanian strata are present farther east, in the Sierra Madre Oriental, where pelagic carbonate and shale successions of the Caracol and San Felipe formations, rich in interbedded tuffs, represent distal deposits of the basin (Figure 2).

East of the Mesa Central, Early Cretaceous carbonate platforms of eastern Mexico were overlapped by clastic strata in Santonian time as a result of eastward migration of the foreland basin foredeep (Figure 1, 2) (Carrillo-Bravo 1971; Wilson and Ward 1993). The youngest deposits of the foreland-basin system include Campanian–Eocene strata of the Difunta Group in the Parras and La Popa basins of northeastern Mexico (e.g. McBride *et al.* 1974; Lawton *et al.* 2009) and the Paleocene–Eocene Chicontepec Formation in the Tampico-Misantla basin of eastern Mexico (Bitter 1993; Alzaga-Ruiz *et al.* 2009).

Methods

Four samples were collected from Mesa Central turbidites for petrographic and detrital zircon analysis. Due to structural complexity, it is not possible to determine the relative stratigraphic positions of the Mesa Central samples within the foreland basin succession. A fine- to medium-grained sandstone was collected from a road

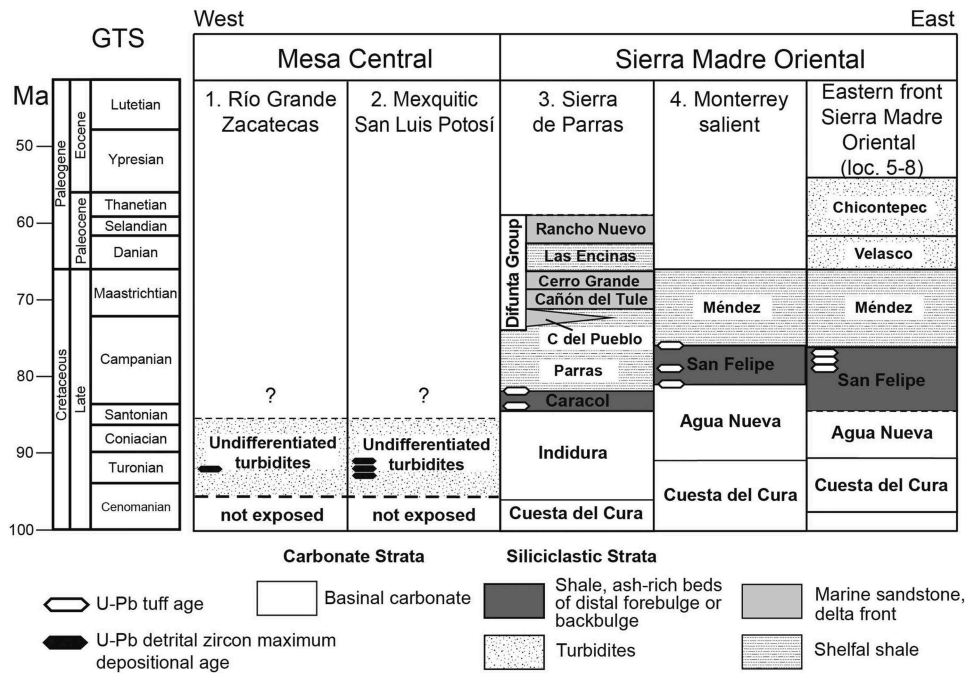


Figure 2. Stratigraphic correlation chart, central and eastern foreland region of Mexico. Lower units of columns represent pre-foreland basin carbonate facies. Lower and upper age limits of turbidites in Mesa Central are unknown due to incomplete sampling and erosion. Siliciclastic environments represented by patterned and dark grey units, migrated eastward with time, toward the exterior part of Mexican orogen.

cut exposure near the city of Río Grande in Zacatecas (sample 14-26IV14; Figure 1(b), locality 1). In the southern part of the Mesa Central, three samples (25-MB02, 26-PST01, and CARN-28; Figure 1(b), locality 2) were collected west of the village of Mexquitic in San Luis Potosí from the bases of medium-grained sandstone beds.

Four samples of reworked tuffs were collected for U-Pb analysis from measured stratigraphic sections of the Caracol and San Felipe formations, as described below (Figure 1, localities 3, 4). Five additional samples (29-TE-01, 36-CL01, 48-AZ02, 04-JC01 and 05-JC02) were collected from ash beds of the San Felipe Formation along the frontal part of the Sierra Madre fold-thrust belt south of the Monterrey salient (Figure 1, localities 5–8).

Each geochronological sample consisted of approximately 3–5 kg of rock, which yielded at least 50 zircon grains per tuff sample and at least 140 grains per detrital sample. Samples were analyzed by LA-ICPMS in the Laboratorio de Estudios Isotópicos (LEI) at the Centro de Geociencias, UNAM, according to the methodology reported in Solari *et al.* (2018) and UT Geo- and Thermochronometry Laboratory at the University of Texas, according to the methodology reported in Hart *et al.* (2016). One sample of the Caracol Formation

(07COA-CA3) was analyzed at the Arizona LaserChron Center, at the University of Arizona, according to the methodology of Gehrels *et al.* (2008). Analyses with discordance >20% or reverse discordance >5% are indicated by strikethrough text in Supplemental Data Tables DR-1 and DR-2 and were not considered further. Concordant grains were plotted as probability distribution functions using Isoplot software (Ludwig 2008). The maximum depositional age (MDA) of each sandstone sample was interpreted from the weighted mean of the concordant, youngest grain ages that overlap at two-sigma (2σ) analytical error (e.g. Dickinson and Gehrels 2009). Tuff ages represent the weighted mean age of the cohort of overlapping (at 2σ error) young grain ages that yielded an MSWD (mean square of weighted deviates) nearest unity, also using Isoplot (Ludwig 2008). We employ the Geologic Time Scale of Cohen *et al.* (2013).

Thin sections were prepared of all samples collected for U-Pb analysis. Sandstone thin sections were point-counted using the Gazzi-Dickinson technique to reduce compositional dependence on grain size (Ingersoll *et al.* 1984). Sandstone and tuff samples were examined to establish the presence or absence of neovolcanic grains (*sensu* Critelli and Ingersoll 1995) that might indicate contemporary volcanism.

Foreland basin

We divide Cenomanian to Campanian strata of the foreland basin into proximal and distal foreland-basin strata on the basis of their inferred distance from the time-equivalent thrust front. Strata of the Mesa Central are considered proximal, whereas strata of the Sierra Madre Oriental are distal.

Proximal foreland basin strata

Extensively folded and faulted turbidites of the Mesa Central were formerly assigned to the Caracol Formation (de Cserna 1976), but our U-Pb data indicate that the turbidites are older than the type Caracol of the Sierra de Parras (Imlay 1937) (Figure 1, locality 3; Figure 2). We refer to the strata as undifferentiated turbidites. They form outcrops of sandstone, siltstone, shale, calcareous shale and calcilithite that are usually limited to fault-truncated successions no more than a few meters to tens of meters thick. Intercalated calciturbidite beds grade from fine-grained calcilithite to laminated calcareous shale. Siliciclastic intervals contain two distinctive lithofacies associations. One association consists of upward-fining and -thinning successions composed of massive to graded lenticular sandstone beds as much as 3.5 m thick interbedded with shale layers. Mudstone clasts are common at the bases of sandstone beds. This lithofacies association is interpreted as deposits of channel systems in a submarine fan system (e.g. Mutti and Normark 1991; Posamentier and Walker 2006). A second lithofacies association consists of graded sandstone beds that alternate with thin layers of shale to form upward-coarsening and -thickening successions as much as 3 m thick. This lithofacies association is interpreted as deposits of submarine-fan lobes (e.g. Mutti and Normark 1991). Limited palaeocurrent data measured on flute casts of siliciclastic sandstone beds indicate generally easterly sediment transport (Figure 3). Calciturbidites were derived from carbonate platforms to the east on the basis of the dominance of carbonate grains and clasts, which in some cases can be matched to Lower Cretaceous rock types of the Sierra Madre Oriental.

Distal foreland basin strata

Ash-rich volcanoclastic and sedimentary strata of Santonian-Campanian age crop out in the northern part of the Mesa Central and in the frontal part of the fold-thrust belt from the eastern part of the Parras transverse sector to the eastern front of the Sierra Madre Oriental (Figure 1, localities 3–8) and continue east into the subsurface (Santamaría-Orozco *et al.*

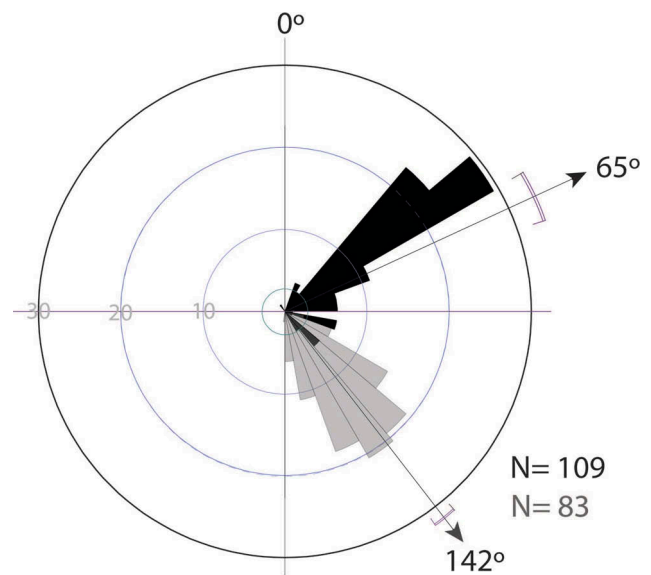


Figure 3. Palaeocurrent rose of flute casts and drag marks at two turbidite outcrops in Mesa Central, Santa Teresa (black shading) and CARN-28 (grey shading) (Figure 1(b), locality 2). Arrows indicate the average direction of palaeocurrent measurements at each outcrop. N values represent the number of measurements.

1990). The volcanoclastic and sedimentary succession is thus distributed along an arcuate belt, approximately 250 km wide by 700 km long, that straddles the present Sierra Madre Oriental thrust front. The succession varies from ~350 m thick in the Parras transverse sector (Figure 1, locality 3; Figure 2), where it is termed the Caracol Formation, to 100–250 m thick in the Monterrey salient and along the Sierra Madre Oriental (Figure 1, localities 4–8; Figure 2), where it is termed the San Felipe Formation (Carrillo-Bravo 1961; Gamper 1977; Sohl *et al.* 1991; Velasco-Tapia *et al.* 2016).

The Caracol Formation in La Casita Canyon (Figure 1 (b), locality 3) concordantly overlies limestone beds of the Indidura Formation (Figure 4(a)). The lower part of the section consists of shale interbedded with ash-rich sandstone or reworked ash beds. The sandstone beds are 3–50 cm thick, rich in tuffaceous grains, volcanic quartz, plagioclase, biotite and microfossils, and normally graded from structureless coarse-grained sandstone to laminated fine-grained sandstone. They are interpreted as Bouma AB turbidites. A coarse-grained sandstone (07COA-CA3) was collected 60 m above the basal contact for U-Pb analysis.

The middle part of the section (m 110–290) consists of thin, bioturbated sandstone beds and thick intervals of shale. *Chondrites* and *Zoophycus* traces indicate the *Zoophycus* ichnofacies. Shale beds are broadly lenticular, 60–80 cm thick, with erosive upward-concave basal contacts that cut subjacent shale layers; overlying shale

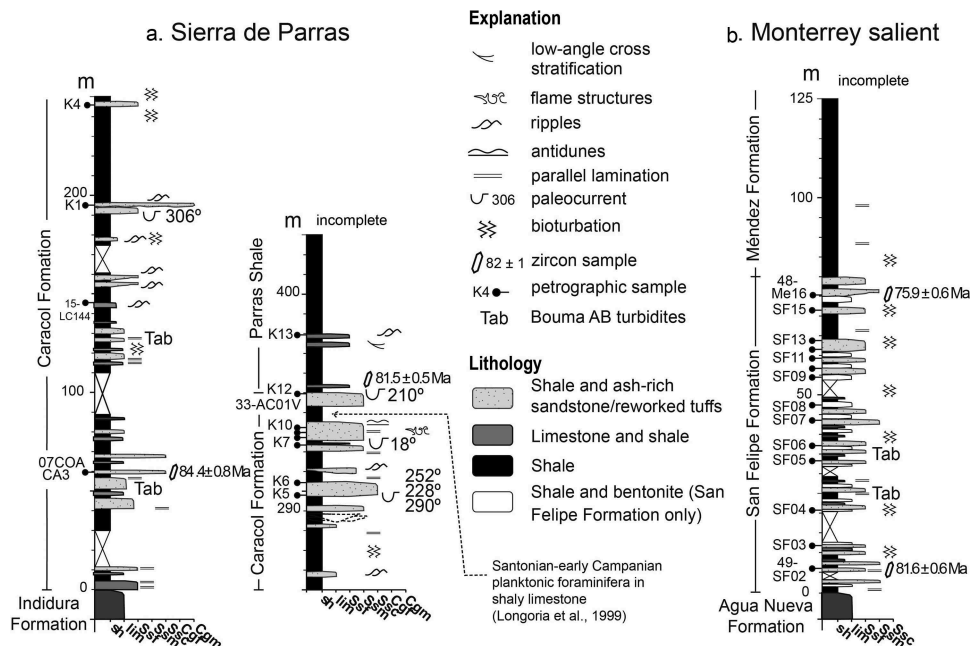


Figure 4. (a) Measured stratigraphic section of Caracol Formation in La Casita Canyon, Sierra de Parras, Coahuila (Figure 1(b), locality 3). Section begins at 25° 13.970'N, 101° 25.977'W and ends at 25° 14.221'N, 101° 25.908'W. Measured palaeocurrent directions indicated as azimuths along the column. Stratigraphic position of a sample reported by Longoria *et al.* (1999) is approximate. (b) Measured stratigraphic section of San Felipe Formation in La Huasteca Canyon, Monterrey salient. Section begins at 25° 35.122'N, 100° 25.535'W and ends at 25° 35.645'N, 100° 26.399'W.

onlaps the erosional contacts. This cut-and-fill geometry results in a broad complex of channelform shale bodies tens of meters wide. We interpret the shale interval as a complex of nested slope channels.

The upper 60 m of the Caracol section consists of interbedded shale and fine- to coarse-grained ash-rich sandstone and reworked tuff beds with soft-sediment deformation structures, flame structures, overlain by medium-grained tuffaceous sandstone with low angle cross-lamination and undulose upward-convex and -concave laminae with wavelengths of tens of centimetres. Flute casts indicate flow to the west and southwest (Figure 4 (a)). The structures in the upper parts of the beds are interpreted as antidunes, indicating sediment deposition during supercritical flow. Observations which support the antidune interpretation include: 1) Morphology of the structures, which consist of upward-convex parallel laminae with low-amplitude rounded crests and absence of swales; 2) presence of traction carpets and horizontal lamination in medium sandstone below the undulating interval, which indicate upper flow regime flow; 3) absence of wave ripples in upper parts of beds; and 4) absence of other structures formed by oscillating currents. The top of the uppermost coarse-grained tuffaceous bed, the level of sample 33-AC01V, is defined as the upper limit of the Caracol Formation (Figure 4(a)). Discrete beds of tuff and ash-rich sandstone form ~13% of the section. The

overlying Parras Shale resembles the shale of the Caracol Formation but lacks tuff beds. The Caracol Formation represents alternating deposits of volcanoclastic turbidites, some of which are resedimented and altered ash falls or bentonites (e.g. Christiansen *et al.* 1994; Christidis and Huff 2009), and hemipelagic mud. The *Zoophycus* ichnofacies indicates low-energy, likely deepwater, conditions (e.g. Pemberton *et al.* 1992). Turbidites and shale-filled channels indicate the presence of a submarine slope. The Caracol Formation has been previously interpreted as shelfal deposits (PEMEX, Petróleos Mexicanos 1988; Barboza-Gudiño *et al.* 2004), but deposition by sediment-gravity flows and the presence of a topographic slope suggest a more distal site in the foreland basin, as discussed below.

We measured a complete section of the San Felipe Formation in La Huasteca Canyon, in the Monterrey salient, where the unit is 75 m thick (Figure 1(b), locality 4). It is dominantly composed of calcareous shale, bentonite, micritic limestone beds as much as 50 cm thick, and rhythmic, thin ash-rich sandstone beds (Figure 4 (b)). The ash-rich beds make up ~20% of the succession and represent Bouma AB turbidites, normally graded from structureless coarse-grained sandstone to laminated fine-grained sandstone. The San Felipe Formation overlies limestone and shale beds of the deepwater Agua Nueva Formation, correlative with

the Indidura Formation, and is overlain by the pale brown Méndez Shale. The lower and upper contacts of the San Felipe Formation are defined to lie at lowermost and uppermost occurrences of coarse-grained ash-rich beds. Two samples of coarse-grained ash-rich sandstone (49-SF02b and 48-Me16) were collected for U-Pb analysis near the base and top of the San Felipe Formation (Figure 4(b)).

The San Felipe Formation has been alternatively interpreted as basinal deposits (e.g. Sohl *et al.* 1991; Ángeles-Villeda *et al.* 2005) or as outer shelf deposits on the basis of lithology, trace fossils, and the ratio of planktonic to benthic foraminifera (e.g. Gamper 1977; López-Ramos 1980; Martínez-Paco 2012). The combination of deepwater deposition, pelagic carbonate deposition, and presence of carbonate extra basinal grains (Lsc) in turbidites derived from a contemporary orogenic belt to the west suggest deposition in a distal part of the foreland basin (sensu DeCelles and Giles 1996).

Younger strata of foreland basin (Difunta group)

The late Campanian-Eocene Difunta Group was deposited in a foredeep depozone adjacent to the frontal Sierra Madre Oriental fold-thrust belt (Soegaard *et al.* 2003; Lawton *et al.* 2009). The Difunta Group consists of sandstone-rich fluvial and deltaic deposits that are coarser grained than the San Felipe and Caracol formations (McBride *et al.* 1974). Published petrographic and detrital zircon results from the Difunta Group (Lawton *et al.* 2009) complement understanding of basin evolution and illustrate the age distribution of detrital zircon grains in younger, Maastrichtian-Eocene units of the foreland basin.

Clastic petrography

Mesa Central sandstones range from lithic arkose to litharenite (classification of Folk 1974). Framework grains are dominated by monocrystalline quartz, plagioclase, volcanic lithic grains and subordinate potassium feldspar that includes microcline, as well as polycrystalline quartz, metamorphic and siliciclastic sedimentary lithic grains (Figure 5(a-b)). Extra basinal carbonate lithic grains (Lsc of Ingersoll *et al.* 1987) derived from erosion of carbonate rocks are uncommon in most samples, except in 26-PST 01, where they are dominant (Figure 6(a)). Altered feldspar and secondary carbonate cement are very common and unstable grains are commonly replaced by calcite (Figure 6(b)). Volcanic lithic grains represent more than 50% of the lithic fragments in two of the samples (Figure 5(c)). Many of the volcanic lithic grains are fresh to altered

felsitic grains (Figure 6(a-f)) that we interpret as neovolcanic grains deposited during penecontemporaneous volcanism in the sediment-source area (e.g. Critelli and Ingersoll 1995). Fresh plagioclase is present in all samples (Figure 6(f-i)). Feldspar and volcanic lithic grains are locally altered to incipient pseudomatrix.

All Caracol and San Felipe tuffs are volcanoclastic sandstones (sensu Critelli and Ingersoll 1995), most having a high degree of alteration, including replacement by calcite, which makes a comparison of grain proportions among samples difficult (Figure 7(a,b)). The framework grains include felsitic volcanic grains, as well as microcrystalline tuffaceous lapilli and glass shards, plagioclase with polysynthetic twins, monocrystalline volcanic quartz and fresh biotite (Figure 7(c-h)). Potassium feldspar is rare; a few grains of microcline and sanidine were observed. Detrital carbonate grains and bioclasts are present (Figure 7(d-i)); carbonate grains can be difficult to discriminate from plagioclase and tuffaceous grains that are replaced by calcite (Figure 7(d-f)).

Zircon grains are common in all tuffs and ash-rich sandstones. All zircon grains consist of elongate euhedral crystals that are colourless or pale yellow; 80–100% of the analyzed grains in individual samples are tetragonal prisms with bipyramidal terminations and well-developed regular oscillatory zoning with parallel domains. A subordinate group of colourless grains lacks zonation. Neither U-Pb analyses nor cathodoluminescent images indicate the presence of inherited cores.

U-Pb geochronology

New U-Pb geochronologic analyses of the undifferentiated turbidites and tuffaceous sandstones include 932 zircon ages (Table 1).

Detrital zircons of undifferentiated turbidites, Mesa Central

Mesa Central turbidite grain ages span ~2940 to ~84 Ma, of which 49% (249 of 509 analyses) are younger than 300 Ma (Figure 8). Precambrian grains constitute a subordinate age component that lacks significant age peaks. Pan-African grains (~652–544 Ma) are present but uncommon in one sample (CARN-28; Figure 8). Early Palaeozoic grains form subordinate age peaks ranging ~469 Ma to ~450 Ma in all samples. Jurassic zircon grains represent an important component (14%; $n = 72$) of all samples, with peaks ranging from ~164 Ma to ~156 Ma. Cretaceous grains ranging from ~145 to ~66 Ma constitute the most abundant ages in the samples (31%, 159 of 509 analyses). A distinctive Early Cretaceous age group

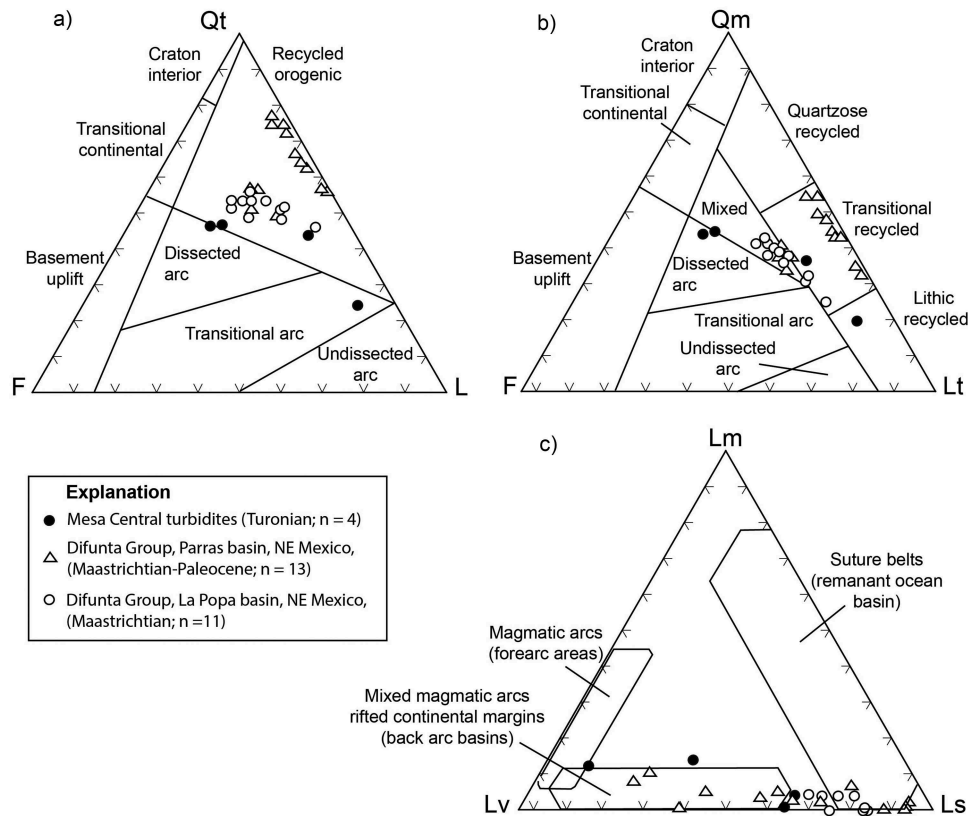


Figure 5. (a) and (b), Total grain plots of detrital modes of Turonian sandstones in Mesa Central (black dots, this study), middle Maastrichtian sandstones in La Popa basin (white dots, Lawton *et al.* 2009), and uppermost Maastrichtian-Paleogene sandstones in Parras basin (white triangles, Lawton *et al.* 2009). Provenance fields after Dickinson (1985). (c) LmLvLs compositional plot of Mesa Central turbidites and Difunta Group sandstones. L = polycrystalline lithic fragments, Lm = metamorphic lithic fragments, Lv = volcanic lithic fragments, Ls = sedimentary lithic fragments, Lt = total lithic fragments. Qt, total quartz = Qm, monocrystalline quartz + Qp, polycrystalline quartz. Lt = L + Qp. Chert is included in Qp and Ls. n = number of samples. Provenance fields of LmLvLs plot after Ingersoll and Suczek (1979).

with an age peak at ~131 Ma is present in sample 26-PST 01 and Early Cretaceous grains are present in 25-MB02 and CARN-28 (Figure 8). Early Late Cretaceous grains form dominant peaks ranging from ~98 Ma to ~92 Ma in the samples. All Mesa Central samples yielded Turonian maximum depositional ages (Table 1).

U-Pb ages of tuffs in distal foreland units

Late Cretaceous zircon grains (98%, 331 of 339 analyzed zircons) dominate our samples of the Caracol and San Felipe formations. All samples yielded mean ages of ~84–76 Ma (Figure 9; Table 1). The lower Caracol sample (07COA-CA3) from our measured section in Sierra de Parras yielded a weighted mean age of 84.4 ± 0.8 Ma and the upper sample (33-AC01V) yielded a weighted mean age of 81.5 ± 0.5 Ma, which we interpret as the depositional ages for the lower part and top of the measured section (Figure 4(a)). The resulting Santonian-early Campanian age range for the Caracol Formation agrees with a Santonian-early

Campanian biostratigraphic age determined for the formation at the same locality (Longoria *et al.* 1999).

The lowermost San Felipe sample (49-SF02B) from our measured section at La Huasteca Canyon yielded a weighted mean age of 81.6 ± 0.6 Ma and the uppermost sample (48-Me16) yielded a weighted mean age of 75.9 ± 0.6 Ma, indicating an early to middle Campanian age for the section (Figure 4(a-b), 9(a-d)). The ages thus indicate alternatively that the lower part of the Sierra de Parras section is equivalent to strata designated as Agua Nueva Formation at La Huasteca Canyon, that the base of the San Felipe Formation is time-transgressive or that there is an unrecognised unconformity at the base of the unit at La Huasteca Canyon that creates a hiatus between the Agua Nueva and San Felipe formations. The second two possibilities could have resulted from deposition of the San Felipe higher on the forebulge than the Caracol Formation.

Five additional tuff samples of the San Felipe Formation were collected along the frontal part of the Sierra Madre Oriental (Figure 1), from incompletely exposed sections, in

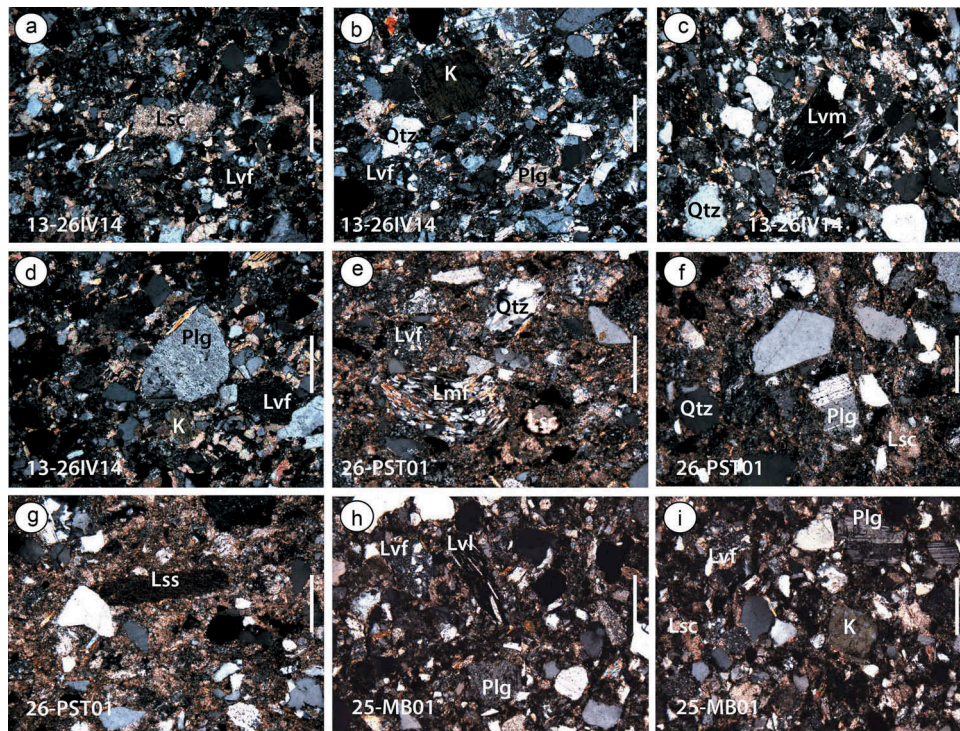


Figure 6. Thin section photomicrographs of Cenomanian-Turonian undifferentiated turbidites, Mesa Central. All photos cross-polarized light; sample numbers indicated in the lower left of photos. **(a)** Detrital carbonate grain (Lsc) and finely crystalline felsitic volcanic lithic fragment (Lvf) in litharenite, Río Grande, Zacatecas. **(b–d)** Angular volcanic lithic fragments in litharenite, Río Grande, Zacatecas, and **(e–i)** metamorphic, volcanic and sedimentary lithic fragments in litharenites, Mexquitic, San Luis Potosí. Abbreviations: Lvf, felsitic volcanic lithic fragment; Lvm, microlitic volcanic lithic fragment; Lvl, lathwork volcanic lithic fragment; Lsc, detrital carbonate fragment; Lss, sedimentary lithic fragment (argillite); Lmf, foliated quartz-mica metamorphic fragment; Qtz, monocrySTALLINE quartz; K, potassium feldspar; Plg, plagioclase. Length of bar is 250 µm in all images.

which their stratigraphic position within the succession is not known. Samples are located in the central Sierra Madre Oriental fold-thrust belt, except 36-CL01, which is from El Alamar Canyon, in the southern part of the Monterrey salient. Weighted mean ages of the samples span late Santonian to middle Campanian (84.4 to 77.0 Ma; [Figure 9\(e–h\)](#); [Table 1](#)).

Discussion

Depositional model

We interpret the units of Turonian to Campanian age described above as deposits of the Late Cretaceous foreland basin developed adjacent to the Cordilleran orogen in Mexico. The turbidite strata of the Mesa Central represent the oldest known deposits within the basin. Eastward and southeastward palaeoflow directions ([Figure 3](#)) indicate sediment transport from the time-equivalent magmatic arc, with flow likely influenced by a foredeep that was oriented NW-SE.

Depositional style changed as basin deposition migrated eastward with time, toward the exterior part

of the Sierra Madre Oriental. Santonian-Campanian pelagic and volcanoclastic facies of the Caracol and San Felipe formations were deposited from suspension in the distal foredeep and by ash falls or mass flows generated on the slight slope between the distal foredeep and forebulge of the foreland-basin system ([Figure 10](#)). Although the Caracol Formation has previously been interpreted as a shelfal deposit, our environmental interpretations indicate deep-water deposition in a foreland basin system. Key features of the deposits include: 1) Local southwest-directed flute casts that indicate sediment transport toward the orogen, rather than away from it, as would be expected in a conventional shelf setting; and 2) broad channelform shale bodies, formed on the flank of a submarine slope susceptible to submarine erosion (e.g. [Collinson et al. 2006](#)). These features indicate the existence of subtle elevated topography in the distal part of the basin, which we interpret as the transition between the foredeep and forebulge depozones (sensu [DeCelles and Giles 1996](#)), where some ash was transferred from the forebulge to distal foredeep by subaqueous gravity-driven transport toward the orogen.

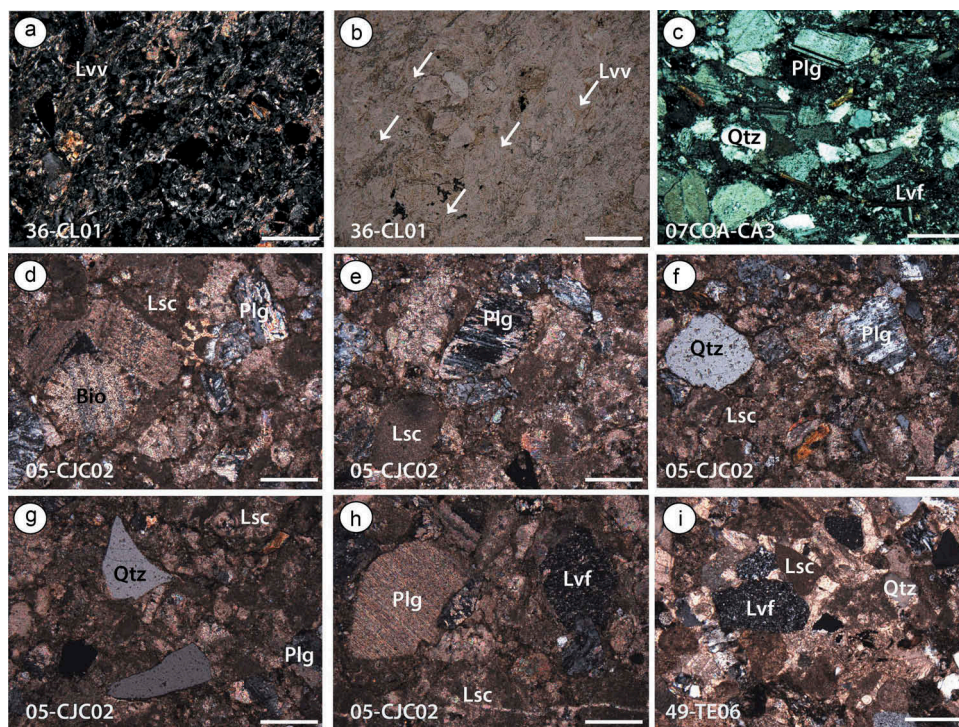


Figure 7. Thin section photomicrographs of Santonian-Campanian tuffs and tuffaceous sandstones of the Mexican foreland basin. All photos cross-polarized light, except **(b)**; sample numbers indicated in the lower left of photos. **(a)** Devitrified tuff containing glass shard, San Felipe Formation, Monterrey salient. **(b)** Devitrified tuff and glass shards (arrows) in tuff layer of the San Felipe Formation, central Sierra Madre Oriental fold-thrust belt (plane-polarized light). **(c)** Detrital biotite grains in the lower part of Caracol Formation, Sierra de Parras, Coahuila. **(d–i)** Ash-rich sandstones of San Felipe Formation, central Sierra Madre Oriental fold-thrust belt with euhedral and broken crystals and a variety of volcanic lithic fragments. Symbols as in Figure 5, and Bio, bioclast. Length of bar is 250 μm in all images.

Neither previous research on the San Felipe Formation nor our observations have documented fan lobes or channel systems. We infer that sediment was not distributed from a single point source, but rather was fed from multiple sources that were active more or less simultaneously. U-Pb zircon ages that approximate the biostratigraphic age (Table 1) and tuffaceous sandstones in the deposits indicate that most of the volcanic grains in this unit were transported to the distal basin by syndepositional ash clouds. Abundant detrital carbonate grains (Lsc) can be explained by erosion of the Early Cretaceous carbonate platforms of eastern Mexico, which were elevated by eastward migration of forebulge. Furthermore, it is possible that sediment reworking toward the distal part of the basin might have been caused by instability that resulted from rapid accumulation of volcanic ash on the forebulge. The resulting remobilization could have caused mass flows, resulting in deposition of debrites and turbidites (Figure 10).

Sediment sources of foreland-basin strata

Potential source regions for the foreland basin fill are interpreted on the basis of clastic petrography and detrital zircon U-Pb ages of the Mesa Central

sandstones and previously published data from the Campanian-Eocene Difunta Group (Lawton *et al.* 2009). Geochronological data and sandstone petrography indicate that the component detritus of the Mesa Central sandstones came from a western source that produced approximately syndepositional zircon grains and a combination of metamorphic, sedimentary and volcanic lithic fragments. The following interpretation of source regions considers Upper Cretaceous and Paleogene volcanic and volcanosedimentary successions that were likely widespread along the western margin of Mexico during the time intervals of interest (e.g. Talavera-Mendoza *et al.* 2007; Bissig *et al.* 2008; Mortensen *et al.* 2008; Centeno-García *et al.* 2011; González-León *et al.* 2017).

Petrographic data demonstrate that Mesa Central and Difunta Group sandstones are in general compositionally similar, but some Mesa Central samples indicate a greater influence of volcanic source rocks. Both Mesa Central turbidites and Difunta Group sandstones plot along the shared boundary of the recycled orogenic and arc provenance fields of Dickinson (1985) (Figure 5(a, b)), with Difunta Group sandstones tending toward lower values of Lv/Ls (Figure 5(c)). Palaeocurrent data for both

Table 1. Calculated ages for Caracol and San Felipe Formations and undifferentiated turbidites in the Mesa Central.

Sample	Unit	Location	Age or MDA	MSWD ¹	Youngest grain (Ma)	n ²	Sample location	Reference
LF-03 ³	San Felipe	La Fábrica	73.0 ± 0.2	1.02	71 ± 1	20	ND ⁴	Velasco-Tapia et al. (2016)
LF-10 ³	San Felipe	La Fábrica	77 ± 1	1.05	69 ± 1.2	8	ND ⁴	Velasco-Tapia et al. (2016)
POB-B6 ³	San Felipe	Pedro Carrizalez	8.0 ± 0.4	1.04	81 ± 1.8	12	ND ⁴	Velasco-Tapia et al. (2016)
CL-24 ³	San Felipe	Cerro Labradores	82 ± 1	1.06	75 ± 2	17	ND ⁴	Velasco-Tapia et al. (2016)
CL-06 ³	San Felipe	Cerro Labradores	82 ± 1	1.2	62 ± 2	6	ND ⁴	Velasco-Tapia et al. (2016)
POB-B1 ³	San Felipe	Pedro Carrizalez	83.0 ± 0.4	0.92	80 ± 4	9	ND ⁴	Velasco-Tapia et al. (2016)
CL-41 ³	San Felipe	Cerro Labradores	83 ± 1	1.01	80 ± 1.8	11	ND ⁴	Velasco-Tapia et al. (2016)
48-Me16	San Felipe	Monterrey salient	75.9 ± 0.6	0.99	73 ± 2.5	8	25° 35.635'N, 100° 26.400'W	This study
04-JC01	San Felipe	Jalpan-Concá	77 ± 1	0.97	69 ± 1.6	6	21° 20.887'N, 99° 33.011'W	This study
48-AZ02	San Felipe	Agua Zarca	77.9 ± 0.5	1.04	77 ± 1.3	9	21° 14.238'N, 99° 06.931'W	This study
05-JC02	San Felipe	Jalpan-Concá	78.7 ± 0.5	1.05	72 ± 2.4	15	21° 20.887'N, 99° 33.011'W	This study
36-CL01	San Felipe	Cañón El Alamar	79.2 ± 1	1.11	77 ± 2.3	5	24° 55-806'N, 99° 53.585'W	This study
33-AC01V	Caracol	Sierra de Parras	81.5 ± 0.5	0.98	79 ± 2.5	26	25° 14.221'N, 101° 25.908'W	This study
49-SF02b	San Felipe	Monterrey salient	81.6 ± 0.6	1.02	79 ± 2.1	6	25° 35.157'N, 100° 25.537'W	This study
29-TE01	San Felipe	Tezapotla	84 ± 0.6	0.99	81 ± 1.7	14	21° 10.674'N, 98° 48.757'W	This study
07COA-CA3 ³	Caracol	Sierra de Parras	84.4 ± 0.8	1.4	81 ± 2.0	5	25° 14.115'N, 101° 26.031'W	Lawton (2012)
CARN-28	Undiff. Turbidite ⁵	Mexquitic	91 ± 3	3.4	84 ± 2.2	6	22° 22.503'N, 101° 17.158'W	This study
13-26IV14	Undiff. Turbidite ⁵	Río Grande	92 ± 1	1	86 ± 1.3	5	23° 48.061'N, 103° 01.009'W	This study
26-PST01	Undiff. Turbidite ⁵	Mexquitic	92 ± 1	0.94	91 ± 1.9	5	22° 21.828'N, 101° 16.835'W	This study
25-MB02	Undiff. Turbidite ⁵	Mexquitic	93 ± 1	0.91	89 ± 1.5	4	22° 22.109'N, 101° 17.895'W	This study

1. MSWD = Mean square of weighted deviates (Ludwig 2008).

2. n = Number of grains used in age calculation for tuff samples or MDA (maximum depositional age) calculation for sandstone samples.

MDA values are in bold text.

3. Parameters recalculated from data in indicated published reference

4. ND = Data not provided in Velasco-Tapia et al. (2016). Locations are indicated on Figure 1 of those authors.

5. Undiff. Turbidite = undifferentiated turbidite

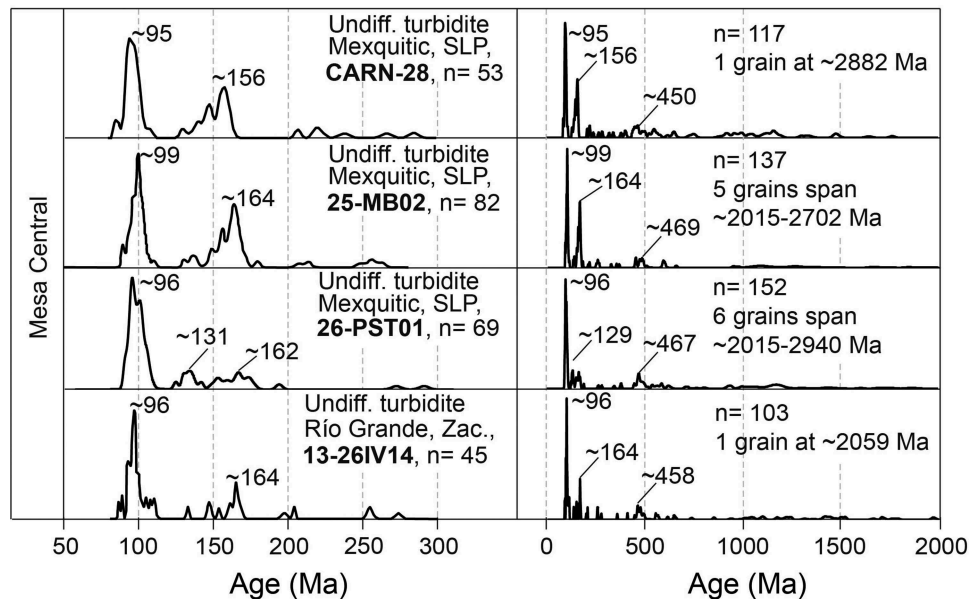


Figure 8. Probability density plots of DZ U-Pb ages in sandstones of Mesa Central. Detrital zircon age probability distribution for zircon grains younger than 300 Ma (left column), and for all grains analyzed (right column). Zircon components are shown with grey and shaded bars. Maximum depositional ages are shown in Table 1.

depositional systems indicate that the source rocks lay generally west of the basin. Thus, plausible sources for the lithic fragments in Mesa Central sandstones include basement of the Guerrero terrane, including magmatic, sedimentary and metamorphic rocks formed prior to its accretion, and a post-accretion continental-margin arc. By the time of deposition of the Difunta Group, crustal deformation had advanced eastward to what is now the front of the Sierra Madre Oriental (Fitz-Díaz *et al.* 2018) and arc magmatism had migrated eastward into Sonora (González-León *et al.* 2011), Sinaloa (Henry *et al.* 2003), and Zacatecas (Velasco-Tapia *et al.* 2016); therefore, younger volcanic rocks and exhumed older rocks of north-western and central Mexico, including the Mesa Central itself, could have provided sediment to the foreland.

Detrital zircon ages compiled from all Mesa Central samples provide insight into U-Pb age distribution in the foreland basin in early Late Cretaceous time (Figure 11). Uncommon old grains (>1 Ga) (Figure 8, 11(a)) are difficult to attribute to a specific source but may represent grains derived from Triassic metasedimentary rocks that constitute the oldest rocks of the Guerrero terrane (e.g. Centeno-García *et al.* 2011). A larger data set of correlative Triassic sedimentary rocks deposited on the west flank of continental Mexico reveals similar grain-age distributions to the Guerrero metasedimentary rocks, including Neoproterozoic, early Palaeozoic and Permian-Triassic grain ages consistent with Mexican basement sources, as well as uncommon Palaeoproterozoic and

Archean grain ages (Barboza-Gudiño *et al.* 2010; Ortega-Flores *et al.* 2014). Most pre-Jurassic zircon grains were thus likely recycled from metasedimentary rocks of Guerrero.

Plots of the combined Mesa Central analyses reveal age peaks in the Middle Jurassic and Late Cretaceous and a minor age peak in the Early Cretaceous (Figure 11 (a)). Jurassic granitoids and volcanic rocks of the Guerrero terrane probably provided the Jurassic zircon grains. Middle to Late Jurassic granitoids are locally exposed in the Cuale area (Mortensen *et al.* 2008), and Jurassic granitoids of the Guerrero terrane farther to the southeast range ~163–145 Ma (e.g. Centeno-García *et al.* 2011). Alternative sources are rhyolites of volcanic sequences in the Guerrero terrane, with ages spanning ~151 to 138 Ma (e.g. Bissig *et al.* 2008; Mortensen *et al.* 2008) and a postulated silicic large igneous province in western Mexico now largely eroded, spanning 170–165 Ma (Kimbrough 2018).

Cretaceous zircon U-Pb ages in the Mesa Central have modes at ~130 Ma and ~96 Ma, separated by a hiatus of about 15 m.y. (~125–110 Ma). We propose two principal sources for the Cretaceous grains: 1) Lower Cretaceous plutonic rocks of the Alisitos arc emplaced in the Guerrero terrane, and 2) Late Cretaceous volcanoes of the Mexican Cordilleran arc. Early Cretaceous ages reported from Guerrero include mica schist with a unimodal zircon age at ~134 Ma and the Ahuacatlán granodiorite exposed near the younger

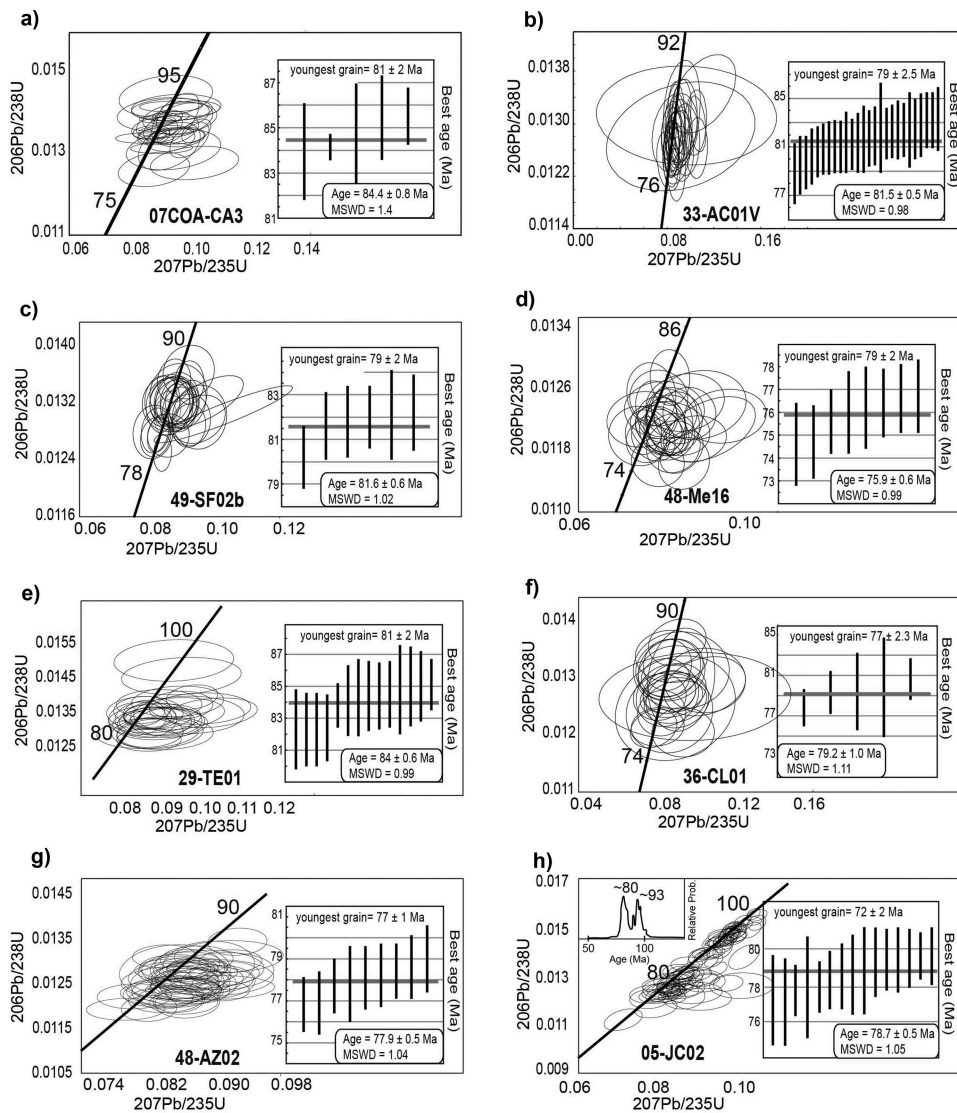


Figure 9. Tera-Wasserburg Concordia diagrams and weighted mean ages for samples of Caracol (**a** and **b**), and San Felipe formations (**c**–**h**). Calculated ages for all samples are listed in [Table 1](#). Data point errors in all samples are 2σ .

Puerto Vallarta batholith (Valencia *et al.* 2013). The group of Late Cretaceous grains with a peak at ~ 96 Ma corresponds with ages of plutons in the Baja Peninsula, especially the Eastern Peninsular Ranges batholith (Kimbrough *et al.* 2001), the Los Cabos batholith (Duque-Trujillo *et al.* 2015), and granitoids of Puerto Vallarta batholith (~ 92 Ma, Valencia *et al.* 2013).

The compiled zircon age distribution from the Maastrichtian-lower Eocene Difunta Group possesses marked differences from, and some important similarities to, the Mesa Central sandstones. Difunta sandstones have an age range of ~ 3037 to ~ 54 Ma, of which 69% (901 of 1302 analyses) are younger than 300 Ma (Figure 11(b)). Like Mesa Central samples, zircon grains of the Difunta Group were derived in part from Mesozoic arc terranes in western Mexico,

but in contrast to Mesa Central sandstones, samples of the Difunta Group include Proterozoic grains of Laurentian derivation (Figure 11(b)) (e.g. 1.7 Ga, 1.4 Ga and 1.1 Ga; e.g. Van Schmus *et al.* 1993; Gehrels *et al.* 2011). The Proterozoic age peaks are subordinate but well defined, and likely were derived directly from the basement or derivative sedimentary rocks, the nearest of which were exposed in northern Sonora, northern Chihuahua, and the southwestern U.S. (e.g. Lawton *et al.* 2009). In addition to the Guerrero basement, a potential source for moderately abundant Triassic grains lies in sedimentary units of southwestern U.S. or northern Sonora (e.g. Barth and Wooden 2006; González-León *et al.* 2009).

Abundant Jurassic and Cretaceous grains in the Difunta Group (Figure 11(b)) can also be attributed

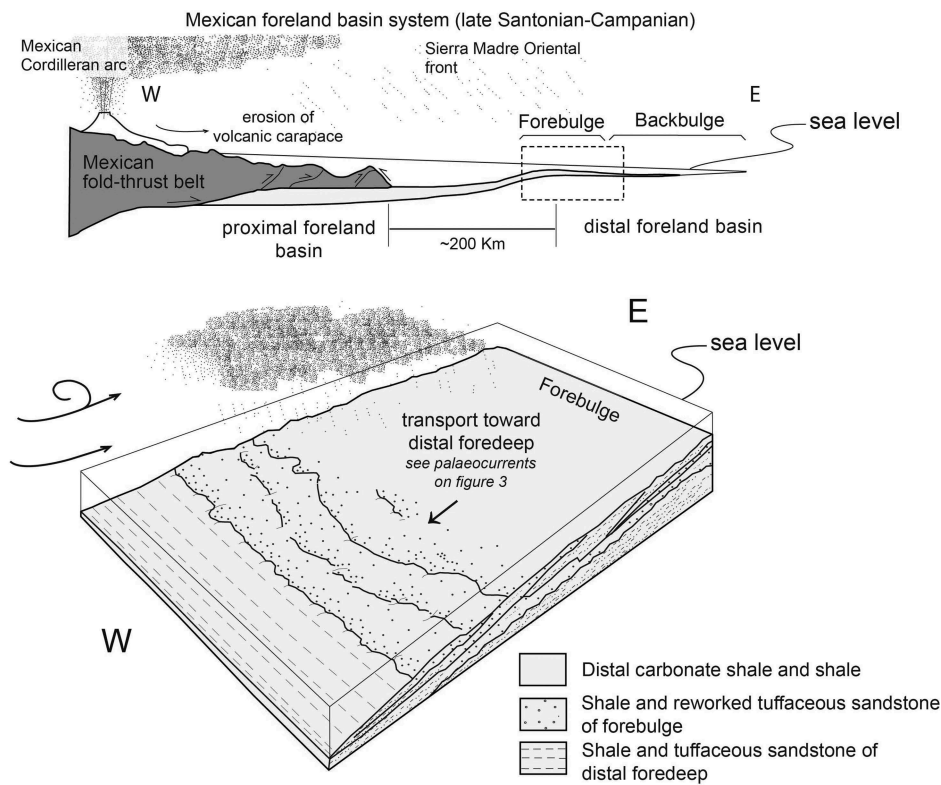


Figure 10. Depositional model for forebulge and distal foredeep deposits of MFB during late Santonian-Campanian time, adapted from foreland-basin system model of DeCelles and Giles (1996). Sediment derived from volcanic carapace was transported by fluvial systems and deposited in basin foredeep by turbidity currents. Volcanic ash from explosive eruptions was transported by westerly winds, and deposited as fall deposits in distal part of the foreland-basin system where some ash was redistributed from the proximal flank of forebulge by subaqueous sediment-gravity flows. Flow direction was toward basin foredeep, where ash was ultimately deposited, as indicated by SW-directed palaeocurrents.

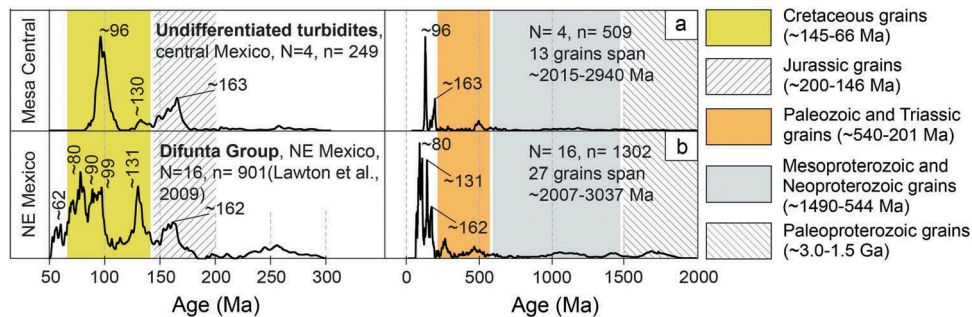


Figure 11. Probability density plots of detrital U-Pb ages of upper Cenomanian(?)–Turonian undifferentiated turbidites of the Mesa Central and sandstones of Difunta Group in northeastern Mexico.

to northwestern Mexico. Jurassic grains have several potential sources because Laramide deformation in the southwestern U.S. and advance of the Mexican orogen to the east likely exhumed pre-Cretaceous rocks in northwestern and central Mexico. Middle Jurassic grains could have been derived from volcano-sedimentary rocks of southern Arizona and California, including ignimbrites of the McCoy Mountains Formation in southern California (Fackler-Adams *et al.*

1997; Haxel *et al.* 2005; Hildebrand and Whalen 2014) or volcano-sedimentary successions such as the Rancho San Martín Formation of northern Sonora, which also contain detrital Proterozoic grain ages similar to those observed in the Difunta Group (Leggett 2009; Mauel *et al.* 2011). Late Jurassic grains could have been derived from the tuff-rich Cucurpe Formation in northern Sonora (Mauel *et al.* 2011). Alternatively, early Late Jurassic zircon grains may

have been supplied in part by rocks of the Nazas continental magmatic arc (Lawton and Molina-Garza 2014).

Thus, Cretaceous grains in the Difunta Group had similar sources to those of the Mesa Central sandstones but could have included more northern parts of the Mexican continental margin. Grains that form a prominent Early Cretaceous age peak at ~131 Ma were likely derived from the Alisitos arc, exposed in the northern part of the Baja Peninsula (Wetmore *et al.* 2002, 2003; Busby *et al.* 2006; Alsleben *et al.* 2012), and from its southern extension, the Western Peninsular Ranges batholith, known primarily from magnetic data (Langenheim and Jachens 2003). Other potential sources for Early Cretaceous zircons are located in southern California, such as plutons of the Ramona plutonic complex, with ages ranging 115–101 Ma (Todd *et al.* 2014). Other possible sources include volcanic rocks of El Encino Formation (~119–98 Ma, Böhnel *et al.* 1989) near Manzanillo, in the Jalisco block, as well as plutonic rocks near Concepción del Oro (Velasco-Tapia *et al.* 2016). Early Late Cretaceous grain ages ranging 99–90 Ma, common in Difunta Group sandstones, were likely derived from voluminous intrusions of the Eastern Peninsular Ranges batholith that crop out in southern California and the entire length of the Baja Peninsula (e.g. Walawender *et al.* 1990; Kimbrough *et al.* 2001; Langenheim and Jachens 2003; Ortega-Rivera 2003). Late Cretaceous grains could also have been contributed by recycling of older foreland-basin deposits containing those ages. A group of grain ages with a peak at ~80 Ma was likely derived by erosion of tuff-rich Santonian-Campanian strata uplifted in the thrust belt. Young grains with ages near 62 Ma, the approximate depositional age of the upper Difunta Group (Figure 11(b)), were likely derived from volcanic and plutonic rocks in northern Sonora described by González-León *et al.* (2011).

In summary, both the Mesa Central and Difunta Group sandstones had important sediment sources in the Mexican Cordilleran arc. Although it is difficult to pinpoint grain sources in an arc that paralleled the length of the foreland basin, slight differences in petrography inferred sediment dispersal, and U-Pb ages of zircon in the sediment suggest primarily sources to the west for the Mesa Central sandstones. The same region of the arc may have continued to provide grains to the Difunta Group of northeastern Mexico, but a more diverse range of lithic fragments and U-Pb detrital grain ages indicates that the Mexican part of the fold-thrust belt, including pre-Campanian foreland basin strata in central Mexico, and younger volcanic rocks in northwestern Mexico supplied sediment to the younger part of the foreland basin,

represented by the Difunta Group. This interpretation is consistent with previous hypotheses that Upper Cretaceous deposits with abundant volcanic grains were derived from a volcanic terrane to the west (e.g. Tardy and Maury 1973; Ocampo-Díaz *et al.* 2016).

A similar Santonian-Campanian set of new and published U-Pb data was assembled for tuffaceous units of the distal MFB. We combined our samples of the Caracol and San Felipe formations ($n = 339$) with seven samples ($n = 247$) by Velasco-Tapia *et al.* (2016) (Figure 12). The combined data set extends the age range of the tuffaceous units to the late Campanian (~74 Ma; Figure 12 and Table 1). This age range matches ages reported from the Sinaloa batholith (Henry *et al.* 2003), Manzanillo batholith (Panseri *et al.* 2007), and Los Cabos batholith (Duque-Trujillo *et al.* 2015), as well as intra-foreland plutons near Concepción del Oro in Zacatecas (Velasco-Tapia *et al.* 2016), located less than 100 km southwest of our Caracol sample localities in Sierra de Parras.

Magmatic events recorded in foreland strata

We propose that the Cenomanian and the late Santonian-Campanian age modes within U-Pb zircon ages in the Mexican foreland basin record two short-lived magmatic events in the continental-margin arc of Mexico. Each magmatic event is characterized by a modal age group defined by continuously distributed grain ages that overlap at 2σ error. The short-lived magmatic events can be observed in individual samples from the Mexican foreland basin; for example, both magmatic events in the arc can be observed in age peaks in sample 05-JC02 (Figure 9(h)). The Cretaceous events and a Paleogene event are also recorded in the detrital ages of the youngest deposits of the foreland basin (e.g. Difunta Group; Figure 11(b)).

The older event took place in Cenomanian-early Turonian time (~98–92 Ma) during the onset of sedimentation in the MFB. The sandstone samples that record this event contain detrital zircon grains with euhedral forms, oscillatory texture, and abundant ages of ~98–92 Ma (Cenomanian-early Turonian time, Figure 13(a)).

Tuff and sandstone of the Caracol and San Felipe formations record a second, more protracted Santonian-Campanian (~85–74 Ma) magmatic event (Figure 12). Widespread distribution of these units along the frontal part of the Sierra Madre Oriental suggests explosive magmatic activity along much of the Mexican margin during this time. The Campanian detrital zircon peak (~80 Ma; Figure 13(a)) and U-Pb ages of the Mexican Cordilleran magmatic arc (~80 Ma; Figure 13(b)) match well. Plutonic rocks approximately coeval with the second magmatic event are

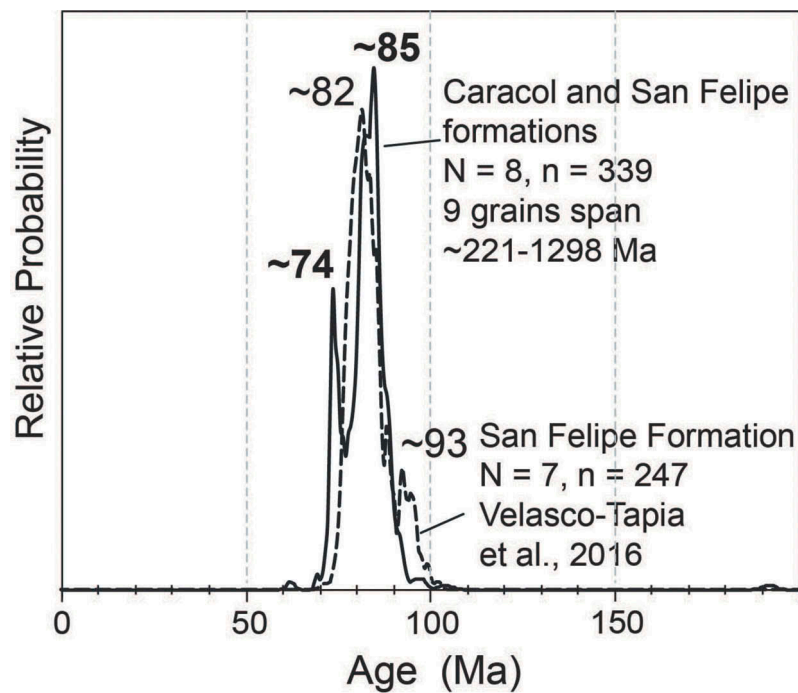


Figure 12. Probability density plots of U-Pb ages of Caracol and San Felipe formations reported in this study and by Velasco-Tapia *et al.* (2016).

quite common along the western Mexican margin (Figure 1). Small intrusive bodies and associated volcanic rocks (~90–70 Ma; McDowell *et al.* 2001; Ramos-Velázquez *et al.* 2008; González-León *et al.* 2017) are present in central Sonora. Plutons that span the Santonian-Campanian time interval are present in the Sinaloa batholith (~100–45 Ma; Henry *et al.* 2003), the Los Cabos batholith (~98–65 Ma; Aranda-Gómez and Pérez-Venzor 1989) and the Puerto Vallarta batholith (~90–80 Ma; Zimmermann *et al.* 1988; Valencia *et al.* 2013). These plutons form an almost continuous batholithic belt between Sonora and Jalisco (Figure 1) that probably represented the main sites of magmatic activity in the arc, as evidenced by their large sizes and long duration, and likely produced large eruptions necessary to generate the tuffs of the MFB.

Relative probability curves for published ages of volcanic and plutonic rocks of the southern North American Cordilleran magmatic arc and detrital zircon ages from strata of the MFB indicate a match in modal ages, especially during Cenomanian time (Figure 13(b)). The Mexican Cordilleran magmatic arc curve has a subordinate peak at ~98 Ma, and the detrital zircon curve has a principal peak at ~96 Ma (Figure 13(a)). Detrital zircon U-Pb age distribution occupy a narrow time interval of ~98–92 Ma, which we interpret as the time span of magmatic activity during early Cenomanian-Turonian time. We infer that postulated rapid

exhumation of the Peninsular Ranges batholith, which caused an important pulse of sedimentation in the early Cenomanian-late Turonian forearc basin (Kimbrough *et al.* 2001), was also recorded simultaneously in the MFB.

An early-middle Coniacian (~90–85 Ma) magmatic minimum is present in the age-probability curves of the Mexican Cordilleran magmatic arc and strata of the MFB (Figure 13(a,b)). The ~90–85 Ma age gap is also observed in the relative flux curves of the Sierra Nevada batholith and batholithic rocks of southern California (Figure 13(c)). Following this reduced magmatic activity, a younger age peak spans nearly 10 m.y., an interval that contains the peak at ~80 Ma (Figure 13(b)).

The imperfect match between the igneous and detrital data sets (Figure 13(a,b)) may result from a combination of geochronological analytical uncertainties, sampling bias in the arc domain, and mixing of sediment from multiple magmatic sources. Large magmatic systems can be difficult to interpret because they are incompletely preserved or exposed, and the ability to resolve absolute age differences decreases as the age of the magmatic system increases (de Silva *et al.* 2015). Another potential reason for a mismatch of igneous and detrital geochronological data sets results from sampling bias in the magmatic arc. Commonly, data for complete arcs are lacking because most studies are focused on segments of a particular (e.g. Cordilleran)

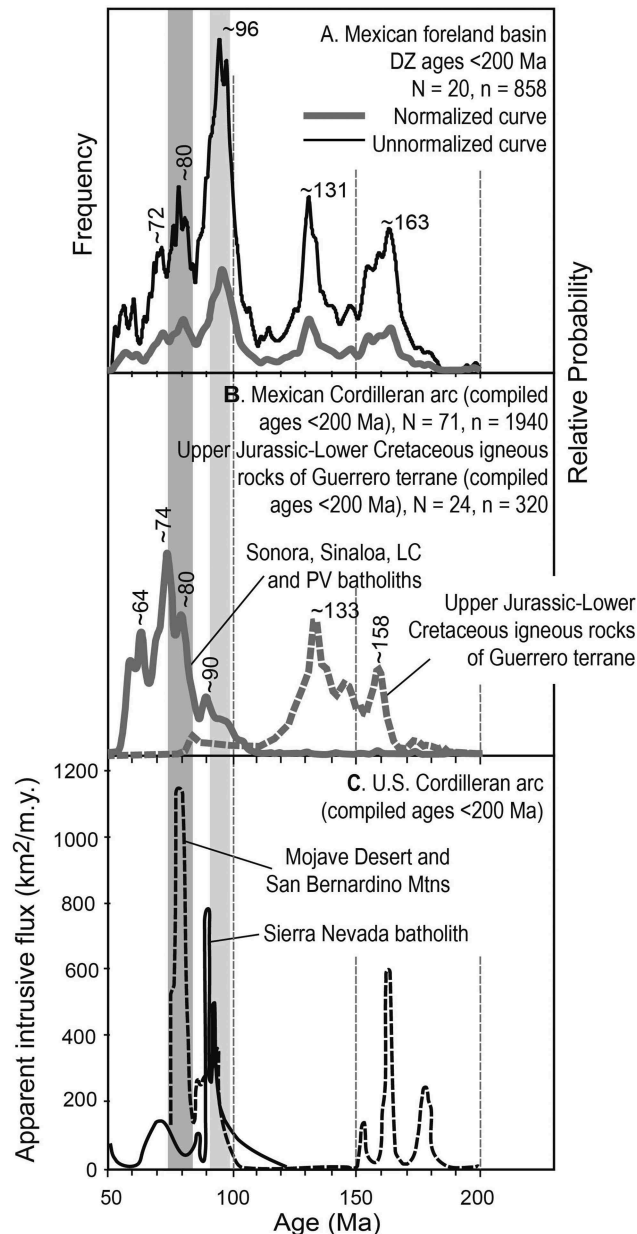


Figure 13. Comparison of age probability plots of Cordilleran batholiths of United States and Mexico with zircon relative age-probability curve of Mexican foreland basin. N = number of samples, n = number of analyses. **(a)** and **(b)** Relative probability density plots based on our zircon U-Pb dataset that include new and published data, according to criteria discussed by de Silva *et al.* (2015). **(a)** Detrital zircon ages <200 Ma from samples of MFB strata of this study and Cretaceous-Eocene samples of Parras and La Popa basins (Lawton *et al.* 2009). Y-axis frequency label refers to this part of the figure only for the unnormalised curve. **(b)** Normalized volcanic and plutonic zircon U-Pb data set <200 Ma of Mexican Cordilleran magmatic arc. LC, Los Cabos batholith; PV, Puerto Vallarta batholith. Vertical shaded grey bars are interpreted age ranges of high magmatic activity events in Mexican Cordilleran arc. Sources of age data: Sonora batholith, Ramos-Velázquez *et al.* (2008); Pérez-Segura *et al.* (2009); González-León *et al.* (2011), González-León *et al.* (2017)); Los Cabos and Sinaloa batholiths, Duque-Trujillo *et al.* (2015); Puerto Vallarta batholith, Valencia *et al.* (2013). Igneous U-Pb data set (<200 Ma) from Upper Jurassic and Lower Cretaceous of the Guerrero terrane. Data sources: Cuale volcanic sequence, Bissig *et al.* (2008); Mortensen *et al.* (2008); Valencia *et al.* (2013); Taxco-Taxco Viejo and Arcelia assemblages, Talavera-Mendoza *et al.* (2007); Tierra Colorada area, Solari *et al.* (2007). **(c)** Relative flux curves of Sierra Nevada batholith and plutonic rocks of southern California. Sources of data: Sierra Nevada batholith, DeCelles *et al.* (2009), Mojave and San Bernardino Mountains (Paterson, unpublished in Ducea *et al.* 2015). Note that main Late Cretaceous magmatic events match with interpreted age ranges of Eastern Peninsular Ranges, Los Cabos, Sinaloa and Puerto Vallarta batholiths of Mexican Cordilleran arc. Jurassic age peaks observed in southern California correspond with ages observed in detrital zircon data of MFB, but Early Cretaceous peak of MFB is not present in California data. Age compilation of part B does not include Early Cretaceous western part of Peninsular Ranges batholith.

arc (e.g. Henry *et al.* 2003; Haxel *et al.* 2005; Gehrels *et al.* 2009) or individual volcanoes or periods of time. Many plutonic and volcanic rocks in the Sonora, Los Cabos and Sinaloa batholiths have been dated recently (e.g. Duque-Trujillo *et al.* 2015; González-León *et al.* 2017), but many igneous rocks in the Mexican Cordilleran magmatic arc remain to be identified and dated. Mineral exploration in central and northern Sonora has been important in the generation of new U-Pb data because these rocks are linked to copper ore deposits (e.g. Valencia *et al.* 2006; Pérez-Segura *et al.* 2009). Sampling strategies are generally dictated by mineral exploration, accessibility of outcrops, or availability of geologic maps, none of which necessarily leads to an unbiased representation of age distributions in the continental crust (Condie and Aster 2009). On the other hand, the sedimentary record of the basin may provide a good correlation with the history of the magmatic arc, depending on whether the arc constitutes a single or merely a dominant, source (de Silva *et al.* 2015). Detrital data typically come from several sedimentary units and analyzed sedimentary successions are likely to record a mixed set of sources through time. Absence of some age components in the foreland basin fill may similarly represent sampling bias, actual absence of sediment due to barriers that prevented delivery of detritus to the basin during some time intervals, preferential loss of zircons with high U content during transport, destruction of small zircon phenocrysts in the magmatic chamber, changes in sediment-dispersal patterns, or inefficient mechanisms of sediment delivery. Thus, some of the histories of a magmatic arc may not be recorded in the basin.

Sediment-dispersal systems in proximal and distal MFB

Volcanic detritus was deposited in the foreland basin at distances between ~200–500 km from the arc during the Cenomanian-Turonian and Santonian-Campanian time intervals as indicated by distances from the principal granite exposures in Sinaloa, Baja California and Jalisco. These batholiths were likely emplaced coevally with the eruption of volcanic equivalents, as has been inferred from other segments of the Cordilleran arc further to the north (e.g. Ducea and Barton 2007).

We propose two mechanisms for sediment transport from the active magmatic arc to the Mexican foreland basin (Figure 14). A principal transport mechanism consisted of fluvial sediment delivery by east-draining transverse river systems with headwaters in the magmatic arc. Fluvial systems likely debouched into the proximal foredeep, with ultimate deposition in the foredeep of the

Mesa Central by turbidity currents. A second transport mechanism entailed the delivery of airborne pyroclastic detritus generated by explosive eruptions directly to the basin (Figure 10). Airborne transport was the principal sediment-delivery mechanism for the Santonian-Campanian tuffaceous sandstones. Voluminous tuffs are recorded in extensive areas far from their potential sources in many worldwide locations, including the western U.S. (Smith 1960; Christiansen *et al.* 1994; Jinnah *et al.* 2009), Indonesia (Matthews *et al.* 2012; Costa *et al.* 2014), and eastern Europe (Marti *et al.* 2016; Smith *et al.* 2016), where prevailing wind patterns played a fundamental role in dispersal of volcanic material. A somewhat different model of axial fluvial transport southeastward along the front of the thrust belt is required to explain sediment delivery from postulated sources in Sonora and the southwestern U.S. to deltaic and marine depositional settings of the upper Campanian-Eocene Difunta Group (Lawton *et al.* 2009). In that transport system, transverse fluvial systems draining the fold-thrust belt contributed sediment to the axial drainage and provided zircon grains eroded from uplifted Santonian-Campanian tuffaceous units. Nevertheless, the younger fluvial transport system was similar to the Cenomanian(?)–Turonian system in the inferred dominance of epiclastic, rather than pyroclastic, sediment transport.

The observed distribution of Santonian-Campanian tuffs relative to batholith locations was evaluated in the context of the atmospheric general circulation model (AGCM) for North America during the Late Cretaceous (Fricke *et al.* 2010). The Campanian simulation suggests that during winter and early springtime, dry atmospheric flow and prevailing winds were from the west (Fricke *et al.* 2010). Farther south, in northwestern Mexico, wind directions to the east were consistent throughout the year (Figure 14). Global and regional atmospheric models of Parrish and Curtis (1982) and Kump and Slingerland (1999) also indicate southeastward atmospheric flow in southwest North America during the Late Cretaceous. For this reason, we infer that pyroclastic material produced along the length of the Mexican Cordilleran magmatic arc, particularly during periods of elevated magmatic activity, could have reached distal parts of the foreland basin through transport by prevailing northwesterly winds, particularly during Santonian-Campanian time.

Conclusions

The Late Cretaceous-Paleogene Mexican foreland basin (MFB), defined herein, represents the southern continuation of the late Mesozoic Cordilleran foreland basin. Sandstone petrography, detrital-zircon U-Pb geochronology, and paleocurrent data indicate that much of the

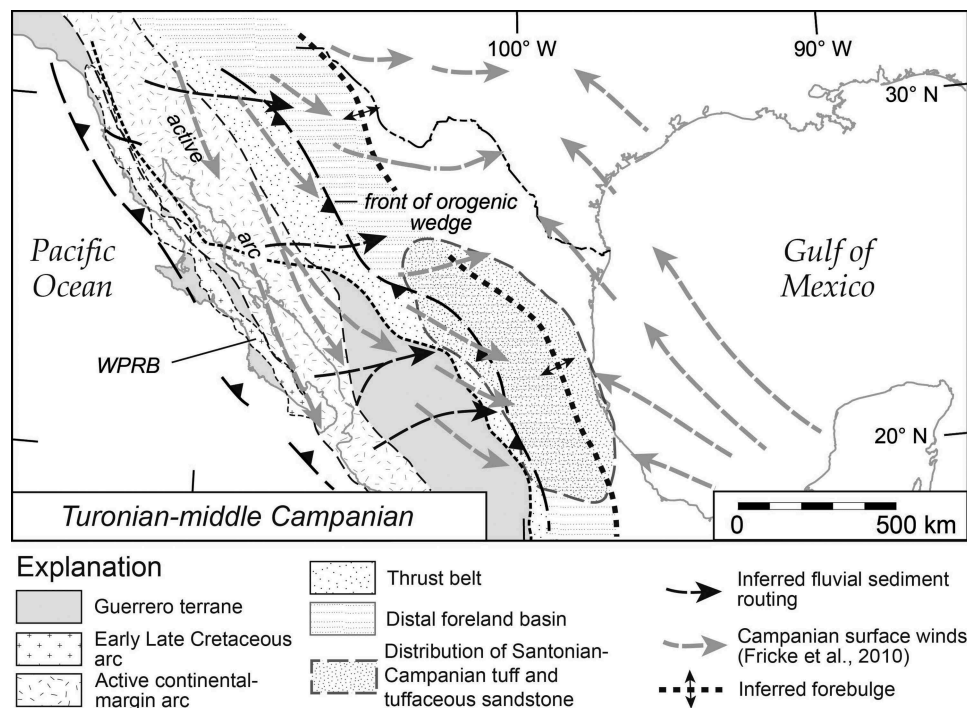


Figure 14. Inferred Late Cretaceous paleogeography of Mexican Cordilleran arc and Mexican foreland basin. Baja Peninsula is restored 475 km to SE according to the reconstruction of Fletcher *et al.* (2007). Black arrows represent fluvial sediment routing from headwaters in arc highlands, across the accreted Guerrero terrane, to foreland basin where sediment was distributed by turbidity currents. Grey arrows indicate simulated Campanian surface winds over North America (Fricke *et al.* 2010). Distribution of tuff and tuffaceous strata of the distal foreland basin based on sources discussed in the text. Volcanic material derived from eruptions along Mexican Cordilleran magmatic arc during periods of high magmatic activity reached distal part of the foreland basin, where the convergence of atmospheric circulation caused extensive accumulation of pyroclastic sediment.

sedimentary fill was derived from an active Late Cretaceous-Paleogene magmatic arc, the Mexican Cordilleran arc, along the western continental margin of Mexico. The oldest known strata of the proximal basin in the Mesa Central consist of calciturbidites that interfinger westward with Cenomanian-Turonian turbidites; abundant DZ ages of ~98–92 Ma indicate that much of the sediment was derived from a voluminous, approximately syndepositional magmatic event. Santonian-Campanian strata in the distal MFB consist of carbonate pelagites with interbedded tuffs and tuffaceous sandstones that form an arcuate outcrop belt ~700 km in length deposited in the forebulge and back-bulge depozones, respectively; detrital zircon U-Pb ages ranging ~85–74 Ma in these successions record a second prominent magmatic event in the source region.

Granites in Sinaloa, Baja California and Jalisco, with published ages within the age range of deposition of the foreland-basin strata, represent the plutonic roots of a volcanic arc, termed here the Mexican Cordilleran arc, that served as the dominant source of detritus for the foreland basin. The arc was eroded during Late Cretaceous time and derivative sediment was transported to the basin from multiple, simultaneously active sources.

Two principal sediment-transport mechanisms delivered volcanogenic sediment to the basin: (1) Transverse east-directed epiclastic sedimentary transport in Cenomanian-Turonian time delivered volcanic-lithic sand and zircon grains westward; and (2) airborne ash clouds transported zircon grains to the distal foreland basin in prevailing Late Cretaceous northwesterly winds in Santonian-Campanian time. Axial sediment transport from active arc sources, Proterozoic basement and derivative sedimentary rocks in northwestern Mexico, in addition to transverse transport from the thrust orogen itself, represents a younger, modified sediment-routing system to the Maastrichtian-Paleogene foreland of northeastern Mexico.

Acknowledgments

The authors thank CONACyT (project CB-240932) and the Coordinación de Estudios de Posgrado of the Universidad Nacional Autónoma de México for financial support to help carry out this research. Additional support was provided by UNAM-PAPIIT Grant IN105714, and Tectonic Analysis Ltd. We acknowledge Carlos Ortega-Obregón at Laboratorio de Estudios Isotópicos (LEI), Centro de Geociencias, and thanks Lisa Stockli of the Geo- and Thermochronometry Laboratory,

Jackson School of Geosciences, University of Texas at Austin for U-Pb isotopic analyses and data reduction. Thanks to Gerardo Aguirre Díaz (Centro de Geociencias) for discussion about magmatism in central Mexico. Juárez Arriaga appreciates the permission of David G. Garrido-Amaya to use information to complement the stratigraphic section at Huasteca Canyon, as well as to Uwe Martens (Source to Sink Geosystems) for discussions on the fine points of U-Pb geochronology. Thanks to Mildred Zepeda-Martínez and Rodrigo Gutiérrez-Navarro for field support. Alexander Iriondo and María Concepción Arredondo de la Rosa assisted with catholuminescence imaging of zircon grains. We thank Juan Tomás Vázquez Ramírez for preparation of the thin sections and Manuel Albarrán Murillo for assistance with mineral separation. Thanks also to Luis Manuel Casiano Casiano and Teresita de Jesús Pérez Cruz who provided much useful information. We thank Cathy Busby and Marty Grove for reviews of an early version of the manuscript and two anonymous persons for reviews of this manuscript. This paper is part of first author's doctoral thesis, supported by the Consejo Nacional de Ciencia y Tecnología (CONACyT).

Disclosure statement

No potential conflict of interest was reported by the authors.

Funding

This work was supported by the Consejo Nacional de Ciencia y Tecnología (CONACyT) [project CB-240932]; Tectonic Analysis Ltd [Pilot Project 2014]; UNAM-PAPIIT [IN105714].

References

- Alsleben, H., Wetmore, P.H., Gehrels, G.E., and Paterson, S.R., 2012, Detrital zircon ages in Palaeozoic and Mesozoic basement assemblages of the Peninsular Ranges batholith: Baja California, Mexico: Constraints for depositional ages and provenance: *International Geology Review*, v. 54, p. 93–110.
- Alzaga-Ruiz, H., Lopez, M., Roure, R., and Séranne, M., 2009, Interactions between the Laramide foreland and the passive margin of the Gulf of Mexico: Tectonics and sedimentation in the Golden Lane area, Veracruz State, Mexico: *Marine and Petroleum Geology*, v. 26, no. 6, p. 951–973. doi:10.1016/j.marpetgeo.2008.03.009
- Ángeles-Villeda, A., Hinojosa-Espinosa, J.J., López-Oliva, J.G., Valdés-González, A., and Livas-Vera, M., 2005, Estratigrafía y microfácies de la parte sur del Cañón La Boca, Santiago, Nuevo León, México: *Revista Mexicana De Ciencias Geológicas*, v. 22, p. 272–281.
- Aranda-Gómez, J.J., and Pérez-Venzor, J.A., 1989, Estratigrafía del complejo cristalino de la región de Todos Santos, estado de Baja California Sur: *Revista Del Instituto De Geología*, v. 8, p. 149–170.
- Barboza-Gudiño, J.R., Hoppe, M., Gómez-Anguiano, M., and Martínez-Macías, P.R., 2004, Aportaciones para la interpretación estratigráfica y estructural de la porción noroccidental de la Sierra de catorce, San Luis Potosí, México: *Revista Mexicana De Ciencias Geológicas*, v. 21, p. 299–319.
- Barboza-Gudiño, J.R., Zavala-Monsiváis, A., Venegas-Rodríguez, G., and Barajas-Nigoche, L.D., 2010, Late Triassic stratigraphy and facies from northeastern Mexico: Tectonic setting and provenance: *Geosphere*, v. 6, p. 621–640. doi:10.1130/GES00545.1
- Barth, A.P., and Wooden, J.L., 2006, Timing of magmatism following initial convergence at a passive margin, southwestern U.S. Cordillera, and ages of lower crustal magma sources: *The Journal of Geology*, v. 114, p. 231–245. doi:10.1086/499573
- Bissig, T., Mortensen, J.K., Tosdal, R.M., and Hall, B.V., 2008, The rhyolite-hosted volcanogenic massive sulfide district of Cuale, Guerrero terrane, west-central Mexico: Silver-rich, base metal mineralization emplaced in shallow marine continental margin setting: *Economic Geology*, v. 103, p. 141–159. doi:10.2113/gsecongeo.103.1.141
- Bitter, M.R., 1993, Sedimentation and provenance of Chicotepec sandstones with implications for uplift of the Sierra Madre Oriental and Teziutlan massif, east-central Mexico: Gulf Coast Section of Society for Sedimentary Geology, in 13th Annual Research Conference Proceedings, p. 155–172. doi:10.1002/bmc.1130070311
- Böhnell, H., Alva-Valdivia, L., González-Huesca, S., Urrutia-Fucugauchi, J., and Morán-Zenteno, D.J., 1989, Paleomagnetic data and the accretion of the Guerrero terrane, southern Mexico continental margin: Deep structure and past kinematics of accreted terranes: Washington DC, American Geophysical Union, Geophysical Monograph Series 50, 73–92 p.
- Busby, C., Adams, B.F., Mattinson, J., and Deoreo, S., 2006, View of an intact oceanic arc, from surficial to mesozonal levels: Cretaceous Alisitos arc, Baja California: *Journal of Volcanology and Geothermal Research*, v. 149, p. 1–46. doi:10.1016/j.jvolgeores.2005.06.009
- Carrillo-Bravo, J., 1961, Geología del anticlinorio Huizachal-Peregrina al NW de Ciudad Victoria Tamaulipas: *Boletín de la Asociación Mexicana de Geólogos Petroleros*, v. 13, p. 98.
- Carrillo-Bravo, J., 1971, La plataforma Valles-San Luis Potosí: *Boletín de la Asociación Mexicana de Geólogos Petroleros*, v. 23, p. 1–102.
- Centeno-García, E., Busby, C., Busby, M., and Gehrels, G., 2011, Evolution of Guerrero composite terrane along the Mexican margin, from extensional fringing arc to contractional continental arc: *Geological Society of America Bulletin*, v. 123, p. 1776–1797. doi:10.1130/B30057.1
- Centeno-García, E., Guerrero-Suastegui, M., and Talavera-Mendoza, O., 2008, The Guerrero composite terrane of western Mexico: Collision and subsequent rifting in a supra-subduction zone, in Draut, A., Clift, P.D., and Scholl, D.W., eds., Formation and applications of the sedimentary record in arc collision zones: Geological Society of America, Special Paper 436, p. 279–308.
- Christiansen, E.H., Kowallis, B.J., and Barton, M.D., 1994, Temporal and spatial distribution of volcanic ash in Mesozoic sedimentary rocks of the Western Interior: An alternative record of Mesozoic magmatism, in Caputo, M. V., Peterson, J.A., and Franczyk, K.J., eds., Mesozoic Systems of the Rocky Mountain Region: USA, Rocky Mountain Section SEPM, p. 73–94.
- Christidis, G.E., and Huff, W.F., 2009, Geological aspects and genesis of bentonites: *Elements*, v. 5, p. 93–98. doi:10.2113/gselements.5.2.93
- Cohen, K.M., Finney, S.C., Gibbard, P.L., and Fan, J.X., 2013, The ICS International Chronostratigraphic Chart: *Episodes*, v. 36, p. 199–204.

- Collinson, J., Mountney, N., and Thompson, D., 2006, *Sedimentary structures: Hertfordshire*, Terra Publishing, 261 p.
- Condie, K.C., and Aster, R.C., 2009, Zircon age episodicity and growth of continental crust: *Eos*, v. 41, p. 364–365. doi:10.1029/2009EO410003
- Costa, A., Smith, V.C., Macedonio, G., and Matthews, N.E., 2014, The magnitude and impact of the youngest Toba Tuff super-eruption: *Frontiers in Earth Science*, v. 2, p. 1–8. doi:10.3389/feart.2014.00016
- Critelli, S., and Ingersoll, R.V., 1995, Interpretation of neovolcanic versus palaeovolcanic sand grains: An example from Miocene deep-marine sandstone of the Topanga Group (Southern California): *Sedimentology*, v. 42, p. 783–804. doi:10.1111/sed.1995.42.issue-5
- de Cserna, Z., 1976, Geology of the Fresnillo area, Zacatecas, Mexico: *Geological Society of America Bulletin*, v. 87, p. 1191–1199. doi:10.1130/0016-7606(1976)87<1191:GOTFAZ>2.0.CO;2
- de Silva, S.L., Riggs, N.R., and Barth, A.P., 2015, Quickening the pulse: Fractal tempos in continental arc magmatism: *Elements*, v. 11, p. 113–118. doi:10.2113/gselements.11.2.113
- DeCelles, P.G., Ducea, M.N., Kapp, P., and Zandt, G., 2009, Cyclicity in Cordilleran orogenic systems: *Nature Geoscience*, v. 2, p. 251–257. doi:10.1038/ngeo469
- DeCelles, P.G., and Giles, K.A., 1996, Foreland basin systems: *Basin Research*, v. 8, p. 105–123. doi:10.1046/j.1365-2117.1996.01491.x
- Dickinson, W.R., 1976, Sedimentary basins developed during evolution of Mesozoic-Cenozoic arc-trench system in western North America: *Canadian Journal of Earth Sciences*, v. 13, p. 1268–1287. doi:10.1139/e76-129
- Dickinson, W.R., 1985, Interpreting provenance relations from detrital modes of sandstones, in Zuffa, G.G., ed., *Provenance of Arenites*: Boston, D. Reidel Publishing Company, p. 333–361.
- Dickinson, W.R., and Gehrels, G.E., 2009, Use of U-Pb ages of detrital zircons to infer maximum depositional ages of strata: A test against a Colorado Plateau Mesozoic database: *Earth and Planetary Science Letters*, v. 288, p. 115–125. doi:10.1016/j.epsl.2009.09.013
- Dickinson, W.R., and Lawton, T.F., 2001, Carboniferous to Cretaceous assembly and fragmentation of Mexico: *Geological Society of America Bulletin*, v. 113, p. 1142–1160. doi:10.1130/0016-7606(2001)113<1142:CTCAAF>2.0.CO;2
- Ducea, M.N., 2001, The California arc: Thick granitic batholiths, eclogitic residues, lithospheric-scale thrusting, and magmatic flare-ups: *GSA Today*, p. 4–10. doi:10.1130/1052-5173(2001)011<0004:TCATGB>2.0.CO;2
- Ducea, M.N., and Barton, M.D., 2007, Igniting flare-up events in Cordilleran arcs: *Geology*, v. 35, p. 1047–1050. doi:10.1130/G23898A.1
- Ducea, M.N., Saleeby, J.B., and Bergantz, G., 2015, The architecture, chemistry, and evolution of continental magmatic arcs: *Annual Review of Earth and Planetary Sciences*, v. 43, p. 299–331. doi:10.1146/annurev-earth-060614-105049
- Duque-Trujillo, J., Ferrari, L., Orozco-Esuivel, T., López-Martínez, M., Lonsdale, P., Bryan, S.E., Kluesner, J., Piñero-Lajas, D., and Solari, L., 2015, Timing of rifting in the southern Gulf of California and its conjugate margins: Insights from the plutonic record: *Geological Society of America Bulletin*, v. 127, p. 702–736. doi:10.1130/B31008.1
- Fackler-Adams, B.N., Busby, C.J., and Mattinson, J.M., 1997, Jurassic magmatism and sedimentation in the Palen Mountains, southeastern California: Implications for regional tectonic control on the Mesozoic continental arc: *Geological Society of America Bulletin*, v. 109, p. 1464–1484. doi:10.1130/0016-7606(1997)109<1464:JMASIT>2.3.CO;2
- Fitz-Díaz, E., Lawton, T.F., Juárez-Arriaga, E., and Chávez-Cabello, G., 2018, Late Cretaceous-Paleogene Mexican orogen: Structure, basin development, and tectonics: *Earth-Science Reviews*, v. 183, p. 56–84. doi:10.1016/j.earscirev.2017.1003.1002
- Fletcher, J.M., Grove, M., Kimbrough, D., Lovera, O., and Gehrels, G.E., 2007, Ridge-trench interactions and the Neogene tectonic evolution of the Magdalena shelf and southern Gulf of California: Insights from detrital zircon U-Pb ages from the Magdalena fan and adjacent areas: *Geological Society of America Bulletin*, v. 119, p. 1313–1336. doi:10.1130/B26067.1
- Folk, R.L., 1974, *Petrology of sedimentary rocks*: Austin, Texas, Hemphill Publishing Company, 182 p.
- Fricke, H.C., Foreman, B.Z., and Sewall, J.O., 2010, Integrated climate model-oxygen isotope evidence for a North American monsoon during the Late Cretaceous: *Earth and Planetary Science Letters*, v. 289, p. 11–21. doi:10.1016/j.epsl.2009.10.018
- Gamper, M.A., 1977, Estratigrafía y microfácies cretácicas del Anticlinorio Huizachal-Peregrina (Sierra Madre Oriental): *Boletín de la Sociedad Geológica Mexicana*, v. 38, p. 1–17. doi:10.18268/BSGM1977v38n2a1
- Gehrels, G., Rusmore, M., Woodsworth, G., Crawford, M., Andronicos, C., Hollister, L., Patchett, J., Ducea, M., Butler, R., Klepeis, K., Davidson, C., Friedman, R., Haggart, J., Mahoney, B., Crawford, W., Pearson, D., and Girardi, J., 2009, U-Th-Pb geochronology of the Coast Mountains batholith in north-coastal British Columbia: Constraints on age and tectonic evolution: *Geological Society of America Bulletin*, v. 121, p. 1341–1361. doi:10.1130/B26404.1
- Gehrels, G.E., Blakey, R., Karlstrom, K.E., Timmons, J.M., Dickinson, B., and Pecha, M., 2011, Detrital zircon U-Pb geochronology of Paleozoic strata in the Grand Canyon: *Arizona: Lithosphere*, v. 3, p. 183–200.
- Gehrels, G.E., Valencia, V.A., and Ruiz, J., 2008, Enhanced precision, accuracy, efficiency, and spatial resolution of U-Pb ages by laser ablation-multicollector-inductively coupled plasma-mass spectrometry: *Geochemistry, Geophysics, Geosystems*, v. 9, p. 13. doi:10.1029/2007GC001805
- González-León, C.M., Solari, L., Solé, J., Ducea, M.N., Lawton, T. F., Bernal, J.P., González Becuar, E., Gray, F., López Martínez, M., and Lozano Santacruz, R., 2011, Stratigraphy, geochronology, and geochemistry of the Laramide magmatic arc in north-central Sonora, Mexico: *Geosphere*, v. 7, p. 1392–1418. doi:10.1130/GES00679.1
- González-León, C.M., Solari, L., Valencia-Moreno, M., Rascon Heimpel, M.A., Solé, J., González Becuar, E., Lozano Santacruz, R., and Pérez Arvizo, O., 2017, Late Cretaceous to early eocene magmatic evolution of the Laramide arc in the Nacozari quadrangle, northeastern Sonora, Mexico and

- its regional implications: *Ore Geology Reviews*, v. 81, p. 1137–1157. doi:10.1016/j.oregeorev.2016.07.020
- González-León, C.M., Valencia, V.A., Lawton, T.F., Amato, J.M., Gehrels, G.E., Leggett, W.J., Montijo-Contreras, O., and Fernández, M.A., 2009, The lower Mesozoic record of detrital zircon U-Pb geochronology of Sonora, México, and its paleogeographic implications: *Revista Mexicana De Ciencias Geológicas*, v. 26, p. 301–314.
- Hart, N.R., Stockli, D.F., and Hayman, N.W., 2016, Provenance evolution during progressive rifting and hyperextension using bedrock and detrital zircon U-Pb geochronology, Mauléon basin, western Pyrenees: *Geosphere*, v. 12, p. 1–21. doi:10.1130/GES01273.1
- Haxel, G.B., Wright, J.E., Riggs, N.R., Tosdal, R.M., and May, D.J., 2005, Middle Jurassic Topawa Group, Baboquivari Mountains, south-central Arizona: Volcanic and sedimentary record of deep basins within the Jurassic magmatic arc, in Anderson, T.H., Nourse, J.A., McKee, J.W., and Steiner, M.B., eds., *The Mojave-Sonora megashear hypothesis: Development, assessment, and alternatives*: Geological Society of America, Special Paper 393, p. 329–357.
- Henry, C.D., McDowell, F.W., and Silver, L.T., 2003, Geology and geochronology of granitic batholithic complex, Sinaloa, México: Implications for Cordilleran magmatism and tectonics, in Johnson, S.E., Paterson, S.R., Fletcher, J. M., Girty, G.H., Kimbrough, D.L., and Martín-Barajas, A., eds., *Tectonic evolution of northwestern México and the southwestern USA*: Geological Society of America, Special Paper 374, p. 37.
- Hildebrand, R.S., and Whalen, J.B., 2014, Arc and slab-failure magmatism in Cordilleran batholiths II – The Cretaceous Peninsular ranges batholith of southern and Baja California: *Geoscience Canada*, v. 41, p. 399–458. doi:10.12789/geocanj.2014.41.059
- Imlay, R.W., 1937, *Geology of the middle part of the Sierra de Parras, Coahuila, Mexico*: Geological Society of America Bulletin, v. 48, p. 587–630. doi:10.1130/GSAB-48-587
- Ingersoll, R.V., 2012, Tectonics of sedimentary basins, with revised nomenclature, in Busby, C., and Azor-Pérez, A., eds., *Tectonics of Sedimentary Basins: Recent Advances*: Oxford, United Kingdom, Blackwell Publishing, p. 3–43.
- Ingersoll, R.V., Bullard, T.F., Ford, R.L., Grimm, J.P., Pickle, J.D., and Sares, S.W., 1984, The effect of grain size on detrital modes: A test of the Gazzi-Dickinson point-counting method: *Journal of Sedimentary Petrology*, v. 54, p. 103–116.
- Ingersoll, R.V., Cavazza, W., Graham, S.A., and Participants, I.U. G.F.S., 1987, Provenance of impure calcilithites in the Laramide foreland of southwestern Montana: *Journal of Sedimentary Petrology*, v. 57, p. 995–1003.
- Ingersoll, R.V., and Sucek, C.A., 1979, Petrology and provenance of Neogene sand from Nicobar and Bengal fans, DSDP sites 211 and 218: *Journal of Sedimentary Petrology*, v. 49, p. 1217–1228.
- Jinnah, Z.A., Roberts, E.M., Deino, A.L., Larsen, J.S., Link, P.K., and Fanning, C.M., 2009, New ⁴⁰Ar-³⁹Ar detrital zircon U-Pb ages for the upper Cretaceous Wahweap and Kaiparowits formations on the Kaiparowits Plateau, Utah: Implications for regional correlation, provenance, and biostratigraphy: *Cretaceous Research*, v. 30, p. 287–299. doi:10.1016/j.cretres.2008.07.012
- Kimbrough, D.L., 2018, The Jurassic arc silicic large igneous province (SLIP) of southwestern North America: Geological Society of America Abstracts with Programs, v. 50, no. 5. doi:10.1130/abs/2018RM-314203
- Kimbrough, D.L., Smith, D.P., Mahoney, J.B., Moore, T.E., Gastil, R. G., Ortega-Rivera, M.A., and Fanning, C.M., 2001, Forearc basin sedimentary response to rapid late Cretaceous batholith emplacement in the Peninsular Ranges of southern and Baja California: *Geology*, v. 29, p. 491–494. doi:10.1130/0091-7613-(2001)029<0491:FBSRTR>2.0.CO;2
- Kump, L.R., and Slingerland, R.L., 1999, Circulation and stratification of the early Turonian Western Interior Seaway: Sensitivity to a variety of forcings: Geological Society of America Special Paper 332, 10 p.
- Langenheim, V.E., and Jachens, R.C., 2003, Crustal structure of the Peninsular Ranges batholith from magnetic data: Implications for Gulf of California rifting: *Geophys Research Letters*, v. 30, no. 1597. doi:10.1029/2003GL017159
- Laskowski, A.K., DeCelles, P.G., and Gehrels, G.E., 2013, Detrital zircon geochronology of Cordilleran retroarc foreland basin strata: western North America: *Tectonics*, v. 32, p. 1–22.
- Lawton, T.F., 2012, Age of the Caracol Formation: Sierra de Parras, Coahuila, Mexico: Cordilleran Section, Geological Society of America Abstracts with Programs, v. 44, no. 3, p. 76.
- Lawton, T.F., Bradford, I.A., Vega, F.J., Gehrels, G.E., and Amato, J.M., 2009, Provenance of upper Cretaceous–Paleogene sandstones in the foreland basin system of the Sierra Madre Oriental: Northeastern Mexico, and its bearing on fluvial dispersal systems of the Mexican Laramide Province: *Geological Society of America Bulletin*, v. 121, p. 820–836.
- Lawton, T.F., Juárez-Arriaga, E., Ocampo-Díaz, Y.Z.E., Beltrán-Triviño, A., Martens, U., and Stockli, D., 2016, Evolution of late Cretaceous–Paleogene foreland sediment-dispersal systems of Northern and Central Mexico, in 35th Annual GCSSEPM, Houston, Texas, Foundation Perkins-Rosen Research Conference Programs and Abstracts, p. 216–233.
- Lawton, T.F., and Molina-Garza, R.S., 2014, U-Pb geochronology of the type Nazas Formation and superjacent strata: Northeastern Durango, Mexico: Implications of a Jurassic age for continental-arc magmatism in north-central Mexico: *Geological Society of America Bulletin*, v. 126, p. 1181–1199.
- Leggett, W.J., 2009, Stratigraphy, sedimentology and geochronology of lower and middle Jurassic rocks near Rancho San Martín del Rincon, north-central Sonora, Mexico [M. S. thesis]: New Mexico State University, 203 p.
- Longoria, J.F., Clowes, D.M., and Monreal, R., 1999, Type Mesozoic succession of northern Mexico: Cañon La Casita: Mesozoic sedimentary and tectonic history of north-central Mexico: Geological Society of America Bulletin Special Paper 340, 32 p.
- López-Ramos, E., 1980, *Geología de México, T II: Tesis Resendiz, México*, 454 p.
- Ludwig, K.R., 2008, ISOPLOT vers. 4.15: Berkeley Geochronology Center (BGC): http://www.bgc.org/isoplot_etc/isoplot.html (accessed February 2017).
- Marti, A., Folch, A., Costa, A., and Engwell, S., 2016, Reconstructing the plinian and co-ignimbrite sources of large volcanic eruptions: A novel approach for the Campanian Ignimbrite: *Scientific Reports*, v. 6, no. 21220, p. 1–11. doi:10.1038/s41598-016-0001-8

- Martínez-Paco, M., 2012, Análisis petrográfico, geoquímico y geocronológico U-Pb de cenizas volcánicas alteradas de la Formación San Felipe (Cretácico Superior), en el Cerro de Labradores, Galeana, N.L., Sierra Madre Oriental [M. S. thesis]: Universidad Autónoma de Nuevo León, 96 p. doi:10.1094/PDIS-11-11-0999-PDN
- Martini, M., Fitz, E., Solari, L., Camprubi, A., Hudleston, P.J., Lawton, T.F., Tolson, G., and Centeno-García, E., 2012, The Late Cretaceous fold-thrust belt in the Peña de Bernal-Tamazunchale area and its possible relationship to the accretion of the Guerrero Terrane, in Aranda-Gómez, A., Tolson, G., and Molina-Garza, R.S., eds., *The southern cordillera and beyond: Geological Society of America Field Guide 25*, p. 19–38.
- Martini, M., Mori, L., Solari, L., and Centeno-García, E., 2011, Sandstone provenance of the Arperos Basin (Sierra de Guanajuato: Central Mexico): Late Jurassic–Early Cretaceous back-arc spreading as the foundation of the Guerrero terrane: *The Journal of Geology*, v. 119, p. 597–617.
- Martini, M., Solari, L., and Camprubi, A., 2013, Kinematics of the Guerrero terrane accretion in the Sierra de Guanajuato: Central Mexico: New insights for the structural evolution of arc-continent collisional zones: *International Geology Review*, v. 55, p. 574–589.
- Martini, M., Solari, L., and López-Martínez, M., 2014, Correlating the Arperos basin from Guanajuato: Central Mexico, to Santo Tomás, southern Mexico: Implications for the paleogeography and origin of the Guerrero terrane: *Geosphere*, v. 10, p. 1385–1401.
- Matthews, N.E., Smith, V.C., Costa, A., Durant, A.J., Pyle, D.M., and Pearce, N.J.G., 2012, Ultra-distal tephra deposits from super-eruptions: Examples from Toba: Indonesia and Taupo Volcanic zone, New Zealand: *Quaternary International*, v. 258, p. 54–79.
- Mauel, D.J., Lawton, T.F., González-León, C., Iriondo, A., and Amato, J.M., 2011, Stratigraphy and age of Upper Jurassic strata in north-central Sonora: Mexico: Southwestern Laurentian record of crustal extension and tectonic transition: *Geosphere*, v. 7, p. 390–414.
- McBride, E.F., Weidie, A.E., Wolleben, J.A., and Laudon, R.C., 1974, Stratigraphy and structure of the Parras and La Popa basins: Northeastern Mexico: *Geological Society of America Bulletin*, v. 84, p. 1603–1622.
- McDowell, F.W., and Clabaugh, S.E., 1979, Ignimbrites of the Sierra Madre Occidental and their relation to the tectonic history of western Mexico: Ash-flow tuffs: *Geological Society of America Special Paper 180*, 12 p.
- McDowell, F.W., Roldán-Quintana, J., and Connelly, J.N., 2001, Duration of late Cretaceous-early tertiary magmatism in east-central Sonora: Mexico: *Geological Society of America Bulletin*, v. 113, p. 521–531.
- Mortensen, J.K., Hall, B.V., Bissig, T., Friedman, R.M., Danielson, T., Oliver, J., Rhys, D.A., Ross, K.V., and Gabites, J.E., 2008, Age and paleotectonic setting of volcanogenic sulfide deposits in the Guerrero terrane of central Mexico: Constraints from U-Pb age and Pb isotope studies: *Economic Geology*, v. 103, p. 117–140. doi:10.2113/gsecongeo.103.1.117
- Mutti, E., and Normark, W.R., 1991, An integrated approach to the study of turbidite systems, in Weimer, P., and Link, M.H., eds., *Seismic facies and sedimentary processes of submarine fans and turbidite systems: New York*, Springer-Verlag, Inc., p. 75–105.
- Ocampo-Díaz, Y.Z.E., Pinzón-Sotelo, M.P., Chávez-Cabello, G., Ramírez-Díaz, A., Martínez-Paco, M., Velasco-Tapia, F., Guerrero-Suastegui, M., and Barboza-Gudiño, J.R., 2016, Propuesta nomenclatural y análisis de procedencia de la Formación Concepción del Oro (antes Formación Caracol): Implicaciones sobre la evolución tectónica del sur de Norteamérica durante el Cretácico Tardío: *Revista Mexicana De Ciencias Geológicas*, v. 33, p. 3–33.
- Ortega-Flores, B., Solari, L., Lawton, T.F., and Ortega-Obregón, C., 2014, Detrital-zircon record of major middle Triassic-early Cretaceous provenance shift: Central Mexico: Demise of Gondwanan continental fluvial systems and onset of back-arc volcanism and sedimentation: *International Geology Review*, v. 56, p. 237–261.
- Ortega-Gutiérrez, F., Elías-Herrera, M., Morán-Zenteno, D.J., Solari, L., Luna-González, L., and Schaaf, P., 2014, A review of batholiths and other plutonic intrusions of Mexico: *Gondwana Research*, v. 26, p. 834–868. doi:10.1016/j.gr.2014.05.002
- Ortega-Rivera, A., 2003, Geochronological constraints on the tectonic history of the Peninsular Ranges batholith of Alta and Baja California: Tectonic implications for western México: Tectonic evolution of northwestern Mexico and the southwestern USA: Boulder: Colorado, Geological Society of America Special Paper, v. 374, p. 297–335.
- Panseri, M., Tunesi, A., Corona-Chávez, P., and Bergomi, M., 2007, Evolution of Manzanillo batholith complex: Structural data, thermobarometry and geochronology, in *Goldschmidt Conference Abstracts*, p. A751. doi:10.1094/PDIS-91-4-0467B
- Parrish, J.T., and Curtis, R.L., 1982, Atmospheric circulation: upwelling, and organic-rich rocks in the Mesozoic and Cenozoic eras: *Palaeogeography, Palaeoclimatology, Palaeoecology*, v. 40, p. 31–66.
- Pemberton, S.G., MacEachern, J.A., and Frey, R.W., 1992, Trace fossil facies models: Environmental and allostratigraphic significance, in Walker, R.G., and James, N.P., eds., *Facies models—Response to sea level change: Geological Association of Canada*, p. 47–72.
- PEMEX, Petróleos Mexicanos, 1988, *Estratigrafía de la República Mexicana: Mesozoico: Subdirección de Producción Primaria, Coordinación Ejecutiva de Exploración*, Report, 229 p. doi:10.3168/jds.S0022-0302(88)79586-7
- Pérez-Segura, E., González-Partida, E., and Valencia, V.A., 2009, Late Cretaceous adakitic magmatism in east-central Sonora: Mexico, and its relation to Cu-Zn-Ni-Co skarns: *Revista Mexicana De Ciencias Geológicas*, v. 26, p. 411–427.
- Posamentier, H.W., and Walker, R.G., 2006, Deep-water turbidites and submarine fans, in Posamentier, H.W., and Walker, R.G., eds., *Facies models revisited: Tulsa: Society for Sedimentary Geology Special Publication 84*, p. 397–520.
- Ramos-Velázquez, E., Calmus, T., Valencia, V., Iriondo, A., Valencia-Moreno, M., and Bellon, H., 2008, U-Pb and ⁴⁰Ar/³⁹Ar geochronology of the coastal Sonora batholith: New insights on Laramide continental arc magmatism: *Revista Mexicana De Ciencias Geológicas*, v. 25, p. 314–333.

- Santamaría-Orozco, D., Arenas Partida, R., and Escamilla Herrera, A., 1990, Normalización de la nomenclatura estratigráfica en las cuencas mesozoicas de México (Etapa I: Zona Norte: Cretácico): Instituto Mexicano del Petróleo, Subdirección de Tecnología de Exploración, Proyecto, v. CAO-3052, p. 140.
- Sigloch, K., and Mihalyuk, M.G., 2013, Intra-oceanic subduction shaped the assembly of Cordilleran North America: *Nature*, v. 496, p. 50–56. doi:10.1038/nature12019
- Sinclair, H.D., 1997, Flysch to molasse transition in peripheral foreland basins: The role of the passive margin versus slab breakoff: *Geology*, v. 25, p. 1123–1126. doi:10.1130/0091-7613(1997)025<1123:FTMTIP>2.3.CO;2
- Smith, R.L., 1960, Ash flows: *Geological Society of America Bulletin*, v. 71, p. 795–842. doi:10.1130/0016-7606(1960)71[795:AF]2.0.CO;2
- Smith, V.C., Isaia, R., Engwell, S.L., and Albert, P.G., 2016, Tephra dispersal during the Campanian Ignimbrite (Italy) eruption: Implications for ultra-distal ash transport during the large caldera-forming eruptio: *Bulletin of Volcanology*, v. 78, p. 1–15. doi:10.1007/s00445-016-1037-0
- Soegaard, K., Ye, H., Halik, N., Daniels, A.T., Arney, J., and Garrick, S., 2003, Stratigraphic evolution of Latest Cretaceous to early Tertiary Difunta foreland basin in north-east Mexico: Influence of salt withdrawal on tectonically induced subsidence by the Sierra Madre Oriental fold and thrust belt, in Bartolini, C., Buffler, R.T., and Blickwede, J., eds., *The Circum-Gulf of Mexico and the Caribbean: Hydrocarbon habitats, basin formation, and plate tectonics*, volume Vol. 79: Tulsa, Oklahoma, American Association of Petroleum Geologists, Memoir, p. 364–394.
- Sohl, N.P., Martínez, E., Salmerón-Urena, P., and Soto-Jaramillo, F., 1991, Upper Cretaceous, in Salvador, A., ed., *The Gulf of Mexico Basin: Boulder, Colorado, Geological Society of America, Geology of North America*, v. J, p. 205–244.
- Solari, L.A., González-León, C.M., Ortega-Obregón, C., Valencia-Moreno, M., and Rascón-Heimpel, M.A., 2018, The Proterozoic of NW Mexico revisited: U-Pb geochronology and Hf isotopes of Sonoran rocks and their tectonic implications: *International Journal of Earth Sciences*, v. 107, p. 845–861. doi:10.1093/ajcn/nqy030
- Solari, L.A., Torres de León, R., Hernández-Pineda, G., Solé, J., and Solís-Pichardo, G., 2007, Tectonic significance of Cretaceous-Tertiary magmatic and structural evolution of the northern margin of the Xolapa Complex, Tierra Colorada area, southern Mexico: *Geological Society of America Bulletin*, v. 119, p. 1265–1279. doi:10.1130/B26023.1
- Talavera-Mendoza, O., Ruiz, J., Gehrels, G.E., Valencia, V.A., and Centeno-García, E., 2007, Detrital zircon U-Pb geochronology of southern Guerrero and western Mixteca arc successions (southern Mexico): New insights for the tectonic evolution of southwestern North America during the late Mesozoic: *Geological Society of America Bulletin*, v. 119, p. 1052–1065. doi:10.1130/B26016.1
- Tardy, M., Lapierre, H., Freyrier, C., Coulon, C., Gill, J.-B., Mercier de Lepinay, B., Beck, C., Martinez, R.J., Talavera, M. O., Ortiz, H.E., Stein, E., Bourdier, J.L., and Yta, M., 1994, The Guerrero suspect terrain (the Greater Antilles and the Western Cordillera of Colombia): A late Mesozoic intra-oceanic arc accreted to cratonal America during the Cretaceous: *Tectonophysics*, v. 230, p. 49–73. doi:10.1016/0040-1951(94)90146-5
- Tardy, M., and Maury, R., 1973, Sobre la presencia de elementos de origen volcánico en las areniscas de los flyschs de edad cretácica superior de los estados de Coahuila y de Zacatecas: México: *Boletín de la Sociedad Geológica Mexicana*, v. 34, p. 5–12.
- Todd, V.R., Hernandez, J.L., and Busch, L.L., 2014, The zoned Ramona plutonic complex: An Early Cretaceous mid- to upper-crustal intrusive sequence, Peninsular Ranges batholith, southern California, in Morton, D.M., and Miller, F.K., eds., *Peninsular Ranges Batholith, Baja California and Southern California*, volume Vol. 211: Boulder, Colorado, Geological Society of America Memoir, p. 583–608.
- Valencia, V.A., Noguez-Alcántara, B., Barra, F., Ruiz, J., Gehrels, G., Quintanar, F., and Valencia-Moreno, M., 2006, Re-Os molybdenite and LA-ICPMS-MC U-Pb zircon geochronology for the Milpillas porphyry copper deposit: Insights for the timing of mineralization in the Cananea District: Sonora, Mexico: *Revista Mexicana De Ciencias Geológicas*, v. 23, p. 39–53.
- Valencia, V.A., Righter, K., Rosas-Elguera, J., López Martínez, M., and Grove, M., 2013, The age and composition of the pre-Cenozoic basement of the Jalisco Block: Implications for and relation to the Guerrero composite terrane: *Contributions to Mineralogy and Petrology*, v. 166, p. 801–824. doi:10.1007/s00410-00013-00908-z
- Van Schmus, W.R., 24 others, 1993, Transcontinental Proterozoic provinces, in Reed, J.C., Jr., Bickford, M.E., Houston, R.S., Link, P.K., Rankin, D.W., Sims, P.W., and Van Schmus, W.R., eds., *Precambrian Conterminous U.S.: Boulder, Colorado, Geological Society of America, Geology of North America*, v. C-2, p. 171–334.
- Velasco-Tapia, F., Martínez-Paco, M., Iriondo, A., Ocampo-Díaz, Y.Z.E., Cruz-Gámez, E.M., Ramos-Ledezma, A., Andaverde, J.A., Ostrooumov, M., and Masuch, D., 2016, Altered volcanic ash layers of the Late Cretaceous San Felipe Formation: Sierra Madre Oriental (northeastern Mexico): U-Pb geochronology, provenance and tectonic setting: *Journal of South American Earth Sciences*, v. 70, p. 18–35.
- Walawender, M.J., Gastil, R.G., Clinkenbeard, J.P., McCormick, W.V., Eastman, B.G., Wernicke, R.S., Wardlaw, M.S., Gunn, S.H., and Smith, B.M., 1990, Origin and evolution of the zoned La Posta-Type plutons, eastern Peninsular Ranges batholith, southern and Baja California, in Anderson, J.L., ed., *The nature and origin of Cordilleran magmatism*, volume Vol. 174: Boulder, Colorado, Geological Society of America Memoir, p. 1–18.
- Wetmore, P.H., Herzig, C., Aisleben, H., Sutherland, M., Schmidt, K.L., Schultz, P.W., and Paterson, S.R., 2003, Mesozoic tectonic evolution of the Peninsular Ranges of southern and Baja California, in Johnson, S.E., Paterson, S.R., Fletcher, J.M., Girty, G.H., Kimbrough, D.L., and Martin-Barajas, A., eds., *Tectonic evolution of northwestern Mexico and the southwestern USA: Geological Society of America Special Paper 374*, p. 93–116.
- Wetmore, P.H., Schmidt, K.L., Paterson, S.R., and Herzig, C., 2002, Tectonic implications for the along-strike variation of the Peninsular Ranges batholith: Southern and Baja California: *Geology*, v. 30, p. 247–250.

Wilson, J.L., and Ward, W.C., 1993, Early Cretaceous carbonate platforms of northeastern and east-central Mexico, *in* Simo, J.A., Scott, R.W., and Masse, J.P., eds., Cretaceous carbonate platforms: American Association of Petroleum Geologists Memoir 56, p. 35–49.

Zimmermann, J.L., Stussi, J.M., González-Partida, E., and Arnold, M., 1988, K-Ar evidence for age and compositional zoning in the Puerto Vallarta-Río Santiago batholith (Jalisco: Mexico): *Journal of South American Earth Sciences*, v. 1, p. 267–274.

III.III Evolución de la cuenca de antepaís mexicana en el centro de México: exhumación y erosión a lo largo del transecto Tolimán-Tamazunchale.

Juárez-Arriaga, E., Lawton, T.F., Stockli, D.F., Solari, L., Martens, U., 2019b. *Late Cretaceous-Paleocene stratigraphic and structural evolution of the central Mexican fold and thrust belt, from detrital zircon (U-Th)/(He-Pb) ages*: Journal of South American Earth Sciences. <https://doi.org/10.1016/j.jsames.2019.102264>



Late Cretaceous-Paleocene stratigraphic and structural evolution of the central Mexican fold and thrust belt, from detrital zircon (U-Th)/(He-Pb) ages



Edgar Juárez-Arriaga^{a,*}, Timothy F. Lawton^{b,1}, Daniel F. Stockli^c, Luigi Solari^b, Uwe Martens^{b,d}

^a Posgrado en Ciencias de la Tierra, Centro de Geociencias, Universidad Nacional Autónoma de México, Querétaro 76001, Mexico

^b Centro de Geociencias, Universidad Nacional Autónoma de México, Querétaro 76001, Mexico

^c Department of Geological Sciences, Jackson School of Geosciences, The University of Texas at Austin, TX 78712-0254, USA

^d Tectonic Analysis Ltd, Chestnut House Burton Park, Duncton West Sussex, GU28 0LH, England, UK

ARTICLE INFO

Keywords:

Foreland basin evolution
Central Mexican fold-thrust belt
Mexican foreland basin
Detrital zircon geochronology
Provenance
Detrital zircon thermochronology

ABSTRACT

Combined U-Pb and (U-Th)/He ages on a small sample set of Cretaceous foreland-basin sandstone from a transect of the fold-thrust belt in east-central Mexico reveal correspondence between episodes of thrust-belt exhumation with previously postulated deformational events and with at least one wedge of synorogenic sediment in the adjacent Tampico-Misantla basin. Detrital zircon U-Pb ages, sandstone petrography and multi-dimensional scaling analysis of the Cenomanian-Turonian Mineral de Pozos sandstone, the Coniacian Soyatal and Campanian San Felipe formations, and the Paleocene Chicontepec Formation indicate sediment sources in the Mexican Cordilleran magmatic arc of western Mexico, the accreted Guerrero arc terrane, and Mesozoic sedimentary rocks of central and western Mexico. (U-Th)/He cooling ages define into three age clusters: (1) ~136–120 Ma, (2) ~99–80 Ma, and (3) ~66–56 Ma. Cooling ages are younger toward the transect's western part, which represents the interior part of the fold-thrust belt. Dominant Early Cretaceous cooling ages in the San Felipe Formation indicate lack of, or partial, resetting of the He system. Late Cretaceous cooling ages are dominant in the Soyatal Formation and are partially equivalent to their maximum depositional age (88 ± 1 Ma), suggesting derivation of grains from adjacent rapidly exhumed thrust sheets. Alternatively, these grains were partially reset. Youngest cooling ages dominate the Mineral de Pozos sandstone samples, indicating Paleocene exhumation and erosion of interior thrust sheets. The Paleocene exhumation event is equivalent to stratal ages of the lower part of the Chicontepec Formation, and sandstone composition of that unit indicates dominant sediment sources in carbonate rocks of the frontal part of the fold-thrust belt. Combined cooling ages and sandstone petrography thus indicate coeval exhumation of the entire width of the orogen in the Paleogene, rather than out-of-sequence thrust-sheet uplift and exhumation of only the interior part of the thrust wedge. Orogen-wide exhumation is corroborated by a previously published early Paleocene illite $^{40}\text{Ar}/^{39}\text{Ar}$ age of 64 ± 2 Ma for thrust deformation at the eastern flank of the Valles-San Luis Potosí carbonate platform, which formed the latest Cretaceous-Paleocene boundary between the fold-thrust belt and foreland basin in which the Chicontepec Formation was deposited.

1. Introduction

The Mexican fold-thrust belt (MFTB) affects more than 90% of Mexican territory; nevertheless, study of shortening and uplift timing in the fold-thrust belt remains in its infancy (see Fitz-Díaz et al., 2018 for a review). In this work, we present new detrital zircon (DZ) U-Pb and (U-Th)/(He-Pb) double ages from a transverse section of the MFTB in

central Mexico to elucidate the role of exhumation on sediment provenance and dispersal. The MFTB, which is part of the North American orogenic system, or Cordilleran orogen, occupies about one-third of the United States and Canada area and extends across the Mexican continent nearly to the western Gulf of Mexico (Fig. 1A). Provenance and stratigraphic data from clastic successions in this part of the MFTB suggest that crustal shortening in Mexico was accompanied by

* Corresponding author.

E-mail address: ejarriaga@geociencias.unam.mx (E. Juárez-Arriaga).

¹ Present address: Bureau of Economic Geology, Jackson School of Geosciences, The University of Texas at Austin, Austin, TX, 78758, USA.

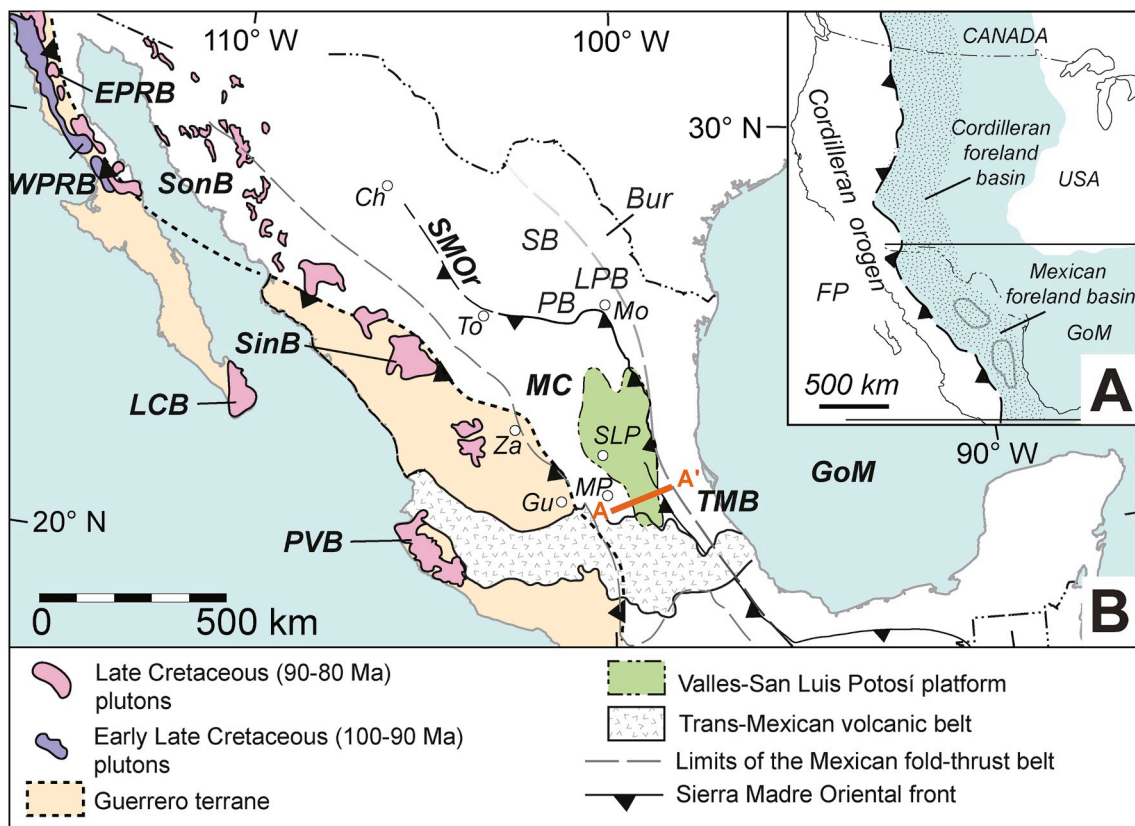


Fig. 1. Location map of Tolimán-Tamazunchale geologic transect (A-A') in central Mexican fold-thrust belt and physiographic elements. (A) Inset rectangle of general paleogeography for Late Cretaceous-early Paleogene time. FP, Farallon plate. (B) Location of Sierra Madre Oriental front (SMOr, dashed line) and geologic features of northern and central Mexico. Basins of Mexican foreland basin system: Bur, Burgos basin; LPB, La Popa basin; PB, Parras basin; SB, Sabinas basin; TMB, Tampico-Misantla basin. Plutonic and volcanic rocks of southern Cordillera: EPRB, Eastern Pensinsular Ranges batholith; WPRB, Western Pensinsular Ranges batholith; LCB, Los Cabos batholith; PVB, Puerto Vallarta batholith; SinB, Sinaloa batholith; SonB, Sonora batholith. Cities (white dots): Ch-Chihuahua; Gu-Guanajuato; Mo-Monterrey; MP-Mineral de Pozos; SLP-San Luis Potosí; To-Torreón; Za-Zacatecas. GoM, Gulf of Mexico; MC, Mesa Central.

development of a Late Cretaceous-Paleogene foreland basin named the Mexican foreland basin (Fig. 1A) (Juárez-Arriaga et al., 2019). Detrital zircon U-Pb ages and sandstone petrography indicate that the component detritus of the Mexican foreland basin came from western sources that produced approximately syndepositional zircon grains and a combination of metamorphic, sedimentary and volcanic lithic fragments (Tardy and Maury, 1973; Lawton et al., 2016; Ocampo-Díaz et al., 2016; Juárez-Arriaga et al., 2019).

Timing of thrust motion has been inferred along the Tolimán-Tamazunchale transect across the fold-thrust belt in central Mexico on the basis of $^{40}\text{Ar}/^{39}\text{Ar}$ ages of neomorphic illite in folds and shear zones. The available ages indicate that two deformational events progressed from west to east during early Campanian (~84-82 Ma), and early Paleocene (~64 Ma) time (Fitz-Díaz et al., 2014). Direct dating of individual structural features in the MFTB suggests that shortening was approximately coeval with episodes of foreland-basin deposition during Late Cretaceous-Eocene time (Suter, 1987; Fitz-Díaz et al., 2011, 2012; Vásquez-Serrano et al., 2018). Regional studies of synorogenic strata in the Mexican foreland basin likewise demonstrate progressive foreland migration of deformation and deposition (Lawton et al., 2016; Fitz-Díaz et al., 2018; Juárez-Arriaga et al., 2019). Nevertheless, basin sedimentary wedges have not yet been explicitly tied to specific thrust sheets as they have in the United States (U.S.) part of the Cordilleran orogenic system (e.g., DeCelles et al., 1995; DeCelles and Coogan, 2006; Yankee and Weil, 2015).

Integration of provenance analysis, direct dating of structural features in the MFTB, and thrust-sheet uplift history in the fold-thrust belt has not previously been attempted. In this study, we present petrographic data, DZ U-Pb geochronology, and detrital zircon (U-Th)/He

(ZHe) thermochronology for foreland-basin strata along a north-northeast-trending traverse in central Mexico. The traverse extends from Tolimán in Querétaro to Tamazunchale in San Luis Potosí and represents the best-documented structural transect in central Mexico (Fig. 1B) (Suter, 1987; Fitz-Díaz et al., 2014). The ZHe thermochronologic data permit reconstruction of the history of exhumation and denudation during Late Cretaceous-Paleogene shortening along the geologic transect and permit us to compare uplift history with existing direct ages on individual thrust structures (Fitz-Díaz et al., 2014; Garduño-Martínez et al., 2015). We also describe the thermochronologic data in the context of new understanding of synorogenic stratigraphy of the foreland basin and inferred provenance relations of those strata. Our goal is to recognize spatial and temporal variations in sedimentation during different stages of evolution of the foreland basin.

2. Geologic background

2.1. The Mexican fold-thrust belt

The MFTB represents the southern extension of the Mesozoic North American Cordilleran orogen through Mexico (Suter, 1987; Fitz-Díaz et al., 2014, 2018). The MFTB is wedge-shaped in cross-section, generally thin-skinned, and was developed during Late Cretaceous-Eocene time (Suter, 1987; Eguiluz et al., 2000; Alzaga-Ruiz et al., 2009; Fitz-Díaz et al., 2012, 2018; Garduño-Martínez et al., 2015). The MFTB has a general NW-SE trend and includes deformed Triassic-Eocene rocks (Campa, 1985; Suter, 1987; Eguiluz et al., 2000; Fitz-Díaz et al., 2012, 2018). To the south, this orogenic belt is buried beneath the Neogene Trans-Mexican volcanic belt (Fig. 1B). Development of the MFTB is

inferred to have begun after accretion of the Guerrero terrane with mainland Mexico, which includes Proterozoic basement rocks and, Triassic and Jurassic deposits, in late Early Cretaceous time (Johnson et al., 1999; Dickinson and Lawton, 2001; Martini et al., 2014; Ortega-Flores et al., 2016; Fitz-Díaz et al., 2018). In this interpretation, rocks of the Guerrero terrane represent the hinterland region of the orogen (Fitz-Díaz et al., 2018).

After accretion of the Guerrero terrane, the Mexican Cordilleran arc was developed along the Baja California Peninsula and the western margin of mainland Mexico during Late Cretaceous-Paleogene time (Juárez-Arriaga et al., 2019). In this work we use the term Mexican Cordilleran arc to distinguish the Late Cretaceous-Paleogene arc from an Early Cretaceous magmatic arc, the Alisitos arc that developed on the Guerrero terrane prior to its accretion (Wetmore et al., 2002, 2003 and references therein).

In the foreland region, pre-orogenic Lower Cretaceous rocks were deposited in a system of carbonate platforms and basins that occupied northern and eastern Mexico following the opening of the Gulf of Mexico (e.g., Wilson, 1990; Wilson and Ward, 1993; Goldhammer, 1999). These carbonate environments were succeeded in Cenomanian time by deepwater siliciclastic deposits in the adjacent foreland of central Mexico. Subsequently, both the carbonate rocks and siliciclastic strata were incorporated into the orogenic wedge. Between the carbonate platforms and the hinterland, strata involved in the fold-thrust belt are mostly Lower Cretaceous carbonates and Upper Cretaceous fine-grained siliciclastic turbidites. Imbricated thick thrust sheets with little internal deformation dominate the platformal carbonate rocks, whereas basinal carbonate strata in more spaced thrust sheets exhibit pervasive meter-scale folding (Fig. 2) (Fitz-Díaz et al., 2011, 2012; Vásquez-Serrano et al., 2018). The structural transect of the study crosses the different paleogeographic elements and Upper Cretaceous-Paleocene foreland deposits of central Mexico (Fig. 2).

2.2. Stratigraphy of Mexican foreland basin

The Mexican foreland basin developed in response to crustal shortening from Late Cretaceous to Eocene time (Fitz-Díaz et al., 2018). The onset of shortening is recorded by a shift from carbonate deposition to siliciclastic turbidites and debris-flow deposits during late Cenomanian in the western part of basin, closest to the hinterland. The oldest succession of the basin is exposed at its western part and is represented by siliciclastic turbidites locally interbedded with calciturbidites (Fig. 3, locality 1). Subsidence continued during the Late Cretaceous as the depocenter of siliciclastic successions migrated eastward with time. During the early Late Cretaceous, turbidite strata were deposited on the western foredeep concurrent with deposition of carbonate pelagites deposited in more distal settings. Pelagic carbonate strata intercalated with tuff beds and ash-rich sandstones were deposited in the distal part of the foreland basin in middle Late Cretaceous time (Santonian-early Campanian; Lawton et al., 2016; Juárez-Arriaga et al., 2019). Subsequent uplift and erosion of proximal foreland basin strata resulted in their erosional truncation. In contrast, Upper Cretaceous strata consisting of sandstone and mudstone are preserved in synclines in the fold belt and near the deformation front (Suter, 1980, 1987; Eguiluz et al., 2000; Fitz-Díaz et al., 2014). Key stratigraphic columns of the foreland region in the Mesa Central and frontal fold belt are indicated in Fig. 3.

Strata deposited in the Mexican foreland basin adjacent to the evolving fold-thrust belt can be divided into (1) proximal strata deposited adjacent to the older parts of the thrust wedge and subsequently imbricated and incorporated into the orogenic wedge (e.g., Mesa Central strata; Fig. 3, locality 1); and (2) distal strata, which are generally coarser deposits that reside in an assemblage of less-deformed foreland basins, such as the Tampico-Misantla basin adjacent to the Gulf of Mexico (Fig. 3, locality 5).

Typically, the age of the proximal foreland basin fill has been

interpreted as Turonian-middle Campanian on the basis of biostratigraphic ages (Carrillo and Suter, 1982; Suter, 1984; Omaña-Pulido, 2012). Nevertheless, in this work we consider the oldest strata from the proximal basin fill to be represented by the Cenomanian Mineral de Pozos sandstone (Fig. 3, locality 1). Turonian-Campanian turbidites of the Soyatal Formation crop out in the central part of the fold-thrust belt (Fig. 3, localities 2–4). Overlying this sedimentary succession are carbonate pelagites with abundant tuffs of the Santonian-Campanian San Felipe Formation, which are distributed along the distal foreland basin (Fig. 3, localities 4–5). Uppermost Cretaceous strata of the Tampico-Misantla basin, the youngest part of the Mexican foreland basin, are represented by shale and thin sandstone layers of the Méndez and Velasco formations, which were deposited in deepwater settings. Paleogene turbidites of the Chicontepec Formation overlie the Upper Cretaceous succession in the Tampico-Misantla basin, the youngest part of the foreland-basin system (Fig. 3, locality 5).

2.3. Lithostratigraphy

The Mineral de Pozos sandstone, an informal unit, is the oldest sedimentary succession yet documented in the foreland basin and lies nearest to the Guerrero terrane (Ortega-Flores et al., 2014). The formation consists of pervasively deformed debrite and turbidite strata; the deformation prevents construction of a single complete stratigraphic section; therefore, the total thickness of this unit is unknown. Thin sandstone layers are folded and foliated whereas thicker, competent ones lack such deformation. Continuous sections a few meters to tens of meters thick include channel deposits and mass-flow deposits with olistoliths, from which samples 06-MP02 and 08-MP04 were collected. These sandstone samples come from the Mineral de Pozos area, ~75 km northwest of transect A-A' (Fig. 1 B). The geology of this area was described by Ortega-Flores et al. (2014; Fig. 2b). DZ U-Pb ages indicate a late Cenomanian maximum depositional age (Ortega-Flores et al., 2014).

The total thickness of the Soyatal Formation is likewise unknown, but the formation has been previously been estimated to be ~1 km thick (Hernández-Jaúregui, 1997). This succession crops out adjacent to the El Doctor platform and in the Zimapán basin (Figs. 2 and 3), where microfossils indicate a late Turonian-Campanian age (e.g., Carrillo and Suter, 1982; Suter, 1984). Westernmost outcrops of Soyatal Formation are located adjacent to the Higuerrillas thrust, where the strata are pervasively deformed. Thin (~20 m) stratigraphically intact sections include turbidite beds and channel bodies containing matrix-supported conglomerate and breccia with exclusively carbonate clasts derived from the adjacent carbonate platform. The Soyatal Formation gradually overlies the Tamaulipas Superior Formation near the town of Vizarrón, few kilometers west of the El Doctor platform (Fig. 3). Within ~15 m of its basal contact, the Soyatal Formation consists of alternating thin beds of limestone, shale and fine-grained sandstone, where we collected the stratigraphically lowest sample (16-CA08). A second section includes fine-grained siliciclastic turbidites, the site of a stratigraphically higher sample (18-CA10). Beds at both sites are pervasively folded and faulted; therefore, the precise stratigraphic relation of the two sections is unknown.

A thick succession of fine-grained turbidites of the San Felipe Formation (Santonian-Campanian) crops out east of the Valles-San Luis Potosí carbonate platform, where we collected two medium-grained sandstone samples (04-JC01 and 05-JC02) (Figs. 2 and 3). U-Pb ages of these samples were previously published (Juárez-Arriaga et al., 2019), and in this work, we have recalculated all discordance filters. In this area the San Felipe Formation displays fault-truncated partial thicknesses, and lower and upper contacts are not exposed.

The Chicontepec Formation (Paleocene-Eocene), which crops out in the Tampico-Misantla basin (Figs. 2 and 3), is the youngest synorogenic sedimentary succession of the foreland basin. It consists of shale and fine- to coarse-grained turbidite sandstone beds deposited in channels

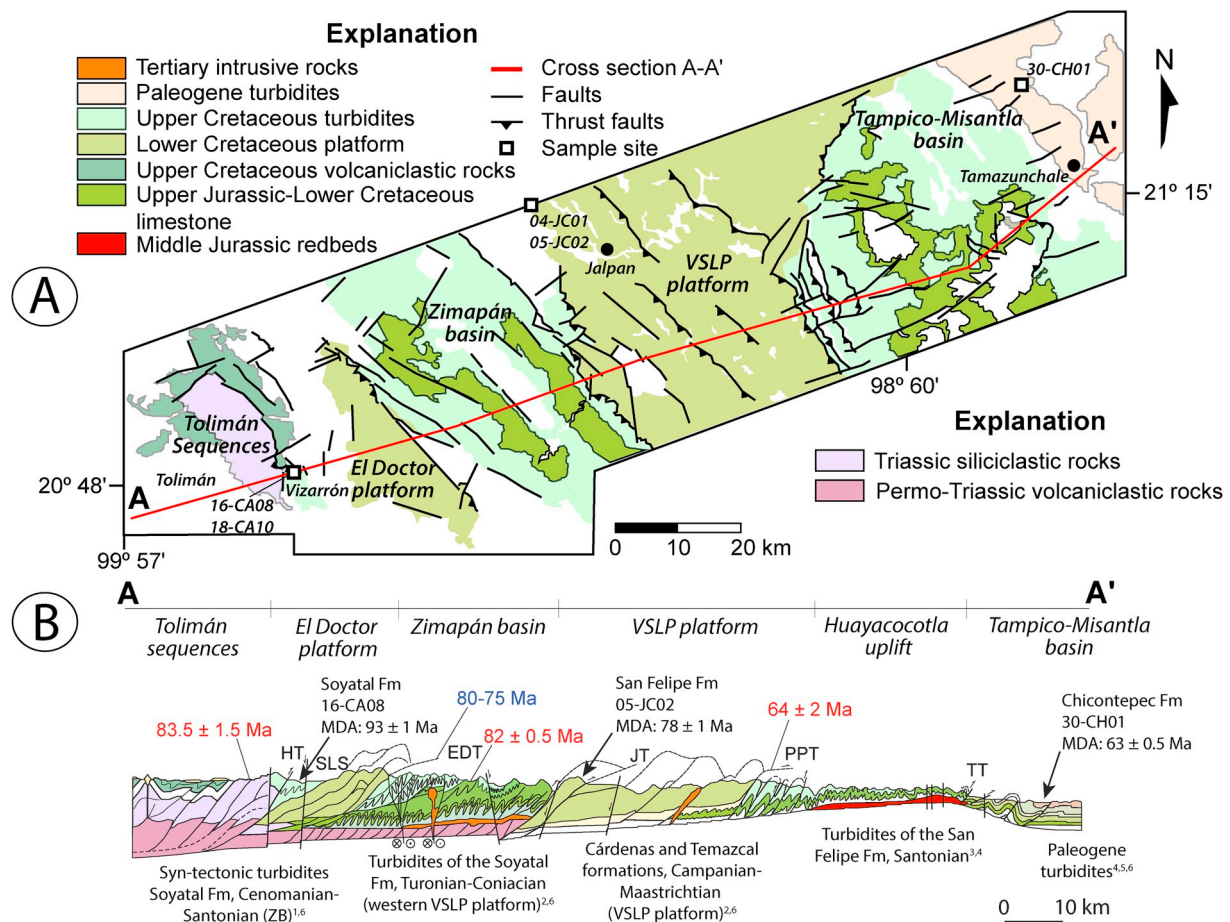


Fig. 2. Locations of paleogeographic elements, deposits of Mexican foreland basin, and geologic features of central Mexico along Tolimán-Tamazunchale transect. Location of cross-section A-A' shown in Fig. 1. (A) Geologic map and location of detrital zircon samples (black squares) along cross-section A-A' (B) Structural cross-section of cross-section A-A' shown in Fig. 1. (A) Geologic map and location of detrital zircon samples (black squares) along cross-section A-A' (B) Structural cross-section of cross-section A-A' shown in Fig. 1. and positions of detrital zircon samples (black arrows). Biostratigraphic ages (below section) of sampled syn-tectonic turbidites from: 1, Hernández-Jauregui (1997), Carrillo and Suter (1982), Suter (1984); 2, Kiyokawa (1981); 3, Omaña-Pulido (2012); 4, Suter (1990); 5, Alzaga-Ruiz et al. (2009); 6, González-Díaz et al. (2017). Explanation: HT, Higuerillas thrust; EDT, El Doctor thrust; JT, Jiliapan thrust; PPT, Puerto de Piedra thrust; TT, Tetitla thrust; ZB, Zimapán basin; VSLP platform, Valles-San Luis Potosí platform. Illite deformation ages (red text) from Fitz-Díaz et al. (2014); illite-mica ages of movement of the El Doctor fault zone (blue text) from Garduño-Martínez et al. (2015). (For interpretation of the references to color in this figure legend, the reader is referred to the Web version of this article.)

and terminal lobes of several submarine-fan systems (Bitter, 1993; Cossey, 2011; Lawton et al., 2016). Total thickness of the Chicontepec Formation is estimated to be as much as 2000 m (Bitter, 1993), but sections in the southern part of the Tampico-Misantla basin are ~500 m thick (Alzaga-Ruiz et al., 2009). We collected a sample from the Chicontepec Formation (30-CH01) from a massive to graded lenticular sandstone bed, which is part of an upward-fining and upward-thinning succession inferred to represent a channel deposit. We also collected two nanofossil samples (17-EMX17SH and 17-EMX1724SH) to help constrain the age of the Chicontepec Formation.

3. Sampling and methods

Rock samples for petrographic, geochronologic and thermochronologic analyses were collected from representative outcrops of the Mineral de Pozos sandstone, Soyatal, San Felipe and Chicontepec formations. New data obtained in this work are integrated with previously published petrographic data and DZ U-Pb ages (e.g., Ortega-Flores et al., 2014; Juárez-Arriaga et al., 2019). We collected five samples of fine-to medium-grained sandstone from five different stratigraphic levels of the Mexican foreland basin along the Tolimán-Tamazunchale transect in central Mexico. Two additional samples of medium-grained sandstone were collected northwest of Tolimán-Tamazunchale. These

samples come from the Mineral de Pozos sandstone, which is not exposed in this transect. The sampling strategy took into account age and stratigraphic position of lithostratigraphic units, and location with respect to paleogeographic elements of the transect A-A', including the El Doctor platform and the Zimapán basin. Sample locations are shown in Fig. 2 and coordinates are given in the supplemental files (Supplemental DT1).

3.1. Petrography of sedimentary samples

Thin sections were stained for potassium feldspar and point counted ($n = 400$ framework grains) using the Gazzi-Dickinson counting technique to minimize compositional dependence on grain size (Ingersoll et al., 1984). Accessory minerals, and bioclastic grains are not included on the ternary diagrams; point counting parameters are shown in Table 1. We use the sandstone classification scheme of Folk (1974).

3.2. Detrital zircon U-Pb geochronology

Standard mineral separation techniques included crushing, grinding, water table concentration, Frantz magnetic separation, and heavy liquids. DZ U-Pb geochronology was performed by laser ablation inductively-coupled plasma mass spectrometry (LA-ICPMS) at the Geo-

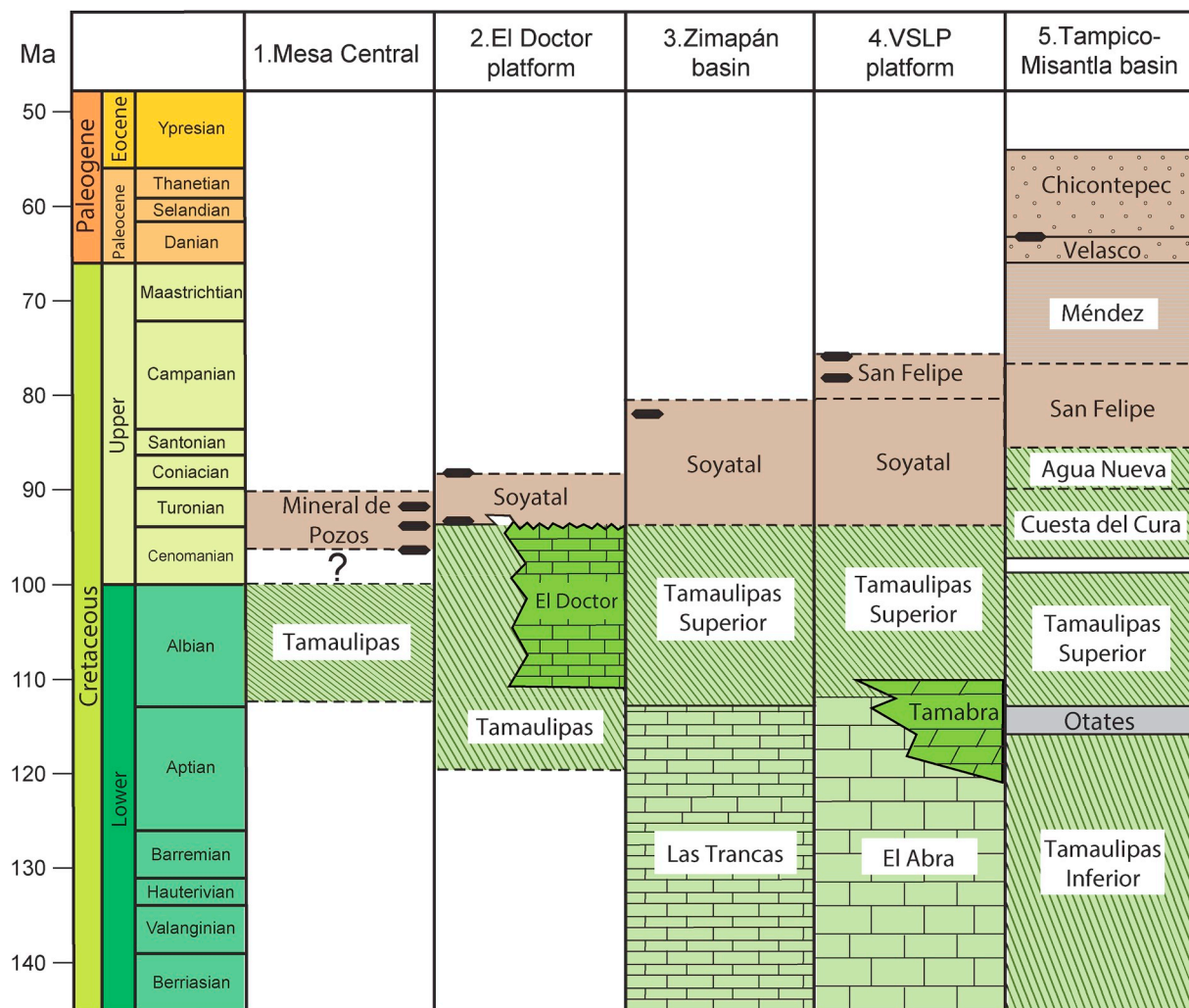


Fig. 3. Stratigraphic correlation chart of central and eastern foreland region of Mexico. Green varieties with shaded textures of this chart indicate carbonate platforms and basins of the Early Cretaceous. Brown color represents units of Mexican foreland basin, which migrated eastward with time. Black zircon symbols indicate stratigraphic positions of detrital and volcanic zircon samples. (For interpretation of the references to color in this figure legend, the reader is referred to the Web version of this article.)

and Thermochronometry Laboratory at the University of Texas at Austin following the methodology reported by Hart (2015), Hart et al. (2016) and Pujols et al. (2018). U-Pb ages are included in supplemental files (Supplemental DT1). To avoid spurious age populations in the probability density plots, the following criteria were applied: (a) The $^{206}\text{Pb}/^{238}\text{U}$ ages were used for zircons younger than 850 Ma and $^{207}\text{Pb}/^{206}\text{Pb}$ ages were used for grains older than 850 Ma (e.g., Kimbrough et al., 2015; Suarez et al., 2017); (b) accepted Jurassic or younger analyses have discordance < 10%, Neoproterozoic and Paleozoic analyses have discordance < 6%, and for Paleoproterozoic grains is < 4%; (c) age errors are < 6%. For each detrital sample ~120 zircon grains were randomly selected for analysis to obtain a statistically representative provenance data set (Vermeesch, 2004). The data were complemented with previously published DZ U-Pb zircon ages (e.g., Mineral de Pozos sandstone; Ortega-Flores et al., 2014). All data are reported at 2σ absolute uncertainties (see Supplemental files). Data were plotted using the Isoplot software (Ludwig, 2008). For temporal context we employ the Geologic Time Scale of Cohen et al. (2013).

We analyzed our data by multidimensional scaling (MDS), a statistical tool useful for comparing large data sets, that employs the dissimilarity matrix (D) of the Kolmogorov-Smirnov test to create a map of “distances” (non-metric) indicative of the dissimilarity between the analyzed age populations (Vermeesch, 2013). We used MDS to compare

the Late Cretaceous sandstones of the central part of the Mexican foreland basin with their potential source rocks located along the western margin of Mexico and in central Mexico. Continuous lines indicate first order distances, and therefore represent high similarity between the analyzed samples. Second order distances between samples with low similarity, are indicated by discontinuous lines. MDS maps were plotted using IsoplotR free software for R (Vermeesch, 2018).

3.3. Detrital zircon (U-Th)/He thermochronology

Forty-three individual zircon grains previously dated by U-Pb were selected for dating by the (U-Th)/He (ZHe) method. Grains were selected on the basis of size (~65–120 μm in length along their longest dimension), lack of inclusions and fractures and relative abundance of DZ U-Pb age components in each sample (for details see Wolfe and Stockli, 2010; Pujols et al., 2018). For each sample we obtained 11–17 ZHe ages, which record the time of cooling through ca. 180 °C, help constrain the time of exhumation, and improve the provenance analysis. We use the difference between crystallization age and cooling age (Δt) to identify first-cycle volcanic zircon grains (e.g., Saylor et al., 2012). If Δt is less than the 2σ uncertainty of the ZHe age, the grain is considered a first-cycle volcanic zircon and is excluded from further consideration. All single zircon (U-Th)/(He-Pb) double dating analyses

Table 1
Point counting parameters.

Symbol	Definition
Qm	Monocrystalline quartz
Qpq	Polycrystalline quartz
Qc	Chert
K	Potassium feldspar
P	Plagioclase feldspar
Lmf	Foliated quartz-mica metamorphic grains
Lmp	Polygonal quartz-mica metamorphic grains
Lmv	Metavolcanic grains with epidote and/or chlorite
Lss	Sedimentary lithic grains: siltstone, argillite, phosphatic grains.
Lsc	Detrital carbonate grains (sensu Zuffa, 1980)
Lvf	Felsitic volcanic lithic grains
Lvl	Lathwork volcanic lithic grains
Lvm	Microilitic volcanic lithic grains
Lvt	Tuffaceous and vitric volcanic lithic grains
Qt	Total quartzose grains (=Qm + Qpq + Qc)
F	Total feldspar (=K + P)
Lm	Total metamorphic grains (=Lmf + Lmp + Lmv)
Lv	Total volcanic grains (=Lvf + Lvl + Lvm + Lvt)
Ls	Total sedimentary grains (=Lss + Lsc)
L	Total unstable lithic grains (=Lm + Lv + Ls)
Qp	Total polycrystalline quartz (=Qpq + Qc)
Lt	Total lithic grains (=L + Qp)
Recalculated parameters	
QtFL%Q	$= 100Qt/(Qt + F + L)$
QtFL%F	$= 100F/(Qt + F + L)$
QtFL%L	$= 100L/(Qt + F + L)$
QmFLt%Qm	$= 100Qm/(Qm + F + Lt)$
QmFLt%F	$= 100F/(Qm + F + Lt)$
QmFLt%Lt	$= 100Lt/(Qm + F + Lt)$
LmLvLs%Lm	$= 100Lm/(Lm + Lv + Ls)$
LmLvLs%Lv	$= 100Lv/(Lm + Lv + Ls)$
LmLvLs%Ls	$= 100Ls/(Lm + Lv + Ls)$
QmPK%Qm	$= 100Qm/(Qm + P + K)$
QmPK%P	$= 100P/(Qm + P + K)$
QmPK%K	$= 100K/(Qm + P + K)$

were performed at the Geo- and Thermochronometry Laboratory of the University of Texas at Austin and are included in supplemental files (Supplemental DT2).

4. Results

4.1. Sandstone petrography

Detrital modes of Upper Cretaceous-Paleogene sandstones adjacent to cross section A-A' were plotted on QtFL and QmFLt ternary plots that illustrate the provenance fields of Dickinson (1985), and LmLvLs ternary plot after Ingersoll and Suczek (1979) (Fig. 4). Point count results are indicated in Table 2. Published petrographic results from the Mineral de Pozos sandstone (Ortega-Flores et al., 2014) complement understanding of sandstone composition evolution in the Mexican foreland basin.

4.1.1. Mineral de Pozos sandstone

The Mineral de Pozos sandstone ranges from feldspathic litharenite (06-MP02: Qt₅₃F₂₂L₂₅; 07-MP03: Qt₄₂F₂₃L₃₅) to arkose (08-MP04: Qt₄₉F₃₉L₁₂). Framework grains include monocrystalline and polycrystalline quartz grains, chert, plagioclase, volcanic lithic grains, which are dominated by felsitic volcanic lithic fragments, and include subordinate microlitic and lathwork volcanic lithic fragments, siliciclastic sedimentary lithic grains, extrabasinal carbonate lithic grains (Lsc of Ingersoll et al., 1987), and metamorphic lithic grains (Table 2). All samples are grain-supported, but grains are locally altered to pseudomatrix (e.g., Dickinson, 1970). Feldspar and felsitic volcanic lithic grains are commonly altered or are partially replaced by carbonate minerals. Common polycrystalline quartz grains have large crystal

domains (> 60 μm), and volcanic lithic grains and fresh plagioclase grains are abundant (e.g., MP-06, 06-MP02, 08-MP04). Micrographic grains are rare and potassium feldspar is absent. Nearly 30% of the framework grains are lithic, and most of the sandstones plot at or near the boundary of the recycled orogenic and dissected arc fields on the QtFL plot (Fig. 4); sample MP-06 (Ortega-Flores et al., 2014) plots in the dissected arc field (Fig. 4). Some samples contain sedimentary lithic grains that include pelitic sedimentary lithic fragments, chert and extrabasinal carbonate lithic fragments (e.g., MP-06, 07-MP03), which indicate the importance of sources in uplifted carbonate strata of the fold-and-thrust belt or of the Guerrero terrane.

4.1.2. Soyatal Formation

Sandstone of the Soyatal Formation is lithic arkose (16-CA08: Qt₄₆F₃₁L₂₄; 18-CA10: Qt₃₈F₃₂L₂₉). Framework grains include monocrystalline and polycrystalline quartz grains, chert, plagioclase, volcanic lithic grains, siliciclastic sedimentary lithic grains, extra-basinal carbonate, and metamorphic lithic grains. The sandstones contain more monocrystalline quartz of apparent volcanic origin (sensu Folk, 1974) than Mineral de Pozos sandstones, whereas polycrystalline quartz grains with domains > 60 μm are less abundant. Volcanic lithic grains, including felsitic, microlitic and rare lathwork volcanic lithic grains, dominate the lithic fraction (~60% of total lithic grains), and pelitic sedimentary lithic grains, chert and lithic sedimentary carbonate grains are also common. Like the Mineral de Pozos samples, the Soyatal sandstones contain uncommon grains of fresh plagioclase, but no potassium feldspar. Feldspar and volcanic lithic grains are commonly partially or completely replaced by carbonate minerals. The sandstones have grain-supported texture and pseudo-matrix formation is rare. Both samples plot in or adjacent to the dissected arc field of the QtFL and QmFLt plots (Fig. 4).

4.1.3. San Felipe Formation

Sandstones of the San Felipe Formation of the eastern part of the Valles-San Luis Potosí carbonate platform contain abundant lithic grains (Fig. 4); samples range from calclithite (05-JC02: Qt₆F₇L₈₄) to feldspathic litharenite (04-JC01: Qt₁₉F₂₁L₆₀). Dominant framework grains consist of subrounded extrabasinal carbonate lithic grains (sensu Zuffa, 1980), including micritic and pelagic bioclastic grains. Subordinate components include volcanic lithic grains, plagioclase, siliciclastic sedimentary lithic grains, volcanic monocrystalline quartz, fresh biotite and carbonate intrabasinal grains. The latter include micritized miliolid shells, fragmental mollusc shells and echinoid spines. A variety of volcanic lithic grains, including microlitic and felsitic volcanic grains, are present in all samples. Volcanic lithic grains and plagioclase grains are commonly slightly altered to small, bright birefringent crystals. Potassium feldspar, including microcline and sanidine, is common in sample 05-JC02.

4.1.4. Chicontepec Formation

The Chicontepec Formation sample is a feldspathic litharenite (30-CH01: Qt₂₄F₂₃L₅₄; Fig. 4). Framework grains include monocrystalline and polycrystalline quartz grains, chert, plagioclase, volcanic lithic grains, siliciclastic sedimentary lithic grains, and extrabasinal carbonate lithic grains. Zircon is the most common accessory mineral. The plagioclase, feldspar and felsitic volcanic lithic grains are partially or totally replaced by carbonate cement. Nearly 80% of the lithic grains are extrabasinal carbonate grains that indicate limestone strata were an important sediment source for this sandstone. Although this sandstone plots in the transitional arc field because the methodology of Dickinson (1985) omitted detrital carbonate grains, we interpret that the sandstone was derived primarily from carbonate strata of the fold-thrust belt. The two calcareous nannofossil samples indicate a biostratigraphic age of middle to late Paleocene based on the presence of *Prinsius bisulcus*, *P. martinii* and *Sphenolithus anarrhopus* (R.W. Morin written communication, 2017). Thus, the age of the nannofossils and the DZ U-Pb maximum depositional ages calculated from young zircon grains

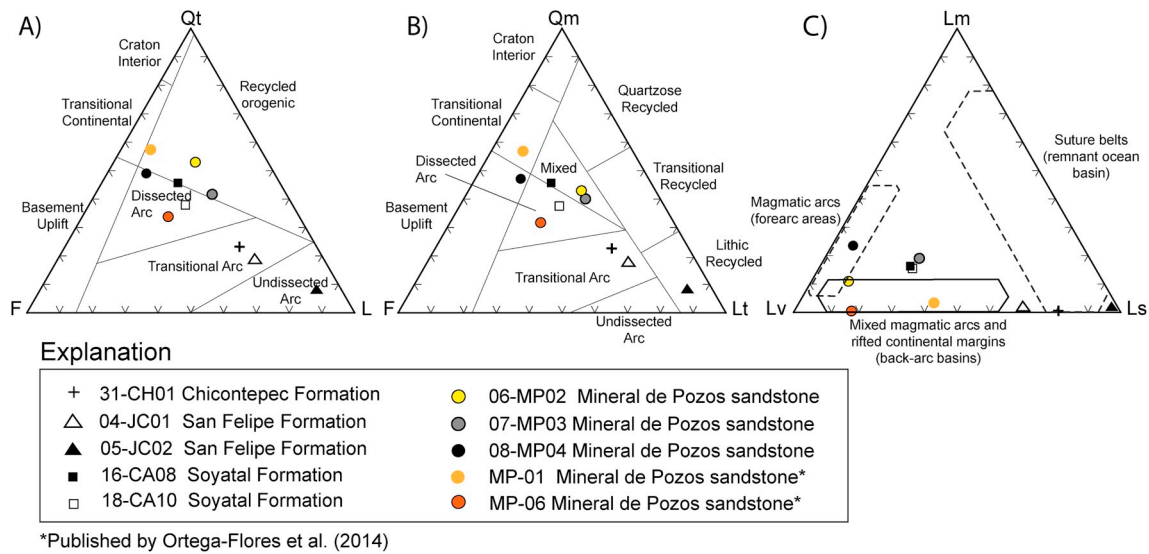


Fig. 4. Detrital modes of Cenomanian-Turonian sandstones in Mesa Central (Mineral de Pozos sandstone), Santonian sandstones and tuff (Soyatal and San Felipe formation), and Paleogene sandstone (Chicontepec Formation) in central MFTB. All samples except Mineral de Pozos sandstone were collected along section A-A'. See Fig. 1 and 2 for sample locations. Data are listed in Table 2. Provenance field of QtFL and QmFLt ternary plots are after Dickinson (1985). Provenance fields indicated by dashed lines on LmLvLs ternary plot are after Ingersoll and Suczek (1979).

Table 2
Recalculated modal point-count data for Tolimán-Tamazunchale transect samples, central Mexican fold-thrust belt.

Sample	QtFL%			QmFLt%			LmLvLs%			QmKP%		
	Qt	F	L	Qm	F	Lt	Lm	Lv	Ls	Qm	K	P
Chicontepec Formation												
30-Ch01	24	23	54	23	23	54	0	19	81	50	0	49
San Felipe Formation												
04-JC01	19	21	60	17	21	62	2	29	70	46	6	48
05-JC02	8	7	84	8	7	84	0	1	99	54	24	22
X	14	14	72	13	14	73	1	15	85	50	15	35
SD	8	10	17	6	10	16	1	20	20	6	13	18
Soyatal Formation												
16-CA08	46	31	24	45	31	24	17	56	27	60	0	40
18-CA10	38	32	29	37	32	31	16	57	27	54	0	46
X	42	32	27	41	32	28	17	57	27	57	0	43
SD	6	1	4	6	1	5	1	1	0	4	0	4
Mineral de Pozos sandstone												
06-MP02	53	22	25	43	22	35	11	78	11	66	0	33
07-MP03	42	23	35	40	23	37	19	52	29	64	0	36
08-MP04	49	39	12	47	39	14	23	71	6	55	1	44
MP-01 ^a	58	33	9	57	33	10	0	82	18	ND ^b	ND ^b	ND ^b
MP-06 ^a	34	40	26	32	40	28	4	56	40	ND ^b	ND ^b	ND ^b
X	47	31	21	44	31	25	11	68	21	65	0	35
SD	9	9	11	9	9	12	10	13	14	6	0.6	6

Notes: Point counting parameters: Qt, total quartzose grains; F, total feldspar; L, total unstable lithic grains; Qm, monocrystalline quartz; Lt, total lithic grains; Lm, total metamorphic grains; Lv, total volcanic grains; Ls, total sedimentary grains; K, potassium feldspar; P, plagioclase feldspar. Total framework counts: 400 per sample.

^a Parameters recalculated from Ortega-Flores et al. (2014).

^b ND = Data not provided in Ortega-Flores et al. (2014).

both are in overall agreement with a depositional age of early to middle Paleocene for the sampled beds. Additionally, a high percentage of reworked Cretaceous nannofossils was found in both samples of the Chicontepec Formation.

4.2. Detrital zircon U-Pb ages in the units of the Tolimán-Tamazunchale transect (A-A')

U-Pb ages of 676 analyzed grains range from 2915 to 61 Ma, and

49% of the analyses (n = 330) yielded ages younger than 200 Ma (Fig. 5). The maximum depositional age (MDA) for each sample was calculated from the weighted mean of the coherent group of youngest grain ages (e.g., Dickinson and Gehrels, 2009); the MDA and the single youngest grain age per sample are summarized in Table 3. Most analyzed detrital zircon grains are colorless, light yellow, and rarely slightly pink. The grains are commonly broken and crystal facets are variably rounded, possibly due to sedimentary transport. Euhedral grains are present in all analyzed samples in a subordinate amount. Archean grains are rare in the sample set and do not form a significant age group. Six main DZ U-Pb age groups were identified from the combined analyses of the transect samples (Fig. 5, Table 4): (1) Paleoproterozoic (1750-1600 Ma), (2) middle Mesoproterozoic-early Neoproterozoic (1230-920 Ma), (3) Cambrian-Silurian (490-420 Ma), (4) Middle Devonian (405-380 Ma), (5) Permian-Triassic (285-220 Ma), and Jurassic-early Paleogene (180-60 Ma).

All samples of the A-A' transect contain DZ U-Pb Jurassic-early Paleogene ages, the dominant age group, albeit in varying proportions (17%–68%; Fig. 6). The three Mineral de Pozos samples show marked differences in their age components (Fig. 6A–F). Sample MP-6, contains abundant Middle Jurassic-early Paleogene (68%) and Permian-Triassic (15%) grains. Paleoproterozoic (4%), middle Mesoproterozoic-early Neoproterozoic (3%), and Cambrian-Silurian (1%) age components are significantly less prominent (Fig. 6A and B). Sample 06-MP02 contains a dominant Jurassic-early Paleogene age group (34%); Paleoproterozoic (12%), Cambrian-Silurian (11%), middle Mesoproterozoic-early Neoproterozoic 10%, and Permian-Triassic (10%) grains represent minor age components (Fig. 6C and D). Sample 08-MP04 is dominated by Permian-Triassic (18%) and Middle Jurassic-early Paleogene (17%) ages, with subordinate but distinctive Middle Devonian (14%) and Cambrian-Silurian (14%) ages. Middle Mesoproterozoic-early Neoproterozoic (10%) ages are less common. Paleoproterozoic grains represent only about 5% of the U-Pb ages (Fig. 6E–F). Mineral de Pozos samples uniformly have an important relative maximum of the curve near ~100–103 Ma that is not present in the other samples of transect (Fig. 6B, D, F).

Two samples from the Soyatal Formation (16-CA08 and 18-CA10; n = 209) contain slightly different age components. The dominant age group of sample 16-CA08 is Middle Jurassic-early Paleogene (44%), with subordinate components of Cambrian-Silurian (13%) and middle Mesoproterozoic-early Neoproterozoic (10%) ages. Minor contributions

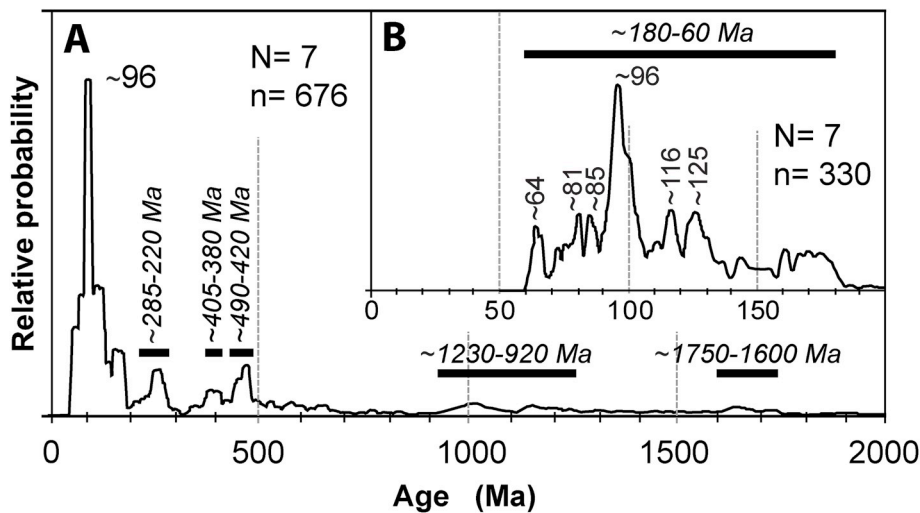


Fig. 5. DZ U-Pb age probability plot for central Mexican fold-thrust belt samples. Horizontal bars indicate age components described in the text. (A) All grain ages from Mineral de Pozos sandstone, Soyatal, San Felipe (sample 04-JC01) and Chicontepec formations, except two grains at 2700 Ma and 2915 Ma. (B) Detrital zircon U-Pb ages younger than 200 Ma. N = number of samples, n = number of analyses.

of Permian-Triassic (5%), Middle Devonian (4%) and Paleoproterozoic (1%) ages are also present (Fig. 6G–H). The main age component for sample 18-CA10 is also Middle Jurassic-early Paleogene (59%); minor age components of middle Mesoproterozoic-early Neoproterozoic (10%), and Cambrian-Silurian (6%) U-Pb ages are present. DZ age components of Permian-Triassic (5%) and Paleoproterozoic (1%) age are significantly less prominent (Fig. 6I–J). Mineral de Pozos sandstone samples and one Soyatal sample (16-CA08) contain a dominant early Late Cretaceous relative maximum of the curve at ~97–95 Ma.

The San Felipe Formation sample (04-JC01; n = 70) (Fig. 6I) has a major Middle Jurassic-early Paleogene age group (50%); Middle Mesoproterozoic-early Neoproterozoic (7%), Cambrian-Silurian (6%), Permian-Triassic (4%), and Paleoproterozoic (1%) ages represent minor components (Fig. 6K–L). Younger age relative maximum of the curve at ~77, 80 and 85 Ma are present in the San Felipe Formation (Fig. 6L).

The Chicontepec Formation sample (n = 132) chiefly yielded Middle Jurassic-early Paleogene grain ages (68%). A subordinate age group is middle Mesoproterozoic-early Neoproterozoic, corresponding to 11% of ages. Minor age groups are Permian-Triassic (2%), Paleoproterozoic (2%), and Cambrian-Silurian (2%) (Fig. 6M–N). This sample (30-CH01) has a dominant early Paleocene relative maximum of the curve at ~64 Ma, and two Late Cretaceous relative maximums of the curve at ~85 and 96 Ma, as well as an important Early Cretaceous relative maximum of the curve at ~126 Ma (Fig. 6N).

The MDS map that compares the A-A' transect sandstones with some possible source rocks in Mexico and the western U.S. (described below) yielded first order distances with detrital samples from Guerrero terrane and volcanic and plutonic samples from the western Mexican magmatic arc (Fig. 7).

4.3. Detrital zircon (U-Th)/He data

A subset of the U-Pb dated zircons was dated by the (U-Th)/He method. These double dated grains are from the following samples: 06-MP02, Mineral de Pozos sandstone; 16-CA08, Soyatal Formation; and 04-JC01, San Felipe Formation. The resulting 43 cooling analyses provide new insight into sediment dispersal and uplift history across the central MFTB.

The ZHe ages for the samples range from Permian to Eocene (Fig. 8). A small number (n = 2) of zircon grains yielded U-Pb ages that are equivalent to their corresponding ZHe ages within 2σ uncertainty; these grains are interpreted to represent first-cycle volcanic grains (e.g., Reiners et al., 2005; Saylor et al., 2012). These two grains, both Campanian of the San Felipe Formation, were not considered in the analysis of ZHe ages to interpret the thermal history along the transect A-A' (Fig. 9a). Three principal ZHe age components (as distinguished from U-Pb age groups) are present in the samples (Fig. 8): Early Cretaceous (~136–120 Ma); Late Cretaceous (~99–80 Ma); and Paleocene (~66–56 Ma). Five main ZHe age groups were identified from the combined analyses of the transect samples: (1) Permian (~271 Ma); (2) Jurassic (~180–159 Ma); Early Cretaceous (~136–107 Ma); Late Cretaceous (~99–66 Ma); and Paleogene (~63–46 Ma). Mineral de Pozos sandstone ZHe ages (n = 11) are largely Paleogene (64%), with minor Late Cretaceous (18%), and Early Cretaceous (18%) ages. Soyatal Formation ZHe ages (n = 15) are dominated by Late Cretaceous (73%), Early Jurassic (13%), and subordinate Paleogene (7%) and Early Cretaceous (7%) ages. The San Felipe Formation (n = 17) yielded mostly Early Cretaceous (35%), Late Cretaceous (29%), Paleogene (12%), Late Jurassic (6%), and Permian (6%) DZHe ages.

Table 3

Calculated ages for Late Cretaceous samples of Mineral de Pozos sandstone and samples of the Tolimán-Tamazuchale transect.

Sample	Unit	Location	MDA	MSWD ^a	Youngest grain (Ma)	n ^b	Reference
06-MP02	Mineral de Pozos sandstone	Mineral de Pozos area	96 ± 1	1.09	94.8 ± 2.7	9	This study
08-MP04	Mineral de Pozos sandstone	Mineral de Pozos area	94 ± 1	1.17	92.8 ± 2	3	This study
MP-06 ^c	Mineral de Pozos sandstone	Mineral de Pozos area	92 ± 1	1.1	91 ± 1	5	Ortega-Flores et al. (2014)
16-CA08	Soyatal Formation	Vizarrón area	93 ± 1	0.92	87 ± 2.6	3	This study
18-CA10	Soyatal Formation	Vizarrón area	88 ± 1	0.62	87.1 ± 1.6	4	This study
04-JC01 ^c	San Felipe Formation	VSLP platform	76 ± 1	0.96	73 ± 1.4	5	Juárez-Arriaga et al. (2019)
05-JC02 ^c	San Felipe Formation	VSLP platform	78 ± 1	1.5	72 ± 2.4	8	Juárez-Arriaga et al. (2019)
30-CH01	Chicontepec Formation	Tampico-Misantla basin	63 ± 0.5	1.07	61.2 ± 1	4	This study

^a MSWD = Mean square of weighted deviates (Ludwig, 2008).

^b n = Number of grains used in age calculation for MDA (maximum depositional age).

^c Parameters recalculated from data in indicated published reference.

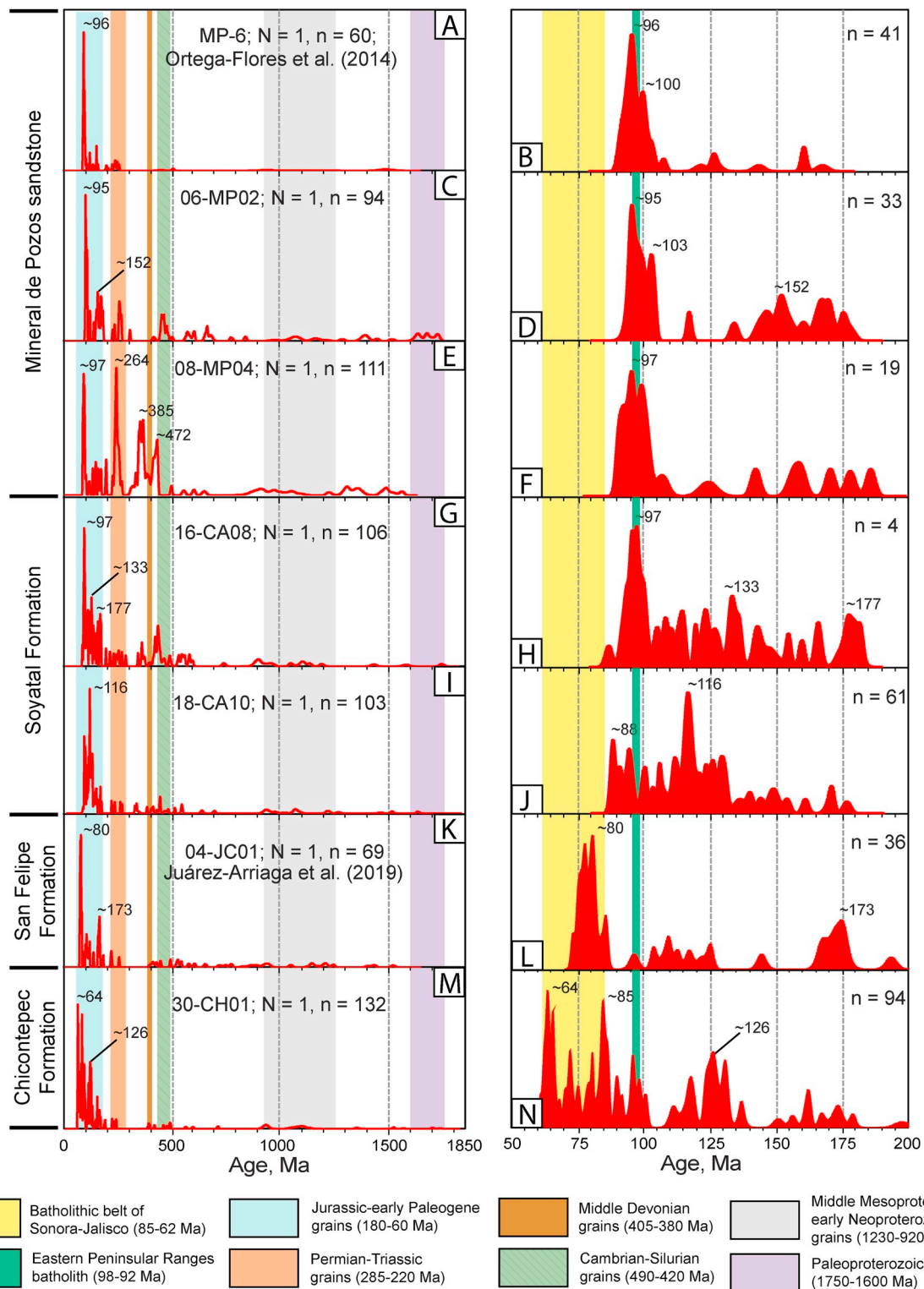


Fig. 6. Probability density plots of DZ U-Pb ages of sandstone samples along A-A' transect in central MFTB. N = number of samples, n = number of analyses. DZ age density plots for all grains (left column); grains younger than 200 Ma (right column). The color columns show the DZ U-Pb age components described in the text. Grains attributable to Mesozoic arc sources (~180-60 Ma) are very common in these sandstones; the Late Cretaceous grain component (~98-92 Ma), which corresponds with ages of the Eastern Peninsular Ranges batholith in the Baja California Peninsula, is the most abundant in the detrital samples. Note that old zircon grain ages (> 1 Ga) (top of the left plots) are not present in younger units. (For interpretation of the references to color in this figure legend, the reader is referred to the Web version of this article.)

Three discrete clusters of DZ grains are defined on the basis of the ranges of their ZHe cooling ages and U-Pb ages, with U-Pb crystallization ages varying widely in each cluster (Fig. 8). Cluster A has ZHe ages older than deformation ages previously reported for the MFTB and

discussed below. Cluster A ZHe ages range from ~136 to 120 Ma and U-Pb ages span ~1450-170 Ma; most grains of cluster A are present in the San Felipe Formation (Fig. 8a). A second, well-defined cluster B, with ZHe ages ranging from ~102 to 80 Ma and U-Pb ages in the range

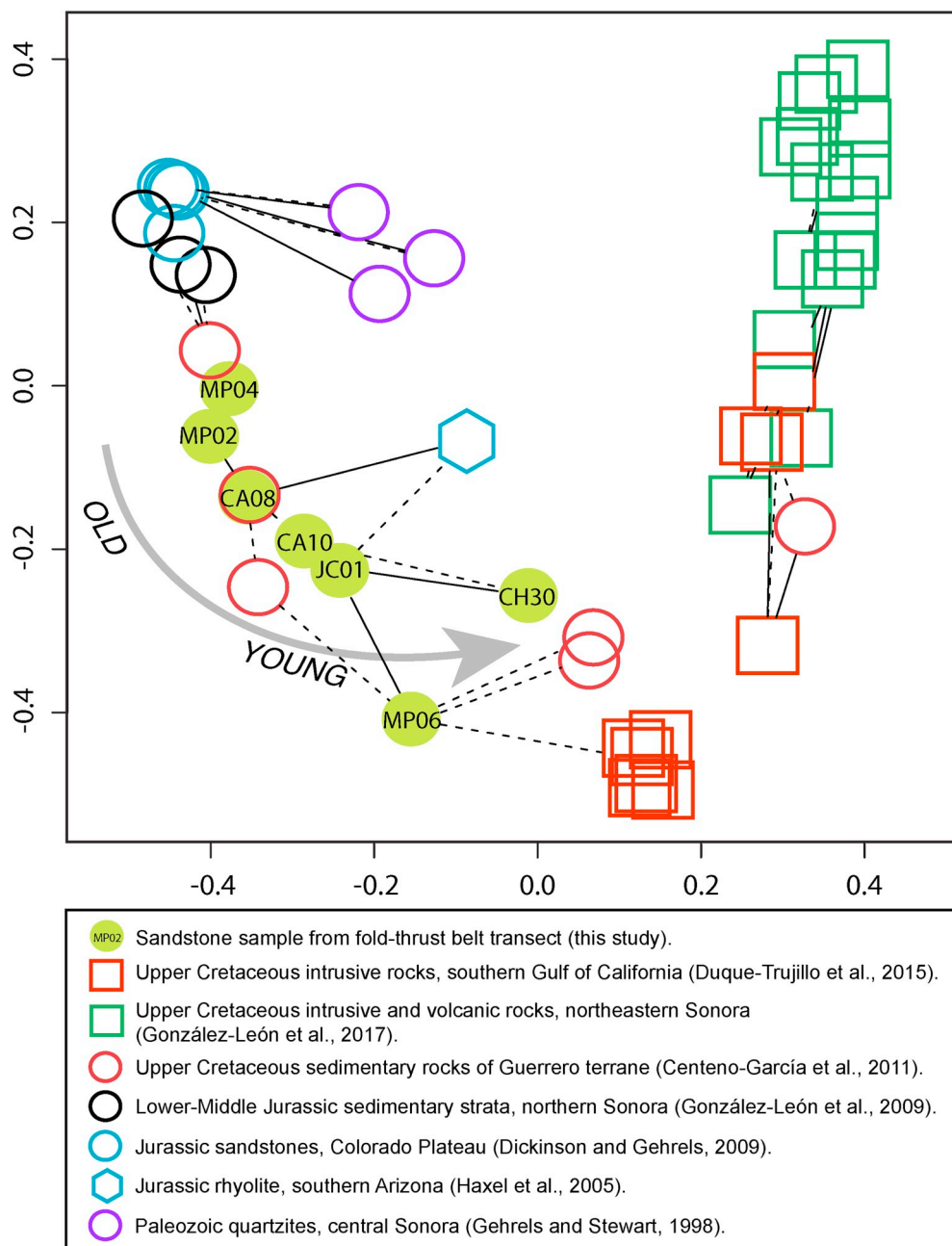


Fig. 7. Multidimensional scaling (MDS) map of transect samples (green circles) and samples interpreted as potential sources discussed in the text. The counterclockwise curved arrow indicates the younging direction of the transect samples (except MP06). Two large groups, not connected in the MDS map, are distinguished: to the left, the detrital samples constitute a well-defined set, to the right, a second set is formed by samples derived from plutonic and volcanic rocks of the batholiths of Sonora, Baja California, Sinaloa and Puerto Vallarta (squares). Continuous lines represent first-order distances (first order similarities between samples), whereas discontinuous lines indicate second-order distances (e.g., Vermeesch, 2013). (For interpretation of the references to color in this figure legend, the reader is referred to the Web version of this article.)

~1150-80 Ma (Fig. 8b), is mostly present in the Soyatal Formation. Cluster C, with the youngest ZHe ages ranging from ~66 to 56 Ma and U-Pb ages spanning ~1638-73 Ma (Fig. 8c), is mostly present in the Mineral de Pozos sandstone. The ZHe ages of the clusters indicate DZ grains derived from sources having different thermal histories.

5. Discussion

5.1. Interpretation DZ U-Pb ages

Most detrital zircon grains are inferred to have been derived from sediment sources in the west (Fig. 10). Sources included magmatic arc rocks for the Jurassic-early Paleogene age component, or the oldest metasedimentary rocks of the arc terrane and uplifted sedimentary strata of the proximal part of the foreland basin for older age components (e.g., Juárez-Arriaga et al., 2019). DZ U-Pb age components of sandstones in the central MFTB and inferred sources are summarized in

Table 4. The U-Pb age components of the Mineral de Pozos sandstone samples were likely derived from Triassic sedimentary rocks deposited on the west flank of mainland Mexico (e.g., Barboza-Gudiño et al., 2010; Ortega-Flores et al., 2014) or from Triassic metasedimentary rocks of the Guerrero terrane (e.g., Martini et al., 2009; Centeno-García et al., 2011). The Triassic rocks contain grain-age distributions similar to those of the transect samples and include late Permian, Ordovician and Grenville grain ages (Figs. 5 and 6). Available geochronologic data indicate that sediment sources of Mineral de Pozos sandstone samples show significant differences in zircon components, even between samples that are lithologically similar and were collected at a short distance to each other. Note that in sample MP-06 almost all grains are younger than Permian age, whereas samples 06-MP02 and 08-MP04 contain Proterozoic and Paleozoic grains. Sample 08-MP04 contains abundant Devonian grains that are absent in the other samples (Fig. 6). Due to the above, we infer a complex sedimentary dispersal history for this unit, an important topic that can be clarified in future research.

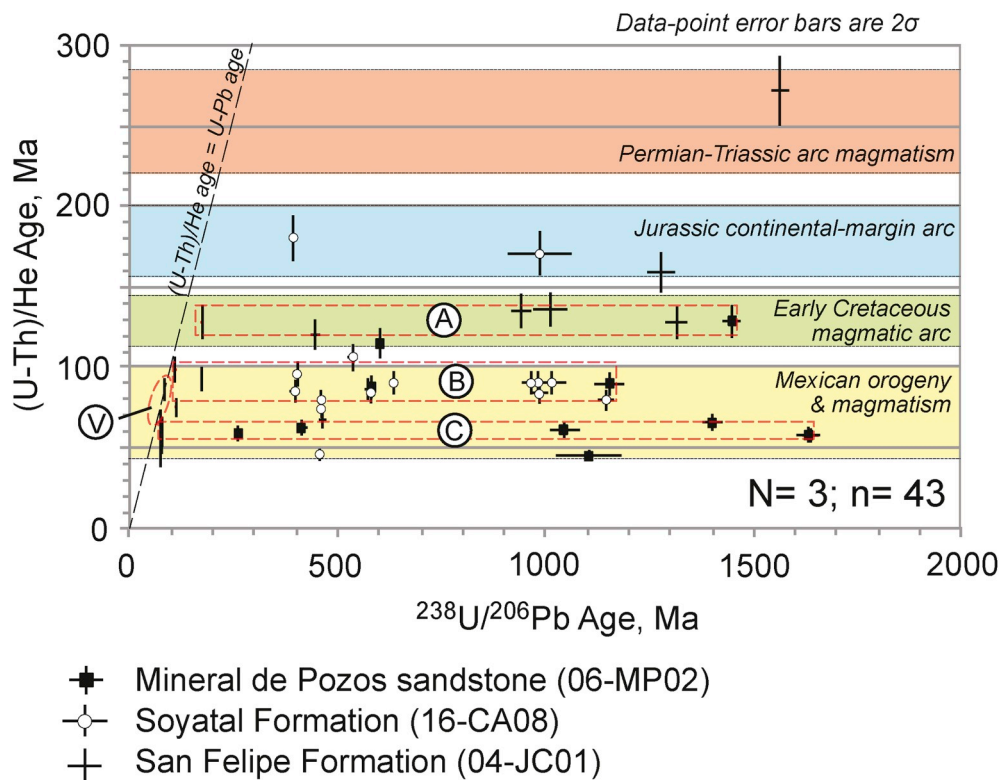


Fig. 8. Plot of double dates (ZHe versus U-Pb ages) of three samples of the central MFTB. First-cycle volcanic grains lying along dashed black line indicating equal U-Pb and ZHe age are shown by dashed polygon V. Dashed rectangles A-C indicate corresponding ZHe and U-Pb age clusters described in text. Colored horizontal fields indicate age ranges of important tectonic events in Mexico (after Fitz-Díaz et al., 2018; Juárez-Arriaga et al., 2019). N = number of samples, n = number of analyses.

In the San Felipe Formation, early Paleozoic and Devonian grains are uncommon; in the Chicontepec Formation, they are rare (Fig. 6). A potential source of these grains lies in peri-Gondwanan terranes that constitute a large part of the suture belt between Laurentia and

Gondwana. The dominant component of ~471 Ma matches the ages of the Esperanza and Palo Liso granitoids of the Acatlán Complex (e.g. Elías-Herrera et al., 2007; Miller et al., 2007; Ortega-Obregón et al., 2009), as well as granite ages of the Taconic orogen, present in the peri-

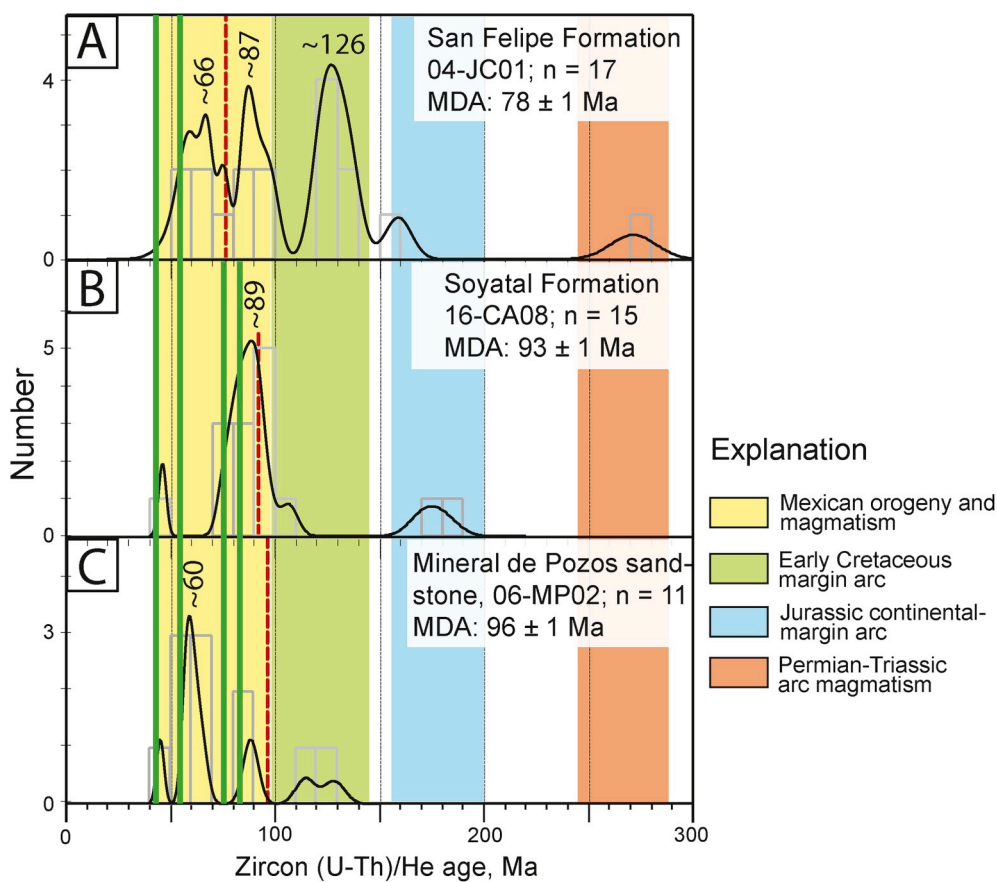


Fig. 9. Probability density plot of ZHe ages from the three samples of central MFTB; n = number of analyses. (A) Multiple age modes in San Felipe Formation indicate only partial resetting of He during burial. (B) Nearly congruent Soyatal ZHe and MDA ages indicate rapid burial and subsequent exhumation of the unit. (C) Strong modal age at ~60 Ma indicates resetting of He in Mineral de Pozos sandstone in interior part of fold-thrust belt prior to exhumation in early Paleocene. Green bars represent illite deformation ages from Fitz-Díaz et al. (2014). Dashed red lines indicate MDA of each sample. Histogram bins equal 10 m.y. (For interpretation of the references to color in this figure legend, the reader is referred to the Web version of this article.)

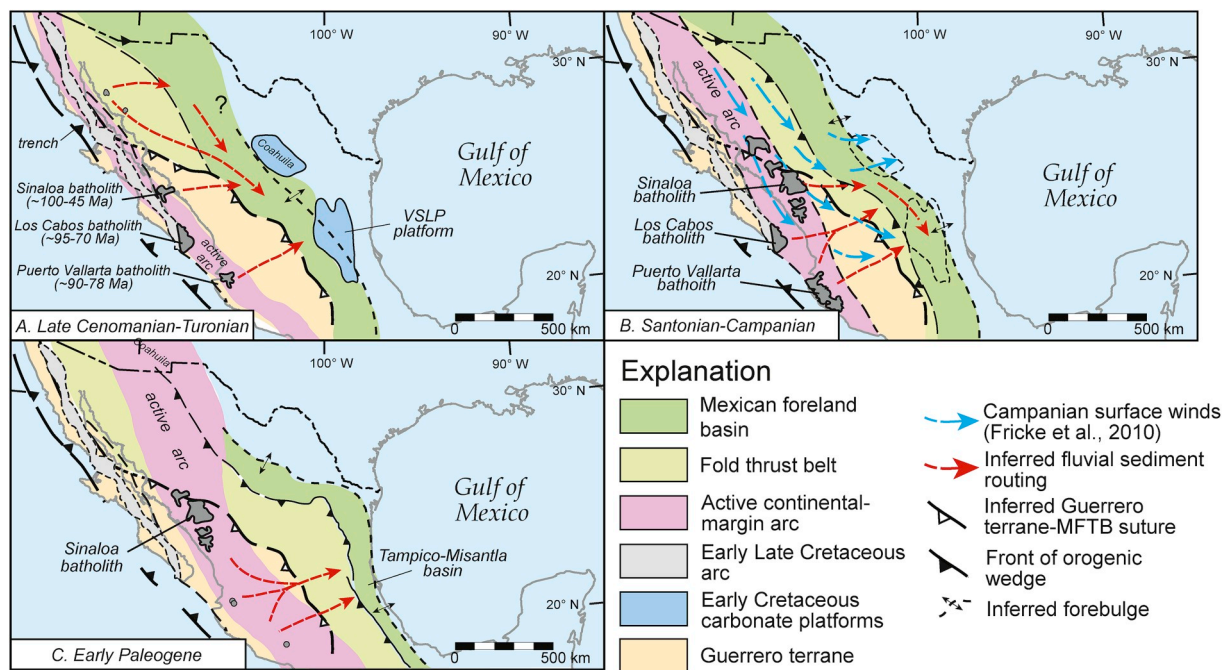


Fig. 10. Paleogeography and inferred sediment-transport routes of evolving foreland basin during Cenomanian-early Paleogene time (Fricke et al., 2010).

Gondwanan terranes that flank Laurentia (Thomas, 2011). An additional potential peri-Gondwanan source is a metapelite of the Jocote unit exposed in southern Chiapas, which is dominated by late Mesoproterozoic grains (~1.2 and 1.0 Ga), and a notable number of early Mesoproterozoic (~1.7–1.5 Ga), Ordovician-Silurian (~480–420 Ma) and Devonian grains (~410–360 Ma) (e.g., Weber et al., 2008; González-Guzmán et al., 2016). Devonian grains constitute a rare component, which is mostly present in sample 08-MP04 of the Mineral de Pozos sandstone.

Permian-Triassic grains (285–220 Ma) are a subordinate component in most of the analyzed samples, possibly originally derived from intrusive units of the Permian-Triassic arc of eastern Mexico (e.g., Torres et al., 1999; Dickinson and Lawton, 2001). Mesozoic arc sources recorded by Middle Jurassic-Paleogene grains (180–60 Ma) constitute the bulk of grains analyzed in sandstones of central MFTB. These grains form a continuous range of ages that overlap at 2σ error. Jurassic grains are a minor age component and suggest a source in volcano-sedimentary rocks such as the Nazas Formation, which has been alternatively interpreted as the record of a continental magmatic arc (Bartolini et al., 2003; Lawton and Molina-Garza, 2014) or of intraplate magmatism and sedimentation during attenuation of continental lithosphere in the backarc region of a coeval continental-margin arc (Martini and Ortega-Gutiérrez, 2018). Grains with ages between ~150 Ma and ~123 Ma, with a prominent ~125 Ma mode (Fig. 5) were probably derived from igneous rocks developed within the Guerrero terrane prior to its accretion with what is now eastern Mexico. This hypothesis is supported by the MDS map, which suggests that the Jurassic grains have a strong similarity with Jurassic granitoids of the Guerrero terrane (e.g., Centeno-García et al., 2011) (Fig. 7). Alternatively, these grains could derive from Late Jurassic felsitic volcanic rocks that were emplaced within the Arperos basin (Martini et al., 2011) and uplifted during Early Cretaceous time (Fitz-Díaz et al., 2018). This source could explain the abundance of felsitic volcanic lithic grains in sandstones from the Tolimán-Tamazunchale transect as well, so these rocks are also a potential source for Jurassic grains.

The early Late Cretaceous relative maximum of the curve (~95–97 Ma), which is dominant in all Mineral de Pozos samples and a Soyatal sample, and Late Cretaceous-Paleogene ages (~85–62 Ma) in the San Felipe and Chicontepec samples, matches well with magmatic

ages reported for the western Mexican continental margin, where they form a continuous batholithic belt between Sonora and Jalisco (Fig. 1). Available U-Pb ages of volcanic and plutonic rocks of the western Mexican magmatic arc (e.g., Kimbrough et al., 2001; McDowell et al., 2001; Henry et al., 2003; Ortega-Rivera, 2003; Ramos-Velázquez et al., 2008; Hildebrand and Whalen, 2014; Todd et al., 2014; Duque-Trujillo et al., 2015; González-León et al., 2017) correspond with DZ U-Pb ages reported here. Framework grains in sandstone samples indicate that most of the sediment was derived from felsic volcanic rocks (Table 2). Felsic to intermediate intrusive rocks are exposed in the Sonora batholith (McDowell et al., 2001; Valencia-Moreno et al., 2001), the Sinaloa batholith (Henry et al., 2003), and the Los Cabos batholith (Aranda-Gómez and Pérez-Venzor, 1989; Kimbrough et al., 2002). We suggest that the volcanic cover of these batholiths was the major source of detritus to the foreland basin.

A quantitative comparison of the distribution of DZ U-Pb ages of the transect samples and potential age sources has been made through the use of a multidimensional scaling (MDS) plot, which uses Kolmogorov-Smirnov D-values as a nonparametric similarity-dissimilarity estimator (e.g., Vermeesch, 2018; Ibañez-Mejía et al., 2018). Results suggest that transect sandstones constitute a closely related set of U-Pb ages (Fig. 7). Two Mineral de Pozos sandstone samples (06-MP02 and 08-MP04) are spatially related to the samples of the Soyatal Formation (16-CA08 and 18-CA10) and these in turn are closely related to the San Felipe Formation sample (04-JC01). The Chicontepec Formation is more distantly linked to the rest of the transect samples, as is Mineral de Pozos sample MP-06. Our petrographic data also indicate a similar grouping of Mineral de Pozos-Soyatal samples, with the Chicontepec sample being compositionally dissimilar (Fig. 4). Geochronological data and the MDS analysis reveal low similarity of the transect samples with Jurassic sedimentary rocks of northwestern Mexico (e.g., Lily, González-León et al., 2009) and the southwestern U.S. (e.g., Ali Molina rhyolite, Haxel et al., 2005) (Fig. 7). Jurassic grains in the Chicontepec Formation were likely derived directly from rocks present in central Mexico, possibly from the Nazas Formation, as suggested by the presence in all samples of zircon grains with ages distributed between ~175 and 150 Ma and the rarity of Proterozoic grains (Fig. 6). Sandstone composition and paleotransport directions measured in the Chicontepec Formation suggest important detrital sources in carbonate rocks of the MFTB directly west

Table 4
U-Pb Detrital-zircon age components of sandstones in central Mexican foreland basin and inferred sources.

Age Group	Age Range (Ma)	Maximums relative of the PDF ^a curve (Ma)	n	% of Total	Inferred Ultimate Source	References
Paleoproterozoic	~1750–1600		4		Basement and sedimentary rocks of SW United States and NW Mexico or South American Gondwana	Iriondo et al. (2004) and refs therein; Barth and Wooden (2006)
Mesoproterozoic-Neoproterozoic	~1230–920	~1000	10		Basement rocks of eastern Mexico (Oaxaquia) or Triassic sedimentary rocks W Mexico	Lawlor et al. (1999); Keppie et al. (2003); Solari et al. (2003; 2004); Barboza-Gudiño et al. (2010)
Early Paleozoic	~490–420	~471	8		Acatlán complex of SW Mexico or peri-Gondwanan terranes	Elias-Herrera et al. (2007); Miller et al. (2007); Ortega-Obregón et al. (2009); Thomas (2011); Weber et al. (2008); González-Guzmán et al. (2016)
Middle Devonian Permian-Triassic	~405–380 ~285–220	~381 ~257	3 8		Peri-Gondwanan terranes Permian-Triassic plutons of E Mexico (via Triassic basement of Guerrero)	Weber et al. (2008); González-Guzmán et al. (2016) Torres et al. (1999); Barboza-Gudiño et al. (2010); Centeno-García et al. (2011); Ortega-Flores et al. (2014)
Jurassic-Paleogene	~180–60	~161, 125, 116, 96, 85, 81, 64	48		Cordilleran arc on Pacific margin of Mexico; uplifted Upper Cretaceous strata of Mexican foreland basin; Middle Jurassic volcanosedimentary rocks of Nazas Formation; Late Jurassic felsitic volcanic rocks emplaced within Arperos basin and their equivalents	Kimbrough et al. (2001); McDowell et al. (2001); Henry et al. (2003); Ramos-Velázquez et al. (2008); Martini et al. (2011); Hildebrand and Whalen (2014); Lawton and Molina-Garza (2014); Todd et al. (2014); Duque-Trujillo et al. (2015); González-León et al. (2017); Juárez-Arriaga et al. (2019)

^a PDF: Probability density function.

of the Tampico-Misantla basin (Bitter, 1993; González-Díaz et al., 2017).

Sample MP-06 (Mineral de Pozos sandstone) has an apparently discrepant position on the MDS plot, which can be explained based on its similarity with rocks of the Guerrero terrane (e.g., Centeno-García et al., 2011) and western Mexican magmatic arc, particularly with the Sinaloa batholith (e.g., Duque-Trujillo et al., 2015). Samples of the Mineral de Pozos sandstone, including the oldest sandstone analyzed (MP-06, MDA = ~94 Ma, late Cenomanian), are rich in sedimentary and volcanic lithic grains (Fig. 4), indicating important sources in sedimentary and volcanic rocks.

During the late Cenomanian, prior to Neogene translation of the Baja California Peninsula, the Sinaloa batholith and the Guerrero terrane were located directly west of the foreland basin (e.g., Fletcher et al., 2007), as were Upper Cretaceous strata of Guerrero, including red beds of the Coalcoman, Estapilla, and Neixpa formations (Centeno-García et al., 2011), suggesting that river catchments drained eastward from the nearby part of the magmatic arc to the basin. This interpretation rests on the abundance of volcanic and sedimentary lithic grains in the Mineral de Pozos and Soyatal samples. Additionally, dominant Early and Late Cretaceous zircon grain ages in sandstones of the transect indicate derivation of sediment from the Guerrero terrane.

5.2. Sources of sediment in the Mexican foreland basin

Continuous overlapping grain ages at 2σ error from the Middle Jurassic to Paleocene (Fig. 6) and abundant volcanic lithic grains in litharenites (Fig. 4) indicate that western volcanic arc sources constituted an important source of igneous detritus during shortening in the fold-thrust belt from Late Cretaceous to early Paleogene time (Fig. 10). The DZ data provide evidence for two intervals of magmatism of the western Mexican magmatic arc, which was a topographic high that flanked the Mexican foreland basin during Late Cretaceous time. The first event, recorded in the Mineral de Pozos sandstone and correlative Cenomanian-Turonian strata of Mexican foreland basin (Juárez-Arriaga et al., 2019) is recognized by abundant Jurassic-early Late Cretaceous zircon grains (Fig. 6). Metamorphic lithic grains present only in the Mineral de Pozos sandstones were likely derived from basement of the Guerrero terrane (e.g., Juárez-Arriaga et al., 2019). The second magmatic event along the western Mexican margin is recorded in younger foreland basin strata, the Soyatal, San Felipe, and Chicontepec samples. Proterozoic and Paleozoic grains were likely recycled from older strata of the Mexican foreland basin, which were uplifted by advance of the thrust wedge (Juárez-Arriaga et al., 2019).

Age components and carbonate lithic grains in the Paleogene Chicontepec turbidites are interpreted as a combination of recycling of age components present in strata of the older foreland successions and erosion of carbonate strata from the thrust belt (Fig. 10). For example, Jurassic and Cretaceous grain ages common in Mineral de Pozos are present but subordinate in the Soyatal and Chicontepec samples. Grain ages (~105–85 Ma) common in the Soyatal Formation are also present in Chicontepec, suggesting recycling of Soyatal strata into the younger foreland. Exhumation and erosion of Lower Cretaceous and lower Upper Cretaceous limestones in the thrust belt to yield sediment for Chicontepec turbidites is supported by abundance of shallow skeletal fossil fragments (e.g., echinoid spines and plates, miliolids) and extra-basinal carbonate lithic grains. Accordingly, ternary diagrams indicate a recycled orogen provenance for the Chicontepec sample (Fig. 4).

5.3. ZHe cooling ages and deformation events

Each cluster of ZHe ages is interpreted as a single exhumation event of sedimentary source rocks in the fold-thrust belt (Fig. 8). Note that Mineral de Pozos sandstone was most strongly affected by burial after deposition, indicated by more complete reserping of ZHe ages to Cretaceous ages. Sample (06-MP02) comes from the older, innermost

portion of the MFTB. The Soyatal sample (16-CA08) has an intermediate position in the MFTB and reflects near-total resetting of the source exhumation ages by deep burial, but preserves the exhumation time by thrusting in the hinterland that yielded sediment to the Mexican foreland basin. The San Felipe sample (04-JC01) is the outermost in the MFTB; this sample displays ZHe ages that predate its depositional age, which suggests that these grains were least affected by burial after deposition. Two of the three significant cooling events indicated by the distribution of nonvolcanic ZHe ages broadly correspond to deformational pulses previously interpreted from $^{40}\text{Ar}/^{39}\text{Ar}$ illite and AFT ages along structural transect A-A' (e.g., Fitz-Díaz et al., 2014; Guerrero-Paz et al., accepted); however, the oldest ZHe cooling age cluster A (~136–120 Ma), recorded on the San Felipe Formation (Fig. 9A), is difficult to assign to a particular uplift event and may represent cooling of rocks in the Guerrero terrane following intrusion of arc plutons there. Alternatively, these cooling ages may be the result of an extension process. This age range coincides with extension in the arc/back-arc region occurred in the western edge of Mexico during Berriasian-Barremian time (Centeno et al., 2008; Martini et al., 2011). In a rift setting, basement rocks could have been exhumed along major normal faults to yield Early Cretaceous cooling ages, and a subsequent source of sediment for early Late Cretaceous rocks of the MFB.

Latest Early Cretaceous to Late Cretaceous ZHe ages cluster B (~102–80 Ma) as a whole span deformation events previously documented in the MFTB. The oldest event, related to thrust movement near Toluimán, previously estimated at 85.5 ± 1.5 Ma from an illite $^{40}\text{Ar}/^{39}\text{Ar}$ age (Fitz-Díaz et al., 2014), is approximately concordant with eleven zircons having ZHe ages between ~91 and 85 Ma. The following event, interpreted from K-Ar illite-mica ages indicating movement of ~80–75 Ma on the El Doctor fault zone near San Joaquín (Garduño-Martínez et al., 2015, Fig. 2) is overlapped by four grains with DZHe ages ranging ~80–75 Ma. This event matches repeated uplift and erosion from ~80 to 75 Ma reported in the western part of the A-A' transect (Guerrero-Paz et al., accepted). The implication is that there were uplift events that produced partial or total resetting during exhumation events of Turonian-Santonian and Campanian age.

Cluster C, with ZHe ages in the range ~66–56 Ma restricted to the Mineral de Pozos sandstone, likely records exhumation-related cooling of the western, interior part of the fold-thrust belt during the early Paleocene. These ZHe ages could represent exhumation by out-of-sequence hinterland thrusts; however, time-equivalent thrusting on the east flank of the Valles-San Luis Potosí platform, near the eastern end of the structural traverse, has been estimated at 64 ± 2 Ma on the basis of an illite $^{40}\text{Ar}/^{39}\text{Ar}$ age (Fig. 2; Fitz-Díaz et al., 2014). The combination of a roughly equivalent interior exhumation related cooling and frontal deformation ages thus suggests that coeval deformation took place across the width of the orogenic wedge rather than simply by interior exhumation by uplift of out-of-sequence interior thrust sheets. Orogenic uplift is substantiated by the age of the synorogenic turbidites near the base of the Chicotepec Formation, with a maximum depositional age of 63 ± 1 Ma (Table 3) and a sediment source in carbonate units of the thrust wedge.

5.4. Cooling age interpretation and uplift evolution of central Mexican fault-thrust belt

Recent stratigraphic and structural investigations in the central MFTB reveal that shortening deformation was coeval with deposition of foreland-basin strata (e.g., Suter, 1987; Fitz-Díaz et al., 2011, 2012; Lawton et al., 2016; Vásquez-Serrano et al., 2018; Juárez-Arriaga et al., 2019). However, there has previously been no combined set of provenance data and deformation ages to better understand the history of deformation and sediment dispersal patterns in the central Mexican fold-thrust belt during Late Cretaceous-Eocene time. Zircon (U-Th)/He data and MDA of A-A' section units shed light on postdepositional burial of foreland strata and their subsequent exhumation in central

Mexico. A plot of the ZHe age probability densities against the direct $^{39}\text{Ar}/^{40}\text{Ar}$ illite ages of individual structures in the fold-thrust belt (Fitz-Díaz et al., 2014) reveals that deformational pulses coincide with exhumation of grains that were subsequently deposited units of the Toluimán-Tamazunchale transect (Fig. 9).

The bulk of the cooling ages of ~66–56 Ma in the Mineral de Pozos sandstone sample is younger than the inferred depositional age and suggests sufficient burial after deposition to result in partial or total He loss. This age range includes the MDA (63 ± 1 Ma) estimated for the Chicotepec Formation. Our combined petrographic and U-Pb data indicate that exhumation of the MFTB resulted in direct transfer of sediment from Lower Cretaceous and earliest Upper Cretaceous limestones in the frontal part of the fold-thrust belt to the Tampico-Misantla basin. This idea is further supported by two independent data sets: 1) Biostratigraphic data indicate that the Campanian-Maastrichtian nanofossils derive from the erosion of the Méndez Formation (located directly on the western flank of the Chicotepec Formation) during the eastward advance of the fold-thrust deformation (González-Díaz et al., 2017); and 2) thrust deformation at the eastern flank of the Valles San Luis Potosí platform on the basis of an early Paleocene illite $^{40}\text{Ar}/^{39}\text{Ar}$ age (Fitz-Díaz et al., 2014) is time-equivalent to MDA from the basal part Chicotepec Formation (Table 3).

In the Soyatal Formation sample, the dominant age mode of the ZHe ages (~80–99 Ma) overlaps the MDA of 93 ± 1 Ma (Fig. 9B). The old DZ U-Pb ages preclude derivation from an active arc and instead suggest total resetting of the exhumation ages of source sedimentary rocks by the combined processes of depositional burial and tectonic stacking in the fault and thrust belt. Importantly, the overlap of the inferred depositional and cooling ages in the Soyatal Formation indicates that thrust sheets within the adjacent culmination of the Toliman sequences above the Higuierillas thrust (Fig. 2) were quickly exhumed and yielded sediment to the foreland.

In the San Felipe Formation sample, most He ages cluster and are within error of the maximum depositional age derived from the U-Pb analyses. We infer that the He system in most zircon grains was partially reset, consistent with derivation from the adjacent Jiliapan thrust sheet, which exhumed the deepest rocks in the area. Grains potentially derived from the Jurassic or Permian-Triassic arcs in Mexico did not preserve their original amounts of He, yielding younger ages; however, most ZHe ages are younger than the U-Pb ages and form poorly defined populations. The lack of clearly defined ZHe age clusters in the San Felipe sample suggests partial He resetting; therefore, the meaning of these data remain unclear.

Based on data presented here, we can predict times of sediment production in central Mexico during Late Cretaceous-Eocene time. The coincidence of deformation events defined from illite $^{40}\text{Ar}/^{39}\text{Ar}$ ages (e.g., Fitz-Díaz et al., 2014) and AFT ages and exhumation ages (e.g., Guerrero-Paz et al., accepted) determined from DZHe analysis independently confirms the ages of the pulses of deformation, and suggests that dated deformation events contributed to episodes of exhumation in the fold-thrust belt. According to DZ U-Pb ages discussed here, the oldest strata are in the western part of the Mexican foreland basin and successive deposits become progressively younger to east. Overall, ZHe ages of those strata are controlled by their relative positions in the fold-thrust belt. Thus, the oldest cooling ages are abundant in the eastern part of the fold-thrust belt and younger cooling ages are dominant to the west.

6. Conclusions

A combination of petrographic and statistical data, and DZ U-Pb and ZHe ages indicate sediment sources in the Guerrero terrane and a long-lived magmatic arc that lay to the west of the Mexican foreland basin. The age components delivered to the sediment varied in proportion during evolution of the foreland basin. Proterozoic and Jurassic grains, common age components in the initial deposits of the central foreland

basin, are less abundant in Turonian and younger foreland basin strata, whose sediment sources were mostly local. In contrast, DZ U-Pb ages spanning the Middle Jurassic to early Paleogene indicate an important and continued magmatic arc source along the western Mexico margin. These younger grains consistently constituted the dominant age group during shortening in the fold-thrust belt and foreland basin history.

On the basis of ZHe age modes and deformational pulses previously documented during growth of the fold-thrust belt in central Mexico, we interpret each cluster of ZHe ages along of the Tolimán-Tamazunchale transect as a single exhumation event of sedimentary source rocks in the fold-thrust belt. The oldest recorded event, represented by Early Cretaceous ZHe ages (~136-120 Ma), predates the history of the Mexican fold-thrust belt and may represent cooling of rocks following intrusion of Guerrero arc plutons or may have resulted from an extensional event before Late Cretaceous-early Paleogene shortening. The Late Cretaceous ZHe ages (~102-80 Ma) represent the first cooling event related to thrust movement of the Mexican fold-thrust belt near Tolimán, as well as movement of the El Doctor fault thrust. Finally, the younger ZHe ages (~66-56 Ma), recorded in both interior and exterior parts of the fold-thrust belt, likely indicate exhumation-related cooling across the width of the orogenic wedge during the early Paleocene.

This event is equivalent to the calculated MDA of the lower part of the Chicontepec Formation and links exhumation to time-equivalent deposition; nevertheless, the DZ U-Pb ages of the Chicontepec Formation do not clearly define sediment provenance sources. Instead, sandstone petrography demonstrates that lithic carbonate grains constitute the dominant component of the framework and further indicates exhumation and erosion of Lower Cretaceous and earliest Upper Cretaceous limestones in the frontal part of the Mexican fold-thrust belt. The results of this study demonstrate that double dating of zircon grains to yield both U-Pb and DZHe ages, in combination with petrographic data from the Mexican fold-thrust belt, can constrain times of sediment production in fold and thrust belts.

Acknowledgments

This study was funded by Consejo Nacional de Ciencia y Tecnología (CONACyT) grant CB-240932 to T.F. Lawton/L. Solari. Additional support was provided by Jim Pindell of Tectonic Analysis Ltd. and the Coordinación de Estudios de Posgrado from Universidad Nacional Autónoma de México. Juárez-Arriaga thanks CONACyT for a PhD scholarship. We thank Lisa Stockli, Edna Rodríguez-Calzado and Rudra Chatterjee of the Geo- and Thermochronometry Laboratory, Jackson School of Geosciences, University of Texas at Austin for isotopic analyses and data reduction. We also thank Luis Manuel Casiano Casiano and Teresita de Jesús Pérez Cruz for library assistance. The biostratigraphic samples were analyzed by Ron Morin, Morin Biostratigraphic Studies.

Appendix A. Supplementary data

Supplementary data to this article can be found online at <https://doi.org/10.1016/j.jsames.2019.102264>.

References

- Alzaga-Ruiz, H., Lopez, M., Roure, R., Séranne, M., 2009. Interactions between the laramide foreland and the passive margin of the Gulf of Mexico: tectonics and sedimentation in the Golden Lane area, Veracruz state, Mexico. *Mar. Pet. Geol.* 26, 951–973.
- Aranda-Gómez, J.J., Pérez-Venzor, J.A., 1989. Estratigrafía del complejo cristalino de la región de Todos Santos, Estado de Baja California Sur. *Revista de la Universidad Nacional Autónoma de México*. 8. Instituto de Geología, pp. 149–170.
- Barboza-Gudiño, J.R., Zavala-Monsiváis, A., Venegas-Rodríguez, G., Barajas-Nigoche, L.D., 2010. Late Triassic stratigraphy and facies from northeastern Mexico: tectonic setting and provenance. *Geosphere* 6, 621–640.
- Barth, A.P., Wooden, J.L., 2006. Timing of magmatism following initial convergence at a passive margin, southwestern U.S. Cordillera, and ages of lower crustal magma sources. *J. Geol.* 114, 231–245.
- Bartolini, C., Lang, H., Spell, T., 2003. Geochronology, geochemistry, and tectonic setting of the Mesozoic Nazas arc in north-central Mexico, and its continuation to northern South America. In: Bartolini, C., Buffler, R.T., Blickwede, J.F. (Eds.), *The Circum-Gulf of Mexico and the Caribbean: Hydrocarbon Habitats, Basin Formation and Plate Tectonics*, vol. 79. American Association of Petroleum Geologists Memoir, pp. 427–461.
- Bitter, M.R., 1993. Sedimentation and provenance of Chicontepec sandstones with implications for uplift of the Sierra Madre Oriental and Teziutlan massif, east-central Mexico. In: 13th Annual Research Conference Gulf Coast Section SEPM Foundation, Proceedings, pp. 155–172.
- Campa, M.F., 1985. The Tectonostratigraphic Terranes and the Thrust Belt in Mexican Territory: Proceedings of the Circum-Pacific Terrane Conference. 18. Stanford University Publications in Geological Sciences, pp. 44–46.
- Carrillo, M., Suter, M., 1982. Tectónica de los alrededores de Zimapán, Hidalgo y Querétaro. In: Alcayde, M., de Cserna, Z. (Eds.), *Libro-guía de la excursión geológica a la región de Zimapán y áreas circundantes, estados de Hidalgo y Querétaro*. Sociedad Geológica Mexicana, pp. 1–20.
- Centeno-García, E., Busby, C.J., Busby, M., Gehrels, G.E., 2011. Evolution of the Guerrero composite terrane along the Mexican margin, from extensional fringing arc to contractional continental arc. *Geol. Soc. Am. Bull.* 123, 1776–1797 DOI: 1710.1130/B30057.30051.
- Centeno-García, E., Guerrero-Suastegui, M., Talavera-Mendoza, O., 2008. The Guerrero Composite Terrane of western Mexico: Collision and subsequent rifting in a supra-subduction zone. In: Draut, A., Clift, P.D., Scholl, D.W. (Eds.), *Formation and Applications of the Sedimentary Record in Arc Collision Zones: Geological Society of America Special Paper 436*, pp. 279–308. [https://doi.org/10.1130/2008.2436\(13\)](https://doi.org/10.1130/2008.2436(13)).
- Cohen, K.M., Finney, S.C., Gibbard, P.L., Fan, J.-X., 2013. The ICS international chronostratigraphic chart. *Episodes* 36, 199–204 updated.
- Cossey, S.P.J., 2011. Mass-transport deposits in the upper Paleocene Chicontepec formation, Mexico. In: Shipp, R.C., Weimer, P., Posamentier, H.W. (Eds.), *Mass-transport Deposits in Deepwater Settings*, vol. 96. Society for Sedimentary Geology SEPM Special Publication, pp. 269–277.
- DeCelles, P.G., Coogan, J.C., 2006. Regional structure and kinematic history of the Sevier fold-and-thrust belt, central Utah. *Geol. Soc. Am. Bull.* 118, 841–864.
- DeCelles, P.G., Lawton, T.F., Mitra, G., 1995. Thrust timing, growth of structural culminations, and synorogenic sedimentation in the type Sevier orogenic belt, western United States. *Geology* 23, 699–702.
- Dickinson, W.R., 1970. Interpreting detrital modes of graywacke and arkose. *J. Sediment. Petrol.* 40, 695–707.
- Dickinson, W.R., 1985. Interpreting Provenance relations from detrital modes of sandstones. In: Zuffa, G.G. (Ed.), *Provenance of Arenites*: Boston, D. Reidel Publishing Company, pp. 333–361.
- Dickinson, W.R., Gehrels, G.E., 2009. Use of U–Pb ages of detrital zircons to infer maximum depositional ages of strata: a test against a Colorado Plateau Mesozoic database. *Earth Planet. Sci. Lett.* 288, 115–125.
- Dickinson, W.R., Lawton, T.F., 2001. Carboniferous to Cretaceous assembly and fragmentation of Mexico. *Geol. Soc. Am. Bull.* 113, 1142–1160.
- Duque-Trujillo, J., Ferrari, L., Orozco-Esuivel, T., López-Martínez, M., Lonsdale, P., Bryan, S.E., Kluesner, J., Piñero-Lajas, D., Solari, L., 2015. Timing of rifting in the southern Gulf of California and its conjugate margins: insights from the plutonic record. *Geol. Soc. Am. Bull.* 127, 702–736.
- Eguiluz, S., Aranda-Gómez, M., Marret, R., 2000. Tectónica de la Sierra Madre Oriental, México. *Bol. Soc. Geol. Mex.* 53, 1–26.
- Elías-Herrera, M., Macías-Romo, C., Ortega-Gutiérrez, F., Reyes, S.M., Sánchez-Zavala, J.L., Iriondo, A., 2007. Conflicting stratigraphic and geochronological data from the Acatlán Complex, “Ordovician” granites intrude metamorphic and sedimentary rocks of Devonian–Permian age. In: AGU 88 (23), EOS Transactions, *Jt. Assem. Suppl.*, Abstract T41A-12.
- Fitz-Díaz, E., Hudleston, P., Tolson, G., 2011. Comparison of tectonic styles in the Mexican and Canadian Rocky Mountain fold-thrust belt. In: Poblet, J., Lisle, R.J. (Eds.), *Kinematic Evolution and Structural Styles of Fold-And-Thrust Belts*, vol. 349. Geological Society of London, Special Publications, pp. 149–167.
- Fitz-Díaz, E., Hudleston, P., Tolson, G., van der Pluijm, B., 2014. Progressive, episodic deformation in the Mexican Fold-Thrust Belt (central Mexico): evidence from isotopic dating of folds and faults. *Int. Geol. Rev.* 56, 734–755.
- Fitz-Díaz, E., Lawton, T.F., Juárez-Arriaga, E., Chávez-Cabello, G., 2018. Late Cretaceous–Paleogene Mexican orogen: structure, basin development, and tectonics. *Earth Sci. Rev.* 183, 56–84. <https://doi.org/10.1016/j.earscirev.2017.03.002>.
- Fitz-Díaz, E., Tolson, G., Hudleston, P., Bolaños-Rodríguez, D., Ortega-Flores, B., Vásquez Serrano, A., 2012. The role of folding in the development of the Mexican fold-and-thrust belt. *Geosphere* 8, 931–949.
- Fletcher, J.M., Grove, M., Kimbrough, D., Lovera, O., Gehrels, G.E., 2007. Ridge-trench interactions and the Neogene tectonic evolution of the Magdalena shelf and southern Gulf of California: insights from detrital zircon U-Pb ages from the Magdalena fan and adjacent areas. *Geol. Soc. Am. Bull.* 119, 1313–1336.
- Folk, R.L., 1974. *Petrology of Sedimentary Rocks*: Austin, second ed. Hemphill Publishing Company, Texas, pp. 182.
- Fricke, H.C., Foreman, B.Z., Sewall, J.O., 2010. Integrated climate model-oxygen isotope evidence for a North American monsoon during the Late Cretaceous. *Earth Planet. Sci. Lett.* 289, 11–21. <https://doi.org/10.1016/j.epsl.2009.10.018>.
- Garduño-Martínez, D.E., Puig, T.P., Solé, J., Martini, M., Alcalá-Martínez, J.R., 2015. K-Ar illite-mica age constraints on the formation and reactivation history of the El Doctor fault zone, central Mexico. *Rev. Mex. Ciencias Geol.* 32, 306–322.
- Goldhammer, R.K., 1999. Mesozoic sequence stratigraphy and paleogeographic evolution of northeast Mexico. In: Bartolini, C., Wilson, J.L., Lawton, T.F. (Eds.), *Mesozoic*

- Sedimentary and Tectonic History of North-Central Mexico, vol. 340. Geological Society of America Special Paper, Boulder, Colorado, pp. 1–58.
- González-Díaz, M.G., Lawton, T.F., Juárez-Arriaga, E., 2017. Estratigrafía, sedimentología y procedencia de la Formación Chicontepec (Paleógeno) en el norte de la cuenca Tampico-Misantla, México. *GEOS Unión Geofísica Mexicana* 37, 135–136.
- González-Guzmán, R., Weber, B., Manjarrez-Juárez, R., Cisneros de León, A., Hecht, L., Herguera-García, J.C., 2016. Provenance, age constraints and metamorphism of Ediacaran metasedimentary rocks from the El Triunfo Complex (SE Chiapas, México): evidence for Rodinia breakup and Iapetus active margin. *Int. Geol. Rev.* 58, 2065–2091. <https://doi.org/10.1080/00206814.2016.1207208>.
- González-León, C.M., Solari, L., Valencia-Moreno, M., Rascon Heimpe, M.A., Solé, J., González Becuar, E., Lozano Santacruz, R., Pérez Arvizo, O., 2017. Late Cretaceous to early Eocene magmatic evolution of the Laramide arc in the Nacozari quadrangle, northeastern Sonora, Mexico and its regional implications. *Ore Geol. Rev.* 81, 1137–1157.
- González-León, C.M., Valencia, V.A., Lawton, T.F., Amato, J.M., Gehrels, G.E., Leggett, W.J., Montijo-Contreras, O., Fernández, M.A., 2009. The lower Mesozoic record of detrital zircon U-Pb geochronology of Sonora, México, and its paleogeographic implications. *Rev. Mex. Ciencias Geol.* 26, 301–314.
- Guerrero-Paz, D.N., Abdullin, F., Ortega-Flores, B., Solari, L., Ortega-Obregón, C., Juárez-Arriaga, E., Accepted. Late cretaceous to Eocene denudation history of the Tolimán area, southern Sierra Madre Oriental, central Mexico. In: Martens, U., Molina, R., and Pindell, J. (Eds.), *Southern and Central Mexico: Basement Framework, Tectonic Evolution, and Provenance of Mesozoic-Cenozoic Basins*, Geological Society of America, Special Paper.
- Hart, N.R., 2015. Ms Sc. Thesis In: Temporal Constraints on Progressive Rifting of a Hyper-Extended Continental Margin Using Bedrock and Detrital Zircon (U-Th)/(Pb-He) Dating, Mauléon Basin, Western Pyrenees. The University of Texas at Austin.
- Hart, N.R., Stockli, D.F., Hayman, W., 2016. Provenance evolution during progressive rifting and hyperextension using bedrock and detrital zircon U-Pb geochronology, Mauléon Basin, western Pyrenees. *Geosphere* 12, 1–21.
- Haxel, G.B., Wright, J.E., Riggs, N.R., Tosdal, R.M., May, D.J., 2005. Middle Jurassic Topawa Group, Baboquivari Mountains, South-Central Arizona: Volcanic and Sedimentary Record of Deep Basins within the Jurassic Magmatic Arc, vol. 393. Geological Society of America, Special Paper, Boulder, Colorado, pp. 329–357.
- Henry, C.D., McDowell, F.W., Silver, L.T., 2003. Geology and geochronology of granitic batholithic complex, Sinaloa, México: implications for Cordilleran magmatism and tectonics. In: Johnson, S.E., Paterson, S.R., Fletcher, J.M., Girty, G.H., Kimbrough, D.L., Martín-Barajas, A. (Eds.), *Tectonic Evolution of Northwestern México and the Southwestern USA*, vol. 374. Geological Society of America Special Paper, pp. 237–273.
- Hernández-Jauregui, R., 1997. Sedimentación sintectónica de la Formación Soyatal (Turoniano medio-Campaniano) y modelado cinemático de la cuenca de flexura de Maconí, Querétaro. Masters thesis. Instituto Politécnico Nacional.
- Hildebrand, R.S., Whalen, J.B., 2014. arc and slab-failure magmatism in cordilleran batholiths II – the cretaceous Peninsular ranges batholith of southern and Baja California. *Geosci. Can.* 41, 399–458.
- Ibañez-Mejía, M., Pullen, A., Pepper, M., Urbani, F., Ghoshal, G., Ibañez-Mejía, J.C., 2018. Use and abuse of detrital zircon U-Pb geochronology—a case from the Río Orinoco delta, eastern Venezuela. *Geology* 46, 1019–1022. <https://doi.org/10.1130/G45596.1>.
- Ingersoll, R.V., Bullard, T.F., Ford, R.I., Grimm, J.P., Pickle, J.D., Sares, S.W., 1984. The effect of grain size on detrital modes: a test of the Gazi-Dickinson point-counting method. *J. Sediment. Petrol.* 54, 103–116.
- Ingersoll, R.V., Cavazza, W., Graham, S.A., Participants, I.U.G.F.S., 1987. Provenance of impure calcilithites in the Laramide foreland of southwestern Montana. *J. Sediment. Petrol.* 57, 995–1003.
- Ingersoll, R.V., Sucek, C.A., 1979. Petrology and provenance of Neogene sand from Nicobar and Bengal fans, DSDP sites 211 and 218. *J. Sediment. Petrol.* 49, 1217–1228.
- Iriondo, A., Premo, W.R., Martínez-Torres, L.M., Budahn, J.R., Atkinson Jr., W.W., Siems, D.F., Guarás-González, B., 2004. Isotopic, geochemical, and temporal characterization of Proterozoic basement rocks in the Quitovac region, northwestern Sonora, México: implications for the reconstruction of the southwestern margin of Laurentia. *Geol. Soc. Am. Bull.* 116, 154–170.
- Johnson, S.E., Tate, M.C., Fanning, C.M., 1999. New geologic mapping and SHRIMP U-Pb zircon data in the Peninsular Ranges batholith, Baja California, Mexico: evidence for a suture? *Geology* 27, 743–746.
- Juárez-Arriaga, E., Lawton, T.F., Ocampo-Díaz, Y.Z.E., Stockli, D.F., Solari, L., 2019. Sediment provenance, sediment-dispersal systems, and major arc-magmatic events recorded in the Mexican foreland basin, north-central and northeastern Mexico. *Int. Geol. Rev.* <https://doi.org/10.1080/00206814.2019.1581848>.
- Keppie, J.D., Dostal, J., Cameron, K.L., Solari, L.A., Ortega-Gutiérrez, F., Lopez, R., 2003. Geochronology and geochemistry of Grenvillian igneous suites in the northern Oaxacan Complex, southern Mexico: tectonic implications. *Precambrian Res.* 120, 365–389.
- Kimbrough, D.L., Grove, M., Gehrels, G.E., Dorsey, R.J., Howard, K.A., Lovera, O., Aslan, A., House, P.K., Pearthree, P.A., 2015. Detrital zircon U-Pb provenance of the Colorado River: a 5 m.y. record of incision into cover strata overlying the Colorado Plateau and adjacent regions. *Geosphere* 11, 1719–1748.
- Kimbrough, D.L., Gastil, R.G., Garrow, P.K., Grove, M., Aranda-Gómez, J.J., Perez-Venzor, J.A., Fletcher, J., 2002. A potential correlation of plutonic suites from the Los Cabos block and Peninsular Ranges batholith. In: VI International Meeting on Geology of the Baja California Peninsula, vol. 9.
- Kimbrough, D.L., Smith, D.P., Mahoney, J.B., Moore, T.E., Gastil, R.G., Ortega-Rivera, M.A., Fanning, C.M., 2001. Forearc basin sedimentary response to rapid Late Cretaceous batholith emplacement in the Peninsular Ranges of southern and Baja California. *Geology* 29, 491–494.
- Kiyokawa, M., 1981. Geological Survey of the Pachuca-Zimapan Area, Central Mexico, Professional Report: Metal Agency of Japan and Mineral Resources Council. pp. 194 United States Mexicans.
- Lawlor, P.J., Ortega-Gutierrez, F., Cameron, K.L., Ochoa-Camarillo, H., Lopez, R., Sampson, D.E., 1999. U-Pb geochronology, geochemistry, and provenance of the Grenvillian Huiznopala Gneiss of eastern Mexico. *Precambrian Res.* 94, 73–99.
- Lawton, T.F., Molina-Garza, R.S., 2014. U-Pb geochronology of the type Nazas Formation and superjacent strata, northeast Durango, Mexico: implications of a Jurassic age for continental-arc magmatism in north-central Mexico. *Geol. Soc. Am. Bull.* 126, 1181–1199.
- Lawton, T.F., Juárez-Arriaga, E., Ocampo-Díaz, Y.Z.E., Beltrán-Triviño, A., Martens, U., Stockli, D., 2016. Evolution of Late Cretaceous-Paleogene foreland sediment-dispersal systems of northern and central Mexico. In: 35th Annual GCSSEPM, Foundation Perkins-Rosen Research Conference Programs and Abstracts, pp. 216–233.
- Ludwig, K.R., 2008. ISOPLOT Vers. 4.1: Berkeley Geochronology Center (BGC). February 2019. http://www.bgc.org/isoplot_etc/isoplot.html.
- Martini, M., Ferrari, L., López-Martínez, M., Cerca-Martínez, M., Valencia, V.A., Serrano-Durán, L., 2009. Cretaceous-Eocene magmatism and laramide deformation in southwestern Mexico: No role for terrane accretion. In: Kay, S.M., Ramos, V.A., Dickinson, W.R. (Eds.), *Backbone of the Americas: Shallow Subduction, Plateau Uplift, and Ridge and Terrane Collision*, vol. 204. Geological Society of America Memoir, pp. 151–182.
- Martini, M., Mori, L., Solari, L., Centeno-García, E., 2011. Sandstone provenance of the Arperos basin (Sierra de Guanajuato, central Mexico): late Jurassic-early cretaceous back-arc spreading as the foundation of the Guerrero terrane. *J. Geol.* 119, 597–617.
- Martini, M., Ortega-Gutiérrez, F., 2018. Tectono-stratigraphic evolution of eastern Mexico during the break-up of Pangea: A review. *Earth Sci. Rev.* 183, 38–55.
- Martini, M., Solari, L., López-Martínez, M., 2014. Correlating the Arperos basin from Guanajuato, central Mexico, to Santo Tomás, southern Mexico: implications for the paleogeography and origin of the Guerrero terrane. *Geosphere* 10, 1–17.
- McDowell, F.W., Roldán-Quintana, J., Connelly, J.N., 2001. Duration of late cretaceous-early Tertiary magmatism in east-central Sonora, Mexico. *Geol. Soc. Am. Bull.* 113, 521–531.
- Miller, B.V., Dostal, J., Keppie, J.D., Nance, R.D., Ortega-Rivera, A., Lee, J.K.W., 2007. Ordovician calc-alkaline granitoids in the Acatlán Complex, southern México: geochemical and geochronologic data and implications for the tectonics of the Gondwanan margin of the Rheic Ocean. In: Linnemann, U., Nance, R.D., Kraft, P., Zulauf, G. (Eds.), *The Evolution of the Rheic Ocean: from Avalonian-Cadomian Active Margin to Alleghenian-Variscan Collision*, vol. 423. Geological Society of America Special Paper, pp. 465–475. [https://doi.org/10.1130/2007.2423\(23\)](https://doi.org/10.1130/2007.2423(23)).
- Ocampo-Díaz, Y.Z.E., Pinzon-Sotelo, M.P., Chñavez-Cabello, G., Ramírez-Díaz, A., Martínez-Paco, M., Velasco-Tapia, F., Guerrero-Suastegui, M., Barboza-Gudiño, J.R., 2016. Propuesta nomenclatural y análisis de procedencia de la Formación Concepción del Oro (antes Formación Caracol): implicaciones sobre la evolución tectónica del sur de Norteamérica durante el Cretácico Tardío. *Rev. Mex. Ciencias Geol.* 33, 3–33.
- Omaña-Pulido, M.L., 2012. Ph.D. Thesis In: Bioestratigrafía, Paleocología y Paleobiogeografía del Cretácico Superior con base en foraminíferos de la parte Occidental de la Plataforma Valles-San Luis Potosí, México. Universidad Nacional Autónoma de México.
- Ortega-Flores, B., Solari, L.A., Escalona-Alcázar, F.J., 2016. The Mesozoic successions of western Sierra de Zacatecas, central Mexico: provenance and tectonic implications. *Geol. Mag.* 153, 696–717.
- Ortega-Flores, B., Solari, L.A., Lawton, T.F., Ortega-Obregón, C., 2014. Detrital zircon record of major Middle Triassic-Early Cretaceous provenance shift, Central Mexico: demise of Gondwanan continental fluvial systems and onset of backarc volcanism and sedimentation. *Int. Geol. Rev.* 56, 237–261.
- Ortega-Obregón, C., Keppie, J.D., Murphy, J.B., Lee, J.K.W., Ortega-Rivera, A., 2009. Geology and geochronology of Paleozoic rocks in western Acatlán Complex, southern Mexico: evidence for contiguity across an extruded high-pressure belt and constraints on Paleozoic reconstructions. *Geol. Soc. Am. Bull.* 121, 1678–1694.
- Ortega-Rivera, A., 2003. Geochronological Constraints on the Tectonic History of the Peninsular Ranges Batholith of Alta and Baja California: Tectonic Implications for Western México: Tectonic Evolution of Northwestern Mexico and the Southwestern USA, vol. 374. Geological Society of America Special Paper, Boulder, Colorado, pp. 297–335.
- Pujols, E.J., Leva López, L., Stockli, D.F., Rossi, V.M., Steel, R.J., 2018. New insights into the stratigraphic and structural evolution of the middle Jurassic S. Neuquén basin from detrital zircon (U-Th)/(He-Pb) and apatite (U-Th)/He ages. *Basin Res.* 30, 1–18.
- Ramos-Velázquez, E., Calmus, T., Valencia, V., Iriondo, A., Valencia-Moreno, M., Bellon, H., 2008. U-Pb and 40Ar/39Ar geochronology of the coastal Sonora batholith: new insights on Laramide continental arc magmatism. *Rev. Mex. Ciencias Geol.* 25, 314–333.
- Reiners, P.W., Campbell, I.H., Nicolescu, S., Allen, C.M., Hourigan, J.K., Garver, J.I., Mattinson, J.M., Cowan, D.S., 2005. (U-Th)/(He-Pb) double dating of detrital zircons. *Am. J. Sci.* 305, 259–311.
- Saylor, J.E., Stockli, D.F., Hurton, B.K., Nie, J., Mora, A., 2012. Discriminating rapid exhumation from syndepositional volcanism using detrital zircon double dating: implications for the tectonic history of the Eastern Cordillera, Colombia. *Geol. Soc. Am. Bull.* 124, 762–779.
- Solari, L.A., Keppie, J.D., Ortega-Gutiérrez, F., Cameron, K.L., Lopez, R., Hames, W.E., 2003. 990 and 1100 Ma Grenvillian tectonohermal events in the northern Oaxacan complex, southern Mexico: roots of an orogen. *Tectonophysics* 365, 257–282.
- Solari, L.A., Keppie, J.D., Ortega-Gutiérrez, F., Cameron, K.L., Lopez, R., 2004. ~990 Ma

- peak granulitic metamorphism and amalgamation of Oaxaquia, Mexico: U-Pb zircon geochronological and common Pb isotopic data. *Rev. Mex. Ciencias Geol.* 21, 212–225.
- Suarez, S.E., Brookfield, M.E., Catlos, E.J., Stockli, D.F., 2017. A U-Pb zircon age constraint on the oldest-recorded air-breathing land animal. *PLoS One* 12, e0179262. <https://doi.org/10.1371/journal.pone.0179262>.
- Suter, M., 1980. Tectonics of the External Part of the Sierra Madre Oriental Foreland Thrust-and-fold Belt between Xilitla and the Moctezuma River (Hidalgo and San Luis Potosí States), vol. 4. *Revista del Instituto de Geología*, pp. 19–31.
- Suter, M., 1984. Cordilleran deformation along the eastern edge of the Valles-San Luis Potosí carbonate platform, Sierra Madre Oriental fold-thrust belt, east-central Mexico. *Geol. Soc. Am. Bull.* 95, 1387–1397.
- Suter, M., 1987. Structural traverse across the Sierra Madre Oriental fold-thrust belt in east-central Mexico. *Geol. Soc. Am. Bull.* 98, 249–264.
- Suter, M., 1990. Sheet Tamazunchale 14Q- (5), with Geology of the Tamazunchale Sheet, States of Hidalgo, Queretaro and San Luis Potosí. Universidad Nacional Autónoma de México, Institute of Geology, scale 1: 100,000.
- Tardy, M., Maury, R., 1973. Sobre la presencia de elementos de origen volcánico en las areniscas de los flyschs de edad cretácica superior de los estados de Coahuila y de Zacatecas, México. *Bol. Soc. Geol. Mex.* 34, 5–12.
- Thomas, W.A., 2011. Detrital-zircon geochronology and sedimentary provenance. *Lithosphere* 3, 304–308 DOI: 310.1130/RF.L1001.1131.
- Todd, V.R., Hernandez, J.L., Busch, L.L., 2014. The zoned Ramona plutonic complex: an Early Cretaceous mid- to upper-crustal intrusive sequence, Peninsular Ranges batholith, southern California. In: Morton, D.M., Miller, F.K. (Eds.), *Peninsular Ranges Batholith, Baja California and Southern California*. Geological Society of America Memoir 211, pp. 583–608.
- Torres, R., Ruiz Joaquin, P., Patchett, P.J., Grajales, J.M., 1999. Permo-Triassic continental arc in eastern Mexico: tectonic implications for reconstructions of southern North America. In: Bartolini, C., Wilson, J.L., Lawton, T.F. (Eds.), *Mesozoic Sedimentary and Tectonic History of North-Central Mexico*. Geological Society of America Special Paper 340, pp. 191–196.
- Valencia-Moreno, M., Ruiz, J., Barton, M.D., Patchett, P.J., Zurcher, L., Hodkinson, D.G., Roldan-Quintana, J., 2001. A Chemical and Isotopic Study of the Laramide Granitic Belt of Northwestern México: Identification of the Southern Edge of the North American Precambrian Basement, vol. 113. *Geological Society of America Bulletin*, pp. 1409–1422.
- Vásquez-Serrano, A., Tolson, G., Fitz-Díaz, E., Chávez-Cabello, G., 2018. Influence of pre-tectonic carbonate facies architecture on deformation patterns of syntectonic turbidites, an example from the central Mexican fold-thrust belt. *J. Struct. Geol.* 109, 127–139.
- Vermeesch, P., 2004. How many grains are needed for a provenance study? *Earth Planet. Sci. Lett.* 224, 441–451.
- Vermeesch, P., 2013. Multi-sample comparison of detrital age distributions. *Chem. Geol.* 341, 140–146.
- Vermeesch, P., 2018. Dissimilarity measures in detrital geochronology. *Earth Sci. Rev.* 178, 310–321. <https://doi.org/10.1016/j.earscirev.2017.11.027>.
- Weber, B., Valencia, V.A., Schaaf, P., Pompa-Mera, V., Ruiz, J., 2008. Significance of provenance ages from the Chiapas massif complex (Southeastern Mexico): redefining the Paleozoic basement of the Maya block and its evolution in a peri-Gondwanan realm. *J. Geol.* 116, 619–639. <https://doi.org/10.1086/591994>.
- Wetmore, P.H., Herzig, C., Alsleben, H., Sutherland, M., Schmidt, K.L., Schultz, P.W., Paterson, S.R., 2003. Mesozoic tectonic evolution of the Peninsular ranges of southern and Baja California. In: Johnson, S.E., Paterson, S.R., Fletcher, J.M., Girty, G.H., Kimbrough, D.L., Martin- Barajas, A. (Eds.), *Tectonic Evolution of Northwestern Mexico and the Southwestern USA*, vol. 374. Geological Society of America Special Paper, pp. 93–116.
- Wetmore, P.H., Schmidt, K.L., Paterson, S.R., Herzig, C., 2002. Tectonic implications for the along-strike variation of the Peninsular ranges batholith: southern and Baja California. *Geology* 30, 247–250.
- Wilson, J.L., 1990. Basement structural controls on Mesozoic carbonate facies in north-eastern Mexico – a review. In: Tucker, M.E., Wilson, J.L., Crevello, P.D., Sarg, R., Read, J.F. (Eds.), *Carbonate Platforms. Facies, Sequences and Evolution*, vol. 9. pp. 235–255.
- Wilson, J.R., Ward, W.C., 1993. Early Cretaceous carbonate platforms of northeastern and east-central Mexico. In: Simon, J.A.T., Scott, R.W., Masse, J.P. (Eds.), *Cretaceous Carbonate Platforms: American Association of Petroleum Geologists Memoir*, vol. 56. pp. 35–50.
- Wolfe, M.R., Stockli, D.F., 2010. Zircon (U-Th)/He thermochronometry in the KTB drill hole, Germany, and its implications for bulk diffusion kinetics in zircon. *Earth Planet. Sci. Lett.* 265, 69–82.
- Yonkee, W.A., Weil, A.B., 2015. Tectonic evolution of the Sevier and laramide belts within the North American Cordillera orogenic system. *Earth Sci. Rev.* 150, 531–593. <https://doi.org/10.1016/j.earscirev.2015.08.001>.
- Zuffa, G.G., 1980. Hybrid arenites: their composition and classification. *J. Sediment. Petrol.* 50, 21–29.

Parte IV

Conclusiones

La aplicación de métodos de estratigrafía clásica y petrografía de areniscas junto el fechamiento isotópico de granos de circón, permitió elucidar la relevancia de la deformación del Cretácico Tardío-Paleógeno sobre la evolución de la cuenca de antepaís mexicana, así como un mejor entendimiento de la generación y dispersión de sedimentos en el cinturón de pliegues y cabalgaduras mexicano. Los resultados de esta investigación permiten hacer las siguientes inferencias.

1. La evolución de la CAM está asociada al evento de acortamiento del orógeno mexicano ocurrido durante el Cretácico Tardío-Paleógeno. Esta cuenca representa la continuación hacia el sur de la cuenca de antepaís cordillerana del Mesozoico tardío.

2. Las edades U-Pb y el análisis petrográfico de areniscas indican que la subsidencia de la CAM inició en el Cenomaniano tardío(?) después de la acreción del terreno Guerrero a la margen occidental de México ocurrida al final del Cretácico Temprano.

3. La CAM se desarrolló sobre el lado continental del orógeno y en la parte posterior del arco cordillerano Mexicano, por lo que corresponde a una cuenca antepaís de retroarco (*retro-foreland basin*). Esta interpretación es sustentada por el abundante material volcánico contenido en el relleno de la CAM, el cual registra la historia del arco al contener un amplio registro del arco volcánico contemporáneo.

4. Los depósitos de la CAM varían a través del tiempo y de acuerdo a su posición paleogeográfica en la cuenca. La variación en la composición modal de las areniscas procedentes de distintas partes de la CAM reflejan cambios en las fuentes y en los patrones de dispersión de sedimentos durante el avance progresivo de la cuña orogénica hacia el este (Fig.5). Los estratos más antiguos conocidos se ubican en la Mesa Central y consisten en calciturbiditas que se interdigitan hacia el oeste con turbiditas del Cenomaniano-Turoniano. En el centro de México, el depósito de turbiditas siliciclásticas predomina a través del Santoniano-Campaniano, las cuales se intercalan con capas de toba y areniscas ricas en detritos volcánicos en las partes más distales de

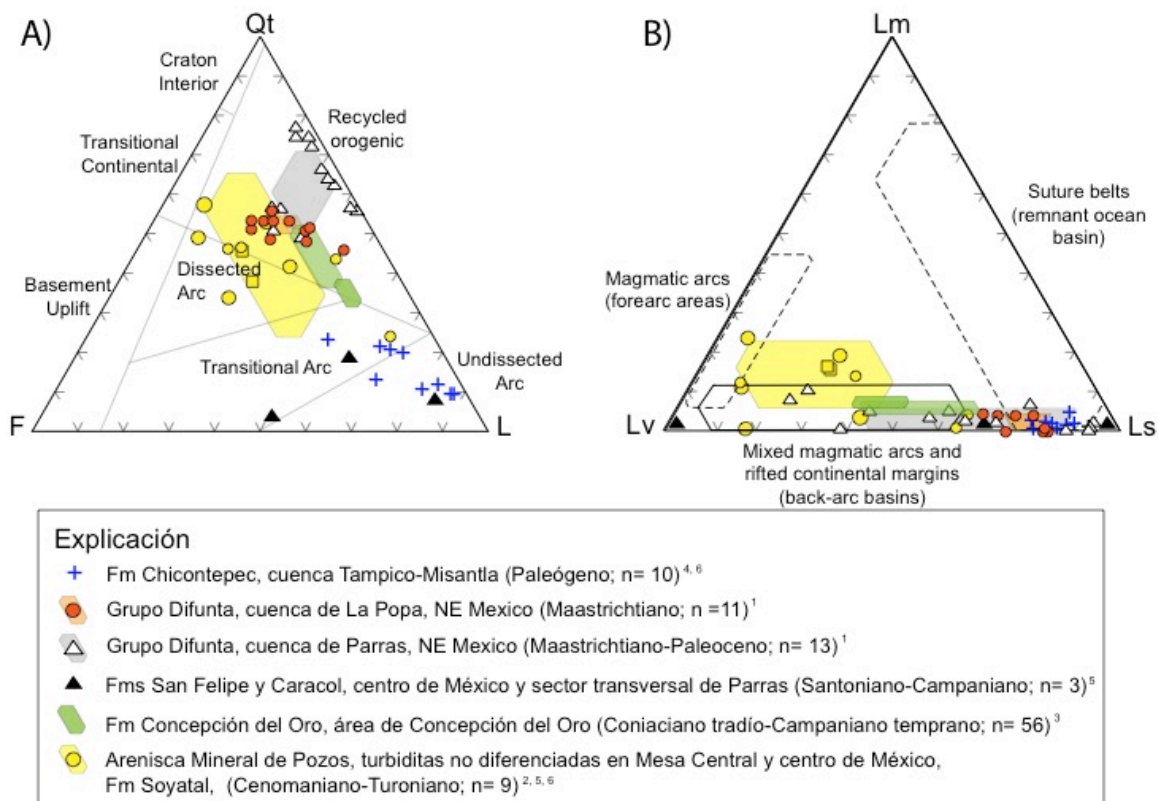


Figura 5. Diagramas ternarios que ilustran la composición de las areniscas de la cuenca de antepaís mexicana. Estos diagramas sintetizan datos documentados en ¹Lawton *et al.* (2009), ²Ortega-Flores *et al.* (2014); ³Ocampo-Díaz *et al.* (2016), ⁴González-Díaz *et al.* (2017) y ^{5,6}Juárez-Arriaga *et al.* (2019a, 2019b). Los polígonos de dispersión fueron construidos con 2 sigma de error y los datos normalizados se encuentran en el Apéndice 5.

la cuenca. Las sucesiones sedimentarias del Cretácico Superior-Paleógeno presentes en la cuenca Tampico-Misantla se depositaron en un ambiente marino profundo y corresponden a los depósitos más jóvenes de la CAM.

5. El arco cordillerano mexicano presente a lo largo de la margen occidental de México, es una de las potenciales fuentes que provieron sedimentos a la CAM. Este arco volcánico se mantuvo activo durante el evento de acortamiento del Cretácico Tardío-Paleógeno con al menos dos prominentes eventos magmáticos en la región, el primero representado por abundantes edades U-Pb entre ~98–92 Ma y un segundo evento definido por el intervalo ~85–74 Ma. Interpretamos que los granitos en Sinaloa, Baja California y Jalisco representan las raíces plutónicas de este arco volcánico, cuyas edades de emplazamiento se corresponden con las

edades de los depósitos sinorogénicos en la CAM. Se infieren dos mecanismos principales de transporte de sedimentos volcanogénicos a la cuenca: (1) el transporte sedimentario epiclástico por sistemas de drenaje transversal durante el Cenomaniano-Turoniano; y (2) nubes de ceniza llevadas por los vientos predominantes durante el Santoniano-Campaniano que alcanzaron la parte distal de la cuenca.

Los resultados de este trabajo también permiten hacer inferencias sobre el desarrollo de la cuña orogénica. Las implicaciones principales se describen a continuación.

6. Las edades de deformación documentadas en la parte central del CPCM (e.g., $^{40}\text{Ar}/^{39}\text{Ar}$ en illita, Fitz-Díaz *et al.*, 2014; K-Ar en illita-mica, Garduño-Martínez *et al.*, 2015; y trazas de fisión en apatito, Guerrero-Paz *et al.*, *aceptado*) combinadas con los nuevos datos de procedencia a partir del análisis petrográfico, edades U-Pb en circón, así como edades de enfriamiento en granos de circón detrítico (ZHe) indican que los eventos de deformación, exhumación y producción de sedimentos se vincularon directamente en el espacio y el tiempo.

7. El magmatismo activo durante toda la historia del acortamiento de MFTB también implica que la subducción de la placa de Farallón es el principal control tectónico de este orógeno.

8. Las sucesiones sedimentarias de la CAM en la parte central del CPCM preservan claras evidencias de cambios en las fuentes que aportaron sedimentos a la cuenca. La integración de datos petrográficos (Fig. 5), edades U-Pb y ZHe indica que estos cambios fueron el resultado de la exhumación y erosión de diferentes hojas de cabalgadura durante el avance progresivo de la cuña orogénica hacia el este. Particularmente, las modas estadísticas de las edades ZHe en granos de circón detrítico coinciden en general con los eventos de deformación previamente documentados en la parte central del cinturón de pliegues y cabalgaduras. El conjunto de edades ZHe definido por el intervalo ~136-120 Ma es el evento más antiguo registrado en el CPCM y representa un evento de enfriamiento anterior a la historia térmica del cinturón de pliegues y cabalgaduras. Estas edades son difíciles de asignar a un evento en particular pero pueden representar el enfriamiento de rocas intrusionadas por plutones en el terreno Guerrero o pueden ser resultado de un evento extensional antes del evento de acortamiento ocurrido durante el Cretácico Tardío-Paleógeno. Las edades de ZHe entre ~102-80 Ma representan el primer evento de enfriamiento relacionado con el movimiento

de empuje del CPCM documentado en su parte occidental, así como el movimiento de la falla El Doctor. Finalmente, las edades ZHe más jóvenes, comprendidas entre ~66-56 Ma, son registradas en las partes interior y exterior del cinturón de pliegues y cabalgaduras, las cuales posiblemente indican un enfriamiento relacionado con la exhumación de la cuña orogénica durante el Paleoceno temprano.

9. La relación temporal entre los eventos de deformación en el CPCM y la generación y dispersión de sedimentos es un aspecto importante para entender tanto la evolución de la CAM como para un mejor entendimiento de la distribución de recursos minerales en la región.

Referencias

- Alzaga-Ruiz, H., Lopez, M, Roure, R., Séranne, M., 2009, Interactions between the Laramide foreland and the passive margin of the Gulf of Mexico: Tectonics and sedimentation in the Golden Lane area, Veracruz State, Mexico: *Marine and Petroleum Geology*, 951-973; doi:10.1016/j.marpetgeo.2008.03.009.
- Busby, C., Adams, B.F., Mattinson, J., Deoreo, S., 2006, View of an intact oceanic arc, from surficial to mesozonal levels: Cretaceous Alisitos arc, Baja California: *Journal of Volcanology and Geothermal Research*, 149, 1-46.
- Calle, A.Z., Horton, B.K., Limachi, R., Stockli, D.F., Uzeda-Orellana, G.V., Anderson, R.B., Long, S.P., 2018, Cenozoic provenance and depositional record of the Sub-Andean foreland basin during growth of the Central Andean fold-thrust belt, southern Bolivia, *in* Zamora, G., McClay, K.R., Ramos, V.A. (eds.), *Petroleum basin and hydrocarbon potential of the Andes of Peru and Bolivia*, American Association of Petroleum Geologist, Memoir 117, p. 483-530.
- Campa, M.F., 1985, The tectonostratigraphic terranes and the thrust belt in Mexican territory: *Proceedings of the Circum-Pacific terrane conference*. Stanford University Publications in Geological Sciences 18, 44-46.
- Carrillo-Bravo, J., 1971, La Plataforma Valles-San Luis Potosí: *Boletín de la Asociación Mexicana de Geólogos Petroleros*, 23(1-6), 102 p.
- Carrillo, M., Suter, M., 1982, Tectónica de los alrededores de Zimapan, Hidalgo y Querétaro: México, D.F., Sociedad Geológica Mexicana, VI Convención geológica Nacional, Libro-guía de la excursión geológica a la región de Zimapan y áreas circundantes, estados de Hidalgo y Querétaro, p. 1-20.
- Centeno-García, E., Guerrero-Suastegui, M., Talavera-Mendoza, 2008, The Guerrero composite terrane of western Mexico: Collision and subsequent rifting in a supra-subduction zone, *in* Draut, A., Clift, P.D., Scholl, D.W. (eds.), *Formation and applications of the sedimentary record in arc collision zones: Geological Society of America Special Paper 436*, p. 279-308.
- Cohen, K.M., Finney, S.C., Gibbard, P.L. Fan, J.-X., 2013 (actualizada), *The ICS International*

- Chronostratigraphic Chart: Episodes, 36, 199-204.
- Coney, P.J., Jones, D.L., Monger, J.W.H., 1980, Cordilleran suspect terranes: *Nature*, 288, 325-333.
- Dahlen, F.A., 1990, Critical taper model of fold-and-thrust belts and accretionary wedges: *Annual Review of Earth and Planetary Sciences*, 18, 55-99.
- Dahlen, F.A., Suppe, J., 1988, Mechanics, growth, and erosion of mountain belts, in Clark, S.P., Burchfiel, B.C., Suppe, J. (eds.) *Processes in continental lithospheric deformation: Geological Society of America Special Paper 218*, p. 161-178.
- de Cserna, Z., 1956, Tectónica de la Sierra Madre Oriental de México, entre Torreón y Monterrey: *International Geological Congress, XX México, D.F., Monograph*, 87 p.
- DeCelles, P.G., 2004, Late Jurassic to Eocene evolution of the Cordilleran thrust belt and foreland basin system, western U.S.A.: *American Journal of Science*, 304, 105-168.
- DeCelles, P.G., Carrapa, B., Gehrels, G.E., 2007, Detrital zircon U-Pb ages provide provenance and chronostratigraphic information from Eocene synorogenic deposits in northwestern Argentina: *Geology*, 35(4), 323-326; doi: 10.1130/G23322A.1.
- DeCelles, P.G., Ducea, M.N., Kapp, P., Zandt, G., 2009, Cyclicity in Cordilleran orogenic systems: *Nature Geoscience*, 2, 251-257.
- DeCelles, P.G., Giles, K.A., 1996, Foreland basin systems: *Basin Research*, 8, 105-123.
- Dewey, J.F., Horsfield, B., 1970, Plate tectonics, orogeny and continental growth: *Nature*, 225(5232), 521-525.
- Dickinson, W.R., 1976, Sedimentary basins developed during evolution of Mesozoic-Cenozoic arc-trench system in western North America: *Canadian Journal of Earth Sciences*, 13, 1268-1287.
- Dickinson, W.R., 1985, Interpreting provenance relations from detrital modes of sandstones, in Zuffa, G.G. (ed.), *Provenance of Arenites*: Boston, D. Reidel Publishing Company, p. 333-361.
- Dickinson, W.R., 2004, Evolution of the North American Cordillera: *Annual Review of Earth and Planetary Sciences*, 32, 13-45; doi:10.1146 / annurev.earth.32.101802.120257.
- Dickinson, W.R., Gehrels, G.E., 2008, Sediment delivery to the Cordilleran foreland basin: Insights from U-Pb ages of detrital zircon in upper Jurassic and Cretaceous strata of the Colorado

- plateau: *American Journal of Science*, 308, 1041-1082; DOI: 10.2475/10.2008.01.
- Dickinson, W.R., Gehrels, G.E., 2009, Use of U-Pb ages of detrital zircons to infer maximum depositional ages of strata: A test against a Colorado Plateau Mesozoic database: *Earth and Planetary Science Letters*, 288, 115-125.
- Dickinson, W.R., Lawton, T.F., 2001, Carboniferous to Cretaceous assembly and fragmentation of Mexico: *Geological Society of America Bulletin*, 113, 1142-1160.
- Dickinson, W.R., Snyder, W.S., 1978, Plate tectonics of the Laramide orogeny, *in* Matthews V. III (ed.), *Laramide folding associated with basement block faulting in the western United States*, Geological Society of America, Memoir 151, pp. 355-366.
- Doglioni, C., Carminati, E., Cuffaro, M., Scrocca, D., 2007, Subduction kinematics and dynamic constraints: *Earth Science Reviews*, 83, 125-175.
- Domènech, M., Teixell, A., Stockli, D.F., 2016, Magnitude of rift-related burial and orogenic contraction in the Marrakech High Atlas revealed by zircon (U-Th)/He thermochronology: *Tectonics*, 35, p. 27; doi:10.1002/2016TC004283.
- Eguiluz, S., 2011, Sinopsis geológica de la cuenca de Burgos, noreste de México: producción y recursos petroleros: *Boletín de la Sociedad Geológica Mexicana*, 63(2), 323-332.
- Eguiluz, S., Aranda-García, M., Marret, R., 2000, Tectónica de la Sierra Madre Oriental, México: *Boletín de la Sociedad Geológica Mexicana*, 53, 1-26.
- Engelbreton, D. C., Cox, A., Thompson, G.A., 1984, Correlation of plate motions with continental tectonics: Laramide to basinrange: *Tectonics*, 3(2), 115-119.
- Fedo, C.M., Sircombe, K., Rainbird, R.H., 2003, Detrital zircon analysis of the sedimentary record, *in* Hancher, J.M., Hoskin, W.O. (eds.), *Zircon, Reviews in Mineralogy and Geochemistry*, 53, p. 277-303.
- Fildani, A., Cope, T.D., Graham, S.A., Wooden, J.L., 2003, Initiation of the Magallanes foreland basin: Timing of the southernmost Patagonian Andes orogeny revised by detrital zircon provenance analysis: *Geology*, 31(12), 1081-1084.
- Fitz-Díaz, E., Hudleston, P., Tolson, G., van der Pluijm, B., 2014, Progressive, episodic deformation in the Mexican Fold–Thrust Belt (central Mexico): Evidence from isotopic dating of folds and

- faults: *International Geology Review*, 56, 734–755.
- Fitz-Díaz, E., Lawton, T.F., Juárez-Arriaga, E., Chávez-Cabello, G., 2018, Late Cretaceous-Paleogene Mexican orogen: Structure, basin development, and tectonics: *Earth-Science Reviews*, 183, 56-84; doi: 10.1016/j.earscirev.2017.03.002.
- Fitz-Díaz, E., Tolson, G., Hudleston, P., Bolaños-Rodríguez, D., Ortega-Flores, B., Vásquez Serrano, A., 2012, The role of folding in the development of the Mexican fold-and-thrust belt: *Geosphere*, 8(4), 931-949; doi: 10.1130/GES00759.1.
- Folk, R.L., 1974, *Petrology of Sedimentary Rocks*: Austin, Texas, second ed. Hemphill Publishing Company, p. 182.
- Fosdick, J.C., Romans, B.W., Fildani, A., Bernhardt, A., Calderón, M., Graham, S.A., 2011, Kinematic evolution of the Patagonian retroarc fold-and-thrust belt and Magallanes foreland basin, Chile and Argentina, 51°30'S: *Geological Society of America Bulletin*, 123(9-10), 1679-1698; doi: 10.1130/B30242.1.
- Freydier, C., Martínez, R.J., Lapierre, H., Tardy, M., Coulon, C., 1996, The Early Cretaceous Arperos oceanic basin (western Mexico). Geochemical evidence for an aseismic ridge formed near a spreading center: *Tectonophysics*, 259, 343-367.
- Garduño-Martínez, D.E., Puig, T.P., Solé, J., Martini, M., Alcalá-Martínez, J.R., 2015, K-Ar illite-mica age constraints on the formation and reactivation history of the El Doctor fault zone, central Mexico: *Revista Mexicana de Ciencias Geológicas*, 32(2), 306-322.
- Garzanti, E., Doglioni, C., Vezzoli, G., Ando, S., 2007, Orogenic belts and orogenic sediment provenance: *The Journal of Geology*, 115(3), 315-334.
- Gehrels, G.E., 2000, Introduction to detrital zircon studies of Paleozoic and Triassic strata in western Nevada and northern California, *in* Soreghan, M.J., Gehrels, G.E. (eds.), *Paleozoic and Triassic paleogeography and tectonics of western Nevada and northern California*: Geological Society of America, Special Paper 347, p. 1-17.
- Gehrels, G.E., Dickinson, W.R., 1995, Detrital zircon provenance of Cambrian to Triassic miogeoclinal and eugeoclinal strata in Nevada: *American Journal of Science*, 295, 18-48.

- Gehrels, G.E., Valencia, V.A., Ruiz, J., 2008, Enhanced precision, accuracy, efficiency, and spatial resolution of U-Pb ages by laser ablation-multicollector-inductively coupled plasma-mass spectrometry: *Geochemistry, Geophysics, Geosystems*, 9, 13 p.
- González-Díaz, M.G., Lawton, T.F., Juárez-Arriaga, E., 2017, Estratigrafía, sedimentología y procedencia de la Formación Chicontepec (Paleógeno) en el norte de la cuenca Tampico-Misantla (resumen): *Geos*, 37(1), 135-136.
- Guerrero-Paz, D.N., Abdullin, F., Ortega-Flores, B., Solari, L., Ortega-Obregón, C., Juárez-Arriaga, E., *aceptado*, Late Cretaceous to Eocene denudation history of the Tolimán area, southern Sierra Madre Oriental, central Mexico, *in* Martens, U., Molina, R., Pindell, J. (eds.), Southern and central Mexico: basement framework, tectonic evolution, and provenance of Mesozoic-Cenozoic basins, Geological Society of America, Special Paper.
- Hart, N.R., 2015, Temporal constraints on progressive rifting of a hyper-extended continental margin using bedrock and detrital zircon (U-Th)/(Pb-He) dating, Mauléon basin, western Pyrenees, tesis de maestría, The University of Texas at Austin, p. 419.
- Hart, N.R., Stockli, D.F., Hayman, W., 2016, Provenance evolution during progressive rifting and hyperextension using bedrock and detrital zircon U-Pb geochronology, Mauléon Basin, western Pyrenees: *Geosphere*, 12, 1-21.
- Henry, C.D., McDowell, F.W., Silver, L.T., 2003, Geology and geochronology of granitic batholithic complex, Sinaloa, México: Implications for Cordilleran magmatism and tectonics, *in* Johnson, S.E., Paterson, S.R., Fletcher, J.M., Girty, G.H., Kimbrough, D.L., Martín-Barajas, A. (eds.), Tectonic evolution of northwestern México and the southwestern USA: Geological Society of America Special Paper 374, 37 p.
- Ingersoll, R.V., 2012, Tectonics of sedimentary basins, with revised nomenclature, *in* Busby C., Azor-Pérez, A., (eds.), Tectonics of Sedimentary Basins: Recent Advances, Blackwell Publishing, p. 3-43.
- Ingersoll, R.V., Bullard, T.F., Ford, R.I., Grimm, J.P., Pickle, J.D., Sares, S.W., 1984, The effect of grain size on detrital modes: A test of the Gazzi-Dickinson point-counting method: *Journal of Sedimentary Petrology*, 54, 103-116.

- Ingersoll, R.V., Suczek, C.A., 1979, Petrology and provenance of Neogene sand from Nicobar and Bengal fans, DSDP sites 211 and 218: *Journal of Sedimentary Petrology*, 49, 1217-1228.
- Johnson, S.E., Tate, M.C., Fanning, C.M., 1999, New geologic mapping and SHRIMP U-Pb zircon data in the Peninsular Ranges batholith, Baja California, Mexico: evidence for a suture?: *Geology*, 27, 743-746.
- Juárez-Arriaga, E., Lawton, T.F., Ocampo-Díaz, Y.Z.E., Stockli, D.F., Solari, L., 2019a, Sediment provenance, sediment-dispersal systems, and major arc-magmatic events recorded in the Mexican foreland basin, north-central and northeastern Mexico: *International Geology Review*.
<https://doi.org/10.1080/00206814.2019.1581848>
- Juárez-Arriaga, E., Lawton, T.F., Stockli, D.F., Solari, L., Martens, U., 2019b, Late Cretaceous-Paleocene stratigraphic and structural evolution of the central Mexican fold and thrust belt, from detrital zircon (U-Th)/(He-Pb) ages: *Journal of South American Earth Sciences*.
<https://doi.org/10.1016/j.jsames.2019.102264>
- Kimbrough, D.L., Smith, D.P., Mahoney, J.B., Moore, T.E., Gastil, R.G., Ortega-Rivera, M.A., Fanning, C.M., 2001, Forearc basin sedimentary response to rapid Late Cretaceous batholith emplacement in the Peninsular Ranges of southern and Baja California: *Geology*, 29, 491-494.
- Lawton, T.F., 2008, Laramide sedimentary basins, *in* Miall, A.D. (ed.) *The sedimentary basins of the United States and Canada*, vol. 5, Elsevier, The Netherlands, 429-450, ISBN: 978-0-444-50425-8
- Lawton, T.F., 2019, Laramide sedimentary basins and sediment-dispersal systems, *in* Miall, A.D. (ed.) *The sedimentary basins of the United States and Canada*, Elsevier, The Netherlands, 529-557, <http://doi.org/10.1016/B978-0-444-63895-3.00013-9>
- Lawton, T.F., Bradford, I.A., Vega, F.J., Gehrels, G.E., Amato, J.M., 2009, Provenance of Upper Cretaceous-Paleogene sandstones in the foreland basin system of the Sierra Madre Oriental, northeastern Mexico, and its bearing on fluvial dispersal systems of the Mexican Laramide Province: *Geological Society of America Bulletin*, 21 (5-6), 820-836.
- Leier, A.L., Gehrels, G.E., 2011, Continental-scale detrital zircon provenance signatures in Lower Cretaceous strata, western North America: *Geology*, 39(4), 399-402; doi: 10.1130/G31762.1.

- López-Ramos, E., 1979, Geología de México, tomo 2, México, p. 454.
- Ludwig, K.R., 2012, Isoplot© versión 4.1 (en línea) Berkeley Geochronology Center (BGC), <http://www.bgc.org/isoplot_etc/isoplot.html> acceso libre, consulta: abril de 2019.
- Malkowski, M.A., Schwartz, T.M., Sharman, G.R., Sickmann, Z.T., Graham, S.A., 2017, Stratigraphic and provenance variations in the early evolution of the Magallanes-Austral foreland basin: Implications for the role of longitudinal versus transverse sediment dispersal during arc-continent collision: Geological Society of America Bulletin, 129(3-4), 349-371, doi: 10.1130/B31549.1.
- Martini, M., Ferrari, L., 2011, Style and chronology of the Late Cretaceous shortening in the Zihuatanejo area (southwestern Mexico): Implications for the timing of the Mexican Laramide deformation: Geosphere, 7(6), 1469-1479.
- Martini, M., Fitz-Díaz, E., Solari, L., Camprubí, A., Hudleston, P.J., Lawton, T.F., Tolson, G., Centeno-García, E., 2012, The Late Cretaceous fold-thrust belt in the Peña de Bernal-Tamazunchale area and its possible relationship to the accretion of the Guerrero Terrane, *in* Aranda-Gómez, J.J., Tolson, G., Molina-Garza, R.S. (eds.), The Southern Cordillera and beyond: Geological Society of America Field Guide 25, p. 19–38, doi:10.1130/2012.0025(02).
- Martini, M., Solari, L., López-Martínez, M., 2014, Correlating the Arperos Basin from Guanajuato, central Mexico, to Santo Tomás, southern Mexico: implications for the paleogeography and origin of the Guerrero terrane: Geosphere, 10, 1-17.
- Martini, M., Solé, J., Garduño-Martínez, D.E., Puig, T.P., Omaña, L., 2016, Evidence for two Cretaceous superposed orogenic belts in central Mexico based on paleontologic and K-Ar geochronologic data from the Sierra de los Cuarzos: Geosphere, 12(4), 1-14.
- Mendoza, O.T., Suastegui, M.G., 2000, Geochemistry and isotopic composition of the Guerrero terrane (western Mexico): Implications for the tectono-magmatic evolution of southwestern North America during the Late Mesozoic: South American Earth Sciences, 13, 297-324.
- Ocampo-Díaz, Y.Z.E., Pinzon-Sotelo, M.P., Chávez-Cabello, G., Ramírez-Díaz, A., Martínez-Paco, M., Velasco-Tapia, F., Guerrero-Suastegui, M., Barboza-Gudiño, J.R., 2016, Propuesta nomenclatural y análisis de procedencia de la Formación Concepción del Oro (antes Formación

- Caracol): implicaciones sobre la evolución tectónica del sur de Norteamérica durante el Cretácico Tardío: *Revista Mexicana de Ciencias Geológicas*, 33(1), 3-33.
- Ortega-Flores, B., Solari, L., Lawton, T.F., Ortega-Obregón, C., 2014, Detrital-zircon record of major Middle Triassic–Early Cretaceous provenance shift, central Mexico: demise of Gondwanan continental fluvial systems and onset of back-arc volcanism and sedimentation: *International Geology Review*, 56(2), 237-261.
- Ortega-Flores, B., Solari, L.A., Escalona-Alcázar, F.J., 2016, The Mesozoic successions of western Sierra de Zacatecas, central Mexico: provenance and tectonic implications: *Geological Magazine*, 153, 696-717.
- Ortega-Gutiérrez, F., Elías-Herrera, M., Morán-Zenteno, D.J., Solari, L., Luna-González, L., Schaaf, P., 2014, A review of batholiths and other plutonic intrusions of Mexico: *Gondwana Research*, 26, 834-868.
- Ortega-Rivera, A., 2003, Geochronological constraints on the tectonic history of the Peninsular Ranges batholith of Alta and Baja California: Tectonic implications for western México: Tectonic evolution of northwestern Mexico and the southwestern USA: Boulder, Colorado, Geological Society of America Special Paper 374, p. 297-335.
- Palacios-García, N.B., Martini, M., 2014, From back-arc rifting to arc accretion: the Late Jurassic–Early Cretaceous evolution of the Guerrero terrane recorded by a major provenance change in sandstones from the Sierra de los Cuarzos area, central Mexico: *International Geology Review*, 56(11), 1377-1394.
- Paton, C., Woodhead, J.D., Hellstrom, J.C., Hergt, J.M., Greig, A., Maas, R., 2010, Improved laser ablation U-Pb zircon geochronology through robust downhole fractionation correction: *Geochemistry Geophysics Geosystems*, 11, Q0AA06, doi:10.1029/2009GC002618.
- Payton, S.L., Carrapa, B., 2013, Thermochronologic techniques, methodology, and applications, *in* Knight, C., Cuzella, J. (eds.), *Application of structural methods to Rocky Mountain hydrocarbon exploration and development*: American Association of Petroleum Geologists, *Studies in Geology* 65, p. 15-36.

- Petrus, J.A., Kamber, B.S., 2012, VisualAge: A novel approach to laser ablation ICP-MS U-Pb Geochronology data reduction: *Geostandards and Geoanalytical Research*, 36(3), 247-270.
- Pujols, E.J., Leva López, L., Stockli, D.F., Rossi, V.M., Steel, R.J., 2018, New insights into the stratigraphic and structural evolution of the middle Jurassic S. Neuquén basin from detrital zircon (U-Th)/(He-Pb) and apatite (U-Th)/He ages: *Basin Research*, 30, 1-18.
- Raines, M.K., Hubbard, S.M., Kukulski, R.B., Leier, A.L., Gehrels, G.E., 2013, Sediment dispersal in an evolving foreland: Detrital zircon geochronology from Upper Jurassic and lowermost Cretaceous strata, Alberta basin, Canada: *Geological Society of America Bulletin*, 125(5-6), 741-755; doi: 10.1130/B30671.1
- Reiners, P.W., 2005, Zircon (U-Th)/He thermochronometry: *Reviews in Mineralogy and Geochemistry*, 58, 151-179.
- Reiners, P.W., Campbell, I.H., Nicolescu, S., Allen, C.M., Hourigan, J.K., Garver, J.I., Mattinson, J.M., Cowan, D.S., 2005, (U-Th)/(He-Pb) double dating of detrital zircons: *American Journal of Science*, 305, 259-311.
- Roigé, M., Gómez-Gras, D., Remacha, E., Daza, R., Boya, S., 2016, Tectonic control on sediment sources in the Jaca basin (Middle and Upper Eocene of the south-central Pyrenees): *Comptes Rendus Geoscience*, 348, 236-245.
- Romans, B.W., Fildani, A., Graham, S.A., Hubbard, S.M., Covault, J.A., 2010, Importance of predecessor basin history on the sedimentary fill of retroarc foreland basin: provenance analysis of the Cretaceous Magallanes basin, Chile (50-52° S): *Basin Research*, 22, 640-658; doi: 10.1111/j.1365-2117.2009.00443.x.
- Ruiz-Arriaga, D., 2018, Historia de la deformación de la margen oriental de la plataforma Guerrero-Morelos, tesis de maestría, Universidad Nacional Autónoma de México, 124 p.
- Ruiz, G.M.H., Seward, D., Winkler, W., 2004, Detrital thermochronology – a new perspective on hinterland tectonics, an example from the Andean Amazon basin, Ecuador: *Basin Research*, 16, 413-430; doi: 10.1111/j.1365-2117.2004.00239.x.
- Saleeby, J., 2003, Segmentation of the Laramide Slab-evidence from the southern Sierra Nevada region: *Geological Society of America Bulletin*, 115(6), 655-668.

- Saylor, J.E., Stockli, D.F., Hurton, B.K., Nie, J., Mora, A., 2012, Discriminating rapid exhumation from syndepositional volcanism using detrital zircon double dating: Implications for the tectonic history of the Eastern Cordillera, Colombia: *Geological Society of America Bulletin*, 124, 762-779.
- Selzer, C., Buiter, S.J.H., Pfiffner, A., 2007, Sensitivity of shear zones in orogenic wedges to surface processes and strain softening: *Tectonophysics*, 437, 51-70.
- Soegaard, K., Ye, H., Halik, N., Daniels, A.T., Arney, J., Garrick, S., 2003, Stratigraphic evolution of Latest Cretaceous to early Tertiary Difunta foreland basin in northeast Mexico: Influence of salt withdrawal on tectonically induced subsidence by the Sierra Madre Oriental fold and thrust belt, *in* Bartolini, C., Buffler, R.T., Blickwede, J. (eds.), *The Circum-Gulf of Mexico and the Caribbean: Hydrocarbon habitats, basin formation, and plate tectonics: American Association of Petroleum Geologists, Memoir 79*, p. 364-394.
- Solari, L.A., Gómez-Tuena, A., Bernal, J.P., Pérez-Arviso, O., Tanner, M., 2010, U-Pb zircon geochronology with an integrated LA-ICP-MS microanalytical workstation: Achievements in precision and accuracy: *Geostandards and Geoanalytical Research*, 34(1), 5-18.
- Solari, L.A., González-León, C.M., Ortega-Obregón, C., Valencia-Moreno, M., Rascón-Heimpel, M.A., 2018, The Proterozoic of NW Mexico revisited: U-Pb geochronology and Hf isotopes of Sonoran rocks and their tectonic implications: *International Journal of Earth Sciences*, 107, 845-861.
- Solari, L.A., Torres de León, R., Hernández-Pineda, G., Solé, J., Solís-Pichardo, G., 2007, Tectonic significance of Cretaceous-Tertiary magmatic and structural evolution of the northern margin of the Xolapa Complex, Tierra Colorada area, southern Mexico: *Geological Society of America Bulletin*, 119(9-10), 1265-1279.
- Suter, M., 1980, Tectonics of the external part of the Sierra Madre Oriental foreland thrust-and-fold belt between Xilitla and the Moctezuma river (Hidalgo and San Luis Potosí states): *Revista del Instituto de Geología*, 4, 19-31.
- Suter, M., 1984, Cordilleran deformation along the eastern edge of the Valles-San Luis Potosí carbonate platform, Sierra Madre Oriental fold-thrust belt, east-central Mexico: *Geological*

- Society of America Bulletin, 95, 1387-1397.
- Suter, M., 1987, Structural traverse across the Sierra Madre Oriental fold-thrust belt in east-central Mexico: Geological Society of America Bulletin, 98, 249-264.
- Suter, M., Contreras-Pérez, J., Ochoa-Camarillo, H., 1997, Structure of the Sierra Madre Oriental fold-thrust belt in east-central Mexico: Pachuca, Hidalgo, Instituto de Investigaciones en Ciencias de la Tierra de la Universidad Autónoma del Estado de Hidalgo e Instituto de Geología de la Universidad Nacional Autónoma de México, II Convención sobre la evolución geológica de México y recursos asociados, Libro-guía de las excursiones geológicas, Excursión 2, p. 45-63.
- Talavera-Mendoza, O., Ruiz, J., Gehrels, G.E., Valencia, V.A., Centeno-García, E., 2007, Detrital zircon U/Pb geochronology of southern Guerrero and western Mixteca arc successions (southern Mexico): New insights for the tectonic evolution of southwestern North America during the late Mesozoic: Geological Society of America Bulletin, 119(9-10), 1052-1065.
- Tardy, M., Maury, R., 1973, Sobre la presencia de elementos de origen volcánico en las areniscas de los flyschs de edad cretácica superior de los estados de Coahuila y de Zacatecas, México: Boletín de la Sociedad Geológica Mexicana, 34, 5-12.
- Valencia, V.A., Richter, K., Rosas-Elguera, J., López Martínez, M., Grove, M., 2013, The age and composition of the pre-Cenozoic basement of the Jalisco Block: Implications for and relation to the Guerrero composite terrane: Contributions to Mineralogy and Petrology, 166, 801-824; doi: 810.1007/s00410-00013-00908-z.
- Velasco-Tapia, F., Martínez-Paco, M., Iriando, A., Ocampo-Díaz, Y.Z.E., Cruz-Gómez, E.M., Ramos-Ledezma, A., Andaverde, J.A., Ostrooumov, M., Masuch, D., 2016, Altered volcanic ash layers of the Late Cretaceous San Felipe Formation, Sierra Madre Oriental (northeastern Mexico): U-Pb geochronology, provenance and tectonic setting: Journal of South American Earth Sciences, 70, 18-35.
- Vermeesch, P., 2004, How many grains are needed for a provenance study?: Earth and Planetary Science Letters, 224, 441-451.
- Wolfe, M.R., Stockli, D.F., 2010, Zircon (U-Th)/He thermochronometry in the KTB drill hole, Germany, and its implications for bulk diffusion kinetics in zircon: Earth and Planetary Science

Letters, 265, 69-82.

Zimmermann, J.L., Stussi, J.M., González-Partida, E., Arnold, M., 1988, K-Ar evidence for age and compositional zoning in the Puerto Vallarta-Río Santiago batholith (Jalisco, Mexico): *Journal of South American Earth Sciences*, 1, 267-274.

Apéndice 1

Parámetros de conteo

Symbol	Definition
Qm	cuarzo monocristalino
Qpq	cuarzo policristalino
Qc	pedernal
K	feldespato potásico
P	plagioclasa
Lmf	grano metamórfico foliado de cuarzo-mica
Lmp	grano metamórfico poligonal de cuarzo-mica
Lmv	grano metavolcánico con epidota y/p clorita
Lss	grano lítico sedimentario: limolita, argilita, granos fosfáticos
Lsc	grano carbonatado detrítico (<i>sensu</i> Zuffa, 1980)
Lvf	grano lítico volcánico felsítico
Lvl	grano lítico volcánico tipo <i>lathwork</i>
Lvm	grano lítico volcánico microlítico
Lvt	granos líticos volcánicos tufáceos y vítreos
Qt	Total de cuarzo (=Qm+Qpq+Qc)
F	Total de feldespatos (=K+P)
Lm	Total de granos metamórficos (=Lmf+Lmp+Lmv)
Lv	Total de granos volcánicos (=Lvf+Lvl+Lvm+Lvt)
Ls	Total de granos sedimentarios (=Lss+Lsc)
L	Total de granos líticos inestables (=Lm+Lv+Ls)
Qp	Total de cuarzo policristalino (=Qpq+Qc)
Lt	Total de granos líticos (=L+Qp)
<hr/> Parámetros recalculados <hr/>	
$QtFL\%Q = 100Qt/(Qt+F+L)$	
$QtFL\%F = 100F/(Qt+F+L)$	
$QtFL\%L = 100L/(Qt+F+L)$	
$QmFLt\%Qm = 100Qm/(Qm+F+Lt)$	
$QmFLt\%F = 100F/(Qm+F+Lt)$	
$QmFLt\%Lt = 100Lt/(Qm+F+Lt)$	
$LmLvLs\%Lm = 100Lm/(Lm+Lv+Ls)$	
$LmLvLs\%Lv = 100Lv/(Lm+Lv+Ls)$	
$LmLvLs\%Ls = 100Ls/(Lm+Lv+Ls)$	
$QmPK\%Qm = 100Qm/(Qm+P+K)$	
$QmPK\%P = 100P/(Qm+P+K)$	
$QmPK\%K = 100K/(Qm+P+K)$	

Apéndice 2

Edades isotópicas y calculadas.

Sediment provenance, sediment-dispersal systems, and major arc-magmatic events recorded in the Mexican foreland basin, North-Central and Northeastern Mexico.

CORRECTED RATIOS ²											CORRECTED AGES (Ma)										
U (ppm)	Th (ppm)	Th/U	²⁰⁷ Pb/ ²⁰⁶ Pb	±2σ abs	²⁰⁷ Pb/ ²³⁵ U	±2σ abs	²⁰⁶ Pb/ ²³⁸ U	±2σ abs	²⁰⁸ Pb/ ²³² Th	±2σ abs	Rho	²⁰⁶ Pb/ ²³⁸ U	±2σ	²⁰⁷ Pb/ ²³⁵ U	±2σ	²⁰⁸ Pb/ ²³² Pb	±2σ	Best age (Ma)	±2σ	Disc %	
San Felipe Formation (sample: 48-Me16), coordinates: 25° 35.635'N, 100° 26.400'W																					
Zircon_41_48-Me16	790	361	0.0492	0.0036	0.0827	0.0051	0.01208	0.00026	0.00411	0.00023	-0.29	77.4	1.7	80.6	4.8	150	160	77.4	1.7	4.0	
Zircon_42	1176	658	0.0486	0.003	0.079	0.0039	0.01193	0.00023	0.00385	0.00019	0.02	76.4	1.5	77.2	3.7	110	130	76.4	1.5	1.0	
Zircon_43	574	323	0.0511	0.0037	0.0845	0.0044	0.01218	0.00036	0.00422	0.00023	-0.11	78	2.3	82.3	4.1	200	150	78	2.3	5.2	
Zircon_44	603	325	0.0467	0.0039	0.0773	0.0059	0.012	0.00032	0.00398	0.0002	-0.02	76.9	2	75.4	5.6	40	170	76.9	2	-2.0	
Zircon_46	526	125	0.0469	0.0045	0.078	0.0068	0.01222	0.0003	0.00399	0.00038	0.08	78.3	1.9	76	6.4	10	190	78.3	1.9	-3.0	
Zircon_47	350	94	0.0493	0.0048	0.0832	0.0077	0.01234	0.00031	0.00437	0.00046	-0.02	79.1	2	80.8	7.2	110	200	79.1	2	2.1	
Zircon_48	899	194	0.05	0.0031	0.0834	0.0041	0.01209	0.00029	0.00395	0.00025	-0.11	77.5	1.8	81.2	3.8	170	130	77.5	1.8	4.6	
Zircon_50	1032	1280	0.0509	0.0029	0.0847	0.0046	0.01199	0.00025	0.00374	0.00016	0.13	76.9	1.6	82.4	4.3	230	130	76.9	1.6	6.7	
Zircon_51	358	107	0.0547	0.0058	0.0913	0.0091	0.01241	0.00037	0.00519	0.00051	0.12	79.5	2.4	88.3	8.4	360	210	79.5	2.4	10.0	
Zircon_52	644	351	0.0533	0.0039	0.0901	0.0063	0.01196	0.00025	0.00388	0.00023	0.12	76.7	1.6	87.4	5.8	290	160	76.7	1.6	12.2	
Zircon_53	678	472	0.051	0.0036	0.0849	0.0049	0.01231	0.00027	0.00388	0.00022	-0.02	78.8	1.7	82.6	4.6	210	150	78.8	1.7	4.6	
Zircon_55	696	292	0.0511	0.004	0.0816	0.0052	0.01207	0.00027	0.00395	0.00022	-0.31	77.3	1.7	80.4	4.7	190	160	77.3	1.7	3.9	
Zircon_56	990	342	0.0482	0.0031	0.0812	0.0039	0.01236	0.0003	0.00406	0.00021	-0.15	79.2	1.9	79.9	3.8	90	140	79.2	1.9	0.9	
Zircon_57	617	287	0.0554	0.0034	0.0878	0.0049	0.01164	0.00028	0.00393	0.00026	0.11	74.6	1.8	85.4	4.6	420	140	74.6	1.8	12.6	
Zircon_58	572	332	0.0526	0.0038	0.0853	0.0052	0.01186	0.00028	0.00364	0.00027	0.08	76	1.8	83	4.9	290	160	76	1.8	8.4	
Zircon_60	1361	1290	0.0533	0.0028	0.0873	0.0041	0.01179	0.00023	0.00393	0.00017	0.36	75.6	1.4	84.9	3.8	330	120	75.6	1.4	11.0	
Zircon_61	949	308	0.05	0.0031	0.0823	0.0041	0.01206	0.00024	0.00388	0.00027	-0.10	77.3	1.5	80.3	3.8	170	130	77.3	1.5	3.7	
Zircon_62	825	268	0.044	0.0032	0.0747	0.0046	0.01223	0.00028	0.00392	0.00028	-0.08	78.4	1.8	73	4.4	-90	140	78.4	1.8	-7.4	
Zircon_63	355	231	0.0556	0.0052	0.0938	0.0088	0.01209	0.00035	0.00439	0.00034	0.43	77.5	2.2	92.3	8.6	400	210	77.5	2.2	16.0	
Zircon_64	651	297	0.0517	0.0036	0.0851	0.0052	0.01216	0.00031	0.00391	0.00026	-0.08	77.9	1.9	82.8	4.8	230	150	77.9	1.9	5.9	
Zircon_65	871	427	0.0532	0.0037	0.0891	0.0051	0.0123	0.00028	0.00403	0.00022	-0.03	78.8	1.8	86.5	4.7	290	140	78.8	1.8	8.9	
Zircon_66	1134	509	0.0477	0.0029	0.0845	0.0038	0.01277	0.0003	0.00403	0.00019	-0.04	81.8	1.9	82.3	3.6	90	130	81.8	1.9	0.6	
Zircon_67	687	221	0.0463	0.0034	0.0751	0.0043	0.01189	0.00029	0.00415	0.00032	-0.15	76.2	1.8	73.5	4.1	10	150	76.2	1.8	-1.7	
Zircon_68	676	278	0.0505	0.0033	0.0865	0.0046	0.01224	0.00028	0.0039	0.00025	-0.07	78.4	1.8	84.2	4.3	220	130	78.4	1.8	6.9	
Zircon_69	561	218	0.0481	0.0039	0.0819	0.0056	0.0125	0.0003	0.00438	0.00038	-0.03	80.1	1.9	79.8	5.3	110	160	80.1	1.9	-0.4	
Zircon_70	515	267	0.0505	0.0048	0.0851	0.0072	0.0121	0.00029	0.00396	0.00029	-0.19	77.5	1.8	82.7	6.8	160	190	77.5	1.8	6.3	
Zircon_71	452	235	0.0463	0.0033	0.0801	0.0047	0.01255	0.00034	0.00404	0.00028	-0.07	80.4	2.1	78.1	4.4	30	140	80.4	2.1	-2.9	
Zircon_72	1415	1549	0.0473	0.0027	0.0783	0.0035	0.01205	0.00024	0.0039	0.00015	0.05	77.2	1.5	76.5	3.3	100	120	77.2	1.5	-0.9	
Zircon_73	874	231	0.0501	0.0039	0.0816	0.0051	0.01165	0.00026	0.00425	0.00031	-0.05	74.7	1.6	79.6	4.8	190	160	74.7	1.6	6.2	
Zircon_74	852	255	0.05	0.003	0.0836	0.0038	0.01216	0.00028	0.00397	0.00025	-0.12	79.1	1.7	81.4	3.6	190	130	79.1	1.7	4.1	
Zircon_75	401	119	0.0443	0.0038	0.076	0.0057	0.01246	0.00039	0.00412	0.00037	0.10	78.8	2.5	74.2	5.4	-70	170	78.8	2.5	-7.5	
Zircon_77	497	155	0.0574	0.005	0.0975	0.0079	0.01226	0.00029	0.00481	0.00044	0.11	78.6	1.9	94.1	7.3	440	190	78.6	1.9	16.5	
Zircon_78	904	212	0.0493	0.003	0.0806	0.0042	0.01196	0.00024	0.00386	0.00027	-0.20	76.6	1.5	79.3	4.1	160	130	76.6	1.5	3.4	
Zircon_79	425	164	0.0518	0.0043	0.0881	0.0075	0.01244	0.00031	0.00408	0.00037	0.13	79.7	1.9	85.4	7	250	180	79.7	1.9	6.7	
Zircon_80_48-Me16	888	251	0.0489	0.0031	0.0825	0.0046	0.01221	0.00025	0.00397	0.00026	-0.14	78.3	1.6	80.4	4.3	120	130	78.3	1.6	2.6	
San Felipe Formation (sample: 49-SF02b), coordinates: 25° 35.157'N, 100° 25.537'W																					
Zircon_01_49-SF02b	897	403	0.0484	0.003	0.089	0.004	0.01317	0.00026	0.00414	0.00022	0.07	84.3	1.6	86.5	3.8	100	130	84.3	1.6	2.5	
Zircon_02	134	52	0.0758	0.004	1.09	0.062	0.1026	0.004	0.0508	0.0023	0.62	629	23	753	28	1120	110	629	23	16.5	
Zircon_03	555	288	0.0487	0.0038	0.0926	0.0063	0.01366	0.00031	0.00471	0.00028	-0.09	87.4	2	89.7	5.9	120	150	87.4	2	2.6	
Zircon_04	1162	601	0.0498	0.0027	0.0903	0.0039	0.01324	0.00023	0.00429	0.00023	0.00	84.8	1.4	87.7	3.6	160	120	84.8	1.4	3.3	
Zircon_05	1674	3060	0.0491	0.002	0.0847	0.0022	0.01251	0.00021	0.00382	0.00015	0.09	80.2	1.4	82.5	2	145	91	80.2	1.4	2.8	
Zircon_06	1068	291	0.0471	0.0031	0.0847	0.0043	0.01325	0.00029	0.00445	0.00025	-0.04	84.9	1.8	82.5	4	60	140	84.9	1.8	-2.9	
Zircon_07	730	338	0.0498	0.0036	0.0865	0.0051	0.01276	0.00025	0.00437	0.00021	-0.04	81.8	1.6	84.1	4.7	200	150	81.8	1.6	2.7	
Zircon_08	795	297	0.0524	0.0036	0.0928	0.0052	0.01298	0.0003	0.00431	0.00024	0.02	83.1	1.9	89.9	4.8	270	150	83.1	1.9	7.6	
Zircon_09	859	687	0.0534	0.0057	1.03	0.17	0.1306	0.00033	0.00419	0.00031	0.93	83.6	2.1	93	11	250	180	83.6	2.1	10.1	
Zircon_10	726	241	0.0505	0.0028	0.0923	0.0045	0.0132	0.00028	0.0044	0.00027	0.28	84.5	1.8	89.5	4.1	210	120	84.5	1.8	5.6	
Zircon_12	1221	501	0.0491	0.0026	0.0928	0.0036	0.01351	0.00025	0.00467	0.00021	0.02	86.5	1.6	90.1	3.4	150	120	86.5	1.6	4.0	
Zircon_13	657	248	0.0453	0.0026	0.0842	0.0037	0.01366	0.00026	0.00411	0.00028	-0.12	87.5	1.7	82	3.5	-30	120	87.5	1.7	-6.7	
Zircon_14	1082	452	0.0475	0.0028	0.0882	0.0041	0.01354	0.00025	0.00456	0.00022	0.07	86.7	1.6	85.8	3.9	80	130	86.7	1.6	-1.0	
Zircon_15	628	209	0.0615	0.0024	0.681	0.049	0.0804	0.0047	0.0338	0.0014	0.94	498	28	523	29	656	84	498	28	4.8	
Zircon_16	847	280	0.0472	0.003	0.0869	0.0049	0.01326	0.00027	0.00447	0.00027	0.13	84.9	1.7	84.5	4.5	50	130	84.9	1.7	-0.5	
Zircon_18	1460	731	0.0473	0.0023	0.0836	0.0028	0.01279	0.00022	0.00412	0.00019	-0.32	82	1.4	81.5	2.6	80	110	82	1.4	0.6	
Zircon_19	439	172	0.0532	0.0044	0.0958	0.0067	0.01302	0.00037	0.00416	0.00036	0.06	83.4	2.4	92.7	6.2	320	170	83.4	2.4	10.0	
Zircon_20	720	246	0.0535	0.004	0.0955	0.0066	0.01299	0.00028	0.00435	0.00027	0.23	80.2	1.8	92.4	6.1	370	150	83.2	1.8	10.0	
Zircon_21	548	223	0.049	0.0043	0.0895	0.007	0.01335	0.00035	0.00412	0.00026	-0.05	85.5	2.2	86.8	6.5	140	180	85.5	2.2	1.5	
Zircon_22	976	368	0.0482	0.0026	0.089	0.0041	0.01325	0.00026	0.00444	0.00028	0.12	84.9	1.7	86.5	3.9	120	120	84.9	1.7	1.8	
Zircon_23	2600	1772	0.0478	0.0022	0.0856	0.0028	0.01302	0.00021	0.00424	0.00016	0.00	83.4	1.3	83.3	2.6	100	100	83.4	1.3	-0.1	
Zircon_25	794	388	0.0488	0.0037	0.0889	0.0055	0.01324	0.00034	0.00436	0.00021	0.11	84.8	2.2	86.3	5.1	110	150	84.8	2.2	1.7	
Zircon_26	595	235	0.0538	0.0054	0.097	0.0098	0.01324	0.0003	0.00505	0.0006	0.67	84.8	1.9	93.6	9	340	200	84.8	1.9	9.4	

Zircon_20	94	96	1.02	0.0492	0.0096	0.087	0.018	0.0124	0.00059	0.00405	0.00086	0.07	79.4	3.8	89	16	160	320	79.4	3.8	10.8
Zircon_21	345	463	1.34	0.0453	0.0052	0.086	0.01	0.01324	0.00037	0.00326	0.00075	0.06	84.8	2.3	83.3	9.2	-30	220	84.8	2.3	-1.8
Zircon_22	824	590	0.72	0.0497	0.0053	0.087	0.011	0.01273	0.00029	0.00404	0.00074	0.19	81.5	1.8	84	10	160	230	81.5	1.8	3.0
Zircon_23	507	738	1.46	0.0508	0.0072	0.088	0.013	0.01266	0.00029	0.00387	0.00074	-0.18	81.1	1.9	85	12	220	270	81.1	1.9	4.6
Zircon_24	784	362	0.46	0.0472	0.0051	0.085	0.01	0.01301	0.00028	0.00389	0.00073	-0.04	83.3	1.8	83.4	9.7	50	220	83.3	1.8	0.1
Zircon_25	656	860	1.31	0.0483	0.0056	0.081	0.011	0.01214	0.00028	0.00385	0.00071	-0.08	77.8	1.8	78.8	9.9	120	240	77.8	1.8	1.3
Zircon_26	342	473	1.38	0.0438	0.0057	0.079	0.011	0.01299	0.00043	0.00321	0.00075	-0.01	83.2	2.7	77	10	-130	240	83.2	2.7	-8.1
Zircon_27	631	1095	1.74	0.0462	0.0051	0.0789	0.0097	0.01211	0.00028	0.00319	0.00066	0.23	77.6	1.8	77	9.2	20	230	77.6	1.8	2.0
Zircon_29	314	305	0.97	0.0486	0.006	0.087	0.013	0.01316	0.00044	0.00402	0.00077	0.17	84.3	2.8	86	12	170	250	84.3	2.8	-0.8
Zircon_30	101	64	0.63	0.061	0.018	0.1	0.04	0.01268	0.00064	0.0042	0.0013	0.06	81.2	4.1	94	34	470	440	81.2	4.1	13.6
Zircon_31	575	362	0.63	0.0486	0.0057	0.093	0.014	0.01298	0.00075	0.0028	0.0011	0.13	83.1	4.8	90	13	130	260	83.1	4.8	7.7
Zircon_32	211	240	1.14	0.0497	0.0069	0.086	0.013	0.0127	0.00045	0.00411	0.00083	0.14	81.3	2.9	84	12	190	290	81.3	2.9	3.2
Zircon_33	284	604	2.13	0.0489	0.007	0.088	0.014	0.01309	0.0004	0.00404	0.00075	0.14	83.8	2.5	85	13	120	270	83.8	2.5	1.4
Zircon_34_36-CL01	203	242	1.19	0.0601	0.0089	0.105	0.017	0.01296	0.00047	0.00439	0.00081	-0.01	83	3	101	15	480	300	83	3	17.8

San Felipe Formation (sample: 29-TE01), coordinates: 21° 10.674'N, 98° 48.757'W

Zircon-004	1360	930	0.68	0.0522	0.0042	0.0904	0.007	0.01266	0.00027	0.00399	0.00013	0.04	81.1	1.7	87.8	6.5	360	100	81.1	1.7	7.6
Zircon-005	263	105	0.40	0.0498	0.0068	0.099	0.013	0.0145	0.00044	0.00522	0.00052	0.16	92.8	2.8	95	12	400	120	92.8	2.8	2.3
Zircon-006	459	202	0.44	0.052	0.0054	0.094	0.0098	0.01314	0.00034	0.00448	0.00027	0.04	84.1	2.2	90.7	9.1	438	91	84.1	2.2	7.3
Zircon-007	472	316	0.67	0.0525	0.0065	0.097	0.011	0.01341	0.00038	0.00458	0.00025	-0.18	85.9	2.4	93	10	500	100	85.9	2.4	7.6
Zircon-008	470	291	0.62	0.0501	0.0047	0.0925	0.0082	0.0132	0.00033	0.00416	0.00023	-0.047	84.5	2.1	89.5	7.6	355	83	84.5	2.1	5.6
Zircon-009	373	160	0.43	0.0494	0.0051	0.0931	0.0093	0.01368	0.00035	0.00475	0.00032	-0.02	87.6	2.2	90	8.7	424	92	87.6	2.2	2.7
Zircon-010	534	197	0.37	0.0477	0.0035	0.0886	0.0062	0.01352	0.00032	0.00436	0.0003	-0.09	86.5	2	86	5.8	301	82	86.5	2	-0.6
Zircon-011	446	248	0.56	0.0594	0.0055	0.1072	0.0098	0.01344	0.00035	0.00432	0.00021	0.24	86.1	2.2	103	9	628	79	86.1	2.2	16.4
Zircon-013	539	276	0.51	0.0516	0.0042	0.0907	0.0072	0.01286	0.00034	0.00462	0.00032	0.10	82.4	2.1	88	6.7	379	90	82.4	2.1	6.4
Zircon-014	766	566	0.74	0.0512	0.0036	0.0958	0.0071	0.01318	0.00034	0.00411	0.00015	0.11	84.4	2.2	92.7	6.6	355	83	84.4	2.2	9.0
Zircon-016	676	191	0.28	0.051	0.0054	0.098	0.01	0.01377	0.00036	0.00475	0.00036	0.12	88.2	2.3	94.2	9.5	440	66	88.2	2.3	6.4
Zircon-017	766	422	0.55	0.0537	0.0029	0.1018	0.0056	0.01389	0.00029	0.00455	0.00016	0.22	88.9	1.8	98.3	5.1	390	66	88.9	1.8	9.6
Zircon-020	509	292	0.57	0.0534	0.0042	0.0989	0.0069	0.01366	0.00033	0.0049	0.00026	-0.06	87.5	2.1	95.6	6.4	426	84	87.5	2.1	8.5
Zircon-021	248	181	0.73	0.0528	0.0063	0.094	0.011	0.01285	0.00039	0.00429	0.00025	-0.04	82.3	2.5	90.6	9.7	550	110	82.3	2.5	9.2
Zircon-022	975	472	0.48	0.0496	0.0033	0.0907	0.0055	0.01329	0.00026	0.00442	0.00019	-0.18	85.1	1.6	88.1	5.1	300	74	85.1	1.6	3.4
Zircon-025	1317	457	0.35	0.049	0.0025	0.0909	0.0045	0.01331	0.00024	0.00451	0.00016	0.02	85.2	1.6	88.3	4.2	238	72	85.2	1.6	3.5
Zircon-026	243	162	0.67	0.0554	0.0061	0.104	0.011	0.01356	0.00037	0.00479	0.00043	0.11	86.8	2.3	100	10	600	100	86.8	2.3	13.2
Zircon-028	291	124	0.43	0.0565	0.0074	0.101	0.012	0.01338	0.00044	0.00574	0.00045	-0.01	86.1	2.8	97	11	660	120	86.1	2.8	11.2
Zircon-029	509	358	0.70	0.0517	0.0061	0.093	0.01	0.01314	0.00039	0.00452	0.00023	-0.12	84.2	2.5	89.8	9.5	501	89	84.2	2.5	6.2
Zircon-030	187	67	0.36	0.046	0.0063	0.097	0.013	0.01495	0.00049	0.00571	0.00061	-0.10	95.7	3.1	95	11	690	200	95.7	3.1	-0.7
Zircon-031	294	136	0.46	0.0498	0.0052	0.0893	0.0083	0.01343	0.00039	0.00477	0.00029	-0.01	86	2.5	89.1	7.8	460	110	86	2.5	3.5
Zircon-032	724	413	0.57	0.0529	0.0038	0.0935	0.0067	0.01318	0.00033	0.00493	0.00028	0.01	84.4	2.1	90.6	6.2	333	74	84.4	2.1	6.8
Zircon-033	388	297	0.77	0.0502	0.0043	0.0896	0.0067	0.01325	0.00043	0.00452	0.00027	0.03	84.8	2.8	86.9	6.3	338	74	84.8	2.8	2.4
Zircon-034	933	552	0.59	0.0505	0.0043	0.0927	0.0073	0.01335	0.0003	0.0042	0.00016	-0.02	85.5	1.9	89.9	6.8	345	83	85.5	1.9	4.9
Zircon-035	548	430	0.78	0.0485	0.0038	0.0873	0.0063	0.01327	0.00039	0.00399	0.00021	0.02	85	2.5	89.8	5.8	252	60	85	2.5	-0.1
Zircon-036	298	183	0.61	0.0517	0.0058	0.092	0.01	0.01328	0.00034	0.00434	0.00027	0.17	85	2.2	88.9	9.4	484	99	85	2.2	4.4
Zircon-038	513	235	0.46	0.0494	0.0058	0.09	0.011	0.01285	0.00036	0.00427	0.00024	-0.14	82.3	2.3	87.2	9.8	480	110	82.3	2.3	5.6
Zircon-039	1300	534	0.41	0.0483	0.0027	0.089	0.0045	0.01343	0.0003	0.00424	0.00021	0.13	86	1.9	86.6	4.2	149	47	86	1.9	0.7
Zircon-040	799	258	0.32	0.0515	0.005	0.0933	0.0094	0.01285	0.00036	0.00457	0.00039	0.17	82.3	2.3	90.4	8.8	400	120	82.3	2.3	9.0

Caracol Formation, Sierra de Parras (sample: 33-AC01V), coordinates: 25° 14.221'N, 101° 25.908'W

Zircon-001_33-AC01	397	270	0.68	0.0508	0.0059	0.0909	0.0078	0.01276	0.00036	0.0043	0.00026	0.09	81.7	2.3	88.1	7	387	95	81.7	2.3	7.3
Zircon-003	292	169	0.58	0.0474	0.0061	0.0888	0.0091	0.01314	0.00044	0.00448	0.00028	0.28	84.1	2.8	86.1	8.5	390	130	84.1	2.8	2.3
Zircon-004	222	111	0.50	0.0539	0.0076	0.095	0.01	0.01275	0.00045	0.00489	0.00036	-0.02	81.6	2.8	93.4	9.5	690	170	81.6	2.8	12.6
Zircon-006	112	52	0.46	0.042	0.0065	0.083	0.011	0.01313	0.00047	0.00436	0.0005	0.24	84.1	3	80	10	510	130	84.1	3	-5.1
Zircon-007	217	132	0.61	0.0538	0.0068	0.0902	0.0097	0.01265	0.00044	0.00397	0.00031	-0.12	81.1	2.8	87.1	9	830	120	81.1	2.8	6.9
Zircon-008	342	258	0.75	0.0461	0.0049	0.0834	0.0069	0.01287	0.00038	0.00417	0.00024	0.16	82.4	2.4	81	6.5	290	110	82.4	2.4	-1.7
Zircon-009	308	184	0.60	0.0521	0.006	0.0903	0.0086	0.01288	0.0004	0.00402	0.00031	0.04	82.5	2.5	87.4	8.2	500	180	82.5	2.5	5.6
Zircon-010	143	67	0.47	0.053	0.0038	0.096	0.063	0.01312	0.00062	0.0047	0.0014	-0.05	84	3.9	93	49	570	430	84	3.9	9.7
Zircon-011	690	421	0.61	0.0491	0.0047	0.0836	0.0049	0.01258	0.00032	0.00406	0.00018	0.11	80.6	2.1	81.5	4.6	311	87	80.6	2.1	1.1
Zircon-012	274	179	0.65	0.053	0.0022	0.091	0.052	0.0128	0.00068	0.0038	0.0013	0.24	82	4.3	88	42	430	350	82	4.3	6.8
Zircon-013	295	222	0.75	0.0481	0.0061	0.0805	0.0081	0.01242	0.00037	0.0043	0.00026	-0.23	79.5	2.4	78.4	7.6	410	130	79.5	2.4	-1.4
Zircon-014	256	150	0.59	0.0511	0.0066	0.0878	0.0094	0.01251	0.00036	0.00409	0.00034	0.29	80.2	2.3	85	8.8	630	130	80.2	2.3	5.6
Zircon-015	539	320	0.59	0.0486	0.0051	0.0872	0.0059	0.01312	0.00042	0.00468	0.00026	-0.06	84	2.7	84.7	5.5	233	87	84	2.7	0.8
Zircon-016	541	278	0.51	0.0487	0.0052	0.0825	0.0056	0.01244	0.00034	0.00378	0.00021	-0.13	79.7	2.2	80.4	5.2	350	110	79.7	2.2	2.0
Zircon-017	528	235																			

Zircon_14	214	209	0.98	0.0555	0.0027	0.549	0.028	0.0717	0.0017	0.02168	0.00089	0.11	446	10	443	18	420	110	446	10	-0.7
Zircon_15	507	296	0.58	0.0518	0.0033	0.269	0.016	0.0376	0.0012	0.01219	0.00048	0.16	237.7	7.4	242	13	310	160	237.7	7.4	1.8
Zircon_16	334	43	0.13	0.0608	0.0021	0.891	0.041	0.1064	0.0033	0.0327	0.0015	0.68	652	19	645	22	623	75	652	19	-1.1
Zircon_17	536	324	0.60	0.1012	0.0029	3.42	0.13	0.2456	0.006	0.0795	0.0018	0.78	1416	31	1512	32	1646	54	1646	31	6.3
Zircon_18	118	41	0.34	0.0712	0.0029	1.668	0.066	0.1685	0.0036	0.0502	0.0021	-0.21	1004	20	998	27	965	79	1004	20	-0.6
Zircon_19	336	223	0.66	0.06	0.0029	0.61	0.031	0.073	0.0019	0.02406	0.00096	0.03	454	11	485	21	610	110	454	11	6.4
Zircon_20	423	214	0.51	0.0926	0.0026	2.96	0.098	0.2295	0.0047	0.0678	0.0019	0.70	1332	25	1397	25	1477	55	1477	25	4.7
Zircon_21	329	157	0.48	0.0605	0.0058	0.123	0.012	0.01474	0.00061	0.00575	0.00057	0.19	94.3	3.9	117	11	610	190	94.3	3.9	19.4
Zircon_22	397	209	0.53	0.0526	0.0026	0.323	0.016	0.0451	0.001	0.01397	0.00055	0.15	284.3	6.4	284	12	300	110	284.3	6.4	-0.1
Zircon_23	178	85	0.48	0.0463	0.0053	0.094	0.011	0.01466	0.00055	0.0047	0.00036	0.10	93.8	3.5	91	9.8	80	210	93.8	3.5	-3.1
Zircon_24	370	202	0.55	0.0488	0.0047	0.0997	0.0094	0.01477	0.00044	0.00483	0.00033	-0.09	94.5	2.8	96.2	8.7	200	200	94.5	2.8	1.8
Zircon_25	177	92	0.52	0.0567	0.0028	0.636	0.031	0.0813	0.0018	0.0259	0.001	0.18	504	11	498	19	470	110	504	11	-1.2
Zircon_26	372	247	0.66	0.0478	0.0036	0.1018	0.0075	0.01538	0.00046	0.00484	0.00026	-0.15	98.4	2.9	98.2	6.9	110	150	98.4	2.9	-0.2
Zircon_27	327	162	0.50	0.0478	0.0031	0.166	0.011	0.02476	0.00068	0.0079	0.00034	0.05	157.7	4.3	155.4	9.8	140	140	157.7	4.3	-1.5
Zircon_28	162	70	0.43	0.0921	0.0032	3.22	0.12	0.2524	0.0048	0.0709	0.0021	-0.02	1451	25	1462	28	1474	61	1474	25	0.8
Zircon_29	244	117	0.48	0.0486	0.0055	0.099	0.011	0.01496	0.00059	0.00496	0.00031	-0.28	95.7	3.7	97	10	100	210	95.7	3.7	1.3
Zircon_30	469	117	0.25	0.0581	0.0044	0.193	0.014	0.02416	0.00062	0.00898	0.00084	0.23	153.9	3.9	179	12	510	170	153.9	3.9	14.0
Zircon_31	195	134	0.69	0.0641	0.0032	1.045	0.053	0.1198	0.0032	0.0364	0.0014	0.40	729	19	725	26	720	100	729	19	-0.6
Zircon_32	186	125	0.67	0.0574	0.0035	0.592	0.034	0.0753	0.0021	0.02447	0.00096	-0.04	468	12	474	21	470	130	468	12	1.3
Zircon_33	577	369	0.64	0.207	0.0053	16.01	0.48	0.567	0.012	0.155	0.0042	0.67	2897	49	2877	29	2882	41	2882	49	-0.7
Zircon_34	94	17	0.18	0.0657	0.004	1.128	0.069	0.1241	0.0038	0.054	0.0044	0.07	754	22	764	33	830	130	754	22	1.3
Zircon_35	199	138	0.69	0.0483	0.0058	0.103	0.012	0.01553	0.00051	0.0047	0.00033	-0.06	99.3	3.2	99	11	150	220	99.3	3.2	-0.3
Zircon_36	299	107	0.36	0.0489	0.0031	0.162	0.01	0.02442	0.0006	0.00775	0.00049	0.15	155.5	3.8	153.6	8.7	160	130	155.5	3.8	-1.2
Zircon_37	125	61	0.48	0.0528	0.0062	0.159	0.018	0.02231	0.00089	0.00702	0.00054	0.07	142.2	5.6	148	15	270	220	142.2	5.6	3.9
Zircon_38	388	12	0.03	0.0629	0.003	0.846	0.037	0.1005	0.0027	0.0345	0.0033	0.22	617	16	631	25	690	100	617	16	2.2
Zircon_39	490	225	0.46	0.0506	0.0031	0.172	0.011	0.02483	0.00057	0.00796	0.00041	0.14	158.1	3.6	161.9	8.8	230	130	158.1	3.6	2.3
Zircon_40	167	74	0.44	0.0804	0.0028	2.233	0.088	0.1997	0.0043	0.0594	0.0019	0.26	1173	23	1190	27	1217	69	1173	23	1.4
Zircon_41	321	279	0.87	0.0499	0.0054	0.109	0.011	0.01574	0.00052	0.00476	0.00028	-0.05	100.7	3.3	107	11	220	210	100.7	3.3	5.9
Zircon_42	79	24	0.31	0.0759	0.0034	1.813	0.089	0.176	0.0044	0.0518	0.0025	0.21	1045	24	1051	31	1071	92	1045	24	0.6
Zircon_43	622	94	0.15	0.0787	0.0022	2.078	0.066	0.1917	0.004	0.0686	0.0022	0.32	1130	21	1141	22	1162	55	1130	21	1.0
Zircon_44	256	124	0.48	0.0523	0.0043	0.154	0.012	0.02191	0.00055	0.00727	0.0004	-0.13	139.7	3.5	147	11	280	170	139.7	3.5	5.0
Zircon_45	329	152	0.46	0.0505	0.0045	0.105	0.0085	0.01521	0.00049	0.0051	0.00035	0.06	97.3	3.1	101.1	7.8	220	170	97.3	3.1	3.8
Zircon_46	1269	348	0.27	0.0512	0.0017	0.2306	0.008	0.03258	0.00065	0.00992	0.00032	0.11	206.7	4.1	210.6	6.6	246	75	206.7	4.1	1.9
Zircon_47	261	65	0.25	0.0795	0.0024	2.089	0.07	0.1921	0.004	0.0569	0.0016	0.20	1133	22	1144	23	1180	59	1133	22	1.0
Zircon_48	380	197	0.52	0.0769	0.0026	1.924	0.09	0.1824	0.0054	0.0547	0.0014	0.70	1080	29	1093	33	1116	67	1080	29	1.2
Zircon_49	76	20	0.26	0.0767	0.0038	1.744	0.08	0.166	0.0041	0.0549	0.0029	-0.14	990	23	1023	30	1110	100	990	23	3.2
Zircon_50	164	128	0.78	0.0613	0.003	0.745	0.035	0.088	0.002	0.02761	0.00086	-0.11	544	12	566	21	650	110	544	12	3.9
Zircon_51	232	130	0.56	0.0508	0.0047	0.117	0.01	0.0161	0.00069	0.00559	0.00044	0.06	103	4.4	112	9.2	240	190	103	4.4	8.0
Zircon_52	388	264	0.68	0.0588	0.0028	0.437	0.021	0.0541	0.0011	0.01744	0.00065	-0.06	339.6	7	368	15	550	100	339.6	7	7.7
Zircon_53	258	178	0.69	0.0503	0.0045	0.1029	0.0098	0.01515	0.00048	0.00497	0.00031	0.02	96.9	3	99.1	9	210	180	96.9	3	2.2
Zircon_54	404	156	0.39	0.0787	0.0027	1.769	0.069	0.1631	0.0039	0.054	0.0017	0.72	974	22	1033	25	1159	69	974	22	5.7
Zircon_55	326	47	0.14	0.0625	0.0019	0.788	0.026	0.0917	0.0018	0.0265	0.0014	0.16	565	10	590	15	693	68	565	10	4.2
Zircon_56	221	126	0.57	0.0531	0.0054	0.108	0.01	0.01512	0.00057	0.00476	0.00036	-0.11	96.8	3.6	103.7	9.4	300	200	96.8	3.6	6.7
Zircon_57	280	95	0.34	0.0932	0.0027	3.28	0.1	0.254	0.0055	0.0751	0.0021	0.46	1459	28	1476	26	1489	55	1489	28	1.2
Zircon_58	256	62	0.24	0.0615	0.0026	0.723	0.034	0.0869	0.0027	0.0286	0.0017	0.55	537	16	552	20	644	92	537	16	2.7
Zircon_59	526	252	0.48	0.0498	0.0029	0.1693	0.0089	0.02474	0.00056	0.00783	0.00035	-0.25	157.5	3.5	158.5	7.7	170	120	157.5	3.5	0.6
Zircon_60	540	266	0.49	0.0797	0.0027	2.073	0.075	0.189	0.0036	0.0564	0.0013	-0.027	1116	20	1139	25	1185	66	1116	20	2.0
Zircon_61	177	255	1.44	0.0857	0.005	1.83	0.1	0.155	0.0037	0.043	0.0018	-0.23	929	20	1060	38	1340	120	929	20	12.4
Zircon_62	619	355	0.57	0.054	0.0044	0.1059	0.0082	0.01446	0.00037	0.00492	0.00024	-0.06	92.6	2.4	102	7.6	410	170	92.6	2.4	9.2
Zircon_63	80	46	0.57	0.0576	0.0046	0.574	0.047	0.0737	0.003	0.0246	0.0012	0.44	458	18	467	34	520	160	458	18	1.9
Zircon_64	431	367	0.85	0.0879	0.0029	2.715	0.092	0.2235	0.0044	0.0647	0.0014	-0.14	1300	23	1332	25	1377	64	1300	23	2.4
Zircon_65	477	122	0.26	0.0711	0.0027	1.488	0.063	0.1529	0.0037	0.0459	0.0021	0.05	917	21	925	26	955	77	917	21	0.9
Zircon_66	290	172	0.59	0.0508	0.0039	0.162	0.013	0.02272	0.00058	0.00729	0.00044	0.11	144.8	3.6	152	11	210	150	144.8	3.6	4.7
Zircon_67	329	85	0.26	0.0558	0.002	0.611	0.023	0.0788	0.0016	0.0237	0.00093	0.12	489.1	9.4	483	14	447	77	489.1	9.4	-1.3
Zircon_68	558	444	0.80	0.087	0.0032	2.75	0.1	0.2289	0.0051	0.0671	0.0017	-0.10	1328	27	1342	27	1370	76	1328	27	1.0
Zircon_69	147	270	1.84	0.0835	0.0038	2.67	0.12	0.2322	0.0061	0.0751	0.0026	-0.03	1346	32	1318	32	1273	88	1346	32	-2.1
Zircon_70	598	260	0.43	0.0745	0.002	1.771	0.055	0.1733	0.0033	0.0531	0.0012	0.15	1030	18	1035	20	1052	54	1030	18	0.5
Zircon_71	287	96	0.33	0.0722	0.0025	1.602	0.056	0.1607	0.0036	0.05	0.002	-0.06	960	20	973	23	984	72	960	20	1.3
Zircon_72	310	188	0.61	0.0534	0.0022	0.449	0.02	0.0608	0.0013	0.01907	0.00073	0.18	380.4	7.9	376	14	332	93	380.4	7.9	-1.2
Zircon_73	214	88	0.41	0.053	0.0032	0.305	0.019	0.0421	0.0012	0.01384	0.00073	0.23	265.9	7.4							

Zircon_109	1269	646	0.51	0.0563	0.0024	0.398	0.016	0.0508	0.0013	0.01522	0.00055	-0.29	319.3	7.9	340	11	453	92	319.3	7.9	6.1
Zircon_110	543	202	0.37	0.05	0.0025	0.1685	0.0091	0.02416	0.00059	0.00798	0.00038	0.18	153.9	3.7	157.9	8	210	110	153.9	3.7	2.5
Zircon_111	223	113	0.51	0.0698	0.0044	0.617	0.038	0.064	0.0017	0.0242	0.0012	0.08	400	11	487	24	910	130	400	11	17.9
Zircon_112	181	117	0.65	0.0474	0.0043	0.13	0.012	0.02027	0.00062	0.00666	0.00035	-0.20	129.4	3.9	125	11	70	170	129.4	3.9	-3.5
Zircon_113	795	172	0.22	0.0467	0.0025	0.1016	0.006	0.01528	0.00035	0.0049	0.0004	-0.02	97.8	2.2	98.1	5.5	50	110	97.8	2.2	0.3
Zircon_114	242	89	0.37	0.0531	0.0035	0.183	0.012	0.02501	0.00066	0.0079	0.00048	0.01	159.2	4.1	170	10	300	140	159.2	4.1	6.4
Zircon_115	258	106	0.41	0.0517	0.0048	0.165	0.014	0.02329	0.00059	0.0074	0.0005	-0.22	148.4	3.7	154	13	230	180	148.4	3.7	3.6
Zircon_116	248	161	0.65	0.0596	0.0059	0.115	0.012	0.01434	0.00068	0.00504	0.00033	-0.06	91.8	4.3	110	11	570	220	91.8	4.3	16.5
Zircon_117	520	87	0.17	0.0464	0.0031	0.16	0.012	0.02434	0.00087	0.00758	0.00055	0.30	155	5.5	150	10	30	120	155	5.5	-3.3
Zircon_118	544	33	0.06	0.0621	0.0031	0.82	0.042	0.0939	0.0022	0.0296	0.0073	0.65	579	13	608	23	670	110	579	13	4.8
Zircon_119	247	166	0.67	0.0564	0.0026	0.626	0.029	0.0805	0.0019	0.02393	0.00086	0.19	499	11	493	18	464	98	499	11	-1.2
Zircon_120	211	274	1.30	0.0542	0.0028	0.494	0.026	0.0646	0.0016	0.01996	0.00058	-0.06	403.3	9.7	406	18	390	120	403.3	9.7	0.7
Zircon_121	589	414	0.70	0.0493	0.0032	0.1003	0.0069	0.01465	0.00041	0.00465	0.00022	0.01	93.7	2.6	96.8	6.4	190	140	93.7	2.6	3.2

Unnamed turbidites near the Mexquitic population, Mesa Central (sample: 25-MB02); coordinates: 22° 22.109'N, 101° 17.895'W

Zircon-001	116	50	0.43	0.0806	0.0044	2.4	0.13	0.2164	0.0053	0.0672	0.0038	0.27	1263	26	1245	39	1202	60	1263	60	-1.4
Zircon-002	362	211	0.58	0.0481	0.0003	0.175	0.01	0.02604	0.00048	0.00794	0.0005	0.37	165.7	3	163.2	8.8	234	95	165.7	3	-1.5
Zircon-003	249	37	0.15	0.1199	0.0059	5.97	0.23	0.3593	0.0045	0.0991	0.0058	0.47	1979	21	1974	32	1958	51	1958	51	-0.3
Zircon-004	650	341	0.52	0.0499	0.0032	0.1089	0.0061	0.01595	0.00033	0.00514	0.0003	0.25	102	2.1	104.8	5.6	232	80	102	2.1	2.7
Zircon-005	219	188	0.86	0.0687	0.0065	0.132	0.012	0.01422	0.00036	0.00513	0.00035	0.16	91	2.3	125	11	880	110	91	2.3	27.2
Zircon-006	306	180	0.59	0.1016	0.0051	4.01	0.16	0.2864	0.0036	0.0882	0.0047	0.02	1623	18	1638	33	1670	53	1670	53	0.3
Zircon-007	578	317	0.55	0.051	0.0034	0.1606	0.0098	0.02327	0.00037	0.00748	0.00044	0.31	148.3	2.3	151	8.8	284	77	148.3	2.3	1.8
Zircon-008	491	156	0.32	0.0597	0.0031	0.806	0.034	0.0974	0.0014	0.0289	0.0017	0.21	599.1	8	600	19	593	75	599.1	8	0.1
Zircon-009	676	35	0.05	0.0589	0.0029	0.78	0.031	0.0956	0.0012	0.029	0.0018	0.21	588.6	6.8	585	18	574	70	588.6	6.8	-0.6
Zircon-010	266	173	0.65	0.0529	0.0034	0.301	0.016	0.0415	0.00077	0.01308	0.00076	0.20	262.1	4.7	267	12	324	78	262.1	4.7	1.8
Zircon-012	203	83	0.41	0.0494	0.0042	0.186	0.014	0.02668	0.00066	0.00932	0.00068	-0.03	169.7	4.1	172	12	380	100	169.7	4.1	1.3
Zircon-013	520	374	0.72	0.0494	0.0033	0.1746	0.0099	0.02545	0.00044	0.00786	0.00045	0.07	162.3	2.7	163.1	8.6	278	83	162.3	2.7	0.5
Zircon-014	610	406	0.67	0.0475	0.0033	0.1084	0.0063	0.0166	0.00031	0.00557	0.00032	-0.16	106.2	2	104.4	5.7	268	75	106.2	2	-1.7
Zircon-015	211	95	0.45	0.0615	0.006	0.181	0.018	0.02135	0.00053	0.00857	0.00079	0.16	136.2	3.3	168	15	720	120	136.2	3.3	18.9
Zircon-017	715	1250	1.75	0.0521	0.0004	0.1079	0.0079	0.01512	0.00035	0.00459	0.0003	0.32	96.7	2.3	103.9	7.2	379	74	96.7	2.3	6.9
Zircon-018	1427	816	0.57	0.0481	0.0028	0.1082	0.0052	0.01625	0.00026	0.00499	0.00028	0.05	103.9	1.6	104.2	4.8	185	49	103.9	1.6	0.1
Zircon-020	367	249	0.68	0.057	0.0053	0.1111	0.0093	0.01438	0.00034	0.00449	0.00031	0.10	92	2.2	108.4	8.5	612	98	92	2.2	15.1
Zircon-021	335	106	0.32	0.0529	0.0038	0.186	0.012	0.02581	0.00057	0.00945	0.00062	-0.12	164.3	3.6	173	9.7	340	71	164.3	3.6	5.0
Zircon-022	709	75	0.11	0.0498	0.0031	0.178	0.01	0.02573	0.00061	0.00902	0.00068	0.35	163.8	3.9	166.1	8.6	258	63	163.8	3.9	1.4
Zircon-023	201	110	0.55	0.053	0.0004	0.166	0.011	0.02294	0.00056	0.00787	0.0005	0.02	146.2	3.5	155.4	9.6	397	87	146.2	3.5	5.9
Zircon-024	189	80	0.42	0.0818	0.0041	2.53	0.11	0.2238	0.0052	0.0643	0.0035	0.17	1302	27	1280	33	1231	54	1231	54	-1.7
Zircon-025	176	107	0.61	0.1077	0.0052	4.18	0.18	0.2803	0.0058	0.0881	0.0045	0.60	1592	29	1669	39	1742	65	1742	65	4.6
Zircon-026	195	151	0.77	0.0724	0.0004	1.579	0.069	0.1586	0.0025	0.0507	0.0026	0.28	949	14	965	27	1006	63	949	14	1.7
Zircon-027	815	942	1.16	0.0584	0.0032	0.574	0.031	0.0722	0.0015	0.022	0.0025	0.33	449.6	9.1	460	20	526	66	449.6	9.1	2.3
Zircon-028	361	175	0.48	0.0517	0.0041	0.177	0.012	0.02578	0.00052	0.00823	0.00056	-0.14	164	3.3	167	11	390	94	164	3.3	1.8
Zircon-029	80	35	0.44	0.0544	0.0051	0.297	0.026	0.0405	0.0011	0.0141	0.0012	0.10	255.6	6.6	265	21	510	120	255.6	6.6	3.6
Zircon-030	506	168	0.33	0.0503	0.0033	0.1772	0.0097	0.02555	0.00045	0.00804	0.00052	-0.03	162.7	2.8	165.4	8.4	321	76	162.7	2.8	1.6
Zircon-031	246	119	0.48	0.0517	0.0048	0.1065	0.009	0.0154	0.00043	0.00518	0.00038	-0.03	98.5	2.7	102.4	8.2	388	95	98.5	2.7	3.8
Zircon-032	567	126	0.22	0.0626	0.0033	0.92	0.04	0.1072	0.0018	0.0399	0.0024	0.43	656.1	9.9	662	21	703	64	656.1	9.9	0.9
Zircon-033	930	960	1.03	0.0488	0.0003	0.1027	0.0059	0.01542	0.00028	0.00485	0.00027	0.29	98.6	1.8	100	5.6	245	99	98.6	1.8	1.4
Zircon-034	412	43	0.10	0.0922	0.0052	2.8	0.21	0.219	0.011	0.0734	0.0052	0.31	1275	60	1354	71	1480	120	1480	120	5.8
Zircon-035	500	173	0.35	0.0499	0.0038	0.1111	0.0085	0.01598	0.00031	0.00527	0.00054	0.25	102.2	2	107.8	7.6	280	140	102.2	2	5.2
Zircon-036	242	314	1.30	0.0496	0.0045	0.157	0.013	0.02332	0.00052	0.00717	0.00042	-0.10	148.6	3.3	149	11	419	78	148.6	3.3	0.3
Zircon-037	713	248	0.35	0.046	0.0031	0.0972	0.0055	0.0151	0.00029	0.00471	0.00031	0.11	96.6	1.9	94	5.1	230	94	96.6	1.9	-2.8
Zircon-038	317	36	0.11	0.0578	0.0033	0.601	0.028	0.0756	0.0012	0.0227	0.0016	0.16	469.6	7.4	477	18	529	60	469.6	7.4	1.6
Zircon-039	143	75	0.53	0.076	0.0043	1.978	0.091	0.1879	0.0027	0.0574	0.0032	0.18	1110	15	1106	31	1091	61	1091	61	-0.4
Zircon-040	134	232	1.73	0.075	0.0045	1.833	0.082	0.176	0.0038	0.054	0.0031	0.27	1045	21	1060	30	1074	72	1074	72	0.4
Zircon-041	262	69	0.26	0.1018	0.0051	4.05	0.16	0.2894	0.0038	0.0867	0.0048	0.46	1638	19	1643	33	1663	42	1663	42	0.3
Zircon-042	564	94	0.17	0.0592	0.0038	0.275	0.016	0.03267	0.00086	0.0155	0.0014	-0.08	207.2	5.4	246	13	601	95	207.2	5.4	15.8
Zircon-043	216	70	0.33	0.055	0.0069	0.192	0.021	0.02433	0.00054	0.0091	0.001	0.09	155	3.4	177	17	480	170	155	3.4	12.4
Zircon-044	868	578	0.67	0.0491	0.0032	0.0942	0.0055	0.01386	0.00023	0.0045	0.00026	-0.03	88.7	1.5	91.3	5.1	280	66	88.7	1.5	2.8
Zircon-045	1592	429	0.27	0.0475	0.0028	0.1041	0.005	0.016	0.00026	0.00513	0.0003	0.04	102.4	1.7	100.5	4.6	159	68	102.4	1.7	-1.9
Zircon-046	225	137	0.61	0.0562	0.0034	0.593	0.031	0.0751	0.0012	0.023	0.0013	-0.09	466.9	7	472	20	459	80	466.9	7	1.1
Zircon-047	725	341	0.47	0.0524	0.0038	0.1108	0.0072	0.01495	0.00026	0.00518	0.00038	0.33	95.7	1.7	106.6	6.5	333	84	95.7	1.7	10.2
Zircon-048	357	142	0.40	0.0586	0.0033	0.779	0.037	0.0962	0.0015	0.0292	0.0016	0.08	591.8	9.1	584	21	568	89	591.8	9.1	0.3
Zircon-049	273	190																			

Zircon-088	468	337	0.72	0.051	0.036	0.1	0.15	0.0152	0.0016	0.0049	0.0029	0.02	97	10	101	89	500	470	97	10	4.0
Zircon-089	75	57	0.76	0.0854	0.0044	2.84	0.14	0.2399	0.0063	0.0685	0.004	0.28	1386	33	1371	36	1334	75	1334	75	-1.1
Zircon-090	245	155	0.63	0.0533	0.0066	0.113	0.015	0.01547	0.00043	0.0052	0.00043	-0.10	98.9	2.7	110	13	500	160	98.9	2.7	10.1
Zircon-091	217	144	0.66	0.0772	0.0039	2.171	0.087	0.2044	0.0029	0.0581	0.003	0.25	1199	15	1171	29	1110	64	1110	64	-2.4
Zircon-092	623	90	0.14	0.0764	0.0038	1.976	0.08	0.1885	0.0029	0.0544	0.003	-0.10	1113	16	1107	27	1095	57	1095	57	-0.5
Zircon-093	302	233	0.77	0.0499	0.0042	0.1107	0.0086	0.01622	0.00039	0.00507	0.00033	0.12	103.7	2.5	106.3	7.8	375	82	103.7	2.5	2.4
Zircon-095	344	87	0.25	0.053	0.0038	0.192	0.012	0.02685	0.00056	0.00798	0.00066	0.10	170.8	3.5	178	10	372	79	170.8	3.5	4.0
Zircon-096	558	353	0.63	0.0541	0.0029	0.419	0.018	0.05602	0.00084	0.01632	0.00088	0.04	351.3	5.1	356	14	382	70	351.3	5.1	1.3
Zircon-097	365	118	0.32	0.075	0.0038	1.864	0.078	0.1803	0.0027	0.0678	0.004	0.52	1068	15	1067	28	1074	58	1074	58	-0.1
Zircon-098	208	157	0.75	0.0542	0.007	0.114	0.014	0.01539	0.00039	0.005	0.00042	-0.23	98.5	2.5	109	12	620	150	98.5	2.5	9.6
Zircon-099	419	58	0.14	0.0536	0.0033	0.1836	0.0096	0.02451	0.00046	0.00762	0.00067	0.09	156.1	2.9	171	8	390	58	156.1	2.9	8.7
Zircon-100	568	245	0.43	0.0482	0.0034	0.1025	0.0064	0.01573	0.00029	0.00503	0.00032	0.05	100.6	1.9	98.9	5.9	250	79	100.6	1.9	-1.7
Zircon-101	308	405	1.31	0.0496	0.0042	0.1071	0.0079	0.01552	0.00036	0.00503	0.00029	-0.02	99.3	2.3	103	7.3	336	80	99.3	2.3	3.6
Zircon-102	741	267	0.36	0.0494	0.0032	0.1027	0.0087	0.01491	0.00074	0.00484	0.0003	0.04	95.4	4.7	99.1	7.9	293	94	95.4	4.7	3.7
Zircon-103	546	412	0.75	0.049	0.0039	0.1062	0.0078	0.01562	0.00026	0.00512	0.00029	-0.08	99.9	1.7	103.1	6.9	261	80	99.9	1.7	3.1
Zircon-104	896	628	0.70	0.0559	0.0032	0.1147	0.006	0.01537	0.00027	0.00516	0.0003	0.29	98.3	1.7	110.1	5.5	461	76	98.3	1.7	10.7
Zircon-105	133	36	0.27	0.0557	0.0043	0.397	0.028	0.0515	0.00097	0.0176	0.0013	-0.23	323.7	6	338	21	470	100	323.7	6	4.2
Zircon-106	226	90	0.40	0.0598	0.0048	0.218	0.017	0.02627	0.00069	0.0096	0.00071	0.37	167.2	4.3	203	14	671	85	167.2	4.3	17.6
Zircon-107	263	222	0.84	0.0492	0.0049	0.1005	0.0084	0.01457	0.00041	0.00505	0.00032	-0.10	93.2	2.6	98.1	7.9	300	100	93.2	2.6	5.0
Zircon-108	356	182	0.51	0.0514	0.0035	0.292	0.017	0.04044	0.00071	0.013	0.00077	-0.07	255.5	4.4	261	13	333	82	255.5	4.4	2.1
Zircon-109	680	130	0.19	0.0564	0.003	0.559	0.024	0.0721	0.001	0.0239	0.0014	-0.03	448.8	6.1	450	16	472	69	448.8	6.1	0.3
Zircon-110	120	42	0.35	0.0773	0.0041	2.145	0.093	0.2001	0.003	0.0605	0.0036	0.15	1176	16	1165	29	1106	65	1106	65	-0.9
Zircon-111	109	163	1.50	0.1158	0.0058	5.83	0.23	0.3613	0.0051	0.1022	0.0053	0.03	1988	24	1950	38	1889	58	1889	58	19.0
Zircon-112	160	86	0.54	0.0577	0.0036	0.628	0.039	0.078	0.00019	0.0234	0.0015	-0.17	484	11	492	23	537	78	484	11	1.6
Zircon-114	97	88	0.91	0.0573	0.0093	0.108	0.019	0.01509	0.00062	0.00553	0.00044	0.22	96.5	3.9	102	17	710	130	96.5	3.9	5.4
Zircon-115	695	364	0.52	0.0485	0.004	0.0995	0.0071	0.01496	0.00026	0.00474	0.0003	-0.16	95.7	1.6	96.1	6.6	301	88	95.7	1.6	0.4
Zircon-116	254	130	0.51	0.0506	0.0034	0.239	0.014	0.03364	0.00062	0.01059	0.00065	0.17	213.3	3.8	217	11	341	79	213.3	3.8	1.7
Zircon-117	450	172	0.38	0.0493	0.0033	0.178	0.01	0.02597	0.00045	0.00829	0.00054	-0.02	165.2	2.8	166.1	8.7	248	52	165.2	2.8	0.5
Zircon-119	80	54	0.67	0.0599	0.0055	0.63	0.05	0.077	0.00019	0.0262	0.0017	-0.06	478	11	498	30	730	110	478	11	4.0
Zircon-121	110	84	0.76	0.0605	0.0055	0.675	0.061	0.0813	0.00021	0.0245	0.0022	-0.02	504	13	522	34	570	120	504	13	3.4
Zircon-122	261	126	0.48	0.0506	0.0048	0.1037	0.0089	0.01494	0.00037	0.00496	0.00037	-0.08	95.6	2.4	99.8	8.2	391	83	95.6	2.4	4.2
Zircon-123	285	170	0.60	0.0485	0.0045	0.1059	0.0089	0.01578	0.00037	0.00519	0.00036	-0.10	100.9	2.3	101.9	8.2	370	100	100.9	2.3	1.0
Zircon-124	394	72	0.18	0.0734	0.004	1.73	0.075	0.1712	0.0025	0.0484	0.0044	0.28	1019	14	1019	27	1022	90	1022	90	0.0
Zircon-125	787	396	0.50	0.0495	0.0033	0.1054	0.006	0.01545	0.00026	0.00465	0.0003	0.11	98.8	1.7	101.6	5.5	237	73	98.8	1.7	2.8
Zircon-126	176	155	0.88	0.0554	0.0035	0.549	0.03	0.0725	0.00014	0.0207	0.0012	0.11	451.2	8.4	445	19	413	83	451.2	8.4	-1.4
Zircon-127	1580	1600	1.01	0.05	0.003	0.177	0.013	0.0259	0.00013	0.00764	0.00072	0.59	164.8	8	166	11	189	63	164.8	8	0.7
Zircon-128	506	317	0.63	0.0551	0.0029	0.582	0.025	0.0759	0.00011	0.0225	0.0012	0.02	471.8	6.5	465	16	424	75	471.8	6.5	6.5
Zircon-129	233	106	0.45	0.0836	0.0042	2.45	0.1	0.215	0.0038	0.0641	0.0035	0.54	1255	20	1257	30	1273	54	1273	54	0.2
Zircon-130	273	219	0.80	0.0495	0.0041	0.193	0.014	0.02817	0.0005	0.00899	0.00056	-0.08	179.1	3.2	179	12	385	98	179.1	3.2	-0.1
Zircon-131	158	91	0.58	0.0551	0.0076	0.118	0.015	0.01581	0.00055	0.00527	0.00049	-0.23	101.1	3.5	113	13	590	110	101.1	3.5	10.5
Zircon-132	318	106	0.33	0.0519	0.0037	0.184	0.013	0.02608	0.00058	0.00944	0.00069	0.03	166	3.6	171	11	319	98	166	3.6	2.9
Zircon-134	1413	522	0.37	0.056	0.0029	0.598	0.024	0.07736	0.00099	0.0231	0.0012	0.24	480.3	5.9	476	16	445	70	480.3	5.9	-0.9
Zircon-135	1077	492	0.46	0.0486	0.003	0.1714	0.0089	0.02558	0.00035	0.00763	0.00043	-0.24	162.8	2.2	160.5	7.7	184	55	162.8	2.2	-1.4
Zircon-136	170	176	1.04	0.0495	0.0064	0.106	0.014	0.01567	0.00054	0.00481	0.00041	0.04	100.2	3.4	102	12	390	160	100.2	3.4	1.8
Zircon-137	363	283	0.78	0.1128	0.0056	4.9	0.19	0.3143	0.0058	0.091	0.0047	-0.11	1762	29	1802	35	1841	39	1841	39	2.2
Zircon-138	154	71	0.46	0.1249	0.0061	6.68	0.29	0.3892	0.0094	0.1105	0.0075	0.12	2119	45	2070	42	2015	49	2015	49	-2.4
Zircon-139	510	296	0.58	0.0508	0.0038	0.168	0.011	0.0245	0.00044	0.0076	0.00044	0.09	156	2.8	158.8	9.8	333	82	156	2.8	1.8
Zircon-140	240	172	0.72	0.0498	0.0046	0.121	0.01	0.01721	0.00045	0.00547	0.00034	0.01	110	2.9	116.5	9.2	383	81	110	2.9	5.6
Zircon-141	280	213	0.76	0.0479	0.0046	0.1042	0.0092	0.01551	0.00035	0.00499	0.00032	0.10	99.2	2.2	100.3	8.4	260	77	99.2	2.2	1.1
Zircon-142	265	183	0.69	0.0571	0.0035	0.573	0.031	0.0723	0.00015	0.0216	0.0013	0.16	450.1	9.2	459	20	484	72	450.1	9.2	1.9
Zircon-143	1477	1530	1.04	0.0503	0.0041	0.169	0.012	0.02436	0.00038	0.00773	0.00045	-0.08	155.1	2.4	159	10	250	110	155.1	2.4	2.5
Zircon-144	509	240	0.47	0.0495	0.0033	0.174	0.011	0.02532	0.00056	0.00794	0.0005	0.35	161.2	3.5	162.8	9.5	212	45	161.2	3.5	1.0
Zircon-145	619	193	0.31	0.0542	0.004	0.198	0.012	0.02631	0.00041	0.00924	0.00073	0.01	167.4	2.6	183.1	9.7	396	94	167.4	2.6	8.6
Zircon-146	275	185	0.67	0.0505	0.0041	0.149	0.01	0.02176	0.00047	0.00713	0.00043	-0.01	138.7	2.9	141	8.9	370	96	138.7	2.9	1.6
Zircon-147	129	99	0.76	0.056	0.0038	0.599	0.035	0.0777	0.00014	0.023	0.0015	0.11	482.6	8.7	478	22	497	93	482.6	8.7	-1.0
Zircon-148	899	631	0.70	0.0471	0.003	0.101	0.0056	0.01557	0.00023	0.00462	0.00026	0.09	99.6	1.5	97.6	5.2	221	72	99.6	1.5	-2.0
Zircon-149	372	282	0.76	0.0478	0.0044	0.0995	0.0084	0.01496	0.00034	0.0046	0.00029	-0.14	95.7	2.2	97.1	7.5	340	94	95.7	2.2	1.4
Zircon-150	274	161	0.59	0.0791	0.004	2.232	0.092	0.2047	0.00026	0.0603	0.00033	0.30	1201	14	1190	29	1163	63	1163	63	-0.9

Unnamed turbidities near the Mexquitic population, Mesa Central (sample: 26-PST01); coordinates: 22° 21.828'N, 101° 16.833'W

Zircon-001

Zircon-036	132	33	0.25	0.0932	0.004	3.57	0.21	0.275	0.011	0.0802	0.004	0.83	1568	55	1545	47	1498	50	1498	50	-1.5
Zircon-037	226	291	1.29	0.0522	0.0048	0.179	0.017	0.02442	0.00065	0.0079	0.0004	0.05	155.5	4.1	166	15	467	88	155.5	4.1	6.3
Zircon-038	264	273	1.03	0.0588	0.0027	0.703	0.033	0.0875	0.0016	0.0266	0.0011	0.11	540.6	9.6	542	20	549	49	540.6	9.6	0.0
Zircon-040	92	106	1.15	0.1126	0.0048	5.5	0.23	0.3538	0.0072	0.1082	0.0046	0.03	1952	34	1898	36	1849	40	1849	40	-2.8
Zircon-042	484	338	0.70	0.0496	0.0038	0.0997	0.0082	0.01488	0.0004	0.00452	0.00028	-0.17	95.2	2.6	96.3	7.5	294	62	95.2	2.6	1.1
Zircon-043	810	623	0.77	0.0496	0.0031	0.1339	0.0082	0.01939	0.00044	0.00583	0.00036	-0.16	123.8	2.8	127.4	7.3	184	67	123.8	2.8	2.8
Zircon-044	242	96	0.40	0.0756	0.003	1.995	0.078	0.1918	0.0034	0.0585	0.0025	0.06	1131	18	1116	27	1088	58	1088	58	-1.3
Zircon-045	735	210	0.29	0.0492	0.0023	0.1758	0.0086	0.02572	0.0005	0.00789	0.00043	0.13	163.7	3.1	164.3	7.4	198	49	163.7	3.1	0.4
Zircon-046	251	327	1.30	0.0503	0.0056	0.099	0.01	0.0143	0.00041	0.00449	0.00024	0.02	91.5	2.6	95	9.5	475	85	91.5	2.6	3.7
Zircon-047	256	28	0.11	0.0561	0.0024	0.585	0.025	0.0754	0.0014	0.0257	0.0017	0.16	468.4	8.2	467	16	442	59	468.4	8.2	-0.3
Zircon-048	29	25	0.86	0.0812	0.005	2.44	0.15	0.2159	0.0051	0.0611	0.0032	0.19	1260	27	1259	44	1239	74	1239	74	-0.1
Zircon-049	381	162	0.43	0.0565	0.0025	0.588	0.025	0.0748	0.0015	0.0235	0.0011	-0.04	465	9	469	16	465	56	465	9	0.9
Zircon-050	248	191	0.77	0.066	0.061	0.14	0.46	0.0163	0.0037	0.006	0.017	0.08	104	23	130	170	850	380	104	23	20.0
Zircon-051	858	1047	1.22	0.0556	0.0023	0.558	0.022	0.0718	0.0013	0.02153	0.00086	0.10	447.1	7.6	450	15	451	55	447.1	7.6	0.6
Zircon-052	100	42	0.42	0.05	0.0081	0.112	0.017	0.01577	0.00058	0.00581	0.00065	-0.04	100.8	3.7	107	15	640	150	100.8	3.7	5.8
Zircon-053	300	338	1.13	0.0541	0.0055	0.191	0.022	0.02649	0.00071	0.0088	0.00053	0.39	168.5	4.5	177	18	420	130	168.5	4.5	4.8
Zircon-054	131	354	2.71	0.0578	0.0031	0.744	0.038	0.092	0.0022	0.0279	0.0011	0.11	567	13	563	22	527	76	567	13	-0.7
Zircon-055	128	68	0.53	0.0525	0.0054	0.111	0.011	0.01597	0.00073	0.00539	0.00045	0.29	102.1	4.7	107	10	530	120	102.1	4.7	4.6
Zircon-056	431	162	0.38	0.0489	0.0036	0.1016	0.0076	0.0149	0.00034	0.00503	0.00029	0.04	95.3	2.1	98.1	6.9	232	61	95.3	2.1	2.9
Zircon-057	167	64	0.38	0.0488	0.0057	0.113	0.012	0.01657	0.0005	0.00536	0.00048	0.03	105.9	3.2	108	11	450	140	105.9	3.2	1.9
Zircon-058	46	21	0.45	0.0595	0.0042	0.796	0.057	0.0956	0.0024	0.0282	0.0022	0.12	589	14	590	33	637	89	589	14	0.2
Zircon-059	304	331	1.09	0.0558	0.0037	0.606	0.047	0.0774	0.0018	0.0221	0.0018	0.40	481	11	480	28	485	93	481	11	-0.2
Zircon-060	124	24	0.19	0.0733	0.0031	1.852	0.078	0.1816	0.0035	0.0514	0.0027	0.08	1076	19	1065	27	1026	45	1026	45	-1.0
Zircon-061	383	99	0.26	0.0515	0.0028	0.316	0.017	0.04461	0.00099	0.0143	0.00078	0.21	281.3	6.1	278	13	341	79	281.3	6.1	-1.2
Zircon-062	161	152	0.94	0.1085	0.0041	4.92	0.18	0.3266	0.006	0.0933	0.0037	0.24	1822	29	1804	31	1769	39	1769	39	-1.0
Zircon-063	222	97	0.44	0.0693	0.0028	1.507	0.065	0.1562	0.0044	0.0507	0.0022	0.43	936	25	932	28	916	60	936	25	-0.4
Zircon-064	269	188	0.70	0.0493	0.0034	0.1046	0.0072	0.01518	0.00037	0.00498	0.00029	0.09	97.1	2.3	100.8	6.6	311	89	97.1	2.3	3.7
Zircon-065	246	162	0.66	0.0503	0.0051	0.099	0.0094	0.01455	0.00046	0.00438	0.00026	-0.08	93.1	2.9	96.9	9.1	460	110	93.1	2.9	3.9
Zircon-066	232	90	0.39	0.0906	0.0036	3.17	0.13	0.2535	0.0051	0.0794	0.0033	0.52	1459	26	1448	32	1441	44	1441	44	-0.8
Zircon-067	66	38	0.57	0.0842	0.0041	2.58	0.12	0.2212	0.0046	0.069	0.0032	-0.01	1288	24	1293	34	1301	52	1301	52	0.4
Zircon-068	249	161	0.65	0.0561	0.003	0.629	0.034	0.0791	0.0016	0.0249	0.0012	0.24	490.7	9.5	494	21	494	70	490.7	9.5	0.7
Zircon-069	261	151	0.58	0.05	0.004	0.1083	0.0086	0.01564	0.00041	0.00521	0.00029	0.00	100	2.6	105.6	7.8	415	85	100	2.6	5.3
Zircon-070	82	39	0.47	0.2132	0.0083	16.61	0.82	0.559	0.019	0.1561	0.0071	0.26	2860	81	2912	59	2940	53	2940	53	1.8
Zircon-071	239	68	0.28	0.0778	0.0031	2.182	0.093	0.2	0.0041	0.0587	0.0026	0.75	1175	22	1173	30	1148	56	1148	56	-0.2
Zircon-072	367	69	0.19	0.0546	0.0031	0.187	0.011	0.02539	0.00059	0.00875	0.00061	0.17	161.6	3.7	174.1	9.5	357	63	161.6	3.7	7.2
Zircon-073	301	33	0.11	0.0787	0.003	2.217	0.086	0.2026	0.004	0.0642	0.0032	0.18	1189	21	1186	27	1174	41	1174	41	-0.3
Zircon-074	91	52	0.57	0.0801	0.0035	2.32	0.1	0.209	0.0043	0.0605	0.0028	0.27	1223	23	1217	31	1203	39	1203	39	-0.5
Zircon-075	60	36	0.61	0.0617	0.0044	0.802	0.055	0.0954	0.0021	0.0286	0.0016	-0.01	587	12	598	32	736	75	587	12	1.8
Zircon-076	338	96	0.28	0.062	0.0025	0.989	0.04	0.1162	0.0023	0.034	0.0017	0.18	708	13	698	20	692	48	708	13	-1.4
Zircon-077	590	195	0.33	0.0796	0.0029	2.205	0.082	0.2018	0.0035	0.0589	0.0024	0.32	1186	19	1182	26	1177	44	1177	44	-0.3
Zircon-078	116	120	1.03	0.0751	0.0039	2.01	0.1	0.1946	0.0041	0.0587	0.0028	0.17	1146	22	1123	33	1064	62	1064	62	-2.0
Zircon-079	648	459	0.71	0.0507	0.0028	0.1107	0.006	0.01603	0.00035	0.00509	0.00025	0.31	102.5	2.2	106.5	5.5	267	53	102.5	2.2	3.8
Zircon-080	73	38	0.53	0.0566	0.0079	0.127	0.017	0.01621	0.00067	0.00574	0.00062	0.22	104.4	4.3	123	15	640	130	104.4	4.3	15.1
Zircon-082	244	470	1.93	0.0577	0.0028	0.573	0.029	0.0772	0.0015	0.02142	0.00094	0.35	448.1	8.9	459	18	559	52	448.1	8.9	2.4
Zircon-083	580	402	0.69	0.0526	0.005	0.11	0.01	0.01515	0.00037	0.00472	0.00035	0.02	96.9	2.3	106	9.7	400	140	96.9	2.3	8.6
Zircon-084	109	73	0.66	0.0582	0.0043	0.742	0.05	0.0895	0.0019	0.0284	0.0015	0.10	553	11	560	29	574	90	553	11	1.3
Zircon-085	100	106	1.06	0.0612	0.0039	0.634	0.038	0.0757	0.0018	0.0222	0.001	-0.33	471	11	496	23	648	77	471	11	5.0
Zircon-086	125	21	0.17	0.0783	0.0035	2.22	0.15	0.2028	0.0096	0.0591	0.0034	0.43	1195	52	1185	51	1173	66	1173	66	-0.8
Zircon-087	285	141	0.49	0.0506	0.0037	0.1421	0.0099	0.02046	0.00055	0.00642	0.00044	-0.06	130.5	3.5	134.6	8.8	356	89	130.5	3.5	3.0
Zircon-088	247	137	0.55	0.0461	0.0033	0.137	0.0096	0.02087	0.00059	0.00647	0.00038	0.29	133.2	3.7	130	8.6	269	64	133.2	3.7	-2.5
Zircon-089	46	26	0.55	0.0624	0.0055	0.647	0.051	0.0748	0.0023	0.0248	0.0016	-0.06	465	14	506	33	730	93	465	14	8.1
Zircon-090	229	173	0.76	0.0522	0.0047	0.1091	0.0094	0.01529	0.00046	0.00479	0.00027	-0.19	97.8	2.9	104.8	8.6	452	74	97.8	2.9	6.7
Zircon-091	192	62	0.32	0.0623	0.0032	0.87	0.046	0.1008	0.002	0.0331	0.0015	0.30	619	12	634	25	687	66	619	12	2.4
Zircon-092	144	73	0.51	0.0526	0.0053	0.125	0.011	0.01688	0.00057	0.00563	0.00044	-0.10	107.9	3.6	119	10	470	110	107.9	3.6	9.3
Zircon-093	454	314	0.69	0.05	0.0033	0.1025	0.0065	0.01499	0.00035	0.00451	0.00027	0.03	95.9	2.2	99	5.9	247	75	95.9	2.2	3.1
Zircon-094	104	69	0.67	0.0531	0.0076	0.113	0.015	0.01569	0.00066	0.00501	0.0004	-0.04	100.4	4.2	110	14	590	120	100.4	4.2	8.7
Zircon-095	411	371	0.90	0.0503	0.0041	0.104	0.0083	0.01501	0.00035	0.00456	0.00025	0.01	96	2.2	100.1	7.6	381	75	96	2.2	4.1
Zircon-096	63	32	0.51	0.0599	0.0039	0.603	0.039	0.0739	0.002	0.024	0.0016	0.33	460	12	483	27	619	64	460	12	4.8
Zircon-097	190	107	0.56	0.055	0.0028	0.607	0.029	0.0796	0.0023	0.0266	0.0013	0.05	494	14	481	19	404	67	494	14	-2.7
Zircon-098	256	146	0.57	0.0482	0.0044	0.1019	0.0089	0.01547	0.												

Zircon-138	155	54	0.35	0.0523	0.0049	0.188	0.017	0.02607	0.00071	0.00838	0.00068	0.23	165.9	4.5	174	15	428	88	165.9	4.5	4.7
Zircon-139	1750	859	0.49	0.0494	0.0022	0.1374	0.0059	0.02009	0.00036	0.00637	0.00027	0.08	128.2	2.2	130.7	5.3	160	54	128.2	2.2	1.9
Zircon-140	277	181	0.65	0.0501	0.0041	0.1046	0.0081	0.01515	0.00039	0.00516	0.00032	0.04	97	2.5	101.7	7.2	373	71	97	2.5	4.6
Zircon-141	53	35	0.67	0.0717	0.0041	1.509	0.08	0.1562	0.0038	0.0496	0.0026	0.25	936	21	935	34	965	57	936	21	-0.1
Zircon-142	279	101	0.36	0.0737	0.003	1.716	0.067	0.1696	0.0031	0.0507	0.0022	0.19	1010	17	1014	25	1026	45	1026	45	0.4
Zircon-143	194	111	0.57	0.0583	0.003	0.624	0.032	0.0785	0.0018	0.025	0.0012	0.40	487	11	493	20	536	67	487	11	1.2
Zircon-144	612	373	0.61	0.0509	0.0032	0.1532	0.0088	0.02194	0.00046	0.00729	0.00034	-0.21	139.9	2.9	144.5	7.7	298	60	139.9	2.9	3.2
Zircon-145	275	193	0.70	0.0591	0.0027	0.702	0.032	0.0869	0.0017	0.0255	0.0012	0.14	537	9.8	541	18	570	50	537	9.8	0.7
Zircon-146	265	173	0.65	0.0525	0.0037	0.305	0.023	0.0418	0.001	0.01331	0.00068	0.14	263.7	6.2	269	18	487	98	263.7	6.2	2.0
Zircon-147	237	216	0.91	0.0623	0.0027	0.999	0.044	0.1184	0.0021	0.0371	0.0015	0.32	721	12	706	21	681	52	721	12	-2.1
Zircon-148	262	109	0.41	0.0725	0.003	1.698	0.069	0.1721	0.0031	0.0533	0.0023	0.20	1024	17	1006	26	989	43	989	43	-1.8
Zircon-149	88	108	1.23	0.1146	0.0046	5.4	0.23	0.343	0.0072	0.0947	0.0039	0.44	1900	35	1883	36	1886	43	1886	43	-0.9
Zircon-150	207	110	0.53	0.0537	0.005	0.155	0.014	0.02092	0.00058	0.00729	0.00052	-0.09	133.4	3.7	145	13	488	89	133.4	3.7	8.0
Zircon-151	167	115	0.69	0.0552	0.0037	0.411	0.027	0.0549	0.0013	0.01749	0.00085	0.23	344.4	7.9	353	20	476	76	344.4	7.9	2.4
Zircon-152	876	270	0.31	0.0534	0.0022	0.447	0.018	0.0608	0.0012	0.01963	0.00083	0.31	380.4	7.1	375	13	357	46	380.4	7.1	-1.4
Zircon-153	471	289	0.61	0.0491	0.0045	0.1104	0.0095	0.01632	0.00042	0.00506	0.00028	-0.27	104.3	2.7	105.9	8.6	354	78	104.3	2.7	1.5
Zircon-154	126	95	0.75	0.0524	0.0076	0.114	0.016	0.01564	0.00053	0.00513	0.00038	-0.12	100.1	3.3	108	14	810	120	100.1	3.3	7.3
Zircon-155	310	126	0.41	0.0732	0.0029	1.764	0.071	0.1748	0.0037	0.0529	0.0024	0.15	1038	20	1032	26	1035	59	1035	59	-0.6
Zircon-156	114	61	0.54	0.0781	0.0032	2.18	0.09	0.2011	0.0039	0.0619	0.0027	0.13	1181	21	1176	28	1146	41	1146	41	-0.4
Zircon-157	203	88	0.43	0.0701	0.0028	1.626	0.064	0.1669	0.0033	0.0504	0.0024	-0.01	995	18	980	25	952	48	995	18	-1.5
Zircon-158	179	105	0.59	0.0588	0.0034	0.647	0.04	0.0802	0.0018	0.0264	0.0014	0.12	497	11	505	24	569	69	497	11	1.6
Zircon-159	76	36	0.48	0.058	0.011	0.113	0.021	0.01482	0.00069	0.00587	0.00074	-0.10	94.9	4.4	107	18	1020	120	94.9	4.4	11.3

Notes:

1: U and Th concentrations are calculated employing an external standard zircon as in Paton et al., 2010, Geochemistry, Geophysics, Geosystems.

2: 2 sigma uncertainties propagated according to Paton et al., 2010, Geochemistry, Geophysics, Geosystems

²⁰⁷Pb/²⁰⁶Pb ratios, ages and errors are calculated according to Petrus and Kamber, 2012, Geostandards Geanalytical Research

Analyzed spots were 23 micrometers, using an analytical protocol modified from Solari et al., 2010, Geostandards Geanalytical Research.

Data measured employing a Thermo iCapQc ICPMS coupled to a Resonetics, Resolun M050 excimer laser workstation.

Mineral separation was carried out using the standard methodology (crushing, sieving, density and magnetic separation, handpicking) at the mineral separation facility of the Centro de Geociencias, UNAM-Juriquilla. Zircons were observed and imaged under cathodoluminescence, using an ELM3R luminoscope connected to a digital camera. Individual zircon ages were obtained by laser ablation inductively coupled plasma mass spectrometry (LA-ICPMS) at LEI, Centro de Geociencias, UNAM. Zircon ablation was performed with a Resolution M-50/Lambda Physik LPX220 Excimer laser, operating at a 193 nm wavelength and coupled to a Thermo XseriesII quadrupole ICPMS. Details of the analytic methodology can be found in Solari et al. (2010) and http://www.geociencias.unam.mx/~solari/index_files/LEI/LA-ICPMS.html

Table . U-Pb geochronologic analyses.

Analysis	Isotope ratios										Apparent ages (Ma)									
	U (ppm)	206Pb 204Pb	U/Th	206Pb* 207Pb* ± (%)	207Pb* 235U* ± (%)	206Pb* 238U ± (%)	error corr.	206Pb* 238U* ± (Ma)	207Pb* 235U ± (Ma)	206Pb* 207Pb* ± (Ma)	Best age (Ma) ± (Ma)	Conc (%)	Disc (%)							
Caracol Formation, Sierra de Parras (sample: 07COA-CA3), coordinates: 25° 14.115'N, 101° 26.031'W																				
07COACA3-10	261	2361	2.30	19.7804	8.6098	0.0879	8.8964	0.0126	2.2400	0.25	80.7864	1.7983	85.5491	7.2992	220.5849	199.5077	80.7864	1.7983	36.6	5.6
07COACA3-4	754	2532	1.59	17.3498	9.3016	0.1015	9.5491	0.0128	2.1600	0.23	81.7862	1.7554	98.1297	8.9322	515.9846	204.6675	81.7862	1.7554	15.9	16.7
07COACA3-34	284	2358	1.15	19.1286	10.6819	0.0945	10.9843	0.0131	2.5600	0.23	83.9348	2.1348	91.6543	9.6269	297.5771	244.3309	83.9348	2.1348	28.2	8.4
07COACA3-21	497	2574	2.12	20.0230	7.4877	0.0905	7.5194	0.0131	0.6900	0.09	84.1490	0.5769	87.9481	6.3349	192.3439	174.3205	84.1490	0.5769	43.7	4.3
07COACA3-40	934	8598	2.05	19.5355	6.6504	0.0930	7.2917	0.0132	2.9900	0.41	84.4281	2.5079	90.3358	6.3026	249.3184	153.1941	84.4281	2.5079	33.9	6.5
07COACA3-30	681	2805	2.18	18.4421	3.7084	0.0998	4.3118	0.0133	2.2000	0.51	85.4509	1.8675	96.5579	3.9716	380.3320	83.3992	85.4509	1.8675	22.5	11.5
07COACA3-24	303	2394	2.45	19.6769	5.4397	0.0936	5.6349	0.0134	1.4700	0.26	85.5241	1.2489	90.8360	4.8962	232.6980	125.6474	85.5241	1.2489	36.8	5.8
07COACA3-7	590	4749	2.77	21.7584	7.5010	0.0848	7.5283	0.0134	0.6400	0.09	85.7343	0.5451	82.6853	5.9781	-4.5010	181.1527	85.7343	0.5451	-1904.8	-3.7
07COACA3-11	396	4986	1.96	19.0754	5.3105	0.0969	5.4444	0.0134	1.2000	0.22	85.8837	1.0238	93.9503	4.8856	303.9455	121.1037	85.8837	1.0238	28.3	8.6
07COACA3-1	529	5367	1.96	21.0866	3.9297	0.0878	4.0624	0.0134	1.0300	0.25	86.0137	0.8801	85.4802	3.3304	70.6057	93.4764	86.0137	0.8801	121.8	-0.6
07COACA3-1	529	5367	1.96	21.0866	3.9297	0.0878	4.0624	0.0134	1.0300	0.25	86.0137	0.8801	85.4802	3.3304	70.6057	93.4764	86.0137	0.8801	121.8	-0.6
07COACA3-9	488	3315	2.60	19.3750	6.2017	0.0956	6.2787	0.0134	0.9800	0.16	86.0397	0.8376	92.7240	5.5640	268.2810	142.3422	86.0397	0.8376	32.1	7.2
07COACA3-23	1015	8982	1.72	21.1845	3.3713	0.0875	3.4768	0.0134	0.8500	0.24	86.0890	0.7269	85.1734	2.8405	59.6017	80.3482	86.0890	0.7269	144.4	-1.1
07COACA3-22	645	6504	1.57	21.4216	4.5917	0.0871	4.6609	0.0135	0.8000	0.17	86.6381	0.6885	84.7878	3.7914	32.9849	110.0170	86.6381	0.6885	262.7	-2.2
07COACA3-25	427	1944	1.51	20.3117	6.4418	0.0920	6.4819	0.0136	0.7200	0.11	86.7760	0.6206	89.3596	5.5447	158.9452	150.8598	86.7760	0.6206	54.6	2.9
07COACA3-3	1509	3828	1.96	18.3400	2.7920	0.1020	3.1460	0.0136	1.4500	0.46	86.8661	1.2511	98.6130	2.9565	392.8046	62.6346	86.8661	1.2511	22.1	11.9
07COACA3-29	379	2544	1.96	20.0413	6.1376	0.0937	6.4220	0.0136	1.8900	0.29	87.1598	1.6362	90.8990	5.5840	190.2218	142.8979	87.1598	1.6362	45.8	4.1
07COACA3-33	573	6345	2.44	21.2867	5.5786	0.0882	5.7397	0.0136	1.3500	0.24	87.1873	1.1691	85.8249	4.7236	48.0882	133.3164	87.1873	1.1691	181.3	-1.6
07COACA3-37	366	4077	2.40	21.0366	5.3888	0.0897	5.6157	0.0137	1.5800	0.28	87.6705	1.3758	87.2673	4.6960	76.2304	128.0970	87.6705	1.3758	115.0	-0.5
07COACA3-15	820	6837	2.08	20.9091	2.8413	0.0911	2.8849	0.0138	0.5000	0.17	88.4573	0.4393	88.5367	2.4460	90.6559	67.3321	88.4573	0.4393	97.6	0.1
07COACA3-28	461	5337	1.98	21.2198	5.1136	0.0901	5.1380	0.0139	0.5000	0.10	88.7431	0.4407	87.5666	4.3106	55.5955	122.0149	88.7431	0.4407	159.6	-1.3
07COACA3-18	377	2871	2.10	19.4861	6.0334	0.0981	6.3225	0.0139	1.8900	0.30	88.7902	1.6666	95.0521	5.7371	255.1914	138.8023	88.7902	1.6666	34.8	6.6
07COACA3-16	377	4074	2.07	20.1246	4.5702	0.0951	5.4724	0.0139	3.0100	0.55	88.8223	2.6552	92.2013	4.8233	180.5197	106.5795	88.8223	2.6552	49.2	3.7
07COACA3-20	395	2814	1.80	19.8212	8.2180	0.0966	8.4237	0.0139	1.8500	0.22	88.8665	1.6328	93.5942	7.5318	215.8447	190.5579	88.8665	1.6328	41.2	5.1
07COACA3-32	706	3498	1.86	20.7623	3.5355	0.0924	3.6205	0.0139	0.7800	0.22	89.1041	0.6902	89.7641	3.1104	107.3702	83.5518	89.1041	0.6902	83.0	0.7
07COACA3-13	752	6660	2.13	20.4319	3.9229	0.0940	3.9685	0.0139	0.6000	0.15	89.1392	0.5312	91.1866	3.4610	145.0783	92.0414	89.1392	0.5312	61.4	2.2
07COACA3-19	354	3774	2.08	21.1678	10.9006	0.0910	11.0808	0.0140	1.9900	0.18	89.4567	1.7679	88.4533	9.3868	61.4370	260.3592	89.4567	1.7679	145.6	-1.1
07COACA3-35	346	2169	2.34	20.6882	9.3562	0.0939	9.4460	0.0141	1.3000	0.14	90.2302	1.1648	91.1678	8.2366	115.8030	221.0825	90.2302	1.1648	77.9	1.0
07COACA3-39	442	4107	1.99	19.4566	6.4098	0.1000	6.4754	0.0141	0.9200	0.14	90.3558	0.8255	96.8016	5.9789	258.6420	147.3947	90.3558	0.8255	34.9	6.7
07COACA3-38	391	3993	1.91	20.4601	10.1997	0.0954	10.3139	0.0142	1.5300	0.15	90.5845	1.3763	92.4877	9.1178	141.8428	239.9188	90.5845	1.3763	63.9	2.1
07COACA3-26	362	3261	2.42	20.8748	7.3457	0.0936	7.3719	0.0142	0.6200	0.08	90.7281	0.5586	90.8685	6.4078	94.5511	174.1167	90.7281	0.5586	96.0	0.2
07COACA3-31	210	2862	2.35	21.6556	10.9142	0.0919	11.1707	0.0144	2.3800	0.21	92.3569	2.1824	89.2482	9.5444	6.8795	263.3950	92.3569	2.1824	1342.5	-3.5

Sample Name:								207/235		206/238		207/206		Best age				
Grain #	[U] ppm	U/Th	207/235	2σ error	206/238	2σ error	RHO	Age Ma	2σ error	Age (Ma)	2σ error	Age (Ma)	2σ error	(Ma)	2σ error	Discordance	Rim/Core	
San Felipe Formation (sample: 04-JC01); coordinates: 21° 20.887'N, 99° 33.011'W																		
04JC-01-2.FIN2	820	2.83	1.5130	0.0280	0.1545	0.0027	0.83	935.0	11.0	926.0	15.0	944.0	24.0	944.0	24.0	1.9		
04JC-01-3.FIN2	339	1.38	0.0893	0.0022	0.0123	0.0002	0.07	86.8	2.1	78.6	1.1	293.0	60.0	78.6	1.1	9.4		
04JC-01-4.FIN2	308	2.29	2.6800	0.0380	0.2243	0.0032	0.81	1323.0	10.0	1306.0	16.0	1359.0	17.0	1359.0	17.0	3.9		
04JC-01-5.FIN2	351	1.29	3.6120	0.0460	0.2685	0.0041	0.69	1552.0	10.0	1533.0	21.0	1567.0	21.0	1567.0	21.0	2.2		
04JC-01-6.FIN2	48	2.46	1.5540	0.0340	0.1638	0.0037	0.53	951.0	13.0	977.0	20.0	909.0	42.0	909.0	42.0	7.5		
04JC-01-7.FIN2	222	3.00	0.1310	0.0052	0.0191	0.0006	0.37	124.9	4.6	121.9	3.9	191.0	91.0	121.9	3.9	2.4		
04JC-01-9.FIN2	102	1.04	0.1944	0.0051	0.0276	0.0005	0.21	180.2	4.4	175.4	3.0	217.0	57.0	175.4	3.0	2.7		
04JC-01-10.FIN2	830	1.28	0.0902	0.0019	0.0134	0.0002	0.72	87.7	1.8	85.8	1.5	102.0	34.0	85.8	1.5	2.2		
04JC-01-11.FIN2	222	3.81	2.2700	0.0300	0.1994	0.0028	0.81	1202.6	9.2	1172.0	15.0	1251.0	17.0	1251.0	17.0	6.3		
04JC-01-12.FIN2	211	0.71	4.0590	0.0690	0.2839	0.0057	0.78	1645.0	14.0	1615.0	29.0	1662.0	22.0	1662.0	22.0	2.8		
04JC-01-13.FIN2	524	11.01	2.2800	0.0300	0.2113	0.0033	0.81	1207.0	9.0	1235.0	17.0	1143.0	19.0	1143.0	19.0	8.0		
04JC-01-16.FIN2	111	1.33	0.0792	0.0027	0.0108	0.0003	0.00	77.4	2.6	69.3	1.6	317.0	94.0	69.3	1.6	10.5		
04JC-01-17.FIN2	226	1.93	2.9860	0.0480	0.2290	0.0039	0.84	1407.0	12.0	1329.0	21.0	1504.0	20.0	1504.0	20.0	11.6		
04JC-01-18.FIN2	314	2.64	0.7180	0.0120	0.0863	0.0010	0.71	549.3	7.3	533.4	6.0	658.0	28.0	533.4	6.0	2.9		
04JC-01-19.FIN2	479	3.69	0.6510	0.0480	0.0731	0.0037	0.27	505.0	28.0	454.0	22.0	710.0	110.0	454.0	22.0	10.1		
04JC-01-20.FIN2	920	1.78	0.1541	0.0032	0.0227	0.0005	0.80	145.5	2.8	144.3	3.2	156.0	33.0	144.3	3.2	0.8		
04JC-01-21.FIN2	179	0.79	0.7650	0.0190	0.0917	0.0023	0.26	576.0	11.0	566.0	14.0	618.0	41.0	566.0	14.0	1.7		
04JC-01-23.FIN2	298	2.45	0.1348	0.0027	0.0196	0.0003	0.35	128.3	2.4	125.1	2.2	193.0	55.0	125.1	2.2	2.5		
04JC-01-24.FIN2	280	2.46	0.0873	0.0025	0.0126	0.0002	0.36	85.0	2.3	80.4	1.3	221.0	59.0	80.4	1.3	5.4		
04JC-01-25.FIN2	253	1.69	0.0849	0.0025	0.0127	0.0002	0.14	82.7	2.3	81.3	1.3	142.0	62.0	81.3	1.3	1.7		
04JC-01-26.FIN2	277	2.03	0.0788	0.0027	0.0119	0.0004	0.46	77.0	2.5	76.5	2.4	66.0	65.0	76.5	2.4	0.6		
04JC-01-27.FIN2	101	2.94	1.6360	0.0360	0.1583	0.0035	0.78	983.0	14.0	947.0	20.0	1031.0	27.0	1031.0	27.0	8.1		
04JC-01-30.FIN2	268	1.54	2.4490	0.0630	0.2109	0.0061	0.79	1256.0	18.0	1233.0	32.0	1279.0	34.0	1279.0	34.0	3.6		
04JC-01-32.FIN2	114	1.47	0.1042	0.0042	0.0151	0.0005	0.44	100.5	3.9	96.3	3.2	181.0	79.0	96.3	3.2	4.2		
04JC-01-33.FIN2	211	21.20	0.6280	0.0220	0.0793	0.0015	0.79	495.0	13.0	491.6	9.2	571.0	59.0	491.6	9.2	0.7	Rim	
04JC-01-33.FIN2	218	4.06	9.4200	0.2600	0.3919	0.0099	0.92	2376.0	26.0	2130.0	46.0	2587.0	19.0	2587.0	19.0	17.7	Core	
04JC-01-34.FIN2	43	1.54	0.5840	0.0210	0.0744	0.0016	0.31	466.0	14.0	462.4	9.7	471.0	75.0	462.4	9.7	0.8		
04JC-01-35.FIN2	278	2.26	0.1894	0.0039	0.0272	0.0006	0.53	176.0	3.3	173.1	3.6	207.0	43.0	173.1	3.6	1.6		
04JC-01-36.FIN2	554	2.96	0.2087	0.0042	0.0304	0.0006	0.69	192.4	3.6	193.1	4.0	179.0	36.0	193.1	4.0	0.4		
04JC-01-38.FIN2	142	2.35	0.0924	0.0039	0.0130	0.0003	0.08	89.6	3.6	83.3	2.0	251.0	94.0	83.3	2.0	7.0		
04JC-01-39.FIN2	156	2.67	1.6320	0.0510	0.1596	0.0053	0.82	981.0	20.0	960.0	31.0	1013.0	40.0	1013.0	40.0	5.2	Core	
04JC-01-40.FIN2	296	1.86	0.1937	0.0064	0.0262	0.0005	0.31	179.6	5.4	166.7	3.3	384.0	79.0	166.7	3.3	7.2		
04JC-01-43.FIN2	428	11.50	1.1590	0.0310	0.1292	0.0037	0.79	783.0	15.0	783.0	21.0	771.0	36.0	783.0	21.0	0.0		
04JC-01-44.FIN2	81	1.86	0.0866	0.0038	0.0124	0.0003	0.24	84.3	3.6	79.4	2.1	293.0	92.0	79.4	2.1	5.8		
04JC-01-45.FIN2	662	2.45	0.1836	0.0035	0.0276	0.0007	0.66	171.1	3.0	175.6	4.7	197.0	46.0	175.6	4.7	2.6		
04JC-01-46.FIN2	286	3.63	0.1154	0.0025	0.0171	0.0003	0.55	111.1	2.2	109.4	2.0	137.0	41.0	109.4	2.0	1.5		
04JC-01-47.FIN2	834	1.68	0.2706	0.0075	0.0369	0.0009	0.75	243.0	6.0	233.7	5.4	333.0	43.0	233.7	5.4	3.8		
04JC-01-48.FIN2	800	6.21	0.2152	0.0071	0.0265	0.0007	0.24	197.7	6.0	168.5	4.2	578.0	84.0	168.5	4.2	14.8		
04JC-01-49.FIN2	145	2.08	0.1255	0.0030	0.0172	0.0004	0.25	120.0	2.7	109.7	2.6	332.0	68.0	109.7	2.6	8.6		
04JC-01-50.FIN2	320	1.52	0.0808	0.0017	0.0121	0.0002	0.32	78.9	1.6	77.8	1.2	80.0	45.0	77.8	1.2	1.4		
04JC-01-51.FIN2	537	1.78	1.7030	0.0350	0.1708	0.0034	0.85	1008.0	13.0	1019.0	19.0	971.0	24.0	971.0	24.0	4.9		
04JC-01-52.FIN2	281	2.03	0.1278	0.0033	0.0183	0.0004	0.45	122.1	2.9	117.0	2.6	238.0	56.0	117.0	2.6	4.2		
04JC-01-53.FIN2	271	2.70	0.0894	0.0044	0.0112	0.0003	0.10	86.8	4.0	71.5	2.1	460.0	110.0	71.5	2.1	17.6		
04JC-01-54.FIN2	261	2.12	0.1339	0.0049	0.0177	0.0004	0.27	128.1	4.5	113.1	2.2	342.0	75.0	113.1	2.2	11.7		
04JC-01-55.FIN2	222	2.19	0.0844	0.0043	0.0119	0.0003	0.18	82.2	3.9	75.9	1.7	201.0	97.0	75.9	1.7	7.7		
04JC-01-56.FIN2	328	2.26	0.0750	0.0029	0.0114	0.0002	0.05	73.4	2.7	73.2	1.4	78.0	82.0	73.2	1.4	0.3		
04JC-01-59.FIN2	498	3.44	0.1841	0.0043	0.0267	0.0005	0.55	171.5	3.7	169.6	3.4	192.0	46.0	169.6	3.4	1.1		
04JC-01-60.FIN2	199	2.04	0.0795	0.0022	0.0117	0.0002	0.06	77.6	2.1	75.0	1.3	147.0	68.0	75.0	1.3	3.4		
04JC-01-61.FIN2	499	1.14	0.0916	0.0024	0.0133	0.0003	0.57	88.9	2.2	85.1	2.0	181.0	57.0	85.1	2.0	4.3		
04JC-01-63.FIN2	261	2.48	0.0818	0.0027	0.0122	0.0003	0.49	79.8	2.5	77.9	2.1	110.0	58.0	77.9	2.1	2.4		
04JC-01-64.FIN2	333	4.92	0.1955	0.0037	0.0275	0.0005	0.60	181.2	3.2	174.5	3.4	233.0	36.0	174.5	3.4	3.7		
04JC-01-65.FIN2	64	2.36	2.2610	0.0580	0.1989	0.0051	0.73	1199.0	18.0	1169.0	27.0	1241.0	37.0	1241.0	37.0	5.8		
04JC-01-66.FIN2	169	2.08	0.1074	0.0031	0.0162	0.0003	0.19	103.5	2.9	103.6	2.2	121.0	71.0	103.6	2.2	0.1		
04JC-01-67.FIN2	323	1.76	0.1087	0.0046	0.0132	0.0003	0.40	104.6	4.2	84.8	1.6	555.0	89.0	84.8	1.6	18.9		
04JC-01-70.FIN2	116	1.74	0.3155	0.0077	0.0434	0.0008	0.11	278.2	5.9	273.6	4.8	316.0	60.0	273.6	4.8	1.7		
04JC-01-71.FIN2	512	1.78	1.7340	0.0200	0.1797	0.0021	0.78	1020.9	7.5	1065.0	12.0	929.0	18.0	929.0	18.0	14.6		
04JC-01-75.FIN2	277	2.41	0.6108	0.0097	0.0780	0.0013	0.61	483.8	6.1	484.1	7.6	509.0	29.0	484.1	7.6	0.1		
04JC-01-76.FIN2	133	3.83	0.0814	0.0025	0.0125	0.0004	0.29	79.4	2.3	80.3	2.2	128.0	74.0	80.3	2.2	1.1		
04JC-01-77.FIN2	320	19.90	0.2558	0.0075	0.0371	0.0010	0.62	231.1	6.1	235.0	6.5	237.0	49.0	235.0	6.5	1.7		

04JC-01-78.FIN2	386	1.42	0.0844	0.0023	0.0125	0.0003	0.57	82.3	2.1	80.1	1.8	195.0	54.0	80.1	1.8	2.7
04JC-01-79.FIN2	185	2.96	2.5990	0.0530	0.2222	0.0052	0.82	1299.0	15.0	1293.0	27.0	1318.0	26.0	1318.0	26.0	1.9
04JC-01-80.FIN2	221	1.28	0.5460	0.0190	0.0696	0.0026	0.61	441.0	13.0	433.0	16.0	478.0	82.0	433.0	16.0	1.8
04JC-01-81.FIN2	315	1.77	0.9980	0.0180	0.1164	0.0025	0.61	702.4	8.9	710.0	14.0	689.0	35.0	710.0	14.0	1.1
04JC-01-82.FIN2	343	1.27	0.0844	0.0017	0.0127	0.0003	0.47	82.3	1.6	81.5	1.6	115.0	44.0	81.5	1.6	1.0
04JC-01-84.FIN2	57	1.15	1.2310	0.0300	0.1347	0.0035	0.60	814.0	13.0	814.0	20.0	794.0	47.0	814.0	20.0	0.0
04JC-01-85.FIN2	147	2.21	0.1120	0.0038	0.0168	0.0005	0.46	107.7	3.5	107.6	3.2	115.0	71.0	107.6	3.2	0.1
04JC-01-89.FIN2	322	3.53	2.5910	0.0310	0.2201	0.0029	0.67	1300.1	8.7	1282.0	16.0	1320.0	21.0	1320.0	21.0	2.9
04JC-01-88.FIN2	271	2.20	10.3080	0.0900	0.4215	0.0042	0.79	2462.4	8.1	2267.0	19.0	2622.0	11.0	2622.0	11.0	13.5
04JC-01-91.FIN2	188	1.03	1.3570	0.0260	0.1396	0.0024	0.64	870.0	11.0	842.0	14.0	927.0	31.0	842.0	14.0	3.2
04JC-01-93.FIN2	318	2.00	3.5030	0.0990	0.2637	0.0065	0.86	1525.0	22.0	1508.0	33.0	1537.0	28.0	1537.0	28.0	1.9
04JC-01-96.FIN2	118	2.12	0.7730	0.0140	0.0929	0.0015	0.42	581.2	8.1	572.7	8.8	613.0	42.0	572.7	8.8	1.5
04JC-01-97.FIN2	157	2.35	0.1912	0.0064	0.0262	0.0007	0.41	177.4	5.4	167.3	4.1	303.0	60.0	167.3	4.1	5.7
04JC-01-99.FIN2	204	1.76	0.5610	0.0140	0.0717	0.0019	0.72	451.2	8.9	446.0	11.0	460.0	47.0	446.0	11.0	1.2
04JC-01-100.FIN2	814	1.31	0.8980	0.0170	0.1071	0.0021	0.88	651.5	9.2	656.0	12.0	593.0	23.0	656.0	12.0	0.7
04JC-01-102.FIN2	93	1.19	0.1885	0.0062	0.0270	0.0005	0.50	175.8	5.2	171.7	2.9	211.0	66.0	171.7	2.9	2.3
04JC-01-103.FIN2	68	2.04	1.6300	0.0320	0.1615	0.0029	0.60	981.0	12.0	965.0	16.0	1017.0	33.0	1017.0	33.0	5.1
04JC-01-105.FIN2	449	2.32	0.8560	0.0170	0.1022	0.0023	0.67	627.5	9.1	627.0	13.0	621.0	35.0	627.0	13.0	0.1
04JC-01-107.FIN2	188	0.81	8.4300	0.1200	0.3702	0.0062	0.80	2280.0	13.0	2029.0	29.0	2510.0	15.0	2510.0	15.0	19.2
04JC-01-109.FIN2	393	4.41	0.8220	0.0140	0.0956	0.0014	0.71	608.7	7.5	588.3	8.1	651.0	24.0	588.3	8.1	3.4
04JC-01-111.FIN2	214	5.58	0.2315	0.0085	0.0299	0.0011	0.80	212.1	7.1	189.8	6.6	470.0	46.0	189.8	6.6	10.5
04JC-01-112.FIN2	143	1.84	0.0818	0.0029	0.0123	0.0003	0.33	79.8	2.7	78.9	2.1	134.0	75.0	78.9	2.1	1.1
04JC-01-116.FIN2	117	1.74	0.0849	0.0035	0.0120	0.0003	0.14	82.6	3.3	77.1	1.9	243.0	92.0	77.1	1.9	6.7
04JC-01-118.FIN2	120	2.09	0.1195	0.0036	0.0176	0.0004	0.39	114.5	3.2	112.6	2.5	135.0	57.0	112.6	2.5	1.7
04JC-01-119.FIN2	272	2.63	0.0789	0.0027	0.0119	0.0004	0.42	77.0	2.6	76.2	2.2	80.0	78.0	76.2	2.2	1.0

San Felipe Formation (sample: 05-JC02); coordinates: 21° 20.887'N, 99° 33.011'W

05JC02_1.FIN2	780	2.62	0.0921	0.0030	0.0137	0.0004	0.30	89.4	2.8	87.9	2.6	134.0	78.0	87.9	2.6	1.7
05JC02_2.FIN2	616	4.57	0.0891	0.0017	0.0134	0.0002	0.44	86.7	1.6	85.7	1.2	103.0	38.0	85.7	1.2	1.2
05JC02_3.FIN2	660	3.63	0.0951	0.0018	0.0140	0.0002	0.40	92.2	1.7	89.6	1.2	148.0	36.0	89.6	1.2	2.8
05JC02_4.FIN2	1112	2.81	0.0932	0.0016	0.0140	0.0002	0.45	90.5	1.4	89.5	1.1	121.0	35.0	89.5	1.1	1.1
05JC02_6.FIN2	689	2.99	0.0916	0.0018	0.0140	0.0002	0.37	89.0	1.6	89.7	1.0	81.0	34.0	89.7	1	0.8
05JC02_7.FIN2	715	3.65	0.0918	0.0015	0.0139	0.0002	0.44	89.2	1.4	88.7	1.2	114.0	35.0	88.7	1.2	0.6
05JC02_8.FIN2	770	3.26	0.0937	0.0024	0.0139	0.0002	0.30	90.9	2.2	89.1	1.2	127.0	49.0	89.1	1.2	2.0
05JC02_9.FIN2	807	2.19	0.0965	0.0017	0.0145	0.0002	0.46	93.5	1.6	92.8	1.1	111.0	34.0	92.8	1.1	0.7
05JC02_10.FIN2	923	2.86	0.0942	0.0016	0.0143	0.0002	0.28	91.3	1.5	91.5	1.1	85.0	33.0	91.5	1.1	0.2
05JC02_11.FIN2	592	2.43	0.0909	0.0019	0.0138	0.0003	0.06	88.3	1.8	88.3	1.6	89.0	51.0	88.3	1.6	0.0
05JC02_12.FIN2	484	1.36	0.5870	0.0100	0.0758	0.0015	0.90	468.6	6.4	470.9	8.9	464.0	19.0	470.9	8.9	0.5
05JC02_13.FIN2	518	2.46	0.1018	0.0030	0.0138	0.0004	0.52	98.4	2.7	88.5	2.7	352.0	79.0	88.5	2.7	10.1
05JC02_15.FIN2	642	3.24	0.0982	0.0017	0.0145	0.0002	0.55	95.1	1.6	93.1	1.4	112.0	36.0	93.1	1.4	2.1
05JC02_16.FIN2	589	2.89	0.0945	0.0022	0.0145	0.0003	0.68	91.6	2.1	92.9	2.0	52.0	37.0	92.9	2	1.4
05JC02_17.FIN2	231	1.80	0.0847	0.0022	0.0124	0.0003	0.38	82.5	2.1	79.4	1.6	161.0	58.0	79.4	1.6	3.8
05JC02_18.FIN2	571	4.66	0.0997	0.0021	0.0146	0.0002	0.48	96.5	1.9	93.5	1.4	144.0	42.0	93.5	1.4	3.1
05JC02_19.FIN2	770	3.00	0.0962	0.0026	0.0145	0.0002	0.47	93.2	2.4	92.8	1.5	102.0	51.0	92.8	1.5	0.4
05JC02_20.FIN2	805	2.98	0.0991	0.0014	0.0151	0.0002	0.44	95.9	1.3	96.7	1.1	94.0	31.0	96.7	1.1	0.8
05JC02_21.FIN2	698	3.52	0.0981	0.0017	0.0146	0.0002	0.05	95.0	1.6	93.3	0.9	137.0	38.0	93.3	0.93	1.8
05JC02_22.FIN2	182	2.08	0.0838	0.0022	0.0125	0.0002	0.10	81.7	2.0	80.3	1.5	146.0	69.0	80.3	1.5	1.7
05JC02_23.FIN2	690	4.11	0.0967	0.0018	0.0145	0.0002	0.35	93.7	1.7	92.8	1.3	115.0	39.0	92.8	1.3	1.0
05JC02_24.FIN2	272	1.84	0.0833	0.0026	0.0126	0.0002	0.28	81.2	2.5	80.4	1.2	96.0	64.0	80.4	1.2	1.0
05JC02_25.FIN2	216	2.57	0.0884	0.0032	0.0130	0.0003	0.46	85.9	3.0	83.1	2.0	135.0	75.0	83.1	2	3.3
05JC02_26.FIN2	669	3.69	0.1002	0.0018	0.0149	0.0002	0.42	96.9	1.7	95.2	1.5	136.0	40.0	95.2	1.5	1.8
05JC02_27.FIN2	1025	2.12	0.0982	0.0021	0.0147	0.0003	0.54	95.1	1.9	94.2	2.2	110.0	51.0	94.2	2.2	0.9
05JC02_28.FIN2	175	1.76	0.0867	0.0035	0.0124	0.0003	0.05	84.4	3.3	79.4	1.7	196.0	89.0	79.4	1.7	5.9
05JC02_29.FIN2	552	3.40	0.0944	0.0019	0.0140	0.0002	0.46	91.5	1.8	89.8	1.2	145.0	40.0	89.8	1.2	1.9
05JC02_30.FIN2	1030	2.42	0.1015	0.0016	0.0153	0.0002	0.40	98.1	1.5	98.1	1.2	95.0	34.0	98.1	1.2	0.0
05JC02_31.FIN2	673	3.03	0.0952	0.0016	0.0145	0.0002	0.34	92.3	1.4	92.6	1.1	89.0	36.0	92.6	1.1	0.3
05JC02_32.FIN2	756	2.53	0.1048	0.0020	0.0156	0.0002	0.35	101.2	1.8	99.6	1.3	136.0	41.0	99.6	1.3	1.6
05JC02_33.FIN2	774	2.57	0.1005	0.0016	0.0150	0.0002	0.13	97.2	1.5	96.2	1.0	119.0	35.0	96.2	1	1.0
05JC02_34.FIN2	774	2.47	0.0997	0.0021	0.0147	0.0002	0.11	96.5	1.9	94.2	1.3	145.0	44.0	94.2	1.3	2.4
05JC02_35.FIN2	997	2.75	0.1048	0.0018	0.0153	0.0003	0.26	101.2	1.6	97.6	1.7	185.0	38.0	97.6	1.7	3.6
05JC02_36.FIN2	142	2.30	0.0875	0.0041	0.0122	0.0004	0.09	85.1	3.8	77.9	2.7	250.0	100.0	77.9	2.7	8.5
05JC02_37.FIN2	1162	1.97	0.0942	0.0013	0.0145	0.0001	0.41	91.4	1.2	92.5	0.9	73.0	29.0	92.5	0.88	1.2
05JC02_38.FIN2	107	3.25	0.1012	0.0062	0.0126	0.0004	0.04	97.7	5.7	80.9	2.8	540.0	140.0	80.9	2.8	17.2

05JC02_39.FIN2	655	1.83	0.1036	0.0019	0.0153	0.0002	0.02	100.1	1.7	98.2	1.0	128.0	40.0	98.2	0.98	1.9
05JC02_40.FIN2	697	3.16	0.0970	0.0031	0.0147	0.0002	0.21	94.0	2.9	94.3	1.4	71.0	61.0	94.3	1.4	0.3
05JC02_41.FIN2	241	1.96	0.0827	0.0032	0.0124	0.0002	0.10	80.6	3.0	79.5	1.5	95.0	73.0	79.5	1.5	1.4
05JC02_42.FIN2	770	2.64	0.0977	0.0014	0.0145	0.0002	0.30	94.8	1.3	92.7	1.1	142.0	33.0	92.7	1.1	2.2
05JC02_43.FIN2	577	5.06	0.0967	0.0019	0.0141	0.0003	0.40	93.7	1.8	90.5	2.0	157.0	54.0	90.5	2	3.4
05JC02_44.FIN2	741	3.57	0.0983	0.0019	0.0148	0.0002	0.30	95.2	1.7	94.5	1.4	106.0	45.0	94.5	1.4	0.7
05JC02_45.FIN2	1092	3.22	0.1001	0.0014	0.0150	0.0002	0.55	96.9	1.2	96.1	1.0	108.0	27.0	96.1	0.96	0.9
05JC02_46.FIN2	270	1.86	0.0924	0.0029	0.0128	0.0002	0.33	90.0	2.7	82.2	1.4	282.0	67.0	82.2	1.4	8.7
05JC02_47.FIN2	730	2.71	0.0989	0.0018	0.0151	0.0002	0.45	95.7	1.7	96.3	1.2	83.0	34.0	96.3	1.2	0.6
05JC02_48.FIN2	672	3.10	0.0984	0.0015	0.0149	0.0002	0.16	95.3	1.4	95.5	1.0	92.0	36.0	95.5	0.97	0.3
05JC02_49.FIN2	759	2.60	0.0997	0.0014	0.0151	0.0001	0.09	96.5	1.3	96.6	0.8	88.0	35.0	96.6	0.82	0.1
05JC02_50.FIN2	837	2.52	0.0992	0.0016	0.0149	0.0002	0.50	96.0	1.5	95.4	1.4	99.0	35.0	95.4	1.4	0.6
05JC02_51.FIN2	556	2.39	0.0946	0.0018	0.0137	0.0002	0.41	91.8	1.7	87.5	1.4	184.0	44.0	87.5	1.4	4.7
05JC02_52.FIN2	732	3.18	0.0974	0.0016	0.0144	0.0002	0.30	94.4	1.4	92.1	1.2	144.0	39.0	92.1	1.2	2.4
05JC02_53.FIN2	696	4.33	0.1022	0.0020	0.0157	0.0003	0.48	98.8	1.9	100.2	1.7	70.0	36.0	100.2	1.7	1.4
05JC02_54.FIN2	734	3.21	0.0986	0.0014	0.0149	0.0002	0.37	95.4	1.3	95.1	0.9	119.0	32.0	95.1	0.92	0.3
05JC02_55.FIN2	768	1.93	0.1005	0.0017	0.0147	0.0002	0.55	97.2	1.6	93.9	1.2	173.0	38.0	93.9	1.2	3.4
05JC02_56.FIN2	765	3.03	0.0999	0.0019	0.0148	0.0002	0.53	96.6	1.8	94.9	1.5	142.0	40.0	94.9	1.5	1.8
05JC02_57.FIN2	437	2.73	0.0957	0.0017	0.0133	0.0002	0.35	92.7	1.6	85.4	1.4	299.0	44.0	85.4	1.4	7.9
05JC02_58.FIN2	942	3.04	0.1014	0.0020	0.0152	0.0002	0.40	98.3	1.8	97.0	1.1	133.0	39.0	97.0	1.1	1.3
05JC02_59.FIN2	1536	2.58	0.1040	0.0013	0.0156	0.0002	0.40	100.4	1.2	99.9	1.2	105.0	29.0	99.9	1.2	0.5
05JC02_60.FIN2	1255	2.75	0.1070	0.0020	0.0161	0.0003	0.52	103.2	1.9	102.7	1.7	108.0	46.0	102.7	1.7	0.5
05JC02_61.FIN2	270	1.68	0.0919	0.0029	0.0129	0.0002	0.45	89.2	2.7	82.5	1.4	260.0	68.0	82.5	1.4	7.5
05JC02_62.FIN2	310	1.74	0.0876	0.0035	0.0129	0.0004	0.20	85.2	3.3	82.6	2.3	156.0	93.0	82.6	2.3	3.1
05JC02_63.FIN2	914	3.17	0.0989	0.0013	0.0149	0.0001	0.23	95.7	1.2	95.5	0.9	97.0	31.0	95.5	0.87	0.2
05JC02_64.FIN2	662	3.15	0.0968	0.0016	0.0142	0.0002	0.34	93.8	1.5	90.9	1.1	151.0	38.0	90.9	1.1	3.1
05JC02_68.FIN2	700	3.70	0.0975	0.0015	0.0148	0.0002	0.38	94.5	1.4	94.6	1.2	80.0	35.0	94.6	1.2	0.1
05JC02_70.FIN2	75	2.41	1.8900	0.0240	0.1850	0.0018	0.42	1076.9	8.5	1094.0	10.0	1053.0	26.0	1053.0	26	3.9
05JC02_72.FIN2	1248	1.41	0.0957	0.0018	0.0145	0.0003	0.47	92.7	1.7	92.9	1.6	90.0	34.0	92.9	1.6	0.2
05JC02a_1.FIN2	764	3.59	0.0838	0.0025	0.0124	0.0002	0.08	81.6	2.3	79.7	1.3	134.0	71.0	79.7	1.3	2.3
05JC02a_2.FIN2	558	3.76	0.0731	0.0037	0.0112	0.0004	0.40	71.5	3.5	71.7	2.4	109.0	94.0	71.7	2.4	0.3
05JC02a_3.FIN2	1065	3.72	0.0852	0.0021	0.0124	0.0002	0.16	83.0	2.0	79.6	1.2	161.0	62.0	79.6	1.2	4.1
05JC02a_4.FIN2	664	3.49	0.0885	0.0029	0.0127	0.0002	0.20	86.0	2.7	81.3	1.3	211.0	70.0	81.3	1.3	5.5
05JC02a_5.FIN2	188	2.24	0.0807	0.0050	0.0123	0.0003	0.14	79.2	4.8	78.6	2.1	90.0	120.0	78.6	2.1	0.8
05JC02a_7.FIN2	1473	3.70	0.0871	0.0017	0.0129	0.0002	0.04	84.8	1.6	82.6	1.1	156.0	53.0	82.6	1.1	2.6
05JC02a_8.FIN2	229	2.68	0.0917	0.0058	0.0121	0.0004	0.08	88.8	5.4	77.2	2.4	390.0	150.0	77.2	2.4	13.1
05JC02a_10.FIN	978	3.44	0.0867	0.0025	0.0130	0.0002	0.20	84.4	2.4	83.2	1.3	96.0	61.0	83.2	1.3	1.4
05JC02a_11.FIN	683	2.83	0.0885	0.0033	0.0125	0.0003	0.20	86.1	3.0	80.1	1.7	234.0	76.0	80.1	1.7	7.0
05JC02a_12.FIN	289	1.80	0.0829	0.0042	0.0125	0.0004	0.05	80.8	3.9	79.9	2.3	110.0	100.0	79.9	2.3	1.1
05JC02a_13.FIN	283	2.04	0.0793	0.0038	0.0121	0.0003	0.09	77.4	3.6	77.3	2.1	100.0	100.0	77.3	2.1	0.1
05JC02a_14.FIN	923	4.63	0.0980	0.0029	0.0127	0.0003	0.20	94.8	2.7	81.5	1.7	425.0	67.0	81.5	1.7	14.0
05JC02a_16.FIN	658	4.06	0.0845	0.0028	0.0127	0.0003	0.16	82.3	2.6	81.2	2.0	104.0	72.0	81.2	2	1.3
05JC02a_17.FIN	765	3.89	0.0846	0.0026	0.0124	0.0002	0.16	82.4	2.4	79.6	1.5	166.0	70.0	79.6	1.5	3.4
05JC02a_19.FIN	1184	3.56	0.0840	0.0022	0.0125	0.0002	0.45	81.9	2.0	80.3	1.5	112.0	51.0	80.3	1.5	2.0
05JC02a_20.FIN	867	3.85	0.0838	0.0036	0.0123	0.0003	0.39	81.6	3.4	78.5	1.7	139.0	84.0	78.5	1.7	3.8
05JC02a_21.FIN	493	3.04	0.0862	0.0034	0.0128	0.0003	0.02	83.8	3.2	82.1	2.0	104.0	94.0	82.1	2	2.0
05JC02a_22.FIN	929	3.92	0.0815	0.0025	0.0122	0.0002	0.33	79.5	2.4	78.3	1.5	126.0	63.0	78.3	1.5	1.5
05JC02a_23.FIN	959	3.95	0.0847	0.0027	0.0121	0.0002	0.04	82.5	2.6	77.7	1.3	209.0	76.0	77.7	1.3	5.8
05JC02a_24.FIN	774	4.55	0.0816	0.0033	0.0126	0.0003	0.15	79.5	3.1	81.0	1.6	41.0	76.0	81.0	1.6	1.9
05JC02a_25.FIN	1561	4.80	0.0849	0.0031	0.0127	0.0003	0.44	82.7	2.9	81.3	2.0	64.0	64.0	81.3	2	1.7
05JC02a_26.FIN	735	3.26	0.0863	0.0031	0.0132	0.0003	0.05	84.0	2.9	84.6	1.6	56.0	69.0	84.6	1.6	0.7
05JC02a_27.FIN	1122	3.32	0.0881	0.0026	0.0131	0.0003	0.18	85.7	2.5	84.0	1.7	121.0	64.0	84.0	1.7	2.0
05JC02a_28.FIN	272	1.60	0.0918	0.0045	0.0128	0.0004	0.00	89.0	4.2	82.1	2.4	270.0	110.0	82.1	2.4	7.8
05JC02a_29.FIN	343	2.09	0.0809	0.0041	0.0117	0.0003	0.32	78.9	3.8	74.7	2.1	200.0	110.0	74.7	2.1	5.3
05JC02a_30.FIN	1343	3.58	0.0879	0.0024	0.0132	0.0002	0.45	85.5	2.2	84.3	1.5	127.0	48.0	84.3	1.5	1.4
05JC02a_31.FIN	751	3.40	0.0812	0.0030	0.0124	0.0003	0.33	79.2	2.9	79.3	1.8	88.0	72.0	79.3	1.8	0.1
05JC02a_32.FIN	963	3.00	0.0866	0.0026	0.0126	0.0003	0.22	84.2	2.4	80.6	1.7	186.0	66.0	80.6	1.7	4.3
05JC02a_33.FIN	824	3.05	0.0882	0.0031	0.0135	0.0002	0.09	85.7	2.9	86.6	1.5	23.0	75.0	86.6	1.5	1.1
05JC02a_34.FIN	1280	3.40	0.0870	0.0024	0.0131	0.0002	0.28	84.6	2.2	83.7	1.1	98.0	58.0	83.7	1.1	1.1
05JC02a_35.FIN	1068	3.69	0.0868	0.0024	0.0132	0.0002	0.06	84.5	2.3	84.3	1.4	110.0	67.0	84.3	1.4	0.2
05JC02a_36.FIN	710	5.21	0.0834	0.0025	0.0128	0.0003	0.11	81.2	2.3	82.1	1.6	66.0	68.0	82.1	1.6	1.1
05JC02a_37.FIN	831	3.94	0.0800	0.0026	0.0122	0.0002	0.06	78.5	2.5	77.9	1.3	111.0	75.0	77.9	1.3	0.8
05JC02a_38.FIN	702	3.85	0.0901	0.0033	0.0131	0.0002	0.21	88.0	3.0	84.0	1.5	220.0	79.0	84.0	1.5	4.5

05JC02a_39.FIN 250 1.38 0.0901 0.0053 0.0123 0.0004 0.14 87.4 4.9 78.8 2.3 300.0 120.0 78.8 2.3 9.8

San Felipe Formation (sample: 48-AZ02); coordinates: 21° 14.238'N, 99° 06.931'W

Lawton3-1.FIN2	347	1.78	0.0899	0.0028	0.0124	0.0002	0.34	87.3	2.6	79.2	1.1	302.0	63.0	79.2	1.1	9.3
Lawton3-2.FIN2	372	2.86	0.0843	0.0027	0.0122	0.0002	0.21	82.1	2.6	77.9	1.5	196.0	71.0	77.9	1.5	5.1
Lawton3-3.FIN2	152	1.35	0.0850	0.0036	0.0125	0.0003	0.34	82.7	3.3	79.8	1.7	166.0	81.0	79.8	1.7	3.5
Lawton3-4.FIN2	233	2.57	0.0826	0.0029	0.0122	0.0002	0.22	80.5	2.7	78.2	1.3	143.0	69.0	78.2	1.3	2.9
Lawton3-5.FIN2	153	1.50	0.0852	0.0034	0.0128	0.0002	0.05	82.8	3.1	82.2	1.4	117.0	81.0	82.2	1.4	0.7
Lawton3-6.FIN2	216	2.66	0.0861	0.0040	0.0127	0.0003	0.30	83.7	3.7	81.3	1.6	142.0	87.0	81.3	1.6	2.9
Lawton3-7.FIN2	75	0.95	0.0839	0.0056	0.0126	0.0003	0.29	81.4	5.2	80.4	1.9	110.0	120.0	80.4	1.9	1.2
Lawton3-8.FIN2	85	0.91	0.0874	0.0063	0.0128	0.0003	0.21	84.7	5.8	82.3	2.2	140.0	130.0	82.3	2.2	2.8
Lawton3-9.FIN2	81	0.64	0.0890	0.0062	0.0124	0.0002	0.02	86.0	5.8	79.7	1.4	210.0	130.0	79.7	1.4	7.3
Lawton3-10.FIN	135	1.09	0.0907	0.0056	0.0131	0.0003	0.01	87.9	5.3	84.1	1.8	190.0	130.0	84.1	1.8	4.3
Lawton3-12.FIN	292	4.47	0.0837	0.0035	0.0129	0.0002	0.18	81.5	3.3	82.6	1.5	65.0	82.0	82.6	1.5	1.3
Lawton3-13.FIN	526	6.71	0.0839	0.0019	0.0126	0.0002	0.06	81.7	1.7	80.5	1.4	121.0	50.0	80.5	1.4	1.5
Lawton3-14.FIN	460	5.12	0.0881	0.0048	0.0129	0.0005	0.14	85.7	4.4	82.8	2.8	160.0	120.0	82.8	2.8	3.4
Lawton3-15.FIN	120	1.14	0.0868	0.0041	0.0128	0.0002	0.12	84.3	3.8	81.8	1.3	140.0	93.0	81.8	1.3	3.0
Lawton3-16.FIN	187	1.81	0.0867	0.0040	0.0125	0.0003	0.30	84.2	3.7	80.0	1.9	158.0	84.0	80.0	1.9	5.0
Lawton3-17.FIN	116	1.14	0.0838	0.0058	0.0128	0.0005	0.29	81.5	5.4	81.9	3.2	100.0	130.0	81.9	3.2	0.5
Lawton3-19.FIN	246	3.14	0.0806	0.0028	0.0120	0.0002	0.33	78.6	2.7	76.7	1.5	140.0	74.0	76.7	1.5	2.4
Lawton3-20.FIN	244	2.48	0.0866	0.0038	0.0131	0.0003	0.22	84.2	3.5	83.7	1.6	107.0	84.0	83.7	1.6	0.6
Lawton3-21.FIN	268	4.51	0.0854	0.0034	0.0130	0.0003	0.36	83.1	3.1	83.1	1.7	108.0	73.0	83.1	1.7	0.0
Lawton3-22.FIN	316	2.75	0.0874	0.0041	0.0126	0.0003	0.14	85.6	4.1	80.8	1.8	210.0	100.0	80.8	1.8	5.6
Lawton3-23.FIN	238	5.61	0.0893	0.0039	0.0126	0.0003	0.40	86.8	3.6	80.5	1.9	236.0	88.0	80.5	1.9	7.3
Lawton3-24.FIN	202	2.19	0.0842	0.0031	0.0127	0.0002	0.02	81.9	2.9	81.1	1.4	102.0	76.0	81.1	1.4	1.0
Lawton3-25.FIN	128	1.59	0.0885	0.0044	0.0126	0.0002	0.05	86.9	4.3	80.8	1.6	230.0	100.0	80.8	1.6	7.0
Lawton3-26.FIN	119	1.72	0.0831	0.0044	0.0124	0.0003	0.05	80.8	4.1	79.3	1.7	130.0	100.0	79.3	1.7	1.9
Lawton3-27.FIN	226	1.31	0.0851	0.0035	0.0125	0.0003	0.32	82.8	3.3	80.3	1.8	143.0	82.0	80.3	1.8	3.0
Lawton3-28.FIN	185	1.46	0.0849	0.0036	0.0121	0.0002	0.15	82.6	3.4	77.5	1.3	220.0	88.0	77.5	1.3	6.2
Lawton3-29.FIN	146	0.73	0.3170	0.0180	0.0424	0.0009	0.28	279.0	13.0	267.9	5.5	360.0	110.0	267.9	5.5	4.0
Lawton3-30.FIN	102	2.73	0.0900	0.0052	0.0128	0.0003	0.02	87.1	4.9	82.0	2.2	230.0	120.0	82.0	2.2	5.9
Lawton3-31.FIN	180	2.41	0.0900	0.0037	0.0128	0.0002	0.22	87.3	3.4	81.7	1.4	224.0	78.0	81.7	1.4	6.4
Lawton3-32.FIN	237	1.69	0.0867	0.0032	0.0129	0.0002	0.12	84.3	3.0	82.5	1.2	130.0	72.0	82.5	1.2	2.1
Lawton3-33.FIN	235	1.16	0.0917	0.0030	0.0135	0.0003	0.15	89.0	2.8	86.2	1.6	162.0	70.0	86.2	1.6	3.1
Lawton3-35.FIN	162	1.02	0.0866	0.0032	0.0128	0.0002	0.08	84.1	3.0	82.3	1.2	146.0	75.0	82.3	1.2	2.1
Lawton3-36.FIN	154	0.71	0.0840	0.0040	0.0128	0.0003	0.25	81.7	3.7	82.0	1.7	94.0	90.0	82.0	1.7	0.4
Lawton3-37.FIN	183	1.74	1.6920	0.0630	0.1692	0.0058	0.90	1002.0	24.0	1007.0	32.0	995.0	33.0	995.0	33	1.2
Lawton3-38.FIN	430	2.02	0.0909	0.0033	0.0130	0.0002	0.03	88.2	3.1	83.5	1.3	207.0	76.0	83.5	1.3	5.3
Lawton3-39.FIN	191	2.07	0.0824	0.0033	0.0131	0.0002	0.31	80.3	3.1	84.2	1.4	3.0	70.0	84.2	1.4	4.9
Lawton3-40.FIN	134	0.80	0.0835	0.0040	0.0128	0.0002	0.19	81.2	3.7	82.2	1.2	67.0	86.0	82.2	1.2	1.2
Lawton3-41.FIN	216	1.34	0.0867	0.0034	0.0124	0.0002	0.29	84.7	3.3	79.2	1.5	221.0	74.0	79.2	1.5	6.5
Lawton3-42.FIN	560	5.44	0.0841	0.0048	0.0125	0.0004	0.39	81.9	4.5	80.3	2.4	160.0	110.0	80.3	2.4	2.0
Lawton3-43.FIN	429	5.03	0.0854	0.0039	0.0129	0.0003	0.44	83.1	3.7	82.4	2.0	122.0	78.0	82.4	2	0.8
Lawton3-45.FIN	55	1.72	0.0838	0.0049	0.0127	0.0003	0.04	82.0	4.7	81.1	1.9	120.0	120.0	81.1	1.9	1.1
Lawton3-47.FIN	117	2.08	0.0886	0.0063	0.0127	0.0003	0.16	86.0	5.9	81.1	2.1	200.0	140.0	81.1	2.1	5.7
Lawton3-48.FIN	192	1.13	0.0840	0.0046	0.0124	0.0003	0.09	81.8	4.3	79.1	1.8	170.0	110.0	79.1	1.8	3.3
Lawton3-49.FIN	93	1.06	0.0787	0.0038	0.0122	0.0002	0.04	77.2	3.7	78.4	1.5	90.0	100.0	78.4	1.5	1.6
Lawton3-50.FIN	169	1.24	0.0850	0.0037	0.0124	0.0002	0.14	82.6	3.4	79.4	1.3	182.0	86.0	79.4	1.3	3.9
Lawton3-51.FIN	160	1.11	0.0849	0.0039	0.0124	0.0002	0.16	82.5	3.7	79.3	1.3	167.0	89.0	79.3	1.3	3.9
Lawton3-52.FIN	294	1.67	0.0854	0.0034	0.0121	0.0003	0.17	83.0	3.2	77.6	1.8	240.0	86.0	77.6	1.8	6.5
Lawton3-53.FIN	126	0.88	0.0826	0.0038	0.0122	0.0002	0.01	80.4	3.6	78.0	1.5	163.0	97.0	78.0	1.5	3.0
Lawton3-54.FIN	156	1.56	0.0823	0.0041	0.0123	0.0002	0.26	80.1	3.9	78.8	1.6	161.0	95.0	78.8	1.6	1.6
Lawton3-55.FIN	147	0.88	0.0776	0.0041	0.0120	0.0002	0.22	75.7	3.8	76.6	1.3	71.0	97.0	76.6	1.3	1.2
Lawton3-57.FIN	120	1.05	0.0834	0.0054	0.0123	0.0003	0.13	81.0	5.0	79.0	1.6	130.0	120.0	79.0	1.6	2.5
Lawton3-59.FIN	170	1.47	0.0853	0.0033	0.0126	0.0002	0.18	82.9	3.0	80.9	1.3	160.0	77.0	80.9	1.3	2.4

Unnamed turbidites near the city Río Grande; Mesa Central (sample: 13-26IV14); coordinates: 23° 48.061'N, 103° 01.009'W

13_26IV14_1	294	2.58	1.9630	0.0580	0.1852	0.0042	0.94	1100.0	20.0	1095.0	23.0	1102.0	19.0	1102.0	19	0.6
13_26IV14_2	299	2.11	3.3520	0.0290	0.2585	0.0021	0.69	1492.9	6.8	1482.0	11.0	1498.0	14.0	1498.0	14	1.1
13_26IV14_3	247	2.54	1.6480	0.0160	0.1615	0.0020	0.40	988.4	6.0	965.0	11.0	1037.0	27.0	1037.0	27	6.9
13_26IV14_4	139	1.37	0.1095	0.0038	0.0154	0.0003	0.16	105.4	3.5	98.4	1.6	253.0	76.0	98.4	1.6	6.6
13_26IV14_5	421	1.83	0.6199	0.0075	0.0762	0.0008	0.67	489.6	4.7	473.6	4.9	550.0	21.0	473.6	4.9	3.3
13_26IV14_6	811	0.94	0.2219	0.0027	0.0320	0.0003	0.56	203.4	2.3	202.8	1.9	210.0	27.0	202.8	1.9	0.3

13_26IV14_7	138	1.71	1.9530	0.0260	0.1853	0.0018	0.41	1099.0	8.9	1095.6	9.6	1090.0	26.0	1090.0	26	0.5	
13_26IV14_8	331	2.05	3.1150	0.0380	0.2473	0.0037	0.77	1436.7	9.5	1424.0	19.0	1437.0	20.0	1437.0	20	0.9	
13_26IV14_9	90	1.09	0.5583	0.0097	0.0713	0.0009	0.41	450.1	6.3	443.6	5.6	478.0	36.0	443.6	5.6	1.4	
13_26IV14_10	616	19.31	0.8340	0.0170	0.0995	0.0015	0.91	615.0	9.2	612.6	8.8	629.0	19.0	612.6	8.8	0.4	
13_26IV14_11	293	1.57	0.1762	0.0037	0.0257	0.0004	0.41	164.7	3.2	163.4	2.2	197.0	45.0	163.4	2.2	0.8	
13_26IV14_13	281	1.24	0.1012	0.0026	0.0143	0.0001	0.08	97.9	2.4	91.3	0.9	280.0	67.0	91.3	0.88	6.7	
13_26IV14_14	239	2.12	3.8740	0.0600	0.2767	0.0042	0.75	1607.0	12.0	1574.0	21.0	1663.0	23.0	1663.0	23	5.4	
13_26IV14_15	101	1.03	3.1710	0.0350	0.2526	0.0031	0.59	1449.3	8.6	1454.0	16.0	1443.0	18.0	1443.0	18	0.8	
13_26IV14_16	253	1.21	0.5994	0.0093	0.0758	0.0011	0.17	476.6	5.9	471.2	6.4	496.0	43.0	471.2	6.4	1.1	
13_26IV14_17	125	1.15	2.6580	0.0390	0.2241	0.0037	0.58	1316.0	11.0	1303.0	19.0	1312.0	26.0	1312.0	26	0.7	
13_26IV14_18	235	1.21	0.1753	0.0049	0.0252	0.0005	0.37	163.9	4.3	160.3	3.2	222.0	64.0	160.3	3.2	2.2	
13_26IV14_20	255	2.08	0.1765	0.0039	0.0262	0.0004	0.42	165.0	3.3	167.3	2.7	152.0	44.0	167.3	2.7	1.4	
13_26IV14_21	157	1.68	0.1430	0.0040	0.0206	0.0003	0.13	135.6	3.5	131.7	1.9	172.0	63.0	131.7	1.9	2.9	
13_26IV14_22	152	0.50	0.7223	0.0098	0.0892	0.0008	0.41	551.7	5.7	551.0	4.9	545.0	28.0	551.0	4.9	0.1	
13_26IV14_23	342	1.99	0.1015	0.0027	0.0150	0.0002	0.27	98.1	2.5	96.2	1.2	143.0	59.0	96.2	1.2	1.9	
13_26IV14_24	116	0.95	4.4350	0.0560	0.2999	0.0054	0.68	1719.0	10.0	1691.0	27.0	1760.0	24.0	1760.0	24	3.9	
13_26IV14_25	210	1.25	2.2670	0.0190	0.2019	0.0018	0.67	1201.9	5.8	1185.3	9.5	1243.0	14.0	1243.0	14	4.6	
13_26IV14_26	333	1.48	1.6620	0.0150	0.1618	0.0017	0.56	994.7	5.7	966.5	9.5	1052.0	19.0	1052.0	19	8.1	
13_26IV14_27	314	1.93	0.1019	0.0026	0.0152	0.0002	0.12	98.4	2.4	97.0	1.1	127.0	53.0	97.0	1.1	1.4	
13_26IV14_28	205	1.05	3.3050	0.0350	0.2568	0.0032	0.68	1481.9	8.2	1473.0	16.0	1512.0	20.0	1512.0	20	2.6	
13_26IV14_29	69	0.88	0.1126	0.0043	0.0163	0.0005	0.01	108.3	4.0	104.0	3.0	210.0	100.0	104.0	3	4.0	
13_26IV14_30	466	1.02	0.4272	0.0062	0.0565	0.0007	0.57	361.0	4.4	354.3	4.3	406.0	27.0	354.3	4.3	1.9	
13_26IV14_31	144	1.14	0.2889	0.0056	0.0401	0.0005	0.30	257.5	4.4	253.3	3.3	271.0	46.0	253.3	3.3	1.6	
13_26IV14_32	87	1.64	1.3410	0.0340	0.1452	0.0020	0.56	862.0	15.0	874.0	12.0	849.0	39.0	849.0	12	1.4	
13_26IV14_33	107	1.23	0.0987	0.0029	0.0154	0.0003	0.01	96.0	2.8	98.4	2.2	95.0	81.0	98.4	2.2	2.5	
13_26IV14_34	315	0.97	0.1010	0.0021	0.0154	0.0002	0.26	97.7	2.0	98.4	1.5	85.0	46.0	98.4	1.5	0.7	
13_26IV14_35	199	1.06	0.3168	0.0086	0.0432	0.0007	0.24	279.3	6.6	272.6	4.1	368.0	63.0	272.6	4.1	2.4	
13_26IV14_37	202	0.54	0.8930	0.0120	0.1050	0.0012	0.59	647.9	6.6	644.6	7.3	667.0	24.0	644.6	7.3	0.5	
13_26IV14_38	80	1.62	1.7040	0.0250	0.1688	0.0020	0.71	1009.1	9.3	1005.0	11.0	1034.0	22.0	1034.0	22	2.8	
13_26IV14_39	98	0.80	0.0983	0.0038	0.0148	0.0003	0.13	95.1	3.5	95.0	2.1	162.0	99.0	95.0	2.1	0.1	
13_26IV14_40	133	1.05	0.0988	0.0050	0.0143	0.0003	0.04	95.6	4.6	91.6	2.1	190.0	110.0	91.6	2.1	4.2	
13_26IV14_41	458	27.50	0.7490	0.0180	0.0905	0.0022	0.53	567.0	10.0	559.0	13.0	615.0	45.0	559.0	13	1.4	
13_26IV14_42	105	1.59	0.1147	0.0056	0.0170	0.0006	0.48	110.6	5.0	108.8	3.8	132.0	87.0	108.8	3.8	1.6	
13_26IV14_43	236	1.05	0.5757	0.0070	0.0736	0.0009	0.43	461.5	4.5	458.0	5.4	467.0	30.0	458.0	5.4	0.8	
13_26IV14_44	22	0.80	4.3710	0.0630	0.2908	0.0043	0.57	1706.0	12.0	1645.0	21.0	1787.0	23.0	1787.0	23	7.9	
13_26IV14_45	54	1.40	3.0810	0.0360	0.2450	0.0025	0.29	1429.2	8.6	1412.0	13.0	1464.0	28.0	1464.0	28	3.6	
13_26IV14_47	321	2.32	1.0690	0.0270	0.1207	0.0024	0.87	738.0	13.0	734.0	14.0	756.0	25.0	734.0	14	0.5	
13_26IV14_48	183	3.02	0.2138	0.0073	0.0309	0.0006	0.34	196.5	6.1	196.2	4.0	183.0	69.0	196.2	4	0.2	
13_26IV14_49	309	1.76	0.0970	0.0024	0.0144	0.0003	0.24	94.0	2.2	92.3	1.6	147.0	60.0	92.3	1.6	1.8	
13_26IV14_50	238	2.17	2.1730	0.0170	0.1992	0.0017	0.63	1172.3	5.4	1170.7	8.9	1171.0	15.0	1171.0	15	0.0	
13_26IV14_51	198	1.33	0.1141	0.0029	0.0171	0.0003	0.27	109.6	2.6	109.1	1.6	142.0	52.0	109.1	1.6	0.5	
13_26IV14_52	272	1.17	0.6120	0.0190	0.0780	0.0022	0.71	485.0	12.0	484.0	13.0	500.0	61.0	484.0	13	0.2	Rim
13_26IV14_52	54	0.84	5.6700	0.1000	0.3459	0.0071	0.73	1926.0	16.0	1915.0	34.0	1975.0	23.0	1975.0	23	3.0	Core
13_26IV14_53	500	11.79	6.5940	0.0800	0.3730	0.0055	0.54	2058.0	11.0	2043.0	26.0	2059.0	24.0	2059.0	24	0.8	
13_26IV14_54	236	1.60	0.1140	0.0046	0.0156	0.0003	0.44	109.6	4.2	99.5	2.2	323.0	84.0	99.5	2.2	9.2	
13_26IV14_55	89	2.01	1.6660	0.0380	0.1668	0.0031	0.68	995.0	14.0	994.0	17.0	987.0	40.0	987.0	40	0.7	
13_26IV14_56	630	15.60	0.5780	0.0160	0.0747	0.0012	0.57	463.0	10.0	464.5	7.2	465.0	50.0	464.5	7.2	0.3	Rim
13_26IV14_56	89	1.67	2.0800	0.0270	0.1864	0.0022	0.36	1142.1	8.9	1102.0	12.0	1216.0	25.0	1216.0	25	9.4	Core
13_26IV14_57	532	1.87	0.5743	0.0055	0.0737	0.0007	0.57	460.6	3.5	458.1	3.9	469.0	20.0	458.1	3.9	0.5	
13_26IV14_58	135	0.93	0.1030	0.0033	0.0148	0.0003	0.16	99.5	3.0	94.9	2.0	223.0	72.0	94.9	2	4.6	
13_26IV14_59	222	1.62	4.2050	0.0350	0.2913	0.0023	0.65	1674.8	6.8	1648.0	12.0	1706.0	12.0	1706.0	12	3.4	
13_26IV14_60	140	6.71	0.9950	0.0240	0.1064	0.0021	0.71	701.0	12.0	652.0	12.0	855.0	33.0	652.0	12	7.0	
13_26IV14_62	211	0.77	0.2917	0.0081	0.0402	0.0008	0.44	260.8	6.1	253.8	4.7	315.0	60.0	253.8	4.7	2.7	
13_26IV14_63	245	24.40	0.6610	0.0460	0.0836	0.0074	0.92	515.0	28.0	517.0	44.0	592.0	87.0	517.0	44	0.4	Rim
13_26IV14_63	102	0.77	5.5140	0.0620	0.3304	0.0042	0.64	1902.2	9.7	1840.0	20.0	1969.0	19.0	1969.0	19	6.6	Core
13_26IV14_64	32	0.95	0.6530	0.0210	0.0791	0.0015	0.21	509.0	13.0	490.5	8.9	623.0	71.0	490.5	8.9	3.6	
13_26IV14_65	135	0.85	0.0991	0.0030	0.0148	0.0003	0.08	95.9	2.8	94.6	2.2	147.0	79.0	94.6	2.2	1.4	
13_26IV14_67	141	0.54	3.0140	0.0370	0.2437	0.0044	0.79	1410.6	9.3	1406.0	23.0	1418.0	22.0	1418.0	22	0.8	
13_26IV14_68	622	1.26	0.1036	0.0044	0.0147	0.0003	0.14	100.0	4.1	94.2	1.9	240.0	100.0	94.2	1.9	5.8	
13_26IV14_70	289	0.85	0.1106	0.0037	0.0150	0.0002	0.18	106.4	3.3	96.1	1.6	305.0	75.0	96.1	1.6	9.7	
13_26IV14_71	31	1.14	0.5840	0.0140	0.0729	0.0012	0.07	466.0	9.2	453.5	7.3	539.0	64.0	453.5	7.3	2.7	
13_26IV14_72	335	1.60	0.1786	0.0030	0.0260	0.0004	0.50	167.1	2.5	165.5	2.4	159.0	34.0	165.5	2.4	1.0	
13_26IV14_73	277	27.60	0.5900	0.0120	0.0746	0.0010	0.49	470.9	7.5	463.7	6.1	469.0	39.0	463.7	6.1	1.5	Rim

13_26IV14_74	337	0.88	0.1005	0.0028	0.0151	0.0002	0.34	97.2	2.6	96.3	1.2	129.0	57.0	96.3	1.2	0.9	
13_26IV14_78	117	0.34	0.1576	0.0048	0.0228	0.0004	0.05	148.4	4.2	145.5	2.2	188.0	73.0	145.5	2.2	2.0	
13_26IV14_79	181	1.79	0.1137	0.0028	0.0167	0.0003	0.21	109.2	2.5	106.7	1.6	157.0	53.0	106.7	1.6	2.3	
13_26IV14_80	199	2.11	0.1098	0.0031	0.0162	0.0003	0.09	105.7	2.8	103.7	1.7	133.0	62.0	103.7	1.7	1.9	
13_26IV14_83	118	1.03	0.6020	0.0110	0.0763	0.0012	0.35	478.4	7.1	474.2	7.4	522.0	44.0	474.2	7.4	0.9	
13_26IV14_84	299	0.76	0.1058	0.0027	0.0158	0.0003	0.20	102.1	2.5	101.0	2.2	180.0	86.0	101.0	2.2	1.1	
13_26IV14_85	257	3.00	1.5980	0.0190	0.1596	0.0018	0.66	970.0	7.3	954.3	9.9	1008.0	18.0	1008.0	18	5.3	
13_26IV14_86	274	2.50	1.7980	0.0160	0.1710	0.0017	0.59	1044.4	5.7	1017.4	9.2	1095.0	19.0	1095.0	19	7.1	
13_26IV14_87	113	1.75	2.3080	0.0250	0.2063	0.0024	0.47	1214.3	7.7	1209.0	13.0	1216.0	27.0	1216.0	27	0.6	
13_26IV14_88	208	1.21	0.0992	0.0024	0.0145	0.0002	0.37	95.9	2.2	92.8	1.3	169.0	52.0	92.8	1.3	3.2	
13_26IV14_89	276	0.42	0.1843	0.0044	0.0258	0.0004	0.29	171.7	3.7	164.1	2.5	256.0	56.0	164.1	2.5	4.4	
13_26IV14_90	138	1.69	2.7070	0.0460	0.2187	0.0033	0.64	1330.0	13.0	1275.0	18.0	1407.0	25.0	1407.0	25	9.4	
13_26IV14_91	471	4.87	0.6120	0.0110	0.0786	0.0022	0.82	484.8	6.7	488.0	13.0	501.0	44.0	488.0	13	0.7	Rim
13_26IV14_91	83	1.78	2.2700	0.0340	0.2034	0.0019	0.58	1202.0	10.0	1194.0	10.0	1228.0	24.0	1228.0	24	2.8	Core
13_26IV14_95	149	1.52	0.0977	0.0032	0.0143	0.0003	0.20	94.6	2.9	91.8	1.8	148.0	66.0	91.8	1.8	3.0	
13_26IV14_96	230	2.57	0.0944	0.0029	0.0134	0.0002	0.21	91.9	2.6	85.7	1.3	245.0	68.0	85.7	1.3	6.7	
13_26IV14_98	452	2.63	0.0908	0.0020	0.0137	0.0002	0.33	88.2	1.8	87.7	1.0	141.0	48.0	87.7	0.97	0.6	
13_26IV14_99	100	1.47	0.1034	0.0042	0.0147	0.0003	0.24	99.8	3.9	94.0	2.0	238.0	88.0	94.0	2	5.8	
13_26IV14_100	226	1.71	1.3790	0.0190	0.1424	0.0016	0.61	879.6	7.9	858.1	8.9	936.0	20.0	936.0	20	8.3	
13_26IV14_101	70	1.46	2.9950	0.0240	0.2420	0.0020	0.39	1406.1	6.1	1397.0	10.0	1417.0	19.0	1417.0	19	1.4	
13_26IV14_102	367	1.31	0.0979	0.0019	0.0149	0.0002	0.23	95.0	1.8	95.0	1.4	101.0	43.0	95.0	1.4	0.0	
13_26IV14_106	114	0.99	0.7460	0.0130	0.0910	0.0016	0.57	565.0	7.6	561.3	9.6	584.0	37.0	561.3	9.6	0.7	
13_26IV14_107	720	1.38	0.1630	0.0046	0.0239	0.0004	0.55	153.3	4.0	152.4	2.2	184.0	58.0	152.4	2.2	0.6	
13_26IV14_108	32	0.82	2.8460	0.0530	0.2247	0.0042	0.29	1370.0	13.0	1306.0	22.0	1479.0	39.0	1479.0	39	11.7	
13_26IV14_109	78	0.75	0.1608	0.0055	0.0230	0.0004	0.24	151.1	4.8	146.8	2.6	244.0	76.0	146.8	2.6	2.8	
13_26IV14_110	170	1.07	0.4952	0.0075	0.0651	0.0006	0.56	408.2	5.1	406.4	3.7	430.0	27.0	406.4	3.7	0.4	
13_26IV14_111	160	0.82	0.1099	0.0028	0.0150	0.0002	0.21	105.8	2.6	95.7	1.5	342.0	61.0	95.7	1.5	9.5	
13_26IV14_112	131	3.45	4.6240	0.0800	0.3189	0.0049	0.85	1753.0	14.0	1784.0	24.0	1719.0	16.0	1719.0	16	3.8	
13_26IV14_113	111	1.24	0.1742	0.0051	0.0251	0.0004	0.27	162.9	4.4	159.7	2.6	210.0	64.0	159.7	2.6	2.0	
13_26IV14_114	407	1.00	0.1787	0.0034	0.0258	0.0003	0.40	166.9	2.9	164.0	1.7	212.0	43.0	164.0	1.7	1.7	
13_26IV14_117	211	1.31	0.1012	0.0026	0.0149	0.0003	0.12	97.8	2.4	95.7	1.5	147.0	61.0	95.7	1.5	2.1	
13_26IV14_118	262	9.80	2.0460	0.0350	0.1872	0.0037	0.78	1131.0	12.0	1106.0	20.0	1178.0	28.0	1178.0	28	6.1	Rim
13_26IV14_118	52	0.96	2.7920	0.0600	0.2356	0.0033	0.50	1353.0	16.0	1367.0	18.0	1358.0	39.0	1358.0	39	0.7	Core
13_26IV14_119	845	3.79	2.9640	0.0350	0.2284	0.0023	0.84	1397.9	9.1	1326.0	12.0	1521.0	13.0	1521.0	13	12.8	

Notes:

Instructions

Best Age Tab

Purpose: Filter out discordant grains, pick a "best age" and will identify rims

Steps

1 Copy and paste the following columns from Iolite "_integrations.xls" sheet into the orange filled cells:

Source file, DateTime, Duration(s), FinalAge206_238,* FinalAge206_238_Int2SE, FinalAge207_235,*FinalAge207_235_Int2SE, FinalAge207_206,*FinalAge207_206_Int2SE

*Be sure to note in the text of your publication if you are using internal or propagated error (if propagated than use Final AgeXXX_XXX_Prop2SE)

Description of Columns

J	% Discordance between 206/238 and 207/206 age
K	% Error for 206/238 age
L	% Discordance between 206/238 and 207/235
M	Picks the 7/6 age if older than *850 Ma, picks the 6/38 age if younger (*modify this number to use a natural gap in your data between 800-1200 Ma)
N	Filters >10% discordant 7/6 ages
O	Filters 6/38 ages with >10% error
P	Filters >10% discordant 6/38 ages
Q	Repopulates grain name
R	Reports the Best Age in Ma
S	Reports the 2 sigma error (if the age is 6/38 than the error is for 6/38, if 7/6 than error for 7/6)
T	% Discordance (*be sure to note in your publication that the discordance reported is 6/38 vs 7/6 if older than 850 Ma and 6/38 vs 7/35 if younger than 850 Ma)
U	Rim or Core or Single Age from grain
V	Notes if the duration of the integration is less than 4 seconds and then calls it "short"

Publication Tab

Steps

- 1 Copy and paste the following columns from lolite " __integrations.xls" sheet into columns A through N:
Source file (Grain #), Approx U ppm, Final_U_Th_Ratio (U/Th), Final207_235 (207/235), Final207_235_Int2SE, Final206_238 (206/238), Final206_238_Int2SE, ErrorCorrelation_6_38vs7_35 (RHO), FinalAge206_238, FinalAge206_238_Int2SE, FinalAge207_235, FinalAge207_235_Int2SE, FinalAge207_206, FinalAge207_206_Int2SE
- 2 Copy and Paste **Values** of "Best Age", "2 sig error" and "% Discordance" from Best Age tab into columns O, P, and Q
- 3 Decide whether DISC grains should be deleted
- 4 In Column A (Grain #). Select all names (not top 2 rows) go to >edit >replace. Find what- .FIN2, Replace with- leave blank. Press Replace All
- 5 Plot your data onto a Concordia Diagram
 - 1 Select all data in rows D through H (Make sure all RHO values are positive or you will get error message. If there are negative values, replace the value with 0)
 - 2 Open Isoplot (Ctrl-I on PC)
 - 3 Boxes to select: Isochron or plot type- U-Pb Concordia, normal; Input errors- 2 sigma, absolute; Symbols- error ellipse, red, not filled
Action- plot, (only calculate if single age or standard); Other-Color, Autoscaled
Hit OK
 - 5 Plot as a line

Apéndice 3

Edades U-Pb isotópicas y calculadas.

Late Cretaceous-Paleocene stratigraphic and structural evolution of the central Mexican fold and thrust belt, from detrital zircon (U-Th)/(He-Pb) ages

Sample Name:								207/235		206/238		207/206		Best age			
Grain #	[U] ppm	U/Th	207/235	2σ error	206/238	2σ error	RHO	Age Ma	2σ error	Age (Ma)	2σ error	Age (Ma)	2σ error	(Ma)	2σ error	% Discordance*	Rim/Core
Soyatal Formation (sample: 18-CA10), coordinates: 20° 56.306'N, 99° 44.090'W																	
18CA10_1.FIN2	344	1.91	0.1806	0.0034	0.0267	0.0005	0.43	168.5	2.9	169.6	3.1	138	42	169.6	3.1	0.7	
18CA10_2.FIN2	227	2.16	0.3032	0.0054	0.0430	0.0005	0.38	269.4	4.1	271.1	2.9	266	42	271.1	2.9	0.6	
18CA10_3.FIN2	29	1.28	1.6690	0.0350	0.1685	0.0026	0.31	996.0	13.0	1003.0	14.0	1007	43	1007.0	43.0	0.4	
18CA10_4.FIN2	95	2.62	0.1318	0.0043	0.0203	0.0004	0.11	125.6	3.9	129.8	2.5	100	66	129.8	2.5	3.3	
18CA10_5.FIN2	88	1.81	0.1140	0.0042	0.0170	0.0004	0.05	110.0	3.7	108.8	2.2	119	77	108.8	2.2	1.1	
18CA10_6.FIN2	95	0.86	1.5990	0.0360	0.1529	0.0030	0.53	972.0	14.0	917.0	17.0	1086	39	1086.0	39.0	15.6	
18CA10_7.FIN2	282	1.59	0.1008	0.0026	0.0148	0.0003	0.00	97.5	2.4	94.9	1.9	157	65	94.9	1.9	2.7	
18CA10_8.FIN2	171	1.64	0.1606	0.0066	0.0231	0.0006	0.11	151.1	5.7	147.1	3.7	207	99	147.1	3.7	2.6	
18CA10_9.FIN2	558	3.40	0.5965	0.0051	0.0763	0.0007	0.57	474.9	3.2	473.7	4.3	478	20	473.7	4.3	0.3	
18CA10_10.FIN2	74	68.40	0.6760	0.0240	0.0821	0.0024	0.66	527.0	15.0	509.0	14.0	599	64	509.0	14.0	3.4	Rim
18CA10_10.FIN2	328	6.02	1.1260	0.0280	0.1230	0.0021	0.36	765.0	14.0	748.0	12.0	801	50	748.0	12.0	2.2	Core
18CA10_11.FIN2	122	1.54	0.1270	0.0046	0.0182	0.0004	0.06	121.3	4.2	116.1	2.6	224	85	116.1	2.6	4.3	
18CA10_12.FIN2	78	2.39	0.2800	0.0076	0.0375	0.0008	0.24	250.4	6.1	237.3	5.1	372	68	237.3	5.1	5.2	
18CA10_13.FIN2	172	2.50	0.1303	0.0048	0.0181	0.0003	0.18	124.3	4.3	115.7	2.2	311	92	115.7	2.2	6.9	
18CA10_14.FIN2	645	1.42	0.1837	0.0025	0.0268	0.0003	0.62	171.2	2.1	170.5	1.8	191	24	170.5	1.8	0.4	
18CA10_15.FIN2	117	2.19	0.1258	0.0039	0.0186	0.0003	0.27	120.8	3.6	119.0	2.0	193	67	119.0	2.0	1.5	
18CA10_16.FIN2	145	2.06	0.1219	0.0030	0.0181	0.0003	0.37	116.7	2.8	115.5	1.7	152	50	115.5	1.7	1.0	
18CA10_17.FIN2	131	1.19	0.0931	0.0030	0.0144	0.0003	0.05	90.8	2.9	92.0	1.7	108	79	92.0	1.7	1.3	
18CA10_18.FIN2	211	2.49	1.7140	0.0360	0.1644	0.0033	0.74	1013.0	13.0	981.0	18.0	1103	27	1103.0	27.0	11.1	
18CA10_19.FIN2	632	38.10	0.6340	0.0180	0.0803	0.0020	0.71	500.0	11.0	498.0	12.0	518	58	498.0	12.0	0.4	# REF!
18CA10_21.FIN2	151	1.05	0.1280	0.0032	0.0192	0.0002	0.15	122.5	2.8	122.9	1.4	149	52	122.9	1.4	0.3	# REF!
18CA10_22.FIN2	47	2.30	0.1490	0.0110	0.0177	0.0009	0.04	140.3	9.8	113.1	5.8	610	180	113.1	5.8	19.4	
18CA10_23.FIN2	111	1.53	0.1243	0.0038	0.0183	0.0003	0.25	119.3	3.4	116.7	2.1	176	67	116.7	2.1	2.2	
18CA10_24.FIN2	279	0.90	0.6560	0.0150	0.0818	0.0017	0.64	511.9	9.3	507.0	10.0	578	47	507.0	10.0	1.0	Rim
18CA10_24.FIN2	315	0.36	0.7676	0.0087	0.0949	0.0012	0.39	579.5	5.4	584.6	7.0	579	31	584.6	7.0	0.9	Core
18CA10_25.FIN2	323	2.45	0.0944	0.0024	0.0141	0.0003	0.36	91.5	2.2	90.1	1.8	97	53	90.1	1.8	1.5	
18CA10_27.FIN2	609	2.19	0.1247	0.0028	0.0184	0.0004	0.62	119.3	2.6	117.5	2.2	173	40	117.5	2.2	1.5	
18CA10_28.FIN2	91	1.98	0.4960	0.0170	0.0600	0.0014	0.61	409.0	12.0	375.3	8.8	596	58	375.3	8.8	8.2	
18CA10_29.FIN2	198	2.50	0.1380	0.0035	0.0204	0.0003	0.38	131.1	3.1	130.4	1.8	138	53	130.4	1.8	0.5	
18CA10_30.FIN2	142	2.30	0.1256	0.0043	0.0179	0.0005	0.28	120.1	3.9	114.2	2.9	240	80	114.2	2.9	4.9	
18CA10_31.FIN2	64	2.70	1.1640	0.0380	0.1166	0.0040	0.66	782.0	18.0	711.0	23.0	972	48	711.0	23.0	9.1	# REF!
18CA10_33.FIN2	221	3.59	0.6860	0.0150	0.0737	0.0020	0.59	529.8	9.4	458.0	12.0	833	49	458.0	12.0	13.6	# REF!
18CA10_33.FIN2	136	4.00	1.0110	0.0290	0.1061	0.0027	0.57	709.0	15.0	650.0	16.0	818	49	650.0	16.0	8.3	Core
18CA10_34.FIN2	168	1.20	0.4197	0.0063	0.0551	0.0007	0.21	355.6	4.5	345.7	4.4	412	37	345.7	4.4	2.8	# REF!
18CA10_36.FIN2	64	1.81	0.1445	0.0081	0.0172	0.0007	0.11	136.8	7.1	110.0	4.2	640	160	110.0	4.2	19.6	# REF!
18CA10_38.FIN2	166	2.90	0.8880	0.0430	0.0928	0.0048	0.83	644.0	23.0	572.0	28.0	895	63	572.0	28.0	11.2	# REF!
18CA10_39.FIN2	365	2.72	0.1537	0.0056	0.0216	0.0006	0.73	145.1	4.9	137.8	3.9	240	71	137.8	3.9	5.0	
18CA10_40.FIN2	189	2.24	0.1506	0.0045	0.0212	0.0005	0.47	142.4	4.0	135.1	3.3	224	87	135.1	3.3	5.1	
18CA10_41.FIN2	700	2.38	0.1637	0.0042	0.0233	0.0005	0.75	153.9	3.6	148.3	2.9	238	37	148.3	2.9	3.6	
18CA10_42.FIN2	261	1.79	0.1272	0.0046	0.0176	0.0005	0.61	121.5	4.2	112.1	3.3	289	69	112.1	3.3	7.7	
18CA10_43.FIN2	119	1.47	0.1699	0.0052	0.0235	0.0005	0.09	159.2	4.5	149.9	3.3	287	83	149.9	3.3	5.8	# REF!
18CA10_45.FIN2	192	2.65	0.6120	0.0170	0.0697	0.0020	0.64	485.0	11.0	435.0	12.0	719	52	435.0	12.0	10.3	# REF!
18CA10_46.FIN2	62	3.22	1.3290	0.0400	0.1264	0.0047	0.64	857.0	17.0	767.0	27.0	1108	59	767.0	27.0	10.5	
18CA10_47.FIN2	44	6.64	0.7190	0.0370	0.0719	0.0030	0.52	549.0	22.0	447.0	18.0	1034	97	447.0	18.0	18.6	Rim
18CA10_47.FIN2	21	5.14	0.9960	0.0480	0.0973	0.0032	0.49	699.0	24.0	599.0	19.0	1072	79	599.0	19.0	14.3	Core
18CA10_48.FIN2	918	4.17	0.5620	0.0110	0.0734	0.0016	0.53	454.2	6.5	456.5	9.6	456	49	456.5	9.6	0.5	
18CA10_49.FIN2	253	40.10	0.7900	0.0110	0.0944	0.0010	0.19	591.2	6.3	581.3	6.2	651	33	581.3	6.2	1.7	
18CA10_50.FIN2	167	1.61	0.1356	0.0058	0.0180	0.0006	0.44	129.1	5.2	115.3	3.6	462	79	115.3	3.6	10.7	
18CA10_51.FIN2	405	1.97	0.1921	0.0037	0.0277	0.0004	0.61	178.3	3.1	176.2	2.8	209	40	176.2	2.8	1.2	
18CA10_52.FIN2	170	1.74	0.1510	0.0037	0.0225	0.0004	0.14	142.7	3.2	143.5	2.4	178	61	143.5	2.4	0.6	
18CA10_53.FIN2	199	2.50	0.1725	0.0032	0.0252	0.0004	0.22	161.6	2.8	160.5	2.3	185	50	160.5	2.3	0.7	
18CA10_54.FIN2	178	1.10	0.1092	0.0036	0.0165	0.0004	0.07	105.2	3.3	105.2	2.6	123	83	105.2	2.6	0.0	
18CA10_55.FIN2	470	48.00	0.6070	0.0180	0.0806	0.0026	0.64	482.0	12.0	500.0	15.0	480	43	500.0	15.0	3.7	Rim
18CA10_55.FIN2	1320	47.40	1.8650	0.0450	0.1804	0.0037	0.77	1068.0	16.0	1069.0	20.0	1058	22	1058.0	22.0	1.0	Core
18CA10_55.FIN2	310	6.27	2.7100	0.0320	0.2276	0.0032	0.43	1331.0	8.8	1322.0	17.0	1376	25	1376.0	25.0	3.9	Core
18CA10_56.FIN2	368	1.17	0.1050	0.0023	0.0157	0.0002	0.44	101.6	2.0	100.5	1.4	138	43	100.5	1.4	1.1	
18CA10_57.FIN2	136	2.03	0.5967	0.0098	0.0758	0.0008	0.31	475.7	6.4	470.8	4.8	506	37	470.8	4.8	1.0	
18CA10_58.FIN2	237	0.85	0.5378	0.0068	0.0654	0.0008	0.35	436.9	4.5	408.5	4.6	593	32	408.5	4.6	6.5	
18CA10_59.FIN2	275	0.98	0.2728	0.0035	0.0384	0.0005	0.37	244.9	2.8	243.0	3.1	272	38	243.0	3.1	0.8	
18CA10_60.FIN2	184	1.44	0.5464	0.0076	0.0702	0.0008	0.39	442.4	4.9	437.3	4.8	483	30	437.3	4.8	1.2	
18CA10_61.FIN2	217	1.95	0.2576	0.0042	0.0358	0.0004	0.36	232.7	3.4	226.6	2.5	280	41	226.6	2.5	2.6	
18CA10_62.FIN2	271	1.84	0.1341	0.0026	0.0197	0.0003	0.21	127.7	2.3	125.6	1.7	126	41	125.6	1.7	1.6	
18CA10_63.FIN2	157	1.21	0.1152	0.0027	0.0174	0.0002	0.00	110.7	2.5	110.9	1.5	116	60	110.9	1.5	0.2	
18CA10_64.FIN2	95	2.58	1.5170	0.0330	0.1506	0.0027	0.65	936.0	13.0	904.0	15.0	1021	33	1021.0	33.0	11.5	
18CA10_65.FIN2	170	2.24	0.1205	0.0037	0.0174	0.0003	0.01	115.5	3.4	111.4	2.1	202	75	111.4	2.1	3.5	# REF!
18CA10_67.FIN2	111	5.11	3.3500	0.1800	0.2564	0.0070	0.81	1491.0	42.0	1471.0	36.0	1589	32	1589.0	32.0	7.4	# REF!
18CA10_68.FIN2	150	5.37	0.1062	0.0052	0.0147	0.0006	0.22	103.2	4.9	94.2	3.8	300	130	94.2	3.8	8.7	
18CA10_69.FIN2	116	2.17	0.1320	0.0036	0.0195	0.0004	0.19	125.8	3.2	124.2	2.2	180	65	124.2	2.2	1.3	

18CA10_70.FIN2	139	1.93	0.1273	0.0035	0.0189	0.0003	0.09	121.6	3.1	120.8	1.8	153	66	120.8	1.8	0.7	
18CA10_71.FIN2	100	1.65	0.1041	0.0044	0.0155	0.0003	0.12	100.4	4.1	99.1	1.9	161	89	99.1	1.9	1.3	
18CA10_72.FIN2	115	1.61	4.6750	0.0580	0.3138	0.0038	0.74	1764.6	9.9	1759.0	19.0	1779	17	1779.0	17.0	1.1	
18CA10_73.FIN2	96	1.58	0.1290	0.0037	0.0189	0.0004	0.07	123.1	3.3	120.5	2.2	196	75	120.5	2.2	2.1	
18CA10_74.FIN2	92	2.33	0.1303	0.0040	0.0199	0.0004	0.22	124.9	3.8	127.0	2.5	134	71	127.0	2.5	1.7	
18CA10_75.FIN2	105	1.42	0.1194	0.0038	0.0179	0.0004	0.20	114.4	3.5	114.8	2.4	118	63	114.8	2.4	0.3	
18CA10_76.FIN2	177	1.95	3.9460	0.0510	0.2873	0.0042	0.86	1624.0	10.0	1628.0	21.0	1648	14	1648.0	14.0	1.2	
18CA10_77.FIN2	125	1.34	1.6640	0.0260	0.1681	0.0020	0.70	995.5	9.7	1002.0	11.0	1008	21	1008.0	21.0	0.6	
18CA10_78.FIN2	235	2.42	0.4330	0.0170	0.0574	0.0024	0.49	365.0	12.0	360.0	15.0	405	77	360.0	15.0	1.4	
18CA10_79.FIN2	58	2.10	1.6300	0.0300	0.1646	0.0027	0.50	981.0	12.0	982.0	15.0	1016	37	1016.0	37.0	3.3	
18CA10_80.FIN2	434	1.66	0.1088	0.0019	0.0161	0.0002	0.35	104.9	1.7	102.9	1.4	184	40	102.9	1.4	1.9	
18CA10_81.FIN2	243	1.50	0.0911	0.0021	0.0137	0.0002	0.18	88.4	1.9	87.9	1.3	120	53	87.9	1.3	0.6	
18CA10_82.FIN2	413	1.84	0.1389	0.0026	0.0203	0.0003	0.49	132.1	2.3	129.2	2.0	179	40	129.2	2.0	2.2	
18CA10_83.FIN2	199	7.29	0.5096	0.0090	0.0651	0.0008	0.52	418.8	6.2	406.3	5.0	505	26	406.3	5.0	3.0	
18CA10_84.FIN2	212	3.21	0.1366	0.0049	0.0174	0.0004	0.21	130.6	4.5	111.0	2.2	499	77	111.0	2.2	15.0	
18CA10_85.FIN2	87	2.75	2.3010	0.0390	0.1896	0.0021	0.51	1212.0	12.0	1119.0	11.0	1399	27	1399.0	27.0	20.0	
18CA10_86.FIN2	110	1.93	0.0902	0.0023	0.0136	0.0003	0.07	87.6	2.2	87.1	1.6	127	64	87.1	1.6	0.6	
18CA10_87.FIN2	126	2.08	0.1105	0.0032	0.0167	0.0003	0.08	106.3	2.9	106.7	2.0	130	66	106.7	2.0	0.4	
18CA10_88.FIN2	227	2.82	0.0989	0.0027	0.0148	0.0004	0.51	95.7	2.5	94.4	2.7	160	66	94.4	2.7	1.4	
18CA10_89.FIN2	149	2.09	0.1229	0.0029	0.0184	0.0003	0.23	117.6	2.6	117.4	1.7	170	54	117.4	1.7	0.2	
18CA10_90.FIN2	287	1.53	0.0959	0.0024	0.0147	0.0002	0.15	92.9	2.2	93.9	1.4	78	57	93.9	1.4	1.1	
18CA10_91.FIN2	487	1.98	0.1088	0.0015	0.0165	0.0002	0.34	104.9	1.4	105.5	1.1	123	31	105.5	1.1	0.6	
18CA10_92.FIN2	105	2.13	0.1228	0.0033	0.0182	0.0003	0.09	117.5	3.0	115.9	2.0	155	64	115.9	2.0	1.4	
18CA10_93.FIN2	134	2.08	0.0925	0.0030	0.0138	0.0002	0.02	89.8	2.8	88.6	1.5	156	73	88.6	1.5	1.3	
18CA10_94.FIN2	333	1.74	0.1026	0.0024	0.0156	0.0003	0.24	99.1	2.2	99.6	1.7	107	55	99.6	1.7	0.5	
18CA10_95.FIN2	286	1.70	0.1703	0.0032	0.0241	0.0004	0.31	159.6	2.7	153.7	2.4	249	46	153.7	2.4	3.7	
18CA10_96.FIN2	65	2.27	0.1343	0.0097	0.0201	0.0009	0.14	127.8	8.7	128.1	5.9	130	160	128.1	5.9	0.2	
18CA10_97.FIN2	191	2.15	0.6690	0.0110	0.0829	0.0012	0.33	520.0	6.5	513.5	7.4	554	39	513.5	7.4	1.3	
18CA10_98.FIN2	296	4.45	1.3170	0.0250	0.1327	0.0027	0.71	853.0	11.0	803.0	15.0	979	33	803.0	15.0	5.9	Rim
18CA10_98.FIN2	124	3.08	1.8770	0.0250	0.1743	0.0033	0.45	1072.6	8.7	1035.0	18.0	1155	30	1155.0	30.0	10.4	Core
18CA10_99.FIN2	25	2.96	0.1025	0.0092	0.0146	0.0006	0.21	98.4	8.4	93.5	3.5	230	160	93.5	3.5	5.0	
18CA10_100.FIN2	425	11.80	2.1240	0.0560	0.1912	0.0043	0.82	1156.0	18.0	1128.0	23.0	1240	34	1240.0	34.0	9.0	Rim
18CA10_100.FIN2	132	1.73	2.3770	0.0310	0.2033	0.0018	0.45	1237.6	9.7	1192.9	9.5	1319	27	1319.0	27.0	9.6	Core
18CA10_101.FIN2	460	2.58	0.1361	0.0027	0.0197	0.0004	0.55	129.8	2.4	125.8	2.2	204	39	125.8	2.2	3.1	
18CA10_102.FIN2	212	2.00	0.0931	0.0022	0.0141	0.0002	0.20	90.4	2.0	90.4	1.5	131	54	90.4	1.5	0.0	
18CA10_103.FIN2	200	2.20	0.1326	0.0029	0.0193	0.0004	0.36	126.4	2.6	123.2	2.4	224	52	123.2	2.4	2.5	
18CA10_104.FIN2	163	3.47	0.5321	0.0080	0.0688	0.0010	0.63	433.0	5.3	428.6	6.2	460	30	428.6	6.2	1.0	
18CA10_105.FIN2	73	0.72	0.9700	0.0190	0.1120	0.0019	0.47	687.8	9.9	684.0	11.0	698	40	684.0	11.0	0.6	
18CA10_106.FIN2	376	2.43	0.3184	0.0049	0.0444	0.0006	0.63	281.1	3.9	280.0	3.6	297	29	280.0	3.6	0.4	
18CA10_107.FIN2	74	0.99	0.6050	0.0130	0.0759	0.0012	0.34	479.8	8.0	471.8	7.0	538	46	471.8	7.0	1.7	
18CA10_108.FIN2	443	2.27	0.1460	0.0028	0.0219	0.0003	0.51	138.3	2.5	139.8	2.1	110	38	139.8	2.1	1.1	
18CA10_109.FIN2	323	3.01	2.0850	0.0220	0.1931	0.0019	0.64	1143.4	7.4	1138.0	10.0	1157	17	1157.0	17.0	1.6	
18CA10_110.FIN2	119	2.94	0.0927	0.0031	0.0137	0.0003	0.29	90.7	3.0	87.9	1.6	134	70	87.9	1.6	3.1	
18CA10_111.FIN2	141	2.95	0.1214	0.0040	0.0184	0.0005	0.15	116.2	3.6	117.6	2.9	104	73	117.6	2.9	1.2	
18CA10_112.FIN2	141	1.36	0.7290	0.0090	0.0887	0.0010	0.34	555.7	5.3	547.5	5.7	618	29	547.5	5.7	1.5	
18CA10_113.FIN2	251	3.17	2.0200	0.0650	0.1911	0.0046	0.85	1125.0	23.0	1127.0	25.0	1162	30	1162.0	30.0	3.0	
18CA10_114.FIN2	276	0.98	0.4163	0.0069	0.0564	0.0006	0.50	353.2	4.9	353.5	3.9	385	31	353.5	3.9	0.1	
18CA10_115.FIN2	279	1.72	0.1367	0.0027	0.0201	0.0003	0.29	130.1	2.4	128.5	1.7	193	44	128.5	1.7	1.2	
18CA10_116.FIN2	177	1.31	2.3990	0.0220	0.2062	0.0021	0.53	1242.0	6.7	1208.0	11.0	1325	21	1325.0	21.0	8.8	
18CA10_118.FIN2	223	2.37	0.1225	0.0033	0.0182	0.0003	0.17	117.3	3.0	116.5	1.7	134	56	116.5	1.7	0.7	
18CA10_119.FIN2	99	2.93	2.1730	0.0390	0.1991	0.0037	0.79	1171.0	12.0	1170.0	20.0	1181	32	1181.0	32.0	0.9	
18CA10_120.FIN2	681	1.60	0.1208	0.0024	0.0176	0.0003	0.40	115.8	2.1	112.3	2.0	173	49	112.3	2.0	3.0	#REF!

Mineral de Pozos sandstone (sample: 06-MP02); coordinates: 21° 13.746'N, 100° 31.108'W

06MP02_1.FIN2	352	6.00	0.5970	0.0140	0.0759	0.0008	0.16	474.9	8.7	471.8	4.9	484	56	471.8	4.9	0.7	
06MP02_2.FIN2	309	0.86	0.5740	0.0140	0.0733	0.0011	0.41	459.7	9.1	456.2	6.6	500	48	456.2	6.6	0.8	
06MP02_3.FIN2	589	4.50	0.8970	0.0130	0.1079	0.0011	0.39	649.7	6.9	660.3	6.6	645	31	660.3	6.6	1.6	
06MP02_4.FIN2	461	3.11	1.0120	0.0200	0.1116	0.0029	0.56	709.0	10.0	682.0	17.0	824	42	682.0	17.0	3.8	
06MP02_5.FIN2	434	1.55	3.0510	0.0480	0.2522	0.0032	0.63	1422.0	12.0	1450.0	17.0	1385	24	1385.0	24.0	4.7	
06MP02_6.FIN2	181	1.47	1.1210	0.0220	0.1272	0.0024	0.24	762.0	11.0	772.0	14.0	735	48	772.0	14.0	1.3	
06MP02_7.FIN2	653	41.00	0.5310	0.0180	0.0660	0.0022	0.19	432.0	12.0	412.0	13.0	530	100	412.0	13.0	4.6	Rim
06MP02_7.FIN2	72	1.58	1.7580	0.0870	0.1762	0.0039	0.14	1027.0	32.0	1046.0	21.0	1000	110	1000.0	110.0	4.6	Core
06MP02_8.FIN2	603	1.08	0.7770	0.0180	0.0969	0.0021	0.57	583.0	10.0	596.0	12.0	577	41	596.0	12.0	2.2	
06MP02_9.FIN2	141	4.17	4.2490	0.0820	0.2974	0.0063	0.59	1682.0	16.0	1677.0	31.0	1669	32	1669.0	32.0	0.5	
06MP02_10.FIN2	128	1.18	0.5680	0.0210	0.0749	0.0015	0.27	457.0	14.0	465.2	9.1	421	72	465.2	9.1	1.8	
06MP02_11.FIN2	550	7.75	4.3780	0.0410	0.3071	0.0026	0.66	1707.6	7.8	1726.0	13.0	1679	14	1679.0	14.0	2.8	
06MP02_12.FIN2	280	1.37	0.8820	0.0130	0.1074	0.0015	0.06	641.7	6.8	657.7	8.9	571	47	657.7	8.9	2.5	
06MP02_13.FIN2	389	1.65	0.1497	0.0047	0.0225	0.0006	0.41	141.5	4.1	143.6	3.7	104	72	143.6	3.7	1.5	
06MP02_14.FIN2	114	0.64	1.9310	0.0390	0.1843	0.0028	0.03	1090.0	14.0	1090.0	15.0	1077	49	1077.0	49.0	1.2	#REF!
06MP02_16.FIN2	699	2.49	0.0997	0.0035	0.0149	0.0002	0.04	96.4	3.2	95.3	1.6	125	76	95.3	1.6	1.1	#REF!
06MP02_17.FIN2	246	1.82	3.9450	0.0700	0.2722	0.0052	0.51	1622.0	14.0	1552.0	26.0	1720	37	1720.0	37.0	9.8	

06MP02_18.FIN2	471	2.22	2.9100	0.0430	0.2382	0.0033	0.61	1389.0	11.0	1377.0	17.0	1398	28	1398.0	28.0	1.5	
06MP02_19.FIN2	298	1.66	1.5220	0.0370	0.1482	0.0035	0.40	938.0	15.0	890.0	20.0	1094	47	1094.0	47.0	18.6	
06MP02_20.FIN2	364	2.12	0.0973	0.0040	0.0148	0.0004	0.17	94.1	3.7	94.8	2.7	134	92	94.8	2.7	0.7	
06MP02_21.FIN2	725	7.87	0.7690	0.0160	0.0940	0.0019	0.74	578.7	9.1	579.0	11.0	597	32	579.0	11.0	0.1	
06MP02_22.FIN2	324	1.17	0.1406	0.0060	0.0210	0.0005	0.09	133.3	5.3	134.2	2.9	103	85	134.2	2.9	0.7	
06MP02_23.FIN2	789	0.88	0.1007	0.0032	0.0153	0.0003	0.07	97.4	2.9	97.8	1.9	91	75	97.8	1.9	0.4	
06MP02_24.FIN2	347	2.36	0.1030	0.0130	0.0149	0.0009	0.41	99.0	12.0	95.5	5.9	230	250	95.5	5.9	3.5	
06MP02_25.FIN2	370	2.43	0.1072	0.0041	0.0150	0.0003	0.15	103.8	3.6	95.7	1.9	259	82	95.7	1.9	7.8	
06MP02_26.FIN2	502	5.91	1.3000	0.0270	0.1386	0.0022	0.68	847.0	11.0	837.0	12.0	875	29	837.0	12.0	1.2	
06MP02_27.FIN2	313	1.30	0.2928	0.0074	0.0406	0.0006	0.26	260.4	5.8	256.4	3.9	299	58	256.4	3.9	1.5	
06MP02_28.FIN2	228	1.69	1.7110	0.0340	0.1685	0.0024	0.52	1011.0	13.0	1003.0	13.0	1045	36	1045.0	36.0	4.0	
06MP02_30.FIN2	222	1.94	3.0600	0.0420	0.2511	0.0035	0.58	1425.0	10.0	1444.0	18.0	1403	24	1403.0	24.0	2.9	# REF!
06MP02_32.FIN2	213	1.98	0.1837	0.0071	0.0262	0.0006	0.11	171.7	5.9	166.7	3.6	254	88	166.7	3.6	2.9	# REF!
06MP02_33.FIN2	268	1.61	0.2853	0.0092	0.0400	0.0009	0.17	254.4	7.3	252.9	5.8	283	77	252.9	5.8	0.6	
06MP02_34.FIN2	324	2.55	2.7970	0.0400	0.2402	0.0032	0.55	1354.0	11.0	1388.0	17.0	1288	25	1288.0	25.0	7.8	
06MP02_35.FIN2	591	0.74	0.5840	0.0170	0.0735	0.0018	0.74	467.0	11.0	457.0	11.0	545	41	457.0	11.0	2.1	
06MP02_36.FIN2	596	1.79	0.3185	0.0072	0.0414	0.0006	0.33	280.5	5.6	261.6	3.8	448	52	261.6	3.8	6.7	
06MP02_38.FIN2	389	1.46	10.4300	0.4000	0.4240	0.0150	0.96	2464.0	35.0	2274.0	67.0	2643	16	2643.0	16.0	14.0	
06MP02_39.FIN2	239	1.21	0.1761	0.0067	0.0260	0.0006	0.05	165.3	6.0	165.3	3.5	178	91	165.3	3.5	0.0	
06MP02_40.FIN2	198	1.40	0.4890	0.0180	0.0585	0.0012	0.45	403.0	12.0	366.7	7.0	598	69	366.7	7.0	9.0	
06MP02_41.FIN2	505	1.15	0.1859	0.0065	0.0280	0.0006	0.42	172.9	5.6	177.8	3.9	112	70	177.8	3.9	2.8	
06MP02_42.FIN2	82	1.11	4.3200	0.1000	0.3078	0.0068	0.27	1699.0	21.0	1729.0	33.0	1623	56	1623.0	56.0	6.5	
06MP02_43.FIN2	440	55.60	0.6330	0.0180	0.0801	0.0021	0.62	498.0	11.0	496.0	13.0	555	57	496.0	13.0	0.4	
06MP02_44.FIN2	187	2.09	0.5460	0.0190	0.0712	0.0012	0.28	441.0	13.0	443.3	7.4	451	81	443.3	7.4	0.5	
06MP02_45.FIN2	349	3.49	3.5880	0.0730	0.2546	0.0052	0.77	1548.0	15.0	1466.0	26.0	1690	22	1690.0	22.0	13.3	
06MP02_47.FIN2	268	4.16	4.3660	0.0630	0.3004	0.0041	0.59	1705.0	12.0	1693.0	21.0	1729	21	1729.0	21.0	2.1	
06MP02_48.FIN2	154	0.59	0.1759	0.0085	0.0244	0.0007	0.15	164.0	7.3	155.1	4.2	320	120	155.1	4.2	5.4	
06MP02_49.FIN2	96	2.34	1.9560	0.0410	0.1894	0.0027	0.36	1100.0	14.0	1118.0	15.0	1082	42	1082.0	42.0	3.3	
06MP02_50.FIN2	176	1.90	0.1033	0.0056	0.0150	0.0005	0.15	99.6	5.2	95.7	3.0	220	120	95.7	3.0	3.9	# REF!
06MP02_52.FIN2	78	2.49	1.6290	0.0370	0.1639	0.0030	0.05	980.0	14.0	978.0	17.0	970	59	970.0	59.0	0.8	# REF!
06MP02_53.FIN2	505	1.01	0.5750	0.0150	0.0721	0.0010	0.51	460.7	9.5	448.5	6.2	531	46	448.5	6.2	2.6	
06MP02_54.FIN2	342	0.79	0.8860	0.0150	0.1059	0.0017	0.45	644.8	8.3	649.0	9.7	644	38	649.0	9.7	0.7	
06MP02_55.FIN2	517	0.52	0.1828	0.0054	0.0252	0.0005	0.21	170.3	4.6	160.5	3.0	297	72	160.5	3.0	5.8	
06MP02_56.FIN2	330	4.25	0.9750	0.0280	0.1097	0.0024	0.62	689.0	15.0	673.0	14.0	742	49	673.0	14.0	2.3	
06MP02_57.FIN2	369	1.25	0.2920	0.0091	0.0401	0.0009	0.16	259.7	7.1	253.6	5.3	286	72	253.6	5.3	2.3	
06MP02_58.FIN2	59	2.11	4.6000	0.1000	0.2961	0.0053	0.35	1746.0	19.0	1671.0	26.0	1810	42	1810.0	42.0	7.7	
06MP02_59.FIN2	1045	0.99	0.1944	0.0045	0.0276	0.0004	0.32	180.3	3.8	175.3	2.4	215	49	175.3	2.4	2.8	
06MP02_60.FIN2	100	1.77	0.1670	0.0100	0.0211	0.0008	0.03	156.4	8.9	134.3	4.7	460	150	134.3	4.7	14.1	
06MP02_61.FIN2	135	4.95	2.2430	0.0360	0.1997	0.0031	0.37	1200.0	13.0	1174.0	17.0	1213	40	1213.0	40.0	3.2	
06MP02_62.FIN2	452	2.00	0.5847	0.0094	0.0739	0.0007	0.27	467.1	6.1	459.7	4.3	464	38	459.7	4.3	1.6	
06MP02_63.FIN2	408	1.31	0.1171	0.0053	0.0161	0.0003	0.15	112.2	4.9	102.8	1.8	300	100	102.8	1.8	8.4	
06MP02_64.FIN2	381	1.43	0.5760	0.0110	0.0726	0.0012	0.18	461.4	7.4	451.8	7.0	479	52	451.8	7.0	2.1	
06MP02_65.FIN2	504	1.69	0.1046	0.0040	0.0156	0.0003	0.07	100.9	3.7	99.8	2.0	127	86	99.8	2.0	1.1	
06MP02_67.FIN2	366	2.25	3.1510	0.0390	0.2483	0.0029	0.57	1444.3	9.5	1430.0	15.0	1448	21	1448.0	21.0	1.2	
06MP02_68.FIN2	249	1.25	0.2566	0.0087	0.0350	0.0008	0.26	231.5	7.0	221.6	4.7	267	72	221.6	4.7	4.3	
06MP02_69.FIN2	166	0.90	2.8730	0.0460	0.2352	0.0038	0.41	1374.0	12.0	1361.0	20.0	1373	33	1373.0	33.0	0.9	
06MP02_71.FIN2	239	2.59	0.1116	0.0061	0.0157	0.0004	0.18	107.1	5.6	100.2	2.8	260	120	100.2	2.8	6.4	
06MP02_72.FIN2	432	2.02	0.1044	0.0051	0.0154	0.0004	0.06	100.6	4.7	98.3	2.6	150	100	98.3	2.6	2.3	
06MP02_73.FIN2	45	0.36	0.1980	0.0200	0.0230	0.0016	0.06	181.0	17.0	146.7	9.9	630	250	146.7	9.9	19.0	
06MP02_74.FIN2	48	1.10	1.7470	0.0650	0.1635	0.0043	0.33	1025.0	25.0	980.0	25.0	1104	78	1104.0	78.0	11.2	# REF!
06MP02_77.FIN2	287	2.85	1.9710	0.0320	0.1907	0.0025	0.49	1104.0	11.0	1125.0	13.0	1072	30	1072.0	30.0	4.9	# REF!
06MP02_78.FIN2	687	2.97	1.6580	0.0430	0.1387	0.0035	0.69	992.0	16.0	837.0	20.0	1350	41	837.0	20.0	15.6	# REF!
06MP02_80.FIN2	1520	3.55	0.2555	0.0043	0.0364	0.0005	0.57	230.9	3.5	230.4	3.3	255	31	230.4	3.3	0.2	# REF!
06MP02_81.FIN2	235	1.76	0.6050	0.0140	0.0770	0.0013	0.16	480.9	8.7	478.1	7.6	497	56	478.1	7.6	0.6	
06MP02_82.FIN2	143	1.56	1.5890	0.0350	0.1547	0.0028	0.27	964.0	14.0	927.0	15.0	1056	43	1056.0	43.0	12.2	
06MP02_83.FIN2	95	1.62	0.7520	0.0320	0.0911	0.0028	0.18	567.0	19.0	562.0	17.0	638	95	562.0	17.0	0.9	
06MP02_84.FIN2	169	2.76	0.1048	0.0069	0.0149	0.0005	0.27	100.9	6.4	95.0	3.4	210	130	95.0	3.4	5.8	
06MP02_85.FIN2	356	0.96	0.4710	0.0130	0.0560	0.0015	0.56	392.6	8.8	351.4	9.2	642	53	351.4	9.2	10.5	
06MP02_86.FIN2	760	1.60	0.1270	0.0041	0.0184	0.0003	0.15	121.3	3.7	117.2	1.8	189	73	117.2	1.8	3.4	
06MP02_87.FIN2	290	1.64	3.8890	0.0670	0.2806	0.0045	0.64	1610.0	14.0	1594.0	23.0	1636	26	1636.0	26.0	2.6	
06MP02_89.FIN2	136	2.06	0.1102	0.0076	0.0155	0.0005	0.09	105.6	7.0	99.1	3.3	250	150	99.1	3.3	6.2	
06MP02_90.FIN2	349	2.34	0.1121	0.0049	0.0161	0.0003	0.12	107.7	4.4	102.8	1.9	245	92	102.8	1.9	4.5	
06MP02_91.FIN2	145	1.10	4.0340	0.0660	0.2830	0.0042	0.58	1643.0	13.0	1606.0	21.0	1700	26	1700.0	26.0	5.5	
06MP02_92.FIN2	429	0.63	0.2026	0.0063	0.0267	0.0004	0.05	187.0	5.3	170.0	2.3	406	68	170.0	2.3	9.1	
06MP02_93.FIN2	784	2.28	0.1653	0.0043	0.0238	0.0005	0.22	155.2	3.7	151.8	2.8	179	62	151.8	2.8	2.2	
06MP02_94.FIN2	191	0.72	0.1656	0.0099	0.0231	0.0008	0.28	157.5	8.3	147.3	5.1	270	130	147.3	5.1	6.5	
06MP02_95.FIN2	280	1.67	0.2980	0.0110	0.0414	0.0008	0.08	265.3	8.4	261.7	4.8	301	82	261.7	4.8	1.4	
06MP02_96.FIN2	331	1.49	3.9800	0.1100	0.2754	0.0063	0.84	1633.0	23.0	1567.0	32.0	1738	24	1738.0	24.0	9.8	
06MP02_97.FIN2	1371	3.74	0.3561	0.0074	0.0479	0.0008	0.62	309.1	5.5	301.8	4.8	412	40	301.8	4.8	2.4	
06MP02_98.FIN2	187	2.10	0.1050	0.0062	0.0151	0.0004	0.04	102.0	5.9	96.4	2.6	270	130	96.4	2.6	5.5	
06MP02_99.FIN2	121	1.51	0.2910	0.0130	0.0400	0.0012	0.05	259.0	10.0	252.8	7.3	38					

06MP02_101.FIN2	526	0.71	0.2947	0.0070	0.0397	0.0006	0.12	262.6	5.4	251.1	3.7	381	62	251.1	3.7	4.4
06MP02_102.FIN2	297	1.50	0.1737	0.0069	0.0238	0.0006	0.13	162.3	6.0	151.9	3.6	271	89	151.9	3.6	6.4
06MP02_103.FIN2	655	13.93	0.5890	0.0140	0.0721	0.0013	0.77	469.9	9.0	448.8	8.0	587	33	448.8	8.0	4.5
06MP02_104.FIN2	156	2.13	0.7640	0.0210	0.0922	0.0015	0.15	575.0	12.0	568.5	9.0	596	67	568.5	9.0	1.1
06MP02_105.FIN2	824	1.26	2.6000	0.0450	0.2086	0.0045	0.88	1299.0	13.0	1221.0	24.0	1429	18	1429.0	18.0	14.6
06MP02_106.FIN2	561	31.70	4.5100	0.1700	0.3126	0.0086	0.80	1742.0	27.0	1761.0	40.0	1721	35	1721.0	35.0	2.3
06MP02_107.FIN2	765	1.77	4.3170	0.0630	0.3118	0.0047	0.72	1700.0	12.0	1749.0	23.0	1638	20	1638.0	20.0	6.8
06MP02_108.FIN2	245	3.91	3.4060	0.0470	0.2619	0.0037	0.55	1508.0	10.0	1499.0	19.0	1517	26	1517.0	26.0	1.2
06MP02_109.FIN2	243	1.60	0.1638	0.0075	0.0230	0.0005	0.25	153.6	6.5	146.8	3.3	233	98	146.8	3.3	4.4
06MP02_110.FIN2	535	1.63	0.1839	0.0052	0.0264	0.0004	0.06	171.2	4.5	167.7	2.7	200	66	167.7	2.7	2.0
06MP02_111.FIN2	228	3.31	2.2340	0.0370	0.2043	0.0027	0.15	1191.0	12.0	1198.0	15.0	1169	35	1169.0	35.0	2.5
06MP02_112.FIN2	150	2.05	4.4230	0.0660	0.3069	0.0038	0.36	1717.0	13.0	1725.0	19.0	1681	27	1681.0	27.0	2.6
06MP02_113.FIN2	370	3.73	0.8140	0.0160	0.0976	0.0015	0.37	605.3	9.0	600.1	8.7	633	39	600.1	8.7	0.9
06MP02_114.FIN2	835	2.10	0.1042	0.0031	0.0163	0.0003	0.22	100.6	2.9	104.1	1.6	46	60	104.1	1.6	3.5
06MP02_115.FIN2	118	0.58	0.1630	0.0100	0.0242	0.0010	0.09	155.2	8.6	153.8	6.2	200	150	153.8	6.2	0.9
06MP02_116.FIN2	244	2.82	4.5620	0.0510	0.3120	0.0029	0.46	1744.0	9.3	1750.0	14.0	1731	17	1731.0	17.0	1.1
06MP02_117.FIN2	358	1.14	0.1909	0.0059	0.0270	0.0005	0.20	177.9	4.9	171.4	3.3	258	74	171.4	3.3	3.7
06MP02_119.FIN2	394	5.16	1.9680	0.0430	0.1820	0.0027	0.53	1103.0	15.0	1078.0	15.0	1153	36	1153.0	36.0	6.5
06MP02_120.FIN2	136	1.94	3.9980	0.0550	0.2894	0.0042	0.43	1633.0	11.0	1638.0	21.0	1632	29	1632.0	29.0	0.4

Soyatal Formation (sample: 16-CA08); coordinates: 20° 56.081'N, 99° 43.754'W

16CA08_1.FIN2	134	2.54	0.1512	0.0045	0.0209	0.0003	0.27	142.8	4.0	133.2	2.1	274	66	133.2	2.1	6.7
16CA08_2.FIN2	315	2.20	0.1221	0.0021	0.0180	0.0003	0.22	116.9	1.9	115.3	1.7	151	45	115.3	1.7	1.4
16CA08_3.FIN2	591	16.63	0.8070	0.0130	0.0988	0.0020	0.50	600.5	7.6	607.0	12.0	581	35	607.0	12.0	1.1
16CA08_4.FIN2	212	1.48	0.1042	0.0026	0.0152	0.0002	0.04	100.9	2.5	97.5	1.2	201	57	97.5	1.2	3.4
16CA08_5.FIN2	51	1.52	0.1630	0.0110	0.0198	0.0011	0.23	152.7	9.4	126.6	6.7	590	190	126.6	6.7	17.1
16CA08_6.FIN2	360	0.85	0.0912	0.0046	0.0136	0.0004	0.49	88.6	4.3	87.0	2.6	135	93	87.0	2.6	1.8
16CA08_7.FIN2	716	2.13	0.1796	0.0030	0.0261	0.0004	0.66	167.7	2.6	166.2	2.4	181	35	166.2	2.4	0.9
16CA08_8.FIN2	248	19.30	1.6340	0.0670	0.1670	0.0080	0.50	982.0	26.0	995.0	44.0	985	77	985.0	77.0	1.0
16CA08_8.FIN2	362	19.40	3.7890	0.0950	0.2804	0.0094	0.92	1590.0	20.0	1593.0	47.0	1570	27	1570.0	27.0	1.5
16CA08_9.FIN2	53	4.43	1.5230	0.0590	0.1527	0.0045	0.40	938.0	24.0	916.0	25.0	1033	73	1033.0	73.0	11.3
16CA08_10.FIN2	163	1.19	0.1327	0.0031	0.0198	0.0003	0.12	126.5	2.8	126.6	2.0	171	63	126.6	2.0	0.1
16CA08_11.FIN2	1170	1.05	0.1593	0.0044	0.0231	0.0007	0.22	150.0	3.9	147.3	4.4	197	62	147.3	4.4	1.8
16CA08_12.FIN2	643	1.84	3.5480	0.0850	0.2554	0.0058	0.86	1537.0	19.0	1466.0	30.0	1659	22	1659.0	22.0	11.6
16CA08_13.FIN2	368	1.39	0.8180	0.0120	0.0986	0.0015	0.72	607.5	6.8	606.0	8.9	613	23	606.0	8.9	0.2
16CA08_14.FIN2	167	2.16	0.0974	0.0043	0.0151	0.0006	0.42	94.3	4.0	96.9	3.6	14	78	96.9	3.6	2.8
16CA08_15.FIN2	73	1.52	2.0780	0.0470	0.1887	0.0035	0.31	1141.0	15.0	1114.0	19.0	1187	43	1187.0	43.0	6.1
16CA08_17.FIN2	360	1.82	0.6420	0.0110	0.0815	0.0014	0.55	503.2	6.7	504.9	8.5	492	39	504.9	8.5	0.3
16CA08_18.FIN2	550	0.87	0.3244	0.0047	0.0457	0.0006	0.43	285.2	3.6	287.8	3.9	284	32	287.8	3.9	0.9
16CA08_19.FIN2	434	1.63	0.1180	0.0025	0.0173	0.0003	0.48	113.2	2.3	110.6	1.9	166	44	110.6	1.9	2.3
16CA08_20.FIN2	252	2.83	0.5970	0.0110	0.0763	0.0017	0.29	475.3	6.9	473.9	9.9	498	63	473.9	9.9	0.3
16CA08_21.FIN2	123	1.38	0.7930	0.0110	0.0961	0.0015	0.56	592.5	6.5	591.4	8.6	609	28	591.4	8.6	0.2
16CA08_22.FIN2	224	0.97	5.7170	0.0950	0.3507	0.0068	0.70	1933.0	14.0	1937.0	33.0	1915	23	1915.0	23.0	1.1
16CA08_23.FIN2	163	1.36	0.1084	0.0026	0.0154	0.0003	0.03	104.5	2.4	98.4	1.8	236	67	98.4	1.8	5.8
16CA08_24.FIN2	290	1.10	0.8100	0.0130	0.0967	0.0016	0.50	602.2	7.2	595.1	9.2	635	34	595.1	9.2	1.2
16CA08_25.FIN2	72	1.58	2.3320	0.0290	0.2002	0.0026	0.33	1221.6	8.8	1176.0	14.0	1312	27	1312.0	27.0	10.4
16CA08_26.FIN2	56	1.34	0.2741	0.0075	0.0389	0.0007	0.01	245.6	5.9	245.7	4.3	255	71	245.7	4.3	0.0
16CA08_27.FIN2	337	2.15	0.1115	0.0026	0.0165	0.0003	0.38	107.3	2.4	105.2	2.0	187	56	105.2	2.0	2.0
16CA08_28.FIN2	110	2.01	0.1311	0.0043	0.0191	0.0004	0.31	125.0	3.8	122.2	2.5	171	71	122.2	2.5	2.2
16CA08_29.FIN2	140	3.00	1.7840	0.0220	0.1729	0.0024	0.58	1038.8	8.1	1028.0	13.0	1049	26	1049.0	26.0	2.0
16CA08_30.FIN2	140	0.93	0.8610	0.0100	0.1030	0.0014	0.47	630.4	5.7	632.6	8.0	635	30	632.6	8.0	0.3
16CA08_31.FIN2	649	1.93	0.2517	0.0051	0.0359	0.0006	0.58	228.3	4.2	227.4	3.7	279	39	227.4	3.7	0.4
16CA08_32.FIN2	531	2.54	0.1086	0.0027	0.0157	0.0003	0.42	104.7	2.4	100.4	1.8	195	46	100.4	1.8	4.1
16CA08_33.FIN2	104	1.76	0.1461	0.0048	0.0209	0.0006	0.41	138.8	4.2	133.1	3.5	227	74	133.1	3.5	4.1
16CA08_34.FIN2	367	4.23	0.6350	0.0120	0.0800	0.0017	0.62	498.9	7.3	496.0	10.0	509	37	496.0	10.0	0.6
16CA08_35.FIN2	164	2.39	0.1028	0.0050	0.0145	0.0003	0.21	99.2	4.6	93.1	2.2	270	110	93.1	2.2	6.1
16CA08_36.FIN2	151	1.14	0.2324	0.0055	0.0326	0.0005	0.20	212.0	4.5	206.9	3.1	259	56	206.9	3.1	2.4
16CA08_37.FIN2	194	1.77	16.0800	0.1500	0.5513	0.0045	0.66	2882.5	8.8	2830.0	19.0	2915	13	2915.0	13.0	2.9
16CA08_38.FIN2	571	4.82	0.1001	0.0017	0.0147	0.0002	0.58	96.8	1.6	93.8	1.5	139	31	93.8	1.5	3.1
16CA08_39.FIN2	228	1.34	0.1034	0.0033	0.0150	0.0003	0.35	100.2	2.9	95.6	1.7	194	70	95.6	1.7	4.6
16CA08_40.FIN2	259	0.92	0.3080	0.0110	0.0424	0.0010	0.53	272.6	8.9	267.6	6.4	248	73	267.6	6.4	1.8
16CA08_41.FIN2	512	2.21	0.1784	0.0025	0.0261	0.0004	0.43	166.6	2.2	165.8	2.5	173	38	165.8	2.5	0.5
16CA08_42.FIN2	46	0.97	9.5800	0.2000	0.4100	0.0110	0.61	2394.0	20.0	2214.0	52.0	2562	40	2562.0	40.0	13.6
16CA08_43.FIN2	352	1.75	0.2885	0.0078	0.0411	0.0008	0.42	257.3	6.1	259.6	4.8	219	61	259.6	4.8	0.9
16CA08_44.FIN2	441	3.23	0.4837	0.0072	0.0645	0.0012	0.42	402.4	5.4	402.8	7.5	397	40	402.8	7.5	0.1
16CA08_45.FIN2	168	2.07	0.6967	0.0090	0.0855	0.0013	0.53	536.5	5.4	529.9	7.7	555	30	529.9	7.7	1.2
16CA08_46.FIN2	294	2.54	0.1055	0.0030	0.0155	0.0003	0.57	101.8	2.8	99.3	2.0	159	52	99.3	2.0	2.5
16CA08_47.FIN2	870	1.76	0.1517	0.0034	0.0225	0.0005	0.59	143.4	3.0	143.3	3.1	165	48	143.3	3.1	0.1
16CA08_48.FIN2	338	1.80	0.1276	0.0023	0.0187	0.0002	0.14	121.9	2.0	119.7	1.4	153	45	119.7	1.4	1.8
16CA08_49.FIN2	264	2.54	0.7830	0.0140	0.0931	0.0018	0.60	586.5	7.9	574.0	11.0	638	36	574.0	11.0	2.1
16CA08_50.FIN2	1100	4.20	0.5260	0.0150	0.0691	0.0023	0.72	429.0	10.0	430.0	14.0	394	50	430.0	14.0	0.2

Rim
Core

#!REF!
#!REF!

16CA08_51.FIN2	275	1.40	0.5988	0.0094	0.0736	0.0009	0.67	476.2	5.9	458.0	5.5	590	27	458.0	5.5	3.8
16CA08_52.FIN2	273	1.81	0.5960	0.0110	0.0758	0.0014	0.51	476.5	7.6	471.1	8.4	475	36	471.1	8.4	1.1
16CA08_53.FIN2	182	3.68	0.3150	0.0063	0.0432	0.0007	0.44	277.8	4.9	272.3	4.4	330	45	272.3	4.4	2.0
16CA08_54.FIN2	151	0.91	0.1227	0.0070	0.0169	0.0006	0.33	117.3	6.3	107.8	3.7	320	120	107.8	3.7	8.1
16CA08_55.FIN2	467	4.60	1.6400	0.0240	0.1652	0.0031	0.78	984.9	9.4	985.0	17.0	984	22	984.0	22.0	0.1
16CA08_56.FIN2	495	2.70	0.1918	0.0034	0.0279	0.0004	0.46	178.1	2.9	177.2	2.3	164	40	177.2	2.3	0.5
16CA08_57.FIN2	555	2.15	0.2032	0.0031	0.0287	0.0003	0.17	187.8	2.6	182.1	2.0	257	39	182.1	2.0	3.0
16CA08_58.FIN2	567	2.16	0.3549	0.0062	0.0489	0.0008	0.25	308.2	4.7	307.4	5.0	317	40	307.4	5.0	0.3
16CA08_60.FIN2	340	1.05	0.4535	0.0060	0.0591	0.0007	0.57	379.5	4.2	370.4	4.1	439	27	370.4	4.1	2.4
16CA08_61.FIN2	314	3.37	0.1440	0.0038	0.0210	0.0004	0.46	136.5	3.3	133.9	2.7	149	60	133.9	2.7	1.9
16CA08_62.FIN2	860	1.88	0.1543	0.0049	0.0235	0.0012	0.67	145.6	4.3	149.4	7.7	142	72	149.4	7.7	2.6
16CA08_63.FIN2	85	0.96	0.5970	0.0130	0.0762	0.0010	0.12	475.0	8.4	473.4	5.8	508	57	473.4	5.8	0.3
16CA08_64.FIN2	223	3.27	0.5780	0.0100	0.0742	0.0011	0.74	463.0	6.7	461.3	6.7	466	32	461.3	6.7	0.4
16CA08_65.FIN2	335	3.09	0.6060	0.0100	0.0766	0.0012	0.61	480.5	6.4	475.6	7.2	510	30	475.6	7.2	1.0
16CA08_66.FIN2	36	0.96	4.5300	0.2100	0.3080	0.0130	0.91	1731.0	37.0	1729.0	63.0	1733	32	1733.0	32.0	0.2
16CA08_67.FIN2	339	0.83	0.5930	0.0094	0.0772	0.0011	0.68	472.5	6.0	479.3	6.6	442	25	479.3	6.6	1.4
16CA08_68.FIN2	127	2.17	1.5390	0.0180	0.1558	0.0015	0.51	945.7	7.1	933.5	8.6	983	22	983.0	22.0	5.0
16CA08_69.FIN2	856	23.20	0.6890	0.0130	0.0866	0.0018	0.73	532.1	8.1	535.0	11.0	480	34	535.0	11.0	0.5
16CA08_70.FIN2	73	1.99	2.3100	0.0300	0.2069	0.0025	0.52	1214.5	9.3	1212.0	13.0	1214	27	1214.0	27.0	0.2
16CA08_71.FIN2	175	0.81	0.5732	0.0082	0.0734	0.0009	0.57	459.8	5.3	456.8	5.5	475	26	456.8	5.5	0.7
16CA08_72.FIN2	345	1.52	0.1166	0.0027	0.0170	0.0003	0.40	111.9	2.5	108.4	1.7	163	51	108.4	1.7	3.1
16CA08_73.FIN2	801	7.34	0.1992	0.0044	0.0281	0.0006	0.61	184.3	3.7	178.9	3.7	245	43	178.9	3.7	2.9
16CA08_74.FIN2	219	2.11	0.1647	0.0031	0.0243	0.0003	0.34	155.5	2.6	154.8	1.8	139	44	154.8	1.8	0.5
16CA08_75.FIN2	247	1.47	0.1386	0.0033	0.0201	0.0004	0.31	131.7	3.0	128.4	2.3	168	52	128.4	2.3	2.5
16CA08_76.FIN2	463	1.38	0.1512	0.0030	0.0224	0.0005	0.68	142.9	2.6	142.7	2.8	117	37	142.7	2.8	0.1
16CA08_77.FIN2	460	8.49	0.7620	0.0100	0.0939	0.0013	0.51	574.7	6.0	578.2	7.5	556	30	578.2	7.5	0.6
16CA08_78.FIN2	402	2.40	0.1423	0.0031	0.0214	0.0003	0.46	135.0	2.8	136.3	1.9	118	40	136.3	1.9	1.0
16CA08_79.FIN2	507	4.80	0.1037	0.0018	0.0153	0.0003	0.37	100.2	1.7	97.8	1.6	135	47	97.8	1.6	2.4
16CA08_80.FIN2	373	1.76	0.1750	0.0031	0.0251	0.0003	0.26	163.7	2.7	159.9	2.1	207	46	159.9	2.1	2.3
16CA08_81.FIN2	314	3.81	0.1031	0.0022	0.0150	0.0003	0.16	99.8	2.1	96.2	1.7	155	65	96.2	1.7	3.6
16CA08_82.FIN2	305	1.45	0.4800	0.0140	0.0634	0.0020	0.71	397.3	9.4	396.0	12.0	410	47	396.0	12.0	0.3
16CA08_83.FIN2	193	1.84	0.1303	0.0047	0.0194	0.0004	0.19	124.3	4.2	123.7	2.6	127	79	123.7	2.6	0.5
16CA08_84.FIN2	605	6.63	1.7630	0.0270	0.1769	0.0036	0.57	1031.6	9.9	1050.0	20.0	1014	35	1014.0	35.0	3.6
16CA08_85.FIN2	56	1.33	0.5900	0.0170	0.0755	0.0014	0.16	470.0	11.0	469.0	8.3	493	73	469.0	8.3	0.2
16CA08_86.FIN2	373	3.96	0.5928	0.0067	0.0757	0.0008	0.47	472.5	4.3	470.5	4.6	478	25	470.5	4.6	0.4
16CA08_87.FIN2	179	1.35	0.1556	0.0065	0.0201	0.0004	0.33	148.1	6.1	128.4	2.4	455	91	128.4	2.4	13.3
16CA08_88.FIN2	628	2.10	0.1058	0.0022	0.0157	0.0004	0.37	102.0	2.0	100.5	2.4	147	53	100.5	2.4	1.5
16CA08_89.FIN2	322	2.43	1.2100	0.0190	0.1334	0.0027	0.68	804.6	8.5	807.0	16.0	792	29	807.0	16.0	0.3
16CA08_90.FIN2	391	2.45	2.4680	0.0370	0.2180	0.0029	0.72	1264.0	10.0	1271.0	15.0	1244	19	1244.0	19.0	2.2
16CA08_91.FIN2	431	1.21	0.4586	0.0066	0.0624	0.0007	0.67	383.6	4.7	390.2	4.2	344	26	390.2	4.2	1.7
16CA08_92.FIN2	301	5.04	0.1025	0.0045	0.0161	0.0007	0.20	100.5	4.9	102.7	4.6	71	97	102.7	4.6	2.2
16CA08_93.FIN2	373	3.11	2.6380	0.0400	0.2250	0.0040	0.77	1311.0	11.0	1308.0	21.0	1305	22	1305.0	22.0	0.2
16CA08_94.FIN2	712	4.21	0.6129	0.0082	0.0779	0.0011	0.65	485.1	5.2	483.6	6.7	493	24	483.6	6.7	0.3
16CA08_95.FIN2	690	2.76	0.1950	0.0036	0.0283	0.0004	0.67	180.8	3.7	179.9	2.7	202	31	179.9	2.7	0.5
16CA08_96.FIN2	631	67.20	0.9070	0.0130	0.1055	0.0016	0.51	655.7	6.8	647.5	9.3	669	32	647.5	9.3	1.3
16CA08_98.FIN2	314	1.44	0.1013	0.0026	0.0150	0.0003	0.43	98.0	2.4	96.1	1.6	179	60	96.1	1.6	1.9
16CA08_99.FIN2	99	2.13	0.1482	0.0051	0.0212	0.0006	0.18	140.2	4.5	135.1	3.6	219	90	135.1	3.6	3.6
16CA08_100.FIN2	237	2.10	0.2052	0.0077	0.0275	0.0006	0.18	189.4	6.5	174.7	4.0	327	80	174.7	4.0	7.8
16CA08_101.FIN2	143	1.70	6.4110	0.0850	0.3543	0.0059	0.69	2034.0	11.0	1954.0	28.0	2096	23	2096.0	23.0	6.8
16CA08_102.FIN2	198	1.52	0.1240	0.0042	0.0178	0.0004	0.44	118.5	3.8	113.9	2.3	220	68	113.9	2.3	3.9
16CA08_103.FIN2	167	1.04	0.2003	0.0080	0.0281	0.0010	0.54	185.2	6.8	178.6	6.3	206	75	178.6	6.3	3.6
16CA08_104.FIN2	198	0.86	2.2650	0.0260	0.2047	0.0028	0.63	1200.8	7.9	1200.0	15.0	1206	22	1206.0	22.0	0.5
16CA08_105.FIN2	464	6.35	1.5660	0.0270	0.1586	0.0033	0.88	957.0	11.0	949.0	19.0	965	23	965.0	23.0	1.7
16CA08_106.FIN2	108	1.55	0.1236	0.0043	0.0177	0.0005	0.22	118.2	3.9	113.3	2.9	196	85	113.3	2.9	4.1
16CA08_107.FIN2	87	2.60	3.1910	0.0580	0.2452	0.0051	0.69	1458.0	14.0	1413.0	26.0	1523	28	1523.0	28.0	7.2
16CA08_108.FIN2	282	7.36	0.8870	0.0150	0.1029	0.0019	0.54	644.3	7.8	631.0	11.0	687	34	631.0	11.0	2.1
16CA08_109.FIN2	526	37.40	2.1600	0.0310	0.2016	0.0031	0.77	1167.4	9.9	1183.0	16.0	1147	19	1147.0	19.0	3.1
16CA08_110.FIN2	123	2.07	0.2064	0.0059	0.0270	0.0006	0.02	190.3	4.9	171.6	3.9	429	83	171.6	3.9	9.8
16CA08_111.FIN2	117	1.79	0.5807	0.0081	0.0721	0.0013	0.48	466.0	5.5	448.7	8.0	551	40	448.7	8.0	3.7
16CA08_112.FIN2	251	4.99	0.0988	0.0025	0.0144	0.0004	0.21	95.6	2.3	92.0	2.2	195	67	92.0	2.2	3.8
16CA08_113.FIN2	312	1.38	0.0997	0.0031	0.0149	0.0003	0.32	96.4	2.9	95.2	1.8	124	65	95.2	1.8	1.2
16CA08_114.FIN2	68	2.53	0.1482	0.0081	0.0199	0.0007	0.35	139.9	7.1	126.9	4.6	420	120	126.9	4.6	9.3
16CA08_115.FIN2	86	3.58	0.5870	0.0110	0.0731	0.0017	0.38	468.4	7.3	455.0	10.0	530	55	455.0	10.0	2.9
16CA08_117.FIN2	64	2.59	0.1483	0.0075	0.0197	0.0005	0.08	140.1	6.6	125.8	3.4	460	130	125.8	3.4	10.2
16CA08_118.FIN2	340	1.49	0.4599	0.0090	0.0622	0.0011	0.77	383.8	6.2	389.1	6.9	369	32	389.1	6.9	1.4
16CA08_119.FIN2	161	7.13	1.6960	0.0350	0.1634	0.0042	0.52	1005.0	13.0	975.0	23.0	1096	44	1096.0	44.0	11.0
16CA08_120.FIN2	259	1.99	0.1299	0.0027	0.0194	0.0004	0.18	124.0	2.4	123.9	2.2	158	54	123.9	2.2	0.1

#REF!
#REF!

Mineral de Pozos sandstone (sample: 08-MP04); coordinates: 21° 13.766'N, 100° 31.691'W

08MP04_1.FIN2	164	1.67	0.1053	0.0074	0.0162	0.0005	0.30	101.2	6.8	103.4	3.2	60	120	103.4	3.2	2.2
08MP04_2.FIN2	102	0.88	4.3470	0.0820	0.3165	0.0073	0.55	1704.0	15.0	1771.0	36.0	1639	38	1639.0	38.0	8.1

08MP04_3.FIN2	103	1.02	0.6110	0.0210	0.0755	0.0017	0.07	483.0	13.0	469.0	10.0	542	85	469.0	10.0	2.9
08MP04_4.FIN2	270	1.34	0.3258	0.0099	0.0439	0.0011	0.42	287.0	7.7	276.8	6.7	332	67	276.8	6.7	3.6
08MP04_5.FIN2	76	1.11	0.2970	0.0130	0.0414	0.0010	0.26	263.0	11.0	261.3	6.4	323	95	261.3	6.4	0.6
08MP04_6.FIN2	177	0.91	0.4810	0.0150	0.0647	0.0014	0.37	398.0	10.0	404.2	8.3	373	63	404.2	8.3	1.6
08MP04_7.FIN2	182	1.24	0.3030	0.0110	0.0430	0.0012	0.43	268.1	8.5	271.5	7.7	263	74	271.5	7.7	1.3
08MP04_8.FIN2	188	1.53	4.0190	0.0980	0.2899	0.0074	0.80	1638.0	19.0	1645.0	38.0	1619	31	1619.0	31.0	1.6
08MP04_9.FIN2	272	1.22	0.4860	0.0110	0.0647	0.0014	0.46	402.8	7.7	403.9	8.7	397	50	403.9	8.7	0.3
08MP04_10.FIN2	252	2.16	0.2998	0.0072	0.0421	0.0009	0.39	266.7	5.5	265.6	5.5	270	55	265.6	5.5	0.4
08MP04_11.FIN2	68	1.52	4.0800	0.1000	0.2905	0.0066	0.51	1648.0	21.0	1650.0	35.0	1643	43	1643.0	43.0	0.4
08MP04_12.FIN2	365	4.70	0.0967	0.0036	0.0148	0.0004	0.30	93.6	3.3	94.6	2.4	118	79	94.6	2.4	1.1
08MP04_13.FIN2	174	1.28	0.5580	0.0140	0.0724	0.0012	0.30	449.7	9.3	451.7	7.5	455	57	451.7	7.5	0.4
08MP04_14.FIN2	702	4.41	0.4950	0.0130	0.0660	0.0014	0.86	408.5	8.7	411.9	8.7	406	30	411.9	8.7	0.8
08MP04_15.FIN2	227	1.39	1.8250	0.0300	0.1803	0.0024	0.42	1054.0	11.0	1068.0	13.0	1010	34	1010.0	34.0	5.7
08MP04_16.FIN2	163	0.98	0.2922	0.0086	0.0417	0.0007	0.10	259.8	6.7	263.6	4.4	193	71	263.6	4.4	1.5
08MP04_17.FIN2	346	1.07	0.4308	0.0082	0.0580	0.0011	0.37	363.4	5.8	363.5	6.5	392	48	363.5	6.5	0.0
08MP04_18.FIN2	106	1.52	0.3250	0.0140	0.0463	0.0010	0.12	287.0	11.0	291.6	6.4	290	110	291.6	6.4	1.6
08MP04_19.FIN2	183	1.39	0.1043	0.0070	0.0160	0.0006	0.14	100.5	6.4	102.2	3.5	90	140	102.2	3.5	1.7
08MP04_20.FIN2	250	1.28	0.2977	0.0076	0.0412	0.0007	0.08	264.3	6.0	259.9	4.0	296	66	259.9	4.0	1.7
08MP04_21.FIN2	134	0.81	0.4840	0.0180	0.0631	0.0014	0.26	400.0	13.0	394.7	8.8	446	86	394.7	8.8	1.3
08MP04_22.FIN2	454	0.61	0.5140	0.0100	0.0671	0.0011	0.53	420.6	6.7	418.7	6.8	427	43	418.7	6.8	0.5
08MP04_23.FIN2	156	2.71	0.6030	0.0170	0.0765	0.0013	0.26	478.0	11.0	474.9	7.7	515	66	474.9	7.7	0.6
08MP04_24.FIN2	650	1.34	0.3126	0.0065	0.0419	0.0008	0.30	276.0	5.0	264.7	4.8	360	53	264.7	4.8	4.1
08MP04_25.FIN2	925	1.35	0.5360	0.0170	0.0694	0.0027	0.48	435.0	11.0	432.0	16.0	465	69	432.0	16.0	0.7
08MP04_26.FIN2	223	1.15	0.2298	0.0099	0.0334	0.0009	0.20	211.1	8.5	211.7	5.4	220	100	211.7	5.4	0.3
08MP04_27.FIN2	130	1.44	2.1170	0.0460	0.1991	0.0043	0.34	1156.0	14.0	1170.0	23.0	1118	55	1118.0	55.0	4.7
08MP04_28.FIN2	238	1.72	3.3510	0.0560	0.2625	0.0045	0.51	1492.0	13.0	1502.0	23.0	1496	32	1496.0	32.0	0.4
08MP04_29.FIN2	242	1.39	0.3070	0.0078	0.0422	0.0008	0.17	271.5	6.1	266.1	4.9	323	67	266.1	4.9	2.0
08MP04_30.FIN2	168	5.56	1.7730	0.0450	0.1778	0.0037	0.41	1034.0	16.0	1055.0	20.0	993	53	993.0	53.0	6.2
08MP04_31.FIN2	281	0.84	0.5020	0.0140	0.0644	0.0013	0.48	414.0	9.1	402.1	7.7	459	57	402.1	7.7	2.9
08MP04_32.FIN2	289	1.81	0.2939	0.0069	0.0418	0.0009	0.22	261.3	5.4	263.6	5.6	279	57	263.6	5.6	0.9
08MP04_33.FIN2	122	1.39	0.6070	0.0180	0.0764	0.0014	0.05	480.0	12.0	474.7	8.4	486	77	474.7	8.4	1.1
08MP04_34.FIN2	651	3.01	2.2040	0.0560	0.2014	0.0046	0.55	1181.0	18.0	1183.0	25.0	1201	51	1201.0	51.0	1.5
08MP04_35.FIN2	112	1.42	0.4620	0.0150	0.0624	0.0014	0.16	387.0	11.0	390.1	8.2	383	78	390.1	8.2	0.8
08MP04_36.FIN2	612	1.61	4.2300	0.1000	0.2984	0.0085	0.74	1678.0	20.0	1682.0	42.0	1679	39	1679.0	39.0	0.2
08MP04_37.FIN2	461	1.10	0.5180	0.0140	0.0595	0.0012	0.53	423.7	9.2	372.7	7.5	691	56	372.7	7.5	12.0
08MP04_38.FIN2	20	1.46	1.5000	0.1200	0.1516	0.0059	0.09	940.0	47.0	909.0	33.0	920	170	920.0	170.0	1.2
08MP04_39.FIN2	341	1.74	0.1008	0.0040	0.0153	0.0004	0.07	97.4	3.6	97.7	2.2	54	89	97.7	2.2	0.3
08MP04_40.FIN2	183	2.36	0.5630	0.0160	0.0732	0.0015	0.36	455.0	11.0	455.2	9.2	464	61	455.2	9.2	0.0
08MP04_41.FIN2	227	1.55	0.1320	0.0080	0.0198	0.0010	0.19	125.8	7.1	126.3	6.3	140	160	126.3	6.3	0.4
08MP04_42.FIN2	380	2.30	0.5550	0.0120	0.0714	0.0014	0.46	449.1	8.3	444.7	8.2	461	52	444.7	8.2	1.0
08MP04_43.FIN2	220	1.40	0.2928	0.0096	0.0402	0.0009	0.16	261.3	7.4	253.7	5.7	306	78	253.7	5.7	2.9
08MP04_44.FIN2	2220	5.29	0.6990	0.0170	0.0882	0.0016	0.04	538.0	10.0	545.0	9.2	444	92	545.0	9.2	1.3
08MP04_45.FIN2	262	2.28	0.4060	0.0160	0.0543	0.0022	0.57	347.0	11.0	340.0	13.0	354	77	340.0	13.0	2.0
08MP04_46.FIN2	265	1.87	0.1818	0.0069	0.0253	0.0006	0.17	169.3	5.9	160.9	3.7	286	90	160.9	3.7	5.0
08MP04_47.FIN2	149	4.64	0.9050	0.0370	0.1079	0.0027	0.51	657.0	21.0	660.0	16.0	603	68	660.0	16.0	0.5
08MP04_47.FIN2	67	1.81	1.5500	0.1100	0.1541	0.0075	0.50	947.0	42.0	924.0	42.0	980	140	980.0	140.0	5.7
08MP04_48.FIN2	229	1.10	0.4580	0.0100	0.0604	0.0011	0.20	382.4	7.2	377.9	6.5	424	58	377.9	6.5	1.2
08MP04_49.FIN2	355	1.56	0.2121	0.0063	0.0294	0.0005	0.11	195.1	5.3	186.7	3.3	263	74	186.7	3.3	4.3
08MP04_50.FIN2	308	4.82	4.2860	0.0540	0.3047	0.0048	0.69	1690.0	10.0	1717.0	24.0	1642	21	1642.0	21.0	4.6
08MP04_51.FIN2	124	1.42	0.5900	0.0140	0.0763	0.0011	0.02	471.3	9.4	474.1	6.5	398	63	474.1	6.5	0.6
08MP04_53.FIN2	316	2.87	0.1717	0.0066	0.0248	0.0007	0.29	160.6	5.7	157.8	4.1	186	80	157.8	4.1	1.7
08MP04_54.FIN2	154	0.97	0.5450	0.0130	0.0693	0.0015	0.01	440.9	8.8	431.8	9.1	421	72	431.8	9.1	2.1
08MP04_55.FIN2	101	1.52	0.1186	0.0090	0.0171	0.0007	0.10	113.4	8.2	109.1	4.3	220	170	109.1	4.3	3.8
08MP04_56.FIN2	289	1.67	0.1046	0.0050	0.0149	0.0004	0.00	100.8	4.6	95.1	2.7	220	120	95.1	2.7	5.7
08MP04_57.FIN2	53	3.09	1.6280	0.0530	0.1651	0.0045	0.27	982.0	21.0	985.0	25.0	969	84	969.0	84.0	1.7
08MP04_58.FIN2	59	1.37	15.8000	0.2600	0.5880	0.0100	0.64	2865.0	15.0	2979.0	40.0	2772	22	2772.0	22.0	7.5
08MP04_59.FIN2	185	2.27	0.1561	0.0069	0.0226	0.0005	0.17	147.8	6.2	143.9	3.3	168	95	143.9	3.3	2.6
08MP04_60.FIN2	94	0.61	3.4280	0.0630	0.2712	0.0045	0.34	1509.0	14.0	1546.0	23.0	1474	35	1474.0	35.0	4.9
08MP04_61.FIN2	330	1.33	0.1958	0.0057	0.0282	0.0006	0.13	181.4	4.8	179.1	3.6	260	79	179.1	3.6	1.3
08MP04_62.FIN2	243	2.03	0.5860	0.0150	0.0750	0.0016	0.36	469.4	9.8	465.9	9.3	506	59	465.9	9.3	0.7
08MP04_63.FIN2	378	0.90	0.4547	0.0093	0.0606	0.0009	0.35	380.2	6.5	379.2	5.3	383	47	379.2	5.3	0.3
08MP04_64.FIN2	235	1.31	0.4760	0.0150	0.0647	0.0014	0.44	395.0	10.0	404.1	8.7	388	73	404.1	8.7	2.3
08MP04_65.FIN2	98	3.50	0.1255	0.0084	0.0159	0.0006	0.13	119.6	7.6	101.9	3.8	450	150	101.9	3.8	14.8
08MP04_66.FIN2	275	1.14	0.4293	0.0098	0.0604	0.0010	0.20	362.3	6.9	378.2	6.2	287	59	378.2	6.2	4.4
08MP04_67.FIN2	135	1.32	0.3100	0.0110	0.0444	0.0012	0.08	273.5	8.8	280.1	7.2	197	86	280.1	7.2	2.4
08MP04_68.FIN2	288	3.17	0.1069	0.0049	0.0158	0.0004	0.06	102.9	4.5	101.0	2.2	140	110	101.0	2.2	1.8
08MP04_69.FIN2	254	3.08	0.4420	0.0130	0.0585	0.0014	0.46	370.8	9.2	366.6	8.8	370	61	366.6	8.8	1.1
08MP04_70.FIN2	212	2.66	0.5230	0.0160	0.0681	0.0014	0.41	426.0	11.0	424.9	8.5	435	72	424.9	8.5	0.3
08MP04_71.FIN2	195	1.77	0.1125	0.0059	0.0160	0.0005	0.15	108.0	5.4	102.4	3.3	170	120	102.4	3.3	5.2
08MP04_72.FIN2	152	0.95	0.3170	0.0120	0.0436	0.0012	0.22	279.9	9.5	275.3	7.3	274	82	275.3	7.3	1.6
08MP04_73.FIN2	611	2.07	0.1336	0.0056	0.0165	0.0007	0.33	127.3	5.0	105.5	4.2	570	100	105.5	4.2	17.1
08MP04_74.FIN2	407	2.72	0.2884	0.0059	0.0405	0.0006	0.19	257.1	4.7	256.0	3.4	264	52	256.0	3.4	0.4

Rim
Core

#|REF!
#|REF!

08MP04_75.FIN2	233	0.97	0.4651	0.0094	0.0617	0.0010	0.30	387.5	6.5	386.0	6.3	377	45	386.0	6.3	0.4	
08MP04_76.FIN2	184	0.91	0.4710	0.0130	0.0621	0.0013	0.35	392.2	8.9	388.4	8.1	401	60	388.4	8.1	1.0	
08MP04_77.FIN2	590	2.03	0.0975	0.0032	0.0145	0.0003	0.09	94.8	3.0	92.8	2.0	117	75	92.8	2.0	2.1	
08MP04_78.FIN2	215	1.36	3.2420	0.0480	0.2586	0.0042	0.58	1468.0	11.0	1482.0	22.0	1440	27	1440.0	27.0	2.9	
08MP04_79.FIN2	160	0.94	0.4570	0.0120	0.0604	0.0011	0.22	382.5	8.2	378.2	6.8	388	65	378.2	6.8	1.1	
08MP04_80.FIN2	839	2.15	0.3243	0.0095	0.0445	0.0013	0.77	286.1	7.6	280.4	7.9	336	46	280.4	7.9	2.0	
08MP04_81.FIN2	63	7.07	1.0270	0.0320	0.1171	0.0036	0.55	715.0	16.0	713.0	21.0	713	60	713.0	21.0	0.3	
08MP04_82.FIN2	224	1.82	0.1097	0.0059	0.0154	0.0006	0.23	105.5	5.4	98.7	3.8	330	120	98.7	3.8	6.4	
08MP04_84.FIN2	161	1.79	0.1033	0.0055	0.0153	0.0004	0.06	99.6	5.0	97.8	2.4	170	120	97.8	2.4	1.8	
08MP04_85.FIN2	426	0.88	0.4710	0.0170	0.0637	0.0016	0.22	394.0	11.0	398.1	9.7	361	97	398.1	9.7	1.0	
08MP04_86.FIN2	676	1.73	0.4710	0.0160	0.0621	0.0019	0.52	392.0	11.0	388.0	12.0	439	68	388.0	12.0	1.0	
08MP04_88.FIN2	509	1.56	0.1883	0.0046	0.0270	0.0005	0.22	175.0	3.9	171.7	3.3	236	61	171.7	3.3	1.9	
08MP04_89.FIN2	315	3.51	0.3010	0.0200	0.0417	0.0010	0.27	267.0	15.0	263.1	6.4	300	160	263.1	6.4	1.5	Rim
08MP04_89.FIN2	345	5.00	2.1470	0.0550	0.1826	0.0053	0.74	1163.0	18.0	1081.0	29.0	1312	34	1312.0	34.0	17.6	Core
08MP04_89.FIN2	194	5.20	3.3900	0.1300	0.2623	0.0088	0.66	1501.0	30.0	1501.0	45.0	1514	54	1514.0	54.0	0.9	Core
08MP04_90.FIN2	291	8.83	1.9130	0.0270	0.1853	0.0026	0.44	1085.1	9.4	1098.0	15.0	1066	32	1066.0	32.0	3.0	
08MP04_91.FIN2	316	1.64	0.3060	0.0130	0.0418	0.0016	0.52	270.0	10.0	264.0	10.0	332	88	264.0	10.0	2.2	
08MP04_92.FIN2	68	0.84	4.6660	0.0930	0.3322	0.0068	0.54	1760.0	17.0	1848.0	33.0	1641	31	1641.0	31.0	12.6	
08MP04_93.FIN2	595	3.61	4.5620	0.0590	0.3119	0.0043	0.57	1742.0	11.0	1750.0	21.0	1723	23	1723.0	23.0	1.6	
08MP04_94.FIN2	711	4.53	3.4770	0.0940	0.2710	0.0100	0.77	1519.0	21.0	1541.0	52.0	1505	42	1505.0	42.0	2.4	
08MP04_95.FIN2	90	1.45	0.5700	0.0240	0.0737	0.0022	0.45	459.0	15.0	458.0	13.0	453	84	458.0	13.0	0.2	
08MP04_96.FIN2	157	5.03	0.3091	0.0093	0.0431	0.0009	0.03	273.1	7.2	272.0	5.7	261	71	272.0	5.7	0.4	
08MP04_97.FIN2	343	19.40	0.5820	0.0170	0.0744	0.0022	0.63	465.0	11.0	462.0	13.0	438	53	462.0	13.0	0.6	
08MP04_98.FIN2	133	1.78	0.5880	0.0240	0.0749	0.0018	0.42	471.0	15.0	465.0	11.0	426	77	465.0	11.0	1.3	
08MP04_99.FIN2	245	4.56	0.3083	0.0094	0.0424	0.0008	0.02	272.4	7.3	267.8	4.8	316	77	267.8	4.8	1.7	
08MP04_100.FIN2	183	0.86	0.4680	0.0140	0.0614	0.0013	0.22	389.1	9.7	383.9	7.9	387	70	383.9	7.9	1.3	
08MP04_101.FIN2	481	1.03	0.2802	0.0067	0.0388	0.0008	0.30	250.6	5.3	245.6	4.6	279	60	245.6	4.6	2.0	
08MP04_102.FIN2	116	1.68	0.4250	0.0270	0.0561	0.0018	0.47	359.0	19.0	352.0	11.0	410	120	352.0	11.0	1.9	# REF!
08MP04_104.FIN2	226	0.93	0.2903	0.0093	0.0412	0.0008	0.18	258.5	7.3	259.9	5.2	199	71	259.9	5.2	0.5	# REF!
08MP04_105.FIN2	102	2.17	1.7890	0.0700	0.1729	0.0056	0.28	1045.0	24.0	1027.0	31.0	1069	78	1069.0	78.0	3.9	
08MP04_106.FIN2	233	1.72	0.4990	0.0140	0.0639	0.0010	0.40	412.4	9.5	399.3	6.0	474	54	399.3	6.0	3.2	
08MP04_107.FIN2	393	3.88	0.4770	0.0130	0.0632	0.0012	0.70	395.5	9.1	395.0	7.4	415	45	395.0	7.4	0.1	
08MP04_108.FIN2	185	1.74	0.5950	0.0140	0.0758	0.0016	0.19	473.2	9.0	470.6	9.8	490	58	470.6	9.8	0.5	
08MP04_109.FIN2	317	2.75	2.8920	0.0570	0.2442	0.0044	0.57	1379.0	15.0	1408.0	23.0	1350	28	1350.0	28.0	4.3	
08MP04_110.FIN2	218	2.44	3.0730	0.0550	0.2474	0.0039	0.60	1425.0	14.0	1425.0	20.0	1445	28	1445.0	28.0	1.4	
08MP04_111.FIN2	138	1.06	0.8240	0.0310	0.0990	0.0031	0.56	609.0	17.0	609.0	18.0	621	75	609.0	18.0	0.0	
08MP04_112.FIN2	61	1.92	0.1100	0.0110	0.0153	0.0008	0.06	106.3	9.7	97.5	5.0	240	200	97.5	5.0	8.3	
08MP04_113.FIN2	525	1.94	0.4798	0.0099	0.0643	0.0013	0.53	397.5	6.8	401.8	7.9	409	41	401.8	7.9	1.1	
08MP04_114.FIN2	153	3.58	2.3220	0.0360	0.2142	0.0032	0.57	1218.0	11.0	1251.0	17.0	1160	32	1160.0	32.0	7.8	
08MP04_115.FIN2	225	0.84	0.4690	0.0120	0.0613	0.0013	0.32	390.0	8.3	383.3	8.2	417	60	383.3	8.2	1.7	
08MP04_116.FIN2	218	1.23	3.3280	0.0620	0.2671	0.0056	0.63	1486.0	15.0	1525.0	28.0	1427	34	1427.0	34.0	6.9	
08MP04_117.FIN2	293	1.27	0.4600	0.0110	0.0617	0.0011	0.16	385.0	7.4	386.2	6.6	408	60	386.2	6.6	0.3	
08MP04_118.FIN2	478	3.59	0.5700	0.0150	0.0731	0.0020	0.57	459.0	10.0	456.0	12.0	475	49	456.0	12.0	0.7	
08MP04_119.FIN2	241	2.78	1.6470	0.0450	0.1666	0.0036	0.76	987.0	17.0	993.0	20.0	971	52	971.0	52.0	2.3	Rim
08MP04_119.FIN2	43	1.97	1.9730	0.0980	0.1890	0.0120	0.58	1104.0	33.0	1117.0	66.0	1096	93	1096.0	93.0	1.9	Core
08MP04_120.FIN2	425	2.33	0.2343	0.0071	0.0335	0.0007	0.31	213.5	5.8	212.6	4.5	214	72	212.6	4.5	0.4	

Chicotepec Formation (sample: 30-CH01); coordinates: 21° 25.345'N, 98° 52.720'W

Lawton4-1.FIN2	83	1.04	0.1317	0.0070	0.0198	0.0005	0.01	125.3	6.3	126.6	3	130	110	126.6	3.0	1.0	
Lawton4-2.FIN2	37	1.44	0.1287	0.0085	0.0184	0.0005	0.15	121.9	7.6	117.4	3.1	190	120	117.4	3.1	3.7	
Lawton4-3.FIN2	182	1.34	0.0663	0.0034	0.0100	0.0002	0.08	65	3.2	63.8	1.1	125	97	63.8	1.1	1.8	
Lawton4-4.FIN2	184	1.26	0.1346	0.0041	0.0193	0.0002	0.06	128	3.6	123.2	1.5	219	69	123.2	1.5	3.8	
Lawton4-5.FIN2	162	0.95	0.0912	0.0039	0.0141	0.0003	0.39	88.9	3.8	90	1.9	94	78	90.0	1.9	1.2	
Lawton4-6.FIN2	61	1.18	2.0580	0.0430	0.1933	0.0031	0.29	1134	14	1139	17	1122	44	1122.0	44.0	1.5	
Lawton4-7.FIN2	306	1.39	0.1876	0.0051	0.0274	0.0005	0.60	174.2	4.3	174.2	3.1	174	51	174.2	3.1	0.0	
Lawton4-8.FIN2	306	2.30	0.2240	0.0046	0.0317	0.0005	0.45	205	3.8	201.4	3.3	249	43	201.4	3.3	1.8	
Lawton4-9.FIN2	134	1.22	0.0929	0.0055	0.0129	0.0004	0.18	89.9	5	82.5	2.2	290	120	82.5	2.2	8.2	
Lawton4-10.FIN2	102	1.24	0.0758	0.0044	0.0110	0.0002	0.09	73.9	4.1	70.4	1.4	180	120	70.4	1.4	4.7	
Lawton4-11.FIN2	43	1.68	0.0838	0.0088	0.0124	0.0005	0.13	81.2	8.2	79.2	3	180	210	79.2	3.0	2.5	
Lawton4-12.FIN2	204	1.91	0.1428	0.0050	0.0206	0.0004	0.22	135.2	4.4	131.2	2.8	214	74	131.2	2.8	3.0	
Lawton4-13.FIN2	305	1.30	0.0834	0.0045	0.0124	0.0004	0.33	81.2	4.2	79.1	2.7	180	110	79.1	2.7	2.6	
Lawton4-14.FIN2	183	1.15	2.2090	0.0300	0.2040	0.0024	0.55	1182.7	9.5	1196	13	1156	24	1156.0	24.0	3.5	
Lawton4-15.FIN2	173	1.03	0.0934	0.0052	0.0140	0.0002	0.13	90.5	4.9	89.7	1.5	110	110	89.7	1.5	0.9	
Lawton4-16.FIN2	187	3.70	1.9810	0.0280	0.1850	0.0028	0.58	1109.2	9.1	1093	15	1133	28	1133.0	28.0	3.5	
Lawton4-17.FIN2	165	1.17	0.1467	0.0047	0.0205	0.0002	0.20	138.8	4.1	130.7	1.5	246	64	130.7	1.5	5.8	
Lawton4-18.FIN2	292	0.83	0.5160	0.0110	0.0681	0.0013	0.48	422.4	7.6	424.5	7.6	403	46	424.5	7.6	0.5	
Lawton4-19.FIN2	147	1.59	0.1915	0.0060	0.0272	0.0004	0.16	178.1	5	172.9	2.6	228	66	172.9	2.6	2.9	
Lawton4-20.FIN2	376	1.45	0.8740	0.0160	0.1053	0.0019	0.48	637	8.8	645	11	610	38	645.0	11.0	1.3	
Lawton4-21.FIN2	687	1.06	2.3940	0.0390	0.2085	0.0036	0.61	1239	12	1220	19	1271	30	1271.0	30.0	4.0	
Lawton4-22.FIN2	518	32.00	0.6210	0.0480	0.0788	0.0048	0.33	489	30	489	29	480	180	489.0	29.0	0.0	Rim
Lawton4-22.FIN2	27	1.32	3.3950	0.0870	0.2599	0.0045	0.33	1498	20	1488	23	1498	50	1498.0	50.0	0.7	Core

Lawton4-23.FIN2	99	1.13	0.1379	0.0063	0.0197	0.0004	0.15	130.6	5.6	125.9	2.3	200	89	125.9	2.3	3.6
Lawton4-24.FIN2	336	0.84	0.2690	0.0046	0.0374	0.0004	0.29	241.7	3.7	236.6	2.5	275	40	236.6	2.5	2.1
Lawton4-25.FIN2	74	1.16	0.1029	0.0052	0.0157	0.0003	0.20	99.1	4.8	100.3	2.1	89	94	100.3	2.1	1.2
Lawton4-26.FIN2	79	0.79	0.0752	0.0054	0.0112	0.0003	0.14	73.3	5.1	72	1.6	120	130	72.0	1.6	1.8
Lawton4-27.FIN2	61	1.39	0.1143	0.0061	0.0174	0.0004	0.11	109.4	5.5	111.4	2.4	120	110	111.4	2.4	1.8
Lawton4-28.FIN2	256	1.43	0.0917	0.0035	0.0132	0.0002	0.23	88.9	3.2	84.5	1	180	71	84.5	1.0	4.9
Lawton4-29.FIN2	291	1.94	1.7460	0.0180	0.1731	0.0018	0.54	1025.7	6.9	1030.2	9.5	1010	20	1010.0	20.0	2.0
Lawton4-30.FIN2	131	1.77	0.6860	0.0130	0.0853	0.0011	0.34	529.1	7.8	527.3	6.7	537	43	527.3	6.7	0.3
Lawton4-31.FIN2	254	1.07	0.1031	0.0034	0.0150	0.0002	0.26	99.5	3.1	96.2	1.3	171	65	96.2	1.3	3.3
Lawton4-32.FIN2	88	1.20	2.1140	0.0480	0.1911	0.0046	0.58	1150	16	1126	25	1198	42	1198.0	42.0	6.0
Lawton4-33.FIN2	50	2.45	0.1295	0.0086	0.0184	0.0005	0.18	122.9	7.6	117.4	3.2	230	120	117.4	3.2	4.5
Lawton4-34.FIN2	54	1.67	0.1550	0.0120	0.0209	0.0006	0.13	146	11	133	3.8	320	150	133.0	3.8	8.9
Lawton4-35.FIN2	289	0.95	0.0666	0.0021	0.0102	0.0001	0.08	65.7	2	65.47	0.86	93	66	65.5	0.9	0.4
Lawton4-36.FIN2	127	0.98	3.2730	0.0340	0.2573	0.0023	0.42	1473.8	8	1476	12	1468	20	1468.0	20.0	0.5
Lawton4-37.FIN2	80	0.81	0.0660	0.0041	0.0103	0.0003	0.13	64.6	3.9	65.9	1.6	70	130	65.9	1.6	2.0
Lawton4-38.FIN2	300	1.52	0.0899	0.0027	0.0135	0.0002	0.23	87.4	2.5	86.7	1.1	117	61	86.7	1.1	0.8
Lawton4-39.FIN2	120	1.45	0.1023	0.0040	0.0152	0.0003	0.33	99.6	3.9	96.9	2	161	78	96.9	2.0	2.7
Lawton4-41.FIN2	297	1.57	0.1080	0.0030	0.0153	0.0002	0.23	104	2.8	98.1	1.3	248	61	98.1	1.3	5.7
Lawton4-42.FIN2	54	2.05	0.1270	0.0073	0.0184	0.0004	0.07	121.5	6.7	117.4	2.6	210	120	117.4	2.6	3.4
Lawton4-43.FIN2	67	1.29	0.1415	0.0066	0.0202	0.0004	0.31	133.8	5.8	128.6	2.5	225	91	128.6	2.5	3.9
Lawton4-44.FIN2	53	1.51	0.1272	0.0090	0.0184	0.0004	0.24	120.8	8.1	117.6	2.5	170	140	117.6	2.5	2.6
Lawton4-45.FIN2	348	2.00	0.0886	0.0058	0.0128	0.0005	0.41	86.1	5.5	81.9	2.9	200	130	81.9	2.9	4.9
Lawton4-45.FIN2	315	1.26	0.0904	0.0051	0.0132	0.0003	0.20	87.7	4.7	84.3	1.8	180	110	84.3	1.8	3.9
Lawton4-46.FIN2	277	1.01	0.1831	0.0048	0.0269	0.0006	0.39	170.5	4.1	170.7	3.8	179	53	170.7	3.8	0.1
Lawton4-47.FIN2	153	1.40	0.6430	0.0130	0.0800	0.0010	0.30	502.9	8	496.2	6.1	525	44	496.2	6.1	1.3
Lawton4-48.FIN2	210	1.14	0.0907	0.0032	0.0125	0.0002	0.20	88	3	80	1.1	307	77	80.0	1.1	9.1
Lawton4-49.FIN2	220	1.60	0.0907	0.0043	0.0131	0.0004	0.23	88	4	84	2.5	199	96	84.0	2.5	4.5
Lawton4-50.FIN2	97	1.46	0.0775	0.0045	0.0110	0.0003	0.16	75.5	4.2	70.5	1.9	240	120	70.5	1.9	6.6
Lawton4-51.FIN2	230	1.38	0.0873	0.0031	0.0133	0.0002	0.13	84.9	2.9	85	1.5	115	73	85.0	1.5	0.1
Lawton4-52.FIN2	301	1.82	0.0870	0.0045	0.0130	0.0006	0.53	84.5	4.2	83.4	3.6	125	92	83.4	3.6	1.3
Lawton4-53.FIN2	369	60.50	4.2560	0.0470	0.3034	0.0031	0.78	1685.9	8.8	1710	16	1655	14	1655.0	14.0	3.3
Lawton4-54.FIN2	162	0.52	5.3920	0.0800	0.3435	0.0040	0.92	1881	14	1903	19	1853	17	1853.0	17.0	2.7
Lawton4-55.FIN2	163	1.46	0.0664	0.0031	0.0101	0.0002	0.04	65.2	3	64.8	1	109	94	64.8	1.0	0.6
Lawton4-56.FIN2	100	1.43	0.1409	0.0061	0.0195	0.0004	0.19	133.4	5.4	124.3	2.3	276	88	124.3	2.3	6.8
Lawton4-57.FIN2	155	1.15	0.5130	0.0120	0.0675	0.0014	0.41	419.6	8.3	421	8.3	385	53	421.0	8.3	0.3
Lawton4-58.FIN2	1173	1.62	0.0749	0.0041	0.0104	0.0004	0.60	73.3	3.9	66.4	2.4	287	98	66.4	2.4	9.4
Lawton4-59.FIN2	598	1.45	0.0955	0.0026	0.0141	0.0002	0.35	92.5	2.4	90.1	1.5	144	55	90.1	1.5	2.6
Lawton4-60.FIN2	101	0.78	0.0774	0.0039	0.0117	0.0002	0.04	75.5	3.7	75.2	1.3	100	100	75.2	1.3	0.4
Lawton4-61.FIN2	95	1.56	1.6210	0.0430	0.1531	0.0029	0.48	981	16	918	16	1098	49	1098.0	49.0	16.4
Lawton4-62.FIN2	115	2.05	13.2700	0.1800	0.5195	0.0072	0.74	2696	13	2694	31	2693	18	2693.0	18.0	0.0
Lawton4-64.FIN2	167	1.60	0.0658	0.0028	0.0098	0.0002	0.09	64.6	2.7	62.6	1.1	152	89	62.6	1.1	3.1
Lawton4-65.FIN2	182	3.57	3.5200	0.1300	0.2596	0.0098	0.57	1531	30	1482	50	1597	62	1597.0	62.0	7.2
Lawton4-66.FIN2	227	0.57	0.8380	0.0170	0.0991	0.0019	0.49	616.8	9.2	609	11	636	43	609.0	11.0	1.3
Lawton4-67.FIN2	265	1.74	0.1448	0.0049	0.0204	0.0003	0.25	137	4.4	129.9	1.7	238	68	129.9	1.7	5.2
Lawton4-68.FIN2	225	1.45	0.0660	0.0027	0.0099	0.0002	0.30	65.1	2.7	63.49	0.99	116	78	63.5	1.0	2.5
Lawton4-69.FIN2	121	0.86	5.2110	0.0640	0.3261	0.0042	0.52	1857	12	1818	21	1892	23	1892.0	23.0	3.9
Lawton4-70.FIN2	225	2.18	0.6240	0.0270	0.0768	0.0034	0.44	492	17	477	20	557	93	477.0	20.0	3.0
Lawton4-70.FIN2	86	1.88	2.0750	0.0380	0.1883	0.0025	0.39	1140	12	1112	14	1184	35	1184.0	35.0	6.1
Lawton4-71.FIN2	120	0.85	0.0820	0.0045	0.0118	0.0002	0.01	79.8	4.2	75.6	1.5	190	110	75.6	1.5	5.3
Lawton4-72.FIN2	150	1.21	0.0676	0.0038	0.0100	0.0003	0.26	66.2	3.6	64.3	1.7	110	110	64.3	1.7	2.9
Lawton4-73.FIN2	381	2.93	4.3860	0.0660	0.3038	0.0044	0.70	1707	13	1709	22	1705	20	1705.0	20.0	0.2
Lawton4-74.FIN2	680	2.79	0.1786	0.0031	0.0253	0.0004	0.26	166.7	2.7	160.9	2.2	245	42	160.9	2.2	3.5
Lawton4-76.FIN2	135	1.84	0.0965	0.0042	0.0135	0.0002	0.24	93.3	3.9	86.4	1.5	249	85	86.4	1.5	7.4
Lawton4-77.FIN2	67	0.97	0.1415	0.0082	0.0214	0.0005	0.01	134	7.3	136.7	3.2	130	120	136.7	3.2	2.0
Lawton4-78.FIN2	314	1.00	0.1344	0.0045	0.0199	0.0003	0.36	127.9	4	127	1.9	142	63	127.0	1.9	0.7
Lawton4-79.FIN2	182	2.74	1.7210	0.0240	0.1702	0.0021	0.42	1014.9	8.8	1013	12	1007	27	1007.0	27.0	0.6
Lawton4-80.FIN2	239	48.50	0.6610	0.0160	0.0828	0.0014	0.46	515	9.7	512.6	8.1	508	49	512.6	8.1	0.5
Lawton4-81.FIN2	304	1.48	0.0977	0.0027	0.0144	0.0002	0.17	94.5	2.5	91.8	1.1	163	55	91.8	1.1	2.9
Lawton4-82.FIN2	539	1.06	0.0688	0.0018	0.0104	0.0002	0.24	67.5	1.7	66.6	1.1	121	56	66.6	1.1	1.3
Lawton4-83.FIN2	426	1.63	0.0726	0.0030	0.0106	0.0002	0.12	71.1	2.9	68.2	1.1	169	88	68.2	1.1	4.1
Lawton4-84.FIN2	305	1.51	0.0846	0.0028	0.0123	0.0003	0.18	82.4	2.6	78.7	1.7	209	77	78.7	1.7	4.5
Lawton4-85.FIN2	394	2.00	0.0896	0.0028	0.0133	0.0003	0.39	87	2.6	85.6	1.7	133	60	85.6	1.7	1.6
Lawton4-86.FIN2	334	1.39	0.1763	0.0037	0.0255	0.0003	0.43	164.7	3.2	162.4	1.7	195	41	162.4	1.7	1.4
Lawton4-87.FIN2	238	2.16	0.1818	0.0049	0.0254	0.0003	0.12	169.4	4.2	161.9	2	274	61	161.9	2.0	4.4
Lawton4-88.FIN2	104	1.01	2.1600	0.0300	0.1984	0.0027	0.55	1167.7	9.5	1166	15	1170	26	1170.0	26.0	0.3
Lawton4-89.FIN2	329	0.61	0.0605	0.0024	0.0095	0.0002	0.06	59.5	2.3	61.1	1	54	82	61.1	1.0	2.7
Lawton4-90.FIN2	294	1.60	0.0824	0.0025	0.0125	0.0003	0.26	80.3	2.4	80	1.7	126	68	80.0	1.7	0.4
Lawton4-91.FIN2	458	2.58	0.1776	0.0035	0.0262	0.0004	0.14	165.9	3	166.9	2.2	157	46	166.9	2.2	0.6
Lawton4-92.FIN2	341	1.57	0.0882	0.0027	0.0134	0.0002	0.19	86	2.6	86	1.3	83	62	86.0	1.3	0.0
Lawton4-93.FIN2	293	1.22	0.0762	0.0024	0.0113	0.0002	0.08	74.5	2.3	72.15	0.94	159	68	72.2	0.9	3.2
Lawton4-94.FIN2	193	0.69	0.1412	0.0043	0.0206	0.0002	0.15	133.8	3.9	131.3	1.5	178	64	131.3	1.5	1.9
Lawton4-95.FIN2	106	1.09	0.1190	0.0059	0.0173	0.0005	0.10	113.9	5.3	110.6	3	220	110	110.6	3.0	2.9

Rim
CoreRim
Core

Lawton4-96.FIN2	83	0.92	0.1352	0.0073	0.0194	0.0004	0.08	128.3	6.5	123.6	2.5	200	110	123.6	2.5	3.7
Lawton4-97.FIN2	103	1.73	0.1044	0.0048	0.0147	0.0004	0.18	100.5	4.4	94.3	2.6	240	98	94.3	2.6	6.2
Lawton4-98.FIN2	420	1.87	0.3821	0.0070	0.0482	0.0006	0.23	328.9	5.3	303.2	3.7	498	47	303.2	3.7	7.8
Lawton4-99.FIN2	502	1.21	0.1002	0.0030	0.0150	0.0002	0.13	96.9	2.8	95.7	1.2	123	63	95.7	1.2	1.2
Lawton4-100.FIN2	308	4.70	0.1713	0.0041	0.0245	0.0004	0.06	160.3	3.6	156	2.5	218	53	156.0	2.5	2.7
Lawton4-101.FIN2	179	1.44	0.1286	0.0044	0.0179	0.0004	0.12	122.6	3.9	114.4	2.7	266	68	114.4	2.7	6.7
Lawton4-102.FIN2	138	1.35	0.1673	0.0071	0.0237	0.0005	0.39	156.4	6.2	150.7	3.4	223	82	150.7	3.4	3.6
Lawton4-103.FIN2	60	0.65	0.6790	0.0200	0.0792	0.0015	0.23	524	12	490.9	9.1	644	66	490.9	9.1	6.3
Lawton4-104.FIN2	225	7.10	1.1610	0.0150	0.1272	0.0015	0.43	782.7	6.8	771.5	8.5	794	28	771.5	8.5	1.4
Lawton4-105.FIN2	162	1.41	0.2743	0.0066	0.0391	0.0005	0.21	245.7	5.2	247.2	3.2	212	52	247.2	3.2	0.6
Lawton4-106.FIN2	131	1.87	2.2750	0.0360	0.2032	0.0027	0.67	1203	11	1192	15	1205	24	1205.0	24.0	1.1
Lawton4-107.FIN2	95	1.14	0.1493	0.0066	0.0205	0.0004	0.20	140.8	5.9	130.5	2.6	286	91	130.5	2.6	7.3
Lawton4-108.FIN2	115	1.51	0.1066	0.0044	0.0158	0.0002	0.12	102.6	4.1	100.9	1.4	131	80	100.9	1.4	1.7
Lawton4-109.FIN2	93	1.36	0.1002	0.0047	0.0149	0.0003	0.12	96.7	4.3	95.5	1.9	139	95	95.5	1.9	1.2
Lawton4-110.FIN2	104	2.01	0.0808	0.0043	0.0113	0.0002	0.12	78.6	4	72.6	1.3	230	110	72.6	1.3	7.6
Lawton4-111.FIN2	396	0.73	0.0663	0.0023	0.0100	0.0001	0.21	65.1	2.2	64.05	0.91	98	65	64.1	0.9	1.6
Lawton4-112.FIN2	145	1.29	0.0718	0.0041	0.0102	0.0003	0.20	70.2	3.9	65.7	1.6	200	110	65.7	1.6	6.4
Lawton4-113.FIN2	298	0.75	0.3013	0.0059	0.0408	0.0004	0.25	267.6	4.7	257.4	2.7	323	42	257.4	2.7	3.8
Lawton4-114.FIN2	294	1.10	0.1463	0.0034	0.0215	0.0003	0.27	138.5	3	136.9	1.7	162	50	136.9	1.7	1.2
Lawton4-115.FIN2	196	1.08	0.0659	0.0027	0.0099	0.0002	0.11	64.7	2.5	63.7	1	95	80	63.7	1.0	1.5
Lawton4-116.FIN2	31	1.47	0.2180	0.0160	0.0311	0.0008	0.20	198	13	197.3	5.2	190	130	197.3	5.2	0.4
Lawton4-117.FIN2	183	0.99	0.0663	0.0036	0.0098	0.0002	0.01	65.5	3.5	62.8	1.1	150	110	62.8	1.1	4.1
Lawton4-118.FIN2	72	2.05	1.5550	0.0330	0.1533	0.0022	0.49	951	13	919	13	997	40	997.0	40.0	7.8
Lawton4-119.FIN2	621	3.36	0.0831	0.0017	0.0126	0.0001	0.36	81	1.6	80.69	0.69	84	40	80.7	0.7	0.4
Lawton4-120.FIN2	255	0.75	0.1957	0.0045	0.0281	0.0004	0.20	181.2	3.8	178.8	2.2	194	49	178.8	2.2	1.3
Lawton4-121.FIN2	93	0.87	0.6980	0.0150	0.0859	0.0011	0.32	536.8	9.2	530.9	6.3	547	48	530.9	6.3	1.1
Lawton4-123.FIN2	107	0.51	0.5780	0.0140	0.0724	0.0011	0.39	462.9	8.5	451.4	6.2	516	49	451.4	6.2	2.5
Lawton4-124.FIN2	331	4.52	2.2920	0.0360	0.2068	0.0022	0.61	1208	11	1211	12	1191	25	1191.0	25.0	1.7
Lawton4-125.FIN2	143	0.94	0.1347	0.0044	0.0198	0.0003	0.16	128.1	3.9	126	1.6	180	71	126.0	1.6	1.6
Lawton4-126.FIN2	108	1.86	0.1386	0.0075	0.0196	0.0005	0.02	131.4	6.6	125.1	3.1	240	120	125.1	3.1	4.8
Lawton4-127.FIN2	120	1.40	0.0766	0.0037	0.0115	0.0003	0.10	74.8	3.5	73.4	1.6	121	92	73.4	1.6	1.9
Lawton4-128.FIN2	379	4.06	0.0888	0.0037	0.0132	0.0003	0.32	86.3	3.4	84.2	1.8	139	82	84.2	1.8	2.4
Lawton4-129.FIN2	681	1.59	0.0691	0.0016	0.0103	0.0001	0.23	67.8	1.5	65.91	0.7	126	45	65.9	0.7	2.8
Lawton4-130.FIN2	123	1.19	0.1294	0.0048	0.0195	0.0003	0.10	123.2	4.3	124.7	1.9	121	76	124.7	1.9	1.2
Lawton4-131.FIN2	109	1.14	0.0635	0.0033	0.0097	0.0002	0.08	62.7	3.2	62.2	1.1	90	98	62.2	1.1	0.8
Lawton4-132.FIN2	60	1.11	0.1395	0.0067	0.0200	0.0004	0.18	132.8	6.2	127.4	2.3	218	96	127.4	2.3	4.1
Lawton4-133.FIN2	197	1.09	0.0867	0.0028	0.0132	0.0002	0.12	84.3	2.6	84.8	1.2	84	64	84.8	1.2	0.6
Lawton4-134.FIN2	143	1.22	0.1252	0.0053	0.0186	0.0004	0.07	119.4	4.7	118.6	2.3	121	94	118.6	2.3	0.7
Lawton4-135.FIN2	125	1.05	0.1017	0.0038	0.0154	0.0002	0.20	99	3.5	98.6	1.5	108	74	98.6	1.5	0.4
Lawton4-136.FIN2	186	1.43	2.3730	0.0280	0.2102	0.0023	0.52	1233.4	8.4	1230	12	1234	22	1234.0	22.0	0.3
Lawton4-138.FIN2	77	1.55	1.5970	0.0270	0.1593	0.0021	0.23	967	10	953	12	999	35	999.0	35.0	4.6
Lawton4-139.FIN2	38	1.13	1.7050	0.0370	0.1657	0.0020	0.20	1008	14	988	11	1040	46	1040.0	46.0	5.0
Lawton4-140.FIN2	77	1.29	1.6690	0.0290	0.1656	0.0019	0.46	995	11	988	11	1011	32	1011.0	32.0	2.3

#REF!

Notes:

Instructions**Best Age Tab****Purpose: Filter out discordant grains, pick a "best age" and will identify rims****Steps**

1 Copy and paste the following columns from lolite "__integrations.xls" sheet into the orange filled cells:

Source file, DateTime, Duration(s), FinalAge206_238,* FinalAge206_238_Int2SE, FinalAge207_235, *FinalAge207_235_Int2SE, FinalAge207_206, *FinalAge207_206_Int2SE

*Be sure to note in the text of your publication if you are using internal or propogated error (if propogated than use Final AgeXXX_XXX_Prop2SE)

Description of Columns

J	% Discordance between 206/238 and 207/206 age
K	% Error for 206/238 age
L	% Discordance between 206/238 and 207/235
M	Picks the 7/6 age if older than *850 Ma, picks the 6/38 age if younger (*modify this number to use a natural gap in your data between 800-1200 Ma)
N	Filters >10% discordant 7/6 ages
O	Filters 6/38 ages with >10% error
P	Filters >10% discordant 6/38 ages
Q	Repopulates grain name
R	Reports the Best Age in Ma
S	Reports the 2 sigma error (if the age is 6/38 than the error is for 6/38, if 7/6 than error for 7/6)
T	% Discordance (*be sure to note in your publication that the discordance reported is 6/38 vs 7/6 if older than 850 Ma and 6/38 vs 7/35 if younger than 850 Ma)
U	Rim or Core or Single Age from grain
V	Notes if the duration of the integration is less than 4 seconds and then calls it "short"

Publication Tab

Steps

- 1 Copy and paste the following columns from lolite " __integrations.xls" sheet into columns A through N:
Source file (Grain #), Approx U ppm, Final_U_Th_Ratio (U/Th), Final207_235 (207/235), Final207_235_Int2SE, Final206_238 (206/238), Final206_238_Int2SE, ErrorCorrelation_6_38vs7_35 (RHO), FinalAge206_238, FinalAge206_238_Int2SE, FinalAge207_235, FinalAge207_235_Int2SE, FinalAge207_206, FinalAge207_206_Int2SE
- 2 Copy and Paste **Values** of "Best Age", "2 sig error" and "% Discordance" from Best Age tab into columns O, P, and Q
- 3 Decide whether DISC grains should be deleted
- 4 In Column A (Grain #). Select all names (not top 2 rows) go to >edit >replace. Find what- .FIN2, Replace with- leave blank. Press Replace All
- 5 Plot your data onto a Concordia Diagram
 - 1 Select all data in rows D through H (Make sure all RHO values are positive or you will get error message. If there are negative values, replace the value with 0)
 - 2 Open Isoplot (Ctrl-I on PC)
 - 3 Boxes to select: Isochron or plot type- U-Pb Concordia, normal; Input errors- 2 sigma, absolute; Symbols- error ellipse, red, not filled
Action- plot, (only calculate if single age or standard); Other-Color, Autoscaled
Hit OK
 - 5 Plot as a line

Apéndice 4

Fechas dobles (U-Th)/(He-Pb) de tres muestras del Cretácico Tardío expuestas en el transecto Tolimán-Tamazunchale.

Late Cretaceous-Paleocene stratigraphic and structural evolution of the central Mexican fold and thrust belt, from detrital zircon (U-Th)/(He-Pb) ages

Table DR2. (U-Th)/He thermochronologic data of Tolimán-Tamazunchale transect, central Mexican fault-thrust belt.

Sample	mineral	Age, Ma	err., Ma	U (ppm)	Th (ppm)	147Sm (ppm)	[U]e	Th/U	He (nmol/g)	mass (ug)	Ft	ESR	U/Pb age	U/Pb age +/-
<i>Mineral de Pozos Fm (06-MP02)</i>														
z06MP02-74	zircon	45.5	3.6	32.9	62.4	4.0	47.3	1.90	8.6	3.61	0.74	45.73	1104.0	78.0
z06MP02-107	zircon	57.9	4.6	299.1	455.9	7.5	404.1	1.52	93.0	3.42	0.73	44.29	1638.0	20.0
z06MP02-120	zircon	58.2	4.7	57.1	34.1	1.9	65.0	0.60	15.3	3.62	0.74	45.60	1632.0	29.0
z06MP02-27	zircon	59.3	4.7	116.5	116.2	3.4	143.2	1.00	29.3	1.24	0.64	31.18	256.4	3.9
z06MP02-28	zircon	61.4	4.9	45.9	37.9	1.1	54.6	0.83	12.9	2.36	0.71	39.75	1045.0	36.0
z06MP02-7	zircon	62.9	5.0	60.5	24.0	2.0	66.0	0.40	15.4	1.71	0.68	35.78	412.0	13.0
z06MP02-30	zircon	66.2	5.3	230.7	186.4	5.7	273.6	0.81	65.8	1.63	0.67	34.58	1403.0	24.0
z06MP02-21	zircon	88.0	7.0	121.6	42.6	9.2	131.4	0.35	44.0	2.14	0.70	38.00	579.0	11.0
z06MP02-119	zircon	89.6	7.2	64.9	34.7	3.6	72.9	0.53	26.5	3.80	0.75	46.23	1153.0	36.0
z06MP02-113	zircon	114.9	9.2	116.7	71.1	5.2	133.1	0.61	57.3	2.14	0.69	36.80	600.1	8.7
z06MP02-67	zircon	128.7	10.3	208.3	144.2	4.2	241.5	0.69	112.1	1.64	0.66	33.68	1448.0	21.0
<i>Soyatal Formation (16-CA08)</i>														
z16CA08-115	zircon	46.1	3.7	151.4	113.2	0.9	177.4	0.75	27.1	1.02	0.61	28.80	455.0	10.0
z16CA08-64	zircon	75.0	6.0	71.0	34.7	3.5	79.0	0.49	22.3	2.13	0.69	37.36	461.3	6.7
z16CA08-109	zircon	79.9	6.4	305.2	61.8	-4.8	319.4	0.20	85.9	0.96	0.62	28.71	1147.0	19.0
z16CA08-71	zircon	79.9	6.4	40.3	53.1	1.7	52.5	1.32	15.2	1.66	0.66	34.64	456.8	5.5
z16CA08-55	zircon	84.7	6.8	238.7	81.7	4.1	257.5	0.34	75.8	1.13	0.64	30.85	984.0	22.0
z16CA08-77	zircon	84.7	6.8	152.6	74.8	10.2	169.9	0.49	48.3	0.99	0.62	29.00	578.2	7.5
z16CA08-82	zircon	85.4	6.8	122.0	114.4	0.0	148.3	0.94	41.4	0.88	0.60	28.10	396.0	12.0
z16CA08-30	zircon	90.6	7.3	30.6	35.5	3.1	38.8	1.16	12.6	1.51	0.66	33.67	632.6	8.0
z16CA08-105	zircon	90.7	7.3	147.7	61.8	3.4	161.9	0.42	50.1	1.09	0.63	29.77	965.0	23.0
z16CA08-68	zircon	90.8	7.3	81.3	70.5	8.9	97.6	0.87	30.7	1.34	0.64	31.23	983.0	22.0
z16CA08-84	zircon	90.9	7.3	294.5	66.4	3.5	309.9	0.23	100.1	1.31	0.66	32.05	1014.0	35.0
z16CA08-44	zircon	96.1	7.7	217.5	128.1	3.4	247.0	0.59	84.7	1.61	0.66	32.96	402.8	7.5
z16CA08-69	zircon	106.5	8.5	72.7	32.1	2.5	80.1	0.44	32.0	2.17	0.69	36.75	535.0	11.0
z16CA08-8	zircon	170.6	13.7	35.2	24.2	2.4	40.8	0.69	22.6	0.77	0.60	27.44	985.0	77.0
z16CA08-91	zircon	180.4	14.4	75.4	41.0	3.3	84.9	0.54	52.5	1.12	0.63	29.95	390.2	4.2
<i>San Felipe Formation (04-JC01)</i>														
z04JC01-56	zircon	56.2	18.1	20.3	13.8	1.5	23.4	0.68	19.8	1.88	0.68	36.19	73.2	1.4
z04JC01-59	zircon	57.6	11.0	90.4	38.3	3.1	99.2	0.42	50.7	1.81	0.68	35.76	75.0	1.3
z04JC01-26	zircon	60.3	9.6	61.4	55.4	3.0	74.2	0.90	34.1	2.74	0.70	38.99	76.5	2.4
z04JC01-34	zircon	67.5	5.4	26.2	25.3	1.2	32.0	0.96	7.8	1.53	0.67	34.52	462.4	9.7
z04JC01-49	zircon	75.3	6.0	37.6	35.5	3.3	45.8	0.94	11.7	1.10	0.63	30.18	109.7	2.6
z04JC01-82	zircon	86.2	6.9	60.8	64.2	3.4	75.5	1.06	23.5	1.64	0.66	34.15	81.5	1.6
z04JC01-96	zircon	86.8	6.9	92.4	58.4	4.7	105.9	0.63	29.5	0.78	0.59	26.96	572.7	8.8
z04JC01-102	zircon	92.8	7.4	36.7	45.6	2.2	47.2	1.24	14.3	0.83	0.60	28.02	171.7	2.9
z04JC01-85	zircon	98.6	7.9	15.6	12.9	1.6	18.6	0.83	7.1	2.81	0.71	40.80	107.6	3.2
z04JC01-99	zircon	120.4	9.6	73.9	71.0	4.9	90.3	0.96	37.9	1.31	0.64	31.53	446.0	11.0
z04JC01-33	zircon	123.7	9.9	50.7	42.5	1.0	60.5	0.84	25.2	0.96	0.62	29.56	2587.0	19.0
z04JC01-79	zircon	127.8	10.2	66.2	36.3	2.7	74.5	0.55	37.4	2.74	0.72	41.49	1318.0	26.0
z04JC01-35	zircon	128.0	10.2	71.9	42.8	3.2	81.7	0.60	36.7	1.43	0.65	31.73	173.1	3.6
z04JC01-2	zircon	135.2	10.8	86.3	84.0	3.7	105.7	0.97	49.8	1.23	0.64	31.56	944.0	24.0
z04JC01-39	zircon	135.8	10.9	25.9	23.0	1.5	31.2	0.89	15.7	1.83	0.68	35.90	1013.0	40.0

z04JC01-30	zircon	159.0	12.7	110.6	71.8	9.3	127.2	0.65	72.2	1.38	0.65	32.72	1279.0	34.0
z04JC01-5	zircon	271.4	21.7	57.4	46.6	2.1	68.2	0.81	61.9	0.88	0.61	28.66	1567.0	21.0

Apéndice 5

Modas detríticas normalizadas para las areniscas de la cuenca de antepaís mexicana

TABLA 1.—*Modas detríticas normalizadas para las areniscas de la cuenca de antepaís mexicana (CAM)*

Muestra	Unidad	QtFL%			LmLvLs%		
		Qt	F	L	Lm	Lv	Ls
Cuenca Tampico-Misantla, E de México							
30-CH01 ⁵	Formación Chicontepec	24	23	54	0	19	81
Grupo Difunta, cuenca de Parras, NE de México							
05DEL08 ¹	Formación Las Imágenes	49	17	35	0	12	88
05FAU01 ¹	Formación Cañón del Tule	55	20	26	1	10	28
05FAU02 ¹	Formación Cañón del Tule	56	20	24	1	6	92
05FAU03 ¹	Formación Cañón del Tule	51	20	29	2	5	93
05FAU04 ¹	Formación Las Imágenes	56	18	26	0	7	93
BT83.5 ¹	N/A	64	4	32	6	17	78
NANL0 ¹	Formación Las Encinas	72	3	25	8	69	24
LH14.5 ¹	Formación Las Encinas	74	5	20	0	61	39
SANL155 ¹	Formación Las Encinas	75	2	23	5	52	43
LH21.8 ¹	Formación Rancho Nuevo	77	4	19	10	63	27
RR147 ¹	Formación Rancho Nuevo	57	3	41	2	33	65
YF10.47 ¹	Formación Rancho Nuevo	63	3	35	5	35	60
LH103.3 ¹	Formación Rancho Nuevo	56	2	42	3	40	57
X		62	9	29	3	32	61
SD		10	8	7	3	24	27
Grupo Difunta, cuenca de La Popa NE México							
06ECT02 ¹	Formación Potrerillos	51	22	27	1	16	83
06ECT04 ¹	Formación Potrerillos	53	20	27	4	25	72
06ECT06 ¹	Formación Potrerillos	55	20	25	0	25	76
06ECT07 ¹	Formación Potrerillos	51	15	35	0	16	84
06ECT09 ¹	Formación Potrerillos	53	23	24	4	21	75
06ECT11 ¹	Formación Potrerillos	53	20	27	4	28	69
06ECM01 ¹	Formación Potrerillos	50	16	34	2	19	79
06ECM02 ¹	Formación Potrerillos	53	17	30	4	17	78
06TWD02 ¹	Formación Potrerillos	53	19	28	1	20	78
06TWD04 ¹	Formación Potrerillos	48	17	36	0	17	83
X		52	19	29	2	20	78
SD		2	3	4	2	4	5
Areniscas del sector transversal de Parras y centro de México							
04-JC01 ⁵	Formación San Felipe	19	21	60	2	29	70
05-JC02 ⁵	Formación San Felipe	8	7	84	0	1	99
07COA-CA3 ⁴	Formación Caracol	4	45	51	0	100	0
X		10	24	65	1	43	56
SD		8	19	17	1	51	51
Areniscas de la Mesa Central y centro de México							
MP-01 ²	arenisca Mineral de Pozos	58	33	9	0	82	18
MP-06 ²	arenisca Mineral de Pozos	34	40	26	4	56	40
06-MP02 ⁵	arenisca Mineral de Pozos	53	22	25	11	78	11
07-MP03 ⁵	arenisca Mineral de Pozos	42	23	35	19	52	29
08-MP04 ⁵	arenisca Mineral de Pozos	49	39	12	23	71	6

CARN-28 ⁴	turbiditas no diferenciadas	44	11	45	35	48	17
13-26IV14 ⁴	turbiditas no diferenciadas	47	30	22	13	75	12
26-PST01 ⁴	turbiditas no diferenciadas	24	9	67	4	31	65
25-MB02 ⁴	turbiditas no diferenciadas	46	33	20	14	51	35
X		44	27	29	14	60	26
SD		21	8	19	8	16	18

Areniscas del área de Concepción del Oro, sector transversal de Parras

Petrofacies A (n=35) Fm Concepción del Oro							
X ³		44	16	40	6	41	53
SD ³		8	3	8	1	13	14
Petrofacies B (n= 21) Fm Concepción del Oro							
X ³		35	14	51	7	49	44
SD ³		4	2	4	1	6	6

Notas: Qt, cuarzo total = Qm, cuarzo monocristalino + Qp, cuarzo policristalino; los granos de pedernal (Qp) se incluyen en esta categoría.

F, feldespato total = K, feldespato potásico + P, plagioclasa.

L = fragmentos líticos microcristalinos

Lt (fragmentos líticos totales) = L + Qp.

Lm = fragmentos líticos metamórficos; Ls = fragmentos líticos sedimentarios; Lv = fragmentos líticos volcánicos.

n = número de muestras analizadas

Notas de superíndice

1. Lawton et al. (2009)
2. Ortega-Flores et al. (2014)
3. Ocampo-Díaz et al. (2016)
4. Juárez-Arriaga et al. (2019a)
5. Juárez-Arriaga et al. (2019b)